Universidade Nova de Lisboa

&

Universidad de Zaragoza

CANCER THERANOSTICS:

MULTIFUNCTIONAL GOLD NANOPARTICLES FOR DIAGNOSTICS AND THERAPY

João Diogo Osório de Castro Conde

Doctorate in Biology

Specialty in Biotechnology

Lisbon 2013

CANCER THERANOSTICS:

MULTIFUNCTIONAL GOLD NANOPARTICLES FOR DIAGNOSTICS AND THERAPY

João Diogo Osório de Castro Conde

Thesis supervised by

Prof. Pedro V. Baptista

Prof. Jesus M. de la Fuente

Doctorate in Biology

Specialty in Biotechnology

COPYRIGHT

Para as minhas princesas,

Catarina e Ritinha

Todo o meu Amor!

TABLE OF CONTENTS

ACKNOWLEDGEMENTS

"Fortune favours the audacious" – *Desiderius Erasmus*

This project has required the input from many people to acquire some of the "amazing" results we could achieved. Although the following words will never be enough to express all my appreciation to them, I would like here to present my admiration for all their support during this long passage. Hence, I would like to thanks:

My supervisor, **Professor Pedro V. Baptista** for giving me the opportunity to be a member of his working group. I would like to thanks for his never ending, dedicated and thoughtful scientific and personal input during my work. I owe him immensely. For his help, guidance, proof reading and scientific contributions with all publications, oral presentations and of course this doctoral thesis.

My co-supervisor, **Professor Jesus M. de la Fuente**, I am especially thankful for his guidance and magnanimity that allowed me to work independently. I would like to thanks for his support. I always enjoyed his commitment to achieve and foster a great working experience at his chair.

Professor João C. Lima for the numerous enthusiastic and successful scientific discussions. You are a great scientist. I want to be like you, someday!

Vanesa Sanz for all the things that I learned from you... and all the funny moments in the lab.

My Thesis Committee members, **Prof. Jorge Gaspar** (Faculdade de Ciências Médicas) and **Prof. Ricardo Franco** (REQUIMTE) for taking some time in evaluating my progress.

I would like to thanks **Fundação para a Ciência e Tecnologia**, for the financial support (SFRH/BD/62957/2009) provided to conduct this thesis and for the projects where I participate: Sensitive and selective detection of DNA/RNA based on functionalised gold nanoparticles - application to pathogen detection; mutation detection and RNA quantification - PTDC/BIO/66514/2006 ; NANOLIGHT - Nanosystems for delivery of caged compounds -

PTDC/QUI-QUI/112597/2009; and Silence is golden (siAu) - Silencing the silencers via multifunctional gold nanoconjugates towards cancer therapy - PTDC/BBB-NAN/1812/2012.

The members of the **lab 315** for the great time in the lab. I believe I have every reason to convey my appreciation to all of you for the cooperation I have received from each and every one of you individually.

A special thanks to a colleague and friend, **Leticia Giestas**. I will always remember the talks on our joys and sorrows about the lab. Your support and judgment always kept me "in line". Thank you for everything.

A todos os meus **Amigos** por estarem sempre lá…. Porque sempre me guiaram, porque sempre me apoiaram, porque sempre me fizeram sorrir…

Um agradecimento muito especial aos meus **Pais**, porque sempre acreditaram que seria possível… porque sempre acreditaram em mim. Pelo apoio incondicional nos melhores e nos piores momentos, especialmente quando achamos que não somos capazes. Muito obrigado. Sem vocês nada teria sido possível.

Por ultimo, não tenho palavras para descrever a gratidão e orgulho que tenho pela minha mulher, **Catarina**. Muito obrigado por todo o amor e carinho. Por todo o apoio e compreensão mesmo quando roubava um pouco do nosso tempo. Obrigado por fazeres de mim um homem melhor… uma pessoa melhor. E um obrigado do tamanho do mundo à nossa princesinha linda, **Ritinha**, que veio unir-nos ainda mais. Amo-vos muito….

Preface

This Thesis compiles the work done during my doctoral studies that I started after invitation by Prof. Pedro V. Baptista for a PhD position at the Research Centre for Human Molecular Genetics, Dept. of Life Sciences at Science and Technology Faculty, New University of Lisbon. In 2010, I was awarded with a PhD Grant funded by the Portuguese Foundation for Science and Technology under the topic "Cancer Theranostics − Multifunctional gold nanoparticles for diagnostics and therapy" (part of the European project NanoScieE+ - NANOTRUCK). Prof. Pedro V. Baptista is an Associate Professor of Molecular Genetics & Nanomedicine at Dept. of Life Sciences, Science and Technology Faculty, New University of Lisbon.

From June 2010 to March 2011, the fellow carried out a part of the PhD Project at the Biofunctional Nanoparticles and Surfaces Group, IUI of Nanoscience of Aragon (INA), Zaragoza, Spain, under supervision of Prof. J.M. de la Fuente. Prof. J.M. de la Fuente established a multidisciplinary Nanotherapy and Nanodiagnostics Group at IUI of Nanoscience of Aragon, University of Zaragoza (Spain) after receiving an ERC Starting Grant.

The NANOTRUCK project intends to develop an innovative kind of multifunctional gold nanoparticles loaded with fluorescent, tumoral markers, cell penetrating peptides and RNAi complementary to the proto-oncogene *c-Myc* for cancer diagnosis and treatment. The fellow worked on the synthesis and functionalization of the multifunctional gold nanoparticles and on the in vitro studies for the silencing of *c-Myc* gene in human cells. From this work, he has broadened his experience in techniques in the molecular genetics field such as the cloning of constructs for applications in gene therapy and techniques related with the small interfering RNA approach for gene silencing. This project implies the collaboration with different groups in Europe with expertise in different subfields: Centre for Cell Engineering (University of Glasgow, UK), Instituto di Cibernetica "E. Caianiello" (Pozzuoli, Italy), Helmholtz Zentrum München (München, Germany), Science and Technology Faculty, New University of Lisbon (Lisbon, Portugal) and IUI of Nanoscience of Aragon at the University of Zaragoza (Zaragoza, Spain). Thanks to these collaborations, the interaction between nanoparticles and biological systems, ranging from in vitro cultured human cells to in vivo animal models (primitive Hydra and complex vertebrate mouse) were studied. From this work, the fellow acquired experience in the diagnostics and therapy fields, as can be seen from his publications on the development of nanosystems for the combined diagnostics/therapeutics (theranostics)

involving DNA/RNA detection with strong impact in genetic diagnostics and for gene delivery and silencing systems of relevance for therapy strategies, with particular focus on enabling the development of safer, more efficient, and specific platforms to human disease.
During the PhD the fellow has acquired experience in molecular biology techniques useful for the biomedical applications of nanoparticles (Human Cell culture, Microbiology, Confocal Microscopy, Electrophoresis, Real-Time PCR, etc), and skills useful in the development of applications of nanoparticles in gene therapy (plasmid DNA cloning, Antisense and RNA interference methodologies, work with reporter vectors such as EGFP and luciferase gene expression) and different techniques for nanoparticle characterization (Atomic Force Microscopy, Scanning Electron Microscopy, Transmission Electron Microscopy, Light-Scattering microscopy, Fluorescence, UV-VIS molecular absorption, etc). With a strong background in nanodiagnostics, nanotherapy and nanotoxicology fields, as can be seen from publications on the development of nanosystems (with ssDNA/ssRNA, siRNA, antibodies, peptides, tumoral markers, polymers and fluorescent dyes) for the combined diagnostics/therapeutics (theranostics) systems. These platforms involves DNA/RNA detection with strong impact in genetic diagnostics and in gene delivery/silencing and tumour targeting systems, with particular focus on enabling the development of safer, more efficient, and specific methods to human disease.

Overall, my doctoral studies have resulted in the following **peer-reviewed publications** with more than **200 citations**:

1. "Gold Nanoparticle-mediated oncogene knockdown in human cancer cells: From cell proliferation to cell-cycle and apoptosis." H.W. Child, Y. Hernandez, **João Conde**, P.V. Baptista, J.M. de la Fuente, C.C. Berry. (Submitted)

2. "Multifunctional Gold Nanocarriers for Cancer Theranostics – From bench to bedside and back again?" **João Conde***, F. Tian, P.V. Baptista and J.M. de la Fuente (Accepted, Invited Book Chapter) (*** Corresponding-author**).

3. "*In vivo* tumour targeting via nanoparticle-mediated therapeutic siRNA coupled to inflammatory response in lung cancer mouse models." **João Conde***, F. Tian*, Y. Hernández, C. Bao, D. Cui, K.P. Janssene, M.R. Ibarra, P.V. Baptista, T. Stoëger and J.M. de la Fuente. (* Co-first authors). **Biomaterials** (2013), Vol. 34, pp. 7744–7753. *Research article (IF=7.604)*

4. "A Gold-nanobeacon system for Gene therapy: evaluation of Genotoxicity, Cell toxicity and Proteome profiling analysis" **João Conde**, M. Larguinho, A. Cordeiro, L.R. Raposo, P.M. Costa, S. Santos, M.S. Diniz, A.R. Fernandes and P.V. Baptista. **Nanotoxicology** (2013). *Research article (IF=7.844)*

5. "Gold-nanobeacons for simultaneous gene specific silencing and intracellular tracking of the silencing events." **João Conde**, J. Rosa, J.M. de la Fuente and P.V. Baptista. **Biomaterials** (2013), Vol. 34, pp. 2516–2523. *Research article (IF=7.604)*

6. "Design of Multifunctional Gold Nanoparticles for In vitro and In vivo Gene Silencing." **João Conde***, A. Ambrosone*, V. Sanz, Y. Hernández, V. Marchesano, F. Tian, H. Child, C.C. Berry, M.R. Ibarra, P.V. Baptista, C. Tortiglione and J.M. de la Fuente. (* Co-first authors). **ACS Nano** (2012), Vol. 6, pp. 8316–8324. *Research article (IF=12.062)*

7. "RNA Quantification Using Noble Metal Nanoprobes: Simultaneous Identification of Several Different mRNA Targets Using Colour Multiplexing and Application to Cancer Diagnostics." **João Conde**, G. Doria, J.M. de la Fuente and P.V. Baptista. Nanoparticles in Biology and Medicine: Methods and Protocols Series. **Methods in Molecular Biology** (2012), Vol. 906, pp. 71-87. Humana Press, *Springer Protocols*.

8. "Effect of PEG biofunctional spacers and TAT peptide on dsRNA loading on Gold Nanoparticles." V. Sanz, **João Conde**, Y. Hernández, P.V. Baptista, M.R. Ibarra and J.M. de la Fuente. **Journal of Nanoparticle Research** (2012), Vol. 14, pp. 1-9. *Research article (IF=3.287)*

9. "Modification of Plasmid DNA Topology by Histone-Mimetic Gold Nanoparticles." **João Conde**, P.V. Baptista, Y. Hernández, V. Sanz and J.M. de la Fuente. **Nanomedicine (Lond).** (2012), Vol. 7, pp. 1657-1666. *Research article (IF=5.260)*

10. "Gold-Nanobeacons for Real-Time Monitoring of RNA Synthesis." J. Rosa*, **João Conde***, J.M. de la Fuente, J.C. Lima and P.V. Baptista. (* Co-first authors). **Biosensors & Bioelectronics** (2012), Vol. 36, pp. 161-167. *Research article (IF=5.437)*

11. "Noble Metal Nanoparticles for Biosensing Applications." G. Doria, **João Conde**, B. Veigas, L. Giestas, C. Almeida, M. Assunção, J. Rosa and P.V. Baptista**. Sensors (Basel)** (2012), Vol. 12, pp. 1657-1687. *Review article (IF= 1.953)*

12. "Noble Metal Nanoparticles Applications in Cancer." **João Conde**, G. Doria and P.V. Baptista. **Journal of Drug Delivery** (2012), Vol. 2012, pp. 1-12. *Review article*

13. "Nanophotonics for Molecular Diagnostics and Therapy Applications." **João Conde**, J. Rosa, J.C. Lima and P.V. Baptista. **International Journal of Photoenergy** (2012), Vol. 2012, pp. 1-11. *Review article (IF= 2.663)*

14. "Alloy Metal Nanoparticles for Multicolour Cancer Diagnostics." P.V. Baptista, G. Doria, **João Conde**. **Proceedings of SPIE** (2011), Vol. 7909, 79090K-1, Colloidal Quantum Dots/Nanocrystals for Biomedical Applications VI. Proceedings article

15. "In vitro Transcription and Translation Inhibition via DNA functionalized Gold-Nanoparticles." **João Conde**, J.M. de la Fuente and P.V. Baptista. **Nanotechnology** (2010), Vol. 21, 505101. *Research article (IF= 3.842)*

16. "RNA Quantification using Gold Nanoprobes - application to Cancer Diagnostics." **João Conde**, J.M. de la Fuente and P.V. Baptista. **Journal of Nanobiotechnology** (2010), Vol. 8, pp. 1-8. *Research article IF=not yet determined by ISI (unofficial=5.09)*

The **three chapters** in this Thesis (**II-IV**) are based on the inclusion of the respective article(s), preceded by a small overview explaining their context and declarations of authorship.

SUMÁRIO

O uso de nanopartículas de ouro tem ganho terreno em diagnóstico molecular, devido às suas propriedades físico-químicas únicas, apresentando inúmeras vantagens, tais como aumento da sensibilidade e especificidade, e do potencial para caracterizar sistemas "single molecule". Devido à sua versatilidade, bem como fácil síntese e funcionalização, nanopartículas de ouro multifuncionais têm, também, sido propostas como sistemas ideais de "delivery" para terapia (nanovectores). Ser capaz de produzir tais sistemas significa o início de uma nova era na área de teragnóstico (diagnóstico e terapia), impulsionada pela criação de veículos fantásticos à nanoescala.

De facto, a Nanotecnologia tem a capacidade de explorar novos sistemas para teragnóstico em cancro, através do desenvolvimento de métodos de diagnóstico, tais como colorimetria e imunoensaios, e em abordagens terapêuticas por meio de terapia génica, "delivery" de fármacos e/ou no "targeting" de tumores.

As características únicas das nanopartículas à nanoescala, tais como a elevada relação de superfície/volume ou as propriedades ópticas dependentes de tamanho e forma, que são radicalmente diferentes das dos seus materiais à macroescala, constituem as principais vantagens para a criação de sistemas utilizados em ensaios clínicos.

Este projecto de doutoramento pretende optimizar a síntese e funcionalização de nanopartículas de ouro para a detecção de transcritos de oncogenes (*c-Myc* e *BCR-ABL*), podendo ser utilizado para a avaliação do perfil de expressão em células cancerígenas e, simultaneamente, o desenvolvimento de uma plataforma inovadora de nanopartículas de ouro multifuncionais, funcionalizadas com marcadores tumorais, péptidos de internalização celular, marcadores fluorescentes e siRNAs capazes de silenciar determinados genes, de forma a avaliar o nível de expressão e determinar a eficiência de silenciamento. Este trabalho é parte de uma colaboração entre o Centro de Investigação em Genética Molecular Humana, Faculdade de Ciências e Tecnologia, Universidade Nova de Lisboa, Portugal e o Instituto de Nanociencia de Aragón, Espanha no âmbito de um projecto europeu [NanoScieE^{+} - NanoTruck].

Por forma a atingir este objetivo, desenvolveram-se estratégias eficazes de conjugação para combinar, de uma forma altamente controlada, biomoléculas à superfície de nanopartículas de ouro com funções específicas, tais como: oligos ssDNA para detectar sequências específicas e para a quantificação de RNA mensageiro; Polímeros biofuncionais: poli(etilenoglicol) (PEG) utilizados para aumentar a solubilidade e biocompatibilidade, conferindo também uma

funcionalidade química através da introdução de um grupo funcional; Péptidos de internalização celular (por exemplo, péptido TAT): usados para superar de forma mais eficiente a barreira lipofílica das membranas celulares, por forma a alcançar mais facilmente o citoplasma das células alvo; amónios quaternários: para introduzir cargas positivas na superfície das nanopartículas de ouro (para fazer ligar/adsorver os RNAs); e siRNA complementar a um proto-oncogene, *c-Myc*, implicado no crescimento celular, proliferação, perda de diferenciação e morte celular programada.

A fim de estabelecer que estas nanopartículas são alternativas viáveis para os métodos disponíveis, estes sistemas inovadores foram extensivamente caracterizados na sua funcionalização química, nível de internalização celular, toxicidade celular e inflamação, e o "knockdown" da expressão da proteína MYC em várias linhagens celulares de cancro e em modelos in vivo.

Palavras-chave: Nanomedicina, Terapia, Diagnóstico, Teragnóstico, Cancro, Nanopartículas de ouro.

ABSTRACT

The use of gold nanoparticles (AuNPs) has been gaining momentum in molecular diagnostics due to their unique physico-chemical properties these systems present huge advantages, such as increased sensitivity, reduced cost and potential for single-molecule characterisation. Because of their versatility and easy of functionalisation, multifunctional AuNPs have also been proposed as optimal delivery systems for therapy (nanovectors). Being able to produce such systems would mean the dawn of a new age in theranostics (diagnostics and therapy) driven by nanotechnology vehicles.

Nanotechnology can be exploit for cancer theranostics via the development of diagnostics systems such as colorimetric and imunoassays, and in therapy approaches through gene therapy, drug delivery and tumour targeting systems.

The unique characteristics of nanoparticles in the nanometre range, such as high surface-to-volume ratio or shape/size-dependent optical properties, are drastically different from those of their bulk materials and hold pledge in the clinical field for disease therapeutics

This PhD project intends to optimise a gold-nanoparticle based technique for the detection of oncogenes' transcripts (*c-Myc* and *BCR-ABL*) that can be used for the evaluation of the expression profile in cancer cells, while simultaneously developing an innovative platform of multifunctional gold nanoparticles (tumour markers, cell penetrating peptides, fluorescent dyes) loaded with siRNA capable of silencing the selected proto-oncogenes, which can be used to evaluate the level of expression and determine the efficiency of silencing. This work is a part of an ongoing collaboration between Research Centre for Human Molecular Genetics, Faculdade de Ciências e Tecnologia, Universidade Nova de Lisboa, Portugal and Biofunctional Nanoparticles and Surfaces Group, Instituto de Nanociencia de Aragón, Spain within a European project [*NanoScieE*$^{+}$ - *NANOTRUCK*].

In order to achieve this goal we developed effective conjugation strategies to combine, in a highly controlled way, biomolecules to the surface of AuNPs with specific functions such as: ssDNA oligos to detect specific sequences and for mRNA quantification; Biofunctional spacers: Poly(ethylene glycol) (PEG) spacers used to increase solubility and biocompatibility and confer chemical functionality; Cell penetrating peptides: to overcome the lipophilic barrier of the cellular membranes and deliver molecules into cells using TAT peptide to achieve cytoplasm and nucleus; Quaternary ammonium: to introduce stable positively charged in gold nanoparticles surface; and RNA interference: siRNA complementary to a master

regulator gene, the proto-oncogene *c-Myc*, that is implicated in cell growth, proliferation, loss of differentiation, and cell death.

In order to establish that they are viable alternatives to the available methods, these innovative nanoparticles were extensively characterized on their chemical functionalization, ease of uptake, cellular toxicity and inflammation, and knockdown of MYC protein expression in several cancer cell lines and in *in vivo* models.

Keywords: Nanomedicine, Therapy, Diagnostics, Theranostics, Cancer, Gold Nanoparticles.

SYMBOLS AND NOTATIONS

AuNPs - gold nanoparticles
cDNA - complementary DNA (DNA synthesized from mRNA template)
CML - chronic myelogenous leukemia
CPPs - Cell penetrating peptides
DEPC - Diethylpyrocarbonate
DLS - Dynamic Light Scattering
DNA - Deoxyribonucleic Acid
dNTPs - Deoxyribonucleotide Triphosphate
dsDNA - double-stranded DNA
DTNB - 5,5'-dithio-bis(2-nitrobenzoic) acid
DTT - Dithiothreitol
EDC - 1-Ethyl-3-(3-dimethylaminopropyl)carbodiimide
EGFP - Enhanced Green Fluorescent Protein
FRET - Förster's or fluorescence resonance energy transfer
GST - Glutathione
LSPR - localized surface plasmon resonance
MDR - multiple-drug resistance
mRNA - Messenger RNA
miRNA - micro RNA
MTT - 3-(4,5-dimethylthiazol-2-yl)-2,5-diphenyltetrazoliumbromide
NIR - near-infrared
NPs - nanoparticles
NHS - N-hydroxysuccinimide
NTP - Ribonucleotide Triphosphate
PBS - Phosphate Buffer Saline
PCR - Polymerase Chain Reaction
PEG - Poly(ethylene glycol)
Prot - Protamine
RGD Arginine-Glycine-Aspartic Acid (peptide)
RNA - Ribonucleic Acid
RNAi - RNA interference
RISC - RNA-Induced Silencing Complex

RT-PCR - Reverse Transcriptase-Polymerase Chain Reaction

SDS - Sodium Dodecyl Sulfate

SEM - Scanning electron microscopy

SERS - Surface-Enhanced Raman Scattering

siRNA - Small interfering RNA

ssDNA - Single-stranded DNA

ssRNA - single-stranded RNA

TAT - Transactivator of transcription (peptide)

TEM - Transmission electron microscopy

❶

INTRODUCTION

1. GENERAL CONSIDERATIONS ON GOLD NANOPARTICLES

Gold has been regarded as precious for as long as humans have existed, and has been associated with gods, kings and immortality. Already synthesized of gold at the times of Faraday, they generated ever-increasing interest since the ability to synthesize those particles in a controlled fashion way and their application in diverse nanosystems have come up in the last few decades [20;21]. Today, nanotechnology is enabling gold to help address critical global problems from cancer treatment to climate change. Although nanotechnology is thought of as a new branch of science that has only emerged over the past decade, gold nanoparticles (AuNPs) have been used, even though unintentionally, for several thousand years [1] (see **Figure 1**).

Gold nanoparticles have gained increasing interest due to their special features, such as extraordinary optical and electronic properties, high stability and biological compatibility, controllable morphology and size dispersion and shapes (see **Figure 2**), and easy surface functionalization.

Figure 1. (**a**) Golden burial mask of Egyptian Pharaoh Tutankhamun (King Tut) of the 18th Dynasty (ca. 1323 BC). (**b**) A gold medal presented at the Games of the II Olympiad (Paris, France; 1900). While bulk gold is highly un-reactive and predominantly reflects light, nanoscale gold can be highly reactive, exhibiting pharmacologic properties and the ability to absorb, transfer, and convert light energy into heat. The mask in (**a**), discovered in 1922 by Howard Cater, consists of solid gold with inlaid glass and stone (21 cm high and ca. 11 kg). Prior to the 1900 Olympics in (**b**), athletes received only silver and copper medals which easily oxidize. The winged goddess Nike is shown on the front in (**b**); a victorious athlete holding a laurel branch is shown on the back with The Acropolis in the background [2].

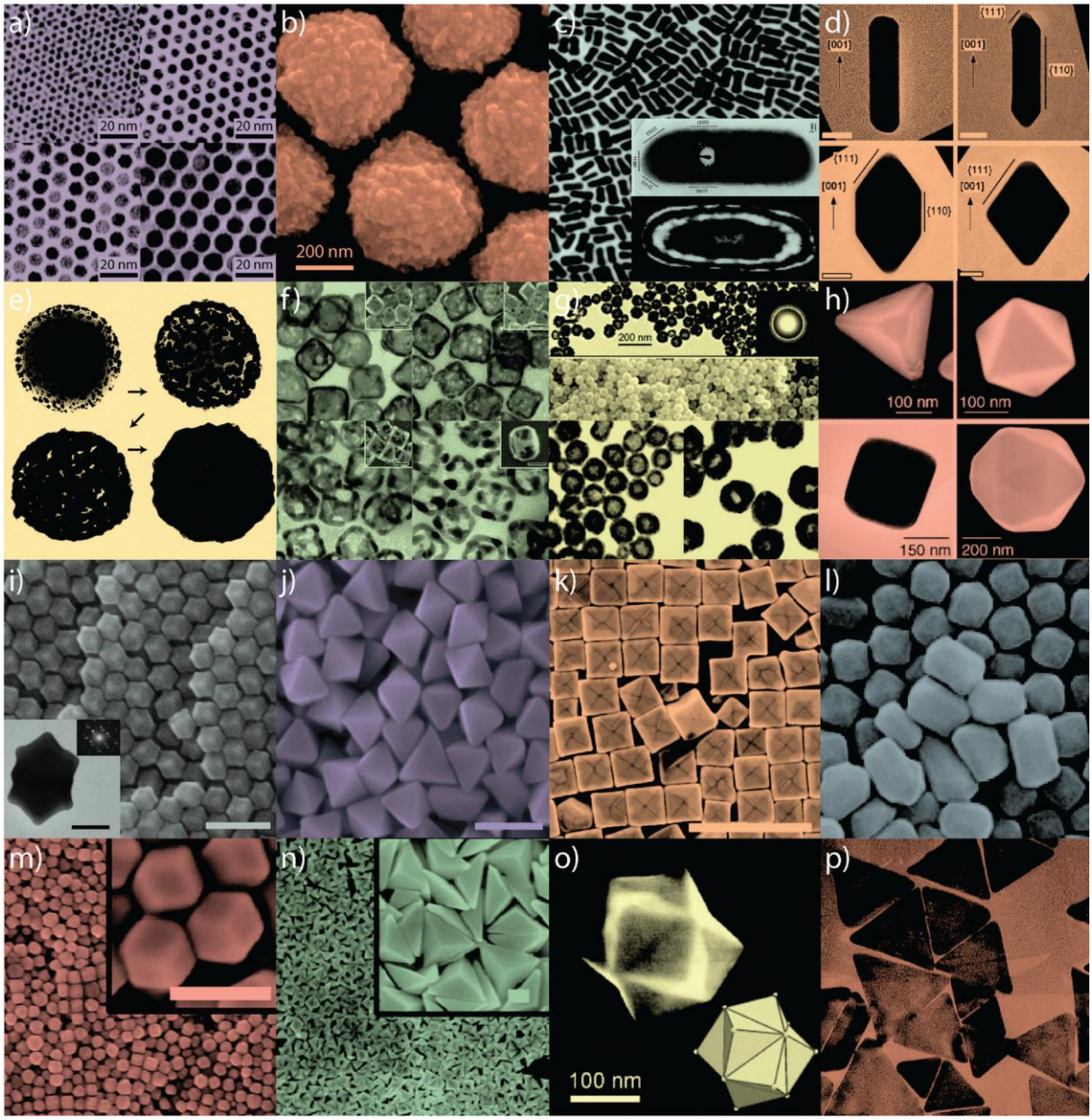

Figure 2. Gold nanoparticles of various size and shape with potential applications in biomedicine. Small (**a**) and large (**b**) nanospheres, (**c**) nanorods, (**d**) sharpened nanorods, (**e**) nanoshells, (**f**) nanocages/frames, (**g**) hollow nanospheres, (**h**) tetrahedra/octahedra/ cubes/icosahedra, (**i**) rhombic dodecahedra, (**j**) octahedra, (**k**) concave nanocubes, (**l**) tetrahexahedra, (**m**) rhombic dodecahedra, (**n**) obtuse triangular bipyramids, (**o**) trisoctahedra, and (**p**) nanoprisms [2].

The main characteristics include the electrical, chemical, and optical properties. The optical properties of AuNPs are significant because its adsorption and emission of the wavelength are within the visible range of light and because of their size- and shape-dependent properties [3]. Of particular interest is the light extinction process in the UV-visible range, which occurs when an electromagnetic wave passes through a metal particle exciting its electronic or

vibrational states [4]. This phenomenon induces dipole moments that oscillate at the respective frequency of the incident wave, and therefore disperse secondary radiation in all directions. This collective oscillation of the free conduction electrons is called localized surface plasmon resonance (LSPR). Surface plasmons are collective charge oscillations that occur at the interface between conductors and dielectrics (**Figure 3**). The oscillation frequency is usually in the visible region giving rise to the strong surface plasmon resonance absorption [25-28]. They can take various forms, ranging from freely propagating electron density waves along metal surfaces to localized electron oscillations on metal nanoparticles (NPs) [4;5]. When light passes through a metal nanoparticle induces dipole moments that oscillate at the respective frequency of the incident wave, consequently dispersing secondary radiation in all directions. Light on NP induces the conduction electrons to oscillate collectively with a resonant frequency that depends on the nanoparticles' size, shape, composition, inter-particle distance and environment (dielectric properties) [30-32;58]. As a result of these SPR modes, the nanoparticles absorb and scatter light so intensely that single NPs are easily observed by eye using dark-field (optical scattering) microscopy.

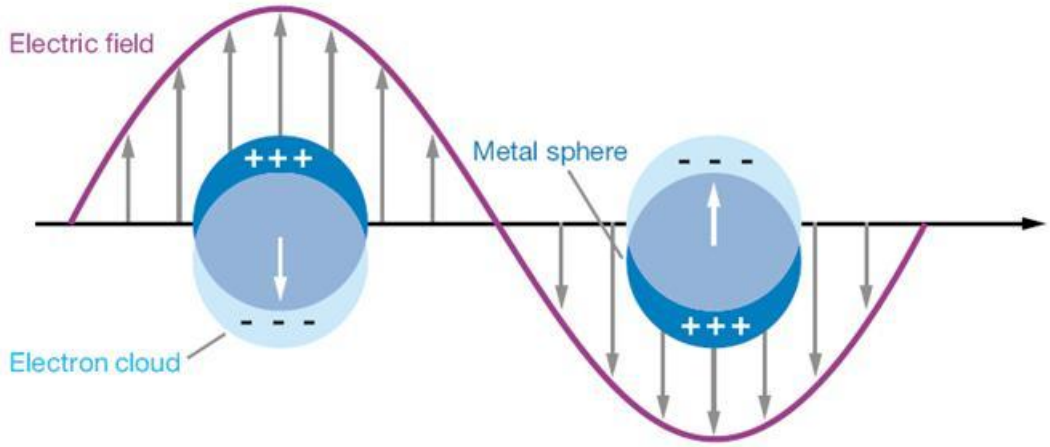

Figure 3. Localized surface plasmon resonance. Schematic representation of how the interaction of the electromagnetic waves with the metal NPs surface electrons generates a surface plasmon resonance [4].

Size provides important control over many of the physical and chemical properties, including luminescence, conductivity, and catalytic activity. AuNPs give rise to both absorption and scattering whose proportions depend on the AuNP size, shell thickness, aspect ratio and percentage of gold [6] (see **Figure 4**). AuNPs with a diameter smaller than 20 nm essentially show absorption, but when the size increase to 80 nm also increases the ratio of scattering to absorption. As the size of the AuNP increases, light can no longer polarize the nanoparticles

homogeneously, and higher order modes at lower energy dominate. This causes a red-shift and broadening of the surface plasmon band. Small AuNPs like the ones with 13 nm of diameter absorb green light, which corresponds to a strong absorption band at 520 nm in the visible light spectrum. However, solutions of AuNPs appear red in colour. For smaller AuNPs (i.e. 5 nm diameter), surface electrons are oscillated by the incoming light in a dipole mode, but the SPR it is very sensitive to the composition, size, shape, inter-particle distance and environment (dielectric properties) of the AuNPs [30-32]. For example, for citrate stabilised particles, the addition of NaCl shields the surface charge and leads to a concomitant decrease in the inter-particle distance and eventual particle aggregation [7]. For instance, 5 nm AuNPs are orange-red, but they turn blue-purple upon aggregation (network formation) to larger AuNPs.

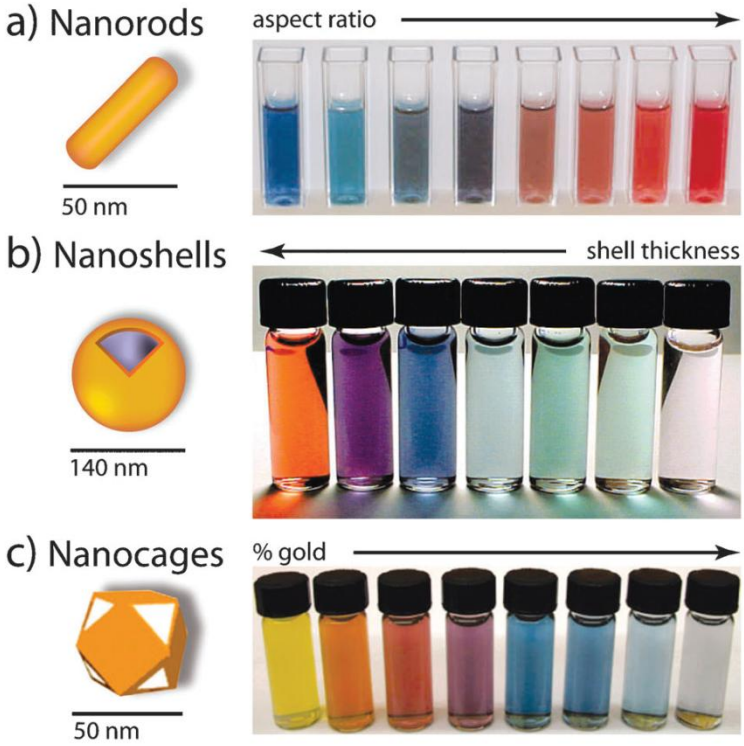

Figure 4. Gold nanoparticles commonly applied in biomedical applications. (**a**) Gold nanorods, (**b**) silica–gold core–shell nanoparticles, and (**c**) gold nanocages. The intense colour of these nanoparticles arises from the collective excitation of their conduction electrons, or surface plasmon resonance modes, which results in photon absorption at wavelengths which varies with (**a**) aspect ratio, (**b**) shell thickness, and/or (**c**) galvanic displacement by gold.

This also explains the corresponding surface plasmon band shifts (red shift), which results in colour changes (red-to-purple) that are observed during the aggregation of small AuNPs. When AuNPs aggregate, their surface plasmons combine (interparticle plasmon coupling),

and the aggregate could be considered as a single large particle, although the detailed interparticle plasmon coupling is rather complex and dependent on many factors, such as aggregate morphology and nanoparticles density [31;32;34].

1.1. GOLD NANOPARTICLE SYNTHESIS

Gold nanoparticles, also known as colloidal gold, is a suspension of sub-micrometre-sized gold metal particles in a fluid and can be obtained in sizes between 3 and 200 nm in diameter. As a colloidal particle is much larger than its constituent atoms, its typical shape mainly results from its surface energy, whose minimization decreases the surface area and favours the formation of spherical objects [8].

The most common methods for the synthesis of spherical gold colloidal particles involve the chemical reduction of Au ions.

Since the pioneering work of *Turkevich* [9] and the modification by *G. Frens* [10], the most widely studied reductant is sodium citrate [37;38]. The method of citrate reduction of Au(III) to Au(0) in water is still used nowadays to subsequently replace the citrate ligand of these AuNPs by appropriate ligands of biological interest.

In the citrate reduction method, sodium citrate reduces the gold cations in hydrogen tetrachloroaurate ($HAuCl_4$). As the gold metal forms, anions coat the outside of the particles preventing them from forming larger particles. The small gold nanoparticles that are formed stay in solution because their coatings are negatively charged and repel each other, preventing aggregation. By other words, the particles are stabilized by citrate ions bound to the surface of the nanoparticles, resulting in negatively charged particles that repel each other by electrostatic repulsion [11].

Recent modifications of the *Turkevitch* method have allowed better size distribution and size control within the 9–120 nm range [32;39;40]. It is now well known that, by varying the citrate/Au ratio, colloidal particles with diameters ranging from 10 to 150 nm may be generated.

The synthesis of gold nanoparticles by reducing agents such as sodium borohydride [12], ascorbic acid in presence of cetyltrimethylammonium bromide (CTAB) [13], sugars (glucose, fructose and sucrose) [14] have also been reported.

1.2. STABILIZATION AGAINST AGGREGATION

In typical synthesis, AuNPs are produced by reduction of gold salts. Usually a stabilizing agent is also added to prevent the particles from aggregating. Because thiol groups bind to

gold surfaces with high affinity, most frequently thiol modified ligands are used as stabilizing agents which bind to the surface of the AuNPs by formation of Au-sulfur bonds [15].

Although AuNPs can be stabilized by a large variety of stabilizers (ligands, surfactants, polymers, dendrimers, biomolecules, etc.), [16] the most robust AuNPs were disclosed by *Giersig* and *Mulvaney* to be stabilized by thiolates using the strong Au–S bond between the soft acid Au and the soft thiolate base [17].

After synthesis, the stabilizing agents surrounding the AuNPs can be replaced by other molecules by ligand exchange reactions [18]. In addition, ligands can also be linked to the shell of stabilizing agents. One of the most common applications is the linkage of amino groups in biological molecules with carboxyl groups at the free ends of the stabilizing agents [19].

Functionalization of AuNPs makes it possible to adjust the surface properties and attach different kinds of molecules to the particles. This has encouraged the development of new forms and modifications of nanoparticles for biomedical, biological and treatment/diagnostic applications, as well as the use of these nanoparticles in self assembly paradigms using biomolecules such as DNA/RNA, oligonucleotides (i.e. siRNA, ssDNA), peptides and antibodies, fluorescent dyes, polymers, drugs, tumoral markers, PEGs, various enzymes and other proteins, that are easily attached to the nanoparticles's surface (**Figure 5**).

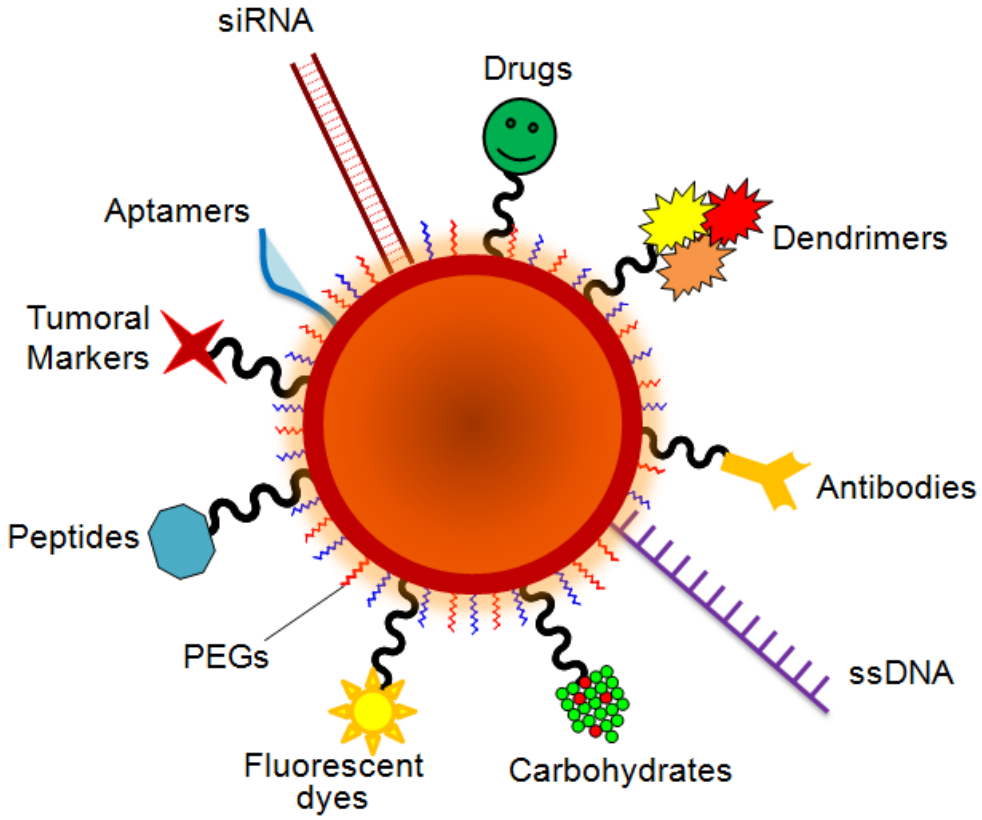

Figure 5. Schematic representation of a multifunctional nanocarrier. These innovative NPs comprise nucleic acids such as RNA and DNA used for gene silencing approaches and in colorimetric assays, respectively. Aptamers and anticancer drug molecules are also used for delivery to the target tissue. Carbohydrates may be useful as sensitive colorimetric probes. PEG is used to improve solubility and decrease immunogenicity. Responsive nanocarriers can also trigger reaction upon external stimuli through the functionality of valuable tumor markers, peptides, carbohydrates, polymers and antibodies that can be used to improve nanocarrier circulation, effectiveness and selectivity. Multifunctional systems can also carry fluorescent dyes that are used as reporter molecules tethered to the particle surface and employed as tracking and/or contrast agents.

1.3. BIOLOGICAL APPLICATIONS

Nanoparticle-based delivery systems in Theranostics (Diagnostics & Therapy) provide better penetration of therapeutic and diagnostic substances within the body at a reduced risk in comparison to conventional therapies [49;50].

Limitations in medical practice are closely associated with the fact that diagnostics, therapy and therapy guidance are three discrete and isolated stages. In order to overcome some of the sensitivity and specificity of current medicines, theranostics unites the three above stages in one single process, supporting early-stage diagnosis and treatment [51-53]. Nowadays, there is an ever-increasing need to enhance the capability of theranostics procedures where nanoparticle-based sensors may provide for the simultaneous detection of several gene-associated conditions and nanodevices with the ability to monitor real-time drug action.

The unique characteristics of nanoparticles in the nanometre range, such as high surface-to-volume ratio or size-dependent optical and magnetic properties, are drastically different from those of their bulk materials and hold pledge in the clinical field for disease therapeutics [54;55].

In spite of these advantages, nanoparticles do have limitations. For example, their small size and large surface area can lead to particle-particle aggregation and may result in limited loading of functional components and burst release.

In fact, only nanoparticles with the appropriate size (and surface chemistry) are not immediately recognized by our immune system and show increased circulation times. The size plays an important role to avoid clearance. Hydrophilic nanoparticles with an effective size in the range of 10 to 100 nm are small enough to slow down activation of the mononuclear phagocyte system and are big enough to avoid renal filtration [20].

However, nanoparticles with unique and broad-based optical properties, ease of synthesis and facile surface chemistry and functionalization, and appropriate size scale are generating much

eagerness in clinical diagnostics and therapy. The most common applications in which gold nanoparticles have been used so far are labelling, delivering, heating, sensing and detection [21] (**Figure 6**).

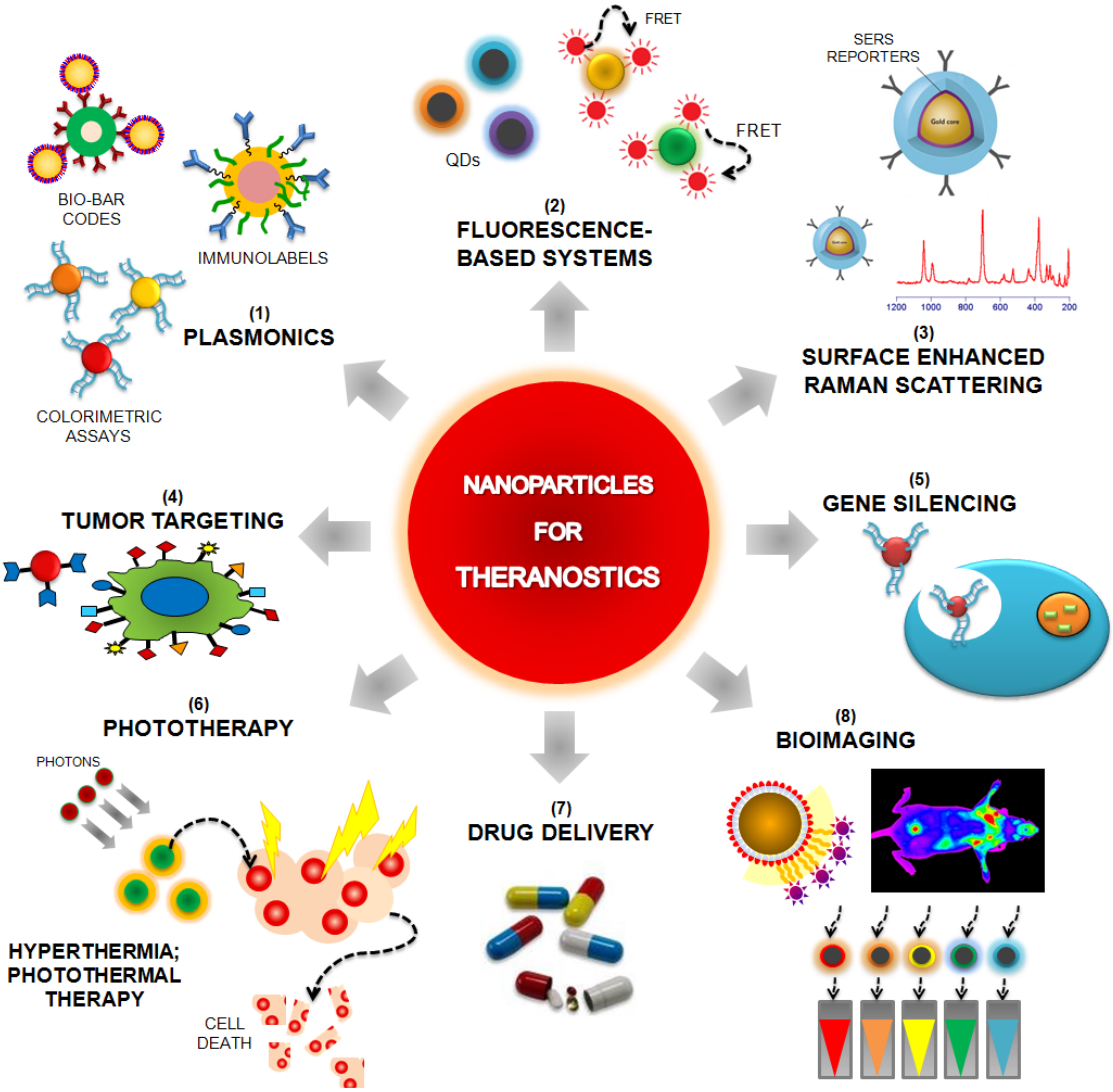

Figure 6. Nanoparticles for Theranostics. Nanoparticles-based strategies can be used for biosensing using plasmonic nanosensors, such as metal nanoparticles functionalized with nucleic acid strand for colorimetric assays; Biobar-codes for protein detection or intense labels for immunoassays (**1**). Some nanoparticle systems can also be used for sensing by exploring a typical FRET system (**2**) or can be surrounded with Raman reporters (**3**) in order to provide *in vivo* detection (**8**), tumour targeting (**4**) and drug delivery (**7**). In fact, NPs symbolize an important class of materials with unique features suitable for biomedical imaging applications (**8**) such as increased sensitivity in detection and high quantum yields for fluorescence. Alternatively, NPs can survey near/far-field enhancing qualities that hold promise for a bounty of novel applications in optics and photonics. Engineered NPs can also act as phototherapeutic agents that can be attached to specific targets for selective gene silencing (**5**) or damage to cancer cells (**6**).

2. NANODIAGNOSTICS

Nanodiagnostics can be defined as the use of nano-sized materials, devices or systems for diagnostics purposes. It is a burgeoning field as more and improved techniques are becoming available for clinical diagnostics with increased sensitivity at lower costs [3-6].

The use of the colloidal gold colour change upon aggregation is the best characterized example for diagnostic systems using AuNPs. In fact, AuNPs functionalized with ssDNA capable of specifically hybridizing to a complementary target for the detection of specific nucleic acid sequences in biological samples have been extensively used [3;5;61;63-68;70;71].

Other approaches are the use of AuNPs as a core/seed that can be tailored with a wide variety of surface functionalities to provide highly selective nanoprobes for diagnosis [22]; the utilization of Surface Plasmon resonance (SPR) scattering imaging or SPR absorption spectroscopy generated from antibody conjugated AuNPs in molecular biosensor techniques for the diagnosis and investigation of oral epithelial living cancer cells *in vivo* and *in vitro* [211]; the use of multifunctional AuNPs which incorporate both cytosolic delivery and targeting moieties on the same particle functioning as intracellular sensors to monitoring actin rearrangement in live fibroblasts [23]; and the employment of AuNPs in electrochemical based methods that can be coupled with metal deposition for signal enhancement [24].

Consequently, the use of thiol-linked ssDNA-modified gold nanoparticles (herein designated Au-nanoprobes) for the colorimetric detection of gene targets represents an inexpensive and easy to perform alternative to fluorescence or radioactivity-based assays [25]. In 1996, *Mirkin* et al. [26] described the use of a cross-linking method that relies on the detection of single-stranded oligonucleotide targets using two different Au-nanoprobes, each of them functionalized with a DNA-oligonucleotide complementary to one half of the given target [60;71].

On the other hand, in 2005 *Baptista* et al. introduced a non-cross linking method where thiol-linked DNA-gold nanoparticles were used in a novel colorimetric method to detect the presence of specific mRNA from a total RNA extract of yeast cells [27]. The method consists in visual and/or spectrophotometric comparison of solutions before and after salt induced Au-nanoprobe aggregation (see **Figure 7**) – the presence of a complementary target prevents aggregation and the solution remains red and has a strong absorbance at ±520 nm; non-complementary/mismatched targets do not prevent Au-nanoprobe aggregation, resulting in a visible change of colour from red to blue and therefore a shift in the surface plasmon absorbance to 600-650 nm. This method has been successfully applied to detect eukaryotic

gene expression without retro-transcription or PCR amplification steps [4;7]; to distinguish fully complementary from mismatched sequences, with a single base mismatch i.e. to detect common mutations within the β-globin gene [28]; and in a fast and straightforward assay for *Mycobacterium tuberculosis* DNA detection in clinical samples [6;62].

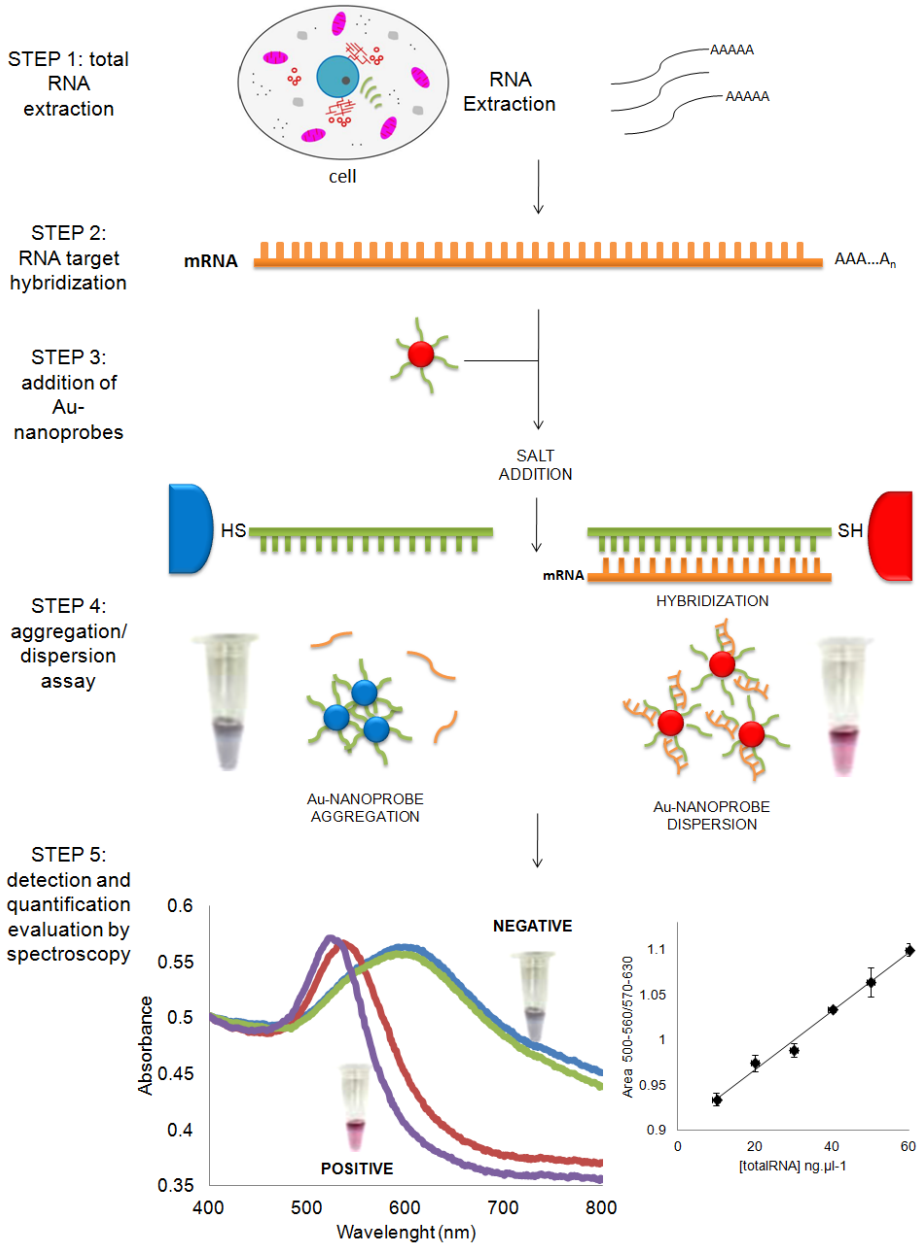

Figure 7. RNA detection using DNA-gold nanoparticles. Detection and quantification of the mRNA using DNA thiol-modified gold nanoparticles. The assay is based on the increased stability of the Au-nanoprobes upon hybridization with the complementary target in solution, while non-hybridized Au-nanoprobes easily aggregate once the solution's ionic strength is increased. This method can be successfully applied to detect eukaryotic gene expression without retro-transcription or PCR amplification steps. Positive: sample in the presence of complementary target (solution remains red); Negative: sample in the presence of non-complementary target (solution turns blue).

To further improve the detection flexibility, simplicity and efficiency, and reduce the cost, advance molecular diagnosis assay that utilizes gold nanoparticles derivatized with thiol modified oligonucleotides is the most simple, rapid and with a great efficiency nanodiagnostic system.

NP-based biosensors provide a new horizon for novel functions with a variety of applications in clinical diagnostics and biological research. Gold NPs have already proven to be one of the most important groups of nanomaterials for biosensing approaches. Highly sensitive and specific biosensors based on AuNPs have open up the possibility of creating new diagnostic platforms for disease markers, biological and infectious agents in the early-stage detection of disease and threats, especially in cancer. [143;213]

2.1. NANOCARRIERS IN CANCER DIAGNOSIS

Cancer is the one of first leading causes of mortality in the modern world, with more than 10 million new cases every year [29]. However, advances in diagnosis and treating this disease that kills millions of people each year worldwide, have not been as effective as for other chronic diseases, and only for some types of cancer there are effective methods of detection [30]. Thus, the main challenge is to find new and more effective diagnostic agents for the monitorization of predictive cell molecular changes that are involved in tumour development. The key to the efficient and ultimately triumphant treatment of cancer is early and accurate diagnosis [31].

It's here that nanotechnology enters the fray in the technological leap of controlling materials at nanoscale by offering a "big revolution" in new medical and healthcare diagnostic systems [20]. In fact, nanotechnology combined with biology and medicine is the most advanced technology both from an academic point-of-view and for commercial applications, producing major advances in cancer diagnostics and bioengineering [22;217].

Nanotechnology can be exploit for cancer theranostics via the development of diagnostics systems such as colorimetric and imunoassays, and in therapy approaches through gene therapy, drug delivery and tumour targeting systems [32].

The unique characteristics of nanoparticles in the nanometre range, such as high surface-to-volume ratio or size-dependent optical properties, are drastically different from those of their bulk materials and hold pledge in the clinical field for disease therapeutics [54;55].

Molecular nanodiagnostics applied to cancer may provide rapid and sensitive detection of cancer related molecular alterations, which would enable early detection even when those alterations occur only in a small percentage of cells. When referring to cancer therapy,

targeting and localized delivery are of utmost importance to enhance the therapeutic effect and decrease undesirable distribution to healthy organs and tissues. Multifunctional gold nanocarriers may potentiate the development of individualized cancer therapy based on the individual's biological information within the tumour (biomolecular profiling). Gold nanocarriers can be modified with multiple cell-targeting and membrane translocating peptides, loaded with DNA/RNA and used as nanovectors [12;13].

A great effort has been applied to the detection of microorganisms and/or virus using gold SPR biosensors but very few were used for the detection of chronic diseases, such as asthma, Alzheimer's disease, diabetes, epilepsy, heart disease and specially cancer. Actually, molecular nanodiagnostics applied to cancer may provide rapid and sensitive detection of cancer related molecular alterations, which would enable early detection even when those alterations occur only in a small percentage of cells.

The high mortality rate in cancer is commonly attributed to the difficulties in detecting the disease at an early treatable stage. Therefore new synthesis, fabrication, and characterization methods are needed for developing highly advanced AuNPs capable of use in sensitive and multiple detection methods with negligible toxicity and high sensitivity. In the future, it might be possible to apply all AuNPs properties together and evolve new chemistry for synthesis of smart materials for diagnostic applications and clinical trials.

3. NANOTHERAPY

In medical term a therapeutic effect is a consequence of a medical treatment of any kind, the results of which are judged to be desirable and beneficial. Conventional therapy methods, for example in cancer, involve the employment of anticancer agents that do not greatly differentiate between cancerous and normal cells. Efficient *in vivo* targeting to heterogeneous population of cancer cells and tissue still requires better selectivity and non-cytotoxicity to surrounding normal cells. This fact leads to systemic toxicity, adverse effects and severe side effects [33].

In another way, universally targeting cells within a tumour is not always feasible because some drugs cannot diffuse efficiently and the random nature of the approach makes it difficult to control the process and may induce multiple-drug resistance (MDR), a situation where chemotherapy treatments fail patients owing to resistance of cancer cells towards one or more drugs [34]. Consequently, nanotechnology could offer a less invasive alternative, enhancing the life expectancy and quality of life of the patient [35].

At the moment, it is expected that the greatest gains in therapeutic selectivity will be achieved by synergistic combinations of several multicomponent targeting strategies. Currently, it is imperative to develop technology for targeting and delivery of multiple therapeutic agents, and for the simultaneous capability of avoiding biological and biophysical barriers. For example, nanoparticles can extravasate into the tumour stroma through the fenestrations of the angiogenic vasculature, demonstrating targeting by enhanced permeation and retention. These particles are able to carry multiple antibodies, which further target them to epitopes on cancer cells, and direct antitumor action, leading to cell death. Irradiation might be use to activate the nanoparticles and set up the release of their cytotoxic action [36].

3.1. TUMOR TARGETING

It is expected that the greatest gains in therapeutic selectivity will be achieved by synergistic combinations of several multicomponent targeting strategies, i.e. capable of simultaneously target and deliver multiple therapeutic agents, while avoiding the organism's biological and biophysiscal barriers. NPs targeting strategies to cancerous tissues have focused on passive and active targeting. In passive targeting, because numerous tumours present defective vasculature and poor lymphatic drainage due to the rapid growth of solid tumours, noble metal NPs can extravasate into the tumour stroma through the fenestrations of the angiogenic vasculature, demonstrating targeting by enhanced permeation and retention, thus accumulation at the tumour site [12;19;109]. Additionally, functionalization of the NP's surface with hydrophilic molecules, such as PEG, can also greatly increase their solubility, help evading macrophage-mediated uptake and, thus, avoid removal from the systemic circulation and protect their carriers from enzymatic degradation when used *in vivo* [16]. For active targeting, NPs can be easily functionalized with a wide variety of biological moieties, such as antibodies, peptides and/or DNA/RNA to specifically target extracellular and intracellular receptors or pathways [16]. The use of NPs functionalized with multiple peptides or antibodies, such as monoclonal antibodies, have been described to successfully target specific cell surface proteins or receptors on cancer cells and further direct their antitumor action, leading to tumour cell death with minimal damage to collateral healthy cells [110-113]. In nucleic-acid functionalized NPs, DNA and RNA macromolecules can be used to simultaneously target specific sequences and exert their genetic-based therapy [114;115].

To help tracking nanoparticles *in vivo* and enhance the imaging properties of such moieties, leading to more efficient control of their therapeutic properties, they can also be

functionalized with chemical moieties, such as Raman [116;117] or fluorescent [92;118] reporters.

3.2. GENE THERAPY

We are in the dawn of a new age in gene therapy driven by nanotechnology vehicles. Although there are technical challenges associated with the therapeutic application of nanoparticles, the integration of therapy with diagnostic profiling has accelerated the pace of discovery of new nanotechnology methods. The development of a safe, efficient, specific and nonpathogenic vehicle for gene delivery is highly attractive [17;18].

Gene therapy is receiving increasing attention and, in particular, small-interference RNA (siRNA) shows significant potential in new molecular approaches to down-regulate specific gene expression in cancerous cells. In fact, this non-viral-vector-mediated delivery of therapeutic siRNAs is highly desirable and constitutes an important challenge to gene therapy [14-16].

In fact, antisense DNA [119;120] and RNA interference (RNAi) via the use of small-interfering RNA [121-124] have emerged as powerful and useful tools to block gene function and for sequence-specific posttranscriptional gene silencing, playing an important role in downregulation of specific gene expression in cancer cells.

siRNAs are 21-23 nucleotide double strand nucleic acid molecules (dsRNA), with symmetric 2-3 nt 3’ overhangs and 5’-phosphate and 3’-hydroxyl groups, that mediate the cleavage of complementary mRNA sequences and thus regulate gene expression [121;129;347;348].

The RNA silencing pathway (**Figure 8**) begins with long dsRNA precursors that are processed to siRNA duplexes by the RNase-III-like enzyme Dicer. These short dsRNAs are subsequently unwound and assembled into an effector complex, RNA Induced Silencing Complex (RISC), which can direct RNA cleavage, mediate translational repression or induce chromatin modification. The antisense strand then binds to its complementary/target mRNA. The strand antisense to the targeted mRNA is often referred to as the guide strand, and its base-paired sense strand is known as the passenger strand, which is destroyed upon incorporation of the guide strand into RISC. The catalytic RISC recognizes mRNAs containing perfect or near-perfect complementary sequence to the guide siRNA and cleaves the mRNAs at a site precisely 10 nucleotides from the 5’-end of the guide strand. Finally, mRNA degradation is achieved by endo- and exonucleases, resulting in knockdown of the expression of the corresponding genes [349-351].

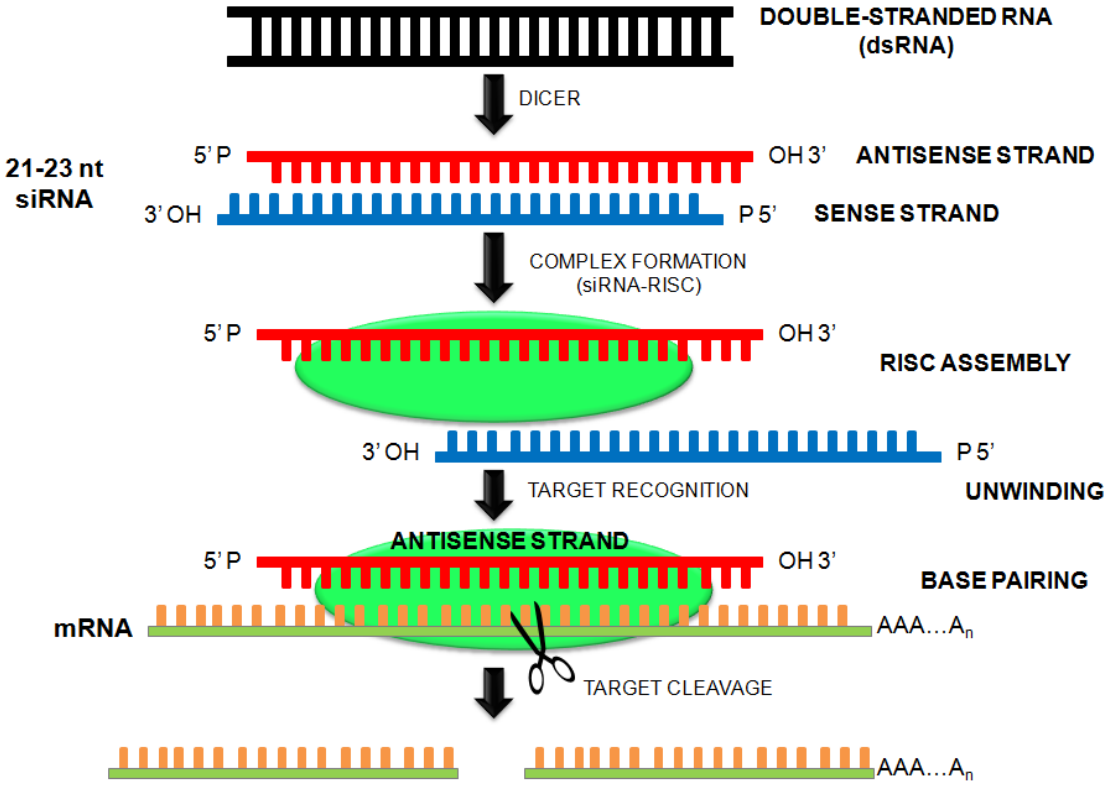

Figure 8. The **RNA interference pathway**, defined as a gene silencing pathway that is triggered by double-stranded RNA (dsRNA). Gene silencing can be the result of nucleolytic degradation of the mRNA, or by translational suppression.

siRNAs can be transfected into mammalian cells by a variety of methods [125-128] that influence the strength and duration of the silencing response, which in turn is affected by the amount of siRNA that is delivered and on the potential of each siRNA to suppress its target. Thus, one drawback of using naked siRNAs is that they show extremely short half-lives, weak protection against action by RNases, poor chemical stability, and common dissociation from vector [37]. In fact, the major obstacle to clinical application is the uncertainty about how to deliver therapeutic RNAs (e.g., miRNA and/or siRNA) with maximal therapeutic impact. Nanotechnology offers an unprecedented opportunity to overcome these problems, as nanoscale devices, due to their small size, can readily interact with biomolecules on both the surface of cells and inside of cells for longer periods of time [38]. AuNPs have shown potential as intracellular delivery vehicles for antisense oligonucleotides [39] and for therapeutic siRNA by providing protection against RNAses and ease of functionalization for selective targeting [114;115]. For example, *Mirkin* and coworkers showed that AuNPs attached to single-stranded oligodeoxynucleotides can be used for gene therapy, providing a highly efficient gene regulator in terms of high loading of the antisense DNA with no toxicity

at the concentrations studied [39]. They have also shown that polyvalent RNA-AuNP conjugates are readily taken up by cells and that the particle bound siRNA could effectively regulate genes in the context of RNA interference [40]. AuNPs modified with the hydrophilic PEG polymer, siRNAs and then coated with poly(β-aminoester)s have been shown to facilitate high levels of *in vitro* siRNA delivery and gene silencing in human cells [41]. Also, Braun et al. developed an Au-nanoshell functionalized with TAT-lipid layer for transfection and selective release of siRNA [42], where the TAT-lipid coating was used to efficiently mediate the cellular uptake of the nanoconjugates and the siRNA release was dependent on near-infrared (NIR) laser pulses. The authors demonstrated that this NIR strategy for siRNA release was proficient and time dependent. Several other studies using engineered NPs modified with siRNA have demonstrated a cytoplasmic delivery system of siRNA and efficient gene silencing using AuNPs [114;131;133;134]. However, almost all nanoconjugates using siRNA have exclusively been tested in cell cultures targeting only reporter genes.

Further research into the fundamental mechanisms of gene therapy *in vivo* using nanodevices could unveil new dimensions of nanoparticle-mediated gene silencing that will have profound implications for understanding gene regulation, and which could also affect the development of functional genomics and therapeutic applications.

4. NANOTOXICITY

The AuNPs have a proclivity *in vivo* and *in vitro* to bioaccumulate within various types of cells with a special affinity for macrophage-type cells (both histiocytes and blood phagocytic cells), and reticuloendothelial cells throughout the body). They also produce varying degrees of bioaccumulation in such tissues as lymph nodes, bone marrow, spleen, adrenals, liver and kidneys [297-299].

Research shows that nanoparticles can stimulate and/or suppress the immune responses, and that their compatibility with the immune system is largely determined by their surface chemistry. In fact, is well known the influence of size, solubility and surface modification on the biocompatibility of nanoparticles and their use in biological applications [43].

AuNPs are generally considered to be benign. However, the size similarity of AuNPs to biological matters could provide “camouflage” to cellular barriers, leading to undesired cellular entry which might be detrimental to normal cellular function [44].

Pan and colleagues recently conducted a systematic investigation of the size-dependent cytotoxicity of AuNPs against four cell lines [45]. They found that AuNPs 1 to 2 nm in size displayed cell-type dependent cyotoxicity with high micromolar IC50s. In contrast, AuNPs 15

nm in size were nontoxic to cells at concentrations 60-fold higher than the IC50 of the smaller AuNPs. These results seemed to confirm size dependent toxicity of AuNPs [277;303-306], an inference that has been somewhat ambivalent.

Now the most imperative question rises up. Are the gold nanoparticles cytotoxic or biocompatible? And how can the gold nanoparticles be design to avoid these effects?

There does not seem to have a simple answer. Even though there is not any general mechanism for making nanoparticles universally 'non-toxic' to all living cells and all organisms, there are important findings that can be applied for increasing nanoparticle biocompatibility and reducing cytotoxic interactions *in vivo* and *in vitro*.

Using the lowest nanoparticle dose to get the desired response for the shortest period of time, in general, seems to promote biocompatibility as well as coating a nanoparticle if the outer coating completely covers the nanoparticle reactive surface (a non-continuous covering, the presence of cracks, roughness or interruptions could lead to complement or antibody attachment, or dissolution of the coating by cell digestion), and cannot be removed and utilized by the living cell [46].

It is essential to test nanoparticle/biological interactions experimentally and modify the nanoparticles for best biocompatibility with the cell in order to eliminate membrane lipid peroxidation; reduce the generation of reactive oxygen species; prevent acute and chronic release of inflammatory factors (and 'complement' activation); guard against alterations in genetic cellular function; and reduce the possibility of nanoparticles becoming 'stuck' during filtration or passage through pores and fenestrations [308] due to size, inflexibility of the nanoparticle core, or protein adsorption and agglomeration [46].

When interpreting nanoparticle interactions with biological cells and organisms, it is important to remember that living systems may appear normal and be capable of growth and function, but they may be genetically altered in subtle ways following nanoparticle exposure, which can produce serious consequences at some time in the distant future. Conversely, other cells that seem to be damaged may, in time, recover from nanoparticle exposure and function normally in the absence of the nanoparticles [46].

In conclusion, the only weapon that we have to insure that these new materials are well designed and safely used is to question and test each new nanoparticle to make sure that it has been designed for safety (with maximum biocompatibility) during handling, use and disposal.

These concepts were extensively reviewed in the **Review Articles A**, **B** and **C** and **Book Chapter A** at the end of this Introduction section.

REFERENCES

1. Salata O. Applications of nanoparticles in biology and medicine. J Nanobiotechnology 2004; 2(1):3.

2. Dreaden EC, Alkilany AM, Huang XH, Murphy CJ, El-Sayed MA. The golden age: gold nanoparticles for biomedicine. Chemical Society Reviews 2012; 41(7):2740-2779.

3. El-Sayed MA. Some interesting properties of metals confined in time and nanometer space of different shapes. Acc Chem Res 2001; 34(4):257-264.

4. Kreibig U, Vollmer M. Optical Properties of Metal Clusters. Springer; 1995.

5. Barnes WL, Dereux A, Ebbesen TW. Surface plasmon subwavelength optics. Nature 2003; 424(6950):824-830.

6. Cao YC, Jin R, Mirkin CA. Nanoparticles with Raman spectroscopic fingerprints for DNA and RNA detection. Science 2002; 297(5586):1536-1540.

7. Storhoff JJ, Lazarides AA, Mucic RC, Mirkin CA, Letsinger RL, Schatz GC. What Controls the Optical Properties od DNA-Linked Gold nanoparticle assemblies? J Am Chem Soc 2000; 122:4640-4650.

8. Daniel MC, Astruc D. Gold nanoparticles: assembly, supramolecular chemistry, quantum-size-related properties, and applications toward biology, catalysis, and nanotechnology. Chem Rev 2004; 104(1):293-346.

9. Turkevich J, Garton G, Stevenson PC. The color of colloidal gold. Journal of Colloidal Science 1954; 9:26-35.

10. Frens G. Controlled nucleation for the regulation of the particle size in monodisperse gold suspensions. Nature (London), Phys Sci 1973; 241:20-22.

11. Wilcoxon JP, Abrams BL. Synthesis, structure and properties of metal nanoclusters. Chem Soc Rev 2006; 35(11):1162-1194.

12. Wagner J, Tshikhudo TR, Koehler JM. Microfluidic generation of metal nanoparticles by borohydride reduction. Chemical Engineering Journal 2008; 135:S104-S109.

13. Cao C, Park S, Sim SJ. Seedless synthesis of octahedral gold nanoparticles in condensed surfactant phase. J Colloid Interface Sci 2008; 322(1):152-157.

14. Panigrahi S, Kundu S, Ghosh SK, Nath S, Pal T. General method of synthesis for metal nanoparticles. Journal of Nanoparticle Research 2004; 6(4):411-414.

15. Templeton AC, Wuelfing WP, Murray RW. Monolayer-protected cluster molecules. Acc Chem Res 2000; 33(1):27-36.

16. Sperling RA, Parak WJ. Surface modification, functionalization and bioconjugation of colloidal inorganic nanoparticles. Philos Transact A Math Phys Eng Sci 2010; 368(1915):1333-1383.

17. Giersig M, Mulvaney P. Preparation of ordered colloid monolayers by electrophoretic deposition. Langmuir 1993; 9(12):3408-3413.

18. Pellegrino T, Kudera S, Liedl T, Munoz JA, Manna L, Parak WJ. On the development of colloidal nanoparticles towards multifunctional structures and their possible use for biological applications. Small 2005; 1(1):48-63.

19. Sperling RA, Pellegrino T, Li JK, Chang WH, Parak WJ. Electrophoretic Separation of Nanoparticles with a Discrete Number of Functional Groups. Adv Funct Mater 2006; 16:943-948.

20. Gil PR, Parak WJ. Composite nanoparticles take aim at cancer. ACS Nano 2008; 2(11):2200-2205.

21. Sperling RA, Rivera GP, Zhang F, Zanella M, Parak WJ. Biological applications of gold nanoparticles. Chem Soc Rev 2008; 37(9):1896-1908.

22. You CC, Miranda OR, Gider B, Ghosh PS, Kim IB, Erdogan B et al. Detection and identification of proteins using nanoparticle-fluorescent polymer 'chemical nose' sensors. Nat Nanotechnol 2007; 2(5):318-323.

23. Kumar S, Harrison N, Richards-Kortum R, Sokolov K. Plasmonic nanosensors for imaging intracellular biomarkers in live cells. Nano Lett 2007; 7(5):1338-1343.

24. Castaneda MT, Merkoci A, Pumera M, Alegret S. Electrochemical genosensors for biomedical applications based on gold nanoparticles. Biosens Bioelectron 2007; 22(9-10):1961-1967.

25. Storhoff JJ, Lucas AD, Garimella V, Bao YP, Muller UR. Homogeneous detection of unamplified genomic DNA sequences based on colorimetric scatter of gold nanoparticle probes. Nat Biotechnol 2004; 22(7):883-887.

26. Mirkin CA, Letsinger RL, Mucic RC, Storhoff JJ. A DNA-based method for rationally assembling nanoparticles into macroscopic materials. Nature 1996; 382(6592):607-609.

27. Baptista P, Doria G, Henriques D, Pereira E, Franco R. Colorimetric detection of eukaryotic gene expression with DNA-derivatized gold nanoparticles. J Biotechnol 2005; 119(2):111-117.

28. Doria G, Franco R, Baptista P. Nanodiagnostics: fast colorimetric method for single nucleotide polymorphism/mutation detection. IET Nanobiotechnol 2007; 1(4):53-57.

29. Siegel R, Naishadham D, Jemal A. Cancer statistics, 2012. CA Cancer J Clin 2012; 62(1):10-29.

30. Hanahan D, Weinberg RA. The hallmarks of cancer. Cell 2000; 100(1):57-70.

31. Etzioni R, Urban N, Ramsey S, McIntosh M, Schwartz S, Reid B et al. The case for early detection. Nat Rev Cancer 2003; 3(4):243-252.

32. Conde J, Doria G, Baptista P. Noble metal nanoparticles applications in cancer. J Drug Deliv 2012; 2012:751075.

33. Liu Y, Miyoshi H, Nakamura M. Nanomedicine for drug delivery and imaging: a promising avenue for cancer therapy and diagnosis using targeted functional nanoparticles. Int J Cancer 2007; 120(12):2527-2537.

34. Peer D, Karp JM, Hong S, Farokhzad OC, Margalit R, Langer R. Nanocarriers as an emerging platform for cancer therapy. Nat Nanotechnol 2007; 2(12):751-760.

35. Cuenca AG, Jiang H, Hochwald SN, Delano M, Cance WG, Grobmyer SR. Emerging implications of nanotechnology on cancer diagnostics and therapeutics. Cancer 2006; 107(3):459-466.

36. Ferrari M. Cancer nanotechnology: opportunities and challenges. Nat Rev Cancer 2005; 5(3):161-171.

37. Hannon GJ, Rossi JJ. Unlocking the potential of the human genome with RNA interference. Nature 2004; 431(7006):371-378.

38. Baptista P. Cancer Nanotechnology - Prospects for Cancer Diagnostics and Therapy. Current Cancer Therapy Reviews 2009.

39. Rosi NL, Giljohann DA, Thaxton CS, Lytton-Jean AK, Han MS, Mirkin CA. Oligonucleotide-modified gold nanoparticles for intracellular gene regulation. Science 2006; 312(5776):1027-1030.

40. Giljohann DA, Seferos DS, Prigodich AE, Patel PC, Mirkin CA. Gene regulation with polyvalent siRNA-nanoparticle conjugates. J Am Chem Soc 2009; 131(6):2072-2073.

41. Lee JS, Green JJ, Love KT, Sunshine J, Langer R, Anderson DG. Gold, poly(beta-amino ester) nanoparticles for small interfering RNA delivery. Nano Lett 2009; 9(6):2402-2406.

42. Braun GB, Pallaoro A, Wu G, Missirlis D, Zasadzinski JA, Tirrell M et al. Laser-Activated Gene Silencing via Gold Nanoshell-siRNA Conjugates. ACS Nano 2009.

43. Dobrovolskaia MA, McNeil SE. Immunological properties of engineered nanomaterials. Nat Nanotechnol 2007; 2(8):469-478.

44. Connor EE, Mwamuka J, Gole A, Murphy CJ, Wyatt MD. Gold nanoparticles are taken up by human cells but do not cause acute cytotoxicity. Small 2005; 1(3):325-327.

45. Pan Y, Neuss S, Leifert A, Fischler M, Wen F, Simon U et al. Size-dependent cytotoxicity of gold nanoparticles. Small 2007; 3(11):1941-1949.

46. Bellucci S. Nanoparticles and Nanodevices in Biological Applications. Lecture Notes in Nanoscale Science and Technology ed. Springer; 2009.

5. REVIEW ARTICLES AND BOOK CHAPTER

In order to complement this introduction, we present three review articles and one book chapter on the application of noble metal nanoparticles in cancer diagnostics and therapy.

Review Article A

"Noble Metal Nanoparticles Applications in Cancer." **João Conde**, G. Doria and P.V. Baptista. **Journal of Drug Delivery** (2012), Vol. 2012, pp. 1-12. *Review article*

Book Chapter A

"Multifunctional Gold Nanocarriers for Cancer Theranostics – From bench to bedside and back again?" **João Conde**, F. Tian, P.V. Baptista and J.M. de la Fuente (Submitted, Invited Book Chapter)

Review Article B

"Noble Metal Nanoparticles for Biosensing Applications." G. Doria, **João Conde**, B. Veigas, L. Giestas, C. Almeida, M. Assunção, J. Rosa and P.V. Baptista**. Sensors (Basel)** (2012), Vol. 12, pp. 1657-1687. *Review article (IF= 1.953)*

Review Article C

"Nanophotonics for Molecular Diagnostics and Therapy Applications." **João Conde**, J. Rosa, J.C. Lima and P.V. Baptista. **International Journal of Photoenergy** (2012), Vol. 2012, pp. 1-11. *Review article (IF= 2.663)*

Review Articles A, B, C and **Book Chapter A**

Declaration of authorship

I, João Diogo Osório de Castro Conde, declare that the manuscripts preparation and writing was carried out by me, Prof. Pedro V. Baptista, Prof. Jesus M. de la Fuente, and all the associated co-authors.

I, Pedro V. Baptista, as supervisor of João Conde hereby acknowledge and confirm that the information above is correct.

João Conde

Pedro V. Baptista

Hindawi Publishing Corporation
Journal of Drug Delivery
Volume 2012, Article ID 751075, 12 pages
doi:10.1155/2012/751075

Review Article

Noble Metal Nanoparticles Applications in Cancer

João Conde,[1,2] Gonçalo Doria,[1] and Pedro Baptista[1]

[1] *CIGMH, Departamento de Ciências da Vida, Faculdade de Ciências e Tecnologia, Universidade Nova de Lisboa, Campus de Caparica, 2829-516 Caparica, Portugal*
[2] *Instituto de Nanociencia de Aragón, Universidad de Zaragoza, Pedro Cerbuna 12, 50009 Zaragoza, Spain*

Correspondence should be addressed to Pedro Baptista, pmvb@fct.unl.pt

Received 23 May 2011; Accepted 2 August 2011

Academic Editor: Paulo Cesar de Morais

Nanotechnology has prompted new and improved materials for biomedical applications with particular emphasis in therapy and diagnostics. Special interest has been directed at providing enhanced molecular therapeutics for cancer, where conventional approaches do not effectively differentiate between cancerous and normal cells; that is, they lack specificity. This normally causes systemic toxicity and severe and adverse side effects with concomitant loss of quality of life. Because of their small size, nanoparticles can readily interact with biomolecules both at surface and inside cells, yielding better signals and target specificity for diagnostics and therapeutics. This way, a variety of nanoparticles with the possibility of diversified modification with biomolecules have been investigated for biomedical applications including their use in highly sensitive imaging assays, thermal ablation, and radiotherapy enhancement as well as drug and gene delivery and silencing. Here, we review the available noble metal nanoparticles for cancer therapy, with particular focus on those already being translated into clinical settings.

1. Introduction

Cancer is one of the leading causes of mortality in the modern world, with more than 10 million new cases every year [1]. It is well established that cancer is a multifactorial disease caused by a complex mixture of genetic and environmental factors [2–4], where considerable advances have led to a more comprehensive understanding of cancer at the genetic, molecular, and cellular levels providing new targets and strategies for therapy [5]. Nevertheless, these advances have yet to be effectively translated into functioning diagnostics and therapy. For example, the effectiveness of many anticancer drugs is limited due to the inability to reach the target site in sufficient concentrations and efficiently exert the pharmacological effect without causing irreversible unwanted injury to healthy tissues and cells [6, 7].

The technological leap of controlling materials at nanoscale provides for a "big revolution" in medical and healthcare treatments and therapies [8, 9]. Nanotechnology offers a wealth of tools to diagnose and treat cancer—new imaging agents, multifunctional, targeted devices capable of bypassing biological barriers to deliver therapeutic agents directly to cells and tissues involved in cancer growth and metastasis, monitor predictive molecular changes allowing preventive action against precancerous cells, and minimizing costs and side effects [5, 10, 11]. Nanotechnology-based therapies for cancer with minimal side effects and high specificity are on the surge, where the main challenge is to develop a system for molecular therapy capable of circulating in the blood stream undetected by the immune system and recognize the desirable target, signaling it for effective drug delivery or gene silencing with minimum collateral cell damage—nanovectorization. As a result, personalized medicine could become a reality in cancer patient management.

Nanoparticles (NPs), and noble metal NPs in particular, are versatile agents with a variety of biomedical applications including their use in highly sensitive diagnostic assays [12, 13], thermal ablation, and radiotherapy enhancement [14–17], as well as drug and gene delivery [18–21]. Moreover, noble metal NPs have been proposed as nontoxic carriers for dru and gene-delivery applications [22–24]. Additionally, the nanoparticle-based systems can provide simultaneous diagnostic and therapy, that is, Theranostics, exploring their unique properties for better penetration of therapeutic

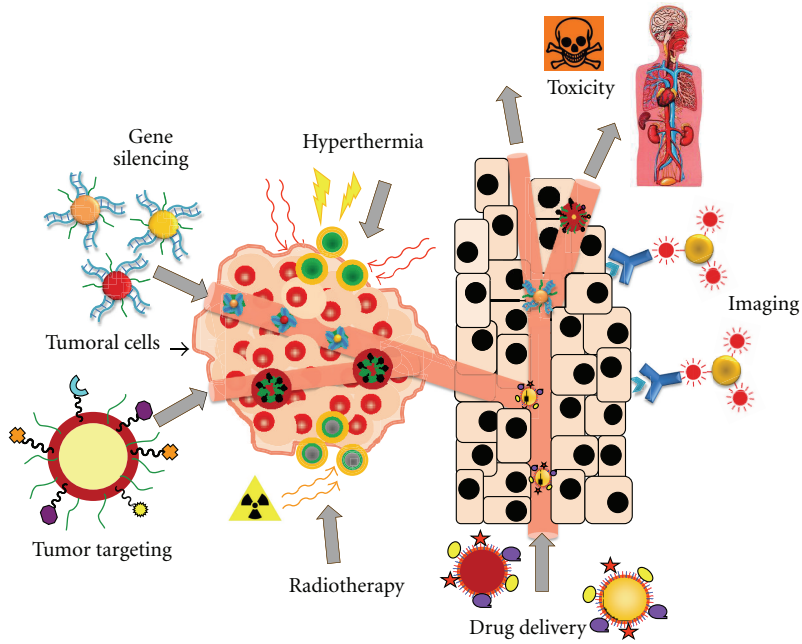

Figure 1: Noble metal NPs for cancer therapy. Once the tumor is directly connected to the main blood circulation system, NPs can exploit several characteristics of the newly formed vasculature and efficiently target tumors. Tumor cells are supplied by blood capillaries that perfuse the cells of the tissue where NPs can (i) passively accumulate or (ii) anchor through targeting moieties to biomarkers overexpress by tumor cells. NPs can act simultaneously as therapeutic agents, inducing hyperthermia, enhancing radiotherapy, silencing genes, and/or delivering drugs to induce tumor cell death, and as imaging enhancers or contrast agents, to help tracking the therapeutic effects in real time.

moieties and tracking within the body, allowing a more efficient therapy with a reduced risk in comparison to conventional therapies [25]—see Figure 1.

The unique characteristics of noble metal NPs, such as high surface-to-volume ratio, broad optical properties, ease of synthesis, and facile surface chemistry and functionalization hold pledge in the clinical field for cancer therapeutics [22, 26, 27]. Noble metal NPs (e.g., gold, silver, or a combination of both) present highly tunable optical properties, which can be easily tuned to desirable wavelengths according to their shape (e.g., nanoparticles, nanoshells, nanorods, etc.), size (e.g., 1 to 100 nm), and composition (e.g., core/shell or alloy noble metals), enabling their imaging and photothermal applications under native tissue [28, 29]. These NPs can also be easily functionalized with various moieties, such as antibodies, peptides, and/or DNA/RNA to specifically target different cells [30] and with biocompatible polymers (e.g., polyethylene glycol and PEG) to prolong their *in vivo* circulation for drug and gene delivery applications [23, 24]. Moreover, they can efficiently convert light or radiofrequencies into heat, thus enabling thermal ablation of targeted cancer cells [31, 32].

In this paper, we will focus on the application of noble metal NPs for cancer therapy with particular emphasis on their use *in vivo* and their potential to be translated into clinical settings.

2. Therapy

In medical terms, a therapeutic effect is a consequence of a medical treatment of any kind, the results of which are judged to be desirable and beneficial [33]. Conventional therapy methods in cancer involve the employment of agents that do not greatly differentiate between cancerous and normal cells, leading to systemic toxicity and adverse and severe side effects [34]. Efficient *in vivo* targeting to heterogeneous population of cancer cells and tissue still requires better selectivity and noncytotoxicity to surrounding healthy cells. However, universally targeting cells within a tumor is not always feasible, because some drugs cannot diffuse efficiently and the random nature of the approach makes it difficult to control the process and may induce multiple-drug resistance—a situation where chemotherapy treatments fail due to resistance of cancer cells towards one or more drugs [7]. Making use of their extraordinary properties, nanotechnology-based systems could offer a less-invasive alternative, enhancing the life expectancy and quality of life of the patient [35]. Among these, the potential therapeutic application of noble metal NPs represents an attractive platform for cancer therapy in a wide variety of targets and clinical settings [36, 37].

2.1. Tumor Targeting. It is expected that the greatest gains in therapeutic selectivity will be achieved by synergistic combinations of several multicomponent targeting strategies that is capable of simultaneously target and deliver multiple therapeutic agents while avoiding the organism's biological and biophysical barriers. NPs targeting strategies to cancerous tissues have focused on passive and active targeting. In passive targeting, because numerous tumors present defective vasculature and poor lymphatic drainage

due to the rapid growth of solid tumors, noble metal NPs can extravasate into the tumor stroma through the fenestrations of the angiogenic vasculature, demonstrating targeting by enhanced permeation and retention, thus accumulation at the tumor site [6, 8, 38]. Additionally, functionalization of the NP's surface with hydrophilic molecules, such as PEG, can also greatly increase their solubility, help evading macrophage-mediated uptake and, thus, avoid removal from the systemic circulation and protect their carriers from enzymatic degradation when used *in vivo* [30]. For active targeting, NPs can be easily functionalized with a wide variety of biological moieties, such as antibodies, peptides, and/or DNA/RNA to specifically target extracellular and intracellular receptors or pathways [30]. The use of NPs functionalized with multiple peptides or antibodies, such as monoclonal antibodies, have been described to successfully target specific cell surface proteins or receptors on cancer cells and further direct their antitumor action, leading to tumor cell death with minimal damage to collateral healthy cells [36, 39–41]. In nucleic-acid functionalized NPs, DNA and RNA macromolecules can be used to simultaneously target specific sequences and exert their genetic-based therapy [42, 43].

To help tracking noble metal NPs *in vivo* and enhance the imaging properties of such moieties, leading to more efficient control of their therapeutic properties, they can also be functionalized with chemical moieties, such as Raman [44, 45] or fluorescent [46, 47] reporters.

2.2. Gene Silencing. Antisense DNA [48, 49] and RNA interference (RNAi) via the use of small-interfering RNA [50–53] have emerged as a powerful and useful tools to block gene function and for sequence-specific posttranscriptional gene silencing, playing an important role in downregulation of specific gene expression in cancer cells.

Small interfering RNAs (siRNAs) can be transfected into mammalian cells by a variety of methods that influence the strength and duration of the silencing response, which in turn is affected by the amount of siRNA that is delivered and on the potential of each siRNA to suppress its target. Thus, one drawback of using naked siRNAs is that they show extremely short half-lives, weak protection against action by RNases, poor chemical stability, and common dissociation from vector [54]. In fact, the major obstacle to clinical application is the uncertainty about how to deliver therapeutic RNAs (e.g., miRNA and/or siRNA) with maximal therapeutic impact. Nanotechnology offers an unprecedented opportunity to overcome these problems, as nanoscale devices, due to their small size, can readily interact with biomolecules on both the surface of cells and inside of cells for longer periods of time [10]. Gold NPs (AuNPs) have shown potential as intracellular delivery vehicles for antisense oligonucleotides [55] and for therapeutic siRNA by providing protection against RNAses and ease of functionalization for selective targeting [42, 43]. For example, Mirkin and coworkers showed that AuNPs attached to single-stranded oligodeoxynucleotides can be used for gene therapy, providing a highly efficient gene regulator in terms of high loading of the antisense DNA with no toxicity at the concentrations studied [55]. They have also shown that polyvalent RNA-AuNP conjugates are readily taken up by cells and that the particle bound siRNA could effectively regulate genes in the context of RNA interference [42]. AuNPs modified with the hydrophilic PEG polymer, siRNAs and then coated with poly(β-aminoester)s have been shown to facilitate high levels of *in vitro* siRNA delivery and gene silencing in human cells [56]. Also, Braun et al. developed an Au-nanoshell functionalized with TAT-lipid layer for transfection and selective release of siRNA [57], where the TAT-lipid coating was used to efficiently mediate the cellular uptake of the nanoconjugates and the siRNA release was dependent on near-infrared (NIR) laser pulses. The authors demonstrated that this NIR strategy for siRNA release was proficient and time dependent.

Several other studies using engineered NPs modified with siRNA have demonstrated a cytoplasmic delivery system of siRNA and efficient gene silencing using AuNPs [42, 56, 58–60].

2.3. Hyperthermia. Hyperthermia is based on the effect increasing temperatures have on living cells, and it is commonly accepted that above 42°C cell viability is strongly reduced. In fact, hyperthermia effects can range from moderate denaturation of blood and extracellular proteins to induction of apoptosis and, above 50°C, to cell death and tissue ablation [61]. Hyperthermia therapy in cancer has been widely used either via direct irradiation or suitable temperature vectors, such as metal NPs [62]. In nanoparticle-mediated hyperthermia for cancer, NPs heat up cancerous cells beyond their temperature tolerance limits, which are lower than normal healthy tissue due to their poor blood supply, killing them selectively. This can be achieved by exposing the entire patient or the targeted area to an alternating current magnetic field, an intense light source or radiofrequencies which will cause the NPs to heat up and induce thermal ablation of the tumor. One of the most widespread examples of hyperthermia mediated by NPs, magnetic NPs have been introduced in the body through magnetic delivery systems or local injection to the affected area [63]. The first *in vivo* Phase II clinical trials of magnetic NP hyperthermia were undertaken in Germany in 2005 [64] by injecting the prostate of cancer patients with biocompatible magnetite NPs. Successful results were obtained using minimally invasive ablation of the tumor in an AC magnetic field after several sessions.

Noble metal NPs have thoroughly been used as photothermal agents for *in vivo* therapy as a less invasive experimental technique that holds great promise for the treatment of cancer [65]. It combines two key components: (i) light source, such as lasers with a spectral range of 650–900 nm [66] for deep tissue penetration and (ii) optical absorbing NPs which efficiently transforms the optical irradiation into heat on a picosecond time scale, thus inducing photothermal ablation [67, 68]. For example, Huang and coworkers demonstrated that Au-nanorods are effective photothermal agents due to their longitudinal absorption band in the NIR on account of their SPR oscillations [65, 66, 69]. Small diameter Au-nanorods are being used as photothermal converters of near infrared radiation (NIR) for *in vivo* applications due

to their high absorption cross-sections beyond the tissue absorption spectra. Since NIR light transmits readily through human skin and tissue, these nanorods can be used as ablation components for cancer [70, 71]. Other gold nanostructures such as Au-nanoshells [72–74], Au-nanocages [67, 75, 76], and spherical AuNPs [77] have also demonstrated effective photothermal destruction of cancer cells and tissue. PEG-modified Au-nanoshells (Silica/Au core/shell NPs) injected intravenously in tumor-bearing mice showed to passively accumulate in the tumor tissue due to the leakiness of the tumor vasculature. The rapid heating of Au-nanoshells upon NIR laser irradiation allowed for effective photothermal ablation of tumor in the mouse [78]. A similar approach was used by Terentyuk et al., where plasmonic silica/gold nanoshells were used to produce a controllable laser hyperthermia in tissues, thus enhancing the photothermal effect in cancer cells [79]. Sirotkina et al. described the use of AuNPs for skin tumor therapy based on local laser-inducing hyperthermia. After intravenous injection, the AuNPs accumulated in the skin tumor cells after 4-5 hours and induced apoptotic death of tumor cells, completely inhibiting the tumor growth after just five days of treatment [80].

The photothermal properties of AuNPs can also be used to generate transient vapor nanobubbles in order to produce a tunable nanoscale theranostic agent, described as plasmonic nanobubbles [81]. These nanobubbles are generated when the AuNPs are locally overheated with short laser pulses, due to the evaporation of a very thin volume of the surrounding medium, which in turn creates a vapor nanobubble that expands and collapses within nanoseconds. Plasmonic nanobubbles have been successfully applied as an *in vivo* tunable theranostic cellular agent in zebrafish hosting prostate cancer xenografts and in leukemia cells of human bone marrow specimens, presenting higher therapeutic selectivity when compared with AuNPs alone [82, 83]. The use of noninvasive radiowaves at 13.56 MHz have also been shown to induce heat in AuNPs and thermally destroy tumor tissue [84]. *In vivo* rat exposures to 35 Watts using direct AuNPs injections resulted in significant thermal injury at subcutaneous injection sites. Radio waves have the advantage of presenting significantly better penetration on tissue than NIR light, making them more efficient for deeper solid tumors [85]. Nonetheless, despite their greater depth of penetration, there is also greater energy attenuation by tissue.

Gold-silver-(AuAg-) nanorods labeled with molecular aptamers proved to require up to six orders of lower laser power irradiation to induce cell death when compared to Au-nanoshells or Au-nanorods [86]. These aptamer Scg8-AuAg-nanorods conjugates presented excellent hyperthermia efficiency and selectivity to CEM cells, exceeding the affinity of the original aptamer probes alone. Bimetallic AuAg-nanostructures with a dendrite morphology and hollow interior have also been developed as photothermal absorbers to destroy A549 lung cancer cells [87]. The photothermal performance of such dendrites required lower NP concentrations and laser power for efficient cancer cell damage when compared to Au-nanorods photothermal therapeutic agents. Likewise, Cheng and coworkers evaluated the photothermal efficiencies of three Au-based nanomaterials (silica@Au-nanoshells, hollow Au/Ag nanospheres and Au-nanorods) at killing three types of malignant cells (A549 lung cancer cells, HeLa cervix cancer cells, and TCC bladder cancer cells) using a CW NIR laser [88]. Silica@Au-nanoshells needed the lowest NP concentration for effective photo-ablation, whereas hollow Au/Ag nanospheres and Au-nanorods needed increasingly higher concentrations.

Gold has also been used together with magnetic or paramagnetic materials to enhance the photothermal effect and, thus, increase cancer cell death [89, 90].

2.4. Drug Delivery. The vast majority of clinically used drugs for cancer are low molecular-weight compounds that diffuse rapidly into healthy tissues being evenly distributed within the body, exhibit a short half-life in the blood stream and a high overall clearance rate. As a consequence, relatively small amounts of the drug reach the target site, and distribution into healthy tissues leads to severe side effects. Poor drug delivery and residence at the target site leads to significant complications, such as multidrug resistance [91]. As seen above, nanoparticles can be used as vectors for targeting cancer tissue/cells so as to optimize biodistribution of drugs. The NPs' performance as drug vectors depends on the size and surface functionalities of the particles, drug release rate, and particle disintegration. These systems show evidence of enhanced delivery of unstable drugs, more targeted distribution and capability to evade/bypass biological barriers.

AuNPs have already been used as vehicles for the delivery of anticancer drugs, such as paclitaxel- [92] or Platinum-(Pt-) based drugs (e.g., cisplatin, oxaliplatin, etc.) [93, 94]. Gibson et al. described the first example of 2 nm AuNPs covalently functionalized with the chemotherapeutic drug paclitaxel [92]. The administrations of hydrophobic drugs require molecular encapsulation, and it is found that nanosized particles are particularly efficient in evading the reticuloendothelial system [95]. Gold-gold sulfide nanoshells covered by a thermosensitive hydrogel matrix have been developed as a photothermal modulated drug-delivery system [96]. These nanoshell-composite hydrogels were designed to strongly absorb NIR light and release multiple bursts of any soluble material held within the hydrogel matrix in response to repeated NIR irradiation. More recently, Yavuz and coworkers developed a similar approach using 50-nm hollow Au-nanocubes (nanocages) with eight lopped-off porous corners covered by a thermosensitive polymer containing a preloaded effector that can be later released in a controllable fashion using an NIR laser [18].

2.5. Radiotherapy. Radiotherapy uses ionizing radiation for cancer treatment to control the proliferation of malignant cells. Nonetheless, the delivery of a lethal dose of radiation to a tumor while sparing nearby healthy tissues remains the greatest challenge in radiation therapy. Noble metal NPs can act as antennas, providing enhanced radiation targeting with lower radiation doses, consequently avoiding damage to healthy tissues. The irradiation may also be used to activate the NPs and set up the release of their cytotoxic action. AuNPs, upon X-ray irradiation, can act as dose enhancers and/or generate radicals that damage cancer cells and induce

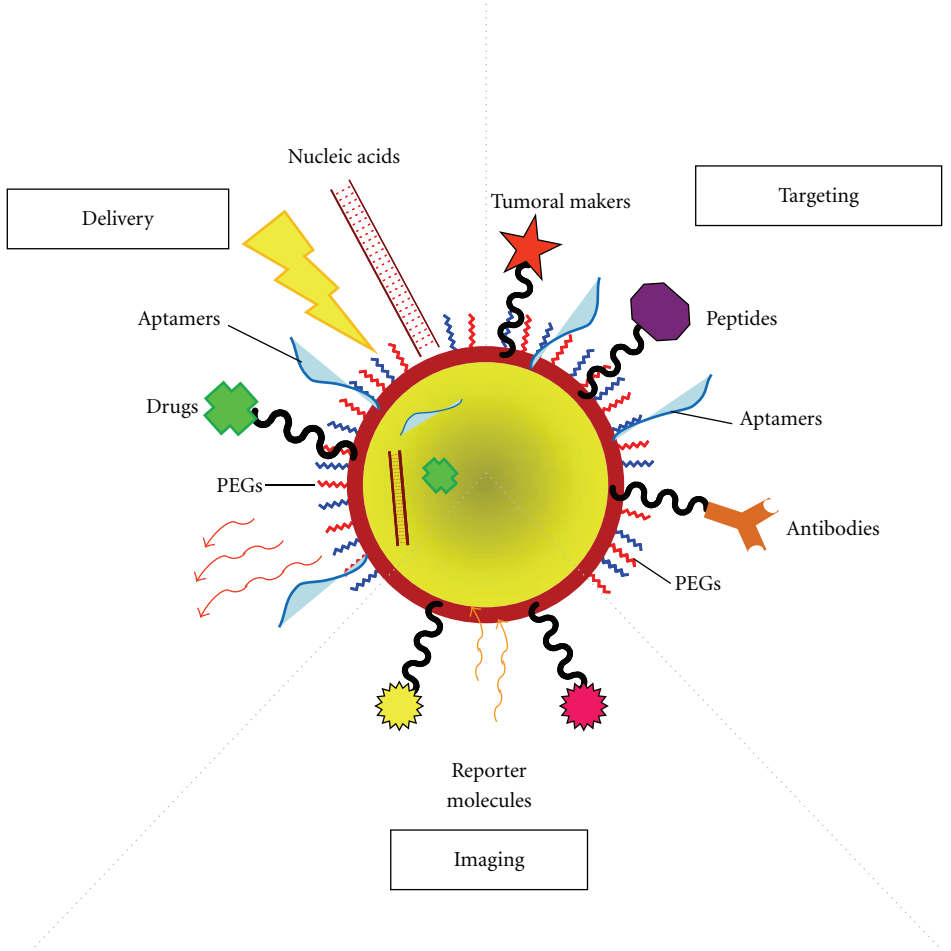

Figure 2: Multifunctional NP-based systems for tumor targeting, delivery and imaging. These innovative NPs comprise nucleic acids, aptamers and anticancer drug molecules for delivery to the target tissue. Depending on the targeting mechanism, they can be on the surface or inside the NPs. Responsive NPs/molecules can also trigger reaction upon external stimuli through the functionality of valuable tumor markers, peptides, polymers and antibodies that can used to improve NP circulation, effectiveness and selectivity. Multifunctional systems can carry reporter molecules tethered to the particle surface and employed as tracking and/or contrast agents.

cell apoptosis and have been proposed as potential radiosensitizers for X-ray cancer therapy [97]. The use of this strategy has led to improvement in the treatment on cancer cells with little or no increase in harm to normal surrounding tissues in mice models [15] and also in breast cancer [98]. More recently, Xu and coworkers studied the potential effects on radiation-induced killing of glioma cells mediated by 10, 20, and 40 nm AuNPs and 20, 50, and 100 nm silver nanoparticles (AgNPs), all modified with proteins from fetal bovine serum [99]. Treating glioma cells with AgNPs led to radiation dose-dependent cytotoxicity, with smaller size particles (20 and 50 nm) being the most cytotoxic at relatively harmless radiation doses. In this study, AuNPs showed little effect on cell survival across different doses of ionizing radiation, which contrasted with the results of previous studies performed with AuNPs coated with PEG or amino acids in mice colorectal adenocarcinoma and breast cancer cells [15, 98]. Hypothetically, the different coatings of the AuNPs used may be responsible for the different outcomes observed.

The use of platinum NPs (PtNPs) as prominent radiation sensitizers in radiotherapy cancer treatment showed strong enhancement of the biological efficiency of radiations, leading to amplified lethal damage in DNA from tumor cells, when compared to metal atoms [37].

3. Imaging

Along with their therapeutic capabilities, most noble metal NPs can be used for the simultaneous actuation and tracking *in vivo*—see Figure 2. Because light absorption from biologic tissue components is minimized at near infrared (NIR) wavelengths, most noble metal NPs for *in vivo* imaging and therapy have been designed to strongly absorb in the NIR so as to be used as effective contrast agents [100]. However, noble metal nanomaterials, such as NPs, nanoshells, nanoclusters, nanocages, and nanorods, have showed widespread application as contrast agents for *in vivo* cancer imaging: those presenting a significant absorbance and scattering in the NIR region [46, 101] or surface-enhanced Raman scattering (SERS) [102], or as contrast agents for computed

tomography (CT) [103], magnetic resonance imaging (MRI) [104], optical coherence tomography (OCT) [105–107], and photoacoustic imaging (PAI) [108]. Moreover, most noble metal nanomaterials are capable of combining multiple imaging modalities that can yield complementary information and offer synergistic advantages over any single imaging technique [109, 110].

Three-dimensional imaging can be achieved by computed tomography (CT), where a series of plane-cross-sectional images along an axis are interlinked by computer to create a 3D image. Typically, the cross-sectional images are acquired using X-ray radiation involving larger radiation doses than the conventional X-ray imaging procedures, which could lead to increased risk to public health [111]. The use of ~30 nm PEG-coated AuNPs for *in vivo* CT contrast agent was shown to increase image contrast, which allows to reduce the radiation dosage needed, allow to overcome the limitations of conventional contrast agents (e.g., iodine-based compounds), such as short imaging times due to rapid renal clearance, renal toxicity, and vascular permeation [103]. Hybrid NPs with a super-paramagnetic iron oxide/silica core and a gold nanoshell, with significant absorbance and scattering in the NIR region, have been used *in vivo* as dual contrast agents for CT and magnetic resonance imaging (MRI) presenting high CT attenuation and a good MR signal in hepatoma, compensating for the weakness of each modality [112].

Optical coherence tomography (OCT) is an imaging modality that provides cross-sectional subsurface imaging of biological tissue with micrometer scale resolution. The extra scattering achieved by using Au-nanoshells has been shown to provide an enhanced optical contrast and brightness for improved diagnostic imaging of tumors in mice due to the preferential accumulation of the nanoshells in the tumor. [78]. Tseng et al. developed nanorings with a localized surface plasmon resonance covering a spectral range of 1300 nm that produced both photothermal and image contrast enhancement effects in OCT when delivered into pig adipose samples [113]. Moreover, the image contrast enhancement effect could be isolated by continuously scanning the sample with a lower scan frequency, allowing to effectively control the therapeutic modality. Similarly, gold capped nanoroses have been used in photothermal OCT to detect macrophages in *ex vivo* rabbit arteries [114].

Photoacoustic imaging (PAI) and photoacoustic tomography (PAT) are noninvasive imaging techniques capable of resolving the optical absorption map of tissue at penetration depths akin with ultrasound imaging. Wang and coworkers have used this technique to image the distribution of Au-nanoshells circulating in the vasculature of a rat brain by achieving a gradual enhancement of the NIR optical absorption in the brain vessels [115]. These Au-nanocages enhanced the contrast between blood and the surrounding tissues by up to 81%, allowing a more detailed image of vascular structures at greater depths. Additionally, these nanocages were shown to be better suited for *in vivo* applications, specially due to their more compact size (<50 nm compared to >100 nm for Au-nanoshells) and larger optical absorption cross sections when compared to Au-nanoshells. Gold-nanorods show the maximum of the plasmon resonance tuned further into the NIR that allowed Motamedi et al. to develop a contrast agent for a laser optoacoustic imaging system for *in vivo* detection of gold nanorods and to enhance the diagnostic power of optoacoustic imaging [116]. Song et al. proposed a noninvasive *in vivo* spectroscopic photoacoustic sentinel lymph node mapping using gold nanorods as lymph node tracers in a rat model [117].

Also, noble metal NP probes can be used for *in situ* diagnostics of cancer. For example, NP-based NIR probes can overcome several limitations of conventional NIR organic dyes, such as poor hydrophilicity and photostability, low quantum yield and detection sensitivity, insufficient stability in biological systems, and weak multiplexing capability. Additionally, the high scattering properties of these NPs can enhance contrast of imaging systems based on microscopy, such as dark-field or dual-photon luminescence microscopy. Zhang et al. developed fluorescent metal nanoshells as molecular imaging agents to detect single microRNA (miRNA) molecules in lung cancer cells [47]. These metal nanoshells were composed of silica spheres with encapsulated $Ru(bpy)_3^{2+}$ complexes as core and thin silver layers as shell. The silver shell allowed to enhance emission intensity up to 6-fold and photostability by 2-fold, as well as to achieve longer lifetime emission signals that overcome cellular autofluorescence interference. Loo et al. demonstrated the use of NIR scattering Au-nanoshells as a contrast agent in dark-field microscopy to target antihuman epidermal growth factor receptor 2 (HER2), a clinically significant breast cancer molecular marker [72]. These Au-nanoshells were also used by Bickford et al. for imaging live HER2-overexpressing cancer cells using two-photon microscopy [118].

Surface-enhanced Raman scattering (SERS) using Au- or AgNPs with an attached reporter species with a Raman signature can be explored to highlight cellular structures and provide molecular structural information on the cellular environment in live cells [119, 120]. The use of such NPs allows for higher spectral specificity, multiplex capabilities, improved contrast and photostability to Raman-based imaging techniques. *In situ* monitoring of photothermal nanotherapy of LNCaP human prostate cancer cells by SERS was a significant enhancement of the Raman signal intensity by several orders of magnitude that have been observed [44].

4. Toxicity

Both *in vivo* and *in vitro*, nanoparticles have a tendency to accumulate within various types of cells with special affinity for macrophage-type cells (both histiocytes and blood phagocytic cells) and reticuloendothelial cells throughout the body. They also produce varying degrees of bioaccumulation in such tissues as lymph nodes, bone marrow, spleen, adrenals, liver, and kidneys [121–123]. The NPs size plays an important role in avoiding immune activation and renal clearance, thus enhancing their circulating time and availability for effective therapy. For example, hydrophilic NPs ranging in size between 10 and 100 nm are small enough to slow down activation of the mononuclear phagocyte

system but are big enough to avoid renal filtration [8]. Research shows that NPs can stimulate and/or suppress the immune responses and that their compatibility with the immune system is largely determined by their surface chemistry. In fact, the influence of size, solubility, and surface modification on the biocompatibility of NPs and their use in biological applications is well known [122]. In terms of acute toxic effects to cells, noble metal NPs have been shown to induce DNA damage and oxidative damage [124–126].

Generally, AuNPs are considered to be benign, but the size similarity to biological molecules could provide "camouflage" to cellular barriers, leading to undesired cellular entry which might be detrimental to normal cellular function [127]. A systematic investigation of the size-dependent cytotoxicity of AuNPs against four cell lines found that 1 to 2 nm AuNPs displayed cell-type-dependent cytotoxicity with high micromolar IC50s, whereas 15 nm AuNPs were nontoxic to cells at concentrations 60-fold higher than the IC50 of the smaller AuNPs [128]. These results seemed to confirm size-dependent toxicity of AuNPs, an inference that has hitherto been shown to be somewhat ambivalent [129–134]. In fact, Yen et al. showed that AuNPs, especially those of smaller sizes, dramatically led to a decrease in the population of the macrophages and upregulated the expressions of proinflammatory genes interlukin-1, interlukin-6, and tumor necrosis factor alpha [135]. Sun et al. studied the *in vivo* toxicity of AuNPs according to their shape in KM mice showing that rod-shaped AuNPs were the most toxic, followed by cube-shaped AuNPs, while sphere-shaped AuNPs displayed the best biocompatibility, revealing that toxicity is shape dependent. Moreover, this study revealed that all AuNPs accumulated preferentially in the liver and spleen organs [136]. Nonetheless, it is worth pointing out that CTAB (a cationic surfactant commonly used for Au-nanorods synthesis) was also recently pointed out as the source of Au-nanorods' cytotoxicity, which may explain their toxicity in the previous studies [137].

Silver NPs are generally considered more toxic than AuNPs, with several studies showing that cell exposure to AgNPs induced significant cytotoxicity [138–141]. Conversely, Yen et al. determined a lower cytotoxicity of AgNPs than that of the AuNPs and attributed this difference to the surface charges between NPs, which can explain the discrepancy with other studies related to AgNPs cytotoxicity [135].

As for platinum, the cytotoxicity of 5–8 nm PtNPs capped with polyvinyl alcohol (PVA) has been addressed in human cells, where PtNPs were shown to enter the cells through diffusion, leading to an increase in DNA damage, proliferating cell nuclear antigen-mediated growth arrest and apoptosis [126]. Asharani et al. performed a comparison between toxicity of 3–10 nm Pt-, 5–35 nm Ag-, and 15–35 nm AuNPs capped with PVA in developing zebrafish embryos, concluding that AgNPs were the most toxic, followed by PtNPs, while AuNPs presented no indication of toxicity [142].

Even though we have focused our attention on the toxicity aspects of the different noble metal nanoparticles based mainly on size and metal, attention should also be brought upon other properties of the nanoconjugates, such as surface chemistry, shape, and administration pathways. In fact, surface chemistry (e.g., functionalization with biomolecules, stabilizers, etc.) constitutes another interface of interaction with the organism's proteins and cells, which in term may be associated with unspecific adsorption or specific recognition by the immune system, thus contributing to the overall effects of the use of the nanoparticles. The interaction with the immune system contributes not only for the specificity of the targeting (passive and/or active), but also towards the toxicological effect of nanoconjugates (see [122] and references therein).

5. Conclusions

Nanotechnology has provided for novel and powerful systems that may be used treatment and diagnostic of cancer. *In vivo* demonstrations of noble metal NPs as theranostic agents are now emerging and serve as important milestones towards clinical application. Nonetheless, the majority of products, reagents and drugs being used for the development of these nanoscale theranostic agents have still to be approved by the main supervising agencies, such as the FDA and EMA. Thus far, there are some questions whose answers still provide no clear understanding about the design and application of NPs, such as pharmacokinetics, biodistribution and side effects of the nanotherapy, and safety profile of NPs before and after conjugation and toxicity [10]. Are noble metal NPs cytotoxic or biocompatible? And how can the NPs be design to avoid these effects? These seem to question more difficult to answer than previously believed. Most therapeutic and imaging approaches based on noble metal NPs rely on AuNPs, mostly due to their higher level of nontoxicity. Nonetheless, a more comprehensive application of core/shell or alloy noble metal NPs, that may allow combination of the benefits of each noble metal into a single carrier, is still to be thoroughly addressed. Even though there is not any general mechanism for making NPs universally "nontoxic" to all living cells and all organisms, there are important findings that can be applied for increasing nanoparticle biocompatibility and reducing cytotoxic interactions *in vivo* and *in vitro*. In general, using the lowest NP dose to get the desired response for the shortest period of time seems to promote biocompatibility. The coating/capping of a nanoparticle is also of the utmost relevance, since a noncontinuous covering, the presence of cracks, roughness, or interruptions could lead to complement or antibody attachment, or dissolution of the coating by cell digestion, decreasing bioavailability at target cell [143]. It is essential to test nanoparticle/biological interactions experimentally and modify the NPs for best biocompatibility with the cell in order to eliminate damage to healthy tissue, guarding against alterations in genetic/molecular function while killing the abnormal cells. When interpreting NPs interactions with biological cells and organisms, it is important to remember that living systems may appear normal and be capable of growth and function, but they may be genetically altered in subtle ways following NP exposure, which can produce serious consequences at some time in the distant future, such as cancer itself.

Noble metal nanoparticles have shown to be powerful tools against cancer though still in need of further optimization and characterization for full understanding of their whole potential. It is now time to start translating these promising platforms to the clinical settings towards widespread effective therapy strategies in the fight against cancer.

Acknowledgments

The authors acknowledge FCT/MCTES (Portugal) and CIGMH for financial support.

References

[1] A. Jemal, R. Siegel, J. Xu, and E. Ward, "Cancer statistics, 2010," *CA Cancer Journal for Clinicians*, vol. 60, no. 5, pp. 277–300, 2010.

[2] A. Balmain, J. Gray, and B. Ponder, "The genetics and genomics of cancer," *Nature Genetics*, vol. 33, pp. 238–244, 2003.

[3] D. Hanahan and R. A. Weinberg, "The hallmarks of cancer," *Cell*, vol. 100, no. 1, pp. 57–70, 2000.

[4] B. A. J. Ponder, "Cancer genetics," *Nature*, vol. 411, no. 6835, pp. 336–341, 2001.

[5] N. P. Praetorius and T. K. Mandal, "Engineered nanoparticles in cancer therapy," *Recent Patents on Drug Delivery & Formulation*, vol. 1, no. 1, pp. 37–51, 2007.

[6] M. Ferrari, "Cancer nanotechnology: opportunities and challenges," *Nature Reviews Cancer*, vol. 5, no. 3, pp. 161–171, 2005.

[7] D. Peer, J. M. Karp, S. Hong, O. C. Farokhzad, R. Margalit, and R. Langer, "Nanocarriers as an emerging platform for cancer therapy," *Nature Nanotechnology*, vol. 2, no. 12, pp. 751–760, 2007.

[8] P. R. Gil and W. J. Parak, "Composite nanoparticles take aim at cancer," *ACS Nano*, vol. 2, no. 11, pp. 2200–2205, 2008.

[9] N. Sanvicens and M. P. Marco, "Multifunctional nanoparticles—properties and prospects for their use in human medicine," *Trends in Biotechnology*, vol. 26, no. 8, pp. 425–433, 2008.

[10] P. V. Baptista, "Cancer nanotechnology—prospects for cancer diagnostics and therapy," *Current Cancer Therapy Reviews*, vol. 5, no. 2, pp. 80–88, 2009.

[11] J. R. Heath and M. E. Davis, "Nanotechnology and cancer," *Annual Review of Medicine*, vol. 59, pp. 251–265, 2008.

[12] S. T. Selvan, T. T. Y. Tan, D. K. Yi, and N. R. Jana, "Functional and multifunctional nanoparticles for bioimaging and biosensing," *Langmuir*, vol. 26, no. 14, pp. 11631–11641, 2010.

[13] P. Baptista, E. Pereira, P. Eaton et al., "Gold nanoparticles for the development of clinical diagnosis methods," *Analytical and Bioanalytical Chemistry*, vol. 391, no. 3, pp. 943–950, 2008.

[14] X. Huang, P. K. Jain, I. H. El-Sayed, and M. A. El-Sayed, "Gold nanoparticles: interesting optical properties and recent applications in cancer diagnostics and therapy," *Nanomedicine*, vol. 2, no. 5, pp. 681–693, 2007.

[15] J. F. Hainfeld, D. N. Slatkin, and H. M. Smilowitz, "The use of gold nanoparticles to enhance radiotherapy in mice," *Physics in Medicine and Biology*, vol. 49, no. 18, pp. N309–N315, 2004.

[16] J. F. Hainfeld, F. A. Dilmanian, D. N. Slatkin, and H. M. Smilowitz, "Radiotherapy enhancement with gold nanoparticles," *Journal of Pharmacy and Pharmacology*, vol. 60, no. 8, pp. 977–985, 2008.

[17] L. R. Hirsch, R. J. Stafford, J. A. Bankson et al., "Nanoshell-mediated near-infrared thermal therapy of tumors under magnetic resonance guidance," *Proceedings of the National Academy of Sciences of the United States of America*, vol. 100, no. 23, pp. 13549–13554, 2003.

[18] M. S. Yavuz, Y. Cheng, J. Chen et al., "Gold nanocages covered by smart polymers for controlled release with near-infrared light," *Nature Materials*, vol. 8, no. 12, pp. 935–939, 2009.

[19] G. Han, P. Ghosh, and V. M. Rotello, "Multi-functional gold nanoparticles for drug delivery," *Advances in Experimental Medicine and Biology*, vol. 620, pp. 48–56, 2007.

[20] M. Thomas and A. M. Klibanov, "Conjugation to gold nanoparticles enhances polyethylenimine's transfer of plasmid DNA into mammalian cells," *Proceedings of the National Academy of Sciences of the United States of America*, vol. 100, no. 16, pp. 9138–9143, 2003.

[21] M. R. Jones, J. E. Millstone, D. A. Giljohann, D. S. Seferos, K. L. Young, and C. A. Mirkin, "Plasmonically controlled nucleic acid dehybridization with gold nanoprisms," *ChemPhysChem*, vol. 10, no. 9-10, pp. 1461–1465, 2009.

[22] S. Bhattacharyya, R. A. Kudgus, R. Bhattacharya, and P. Mukherjee, "Inorganic nanoparticles in cancer therapy," *Pharmaceutical Research*, vol. 28, no. 2, pp. 237–259, 2011.

[23] P. Ghosh, G. Han, M. De, C. K. Kim, and V. M. Rotello, "Gold nanoparticles in delivery applications," *Advanced Drug Delivery Reviews*, vol. 60, no. 11, pp. 1307–1315, 2008.

[24] N. Nishiyama, "Nanomedicine: nanocarriers shape up for long life," *Nature Nanotechnology*, vol. 2, no. 4, pp. 203–204, 2007.

[25] J. Xie, S. Lee, and X. Chen, "Nanoparticle-based theranostic agents," *Advanced Drug Delivery Reviews*, vol. 62, no. 11, pp. 1064–1079, 2010.

[26] T. K. Sau, A. L. Rogach, F. Jäckel, T. A. Klar, and J. Feldmann, "Properties and applications of colloidal nonspherical noble metal nanoparticles," *Advanced Materials*, vol. 22, no. 16, pp. 1805–1825, 2010.

[27] R. A. Sperling, P. R. Gil, F. Zhang, M. Zanella, and W. J. Parak, "Biological applications of gold nanoparticles," *Chemical Society Reviews*, vol. 37, no. 9, pp. 1896–1908, 2008.

[28] P. K. Jain, X. Huang, I. H. El-Sayed, and M. A. El-Sayed, "Noble metals on the nanoscale: optical and photothermal properties and some applications in imaging, sensing, biology, and medicine," *Accounts of Chemical Research*, vol. 41, no. 12, pp. 1578–1586, 2008.

[29] K. S. Lee and M. A. El-Sayed, "Gold and silver nanoparticles in sensing and imaging: sensitivity of plasmon response to size, shape, and metal composition," *Journal of Physical Chemistry B*, vol. 110, no. 39, pp. 19220–19225, 2006.

[30] R. A. Sperling and W. J. Parak, "Surface modification, functionalization and bioconjugation of colloidal Inorganic nanoparticles," *Philosophical Transactions of the Royal Society A*, vol. 368, no. 1915, pp. 1333–1383, 2010.

[31] H. Chen, L. Shao, T. Ming et al., "Understanding the photothermal conversion efficiency of gold nanocrystals," *Small*, vol. 6, no. 20, pp. 2272–2280, 2010.

[32] E. S. Day, J. G. Morton, and J. L. West, "Nanoparticles for thermal cancer therapy," *Journal of Biomechanical Engineering*, vol. 131, no. 7, Article ID 740011, 2009.

[33] P. Chandra, D. Das, and A. A. Abdelwahab, "Gold nanoparticles in molecular diagnostics and therapeutics," *Digest Journal of Nanomaterials and Biostructures*, vol. 5, no. 2, pp. 363–367, 2010.

[34] Y. Liu, H. Miyoshi, and M. Nakamura, "Nanomedicine for drug delivery and imaging: a promising avenue for cancer therapy and diagnosis using targeted functional nanoparticles," *International Journal of Cancer*, vol. 120, no. 12, pp. 2527–2537, 2007.

[35] A. G. Cuenca, H. Jiang, S. N. Hochwald, M. Delano, W. G. Cance, and S. R. Grobmyer, "Emerging implications of nanotechnology on cancer diagnostics and therapeutics," *Cancer*, vol. 107, no. 3, pp. 459–466, 2006.

[36] A. C. Powell, G. F. Paciotti, and S. K. Libutti, "Colloidal gold: a novel nanoparticle for targeted cancer therapeutics," *Methods in Molecular Biology*, vol. 624, pp. 375–384, 2010.

[37] E. Porcel, S. Liehn, H. Remita et al., "Platinum nanoparticles: a promising material for future cancer therapy?" *Nanotechnology*, vol. 21, no. 8, p. 85103, 2010.

[38] C. Minelli, S. B. Lowe, and M. M. Stevens, "Engineering nanocomposite materials for cancer therapy," *Small*, vol. 6, no. 21, pp. 2336–2357, 2010.

[39] T. Stuchinskaya, M. Moreno, M. J. Cook, D. R. Edwards, and D. A. Russell, "Targeted photodynamic therapy of breast cancer cells using antibody-phthalocyanine-gold nanoparticle conjugates," *Photochemical and Photobiological Sciences*, vol. 10, no. 5, pp. 822–831, 2011.

[40] V. Raji, J. Kumar, C. S. Rejiya, M. Vibin, V. N. Shenoi, and A. Abraham, "Selective photothermal efficiency of citrate capped gold nanoparticles for destruction of cancer cells," *Experimental Cell Research*, vol. 317, no. 14, pp. 2052–2058, 2011.

[41] P. Mukherjee, R. Bhattacharya, N. Bone et al., "Potential therapeutic application of gold nanoparticles in B-chronic lymphocytic leukemia (BCLL): enhancing apoptosis," *Journal of Nanobiotechnology*, vol. 5, p. 4, 2007.

[42] D. A. Giljohann, D. S. Seferos, A. E. Prigodich, P. C. Patel, and C. A. Mirkin, "Gene regulation with polyvalent siRNA-nanoparticle conjugates," *Journal of the American Chemical Society*, vol. 131, no. 6, pp. 2072–2073, 2009.

[43] K. A. Whitehead, R. Langer, and D. G. Anderson, "Knocking down barriers: advances in siRNA delivery," *Nature Reviews Drug Discovery*, vol. 8, no. 2, pp. 129–138, 2009.

[44] W. Lu, A. K. Singh, S. A. Khan, D. Senapati, H. Yu, and P. C. Ray, "Gold nano-popcorn-based targeted diagnosis, nanotherapy treatment, and in situ monitoring of photothermal therapy response of prostate cancer cells using surface-enhanced raman spectroscopy," *Journal of the American Chemical Society*, vol. 132, no. 51, pp. 18103–18114, 2010.

[45] X. Qian, X. H. Peng, D. O. Ansari et al., "In vivo tumor targeting and spectroscopic detection with surface-enhanced Raman nanoparticle tags," *Nature Biotechnology*, vol. 26, no. 1, pp. 83–90, 2008.

[46] X. He, J. Gao, S. S. Gambhir, and Z. Cheng, "Near-infrared fluorescent nanoprobes for cancer molecular imaging: status and challenges," *Trends in Molecular Medicine*, vol. 16, no. 12, pp. 574–583, 2010.

[47] J. Zhang, Y. Fu, Y. Mei, F. Jiang, and J. R. Lakowicz, "Fluorescent metal nanoshell probe to detect single mirna in lung cancer cell," *Analytical Chemistry*, vol. 82, no. 11, pp. 4464–4471, 2010.

[48] Y. Fichou and C. Férec, "The potential of oligonucleotides for therapeutic applications," *Trends in Biotechnology*, vol. 24, no. 12, pp. 563–570, 2006.

[49] N. Toub, C. Malvy, E. Fattal, and P. Couvreur, "Innovative nanotechnologies for the delivery of oligonucleotides and siRNA," *Biomedicine and Pharmacotherapy*, vol. 60, no. 9, pp. 607–620, 2006.

[50] A. Fire, S. Xu, M. K. Montgomery, S. A. Kostas, S. E. Driver, and C. C. Mello, "Potent and specific genetic interference by double-stranded RNA in caenorhabditis elegans," *Nature*, vol. 391, no. 6669, pp. 806–811, 1998.

[51] M. Baker, "RNA interference: from tools to therapies," *Nature*, vol. 464, no. 7292, p. 1225, 2010.

[52] O. Milhavet, D. S. Gary, and M. P. Mattson, "RNA interference in biology and medicine," *Pharmacological Reviews*, vol. 55, no. 4, pp. 629–648, 2003.

[53] N. R. Wall and Y. Shi, "Small RNA: can RNA interference be exploited for therapy?" *The Lancet*, vol. 362, no. 9393, pp. 1401–1403, 2003.

[54] G. J. Hannon and J. J. Rossi, "Unlocking the potential of the human genome with RNA interference," *Nature*, vol. 431, no. 7006, pp. 371–378, 2004.

[55] N. L. Rosi, D. A. Giljohann, C. S. Thaxton, A. K. R. Lytton-Jean, M. S. Han, and C. A. Mirkin, "Oligonucleotide-modified gold nanoparticles for infracellular gene regulation," *Science*, vol. 312, no. 5776, pp. 1027–1030, 2006.

[56] J. S. Lee, J. J. Green, K. T. Love, J. Sunshine, R. Langer, and D. G. Anderson, "Gold, poly(β-amino ester) nanoparticles for small interfering RNA delivery," *Nano Letters*, vol. 9, no. 6, pp. 2402–2406, 2009.

[57] G. B. Braun, A. Pallaoro, G. Wu et al., "Laser-activated gene silencing via gold nanoshell-siRNA conjugates," *ACS Nano*, vol. 3, no. 7, pp. 2007–2015, 2009.

[58] S. Guo, Y. Huang, Q. Jiang et al., "Enhanced gene delivery and siRNA silencing by gold nanoparticles coated with charge-reversal polyelectrolyte," *ACS Nano*, vol. 4, no. 9, pp. 5505–5511, 2010.

[59] S. H. Lee, K. H. Bae, S. H. Kim, K. R. Lee, and T. G. Park, "Amine-functionalized gold nanoparticles as non-cytotoxic and efficient intracellular siRNA delivery carriers," *International Journal of Pharmaceutics*, vol. 364, no. 1, pp. 94–101, 2008.

[60] A. R. Wadhwani, W. L. Klein, and P. N. Lacor, "Efficient gene silencing in neural cells by functionalized gold nanoparticles," *Nanoscape*, vol. 7, no. 1, pp. 6–10, 2010.

[61] R. B. Roemer, "Engineering aspects of hyperthermia therapy," *Annual Review of Biomedical Engineering*, vol. 1, pp. 347–376, 1999.

[62] P. Cherukuri, E. S. Glazer, and S. A. Curley, "Targeted hyperthermia using metal nanoparticles," *Advanced Drug Delivery Reviews*, vol. 62, no. 3, pp. 339–345, 2010.

[63] D. P. O'Neal, L. R. Hirsch, N. J. Halas, J. D. Payne, and J. L. West, "Photo-thermal tumor ablation in mice using near infrared-absorbing nanoparticles," *Cancer Letters*, vol. 209, no. 2, pp. 171–176, 2004.

[64] M. Johannsen, U. Gneveckow, L. Eckelt et al., "Clinical hyperthermia of prostate cancer using magnetic nanoparticles: presentation of a new interstitial technique," *International Journal of Hyperthermia*, vol. 21, no. 7, pp. 637–647, 2005.

[65] X. Huang, P. K. Jain, I. H. El-Sayed, and M. A. El-Sayed, "Determination of the minimum temperature required for selective photothermal destruction of cancer cells with the use of immunotargeted gold nanoparticles," *Photochemistry and Photobiology*, vol. 82, no. 2, pp. 412–417, 2006.

[66] X. Huang, I. H. El-Sayed, W. Qian, and M. A. El-Sayed, "Cancer cell imaging and photothermal therapy in the near-infrared region by using gold nanorods," *Journal of the American Chemical Society*, vol. 128, no. 6, pp. 2115–2120, 2006.

[67] J. Chen, D. Wang, J. Xi et al., "Immuno gold nanocages with tailored optical properties for targeted photothermal

destruction of cancer cells," *Nano Letters*, vol. 7, no. 5, pp. 1318–1322, 2007.

[68] Y. Haba, C. Kojima, A. Harada, T. Ura, H. Horinaka, and K. Kono, "Preparation of poly(ethylene glycol)-modified poly(amido amine) dendrimers encapsulating gold nanoparticles and their heat-generating ability," *Langmuir*, vol. 23, no. 10, pp. 5243–5246, 2007.

[69] X. Huang, I. H. El-Sayed, and M. A. El-Sayed, "Applications of gold nanorods for cancer imaging and photothermal therapy," *Methods in Molecular Biology*, vol. 624, pp. 343–357, 2010.

[70] W. S. Kuo, C. N. Chang, Y. T. Chang et al., "Gold nanorods in photodynamic therapy, as hyperthermia agents, and in near-infrared optical imaging," *Angewandte Chemie—International Edition*, vol. 49, no. 15, pp. 2711–2715, 2010.

[71] L. Tong, Q. Wei, A. Wei, and J. X. Cheng, "Gold nanorods as contrast agents for biological imaging: optical properties, surface conjugation and photothermal effects," *Photochemistry and Photobiology*, vol. 85, no. 1, pp. 21–32, 2009.

[72] C. Loo, A. Lowery, N. Halas, J. West, and R. Drezek, "Immunotargeted nanoshells for integrated cancer imaging and therapy," *Nano Letters*, vol. 5, no. 4, pp. 709–711, 2005.

[73] C. Loo, L. Hirsch, M. H. Lee et al., "Gold nanoshell bioconjugates for molecular imaging in living cells," *Optics Letters*, vol. 30, no. 9, pp. 1012–1014, 2005.

[74] S. Lal, S. E. Clare, and N. J. Halas, "Nanoshell-enabled photothermal cancer therapy: impending clinical impact," *Accounts of Chemical Research*, vol. 41, no. 12, pp. 1842–1851, 2008.

[75] S. E. Skrabalak, L. Au, X. Lu, X. Li, and Y. Xia, "Gold nanocages for cancer detection and treatment," *Nanomedicine*, vol. 2, no. 5, pp. 657–668, 2008.

[76] Y. Xia, W. Li, C. M. Cobley et al., "Gold nanocages: from synthesis to theranostic applications," *Accounts of Chemical Research*. In press.

[77] X. Huang, P. K. Jain, I. H. El-Sayed, and M. A. El-Sayed, "Plasmonic photothermal therapy (PPTT) using gold nanoparticles," *Lasers in Medical Science*, vol. 23, no. 3, pp. 217–228, 2008.

[78] A. M. Gobin, M. H. Lee, N. J. Halas, W. D. James, R. A. Drezek, and J. L. West, "Near-infrared resonant nanoshells for combined optical imaging and photothermal cancer therapy," *Nano Letters*, vol. 7, no. 7, pp. 1929–1934, 2007.

[79] G. S. Terentyuk, G. N. Maslyakova, L. V. Suleymanova et al., "Laser-induced tissue hyperthermia mediated by gold nanoparticles: toward cancer phototherapy," *Journal of Biomedical Optics*, vol. 14, no. 2, Article ID 021016, 2009.

[80] M. A. Sirotkina, V. V. Elagin, M. V. Shirmanova et al., "OCT-guided laser hyperthermia with passively tumor-targeted gold nanoparticles," *Journal of Biophotonics*, vol. 3, no. 10-11, pp. 718–727, 2010.

[81] E. Y. Lukianova-Hleb, A. O. Oginsky, A. P. Samaniego et al., "Tunable plasmonic nanoprobes for theranostics of prostate cancer," *Theranostics*, vol. 1, pp. 3–17, 2011.

[82] D. S. Wagner, N. A. Delk, E. Y. Lukianova-Hleb, J. H. Hafner, M. C. Farach-Carson, and D. O. Lapotko, "The in vivo performance of plasmonic nanobubbles as cell theranostic agents in zebrafish hosting prostate cancer xenografts," *Biomaterials*, vol. 31, no. 29, pp. 7567–7574, 2010.

[83] D. O. Lapotko, E. Lukianova, and A. A. Oraevsky, "Selective laser nano-thermolysis of human leukemia cells with microbubbles generated around clusters of gold nanoparticles," *Lasers in Surgery and Medicine*, vol. 38, no. 6, pp. 631–642, 2006.

[84] J. Cardinal, J. R. Klune, E. Chory et al., "Noninvasive radiofrequency ablation of cancer targeted by gold nanoparticles," *Surgery*, vol. 144, no. 2, pp. 125–132, 2008.

[85] P. Bernardi, M. Cavagnaro, S. Pisa, and E. Piuzzi, "Specific absorption rate and temperature elevation in a subject exposed in the far-field of radio-frequency sources operating in the 10–900-MHz range," *IEEE Transactions on Biomedical Engineering*, vol. 50, no. 3, pp. 295–304, 2003.

[86] Y. F. Huang, K. Sefah, S. Bamrungsap, H. T. Chang, and W. Tan, "Selective photothermal therapy for mixed cancer cells using aptamer-conjugated nanorods," *Langmuir*, vol. 24, no. 20, pp. 11860–11865, 2008.

[87] K. W. Hu, C. C. Huang, J. R. Hwu, W. C. Su, D. B. Shieh, and C. S. Yeh, "A new photothermal therapeutic agent: core-free nanostructured Au x Ag1-x dendrites," *Chemistry*, vol. 14, no. 10, pp. 2956–2964, 2008.

[88] F. Y. Cheng, C. T. Chen, and C. S. Yeh, "Comparative efficiencies of photothermal destruction of malignant cells using antibody-coated silica@Au nanoshells, hollow Au/Ag nanospheres and Au nanorods," *Nanotechnology*, vol. 20, no. 42, p. 425104, 2009.

[89] F. Mohammad, G. Balaji, A. Weber, R. M. Uppu, and C. S. S. R. Kumar, "Influence of gold nanoshell on hyperthermia of superparamagnetic iron oxide nanoparticles," *Journal of Physical Chemistry C*, vol. 114, no. 45, pp. 19194–19201, 2010.

[90] D. H. Kim, E. A. Rozhkova, T. Rajh, S. D. Bader, and V. Novosad, "Synthesis of hybrid gold/iron oxide nanoparticles in block copolymer micelles for imaging, drug delivery, and magnetic hyperthermia," *IEEE Transactions on Magnetics*, vol. 45, no. 10, Article ID 5257027, pp. 4821–4824, 2009.

[91] B. Ehdaie, "Application of nanotechnology in cancer research: review of progress in the National Cancer Institute's alliance for nanotechnology," *International Journal of Biological Sciences*, vol. 3, no. 2, pp. 108–110, 2007.

[92] J. D. Gibson, B. P. Khanal, and E. R. Zubarev, "Paclitaxel-functionalized gold nanoparticles," *Journal of the American Chemical Society*, vol. 129, no. 37, pp. 11653–11661, 2007.

[93] S. Dhar, W. L. Daniel, D. A. Giljohann, C. A. Mirkin, and S. J. Lippard, "Polyvalent oligonucleotide gold nanoparticle conjugates as delivery vehicles for platinum(IV) warheads," *Journal of the American Chemical Society*, vol. 131, no. 41, pp. 14652–14653, 2009.

[94] S. D. Brown, P. Nativo, J. A. Smith et al., "Gold nanoparticles for the improved anticancer drug delivery of the active component of oxaliplatin," *Journal of the American Chemical Society*, vol. 132, no. 13, pp. 4678–4684, 2010.

[95] J. R. Hwu, Y. S. Lin, T. Josephrajan et al., "Targeted paclitaxel by conjugation to iron oxide and gold nanoparticles," *Journal of the American Chemical Society*, vol. 131, no. 1, pp. 66–68, 2009.

[96] S. R. Sershen, S. L. Westcott, N. J. Halas, and J. L. West, "Temperature-sensitive polymer-nanoshell composites for photothermally modulated drug delivery," *Journal of Biomedical Materials Research*, vol. 51, no. 3, pp. 293–298, 2000.

[97] H. C. Sang, "Estimation of tumour dose enhancement due to gold nanoparticles during typical radiation treatments: a preliminary Monte Carlo study," *Physics in Medicine and Biology*, vol. 50, no. 15, pp. N163–N173, 2005.

[98] T. Kong, J. Zeng, X. Wang et al., "Enhancement of radiation cytotoxicity in breast-cancer cells by localized attachment of gold nanoparticles," *Small*, vol. 4, no. 9, pp. 1537–1543, 2008.

[99] R. Xu, J. Ma, X. Sun et al., "Ag nanoparticles sensitize IR-induced killing of cancer cells," *Cell Research*, vol. 19, no. 8, pp. 1031–1034, 2009.

[100] J. H. Lee, Y. M. Huh, Y. W. Jun et al., "Artificially engineered magnetic nanoparticles for ultra-sensitive molecular imaging," *Nature Medicine*, vol. 13, no. 1, pp. 95–99, 2007.

[101] E. I. Altinoğlu and J. H. Adair, "Near infrared imaging with nanoparticles," *Wiley Interdisciplinary Reviews: Nanomedicine and Nanobiotechnology*, vol. 2, no. 5, pp. 461–477, 2010.

[102] J. Kneipp, H. Kneipp, B. Wittig, and K. Kneipp, "Novel optical nanosensors for probing and imaging live cells," *Nanomedicine: Nanotechnology, Biology, and Medicine*, vol. 6, no. 2, pp. 214–226, 2010.

[103] D. Kim, S. Park, H. L. Jae, Y. J. Yong, and S. Jon, "Antibiofouling polymer-coated gold nanoparticles as a contrast agent for in vivo X-ray computed tomography imaging," *Journal of the American Chemical Society*, vol. 129, no. 24, pp. 7661–7665, 2007.

[104] P. Vartholomeos, M. Fruchard, A. Ferreira, and C. Mavroidis, "MRI-guided nanorobotic systems for therapeutic and diagnostic applications," *Annual Review of Biomedical Engineering*, vol. 13, pp. 157–184, 2011.

[105] E. V. Zagaynova, M. V. Shirmanova, M. Y. Kirillin et al., "Contrasting properties of gold nanoparticles for optical coherence tomography: phantom, in vivo studies and Monte Carlo simulation," *Physics in Medicine and Biology*, vol. 53, no. 18, pp. 4995–5009, 2008.

[106] J. C. Kah, M. Olivo, T. H. Chow et al., "Control of optical contrast using gold nanoshells for optical coherence tomography imaging of mouse xenograft tumor model in vivo," *Journal of Biomedical Optics*, vol. 14, no. 5, p. 054015, 2009.

[107] A. L. Oldenburg, M. N. Hansen, T. S. Ralston, A. Wei, and S. A. Boppart, "Imaging gold nanorods in excised human breast carcinoma by spectroscopic optical coherence tomography," *Journal of Materials Chemistry*, vol. 19, no. 35, pp. 6407–6411, 2009.

[108] X. Yang, E. W. Stein, S. Ashkenazi, and L. V. Wang, "Nanoparticles for photoacoustic imaging," *Wiley Interdisciplinary Reviews. Nanomedicine and Nanobiotechnology*, vol. 1, no. 4, pp. 360–368, 2009.

[109] D. B. Chithrani, "Nanoparticles for improved therapeutics and imaging in cancer therapy," *Recent Patents on Nanotechnology*, vol. 4, no. 3, pp. 171–180, 2010.

[110] E. C. Cho, C. Glaus, J. Chen, M. J. Welch, and Y. Xia, "Inorganic nanoparticle-based contrast agents for molecular imaging," *Trends in Molecular Medicine*, vol. 16, no. 12, pp. 561–573, 2010.

[111] D. J. Brenner and E. J. Hall, "Computed tomography—an increasing source of radiation exposure," *The New England Journal of Medicine*, vol. 357, no. 22, pp. 2277–2284, 2007.

[112] D. Kim, M. K. Yu, T. S. Lee, J. J. Park, Y. Y. Jeong, and S. Jon, "Amphiphilic polymer-coated hybrid nanoparticles as CT/MRI dual contrast agents," *Nanotechnology*, vol. 22, no. 15, p. 155101, 2011.

[113] H. Y. Tseng, C. K. Lee, S. Y. Wu et al., "Au nanorings for enhancing absorption and backscattering monitored with optical coherence tomography," *Nanotechnology*, vol. 21, no. 29, p. 295102, 2010.

[114] A. S. Paranjape, R. Kuranov, S. Baranov et al., "Depth resolved photothermal OCT detection of macrophages in tissue using nanorose," *Biomedical Optics Express*, vol. 1, no. 1, pp. 2–16, 2010.

[115] Y. Wang, X. Xie, X. Wang et al., "Photoacoustic tomography of a nanoshell contrast agent in the in vivo rat brain," *Nano Letters*, vol. 4, no. 9, pp. 1689–1692, 2004.

[116] M. Eghtedari, A. Oraevsky, J. A. Copland, N. A. Kotov, A. Conjusteau, and M. Motamedi, "High sensitivity of in vivo detection of gold nanorods using a laser optoacoustic imaging system," *Nano Letters*, vol. 7, no. 7, pp. 1914–1918, 2007.

[117] K. H. Song, C. Kim, K. Maslov, and L. V. Wang, "Noninvasive in vivo spectroscopic nanorod-contrast photoacoustic mapping of sentinel lymph nodes," *European Journal of Radiology*, vol. 70, no. 2, pp. 227–231, 2009.

[118] L. Bickford, J. Sun, K. Fu et al., "Enhanced multi-spectral imaging of live breast cancer cells using immunotargeted gold nanoshells and two-photon excitation microscopy," *Nanotechnology*, vol. 19, no. 31, p. 315102, 2008.

[119] J. Kneipp, H. Kneipp, M. McLaughlin, D. Brown, and K. Kneipp, "In vivo molecular probing of cellular compartments with gold nanoparticles and nanoaggregates," *Nano Letters*, vol. 6, no. 10, pp. 2225–2231, 2006.

[120] A. Matschulat, D. Drescher, and J. Kneipp, "Surface-enhanced Raman scattering hybrid nanoprobe multiplexing and imaging in biological systems," *ACS Nano*, vol. 4, no. 6, pp. 3259–3269, 2010.

[121] Y. S. Chen, Y. C. Hung, I. Liau, and G. S. Huang, "Assessment of the in vivo toxicity of gold nanoparticles," *Nanoscale Research Letters*, vol. 4, no. 8, pp. 858–864, 2009.

[122] M. A. Dobrovolskaia and S. E. McNeil, "Immunological properties of engineered nanomaterials," *Nature Nanotechnology*, vol. 2, no. 8, pp. 469–478, 2007.

[123] C. Lasagna-Reeves, D. Gonzalez-Romero, M. A. Barria et al., "Bioaccumulation and toxicity of gold nanoparticles after repeated administration in mice," *Biochemical and Biophysical Research Communications*, vol. 393, no. 4, pp. 649–655, 2010.

[124] J. J. Li, D. Hartono, C. N. Ong, B. H. Bay, and L. Y. L. Yung, "Autophagy and oxidative stress associated with gold nanoparticles," *Biomaterials*, vol. 31, no. 23, pp. 5996–6003, 2010.

[125] S. Hackenberg, A. Scherzed, M. Kessler et al., "Silver nanoparticles: evaluation of DNA damage, toxicity and functional impairment in human mesenchymal stem cells," *Toxicology Letters*, vol. 201, no. 1, pp. 27–33, 2011.

[126] P. V. Asharani, N. Xinyi, M. P. Hande, and S. Valiyaveettil, "DNA damage and p53-mediated growth arrest in human cells treated with platinum nanoparticles," *Nanomedicine*, vol. 5, no. 1, pp. 51–64, 2010.

[127] E. E. Connor, J. Mwamuka, A. Gole, C. J. Murphy, and M. D. Wyatt, "Gold nanoparticles are taken up by human cells but do not cause acute cytotoxicity," *Small*, vol. 1, no. 3, pp. 325–327, 2005.

[128] Y. Pan, S. Neuss, A. Leifert et al., "Size-dependent cytotoxicity of gold nanoparticles," *Small*, vol. 3, no. 11, pp. 1941–1949, 2007.

[129] I. H. El-Sayed, X. Huang, and M. A. El-Sayed, "Surface plasmon resonance scattering and absorption of anti-EGFR antibody conjugated gold nanoparticles in cancer diagnostics: applications in oral cancer," *Nano Letters*, vol. 5, no. 5, pp. 829–834, 2005.

[130] M. E. H. El-Sayed, A. S. Hoffman, and P. S. Stayton, "Smart polymeric carriers for enhanced intracellular delivery of therapeutic macromolecules," *Expert Opinion on Biological Therapy*, vol. 5, no. 1, pp. 23–32, 2005.

[131] X. L. Huang, B. Zhang, L. Ren et al., "In vivo toxic studies and biodistribution of near infrared sensitive Au-Au2S nanoparticles as potential drug delivery carriers," *Journal of Materials Science: Materials in Medicine*, vol. 19, no. 7, pp. 2581–2588, 2008.

[132] C. K. Kim, P. Ghosh, C. Pagliuca, Z. J. Zhu, S. Menichetti, and V. M. Rotello, "Entrapment of hydrophobic drugs in nanoparticle monolayers with efficient release into cancer cells," *Journal of the American Chemical Society*, vol. 131, no. 4, pp. 1360–1361, 2009.

[133] G. F. Paciotti, L. Myer, D. Weinreich et al., "Colloidal gold: a novel nanoparticle vector for tumor directed drug delivery," *Drug Delivery*, vol. 11, no. 3, pp. 169–183, 2004.

[134] R. K. Visaria, R. J. Griffin, B. W. Williams et al., "Enhancement of tumor thermal therapy using gold nanoparticle-assisted tumor necrosis factor-α delivery," *Molecular Cancer Therapeutics*, vol. 5, no. 4, pp. 1014–1020, 2006.

[135] H. J. Yen, S. H. Hsu, and C. L. Tsai, "Cytotoxicity and immunological response of gold and silver nanoparticles of different sizes," *Small*, vol. 5, no. 13, pp. 1553–1561, 2009.

[136] Y. N. Sun, C. D. Wang, X. M. Zhang, L. Ren, and X. H. Tian, "Shape dependence of gold nanoparticles on in vivo acute toxicological effects and biodistribution," *Journal of Nanoscience and Nanotechnology*, vol. 11, no. 2, pp. 1210–1216, 2011.

[137] Y. Qiu, Y. Liu, L. Wang et al., "Surface chemistry and aspect ratio mediated cellular uptake of Au nanorods," *Biomaterials*, vol. 31, no. 30, pp. 7606–7619, 2010.

[138] L. Braydich-Stolle, S. Hussain, J. J. Schlager, and M. C. Hofmann, "In vitro cytotoxicity of nanoparticles in mammalian germline stem cells," *Toxicological Sciences*, vol. 88, no. 2, pp. 412–419, 2005.

[139] S. M. Hussain, K. L. Hess, J. M. Gearhart, K. T. Geiss, and J. J. Schlager, "In vitro toxicity of nanoparticles in BRL 3A rat liver cells," *Toxicology in Vitro*, vol. 19, no. 7, pp. 975–983, 2005.

[140] K. F. Soto, A. Carrasco, T. G. Powell, K. M. Garza, and L. E. Murr, "Comparative in vitro cytotoxicity assessment of some manufacture dnanoparticulate materials characterized by transmission electron microscopy," *Journal of Nanoparticle Research*, vol. 7, no. 2-3, pp. 145–169, 2005.

[141] R. Foldbjerg, D. A. Dang, and H. Autrup, "Cytotoxicity and genotoxicity of silver nanoparticles in the human lung cancer cell line, A549," *Archives of Toxicology*, vol. 85, no. 7, pp. 743–750, 2011.

[142] P. V. Asharani, Y. Lianwu, Z. Gong, and S. Valiyaveettil, "Comparison of the toxicity of silver, gold and platinum nanoparticles in developing zebrafish embryos," *Nanotoxicology*, vol. 5, no. 1, pp. 43–54, 2011.

[143] S. Bellucci, "Nanoparticles and nanodevices in biological applications," *Lecture Notes in Nanoscale Science and Technology*, vol. 4, pp. 1–198, 2009.

Multifunctional Gold Nanocarriers for Cancer Theranostics – From bench to bedside and back again?

João Conde [a, b,*], *Furong Tian* [c], *Pedro V. Baptista* [b], *Jesús M. de la Fuente* [a]

[a] Instituto de Nanociencia de Aragon (INA), Universidad de Zaragoza, Zaragoza, 50018, Spain.

[b] CIGMH, Departamento de Ciências da Vida, Faculdade de Ciências e Tecnologia, Universidade Nova de Lisboa, Campus de Caparica, 2829-516 Caparica, Portugal.

[c] Comprehensive Pneumology Centre, Institute of Lung Biology and Disease, Helmholtz Zentrum München, Neuherberg, Germany.

[*] Corresponding-Author, j.conde@campus.fct.unl.pt

Abstract

After a quarter of century of rapid technological advances, research has revealed the complexity of cancer, a disease intimately related to the dynamic transformation of the genome. However, the full understanding of the molecular onset of this disease is still far from achieved and the search for mechanisms of treatment will follow closely.

It is here that Nanotechnology enters the fray offering a wealth of tools to diagnose and treat cancer. It is indisputable that the use of gold nanocarriers has been gaining momentum as vectors for therapy and diagnostic strategies, combining the AuNPs' ease of functionalization with numerous biomolecules, high loading capacity and fast uptake by target cells. In fact, over the last decade nearly 12.000 research papers focusing on multifunctional gold nanocarriers have been published in peer-reviewed journals. Some of the described nanosystems will most likely revolutionize our understanding of biological mechanisms and push forward the clinical practice through their integration in future diagnostics platforms. Nevertheless, very little gave fruitful results in order to

improve a bench-to-bedside approach to translational research. On the basis of theoretical and experimental results obtained so far are we or not at the point: from bench to bedside and back again? As you will see, the answers to this question are complex, but one thing is clear: Translation into clinics is a tortuous and difficult path. Here, we provide a critical review about the available multifunctional gold nanocarriers for in vitro application and in vivo cancer targeting on nanodiagnostics and therapy. Finally, the correct choices of chemical modifications to incorporate into the multifunctional gold nanocarriers to avoid activation off-target, side effects and toxicity are illustrated toward the development of new clinical strategies.

Keywords: cancer; gold nanoparticles; nanomedicine; nanotheranostics; nanotoxicity.

1. Introduction

The National Cancer Institute predicts that over the next years, nanotechnology will result in important advances in early detection, molecular imaging, targeted and multifunctional therapeutics, prevention and control of cancer [1]. Nanotechnology offers numerous tools to diagnose and treat cancer, such as new imaging agents, multifunctional devices capable of overcome biological barriers to deliver therapeutic agents directly to cells and tissues involved in cancer growth and metastasis, and devices capable of predicting molecular changes to prevent action against precancerous cells [2]. Nanoparticle-based delivery systems in Theranostics (Diagnostics & Therapy) provide better penetration of therapeutic and diagnostic substances within the body at a reduced risk in comparison to conventional therapies [3;4]. Limitations in medical practice are intimately associated with the fact that diagnostics, therapy and therapy guidance are mostly separate from each other. It is here that theranostics unites the three stages in one single process, supporting early-stage diagnosis and treatment, overcoming some of the sensitivity and specificity of current medicines [5-7]. At the present time, there is a growing need to enhance the capability of theranostics procedures where

nanoparticle-based sensors may provide for the simultaneous detection of several gene-associated conditions and nanodevices with the ability to monitor real-time drug action. These innovative multifunctional nanocarriers for cancer theranostics may allow the development of diagnostics systems such as colorimetric and immunoassays, and in therapy approaches through gene therapy, drug delivery and tumor targeting systems (**Figure 1**).

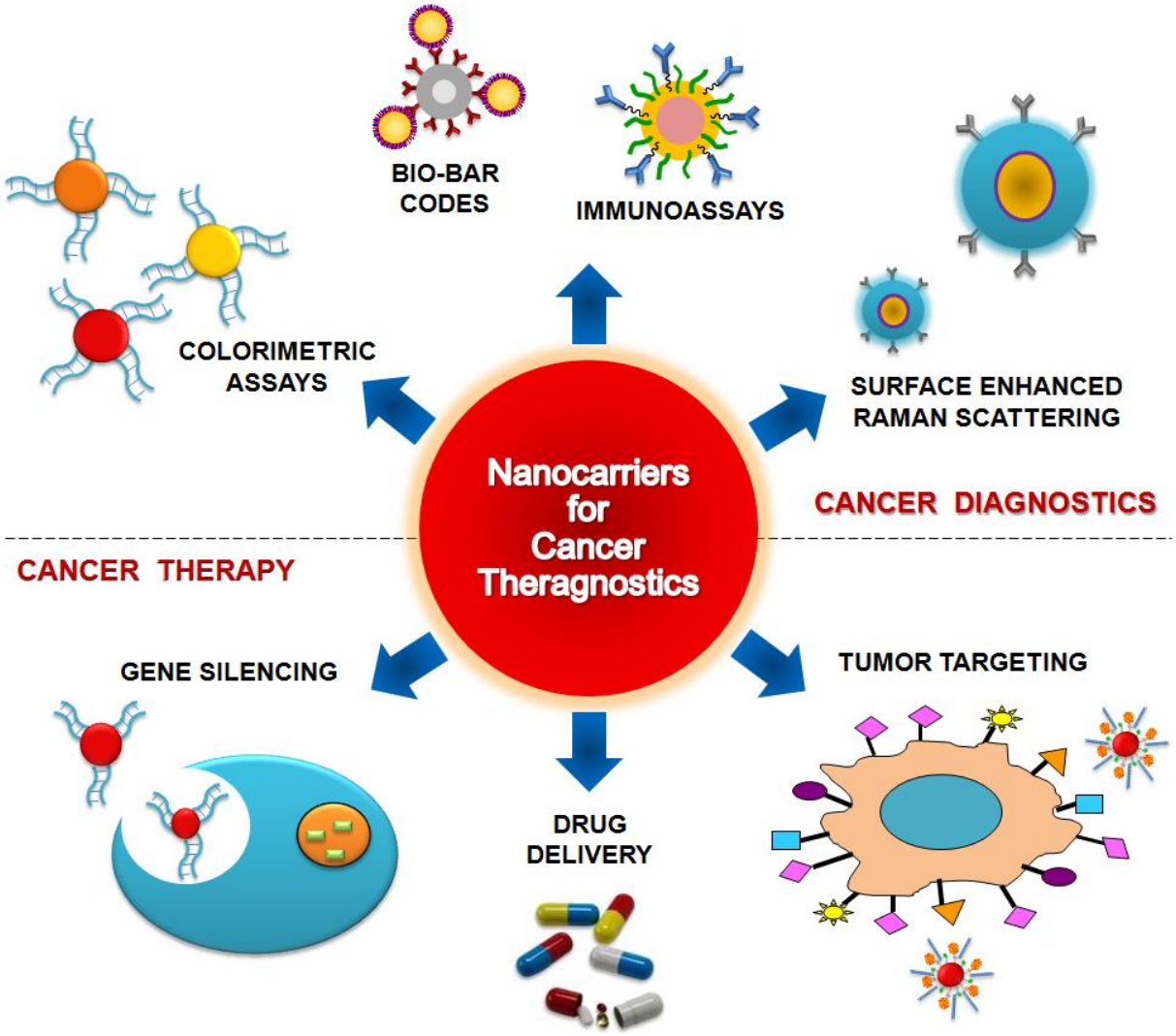

Figure 1. Nanocarriers for Cancer Theranostics. Nanoparticles-based strategies can be used for biosensing using plasmonic nanosensors for colorimetric assays and bio-bar codes for protein detection or intense labels for immunoassays. Moreover, the use of metal surfaces to enhance the Raman scattering signal of target molecules may be used for cancer diagnostics. Engineered nanocarriers can also act as therapeutic agents via gene silencing and drug delivery systems. Some nanocarriers can be attached to specific targets for selective damage to cancer cells through tumor targeting approaches.

Nowadays the main challenge is to develop a system for molecular therapy capable of circulating in the blood stream undetected by the immune system and capable to recognize the desirable target and signal it for effective drug delivery or gene silencing. As a result, nanotechnology is playing a role in providing new types of nanotherapeutics for cancer that have the potential to provide effective therapies with minimal side effects and with high specificity [8]. The interdisciplinary and vibrant field of nanotechnology continues giving us hope of a personalized medicine as a part of cancer patient management. Gold nanoparticles (AuNPs) are one of those nanosystems that provide non-toxic carriers for drug and gene delivery applications [9;10]. They are versatile agents with a variety of biomedical applications including use in highly sensitive diagnostic assays [11], thermal ablation and radiotherapy enhancement [12-14], as well as drug and gene delivery [15;16].

The unique characteristics of AuNPs in the nanometer range, such as high surface-to-volume ratio or size-dependent optical properties, are drastically different from those of their bulk materials and hold pledge in the clinical field for disease therapeutics [8;17]. Nanoparticles (NPs) exhibiting these unique and broad-based optical properties, ease of synthesis and facile surface chemistry and functionalization, and appropriate size scale are generating much eagerness in clinical diagnostics and therapy. The most common applications in which gold nanocarriers have been used so far are labeling, delivering, heating, sensing and detection [18].

In spite of these advantages, nanoparticles show some limitations, such as their small size and large surface area can lead to particle-particle aggregation and may result in limited loading of functional components and burst release. In fact, only NPs with the appropriate size (and surface chemistry) will not be immediately recognized by our immune system and committed to removal from the organism, thus showing increased circulation times. Also, size and surface properties play an important role to avoid clearance [19]. For example, hydrophilic nanoparticles with an effective size in the range of 10 to 100 nm are small enough to slow down activation of the mononuclear phagocyte system and are big enough to avoid renal filtration [20]. The unique characteristics of

nanoparticles (NPs) in the nanometer range, such as high surface-to-volume ratio or size-dependent optical properties, are drastically different from those of their bulk materials and hold pledge in the clinical field for disease therapeutics [21].

When referring to cancer therapy, targeting and localized delivery are of utmost importance to enhance the therapeutic effect and decrease an adverse distribution to healthy organs and tissues. Multifunctional gold nanocarriers may potentiate the development of individualized cancer therapy based on the individual's biological information within the tumor (i.e. biomolecular profiling). Gold nanocarriers can be modified with multiple cell-targeting and membrane translocating peptides, loaded with DNA/RNA and used as nanovectors [20;22].

In this paper, we will focus on the exciting new methods and applications of AuNPs for cancer diagnosis and therapy with particular emphasis on their use in vivo and their potential to be translated into clinical settings.

1. Nanodiagnostics

Nanodiagnostics can be defined as the use of nano-sized materials, devices or systems for diagnostics purposes [23]. It is a promising field as more and improved techniques are becoming available for clinical diagnostics with increased sensitivity at lower costs [24-27].

The use of the colloidal gold color change upon aggregation is the best characterized example for diagnostic systems using AuNPs. In fact, AuNPs functionalized with ssDNA capable of specifically hybridizing to a complementary target for the detection of specific nucleic acid sequences in biological samples have been extensively used [24;26;28-36].

The use of thiol-linked ssDNA-modified gold nanoparticles for the colorimetric detection of gene targets represents an inexpensive and easy to perform alternative to fluorescence or radioactivity-based assays [37]. In 1996, *Mirkin* et al. [29] described the use of a cross-linking method that relies on the detection of single-stranded oligonucleotide targets using two different Au-nanoprobes, each

of them functionalized with a DNA-oligonucleotide complementary to one half of the given target. A mixture of gold nanoparticles with surface-immobilized non-complementary DNA sequences appears red in color and has a strong absorbance at 520 nm. When a complementary DNA sequence is added, the nanoparticles are reversibly aggregated causing a red shift in the surface plasmon absorbance to 574 nm, and the solution becomes purple in color. Consequently, these AuNPs reversibly assemble by the formation of the DNA duplex, linking the particles together. These pioneer work gave the research community the idea of an easy method to sensitized oligonucleotide–AuNP conjugates, with intense and highly tunable optical properties, ease of conjugation though the gold–thiol bond, catalytic properties, and relative biocompatibility [30;38].

On the other hand, in 2005 Baptista et al. introduced a non-cross linking method where thiol-linked DNA-gold nanoparticles were used in a novel colorimetric method to detect the presence of specific mRNA from a total RNA extract of yeast cells [25]. The method consists in visual and/or spectrophotometric comparison of solutions before and after salt induced Au-nanoprobe aggregation (see **Figure 2**) – the presence of a complementary target prevents aggregation and the solution remains red and has a strong absorbance at ±520 nm; non-complementary/mismatched targets do not prevent Au-nanoprobe aggregation, resulting in a visible change of color from red to blue and therefore a shift in the surface plasmon absorbance to 600-650 nm. This method has been successfully applied to detect eukaryotic gene expression without retro-transcription or PCR amplification steps [25;39]; to distinguish fully complementary from mismatched sequences, with a single base mismatch i.e. to detect common mutations within the β-globin gene [26]; and in a fast and straightforward assay for Mycobacterium tuberculosis DNA detection in clinical samples [27;40].

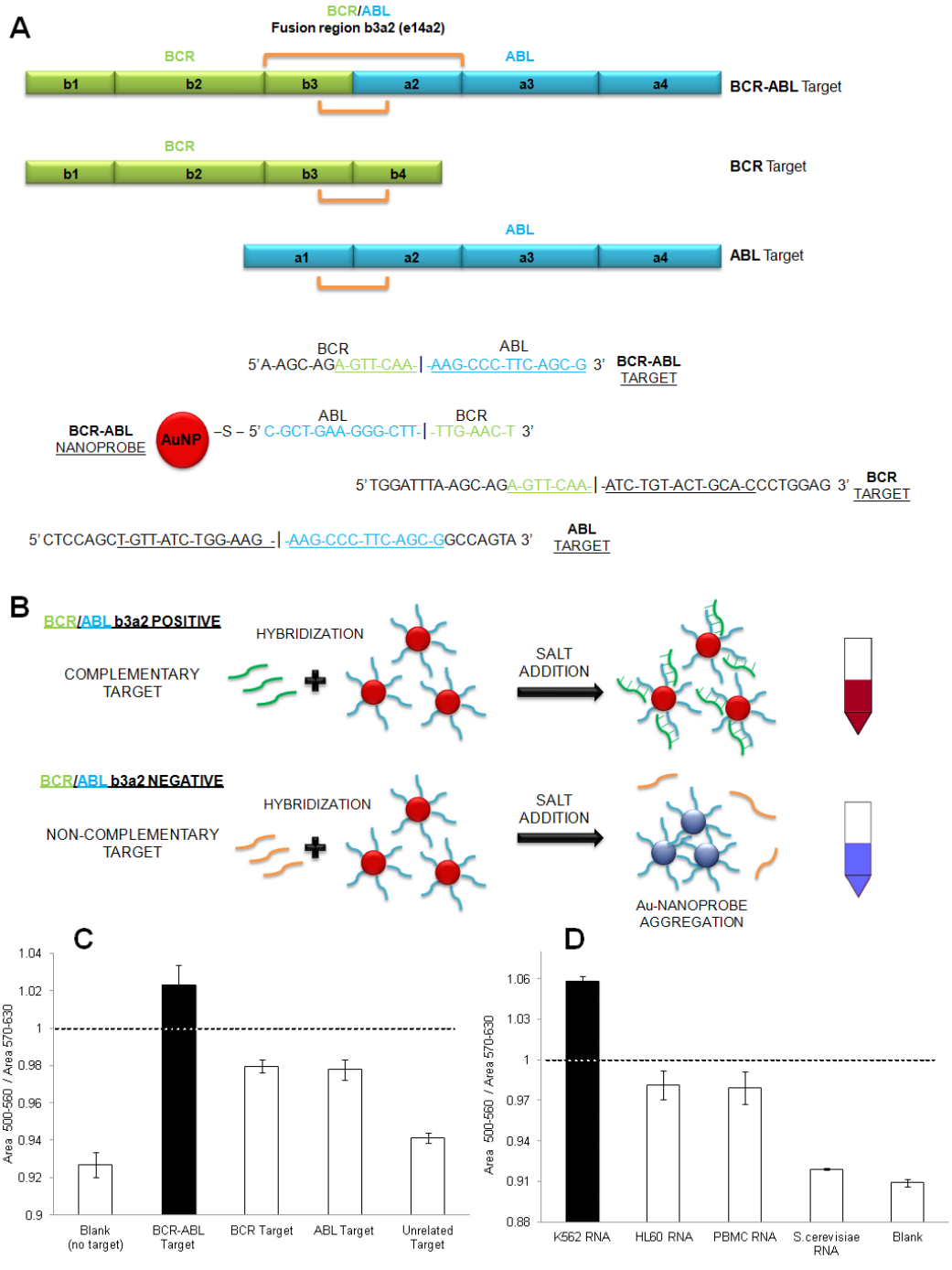

Figure 2. The colorimetric assay. (**A**) Oligonucleotide probe and target sequences designed for BCR-ABL b3a2 (e14a2) junction and for BCR and ABL genes. Complementary and non-complementary target sequences were used to study the level of specific interaction between the target and the Au-nanoprobes. BCR-ABL fusion positive (100% complementary); BCR and ABL gene sequences were used as controls (50% non-complementary); and a completely unrelated sequence (100% non-complementary) was used as negative control. (**B**) The assay is based on the increased stability of the Au-nanoprobes upon hybridization with the complementary target in solution, while non-hybridized Au-nanoprobes easily aggregate once the solution's ionic strength is increased. The absence of full complementarity is revealed by a change of color from red to blue due to A-nanoprobe aggregation which is corroborated by naked eye and UV/vis spectroscopy. BCR-ABL Positive: sample in the presence of complementary target (solution remains red); BCR-ABL

Negative: sample in the presence of non-complementary target (solution turns blue). (**C**) Spectrophotometry relative to the detection of synthetic BCR-ABL oligonucleotide target. Oligonucleotides with BCR or ABL sequence only (showing 50% complementarity) were used as controls and an unrelated target (showing 100% non-complementarity to the Au-nanoprobe) as negative control. (**D**) Detection of BCR-ABL in total RNA from K562 cell line, HL-60 cell line and human PBMC (harboring 50% complementary targets to the nanoprobe) and S. cerevisiae cells (100% non-complementary). Nanoprobe aggregation as measured by ratio of area under the curve AUC500 nm-560 nm/AUC570 nm-630 nm. The dashed line represents the threshold of 1 considered for discrimination between Positive and Negative.

Other approaches are the use of AuNPs as a core/seed that can be tailored with a wide variety of surface functionalities to provide highly selective nanoprobes for diagnosis [41]; the utilization of Surface Plasmon resonance (SPR) scattering imaging or SPR absorption spectroscopy generated from antibody conjugated AuNPs in molecular biosensor techniques for the diagnosis and investigation of oral epithelial living cancer cells *in vivo* and *in vitro* [42]; the use of multifunctional AuNPs which incorporate both cytosolic delivery and targeting moieties on the same particle functioning as intracellular sensors to monitoring actin rearrangement in live fibroblasts [43]; and the employment of AuNPs in electrochemical based methods that can be coupled with metal deposition for signal enhancement [44].

Gold NPs have already proven to be one of the most important groups of nanomaterials for biosensing approaches. Highly sensitive and specific biosensors based on AuNPs have open up the possibility of creating new diagnostic platforms for disease markers, biological and infectious agents in the early-stage detection of disease and threats, especially in cancer [21;45].

1.1. Gold nanocarriers in Cancer Diagnosis

Cancer is the one of first leading causes of mortality in the modern world, with more than 10 million new cases every year [46;47]. Some continue to argue that the search for the origin and treatment of this disease will continue through the next quarter of century, adding successive layers of complexity to an investigation that per se is very complex. In fact, advances in diagnosis and treating this disease that kills millions of people each year worldwide, have not been as effective as for other chronic

diseases, and only for some types of cancer there are effective methods of detection [46]. The high mortality rate in cancer is commonly attributed to the difficulties in detecting the disease at an early treatable stage. The main challenge is to find new and more effective diagnostic agents for the monitorization of predictive cell molecular changes that are involved in tumor development as the key to the efficient and ultimately triumphant treatment of cancer is early and accurate diagnosis [48].

It is here that nanotechnology enters the fight in the technological leap of controlling materials at nanoscale by offering a "big revolution" in new medical and healthcare diagnostic systems [20]. In fact, nanotechnology combined with biology and medicine is the most advanced technology both from an academic point-of-view and for commercial applications, producing major advances in molecular diagnostics and bioengineering [49;50]. AuNPs are one of those nanosystems that provide non-toxic carriers with a variety of biomedical applications including use in highly sensitive diagnostic assays [21;45].

In reality the multiplexed marker protein assays are critical in the diagnosis of complex diseases like cancer. In fact, AuNP probes barcoded with reporter DNAs and a capture antibody have been extensively used with great promise [51;52]. For instance, AuNP imunoassays are one of the most used nanosystems in cancer detection. Mirkin and co-workers developed an ultrasensitive method for detecting protein analytes. This facile immunoassay was used for the detection of prostate specific antigen (PSA, a valuable biomarker for prostate cancer screening) and had an almost one million-fold higher sensitivity than a conventional ELISA-based assay [53]. This study was the first step to use six years later the AuNP bio-barcode assay probe for the detection of PSA in a clinical pilot study with 18 men who have undergone radical prostatectomy for prostate cancer. This new bio-barcode PSA assay is approximately 300 times more sensitive than commercial immunoassays [54]. Also, Huang et al. have reported a PSA immunoassay on a commercially available surface plasmon resonance biosensor. This sandwich assay with AuNPs was used for a major enhancement in

sensitivity of PSA detection at clinical relevant concentrations [55]. Other study demonstrated a highly sensitive organic electrochemical transistor based immunosensor with secondary antibody-conjugated AuNPs with a low detection limit for PSA. These sensor performances were particularly improved in the lower concentration range where the detection is clinically important for the preoperative diagnosis and screening of prostate cancer [55].

Additionally, AuNP probes coupled with dynamic light scattering (DLS) measurements can also be used for the development of a one-step homogeneous immunoassay for the detection of free-PSA. The light scattering intensity of nanoparticles and nanoparticle oligomers is several orders of magnitude higher than proteins, making it possible to detect nanoparticle probes in the low picomolar concentration range [56].

AuNPs scatter light intensely at or near their surface plasmon wavelength region and when coupled with DLS detection can be very useful for serum protein biomarker detection and analysis. Huo et al. reported the use of citrate-AuNP to absorb proteins from the serum and form a protein corona on the nanoparticle surface. The protein corona formation and the subsequent binding of antibody to the target proteins in the protein corona were detected by DLS. Using this simple assay, the authors discovered multiple molecular aberrations associated with prostate cancer from both mice and human blood serum samples [57;58].

Other authors have taken a different approach to addressing the use of AuNPs in cancer biomarker detection by employing the biological applications of antibody-conjugated AuNPs in several types of cancer, such as breast cancer [59;60], pancreatic adenocarcinoma [61], cervical cancer [62], epithelial cancer [63], liver cancer [64], prostate cancer [65] and oral cancer [42].

The mechanism of selectivity and all these immunoassay's response open up a new possibility of rapid, simple, clean, easy, economically very cheap, non-toxic and reliable diagnosis of cancer. In fact, antibody-conjugated AuNPs are one of the most used nanosystems in cancer diagnostics, being useful in molecular biosensor techniques for the diagnosis and investigation of cancer cells *in vivo*

and *in vitro*. The importance of these nanosystems can be demonstrated by a significant number of companies involved in the synthesis and applications of antibody-conjugated nanoparticles, such as Magnisense SAS, Diagnostic Biosensors, LLC, Alnis Biosciences Inc. and Invitrogen Corp [66]. Direct detection of cancer cells using colorimetric assays with AuNPs has been extensively used due to their simplicity and versatility, among which those based on LSPR. LSPR is the collective oscillation of the electrons in the conduction band, which is usually in the visible region giving rise to the strong surface plasmon resonance absorption [67]. These AuNPs are commonly functionalized with biomolecules (e.g., DNA, RNA, peptides, enzymes) and capable of recognizing molecular events associated with cancer development down to femtomolar level with single base discrimination resolution [68-70]. Molecular nanodiagnostics applied to cancer may provide rapid and sensitive detection of cancer related molecular alterations, which would enable early detection even when those alterations occur only in a small percentage of cells. For instance, Conde et al. present an AuNPs based approach for the molecular recognition and quantification of the *BCR-ABL* fusion transcript, which is responsible for chronic myeloid leukemia (CML). This inexpensive and very easy to perform method allows quantification of unamplified total human RNA and specific detection of the oncogene transcript. This assay may constitute a promising tool in early diagnosis of CML and could easily be extended to further target genes with proven involvement in cancer development [39;71]. The sensitivity settled by the Au-nanoprobes allows differential gene expression from 10 ng/μl of total RNA and takes less than 30 minutes to complete after total RNA extraction, minimizing RNA degradation (see **Figure 2**).

Also, aptamer-conjugated AuNPs have become a powerful tool for point of care diagnostics [72]. Most of the common aptamer-AuNP assays are able to differentiate between different types of target and control cells based on the aptamer used in the assay, indicating the wide applicability for cancer cell detection. For instance, Liu et al. reported the use of an aptamer-nanoparticle strip biosensor for the rapid, specific, sensitive, and low-cost detection of circulating cancer cells in human blood,

showing great promise for in-field and point-of-care cancer diagnosis and therapy [73]. In another study, Medley et al. have developed a colorimetric assay for the direct detection of diseased cells and thus capable of distinguish between cancer cells and noncancerous cells. This assay combines the selectivity and affinity of aptamers and the spectroscopic advantages of AuNPs to allow for the sensitive detection of cancer cells with both the naked eye and based on absorbance measurements [70]. Another important aspect correlated with disease state in cancer patients is the presence of circulating tumor cells in the bloodstream. In order to induce optical contrast in non-pigmented cancer cells, Viator et al. attached AuNPs to a prostate cancer cell line, using optical absorption to detect such cells in a photoacoustic flowmeter designed to find circulating tumor cells in blood samples [74].

Another application of AuNPs in cancer is their capability to target and provide *in vivo* tumor detection using Surface-enhanced Raman scattering - SERS. Actually, Lin et al. described the tremendous potential of using AuNP based-SERS to obtain blood serum biochemical information for non-invasive colorectal cancer detection [75]. Raman reporters when combined with AuNPs can elicit an optical contrast to discriminate between cancerous and normal cells and their conjugation with antibodies allowed them to map the expression of relevant biomarkers for molecular imaging [76], as well as detect and characterized circulating tumor cells. These SERS nanoparticles constitute an important tool for clinical research once they can successfully identified circulating tumor cells in the peripheral blood of 19 patients with squamous cell carcinoma of the head and neck [77].

The papers discussed earlier report the development of nanoscale devices and platforms that can be used for improved biomarker detection, such as nucleic acids (DNA or RNA) or proteins. However, the development of molecular diagnosis of cancer and at the same time the selective delivery of a specific anticancer agent by joining diagnostics and therapy (theranostics) on a single nanodevice will most definitely revolutionizing the way we manage cancer [78].

Table 1 summarizes the latest types of AuNP-based biosensors for cancer dignostics, according to their methodology principle. Some of the described nanosystems will most likely revolutionize our understanding of biological mechanisms and push forward the clinical practice through their integration in future diagnostics platforms. Nevertheless, very little gave successful results or went to clinical trials. Therefore new synthesis, fabrication, and characterization methods are needed for developing highly advanced AuNPs capable of use in sensitive and multiple detection methods with negligible toxicity and high sensitivity. In the future, it might be possible to apply all AuNPs properties together and evolve new chemistry for synthesis of smart materials for diagnostic applications and clinical trials.

Table 1. Summary of the latest AuNP-based biosensors used in cancer diagnostics according to the type of NP, surface modification, type of cancer and explored methodology principle.

Method	Type of NP	Surface modification	Target/Cells/ Samples	Type of Cancer	Comments [Reference]
Colorimetric Scanometric	40 nm spherical	dA-tailed probe applied to the strip, which contains oligo(dT)-conjugated AuNPs in dry form	Fusion genes in K562 cell line	acute and chronic leukemia	Dry-reagent, disposable, dipstick test for molecular screening of seven chromosomal translocations associated with acute and chronic leukemia [79]
	13 nm spherical	ssDNA	BCR-ABL b3a2 (e14a2) fusion transcript	Chronic myeloid leukemia	Detection and quantification of the BCR-ABL gene fusion using thiol-DNA modified AuNPs [39]
	30 nm spherical	thiol-terminated DNA barcodes; anti-PSA antibodies	Prostate-specific antigen PSA (biomarker for prostate cancer screening)	Prostate cancer	Nanoparticle based bio-barcode for PSA detection [54]
	15 nm spherical	antibody anti-CA15-3−HRP (horseradish peroxidase)	CA15-3 breast cancer biomarker in human serum	Breast cancer	Enhanced AuNP based ELISA for a breast cancer biomarker detection [59]
	oval-shaped	monoclonal anti-HER2/c-erb-2 antibody; S6 RNA aptamer-conjugated	SK-BR-3 cells	Breast cancer	Colorimetric and highly sensitive two-photon scattering assay for highly selective and sensitive detection of breast cancer [60]
Immunoassays	15 nm spherical	dithiol-PEG-COOH; F19 monoclonal antibodies	Tissues from cancerous and healthy human pancreas (patients	Pancreatic adenocarcinoma	pancreatic adenocarcinoma [61]

			undergoing pancreatic resection)		
	25 nm spherical	anti-EGFR and non-specific IgG antibodies	SiHa cervical cancer cells	Cervical cancer	Optical imaging of cervical pre-cancers using AuNPs and CdSe QDs for reflectance and fluorescence imaging [62]
	10 nm spherical	antibody (Cetuximab)	epidermal growth factor receptor (EGFR) in A431 cells	Liver cancer	High-performance probes based on AuNPs for detection of live cancer cell [63]
	16 nm spherical	NHS-PEG; mouse anti-human AFP antibodies (antibody-1 and antibody-2)	liver cancer biomarker alpha-fetoprotein (AFP)	Liver cancer	One-step homogeneous detection of cancer marker using antibody-AuNP probes [64]
	60 nm spherical	PSMA (prostate specific membrane antigen); C225 (Erbitux, the antibody raised against human EGF receptor)	living bone metastatic prostate cancer (C4-2B); human bone marrow stromal (HS-5) cells	Prostate cancer	Tunable plasmonic nanoprobes for theranostics of prostate Cancer [65]
	35 nm spherical	monoclonal anti-epidermal growth factor receptor (anti-EGFR)	nonmalignant epithelial cells (HaCaT); malignant oral epithelial cells (HOC 313 clone 8 and HSC 3)	Oral cancer	Surface plasmon resonance scattering and absorption of antibody-AuNPs in oral cancer diagnostics [42]
Surface-enhanced Raman scattering - SERS	30 nm spherical	mouse anti-human free PSA clone PSA-F65 and clone PSA-66	Prostate-specific antigen (PSA) in human serum	Prostate cancer	Detection of PSA with an immunoassay based on SERS and immunogold labels [80]
	43 nm spherical	human serum	human serum	Colorectal cancer	AuNP based-SERS to obtain blood serum biochemical information for non-invasive colorectal cancer detection [75]
	60 nm spherical	QSY reporter molecules; thiol-PEG-COOH; epidermal growth factor (EGF) peptide	epidermal growth factor (EGF)	Squamous cell carcinoma of the head and neck	SERS AuNPs identified circulating tumor cells in the peripheral blood of cancer patients [77].
	35-50 nm spherical	Thiol-DNA hairpin tagged with a Raman label	BRCA1 SNPs	Breast cancer	Plasmonic nanoprobes for detection of SNPs in breast cancer BRCA1 gene [81]
Electrochemical	5 nm spherical	Glutathione (GSH); primary antibodies for human Interleukin-8	Interleukin-8 (IL-8) cancer biomarker in human serum	Cancer biomarker	Ultrasensitive immunosensor based on a glutathione-protected AuNP sensor surface [82]
	4 nm spherical	antibodies for IL-6; biotinylated secondary antibody with 16-18 horseradish peroxidase labels	Interleukin-6 (IL-6) cancer biomarker in calf serum	Cancer biomarker	Inkjet printed AuNP electrochemical arrays for immunodetection of a cancer biomarker protein [83]

	13 nm spherical	Alkaline phosphatase; poly (styrene-co-acrylic acid); TNF-α antibody	Tumor necrosis factor α (TNF-α) in human serum	Tumor necrosis factor	Electrochemical immunosensor of tumor necrosis factor based on alkaline phosphatase functionalized NPs [84]

2. NanoBioimaging

Nanoparticles are within the same size domain as many biomaterials including: enzymes, antibodies and protein receptors. This combined with the unique properties of materials in the nano-size range provides scope for making measurements more efficiently than existing molecular materials. Because light absorption from biologic tissue components is minimized at near infrared (NIR) wavelengths, most NPs for in vivo imaging have been designed to strongly absorb in the NIR so as to be used as effective contrast agents [45].

Gold nanoparticles have been used as exceptional contrast agents *in vivo*, giving a higher contrast when compared to traditional agents [85]. Ji et al. described the characterization of hybrid nanoparticles with a superparamagnetic iron oxide (SPIO)−silica core and a gold nanoshell, that displayed superparamagnetic characteristics and a significant absorbance in the near-infrared (NIR) region of the electromagnetic spectrum [86]. Examples include a superparamagnetic magnetite core with a layer of silica, before gold en-capsulation and the poly(ethylene glycol) (PEG) coating of magnetite/gold NPs to ensure biocompatibility. These poly(ethylene glycol) (PEG) coated hybrid nanoparticles comprising an iron oxide nanoparticle core and a thin gold layered shell show a potential as Computed tomography/Magnetic resonance imaging dual contrast agents [87].

Recently, the exploit of the high scattering ability of gold nanoshells as a contrast agent in vivo has been used by Optical Coherence Tomography (OCT) [88]. OCT is an imaging modality that provides cross-sectional subsurface imaging of biological tissue with micrometerscale resolution. The extra scattering achieved using a gold nanoshell, which possess both absorption and scattering properties in the NIR, provide optical contrast for improved diagnostic imaging and, at higher light intensity.

This property has been used to increase the contrast of tumours in mice. The gold nanoshells accumulated preferentially in the tumour and increased the contrast more than in other tissue [88].

PEG-coated gold nanoshells have been used as a contrast agent to image their distribution circulating in the vasculature in rat brain using photoacoustic imaging [89]. In this study, the images of the distribution of nanoshells circulating in the vasculature of a rat brain achieved by deep penetrating near-infrared light present a gradual enhancement of the optical absorption in the brain vessels (see **Figure 3**). Gold-nanorods and gold-nanoprisms have also been extensively used in bioimaging due to their ability to have the maximum of the plasmon resonance tuned further into the near infrared (NIR). Actually Motamedi et al. reported a contrast agent for a laser optoacoustic imaging system for in vivo detection of gold nanorods as well as to enhance the diagnostic power of photoacoustic imaging [90]. Song et al. also proposed a noninvasive in vivo spectroscopic photoacoustic sentinel lymph node mapping in a rat model using gold nanorods as lymph node tracers [91]. More recently, Daxiang Cui and co-workers reported the use of gold-nanoprisms a novel contrast agent for the hybrid technique of optoacoustic imaging. The authors demonstrated an in silico electron tomographic reconstruction of such gold nanostructures, which show promise for application in biomedical imaging, drug delivery, and photothermal therapy [92].

Some of the studies reported here can be useful for in situ diagnostics of cancer, by overcoming several limitations of conventional dyes, such as poor hydrophilicity and photostability, low quantum yield and detection sensitivity, insufficient stability in biological systems, and weak multiplexing capability. Additionally, the high scattering properties of these kind of NPs can enhance contrast of imaging systems based on microscopy.

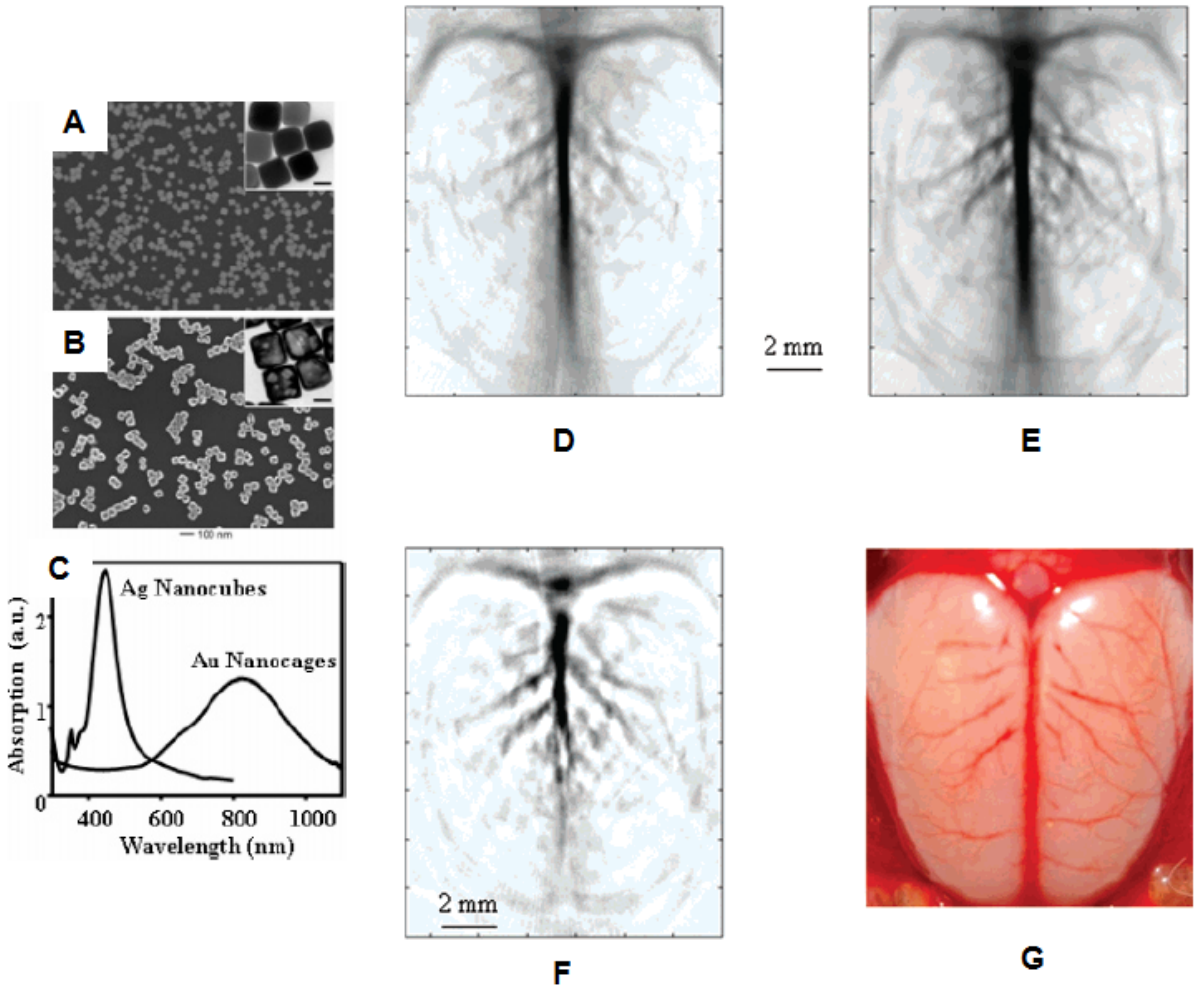

Figure 3. NanoBioimaging. Poly(ethylene glycol)-coated Au nanocages as a potential near-infrared (NIR) contrast agent for photoacoustic tomography (PAT). (**A**) SEM image of the as-synthesized silver nanocubes and (**B**) SEM image of gold nanocages. (**C**) Absorption spectra of Ag nanocubes and Au nanocages. The insets in panels **A** and **B** show TEM images of the nanocubes and nanocages, respectively (scale bars, 25 nm). Noninvasive PAT imaging of a rat's cerebral cortex (**D**) before the injection of nanocages and (**E**) about 2 h after the final injection of nanocages, which is the peak enhancement point. (**F**) A pixelwise differential image (image **D** - image **E**). (**G**) An openskull photograph of the rat's cerebral cortex.

3. Nanotherapy

In medical terms, a therapeutic effect is a consequence of a medical treatment of any kind, the results of which are judged to be desirable and beneficial. Conventional therapy methods in cancer involve the employment of anticancer agents that do not greatly differentiate between cancerous and normal cells [93]. Efficient in vivo targeting to heterogeneous population of cancer cells and tissue still requires better selectivity and decreased toxicity to surrounding normal cells, towards a decrease of systemic toxicity, adverse and severe side effects [94].

In another way, universally targeting cells within a tumor is not always feasible because some drugs cannot diffuse efficiently and the random nature of the approach makes it difficult to control the process and may induce multiple-drug resistance (MDR) – a situation where chemotherapy treatments fail patients owing to resistance of cancer cells towards one or more drugs [22]. Consequently, nanotechnology could offer a less invasive alternative, enhancing the life expectancy and quality of life of the patient [95].

At the moment, it is expected that the greatest gains in therapeutic selectivity will be achieved by synergistic combinations of several multicomponent targeting strategies. Currently, it is essential to develop technology for target and delivery of multiple therapeutic agents, and for the simultaneous capability of avoiding biological and biophysiscal barriers. For example, nanoparticles can extravasate into the tumor stroma through the fenestrations of the angiogenic vasculature, demonstrating targeting by enhanced permeation and retention. These particles are able to carry multiple antibodies, which further target them to epitopes on cancer cells, and direct antitumor action, leading to cell death. Irradiation might be use to activate the nanoparticles and set up the release of their cytotoxic action [96].

Due to advances in nanobiotechnology, potential therapeutic application of gold nanocarriers represent are an attractive platform for cancer therapy and has been investigated by different coworkers and used in a broad range of applications [95]. **Table 2** summarizes the latest progresses and general considerations for AuNP delivery and targeting in cancer therapy, according to their methodology principle, type of incubation/exposure and target organs.

Table 2. Summary of AuNPs used in cancer therapy according to the type of NP, surface modification, type of cancer, target cells/organs/organisms and explored methodology principle.

Method	Type of AuNP	Surface modification	Target cells/organs/organisms	Comments [Reference]
Gene therapy	13 nm spherical	thiol-ssDNA	RAW 264.7 (macrophage); HeLa cells (cervical carcinoma); NIH-3T3 (fibroblast); MDCK	***In vitro*** intracellular gene Regulation; control of protein expression in cells [97]

			cells (kidney)	
	13 nm spherical	PEG-block-poly(2-(N,N-dimethylamino)ethyl methacrylate) copolymer (PEG-PAMA); siRNA	HuH-7 cells (hepatocarcinoma)	Smart PEGylated AuNPs for the ***in vitro*** delivery of siRNA and to induce gene silencing [98]
	13 nm spherical	thiol-siRNA	HeLa cells (cervical carcinoma)	Polyvalent RNA-nanoparticle conjugates for ***in vitro*** luciferase knockdown [99]
	14 nm spherical	thiol-siRNA; naked siRNA; PEG-COOH; PEG-N_3; HIV-derived TAT peptide; RGD peptide; quaternary ammonium.	HeLa cells (cervical carcinoma); (freshwater polyp, Hydra); mice (C57BL/6j)	***In vitro*** and ***in vivo*** RNAi triggering using hierarchical approach with three biological systems of increasing complexity [100]
	15 nm spherical	cationic polymers: PEI; charge-reversal PAH-Cit; MUA (mercaptoundecanoic acid)	HeLa cells (cervical carcinoma)	Charge-reversal functional AuNPs to deliver siRNA and plasmid DNA into cancer cells (***in vitro***) [101]
	14 nm spherical	Cy3 labeled hairpin-DNA	HCT-116 cells (carcinoma of colon)	Au-nanobeacons capable of intersecting both pathways of ***in vitro*** RNA interference, blocking exogenous siRNA and endogenous microRNA [102]
	13 nm spherical	PEG-NH_2; siRNA; poly(β-amino ester)s (PBAEs)	HeLa cells (cervical carcinoma)	gold, Poly(β-amino ester) nanoparticles that facilitate high levels of ***in vitro*** siRNA delivery [103]
	40 nm spherical	Protease-degradable poly-L-lysine (PLL); siRNA	MDA-MB231-luc cells (breast cancer; LNCaP-luc cells (prostate adenocarcinoma)	multilayer siRNA coated AuNPs using siRNA and PLL as the charged polyelectrolytes for ***in vitro*** luciferase knockdown [104]
	Au-nanospheres	Folate receptor; siRNA	nude mice bearing HeLa cervical cancer xenografts	near-IR light-inducible NF-kappaB ***in vivo*** downregulation through folate receptor-targeted hollow Au-nanospheres carrying siRNA recognizing NF-kappaB p65 subunit [105]
	40 nm Au-nanoshells	PEG-NH_2; TAT-lipid; Cy3-siRNA	mouse endothelial cells	NIR laser-induced release of siRNA from the nanoshells and ***in vitro*** GFP silencing [106]
	spherical nucleic acid NP	siRNA	HeLa cells (cervical carcinoma); SKH-1E and C57BL/6J mice	*In vitro* and *in vivo* topical delivery of siRNA-based spherical nucleic acid AuNP conjugates for gene regulation [107]
Tumor targeting	spherical	pH Low Insertion Peptide (pHLIP)	Mouse model	nanogold-pHLIP conjugates used ***in vivo*** to target tumors [108]
	6 nm spherical	amine-terminated generation 5 (G5) poly(amidoamine) (PAMAM) dendrimers pre-functionalized with folic acid (FA) and fluorescein isothiocyanate (FI)	KB-HFAR cells (human epithelial carcinoma)	multifunctional dendrimer-stabilized AuNPs can specifically target cancer cells expressing high-affinity FA receptors ***in vitro*** [109]
	30 nm spherical	PEGylated trastuzumab (Herceptin)	MDA-MB-361 (breast cancer) tumors	Human Epidermal Growth Factor Receptor-2 (HER-2)-targeted AuNPs that enhance the radiation response of ***in vitro*** breast cancer cells and ***in vivo*** tumor xenografts to X-radiation

				[110]
	4 nm spherical	VEGF antibody (AbVF)	CLL B cells (B-Chronic Lymphocytic Leukemia)	AuNPs enhance ***in vitro*** apoptosis in B-chronic lymphocytic leukemia [111]
	60 nm spherical	PEG-COOH; malachite green isothiocyanate (MGITC); ScFv B10 (antibody fragment for human EGFR)	Tu686 and H520 cells (EGFR-positive cancer cells); nude mouse xenografted with Tu686 cells	Pegylated SERS AuNPs for ***in vitro*** and ***in vivo*** tumor targeting and detection [112]
	Ultra-small Au-nanoclusters	folic acid (FA); near-infrared fluorescent dye (MPA); Doxorubicin (DOX)	A549 cells (lung cancer); HepG-2 (liver cancer); MDA-MB-231 (breast cancer); HTC116 (carcinoma of colon)	***Cellular*** and ***in vivo*** studies with Au-FA-MPA and Au-FA-DOX show high affinity and anti-tumor activity to different tumors [113]
	30 nm spherical	PEGylated trastuzumab (FDA-approved humanized monoclonal antibody); radiolabeled polymer	MDA-MB-361 cells (breast cancer); athymic CD-1 mice bearing MDA-MB-361tumors	AuNPs that enhance tumor uptake and intracellular delivery (***in vitro*** and ***in vivo***) while reducing the systemic exposure by evaluation of the impact of targeting and route of administration on organ distribution [114]
Drug delivery	2.5 nm spherical	hydrophobic drugs: tamoxifen (TAF) and β-lapachone (LAP); Bodipy (fluorescent probe)	MCF-7 cells (breast cancer)	Entrapment of hydrophobic drugs in AuNP monolayers with efficient ***in vitro*** release into cancer cells [115]
	30 nm spherical	prostate-specific membrane antigen (PSMA) RNA aptamer; Doxorubicin (DOX)	LNCaP cells (prostate adenocarcinoma)	A drug-loaded aptamer−AuNP bioconjugate for ***in vitro*** imaging and therapy of prostate cancer [116]
	25 nm spherical	thiol-PEGylated; tamoxifen (TAM)	MDA-MB-361 cells (breast cancer); MCF-7 cells (breast cancer)	Tamoxifen−poly(ethylene glycol)−thiol AuNPs that enhance potency and selective delivery for ***in vitro*** breast cancer treatment [117]
	180 nm spherical	PEG; Oxaliplatin	A549 cells (lung epithelial cancer); HCT116, HCT15, HT29, RKO cells (all for colon cancer)	AuNPs for the improved anticancer drug delivery ***in vitro*** of the active component of oxaliplatin [118]
	13 nm spherical	cisplatin	A549 cells (lung cancer); tumor-bearing SCID mice	***In vitro*** and ***in vivo*** antitumoral drugs conjugated to AuNPs [119]
	spherical	Cyclic peptide	CCRF-CEM cells (human leukemic lymphoblasts); SK-OV-3 cells (human ovarian adenocarcinoma)	Cyclic peptide-capped AuNPs for ***in vitro*** drug delivery [120]
	40 nm Au-nanospheres	NH_2-PEG-COOH; Doxorubicin (DOX); Cyclic peptide c(TNYL-RAW), a second-generation EphB4-binding antagonist	mice bearing Hey tumors	***In vivo*** photothermal chemotherapy using doxorubicin-loaded Au-nanospheres that target EphB4 receptors in tumors [121]
	plasmonic vesicles assembled from 14 nm spherical AuNPs	Raman reporter; PEG; hydrophobic copolymer (PMMAVP) of methyl methacrylate (MMA) and 4-vinylpyridine (4VP)	SKBR-3 cells (breast adenocarcinoma)	Self-assembled plasmonic vesicles of SERS-encoded amphiphilic AuNPs for ***in vitro*** cancer cell targeting and traceable intracellular drug delivery [122]

In this panorama we can see that over the last 10 years, the majority (approximately 80%) of gold nanoformulations for gene therapy, tumor targeting and drug delivery in cancer have been tested in cell cultures and normally targeting reporter genes, such as luciferase or GFP. In the future, it is imperative to develop new therapy vehicles and extensive testing in animal models in order to develop the next-generation nanoparticle translation into the clinics. There is only one active clinical trial reporting the use of AuNPs. This phase I trial is studying the side effects and best dose of TNF-bound colloidal gold in treating patients with advanced solid tumors (clinical trial number NCT00356980), sponsored by the National Institutes of Health Clinical Center (CC) and National Cancer Institute (NCI). As it can be seen in **Figure 4** there is a disproportional level between nanoparticle production and their translation into clinics.

In fact, clinical trials require the coordinated effort of interdisciplinary research groups, institutes and pharmaceuticals. Clinical-stage programs will probably have to deal with more and more human data and financial investment, before they can be viewed as a mainstream proposition for resourceful nanotherapy vehicle developers. The current generation of nanoparticles varies widely in size, chemical composition, surface charge, tissue tropism and sensitivity that makes difficult to translate them into the manufacturing process. The community has to learn how to deal with all the dat produced so far. The rules for understanding how nanoparticles interact with different organs and organisms are starting to emerge, although most of the valuable evidences has to come from animal models.

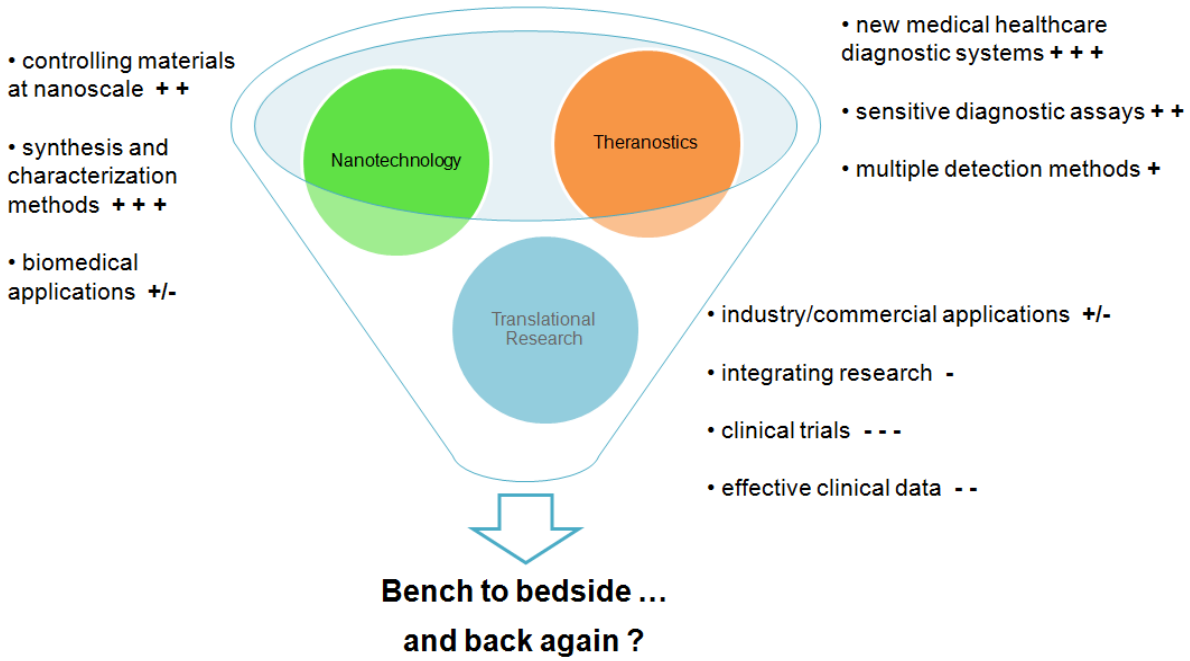

Figure 4. Disproportional level between nanoparticle production and their translation into clinics. Thousands of systems were published describing different synthesis, biofunctionalization and characterization methods that will most likely revolutionize our understanding of chemical and biological mechanisms and push forward efficient diagnostics and therapeutic platforms. Nevertheless, very few were produced to improve a bench-to-bedside approach to translational research. Outcomes like this must be followed by extensive laboratory work, which results in improved screening procedures and a new therapy of great potential, although the final product should always be part of a two way interaction between laboratory scientists and clinicians.

3.1.Gene therapy

We are in the dawn of a new age in gene therapy driven by nanotechnology vehicles. Although there are technical challenges associated with the therapeutic application of nanoparticles, the integration of therapy with diagnostic profiling has accelerated the pace of discovery of new nanotechnology methods. The development of a safe, efficient, specific and nonpathogenic vehicle for gene delivery is highly attractive [123;124].

Gene therapy is receiving increasing attention and, in particular, small-interference RNA (siRNA) shows importance in novel molecular approaches in the knockdown of specific gene expression in cancerous cells (see **Figure 5**). In fact, this non-viral-vector-mediated delivery of therapeutic siRNAs is highly desirable and constitutes an important challenge to gene therapy [125-127].

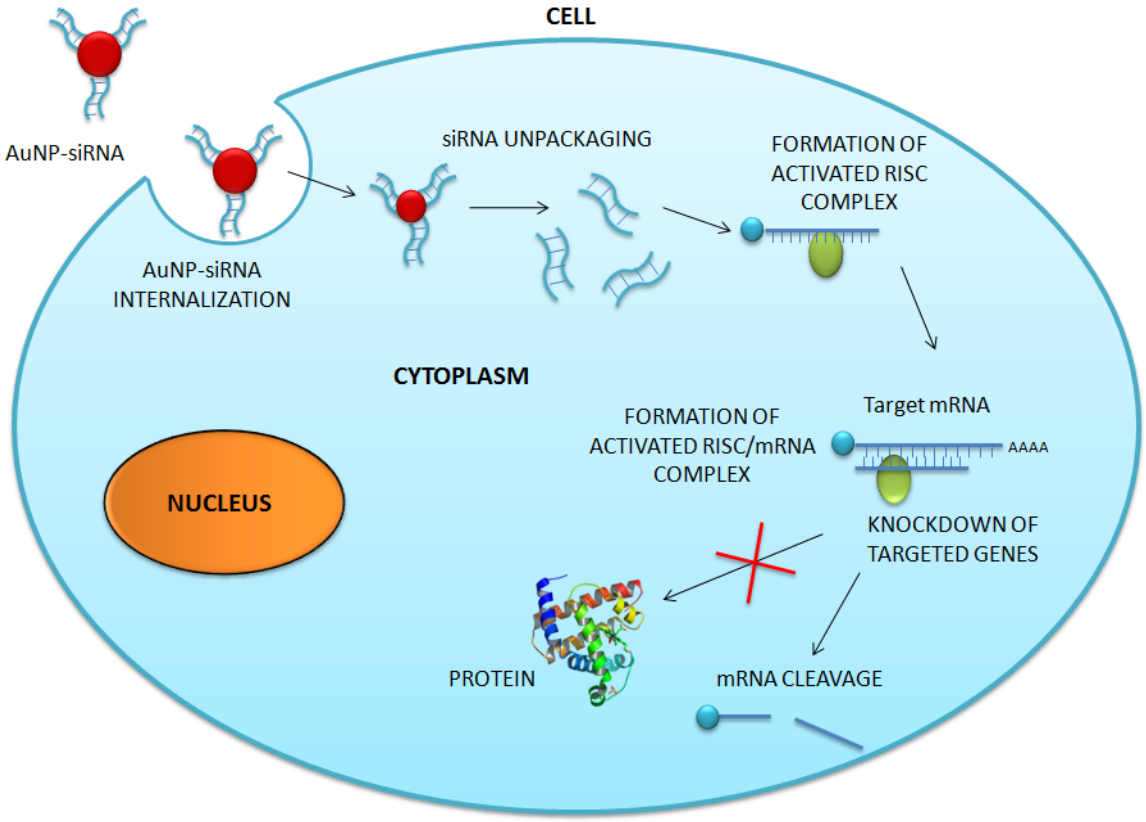

Figure 5. Regulation of gene expression via siRNA-gold nanoparticles. Engineered nanoparticles modified with siRNA can represent a delivery system of siRNA and a useful tool to block gene function and for sequence-specific post-transcriptional gene silencing. siRNA-modified nanocarriers can enter cells and subsequently unwound siRNA strands and assembled into an effector complex, RNA Induced Silencing Complex (RISC), which can direct RNA cleavage, mediate translational repression or induce chromatin modification. The antisense strand then binds to its complementary/target mRNA (activated RISC/mRNA complex). The catalytic RISC recognizes mRNAs containing perfect or near-perfect complementary sequence to the guide siRNA and cleaves the mRNAs at a site precisely 10 nucleotides from the 5'-end of the guide strand. Finally, mRNA degradation is achieved by endo- and exonucleases, resulting in knockdown of the expression of the corresponding genes.

In fact, antisense DNA [128;129] and RNA interference (RNAi) via the use of small-interfering RNA [130-133] have emerged as powerful and useful tools to block gene function and for sequence-specific posttranscriptional gene silencing, playing an important role in downregulation of specific gene expression in cancer cells. Thus, one drawback of using naked siRNAs is that they show extremely short half-lives, weak protection against action by RNases, poor chemical stability, and

common dissociation from vector [134]. In fact, the major obstacle to clinical application is the uncertainty about how to deliver therapeutic RNAs (e.g., miRNA and/or siRNA) with maximal therapeutic impact. AuNPs have shown potential as intracellular delivery vehicles for antisense oligonucleotides [97] and for therapeutic siRNA by providing protection against RNAses and ease of functionalization for selective targeting [99;135]. For example, Mirkin and coworkers reported the use of polyvalent RNA-AuNP conjugates that are readily taken up by cells and that the particle bound siRNA can effectively regulate genes in the context of RNA interference [99].

Several other studies using engineered NPs modified with siRNA have demonstrated a cytoplasmic delivery system of siRNA and efficient gene silencing using AuNPs [99;101;103;136]. However, almost all nanoconjugates using siRNA have exclusively been tested in cell cultures targeting only reporter genes.

Recently, Conde et al. provided evidence of in vitro and in vivo RNAi triggering via the synthesis of a library of novel multifunctional AuNPs, using a hierarchical approach including three biological systems of increasing complexity: in vitro cultured human cells, in vivo freshwater polyp (*Hydra vulgaris*), and in vivo mice models [100]. The authors developed effective conjugation strategies to combine, in a highly controlled way, specific biomolecules to the surface of AuNPs such as: (a) biofunctional spacers: Poly(ethylene glycol) (PEG) spacers used to increase solubility and biocompatibility; (b) cell penetrating peptides such as TAT and RGD peptides: A novel class of membrane translocating agents named cell penetrating peptides (CPPs) that exploit more than one mechanism of endocytosis to overcome the lipophilic barrier of the cellular membranes and deliver large molecules and even small particles inside the cell for their biological actions; and (c) siRNA complementary to a master regulator gene, the protooncogene c-myc, were bond covalently (SH-siRNA) and ionically (naked siRNA) to AuNPs [100].

However, efforts to target siRNA-nanoparticles to organs are less advanced. Some organs need smaller and novel NPs to access different kinds of tissue. Another challenge, which also requires

novel materials, is the endosomal release of siRNA, once it is transported across the cell membrane. Most of the described systems also get trapped by the the lysosomes and their siRNA cargo gets compromised. Probably the endosomal escape or siRNA accessibility to form the RNA-induced silencing complex (RISC) requires substantially more circulation time.

While the AuNPs for gene therapy discussed thus far employ the load of siRNA to nanoparticles, AuNPs have also shown potential as intracellular delivery vehicles for antisense oligonucleotides (ssDNA,dsDNA) by providing protection against intracellular nucleases and ease of functionalization for selective targeting [99;135]. So far, several strategies for gene delivery systems have been developed, including mixed monolayer protected AuNPs [137;138], polymer-AuNPs complexes [139;140] and dsDNA and ssDNA functionalized AuNPs [141;142].

Recently, Conde et al developed a new theranostic system capable of intersecting all RNA pathways: from gene specific downregulation to silencing the silencers, i.e. siRNA and miRNA pathways. The authors reported the development AuNPs functionalized with a fluorophore labeled hairpin-DNA, i.e. Gold nanobeacons, capable of efficiently silencing single gene expression, exogenous siRNA and endogenous miRNAs while yielding a quantifiable fluorescence signal directly proportional to the level of silencing [102].

From a synthetic point of view it is still unclear the differences between DNA–AuNPs and siRNA–AuNPs. From the papers reported so far the siRNA and DNA gold nanoconjuates are almost from the same size and charge, and show similar efficiencies. Nevertheless siRNA–AuNP conjugates require functionalization with thiol-PEG molecules to achieve equivalent stability to DNA–AuNPs, which may have something to do with the capacity loading of the different molecules due to singular hydrophobicity and/or hydrophilicity, molecular weight and charge density properties between RNA and DNA [143]. However, this fact needs additional clarification.

Further research into the fundamental mechanisms of *in vivo* gene therapy using nanodevices could unveil new dimensions of nanoparticle-mediated gene silencing that will have profound implications

for understanding gene regulation, and which could also affect the development of functional genomics and therapeutic applications. One of the most important issues that is still unclear is how biocompatible AuNPs will be following intraveneous injection, in particular when the ultimate destination is the cytoplasm and/or nucleus inside cells. Future *in vivo* work will need to cautiously consider the accurate option of chemical modifications to incorporate into the nanoparticles to avoid off-target effects. Though nanoparticles' potential against cancer is still in need of further optimization and characterization, it is now time to start translating these promising platforms to the clinical settings towards widespread effective therapy strategies in the fight against cancer.

3.2. Tumor targeting

Nanoparticles are excellent tumor-targeting vehicles because of a unique inherent property of solid tumors. Numerous tumors present with defective vasculature and poor lymphatic drainage, due to the rapid growth of solid tumors, resulting in an enhanced permeability and retention effect. This effect allows nanoparticles to accumulate specifically at the tumor site [20;93]. Once the tumor is directly connected to the main blood circulation system, multifunctional nanocarriers can exploit several characteristics of the newly formed vasculature and efficiently target tumors. Tumor cells are supplied by blood capillaries that perfuse the cells of the tissue where nanocarriers can passively accumulate or anchor through targeting moieties to biomarkers overexpress by tumor cells (see **Figure 6**) [45].

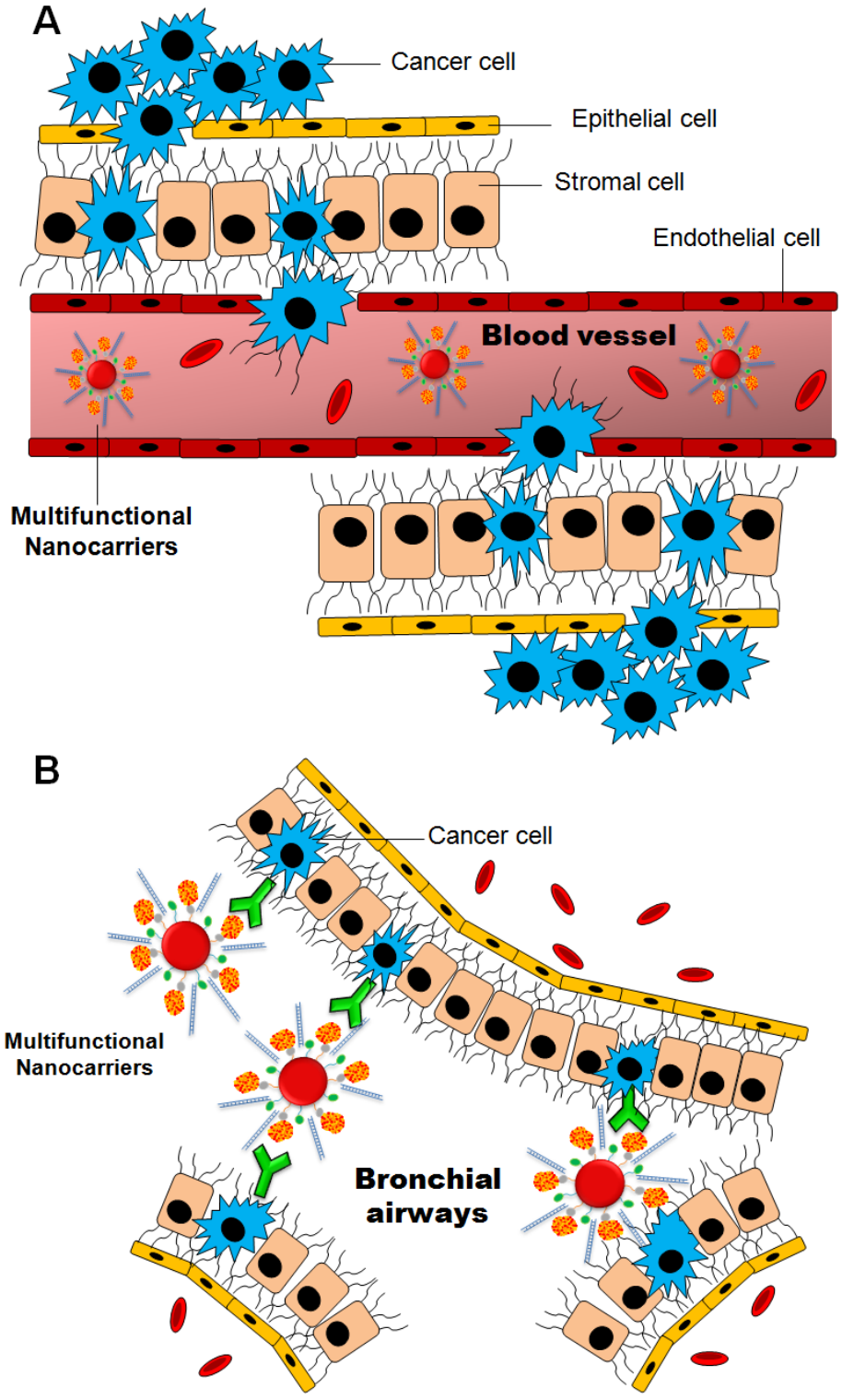

Figure 6. Tumor targeting via multifunctional nanocarriers. Cancer cells reduce adhesion to neighboring cells and migrate into the vasculature-rich stroma. Once at the vasculature, cells can freely enter the bloodstream (**A**). Once the tumor is directly connected to the main blood circulation system, multifunctional nanocarriers can interact directly with cancer cells and effectively target tumors. Engineered NPs maybe also administered directly to bronchial airways (**B**). These nanocarriers may bind to unique moieties that are presented by the cancer cell that can upregulate certain cell-surface molecules and secreted factors.

Shi *et al.* developed a simple system with multifunctional amine terminated poly(amidoamine) (PAMAM) dendrimers, folic acid (FA) and fluorescein isothiocyanate functionalized in gold nanoparticles. This approach can specifically target cancer cells expressing high-affinity FA receptors in vitro [109].

Further work in tumor targeting was reported in a subcutaneous model of colon cancer, where it was demonstrated that systemically delivered AuNPs (size, approximately 33 nm) conjugated to tumor necrosis factor (TNF) accumulated in tumors [144]. This study outlines the development of a colloidal gold nanoparticle vector that targets the delivery of tumor necrosis factor (TNF) to a solid tumor growing in mice.

Mukherjee et al. studied B-Chronic Lymphocytic Leukemia (CLL) which is characterized by apoptosis resistance. They found induction of significantly more apoptosis in CLL B cells by co-culture with an anti-VEGF antibody. To increase the efficacy of these agents in CLL therapy they focused on the use of AuNPs, by attaching VEGF antibody to the nanoparticle's surface. The AuNP–VEGF antibody treated cells showed significant down regulation of anti-apoptotic proteins [111].

In cancer research, colloidal gold can be used to target tumors and provide detection using SERS (Surface Enhanced Raman Spectroscopy) in vivo. These AuNPs are surrounded with Raman reporters which provide light emission that is over 200 times brighter than quantum dots [145;146]. It was found that the Raman reporters were stabilized when the nanoparticles were encapsulated with a thiol-modified polyethylene glycol coat and gave large optical enhancements. This allows for compatibility and circulation in vivo. When conjugated to tumor-targeting ligands, these conjugated SERS nanoparticles were able to target tumor markers such as epidermal growth factor receptor (EGFR), which is sometimes overexpressed in cells of certain cancer types, [42;147] and then detect the location of the tumor on human cancer cells and in xenograft tumor models [112]. Qian et al.

described biocompatible and nontoxic nanoparticles for in vivo tumor targeting and detection based on pegylated gold nanoparticles and surface-enhanced Raman scattering. These conjugated nanoparticles were able to target tumor biomarkers such as epidermal growth factor receptors on human cancer cells and in xenograft tumor models [112].

Although cancer therapies are improving, some formulations are not reaching with high efficiency tumor cells or tissues, and countless doubts remains over the efficacy of those that do. To efficiently target a cancer cell, either a circulation cell or a cell from the primary tumor or one hidden within a population of normal cells, represents an exceptional challenge. In fact, there are a lot of limitations for tumor targeting as some nanocarriers can also target normal proteins which are not exclusively expressed by the cancer cell. Targeting specific cells may be completely different to target the organ. The most important aspects that the researchers need to take into account are the specificity of the nanoparticle to the target molecules, as well as toxicological and immunological effects [148]. For example, the combination of small size nanoparticles with their special thermal, imaging, drug/gene carrier, or optical characteristics with the specific and selective recognition abilities of antibodies will definitely produce a hybrid product that shows versatility and specificity. Therefore, multifunctional nanocarriers have the potential to join numerous therapeutic functions into a single platform, by targeting specific tumor cells, tissues and organs.

3.3. Drug delivery

The vast majority of FDA approved used drugs exhibit a short half-life in the blood stream and a high overall clearance rate. In fact, the major obstacles/limitations in drug delivery are: cytoplasmic and systemically delivery of the drug, renal clearance, target site accumulation after administration and heterogeneous vascular perfusion and diffusion. Actually, these small drug molecules usuaaly diffuse rapidly into healthy tissues and are dispersed consistently within the body. As a consequence, just a small amount of the drug can reach the target site, which often leads to side effects. These

obstacles usually occur with drugs that exhibit a narrow therapeutic index, such as anticancer biomolecules, immunosuppressive agents, as well as antirheumatic medicines. Poor drug delivery and accumulation at the target site frequently leads to significant limitations, such as multi-drug resistance, which leads many cancers to develop severe resistance to chemotherapy drugs [149]. Nanocarriers can also be used to optimize the biodistribution of drugs to diseased organs, tissues or cells, in order to improve and target drug delivery [150].

It is important to realize that the nanoparticle-mediated drug delivery is feasible only if the drug distribution is otherwise inadequate. These cases include drug targeting of difficult, unstable molecules (proteins, siRNA, DNA), delivery to the difficult sites (brain, retina, tumors, intracellular organelles) and drugs with serious side effects (e.g. anti-cancer agents). The performance of the nanoparticles depends on the size and surface functionalities in the particles. Also, the drug release and particle disintegration can vary depending on the system (eg. biodegradable polymers sensitive to pH). An optimal nanodrug delivery system ensures that the active drug is available at the site of action for the correct time and duration, and their concentration should be above the minimal effective concentration (MEC) and below the minimal toxic concentration (MTC) [151;152].

AuNPs are also being investigated as vehicles for drug delivery such as paclitaxel [153]. *Gibson* et al. describe the first example of 2 nm AuNPs covalently functionalized with the chemotherapeutic drug paclitaxel. The administrations of hydrophobic drugs require molecular encapsulation and it is found that nanosized particles are particularly efficient in evading the reticuloendothelial system. This approach gives a rare opportunity to prepare hybrid particles with a well-defined amount of drug and offers a new alternative for the design of nanosized drug-delivery systems [115;153;154] (see **Figure 7**)

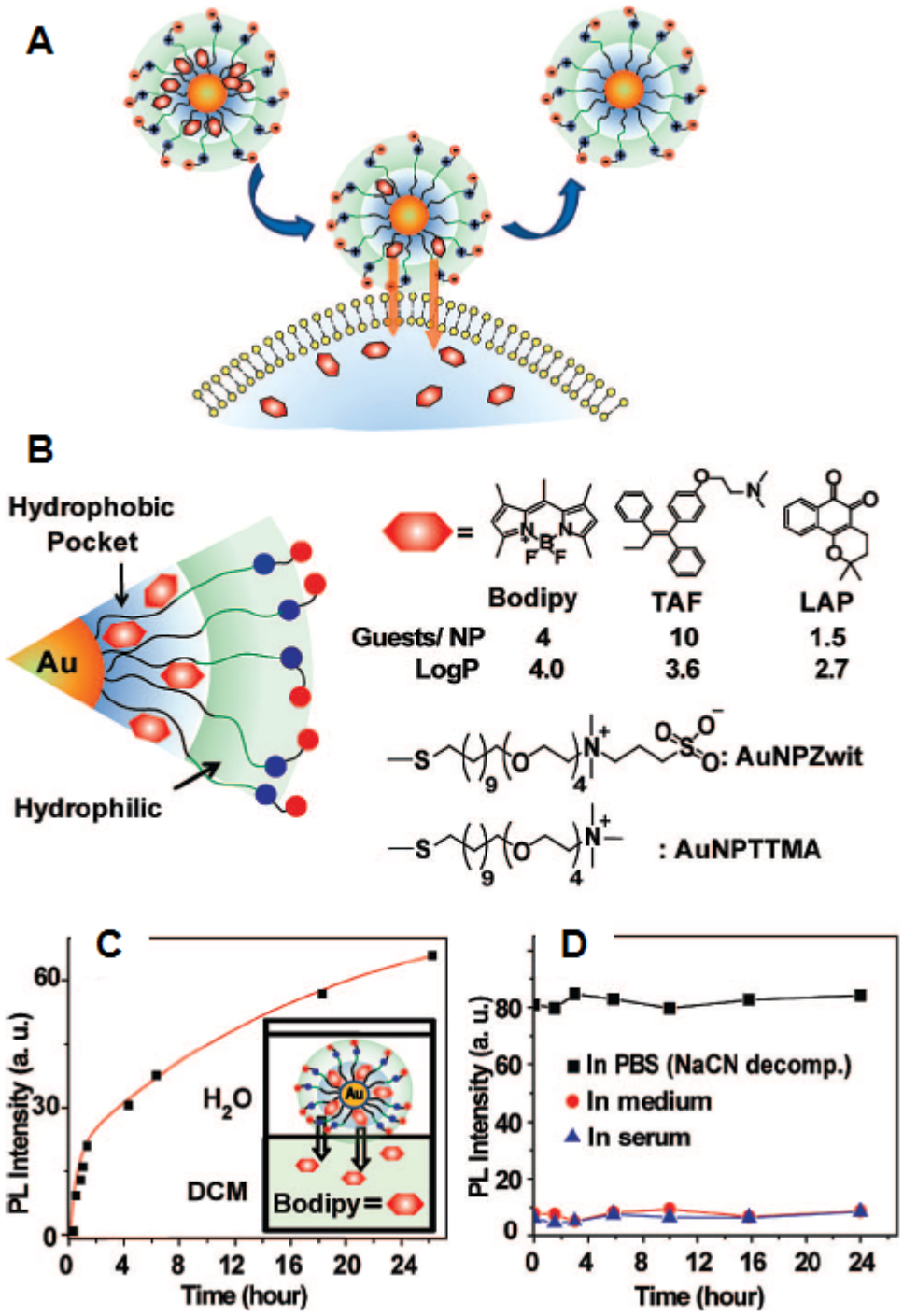

Figure 7. Drug delivery. Entrapment of hydrophobic drugs in nanoparticle monolayers with efficient release into cancer cells (**A**) Delivery of payload to cell through monolayer-membrane interactions. (**B**) Structure of particles and guest compounds: Bodipy, TAF, and LAP, the number of encapsulated guests per particle, and log P of the guests. (**C**) Release of Bodipy from AuNPZwit Bodipy in DCM-aqueous solution two-phase systems (λex=499 nm, (λem=517 nm). (**D**) PL intensity of AuNPZwit-Bodipy in cell culture medium and 100% serum, indicating little or no release relative to AuNPZwit-Bodipy in PBS after NaCN induced release of guest molecules (λex=499 nm, λem=510 nm).

Nanotechnology has provided for novel and powerful systems that may be used treatment of human diseases. However the majority of products, reagents and drugs being used for the development of these nanoscale systems have to be approved by the main supervising agencies, such as the FDA and EMA [2].

Thus far, some limitations for the correct design and application of nanoparticles, such as pharmacokinetics, biodistribution, and side effects of the nanotherapy; safety profile of nanoparticles before and after conjugation and toxicity, needs to be clarified to validate efficient clinical appliance [2].

4. NanoToxicity

The AuNPs have a proclivity in vivo and in vitro to bioaccumulate within various types of cells with a special affinity for macrophage-type cells (both histiocytes and blood phagocytic cells), and reticuloendothelial cells throughout the body). They also produce varying degrees of bioaccumulation in such tissues as lymph nodes, bone marrow, spleen, adrenals, liver and kidneys [155-157].

Research shows that nanoparticles can stimulate and/or suppress the immune responses, and that their compatibility with the immune system is largely determined by their surface chemistry. In fact, is well known the influence of size, solubility and surface modification on the biocompatibility of nanoparticles and their use in biological applications [158] (see **Figure 8**).

AuNPs are generally considered to be benign. However, the size similarity of AuNPs to biological matters could provide "camouflage" to cellular barriers, leading to undesired cellular entry which might be detrimental to normal cellular function [159].

Pan and colleagues recently conducted a systematic investigation of the size-dependent cytotoxicity of AuNPs against four cell lines [160]. They found that AuNPs 1 to 2 nm in size displayed cell-type dependent cyotoxicity with high micromolar IC50s. In contrast, AuNPs 15 nm in size were nontoxic

to cells at concentrations 60-fold higher than the IC50 of the smaller AuNPs. These results seemed to confirm size dependent toxicity of AuNPs [115;144;161-163], an inference that has hitherto been somewhat ambivalent. On the other hand, found that the presence of sodium citrate residues on AuNPs impaired the viability in the alveolar type-II cell lines A549 and NCIH441. Interestingly, the presence of an excess of sodium citrate on the surface of NPs not only reduced the *in vitro* viability of A549 and NCIH441cell lines, but also affected cellular proliferation and increased the release of lactate dehydrogenase (marker for apoptotic cell degradation) [164].

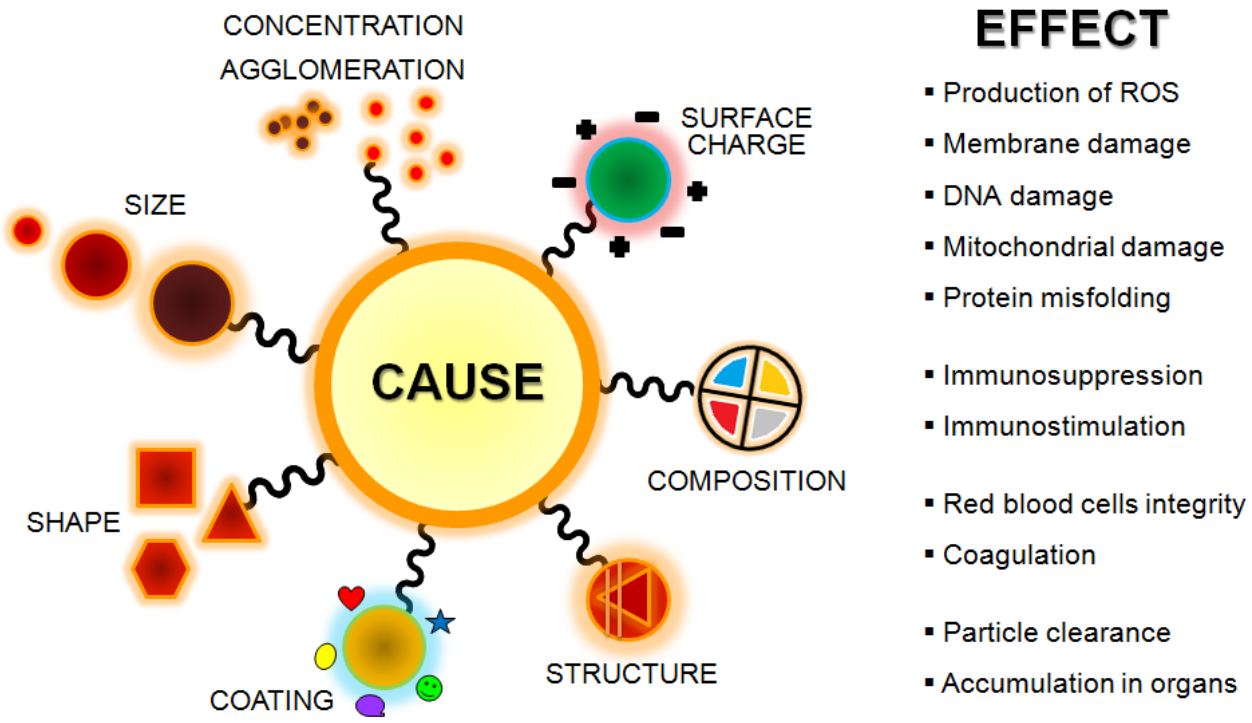

Figure 8. NanoToxicity: Causes and Effects. Nanoparticles biocompatibility/effects and their use in biological applications can be influenced by size, shape, solubility, composition and surface charge and modification/chemistry.

Although AuNPs are generally considered as highly biocompatible, previous in vitro studies have also shown that cytotoxicity of AuNPs in certain human epithelial cells was observed [165;166].

Now the most imperative question rises up. Are the gold nanoparticles cytotoxic or biocompatible? And how can the gold nanoparticles be design to avoid these effects?

There does not seem to have a simple answer. Even though there is not any general mechanism for making nanoparticles universally 'non-toxic' to all living cells and all organisms, there are important findings that can be applied for increasing nanoparticle biocompatibility and reducing cytotoxic interactions in vivo and in vitro.

Using the lowest nanoparticle dose to get the desired response for the shortest period of time, in general, seems to promote biocompatibility as well as nanoparticle´s coating. For example, if the outer coating does not completely covers the nanoparticle reactive surface, the presence of cracks, roughness or interruptions could lead to complement or antibody attachment, or dissolution of the coating by cell digestion [167].

It is essential to test nanoparticle/biological interactions experimentally and modify the nanoparticles for best biocompatibility with the cell in order to eliminate some obstacle, like the peroxidation of membrane lipids, the generation of reactive oxygen species, the acute and chronic release of pro-inflammatory factors, modification in genetic cellular function, and the possibility of nanoparticles becoming inactive/unavailable during filtration or passage through pores and fenestrations [168,169] due to size, inflexibility of the nanoparticle core, or protein adsorption and agglomeration [167].

When interpreting nanoparticle interactions with cells and organisms, it is important to remember that living systems may appear normal and be capable of growth and function, but they may be genetically altered in subtle ways following nanoparticle exposure, which can produce serious consequences at some time in the distant future. Conversely, other cells that seem to be damaged may, in time, recover from nanoparticle exposure and function normally in the absence of the nanoparticles [167,169].

In conclusion, the only weapon that we have to insure that these new materials are well designed and safely used is to question and test each new nanoparticle to make sure that it has been designed for

safety (with maximum biocompatibility) during handling, use and disposal. Evaluating the biocompatibility of nanomaterials is imperative. In fact, it is important to carefully characterize the biocompatibility and safety of the nanomaterials if they are to be used for medical purposes. Despite the major scientific advances made in the field of molecular and cell biology and biotechnology, the basic concepts of regulatory toxicology have hardly changed over the past decades [158]. Actually, the vast majority of studies report the biocompatibility of nanomaterials only trough the study of cell viability. Almost no importance is given when testing nanomaterials in the detection of genetic damages (DNA strand breaks and the formation of nuclear abnormalities), or in identifying protein markers of toxicity, or measuring the level of oxidative stress. For example, when using gene silencing technologies, the function of specific genes and proteins in toxicity pathways could be identified, once DNA-damage response (DNA repair, cell-cycle regulation and apoptosis) encompasses gene-expression regulation at the transcriptional and post-translational levels.
In fact, Conde et al. reported a gold-nanobeacon system [102] used for gene therapy that was extensively evaluated for the genotoxic, cytotoxic and proteomic effects after incubation in cancer cells [170]. The exposure was evaluated by two-dimensional protein electrophoresis followed by mass spectrometry to perform a proteomic profile and MTT assay, glutathione-S-transferase assay, micronucleus test and comet assay to assess the genotoxicity. An assessment of genome-related toxicity revealed no significant DNA damage increase, as well as no potential mutagenic or clastogenic consequences to the cell [170].

5. Conclusions and Future perspectives

Over the last decade, thousands of different gold nanocarriers were developed and published. Almost 20% of these papers were published in 2010 alone. It is indisputable that the use of gold nanocarriers has been gaining momentum as vectors for therapy and diagnostic strategies, combining the AuNPs'

ease of functionalization with numerous biomolecules, high loading capacity and fast uptake by target cells.

Here, we have reviewed part of this exciting progress and research advances within the context of multifunctional gold nanocarriers for cancer theranostics. Despite the significant efforts towards the use of gold nanocarriers in biologically relevant research, more *in vivo* studies are needed to assess the applicability of these materials as delivery agents. In fact, only a few went through feasible clinical trials. Nanoparticles have to serve as the norm rather than an exception in the future conventional cancer treatments. Future *in vivo* work will need to carefully consider the correct choice of chemical modifications to incorporate into the multifunctional gold nanocarriers to avoid activation off-target, side effects and toxicity. Moreover the majority of studies on nanomaterials do not consider the final application to guide the design and functionalization of NP. Instead, the focus is predominantly on engineering materials with specific physical or chemical properties.

To improve medicine, scientific discoveries must be translated into clinical applications. Such discoveries typically begin at "the bench" with basic/fundamental research in which scientists study disease at a molecular or cellular level then progress to the clinical level, which is the patient's "bedside". Scientists and clinicians are increasingly aware that this bench-to-bedside approach to translational research is really a two-way interaction. However, an additional effort should appear towards the development of new clinical strategies.

For that reason, it is imperative to learn how advances in nanosystem's capabilities are being used to identify new diagnostic and therapy tools driving the development of personalized medicine in oncology; discover how integrating cancer research and nanotechnology modeling can help patient diagnosis and treatment; recognize how to translate nanotheranostics data into an actionable clinical strategy; discuss with industry leaders how nanotheranostics is evolving and what the impact is on current research efforts; and last but not least, learn what approaches are proving fruitful in turning promising clinical data into treatment realities.

Although all studies described here provide a baseline level of data in support of the effectiveness and safety of nanomaterials, we wonder how useful the data generated will be in successfully predicting and preventing scientists from jeopardizing the safety of the future patients?
With chemists, biologists and materials scientists working together with clinicians and engineers, but especially with "translational innovators" new solutions to crucial nanobiomedical problems will hopefully be found.

Competing interests

The authors declare that they have no competing interests.

Authors' contributions

JC conceptualized the manuscript and wrote the draft. FT, PVB and JMF contributed in the draft and concept of the paper. All authors contributed in the revision process. All authors read and approved the final manuscript.

Acknowledgements

Authors thank ERANET-NANOSCIERA NANOTRUCK project for financial support. JMF thanks ARAID and Fondo Social Europeo for financial support. PVB thanks CIGMH/FCT/MCES (PEst-OE/SAU/UI0009/2011). JC acknowledges FCT grant (SFRH/BD/62957/2009).

BOOK CHAPTER: "Nano-oncologicals: new targeting and delivery approaches"

References

[1] http://nano.cancer.gov/, in 2010.

[2] Baptista P. Cancer Nanotechnology - Prospects for Cancer Diagnostics and Therapy. Current Cancer Therapy Reviews 2009.

[3] Ma X, Zhao Y, Liang XJ. Theranostic nanoparticles engineered for clinic and pharmaceutics. Acc Chem Res 2011 Oct 18;44(10):1114-22.

[4] Praetorius NP, Mandal TK. Engineered nanoparticles in cancer therapy. Recent Pat Drug Deliv Formul 2007;1(1):37-51.

[5] Lammers T, Kiessling F, Hennink WE, Storm G. Nanotheranostics and image-guided drug delivery: current concepts and future directions. Mol Pharm 2010 Dec 6;7(6):1899-912.

[6] Pene F, Courtine E, Cariou A, Mira JP. Toward theragnostics. Crit Care Med 2009 Jan;37(1 Suppl):S50-S58.

[7] Lammers T, Aime S, Hennink WE, Storm G, Kiessling F. Theranostic nanomedicine. Acc Chem Res 2011 Oct 18;44(10):1029-38.

[8] Heath JR, Davis ME. Nanotechnology and cancer. Annu Rev Med 2008;59:251-65.

[9] Nishiyama N. Nanomedicine: nanocarriers shape up for long life. Nat Nanotechnol 2007 Apr;2(4):203-4.

[10] Ghosh P, Han G, De M, Kim CK, Rotello VM. Gold nanoparticles in delivery applications. Adv Drug Deliv Rev 2008 Aug 17;60(11):1307-15.

[11] Goodman CM, McCusker CD, Yilmaz T, Rotello VM. Toxicity of gold nanoparticles functionalized with cationic and anionic side chains. Bioconjug Chem 2004 Jul;15(4):897-900.

[12] Hirsch LR, Stafford RJ, Bankson JA, Sershen SR, Rivera B, Price RE, et al. Nanoshell-mediated near-infrared thermal therapy of tumors under magnetic resonance guidance. Proc Natl Acad Sci U S A 2003 Nov 11;100(23):13549-54.

[13] Hainfeld JF, Slatkin DN, Smilowitz HM. The use of gold nanoparticles to enhance radiotherapy in mice. Phys Med Biol 2004 Sep 21;49(18):N309-N315.

[14] Hainfeld JF, Dilmanian FA, Slatkin DN, Smilowitz HM. Radiotherapy enhancement with gold nanoparticles. J Pharm Pharmacol 2008 Aug;60(8):977-85.

[15] Hong R, Han G, Fernandez JM, Kim BJ, Forbes NS, Rotello VM. Glutathione-mediated delivery and release using monolayer protected nanoparticle carriers. J Am Chem Soc 2006 Feb 1;128(4):1078-9.

[16] Thomas M, Klibanov AM. Conjugation to gold nanoparticles enhances polyethylenimine's transfer of plasmid DNA into mammalian cells. Proc Natl Acad Sci U S A 2003 Aug 5;100(16):9138-43.

[17] Kim KY. Nanotechnology platforms and physiological challenges for cancer therapeutics. Nanomedicine 2007 Jun;3(2):103-10.

[18] Sperling RA, Rivera GP, Zhang F, Zanella M, Parak WJ. Biological applications of gold nanoparticles. Chem Soc Rev 2008 Sep;37(9):1896-908.

[19] Sperling RA, Parak WJ. Surface modification, functionalization and bioconjugation of colloidal inorganic nanoparticles. Philos Transact A Math Phys Eng Sci 2010 Mar 28;368(1915):1333-83.

[20] Gil PR, Parak WJ. Composite nanoparticles take aim at cancer. ACS Nano 2008 Nov 25;2(11):2200-5.

[21] Doria G, Conde J, Veigas B, Giestas L, Almeida C, Assuncao M, et al. Noble metal nanoparticles for biosensing applications. Sensors (Basel) 2012;12(2):1657-87.

[22] Peer D, Karp JM, Hong S, Farokhzad OC, Margalit R, Langer R. Nanocarriers as an emerging platform for cancer therapy. Nat Nanotechnol 2007 Dec;2(12):751-60.

[23] Doria G, Franco R, Baptista P. Nanodiagnostics: fast colorimetric method for single nucleotide polymorphism/mutation detection. IET Nanobiotechnol 2007 Aug;1(4):53-7.

[24] Baptista P, Pereira E, Eaton P, Doria G, Miranda A, Gomes I, et al. Gold nanoparticles for the development of clinical diagnosis methods. Anal Bioanal Chem 2008 Jun;391(3):943-50.

[25] Baptista P, Doria G, Henriques D, Pereira E, Franco R. Colorimetric detection of eukaryotic gene expression with DNA-derivatized gold nanoparticles. J Biotechnol 2005 Sep 23;119(2):111-7.

[26] Doria G, Franco R, Baptista P. Nanodiagnostics: fast colorimetric method for single nucleotide polymorphism/mutation detection. IET Nanobiotechnol 2007 Aug;1(4):53-7.

[27] Baptista PV, Koziol-Montewka M, Paluch-Oles J, Doria G, Franco R. Gold-nanoparticle-probe-based assay for rapid and direct detection of Mycobacterium tuberculosis DNA in clinical samples. Clin Chem 2006 Jul;52(7):1433-4.

[28] Li H, Rothberg L. Colorimetric detection of DNA sequences based on electrostatic interactions with unmodified gold nanoparticles. Proc Natl Acad Sci U S A 2004 Sep 28;101(39):14036-9.

[29] Mirkin CA, Letsinger RL, Mucic RC, Storhoff JJ. A DNA-based method for rationally assembling nanoparticles into macroscopic materials. Nature 1996 Aug 15;382(6592):607-9.

[30] Thaxton CS, Georganopoulou DG, Mirkin CA. Gold nanoparticle probes for the detection of nucleic acid targets. Clin Chim Acta 2006 Jan;363(1-2):120-6.

[31] Cheng MM, Cuda G, Bunimovich YL, Gaspari M, Heath JR, Hill HD, et al. Nanotechnologies for biomolecular detection and medical diagnostics. Curr Opin Chem Biol 2006 Feb;10(1):11-9.

[32] Taton TA, Mirkin CA, Letsinger RL. Scanometric DNA array detection with nanoparticle probes. Science 2000 Sep 8;289(5485):1757-60.

[33] Qin WJ, Yung LY. Nanoparticle-based detection and quantification of DNA with single nucleotide polymorphism (SNP) discrimination selectivity. Nucleic Acids Res 2007;35(17):e111.

[34] Sato K, Hosokawa K, Maeda M. Non-cross-linking gold nanoparticle aggregation as a detection method for single-base substitutions. Nucleic Acids Res 2005;33(1):e4.

[35] Sato K, Hosokawa K, Maeda M. Rapid aggregation of gold nanoparticles induced by non-cross-linking DNA hybridization. J Am Chem Soc 2003 Jul 9;125(27):8102-3.

[36] Elghanian R, Storhoff JJ, Mucic RC, Letsinger RL, Mirkin CA. Selective colorimetric detection of polynucleotides based on the distance-dependent optical properties of gold nanoparticles. Science 1997 Aug 22;277(5329):1078-81.

[37] Storhoff JJ, Lucas AD, Garimella V, Bao YP, Muller UR. Homogeneous detection of unamplified genomic DNA sequences based on colorimetric scatter of gold nanoparticle probes. Nat Biotechnol 2004 Jul;22(7):883-7.

[38] Cao YC, Jin R, Thaxton CS, Mirkin CA. A two-color-change, nanoparticle-based method for DNA detection. Talanta 2005 Sep 15;67(3):449-55.

[39] Conde J, de la Fuente JM, Baptista PV. RNA quantification using gold nanoprobes - application to cancer diagnostics. J Nanobiotechnology 2010;8:5.

[40] Costa P, Amaro A, Botelho A, Inacio J, Baptista PV. Gold nanoprobes assay for identification of mycobacteria from the Mycobacterium tuberculosis complex. Clin Microbiol Infect 2009 Nov 20.

[41] You CC, Miranda OR, Gider B, Ghosh PS, Kim IB, Erdogan B, et al. Detection and identification of proteins using nanoparticle-fluorescent polymer 'chemical nose' sensors. Nat Nanotechnol 2007 May;2(5):318-23.

[42] El-Sayed IH, Huang X, El-Sayed MA. Surface plasmon resonance scattering and absorption of anti-EGFR antibody conjugated gold nanoparticles in cancer diagnostics: applications in oral cancer. Nano Lett 2005 May;5(5):829-34.

[43] Kumar S, Harrison N, Richards-Kortum R, Sokolov K. Plasmonic nanosensors for imaging intracellular biomarkers in live cells. Nano Lett 2007 May;7(5):1338-43.

[44] Castaneda MT, Merkoci A, Pumera M, Alegret S. Electrochemical genosensors for biomedical applications based on gold nanoparticles. Biosens Bioelectron 2007 Apr 15;22(9-10):1961-7.

[45] Conde J, Doria G, Baptista P. Noble metal nanoparticles applications in cancer. J Drug Deliv 2012;2012:751075.

[46] Hanahan D, Weinberg RA. The hallmarks of cancer. Cell 2000 Jan 7;100(1):57-70.

[47] Siegel R, Naishadham D, Jemal A. Cancer statistics, 2012. CA Cancer J Clin 2012 Jan;62(1):10-29.

[48] Etzioni R, Urban N, Ramsey S, McIntosh M, Schwartz S, Reid B, et al. The case for early detection. Nat Rev Cancer 2003 Apr;3(4):243-52.

[49] Giljohann DA, Seferos DS, Daniel WL, Massich MD, Patel PC, Mirkin CA. Gold Nanoparticles for Biology and Medicine. Angew Chem Int Ed Engl 2010 Apr 16;49(19):3280-94.

[50] Salata O. Applications of nanoparticles in biology and medicine. J Nanobiotechnology 2004 Apr 30;2(1):3.

[51] Stoeva SI, Lee JS, Smith JE, Rosen ST, Mirkin CA. Multiplexed detection of protein cancer markers with biobarcoded nanoparticle probes. J Am Chem Soc 2006 Jul 5;128(26):8378-9.

[52] Son SJ, Lee SB. A platform for ultrasensitive and selective multiplexed marker protein assay toward early-stage cancer diagnosis. Nanomedicine (Lond) 2007 Feb;2(1):79-82.

[53] Nam JM, Thaxton CS, Mirkin CA. Nanoparticle-based bio-bar codes for the ultrasensitive detection of proteins. Science 2003 Sep 26;301(5641):1884-6.

[54] Thaxton CS, Elghanian R, Thomas AD, Stoeva SI, Lee JS, Smith ND, et al. Nanoparticle-based bio-barcode assay redefines "undetectable" PSA and biochemical recurrence after radical prostatectomy. Proc Natl Acad Sci U S A 2009 Nov 3;106(44):18437-42.

[55] Huang L, Reekmans G, Saerens D, Friedt JM, Frederix F, Francis L, et al. Prostate-specific antigen immunosensing based on mixed self-assembled monolayers, camel antibodies and colloidal gold enhanced sandwich assays. Biosens Bioelectron 2005 Sep 15;21(3):483-90.

[56] Liu X, Dai Q, Austin L, Coutts J, Knowles G, Zou J, et al. A one-step homogeneous immunoassay for cancer biomarker detection using gold nanoparticle probes coupled with dynamic light scattering. J Am Chem Soc 2008 Mar 5;130(9):2780-2.

[57] Huo Q, Litherland SA, Sullivan S, Hallquist H, Decker DA, Rivera-Ramirez I. Developing a nanoparticle test for prostate cancer scoring. J Transl Med 2012;10:44.

[58] Huo Q, Colon J, Cordero A, Bogdanovic J, Baker CH, Goodison S, et al. A facile nanoparticle immunoassay for cancer biomarker discovery. J Nanobiotechnology 2011;9:20.

[59] Ambrosi A, Airo F, Merkoci A. Enhanced gold nanoparticle based ELISA for a breast cancer biomarker. Anal Chem 2010 Feb 1;82(3):1151-6.

[60] Lu W, Arumugam SR, Senapati D, Singh AK, Arbneshi T, Khan SA, et al. Multifunctional oval-shaped gold-nanoparticle-based selective detection of breast cancer cells using simple colorimetric and highly sensitive two-photon scattering assay. ACS Nano 2010 Mar 23;4(3):1739-49.

[61] Eck W, Craig G, Sigdel A, Ritter G, Old LJ, Tang L, et al. PEGylated gold nanoparticles conjugated to monoclonal F19 antibodies as targeted labeling agents for human pancreatic carcinoma tissue. ACS Nano 2008 Nov 25;2(11):2263-72.

[62] Rahman M, Abd-El-Barr M, Mack V, Tkaczyk T, Sokolov K, Richards-Kortum R, et al. Optical imaging of cervical pre-cancers with structured illumination: an integrated approach. Gynecol Oncol 2005 Dec;99(3 Suppl 1):S112-S115.

[63] Yang J, Eom K, Lim EK, Park J, Kang Y, Yoon DS, et al. In situ detection of live cancer cells by using bioprobes based on Au nanoparticles. Langmuir 2008 Nov 4;24(21):12112-5.

[64] Lan T, Dong C, Huang X, Ren J. Single particle technique for one-step homogeneous detection of cancer marker using gold nanoparticle probes. Analyst 2011 Oct 21;136(20):4247-53.

[65] Lukianova-Hleb EY, Oginsky AO, Samaniego AP, Shenefelt DL, Wagner DS, Hafner JH, et al. Tunable plasmonic nanoprobes for theranostics of prostate cancer. Theranostics 2011;1:3-17.

[66] Arruebo M, Valladares M, Gonzalez-Fernandez A. Antibody-Conjugated Nanoparticles for Biomedical Applications. Journal of Nanomaterials 2009.

[67] Daniel MC, Astruc D. Gold nanoparticles: assembly, supramolecular chemistry, quantum-size-related properties, and applications toward biology, catalysis, and nanotechnology. Chem Rev 2004 Jan;104(1):293-346.

[68] Kang JH, Asami Y, Murata M, Kitazaki H, Sadanaga N, Tokunaga E, et al. Gold nanoparticle-based colorimetric assay for cancer diagnosis. Biosens Bioelectron 2010 Apr 15;25(8):1869-74.

[69] Li J, Chu X, Liu Y, Jiang JH, He Z, Zhang Z, et al. A colorimetric method for point mutation detection using high-fidelity DNA ligase. Nucleic Acids Res 2005;33(19):e168.

[70] Medley CD, Smith JE, Tang Z, Wu Y, Bamrungsap S, Tan W. Gold nanoparticle-based colorimetric assay for the direct detection of cancerous cells. Anal Chem 2008 Feb 15;80(4):1067-72.

[71] Conde J, Doria G, de la Fuente JM, Baptista PV. RNA quantification using noble metal nanoprobes: simultaneous identification of several different mRNA targets using color multiplexing and application to cancer diagnostics. Methods Mol Biol 2012;906:71-87.

[72] Mukerjee A, Ranjan AP, Vishwanatha JK. Combinatorial nanoparticles for cancer diagnosis and therapy. Curr Med Chem 2012;19(22):3714-21.

[73] Liu G, Mao X, Phillips JA, Xu H, Tan W, Zeng L. Aptamer-nanoparticle strip biosensor for sensitive detection of cancer cells. Anal Chem 2009 Dec 15;81(24):10013-8.

[74] Viator JA, Gupta S, Goldschmidt BS, Bhattacharyyal K, Kannan R, Shukla R, et al. Gold nanoparticle mediated detection of prostate cancer cells using photoacoustic flowmetry with optical reflectance. J Biomed Nanotechnol 2010 Apr;6(2):187-91.

[75] Lin D, Feng S, Pan J, Chen Y, Lin J, Chen G, et al. Colorectal cancer detection by gold nanoparticle based surface-enhanced Raman spectroscopy of blood serum and statistical analysis. Opt Express 2011 Jul 4;19(14):13565-77.

[76] Kah JC, Kho KW, Lee CG, James C, Sheppard R, Shen ZX, et al. Early diagnosis of oral cancer based on the surface plasmon resonance of gold nanoparticles. Int J Nanomedicine 2007;2(4):785-98.

[77] Wang X, Qian X, Beitler JJ, Chen ZG, Khuri FR, Lewis MM, et al. Detection of circulating tumor cells in human peripheral blood using surface-enhanced Raman scattering nanoparticles. Cancer Res 2011 Mar 1;71(5):1526-32.

[78] Baptista PV. Could gold nanoprobes be an important tool in cancer diagnostics? Expert Review of Molecular Diagnostics 2012 Jul;12(6):541-3.

[79] Kalogianni DP, Bravou V, Christopoulos TK, Ioannou PC, Zoumbos NC. Dry-reagent disposable dipstick test for visual screening of seven leukemia-related chromosomal translocations. Nucleic Acids Research 2007 Feb;35(4).

[80] Grubisha DS, Lipert RJ, Park HY, Driskell J, Porter MD. Femtomolar detection of prostate-specific antigen: An immunoassay based on surface-enhanced Raman scattering and immunogold labels. Analytical Chemistry 2003 Nov 1;75(21):5936-43.

[81] Wabuyele MB, Yan F, Vo-Dinh T. Plasmonics nanoprobes: detection of single-nucleotide polymorphisms in the breast cancer BRCA1 gene. Analytical and Bioanalytical Chemistry 2010 Sep;398(2):729-36.

[82] Munge BS, Coffey AL, Doucette JM, Somba BK, Malhotra R, Patel V, et al. Nanostructured Immunosensor for Attomolar Detection of Cancer Biomarker Interleukin-8 Using Massively Labeled Superparamagnetic Particles. Angewandte Chemie-International Edition 2011;50(34):7915-8.

[83] Jensen GC, Krause CE, Sotzing GA, Rusling JF. Inkjet-printed gold nanoparticle electrochemical arrays on plastic. Application to immunodetection of a cancer biomarker protein. Physical Chemistry Chemical Physics 2011;13(11):4888-94.

[84] Yin ZZ, Liu Y, Jiang LP, Zhu JJ. Electrochemical immunosensor of tumor necrosis factor alpha based on alkaline phosphatase functionalized nanospheres. Biosensors & Bioelectronics 2011 Jan 15;26(5):1890-4.

[85] Lee JH, Huh YM, Jun YW, Seo JW, Jang JT, Song HT, et al. Artificially engineered magnetic nanoparticles for ultra-sensitive molecular imaging. Nat Med 2007 Jan;13(1):95-9.

[86] Ji X, Shao R, Elliott AM, Stafford RJ, Esparza-Coss E, Liang G, et al. Bifunctional Gold Nanoshells with a Superparamagnetic Iron Oxide-Silica Core Suitable for Both MR Imaging and Photothermal Therapy. J Phys Chem C Nanomater Interfaces 2007 Apr 6;111(17):6245.

[87] Kim D, Kim JW, Jeong YY, Jon S. Antibiofouling Polymer Coated Gold@Iron Oxide Nanoparticle (GION) as a Dual Contrast Agent for CT and MRI. Bulletin of the Korean Chemical Society 2009 Aug;30(8):1855-7.

[88] Gobin AM, Lee MH, Halas NJ, James WD, Drezek RA, West JL. Near-infrared resonant nanoshells for combined optical imaging and photothermal cancer therapy. Nano Lett 2007 Jul;7(7):1929-34.

[89] Yang X, Skrabalak SE, Li ZY, Xia Y, Wang LV. Photoacoustic tomography of a rat cerebral cortex in vivo with au nanocages as an optical contrast agent. Nano Lett 2007 Dec;7(12):3798-802.

[90] Eghtedari M, Oraevsky A, Copland JA, Kotov NA, Conjusteau A, Motamedi M. High sensitivity of in vivo detection of gold nanorods using a laser optoacoustic imaging system. Nano Lett 2007 Jul;7(7):1914-8.

[91] Song KH, Kim C, Maslov K, Wang LV. Noninvasive in vivo spectroscopic nanorod-contrast photoacoustic mapping of sentinel lymph nodes. Eur J Radiol 2009 May;70(2):227-31.

[92] Bao C, Beziere N, del PP, Pelaz B, Estrada G, Tian F, et al. Gold nanoprisms as optoacoustic signal nanoamplifiers for in vivo bioimaging of gastrointestinal cancers. Small 2013 Jan 14;9(1):68-74.

[93] Minelli C, Lowe SB, Stevens MM. Engineering nanocomposite materials for cancer therapy. Small 2010 Nov 5;6(21):2336-57.

[94] Liu Y, Miyoshi H, Nakamura M. Nanomedicine for drug delivery and imaging: a promising avenue for cancer therapy and diagnosis using targeted functional nanoparticles. Int J Cancer 2007 Jun 15;120(12):2527-37.

[95] Cuenca AG, Jiang H, Hochwald SN, Delano M, Cance WG, Grobmyer SR. Emerging implications of nanotechnology on cancer diagnostics and therapeutics. Cancer 2006 Aug 1;107(3):459-66.

[96] Ferrari M. Cancer nanotechnology: opportunities and challenges. Nat Rev Cancer 2005 Mar;5(3):161-71.

[97] Rosi NL, Giljohann DA, Thaxton CS, Lytton-Jean AK, Han MS, Mirkin CA. Oligonucleotide-modified gold nanoparticles for intracellular gene regulation. Science 2006 May 19;312(5776):1027-30.

[98] Oishi M, Nakaogami J, Ishii T, Nagasaki Y. Smart PEGylated gold nanoparticles for the cytoplasmic delivery of siRNA to induce enhanced gene silencing. Chemistry Letters 2006 Sep 5;35(9):1046-7.

[99] Giljohann DA, Seferos DS, Prigodich AE, Patel PC, Mirkin CA. Gene regulation with polyvalent siRNA-nanoparticle conjugates. J Am Chem Soc 2009 Feb 18;131(6):2072-3.

[100] Conde J, Ambrosone A, Sanz V, Hernandez Y, Marchesano V, Tian F, et al. Design of Multifunctional Gold Nanoparticles for In Vitro and In Vivo Gene Silencing. ACS Nano 2012 Aug 22.

[101] Guo S, Huang Y, Jiang Q, Sun Y, Deng L, Liang Z, et al. Enhanced gene delivery and siRNA silencing by gold nanoparticles coated with charge-reversal polyelectrolyte. ACS Nano 2010 Sep 28;4(9):5505-11.

[102] Conde J, Rosa J, de la Fuente JM, Baptista PV. Gold-nanobeacons for simultaneous gene specific silencing and intracellular tracking of the silencing events. Biomaterials 2013 Mar;34(10):2516-23.

[103] Lee JS, Green JJ, Love KT, Sunshine J, Langer R, Anderson DG. Gold, poly(beta-amino ester) nanoparticles for small interfering RNA delivery. Nano Lett 2009 Jun;9(6):2402-6.

[104] Lee SK, Han MS, Asokan S, Tung CH. Effective Gene Silencing by Multilayered siRNA-Coated Gold Nanoparticles. Small 2011 Feb 7;7(3):364-70.

[105] Lu W, Zhang GD, Zhang R, Flores LG, Huang Q, Gelovani JG, et al. Tumor Site-Specific Silencing of NF-kappa B p65 by Targeted Hollow Gold Nanosphere-Mediated Photothermal Transfection. Cancer Research 2010 Apr 15;70(8):3177-88.

[106] Braun GB, Pallaoro A, Wu G, Missirlis D, Zasadzinski JA, Tirrell M, et al. Laser-Activated Gene Silencing via Gold Nanoshell-siRNA Conjugates. ACS Nano 2009 Jun 15.

[107] Zheng D, Giljohann DA, Chen DL, Massich MD, Wang XQ, Iordanov H, et al. Topical delivery of siRNA-based spherical nucleic acid nanoparticle conjugates for gene regulation. Proceedings of the National Academy of Sciences of the United States of America 2012 Jul 24;109(30):11975-80.

[108] Yao L, Danniels J, Moshnikova A, Kuznetsov S, Ahmed A, Engelman DM, et al. pHLIP peptide targets nanogold particles to tumors. Proc Natl Acad Sci U S A 2013 Jan 8;110(2):465-70.

[109] Shi XY, Wang SH, Van Antwerp ME, Chen XS, Baker JR. Targeting and detecting cancer cells using spontaneously formed multifunctional dendrimer-stabilized gold nanoparticles. Analyst 2009;134(7):1373-9.

[110] Chattopadhyay N, Cai ZL, Kwon YL, Lechtman E, Pignol JP, Reilly RM. Molecularly targeted gold nanoparticles enhance the radiation response of breast cancer cells and tumor xenografts to X-radiation. Breast Cancer Research and Treatment 2013 Jan;137(1):81-91.

[111] Mukherjee P, Bhattacharya R, Bone N, Lee YK, Patra CR, Wang S, et al. Potential therapeutic application of gold nanoparticles in B-chronic lymphocytic leukemia (BCLL): enhancing apoptosis. J Nanobiotechnology 2007;5:4.

[112] Qian X, Peng XH, Ansari DO, Yin-Goen Q, Chen GZ, Shin DM, et al. In vivo tumor targeting and spectroscopic detection with surface-enhanced Raman nanoparticle tags. Nat Biotechnol 2008 Jan;26(1):83-90.

[113] Chen HY, Li SL, Li BW, Ren XY, Li SN, Mahounga DM, et al. Folate-modified gold nanoclusters as near-infrared fluorescent probes for tumor imaging and therapy. Nanoscale 2012;4(19):6050-64.

[114] Chattopadhyay N, Fonge H, Cai ZL, Scollard D, Lechtman E, Done SJ, et al. Role of Antibody-Mediated Tumor Targeting and Route of Administration in Nanoparticle Tumor Accumulation in Vivo. Molecular Pharmaceutics 2012 Aug;9(8):2168-79.

[115] Kim CK, Ghosh P, Pagliuca C, Zhu ZJ, Menichetti S, Rotello VM. Entrapment of hydrophobic drugs in nanoparticle monolayers with efficient release into cancer cells. J Am Chem Soc 2009 Feb 4;131(4):1360-1.

[116] Kim D, Jeong YY, Jon S. A Drug-Loaded Aptamer-Gold Nanoparticle Bioconjugate for Combined CT Imaging and Therapy of Prostate Cancer. ACS Nano 2010 Jul;4(7):3689-96.

[117] Dreaden EC, Mwakwari SC, Sodji QH, Oyelere AK, El-Sayed MA. Tamoxifen-Poly(ethylene glycol)-Thiol Gold Nanoparticle Conjugates: Enhanced Potency and Selective Delivery for Breast Cancer Treatment. Bioconjugate Chemistry 2009 Dec;20(12):2247-53.

[118] Brown SD, Nativo P, Smith JA, Stirling D, Edwards PR, Venugopal B, et al. Gold nanoparticles for the improved anticancer drug delivery of the active component of oxaliplatin. J Am Chem Soc 2010 Apr 7;132(13):4678-84.

[119] Comenge J, Sotelo C, Romero F, Gallego O, Barnadas A, Parada TGC, et al. Detoxifying Antitumoral Drugs via Nanoconjugation: The Case of Gold Nanoparticles and Cisplatin. Plos One 2012 Oct 17;7(10).

[120] Nasrolahi SA, Mandal D, Tiwari RK, Guo L, Lu W, Parang K. Cyclic Peptide-Capped Gold Nanoparticles as Drug Delivery Systems. Mol Pharm 2012 Oct 5.

[121] You J, Zhang R, Xiong CY, Zhong M, Melancon M, Gupta S, et al. Effective Photothermal Chemotherapy Using Doxorubicin-Loaded Gold Nanospheres That Target EphB4 Receptors in Tumors. Cancer Research 2012 Sep 15;72(18):4777-86.

[122] Song JB, Zhou JJ, Duan HW. Self-Assembled Plasmonic Vesicles of SERS-Encoded Amphiphilic Gold Nanoparticles for Cancer Cell Targeting and Traceable Intracellular Drug Delivery. Journal of the American Chemical Society 2012 Aug 15;134(32):13458-69.

[123] Akhtar S, Benter IF. Nonviral delivery of synthetic siRNAs in vivo. J Clin Invest 2007 Dec;117(12):3623-32.

[124] Kim SS, Garg H, Joshi A, Manjunath N. Strategies for targeted nonviral delivery of siRNAs in vivo. Trends Mol Med 2009 Nov;15(11):491-500.

[125] Castanotto D, Rossi JJ. The promises and pitfalls of RNA-interference-based therapeutics. Nature 2009 Jan 22;457(7228):426-33.

[126] Li H, Li WX, Ding SW. Induction and suppression of RNA silencing by an animal virus. Science 2002 May 17;296(5571):1319-21.

[127] Soutschek J, Akinc A, Bramlage B, Charisse K, Constien R, Donoghue M, et al. Therapeutic silencing of an endogenous gene by systemic administration of modified siRNAs. Nature 2004 Nov 11;432(7014):173-8.

[128] Fichou Y, Ferec C. The potential of oligonucleotides for therapeutic applications. Trends Biotechnol 2006 Dec;24(12):563-70.

[129] Toub N, Malvy C, Fattal E, Couvreur P. Innovative nanotechnologies for the delivery of oligonucleotides and siRNA. Biomed Pharmacother 2006 Nov;60(9):607-20.

[130] Fire A, Xu S, Montgomery MK, Kostas SA, Driver SE, Mello CC. Potent and specific genetic interference by double-stranded RNA in Caenorhabditis elegans. Nature 1998 Feb 19;391(6669):806-11.

[131] Baker M. RNA interference: From tools to therapies. Nature 2010 Apr 22;464(7292):1225.

[132] Milhavet O, Gary DS, Mattson MP. RNA interference in biology and medicine. Pharmacol Rev 2003 Dec;55(4):629-48.

[133] Wall NR, Shi Y. Small RNA: can RNA interference be exploited for therapy? Lancet 2003 Oct 25;362(9393):1401-3.

[134] Hannon GJ, Rossi JJ. Unlocking the potential of the human genome with RNA interference. Nature 2004 Sep 16;431(7006):371-8.

[135] Whitehead KA, Langer R, Anderson DG. Knocking down barriers: advances in siRNA delivery. Nat Rev Drug Discov 2009 Feb;8(2):129-38.

[136] Lee SH, Bae KH, Kim SH, Lee KR, Park TG. Amine-functionalized gold nanoparticles as non-cytotoxic and efficient intracellular siRNA delivery carriers. Int J Pharm 2008 Nov 19;364(1):94-101.

[137] Rana S, Bajaj A, Mout R, Rotello VM. Monolayer coated gold nanoparticles for delivery applications. Adv Drug Deliv Rev 2012 Feb;64(2):200-16.

[138] Ghosh P, Han G, De M, Kim CK, Rotello VM. Gold nanoparticles in delivery applications. Adv Drug Deliv Rev 2008 Aug 17;60(11):1307-15.

[139] Thomas M, Klibanov AM. Conjugation to gold nanoparticles enhances polyethylenimine's transfer of plasmid DNA into mammalian cells. Proc Natl Acad Sci U S A 2003 Aug 5;100(16):9138-43.

[140] Ghosh PS, Kim CK, Han G, Forbes NS, Rotello VM. Efficient gene delivery vectors by tuning the surface charge density of amino acid-functionalized gold nanoparticles. ACS Nano 2008 Nov 25;2(11):2213-8.

[141] Conde J, de la Fuente JM, Baptista PV. In vitro transcription and translation inhibition via DNA functionalized gold nanoparticles. Nanotechnology 2010 Dec 17;21(50):505101.

[142] McIntosh CM, Esposito EA, III, Boal AK, Simard JM, Martin CT, Rotello VM. Inhibition of DNA transcription using cationic mixed monolayer protected gold clusters. J Am Chem Soc 2001 Aug 8;123(31):7626-9.

[143] Gary DJ, Puri N, Won YY. Polymer-based siRNA delivery: Perspectives on the fundamental and phenomenological distinctions from polymer-based DNA delivery. Journal of Controlled Release 2007 Aug 16;121(1-2):64-73.

[144] Paciotti GF, Myer L, Weinreich D, Goia D, Pavel N, McLaughlin RE, et al. Colloidal gold: a novel nanoparticle vector for tumor directed drug delivery. Drug Deliv 2004 May;11(3):169-83.

[145] Cai W, Gao T, Hong H, Sun J. Applications of gold nanoparticles in cancer nanotechnology. Nanotechnology Science and Applications 1, 17-32. 2008.

[146] Kneipp J, Kneipp H, McLaughlin M, Brown D, Kneipp K. In vivo molecular probing of cellular compartments with gold nanoparticles and nanoaggregates. Nano Lett 2006 Oct;6(10):2225-31.

[147] El-Sayed IH, Huang X, El-Sayed MA. Selective laser photo-thermal therapy of epithelial carcinoma using anti-EGFR antibody conjugated gold nanoparticles. Cancer Lett 2006 Jul 28;239(1):129-35.

[148] Schroeder A, Heller DA, Winslow MM, Dahlman JE, Pratt GW, Langer R, et al. Treating metastatic cancer with nanotechnology. Nat Rev Cancer 2012 Jan;12(1):39-50.

[149] Ehdaie B. Application of nanotechnology in cancer research: review of progress in the National Cancer Institute's Alliance for Nanotechnology. Int J Biol Sci 2007;3(2):108-10.

[150] Han G, Ghosh P, Rotello VM. Multi-functional gold nanoparticles for drug delivery. Adv Exp Med Biol 2007;620:48-56.

[151] Han G, Ghosh P, Rotello VM. Functionalized gold nanoparticles for drug delivery. Nanomedicine (Lond) 2007 Feb;2(1):113-23.

[152] Langer R. Biomaterials in drug delivery and tissue engineering: one laboratory's experience. Acc Chem Res 2000 Feb;33(2):94-101.

[153] Gibson JD, Khanal BP, Zubarev ER. Paclitaxel-functionalized gold nanoparticles. J Am Chem Soc 2007 Sep 19;129(37):11653-61.

[154] Hwu JR, Lin YS, Josephrajan T, Hsu MH, Cheng FY, Yeh CS, et al. Targeted Paclitaxel by conjugation to iron oxide and gold nanoparticles. J Am Chem Soc 2009 Jan 14;131(1):66-8.

[155] Lasagna-Reeves C, Gonzalez-Romero D, Barria MA, Olmedo I, Clos A, Sadagopa Ramanujam VM, et al. Bioaccumulation and toxicity of gold nanoparticles after repeated administration in mice. Biochem Biophys Res Commun 2010 Mar 19;393(4):649-55.

[156] Chen YS, Hung YC, Liau I, Huang GS. Assessment of the In Vivo Toxicity of Gold Nanoparticles. Nanoscale Res Lett 2009;4(8):858-64.

[157] Dobrovolskaia MA, Aggarwal P, Hall JB, McNeil SE. Preclinical studies to understand nanoparticle interaction with the immune system and its potential effects on nanoparticle biodistribution. Mol Pharm 2008 Jul;5(4):487-95.

[158] Dobrovolskaia MA, McNeil SE. Immunological properties of engineered nanomaterials. Nat Nanotechnol 2007 Aug;2(8):469-78.

[159] Connor EE, Mwamuka J, Gole A, Murphy CJ, Wyatt MD. Gold nanoparticles are taken up by human cells but do not cause acute cytotoxicity. Small 2005 Mar;1(3):325-7.

[160] Pan Y, Neuss S, Leifert A, Fischler M, Wen F, Simon U, et al. Size-dependent cytotoxicity of gold nanoparticles. Small 2007 Nov;3(11):1941-9.

[161] Visaria RK, Griffin RJ, Williams BW, Ebbini ES, Paciotti GF, Song CW, et al. Enhancement of tumor thermal therapy using gold nanoparticle-assisted tumor necrosis factor-alpha delivery. Mol Cancer Ther 2006 Apr;5(4):1014-20.

[162] El-Sayed ME, Hoffman AS, Stayton PS. Smart polymeric carriers for enhanced intracellular delivery of therapeutic macromolecules. Expert Opin Biol Ther 2005 Jan;5(1):23-32.

[163] Huang XL, Zhang B, Ren L, Ye SF, Sun LP, Zhang QQ, et al. In vivo toxic studies and biodistribution of near infrared sensitive Au-Au(2)S nanoparticles as potential drug delivery carriers. J Mater Sci Mater Med 2008 Jul;19(7):2581-8.

[164] Uboldi C, Bonacchi D, Lorenzi G, Hermanns MI, Pohl C, Baldi G, et al. Gold nanoparticles induce cytotoxicity in the alveolar type-II cell lines A549 and NCIH441. Part Fibre Toxicol 2009;6:18.

[165] Freese C, Uboldi C, Gibson MI, Unger RE, Weksler BB, Romero IA, et al. Uptake and cytotoxicity of citrate-coated gold nanospheres: Comparative studies on human endothelial and epithelial cells. Part Fibre Toxicol 2012;9:23.

[166] Rothen-Rutishauser B, Muhlfeld C, Blank F, Musso C, Gehr P. Translocation of particles and inflammatory responses after exposure to fine particles and nanoparticles in an epithelial airway model. Part Fibre Toxicol 2007;4:9.

[167] Bellucci S. Nanoparticles and Nanodevices in Biological Applications. Lecture Notes in Nanoscale Science and Technology ed. Springer; 2009.

[168] Sun X, Rossin R, Turner JL, Becker ML, Joralemon MJ, Welch MJ, et al. An assessment of the effects of shell cross-linked nanoparticle size, core composition, and surface PEGylation on in vivo biodistribution. Biomacromolecules 2005 Sep;6(5):2541-54.

[169] Panessa-Warren BJ, Warrren JB, Maye MM, Schiffer W, Nanoparticle interactions with living systems: in vivo and in vitro biocompatibility", Nanoparticles and Nanodevices in Biological Applications; 2009.

[170] Conde J, Larguinho M, Cordeiro A, Raposo LR, Costa PM, Santos S, et al. Gold-nanobeacons for gene therapy: evaluation of genotoxicity, cell toxicity and proteome profiling analysis. Nanotoxicology 2013 May 28.

Sensors **2012**, *12*, 1657-1687; doi:10.3390/s120201657

OPEN ACCESS

sensors

ISSN 1424-8220

www.mdpi.com/journal/sensors

Review

Noble Metal Nanoparticles for Biosensing Applications

Gonçalo Doria [1], João Conde [1,2], Bruno Veigas [1,3], Leticia Giestas [1], Carina Almeida [1], Maria Assunção [1], João Rosa [1,4] and Pedro V. Baptista [1,*]

[1] CIGMH, Departamento de Ciências da Vida, Faculdade de Ciências e Tecnologia, Universidade Nova de Lisboa, Campus de Caparica, 2829-516 Caparica, Portugal;
E-Mails: doria_go@fct.unl.pt (G.D.); conde.bio@gmail.com (J.C.); bmrveigas@gmail.com (B.V.); l.giestas@fct.unl.pt (L.G.); msa.carina@gmail.com (C.A.); maria.sm.assuncao@gmail.com (M.A.); joao.rosa@fct.unl.pt (J.R.)

[2] Instituto de Nanociencia de Aragón, Universidad de Zaragoza, Campus Río Ebro, Edifício I+D, Mariano Esquillor, s/n, 50018 Zaragoza, Spain

[3] CENIMAT/I3N, Departamento de Ciência dos Materiais, Faculdade de Ciências e Tecnologia, Universidade Nova de Lisboa, Campus de Caparica, 2829-516 Caparica, Portugal

[4] REQUIMTE, Departamento de Química, Faculdade de Ciências e Tecnologia, Universidade Nova de Lisboa, Campus de Caparica, 2829-516 Caparica, Portugal

* Author to whom correspondence should be addressed; E-Mail: pmvb@fct.unl.pt; Tel.: +351-21-294-8530; Fax: +351-21-294-8530.

Received: 20 December 2011; in revised form: 29 January 2012 / Accepted: 2 February 2012 / Published: 7 February 2012

Abstract: In the last decade the use of nanomaterials has been having a great impact in biosensing. In particular, the unique properties of noble metal nanoparticles have allowed for the development of new biosensing platforms with enhanced capabilities in the specific detection of bioanalytes. Noble metal nanoparticles show unique physicochemical properties (such as ease of functionalization via simple chemistry and high surface-to-volume ratios) that allied with their unique spectral and optical properties have prompted the development of a plethora of biosensing platforms. Additionally, they also provide an additional or enhanced layer of application for commonly used techniques, such as fluorescence, infrared and Raman spectroscopy. Herein we review the use of noble metal nanoparticles for biosensing strategies—from synthesis and functionalization to integration in molecular diagnostics platforms, with special focus on those that have made their way into the diagnostics laboratory.

Keywords: nanotechnology; noble metal nanoparticles; biosensors; molecular diagnostics; immunoassays; DNA; RNA; nucleic acids; proteins; antibody

1. Introduction

In the era of nanotechnology, noble metal nanoparticles (NPs) have played an important role in the development of new biosensors and/or in the enhancement of existing biosensing techniques to fulfill the demand for more specific and highly sensitive biomolecular diagnostics. The unique physicochemical properties of such metals at the nanoscale have led to the development of a wide variety of biosensors, such as: (i) nanobiosensors for point of care disease diagnosis, (ii) nanoprobes for *in vivo* sensing/imaging, cell tracking and monitoring disease pathogenesis or therapy monitoring and (iii) other nanotechnology-based tools that benefit scientific research on basic biology [1–5]. In fact, NPs are, in general, one of the most common nanotechnology-based approaches for developing biosensors, due to their simplicity, physiochemical malleability and high surface areas [6]. They can measure between 1 to 100 nm in diameter, have different shapes and can be composed of one or more inorganic compounds, such as noble metals, heavy metals, iron, *etc.* The majority of them exhibit size-related properties that differ significantly from those observed in microparticles or bulk materials. Depending on their size and composition we can observe peculiar properties, such as quantum confinement in semiconductor nanocrystals, surface plasmon resonance in some metal NPs and superparamagnetism in magnetic materials. Noble metal NPs, in particular gold and silver NPs, are among the most extensively studied nanomaterials and have led to the development of innumerous techniques and methods for molecular diagnostics, imaging, drug delivery and therapeutics. Most of their unique physicochemical properties at the nanoscale, such as Localized Surface Plasmon Resonance (LSPR), have been explored for the development of new biosensors. This review will focus on these unique physicochemical properties of noble metal NPs that have thus far been explored for the development of new highly sensitive and specific biosensing techniques, favoring those that have already been successfully tested with biological samples. While some recent reports have addressed specific bio-application for noble metal NPs, such as molecular diagnostics and therapy [5,7] or cancer applications [8], and others have focused on the bio-applications of a specific type of noble metal NP, mostly gold NPs [9], here we aim at presenting an overview on the general principals and up to date applications of all noble metal NPs used for the development of biosensors.

2. Noble Metal Nanoparticles for Biosensing

2.1. Synthesis and Functionalization of Noble Metal Nanoparticles

Numerous techniques have been developed to synthesize noble metal NPs, including chemical methods (e.g., chemical reduction, photochemical reduction, co-precipitation, thermal decomposition, hydrolysis, *etc.*) and physical methods (e.g., vapor deposition, laser ablation, grinding, *etc.*), whose ultimate goal is to obtain NPs with a good level of homogeneity and provide fine control over size,

shape and surface properties, in order to better take advantage of their unique physicochemical properties for biosensing [10].

The majority of the biosensing applications based on NPs that have been developed thus far are based on gold NPs, due to their unique optical properties and ease of derivatization with different biomarkers in aqueous solution [11–13]. These gold NPs, also known as colloidal gold, can be easily synthesized in sizes ranging between 3 and 200 nm in diameter and in different shapes, being the most common the quasi-spherical shape, mainly due to their surface energy that favors the formation of spherical particles. Generally, the method of choice to synthesize quasi-spherical gold NPs is the chemical reduction of Au(III) to Au(0) ions using sodium citrate as a reducing agent, a method first developed by Turkevich [14] and latter optimized by Frens [15]. In this approach, the citrate acts both as reducing agent and as capping agent which, as the gold NPs form, prevents the NPs from forming larger particles and simultaneously conferring them a mild stability due to electrostatic repulsion between citrate-capped gold NPs [16]. Recent modifications of the Turkevich method have allowed a better distribution and control over the size of the gold NPs, where a range between 9–120 nm can be achieved just by varying the citrate/Au ratio [17–19]. Alternatively, many other aqueous- and organic-based methodologies have been developed for the controlled synthesis of different noble metal NPs, including spherical or non-spherical, pure, alloy or core/shell NPs of gold, silver, platinum, palladium and/or rhodium [20–22]. The development of new biosensing and therapeutic applications based on noble metal NPs has been pushing forward the chemistry for their functionalization with different moieties such as nucleic acids, antibodies, biocompatible polymers, enzymes and other proteins, in a quest for an increased biocompatibility and targeting specificity [10,23].

Table 1. Types of conjugations between biomolecules and noble metal NPs.

Type of conjugation	Pros	Cons
Electrostatic interactions (e.g., adsorption of negative charged DNA to positive charged gold NP)	- Very simple and straightforward to perform.	- Restricted to opposite charged biomolecules and NPs; - Very sensitive to environmental properties (e.g., pH, ionic strength, *etc*.); - Weak functionalization.
Chemisorption (e.g., quasi-covalent binding of thiol-functionalized biomolecule to gold NP)	- Allows oriented functionalization; - Very robust functionalization.	- Requires NPs with capping agents with weaker adsorption than the derivatization moiety; - Usually requires modification of the biomolecule; - Subject to interference by other chemical groups available for adsorption within the biomolecule; - Affected by chemical degradation and surface oxidation of some NPs (e.g., silver).
Affinity-based (e.g., His-tag protein binding to Ni-NTA derivatized gold NP)	- Allows oriented functionalization; - Very straightforward binding between affinity pairs.	- Requires modification of both NPs and biomolecules with an affinity pair; - Limited to availability of suitable binding affinity pairs.

Table 1 summarizes the different approaches for the biofunctionalization of noble metal NPs, including the main pros and cons of each approach, which can be consulted in more detail in the excellent review made by Sperling *et al.* [10].

A range of highly sensitive biosensing methods for nucleic acids, proteins, antibodies, enzymes and other biological molecules have been developed by exploring different physicochemical properties of the noble metal NPs, such as LSPR, fluorescence enhancement/quenching, surface-enhanced Raman scattering (SERS), electrochemical activity, *etc*. Among these biosensing methods, the colorimetric approaches have been the most explored and, due to their simplicity and portability, are one the most promising for future diagnostic methods at point-of-care. For this reason also, most methods have been based on silver and gold NPs, since these present unique optical properties within the visible wavelength range and are easy to synthesize and functionalize, with gold NPs being the most explored of all noble metal NPs. Nonetheless, even though in much less extension than silver and gold NPs, other noble metal NPs, such as platinum NPs, have also been used in biosensing applications, mostly by exploring their unique electrochemical properties.

2.2. Localized Surface Plasmon Resonance

One of the most explored characteristic of noble metal NPs for biosensing is their LSPR arising from the electromagnetic waves that propagate along the surface of the conductive metal [24]. When excited with an electromagnetic wave, such as light, most noble metal NPs produce an intense absorption and scattering due to the collective oscillation of the conduction electrons located at the NPs' surface. In the particular case of gold and silver NPs, the LSPR yields exceptionally high absorption coefficients and scattering properties within the UV/visible wavelength range that allows them to have a higher sensitivity in optical detection methods than conventional organic dyes, making them the perfect candidates for colorimetric biosensing applications [25,26]. Moreover, their LSPR properties can be easily modulated according to their size, shape and composition [22,27]. Figure 1 illustrates the effect of nanoparticle composition in LSPR that has been already demonstrated beneficial for the development of new and highly sensitive biosensing methods [28,29].

Typically, colloidal solutions of spherical gold NPs (<40 nm) present a red color with their LSPR band centered at ca. 520 nm, while spherical silver NPs present a yellow color with their LSPR band centered at *ca.* 420 nm [25]. Both metals can also be combined in an alloy or core-shell conformation, presenting a LSPR band that can vary within the wavelength limits of pure metal NPs LSPR bands. In the case of the core-shell conformation, a dual LSPR peak characteristic of each pure metal can be observed, depending on the thickness of the metallic shell [27]. These LSPR bands are usually weakly dependent on the size of the NPs and the refractive index of the surrounding media, but strongly change with inter-particle distance, for example aggregation of NPs leads to a pronounced color change as a consequence of the plasmon coupling between NPs and a concomitant red-shift of the LSPR absorption band peak [30]. Most of the colorimetric biosensors based on gold and/or silver NPs have been developed considering these changes in color generated by the plasmon coupling between NPs upon aggregation, while other methods have used the LSPR properties of the noble metal NPs just as a colorful reporter (*i.e.*, making use of their superb scattering and/or absorbance properties). Some

are based on the unspecific adsorption of biomolecules to non-functionalized noble metal NPs, while others are based on functionalized noble metal NPs for increased specificity.

Figure 1. Example of LSPR modulation through different NP compositions. The LSPR absorption band of gold/silver alloy NPs increases to longer wavelengths with increasing amounts of gold.

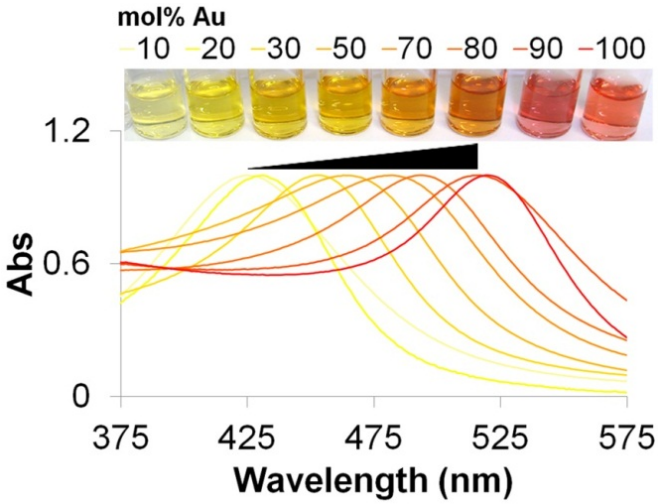

In the case of the non-functionalized NPs, Li *et al.* took advantage of the differential propensity of ssDNA and dsDNA adsorption to gold NPs to develop a biosensor for DNA detection [31]. The free bases of ssDNA molecules interact electrostatically with the negatively charged surface of gold NPs harboring a citrate capping, which confers an increased stability to the NPs upon increasing ionic strength. On the other hand, dsDNA molecules adsorb much less to the NPs' surface and do not provide stability to increasing ionic strength induced aggregation of the NPs. Based on these observations, Li and co-workers combined gold NPs with citrate capping with a polymerase chain reaction (PCR) procedure, using ssDNA probes complementary to the amplicon. Whenever the template of the PCR is amplified, the ssDNA probes hybridize with the amplicon and consequently become unavailable to adsorb to the gold NPs' surface and confers them with increased stability to salt induced aggregation. This way, a positive result (*i.e.*, target amplification) yields a colorimetric change from red to blue upon salt addition, while in a negative result the color remains unchanged. This approach has also been successfully explored for the detection of SNPs [32,33], ultraviolet (UV)-induced mutagenic or carcinogenic DNA dimers [34], or to directly detect unamplified hepatitis C virus RNA isolated from clinical specimens [35]. Similarly, Xia and co-workers used the same approach to develop a nearly "universal" biosensor to detect a broad range of targets including nucleic acids, proteins, small molecules and inorganic ions, using conjugated polyelectrolytes and different ssDNA aptamers or probe molecules that mediated the target detection [36]. Ma *et al.* used gold nanorods in a CTAB solution to achieve a DNA target detection limit down to 0.1 pM [37] and Kanjanawarut *et al.* used peptide nucleic acids instead of ssDNA oligonucleotide probes to improve the differential aggregation between complementary and non-complementary targets [38]. Non-functionalized citrate-capped NPs have also been used to develop colorimetric biosensors for thiourea and melamine [39,40]. In these approaches, the presence of thiourea or melamine in the colloidal solution reduced the overall surface

charges of silver or gold NPs, respectively, resulting in their aggregation and a colorimetric response correlating with the concentration of the targets (up to 0.8 nM for thiourea and 40 ppb for melamine).

Other approaches have used noble metal NPs functionalized with different biosensing molecules (e.g., ssDNA, antibodies, proteins or enzymes) in order to increase specificity of the methods. In 1996, Mirkin *et al.* described the use gold NPs functionalized with thiol-modified ssDNA probes (*i.e.*, gold nanoprobes) that would form a cross-linking network upon detection of a complementary ssDNA target by both gold nanoprobes [41]. This cross-linking network lead to the aggregation of the gold NPs causing a red-shift in the LSPR absorbance band to 574 nm. It was also possible to detect a single base mismatch through this cross-linking approach by controlling the temperature of denaturation of the cross-linked network, which presents a sharp melting transition [42]. This cross-linking approach has also been combined with a rolling circle amplification technique allowing the detection of single point mutations with 1 fM sensitivity [43]. Other methods for specific nucleic acid detection using gold NPs functionalized with ssDNA probes have been developed based on their differential non-cross-linking aggregation mediated by the increasing ionic strength of the solution [44–50]. In the case of the non-cross-linking method developed by Baptista and co-workers, the differential aggregation of the gold nanoprobes is evaluated upon salt addition to discriminate the presence of complementary, mismatched and non-complementary targets in solution [45–50]. Only the presence of a fully complementary target provides stability to the gold nanoprobes, while mismatched and non-complementary targets allow the nanoprobes to aggregate upon salt addition. This method has been thus far successfully applied to the detection of pathogenic agents [46,48] and single-nucleotide polymorphism (SNP)/single point mutations [50,28], as well as in gene expression analysis without the need for retro-transcription [47,49]. Moreover, the use of different gold/silver alloy nanoprobes in combination with the pure gold nanoprobes has allowed to create a multiplex DNA biosensor following this non-cross-linking approach [28,29]. Jian and co-workers also developed a non-cross-linking assay for the specific detection of a gene associated with sickle-cell anemia using fibrinogen-functionalized 56 nm gold NPs and a thrombin-binding aptamer assembled on gold NPs [51]. The detection was mediated through thrombin-induced aggregation of the fibrinogen-functionalized gold NPs allowing to achieve a limit of detection of 12 pM. The potency of the inhibition mediated by the thrombin-binding aptamer conjugated with gold NPs relative to thrombin also demonstrated to be highly dependent on the concentration of fully complementary DNA targets presenting a linear sensitivity in the concentration range of 20–500 pM.

Apart from the methods based on colorimetric alterations, other colorimetric methods have been developed using the noble metal NPs as a reporter. One example is the method for detecting nucleic acid sequences through the hybridization with gold nanoprobes in a chromatographic strip, also known as dipstick, as described by Kalogianni *et al.* [52]. In this approach, similarly to current pregnancy tests, biotinylated PCR products are hybridized to a specific oligo(dA)-tailed probe and loaded on the chromatographic stripe. As the buffer migrates through the stripe, the biotinylated PCR products are immobilized by streptavidin spotted in a specific location of the stripe. Finally, to detect the presence of the DNA target in the streptavidin spot, poly-dT gold nanoprobes are used to hybridize with the poly-dA probe. Other variants of this technique have also been described by Kalogianni *et al.* to fit a specific application (e.g., SNP detection, multiplex analysis) [53–55] and by Fan *et al.* to monitor protein-protein interactions using silver NPs instead of gold NPs [56]. Using a high-throughput

microarray approach, Mirkin's group used gold nanoprobes to substitute the conventional fluorescence-labeled probes usually used to report target hybridization [57]. In this approach, the scattered light incident on the gold NPs reported complementary target hybridization. Moreover, using an additional step of silver(I) reduction over the gold nanoprobes surface, the scattering intensity increased and up to 200 fM of genomic DNA target was successfully detected [58]. The detection of single base mismatches was also possible at controlled temperatures with increased selectivity when compared to standard fluorescent probes. Zhou *et al.* added a biomineralization-assisted amplification methodology to this approach that allowed to discriminate single-base mismatches upon a salt-based stringency wash using a target concentration as low as 50 aM [59]. The assay involves two types of derivatized gold NPs: one simultaneously functionalized with both target-recognition oligonucleotide and biomineralization-capable silicatein (probe A) and the other derivatized with an oligo(ethylene glycol) derivative (probe B). These two probes allowed detection of DNA through a cascade signal amplification process: first, a transparent solid support surface modified with a capture oligonucleotide was used to hybridize to both target and probe A in a sandwich manner; then, the silicatein from probe A catalyzes the synthesis of silica simultaneously allowing for the entrapment of probe B and yielding the first signal amplification. The signal can be further enhanced by selective deposition of silver metals on both probes.

Mirkin's group also developed the microarray approach to detect protein cancer markers using antibody microarrays and gold NPs functionalized with antibodies [60]. This time, they used an electroless gold deposition as a light scattering signal enhancer allowing to detect as low as 300 aM (9,000 copies) of prostate specific antigen in buffer and 3 fM in 10% serum. They have also developed a bio-barcode assay high sensitivity for nucleic acid or protein targets, by combining such microarray approaches with magnetic microparticles holding recognition elements (antibodies or DNA) for specific targets and gold nanoprobes that harbored a secondary recognition agent and hundreds of ssDNA barcodes strands [61,62]. Through this approach they have been able to successfully detected prostate-specific antigen (PSA) in clinical samples with 300 times more sensitivity than commercial PSA immunoassays [63]. In fact, the microarray approach developed by Mirkin's group is already being commercialized by Nanosphere, Inc. (known as Verigene® system) and was one of the first nanotechnology-based diagnostic platforms to be approved by U.S. Food and Drug Administration (FDA).

Gold NPs functionalized with an antibody anti-CA15-3-HRP were also implemented in a traditional ELISA immunoassay to detect a breast cancer biomarker present in blood (*i.e.*, CA15-3 antigen) such as to improve the optical signal of the assay [64]. When compared to classical ELISA procedures, the gold NPs based ELISA presented a higher sensitivity and shorter assay time allowing to detect a target within the 0–60 U/mL range. Zhang *et al.* also developed a human serum albumin (HSA) immunosensor based on a chitosan-modified glass slide harboring a polymer with amino groups that served as linking sites (using glutaraldehyde) for anti-HAS antibody [65]. The antigen (HSA) and gold NP-labeled anti-HSA were then added to complete the sandwich-type immunocomplex and a linear correlation was obtained between the logarithm of HSA concentration and the absorbance intensity, as measured by UV-visible spectroscopy. Mayer *et al.* have also explored the shifts in the LSPR spectral extinction peak of gold nanorods and bipyramids NPs conjugated with antibodies to monitor real-time dynamic interactions with a specific secondary antibody [66,67].

2.3. Infrared Imaging and Enhanced-Spectroscopy

Noble metal NPs presenting a significant absorbance and scattering in the near infrared (NIR) region, such as gold nanoshells, nanorods or silver NPs, have found wide application as contrast agents for *in vivo* imaging [68–70] and also as nanostructures for surface-enhanced infrared absorption spectroscopy (SEIRAS)-mediated biosensing [71].

Several authors have taken advantage of the high permeability of human skin and tissue to NIR radiation to develop minimally invasive deep tissue diagnostic imaging techniques using such NPs as contrast agents. In general, the use of such noble metal NPs in *in vivo* imaging applications allows one to overcome several limitations of conventional NIR organic dyes, such as rapid photobleaching, detection sensitivity, insufficient stability in biological systems and weak multiplexing capability [69]. The high scattering properties of these NPs permits to enhance the contrast of imaging systems based on microscopy, such as dark-field or dual-photon luminescence microscopy, and even combine multiple imaging modalities such as to explore synergistic advantages over single imaging techniques [72,73]. Additionally, the synergy of such biosensing aptitudes with their intrinsic therapeutical capabilities, *i.e.*, theranostics, can provide for more efficient and focused therapies of different diseases, such as cancer [4]. These noble NPs, with a LSPR located within the NIR region, have been applied to different imaging techniques, such as Photoacoustic Imaging (PAI), Photoacoustic Tomography (PAT), dark-field microscopy and two-photon microscopy. PAI and PAT techniques allow noninvasive imaging with the capacity of resolving the optical absorption map of tissue at penetration depths akin with ultrasound imaging. For example, Agarwal and co-workers combined antibody functionalized gold nanorods tuned to the NIR region with PAI to effectively target and image early stage prostate cancer cells. These gold nanorods allowed them to produce high contrast images between targeted tissue and non-targeted tissue [74]. Similarly, Eghtedari *et al.* used gold nanorods as a contrast agent for *in vivo* detection using a laser based PAI system [75], while Pan *et al.* used NIR absorbing 2–4 nm gold nanobeacons (*i.e.*, gold NP functionalized with ssDNA strands that form a hairpin structure) to detect sentinel lymph nodes through PAI in *ex vivo* tissue samples [76]. On the other hand, Wang's group has used PAT technique to image the distribution of gold nanoshells circulating in the vasculature of a rat brain by achieving a gradual enhancement of the NIR optical absorption in the brain vessels [77,78]. They concluded that these NPs presented a high spatial resolution and enhanced sensitivity with an increased photoacoustic contrast up to 81% greater than blood, in their latest report. Lu *et al.* have also observed this increase in contrast by using similar NIR absorbing 40 nm gold nanoshells functionalized with thiolated-PEG as contrast agents for PAT in nude mice [79].

NIR scattering gold nanoshells were used by Loo and co-workers as a contrast agent in dark-field microscopy to target human epidermal growth factor receptor 2 (HER2), a clinically significant breast cancer molecular marker [80]. Similarly, Bickford *et al.* also used these type of gold nanoshells to image live HER2-overexpressing cancer cells using two-photon microscopy [81].

The LSPR of noble metal NPs when tuned into the NIR part of the spectrum can also be exploited for surface enhanced infrared absorption (SEIRA) spectroscopy, taking advantage of the direct NIR excitation of molecules adsorbed to metal NPs' surface. Some applications have benefited from SEIRA, namely in chemical analysis and biochemical sensing [82]. Mostly, gold and silver NPs have been used for the development of SEIRA based biosensors. As an example, by depositing gold NPs

functionalized with specific antibodies over a SiO_2/Si wafer surface, Enders and co-workers were able to detect antibody-antigen coupling with a 25-fold enhancement over a SiO_2/Si wafer surfaces' lacking the gold NP layer [71]. The IR transmission spectra (normal incidence) of non-specific antibody–antigen coupling and of specific antibody–antigen coupling was studied using a monolayer of anti-rabbit antibodies from goat immobilized on gold NP/(aminopropyl)-triethoxysilane/SiO_2/Si wafer as reference. The specific antibody–antigen reaction could clearly be detected via the characteristic absorption bands of proteins that are not coupled to the non-specific antigens.

2.4. Raman-Spectroscopy and Imaging

In 1974, Fleishmann and co-workers demonstrated for the first time that Raman signals from different types of molecules could be dramatically enhanced by their adsorption to silver surfaces [83], as well as on other metals, as later demonstrated. Since then, the use of metal NPs for surface-enhanced Raman scattering (SERS), mostly gold and silver NPs, has led to the development of a wide variety of new biosensors for the detection of nucleic acids, antibodies, proteins and other biological molecules [84,85]. Raman scattering arises from the inelastic scattering of photons that hit the analyte molecule and either gain or lose energy from the molecule's vibrational and rotation motion. This interaction generates a very narrow spectrum of bands that is unique for each analyte, and which can be greatly enhanced by metal nanostructures in the order of 10^5 to 10^6 times more than non-SERS Raman signals [86]. This enhancement is mainly attributed to the LSPR of the metal nanostructures and can be greater enhanced when the analyte molecules are placed in "hot spots" where LSPR fields overlap, such as junctions between aggregates of noble metal NPs [87].

The SERS detection of specific biomolecules mediated by noble metal NPs can be either accomplished directly or indirectly, through the association with a molecule with an intense and characteristic Raman signature, typically a fluorescent dye. Most of the methods based on SERS have taken similar approaches to those already described in colorimetric and fluorescent assays. For example, by exploring the electrostatic adsorption of some biomolecules to the NPs' metal surface some groups have created a metallic layer made of gold or silver NP aggregates to perform the detection of biomolecules and metabolites by SERS. Gogotsi *et al.* developed a SERS label-free biosensor based on a glass coated with gold NPs to detect and quantify nicotinic acid adenine dinucleotide phosphate (NAADP) molecules, which is a calcium secondary messenger that plays a crucial role for intracellular Ca^{2+} release [88]. This system allowed for the rapid detection of 100 μM NAADP without any special sample purification or labeling, making it an important tool for the study of normal cell function and cancer development. Ozaky's group used a similar approach using a surface covered with silver NPs instead of gold to detect bombesin, a neurotransmitter tumor marker, and its modified analogues by SERS [89]. They have also developed a protocol to monitor protein-protein and protein-small molecule interactions employing colloidal silver staining of the samples for producing active substrates for SERS [90,91]. Similarly, Van Duyne's group used SERS to detect and monitor glucose levels by adding a self-assembled monolayer of decanethiol over an aggregated silver NPs film in order to increase glucose adsorption which is minimal for bare-SERS active substrates, such as roughened silver [92,93]. The initial glucose detection limit of this system was lower than 5 mM, but was subsequently improved by the use of mixed decanethiol and

mercaptohexanol or (1-mercaptoundeca-11-yl)tri(ethylene glycol) layers and use of gold NPs instead of silver [94–96].The detection of ssDNA using SERS was carried out by Fabris and co-workers using a slide derivatized with uncharged peptide nucleic acids (PNAs) that recognized specific negatively charged ssDNA targets, which upon hybridization mediated the adsorption of positively charged silver NP [97]. A further addition of rhodamine6G dye to this system gave rise to SERS signals that allowed monitoring the hybridization event.

The use of conjugated noble metal NPs was also explored in SERS-based biosensors for a more versatile and specific detection of biomolecules. In most cases, a probe (e.g., DNA, antibody) is functionalized to the NP or an aggregated layer of NPs such as to create a sandwich conjugation with a Raman-labeled probe upon target detection, thus generating the SERS signal. Some variations of this cross-linking approach (Figure 2) have been explored by (i) Bonham *et al.* in the detection of DNA-binding proteins through the use of DNA functionalized gold NPs and an electroless silver plating of the conjugates to enhance the output signal [98]; (ii) Ryu *et al.*, to detect a specific Anthrax biomarker by means of peptide derivatized gold NPs [99] (iii) Vo-Dinh and co-workers for the detection of specific DNA sequences, such as HIV DNA, using Raman-active dye-labeled DNA on silver or gold NPs [100–103]; (iv) Ozaki's group to detect hepatitis B virus antigen using surface immobilized antibodies and gold NPs conjugated to antibodies and 4-mercaptobenzoic acid (MBA), acting as a Raman-active probe. In this case the signal was further enhanced by silver staining allowing to detect as low as 0.5 μg/mL of target [104]; (v) Driskell *et al.* in the detection of viral pathogens, such as feline calicivirus, using gold NP conjugated with a monoclonal antibody and a Raman reporter moiety, namely 5,5'-dithiobis(succinimidyl-2-nitrobenzoate) [105]; among others [106–108].

Figure 2. Examples of different variations of cross-linking approaches for SERS. The schematics depicts different approaches to the use of Raman-active moieties to enhance SERS signal output via cross-linking strategies: the Raman-active moiety can be bond to the target (two illustrations to the left) or to the surface of the film and/or NP (two illustrations to the right). Signal enhancement will occur upon cross-linking of the involved moieties derived from target recognition and binding.

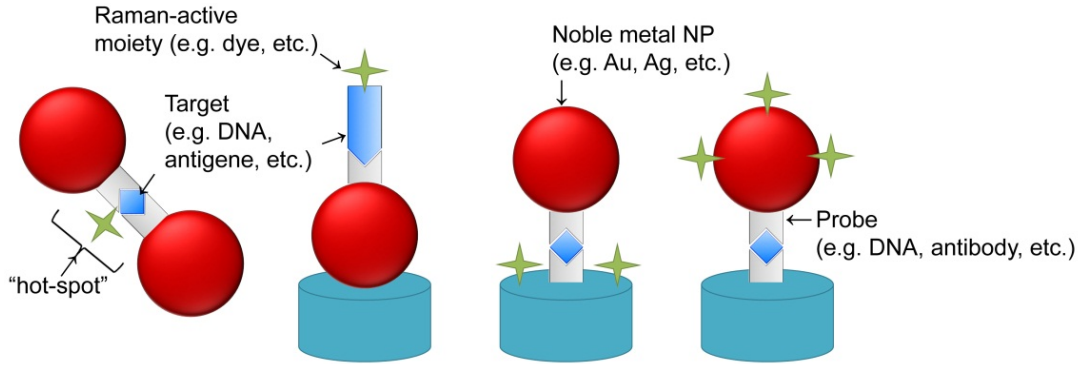

The cross-linking approach can also be used to entrap the Raman reporter moiety in "hot-spots" between NPs upon target detection, benefiting from an additional enhancement of SERS signal. For example, ssDNA functionalized silver [109] or gold [110,111] Raman dye-labeled NPs were used to detect the presence of a complementary ssDNA target that would generate a cross-linked nanostructure of NPs and, therefore, entrap the Raman-dye within it.

Vo-Dinh's group also explored a molecular nanobeacon approach using a Raman dye-labeled DNA functionalized on silver NPs where the presence of a complementary target would decrease SERS signal. This decrease was a consequence of the disruption of the hairpin structure that, otherwise, leads the Raman dye to the proximity of NPs' metallic surface [112]. Through this approach they were able to detect and quantify a gag gene sequence of the human immunodeficiency virus type 1 (HIV-1) within the range of 0.5 and 2 μM of DNA target. They have also expanded this method for multiplexing capability using two different Raman dyes-labeled gold nanobeacons to successfully detect the presence of the erbB-2 and ki-67 breast cancer biomarkers [113].

Other multiplex SERS methods have also been developed for biosensing based on a microarray approach [114,115], multiple dye-labeling [116,117], or even on "bar-coded" noble metal NPs [118–120]. An example of the latter, are the gold barcode nanodisks fabricated by Mirkin's group using on-wire lithography to create a barcode with 2 nm separated patterns of nanodisks over nickel wires [119]. The gaps located between the gold nanodisks acted both as "hot-spots", to enhance the SERS signal from the Raman-active dyes, and as a physical encoded "barcode" pattern, for multiplex detection of biomolecules using confocal Raman spectroscopy. As proof-of-concept, they demonstrated that multiplexing detection of DNA was possible with targets concentrations as low as 100 fM. More recently, the group also developed silver nanorods with etched gaps for multiplex biosensing by SERS [120].

The application of SERS mediated by noble metal NPs has also been described for *in situ* detection of specific reactions and intracellular molecular imaging of living cells and tissues. As an example, Qian and co-workers derivatized 60-80 nm gold NPs with PEG and a tumor targeting ligand, namely single-chain variable fragment antibodies, to detect tumors both *in vitro* and *in vivo* through SERS imaging [121]. These NPs were able to detect tumor biomarkers, such as epidermal growth factor receptors on human cancer cells and in xenograft tumor models, being more than 200 times brighter than NIR-emitting quantum dots (QDs). They were able to detect tumors up to 2 cm below the skin of live animals, mainly due to the fact that the LSPR peaks of such NPs was tuned within the 630–785 nm region, where the optical absorption of water is minimal. Specific cancer markers (phopholipase Cg1 biomarker proteins—PCg1) were also imaged in live human embryonic kidney cells (HEK293) by SERS microscopy using derivatized gold/silver core/shell NPs with R6G Raman tags and IgG antibodies [122]. Multiplexed SERS imaging has also been demonstrated in living mouse upon the injection of five different 60 nm gold NPs derivatized with a silica shell and a unique Raman active moiety for each NP (making up a total of 120 nm NP in diameter) [123]. These conjugated SERS-NPs naturally accumulated in the liver 24 h after the injection and presented five distinguishable SERS spectra signals up to 5 mm of tissue depth, which limited the mapping of the total liver for deeper tissue levels.

2.5. Fluorescence Spectroscopy

The exceptional quenching of fluorescent dyes mediated by noble metal NPs has allowed increased sensitivity and efficiency of Förster resonance energy transfer (FRET)-based biosensors. Two approaches have been used thus far: the so called molecular beacons that rely on NPs functionalized with fluorescent-labeled ssDNA strands that form a hairpin structure; and noble metal nanoprobes

consisting of NPs functionalized with single strand nucleic acid strands that are hybridized to another fluorescent-labeled single strand nucleic acid probe (Figure 3).

Figure 3. Different approaches for fluorescent-based noble metal NPs biosensing. (**A**) molecular nanobeacons and (**B**) other nanoprobes. Distance to the nanoparticle determine the fluorescence signal that is observed. Distances are not represented to the scale.

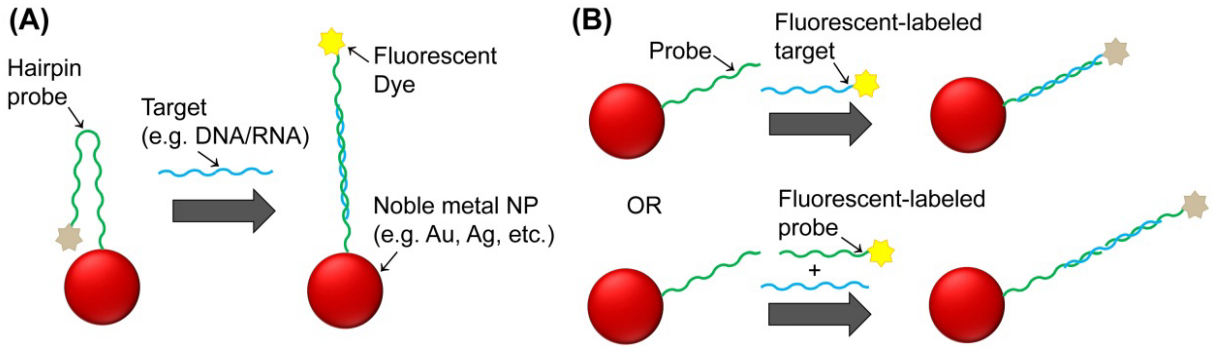

In the case of the molecular beacons, the hairpin structure leads the fluorescent dye moiety to the proximity of the NP's surface and, consequently, to the quenching of fluorescence due to Nanoparticle Surface Energy Transfer (NSET) occurring between the dye (donor molecule) and the NP's surface (acceptor)—a phenomenon that has been described to permit energy transfer for distances nearly twice as far as FRET [124,125]. In the presence of a complementary DNA/RNA target, the hairpin structure is disrupted by target hybridization and fluorescence is restored. Several methods have been developed based on this approach to monitor specific nucleic acid hybridizations as well as cleavage processes mediated by nucleases, mainly using gold NPs [126]. For example, Dubertret and co-workers reported the use of molecular nanobeacons based on 1.4 nm gold NPs to detect single-base mismatches in DNA with a 100-fold increase in sensitivity when compared to conventional molecular beacons [127]. Similarly, Benia *et al.* used molecular nanobeacons based on 13 nm gold NPs to successfully detect a mutation associated to cystic fibrosis using just 1 nM of target [128]. They have also shown that the use of gold NPs larger than 13 nm for molecular nanobeacons is not recommended due to the fact that larger NPs present relevant quenching efficiency even at large fluorophore–NP separation lengths, despite the fact that they could carry a higher number of molecular beacons.

On another approach, noble metal nanoprobes can be combined with dye-labeled ssDNA probes to detect specific nucleic acid targets by FRET/NSET mediated mechanisms. One method is to design such probes to harbor complementary and contiguous sequences to the target, in such way that upon target hybridization the dye is forced to approach the NP's surface and the fluorescent signal consequently decreases [129]. Another method is to hybridize the dye-labeled ssDNA directly to the nanoprobes and detect specific target DNA sequences based on strand displacement of the fluorescent probe [130]. For example, in the presence of a fully complementary long ssDNA targets, the short dye-labeled DNA strand is displaced and, as a result, the fluorescence that was initially quenched by the NP is restored. Through this approach, the signal-to-noise ratio and detection limit of 50 pM is significantly improved when compared with similar probes using organic acceptors as reported by Mo and co-workers [130]. A similar approach was used by Wang and co-workers to detect proteins using the dye-labeled ssDNA hybridized to an aptamer that is immobilized on gold NPs [131]. Whenever a

protein binds to the aptamer, the dye-labeled ssDNA is released and fluorescence is restored, allowing to detect proteins with high sensitivity and specificity. Similarly, Ray and co-workers demonstrated that the DNA cleavage by specific nucleases can also be easily and quickly monitored using Au-nanoprobes hybridized with complementary Cy3-labeled nucleic acid strands with a sensitivity several orders of magnitude greater than the conventional gel electrophoresis or HPLC techniques, or even a few orders of magnitude greater than UV assays [132]. The presence of a S1 nuclease leads to the cleavage of the dye-labeled dsDNA bound to the NP and consequently to an enhancement of the fluorescence signal by a factor of 120. Jennings *et al.* also developed a method based on this approach using NSET to measure Mg^{2+}-induced conformational changes and kinetics of a hammerhead ribozyme using a fluorescent labeled RNA that hybridized with a complementary strand attached to 1.4 nm gold NPs and formed the hammerhead structure [133]. Mayilo *et al.* described a sandwich immunoassay using gold NPs quenching upon detecting a cardiac troponin T protein by its interaction with two different antibodies, one attached to gold NPs and the other labeled with fluorescent dyes [134]. Guirgis and co-workers developed an immunoassay to detect malaria based on the fluorescence quenching of Cy3B-labeled recombinant *Plasmodium falciparum* heat shock protein 70 (PfHsp70) upon binding to gold NPs functionalized with an anti-Hsp70 monoclonal antibody [135]. Upon competition with the free antigen, the Cy3B-labeled recombinant PfHsp70 is released to solution resulting in an increase of fluorescence intensity. The interaction of human blood proteins with gold NPs has also been studied by letting the proteins interact with fluorescent gold NPs and performing the detection through quenching [136].

The combination of noble metal NPs and semiconductor QDs as a FRET donor–acceptor couple has also been explored by several authors to develop fluorescence competition assays for nucleic acid, protein and antibody/antigen detection following the same approaches described above, simply by substituting the dye with QDs [137–139]. Additionally, more than one dye can also be simultaneously used to develop multiplexing approaches of all the previously described methods by tracking the specific emission of each dye, since the quenching effectiveness of noble metal NPs is widespread across the UV/visible spectra. Namely multiplex methods for DNA detection [140,141], endonucleases monitoring [142], small analytes detection (adenosine, potassium and cocaine) using aptamers [143] have been described.

The use of noble metal NPs to enhance the fluorescence signal of dyes used in a DNA assay has been reported by Dragan *et al.* [144]. A 2-color DNA assay based on the combination of the Metal-Enhanced Fluorescence (MEF) effect and microwave-accelerated DNA hybridization allowed to detect dye-labeled targets in a microarray format. The microarray ssDNA probes are functionalized over a monolayer film of silver NPs which contributed for the large enhancement of the target's fluorescent label due to a short-range (0–30 nm) coupling effect of a dye's excited state electronic system with NPs plasmons.

Different noble metal NPs with inherent fluorescent properties or directly functionalized with fluorescent dyes have also been used for *in vivo* biosensing. Zhang and co-workers have developed fluorescent metal nanoshells composed of silica spheres with encapsulated $[Ru(bpy)3]^{2+}$ complexes as cores and thin silver layers as shells to detect single microRNA molecules in cells positive to lung cancer [145]. These nanoshells harbored a covalently bound ssDNA probe that recognized the micro RNA (miRNA) target in the cells and presented highly contrast images against cellular autofluorescence,

mainly due to their strong intensity emission and longer lifetimes. The same authors have also reported similar fluorescence enhancements of different fluorophores when functionalized to different silver NPs, which were used to target different receptors within cell membranes [146,147]. Using a different approach, Phillips and co-workers developed an array of gold NP–conjugated polymer constructs for bacterial sensing [148]. The efficient quenching ability of gold NPs coupled with the molecular-wire effect of conjugated polymer compounds generated a pronounced fluorescence response mediated by the binding strength of the bacterium to the gold NP. Through this approach, the authors successfully differentiated twelve different bacteria using only three systems.

2.6. Electric and Electrochemical Approaches

The unique physicochemical properties of noble metal NPs, such as high surface area, high mechanical strength, rich electronic and catalytic properties, have been explored to detect biological recognition events through electrical signals or electrochemical transductions and design a new generation of electronic biosensor devices [149,150]. These electrical and electrochemical approaches generally rely on the changes in the ohmic response of an electrical circuit or the flow of electrons arising from faradaic processes (*i.e.*, oxidation or reduction) near the surface of an electrode, respectively, to achieve biosensing. Although the direct electrical and electrochemical detection of biomolecules is possible, many have benefited from the electroactive or catalytic properties of NPs as reporters for biosensing with unprecedented levels of sensitivity [151].

The key aspect of electrical biosensors is the generation or modulation of electrical current in an electronic circuit by molecular binding of the biomolecule of interest, such as the completion of a broken circuit or altering the electrical properties of an electro-mechanical sensor (e.g., piezoelectric sensor). An example of the latter case, is the piezoelectric biosensor developed by Chen and co-workers using gold NP functionalized with DNA probes for the detection of the foodborne pathogen *Escherichia coli* O157:H7 [152]. In this application, the authors used gold nanoprobes as a mass enhancer and, thus, further amplify the changes in the signal and the sensitivity of the piezoelectric sensor, as well as increase the specificity of the method. The oscillation frequency of the piezoelectric sensor decreased in real-time as the weight at the sensor's surface increased due to the sandwich hybridization occurring between the target oligonucleotide, the sensor’s probe oligonucleotides and the circulating DNA functionalized gold NP. Similarly, Pang *et al.* used this piezoelectric approach to detect a DNA single-base mutation within an artificial codon CD17 of the β-thalassemia gene, complementing the method with a DNA ligase reaction [153]. Immunoassays were also developed using piezoelectric sensors in which the specific agglutination of antigen-coated gold NPs causes a frequency change in the signal when in the presence of the corresponding antibody [154,155].

Another electrical approach for biosensing is to explore the conductivity of noble metal NPs and use them as conductive tags to act as a “switch” on an electrical circuit. Following this idea, several groups developed DNA sensors based on electrode gaps in which the binding of noble metal NPs functionalized with oligonucleotides leaded to conductivity changes associated with target-probe binding events [156–160]. In the case of the Mirkin’s group approach [156], the presence of a complementary target allowed the gold nanoprobes to form a sandwich hybridization with the probes

functionalized within the electrode gaps, thus filling the gaps and facilitating silver deposition to further increase conductivity between electrodes, allowing to detect DNA concentrations as low as 500 fM with a single base resolution.

In general, electrochemical biosensors employ potentiometric, amperometric or impedimetric transducers to convert the biosensing information into a measurable signal. Some authors have described the use of potentiometric stripping analysis to detect and quantify gold, silver or gold/silver NPs that worked as tags for biosensing DNA [161–164], antibodies [165–167] or aptamers [168], with sensitivities of down to 600 aM, 3 fM and 1 nM, respectively. Others have described the use of cyclic voltammetry [169,170], differential pulse voltammetry [171], chronocoulometry [172] electrochemical methods to perform biosensing of DNA and proteins mediated by noble metal NPs acting as electrochemical labels. Ozsoz and co-workers described an electrochemical genosensor based on gold NP and disposable pencil graphite electrodes for the detection of a Factor V Leiden mutation in PCR products amplified from clinical samples [173]. The method allowed detection of as little as 0.78 fmol of PCR amplicons using the oxidation signal of colloidal gold nanoprobes that hybridized to the complementary DNA targets. More recently, Yu *et al.* used gold NP in combination with apoferrition NPs to further increase the sensitivity of electrochemical DNA biosensing down to 51 aM [174].

Several authors have described the development of amperometric-based biosensors, which are usually more suited for mass production than potentiometric biosensors [175]. In this approach the working electrode is usually a noble metal NP covered by the biorecognition component, which enables the amperometric signal. Namely, using this amperometric approach: Polsky and co-workers used platinum NPs functionalized with nucleic acid aptamers to detect thrombin with a sensitivity limit corresponding to 1 nM [176]; Munge *et al.* developed an immunosensor to detect attomoles of the cancer biomarker interleukin-8 using glutathione derivatized gold NPs [177]; Jensen and co-workers used inkjet printed arrays with gold NPs to detect the cancer biomarker interleukin-6 directly in serum with a detection limit of 20 pg/mL [178]; Yin *et al.* used gold NPs over a surface of poly(styrene-acrylic acid) nanospheres, that served as a matrix to conjugate alkaline phosphatase, to detect the tumor necrosis factor α up to 0.01 ng/mL [179]; Meng *et al.* used gold NPs combined with ferric oxide NPs and carbon nanotubes to detect up to 0.04 ng/mL of the tumor biomarker alpha fetoprotein [180]; Sharma and co-workers used gold NPs and screen printed electrodes modified with multiwall carbon nanotubes to detect *Plasmodium falciparum* histidine-rich protein 2 in serum of humans with malaria [181]. In this case, the authors compared the method with a commercial kit, Paracheck Pf test (Orchid Biomedical Systems, Goa, India), and determined that their method was more sensitive and specific than the kit, having a detection limit of 8 ng/mL; Merkoçi's group used gold NP and magnetic beads to develop a magneto-immunosensor for the detection of anti-hepatitis B virus antibodies and human IgG in human serum [182,183]; Che and co-workers used gold NPs with multi-walled carbon nanotube-silver composites to detect down to 0.08 ng/mL of alpha-1-fetoprotein [184]; Scodeller *et al.* used gold-silver core-shell NPs to develop a system responsive to glucose based on the enzymatic reduction of FAD by glucose [185].

Some impedimetric based electrochemical biosensors have also been reported, following either impedance (Z) or its components resistance (R), capacitance (C) and inductance (L). Mahmoud and co-workers developed an assay based on a modified gold electrode with single-walled carbon nanotube/gold NPs derivatized with thiol terminated ferrocene-pepstatin conjugates able to detect

picomolar levels of HIV-1 protease and screen its potent inhibitors using electrochemical impedance spectroscopy [186]. Yang *et al.* fabricated a capacitive immunosensor based on grafted ethylene diamine and self-assembled gold NPs monolayer on glassy carbon electrode for the detection of *Salmonella* spp. using also electrochemical impedance spectroscopy [187]. This assay was successfully used for the detection of *Salmonella* spp. in lab-processed commercial pork samples and presented a detection limit of 100 CFU/mL.

Recently, Tian and co-workers developed an electrochemiluminescence biosensor using luminol functionalized gold NPs as labels [188,189]. The electrochemiluminescence of luminol is enhanced 2 to 3-orders of magnitude on gold NPs when compared to bare gold electrodes and allowed this sandwich-type immunocomplex sensor to achieve a detection limit of 1 pg/mL for human IgG in human sera.

Multiplex approaches based on some of the methods previously described have also been described. Li and co-workers used gold surface DNA arrays functionalized with multiple probes in combination with reporting probes made of silver NPs to detect herpes simplex virus (HSV), Epstein-Barr virus (EBV) and cytomegalovirus (CMV) sequences by differential pulse voltammetry [190]. The silver NPs-based tag allowed for the detection down to 5 aM of target DNA by producing a 103-fold amplification in the differential pulse voltammetry signal, due to the excellent electroactive properties of silver NPs.

Enzyme-functionalized gold NPs harboring specific DNA sequences were also used as catalytic labels for multiplex DNA detection [191]. A sandwich hybridization strategy was used in this method, involving DNA probes functionalized on a glassy carbon electrode which registered the electrochemical signals generated by the enzymatic products produced from the substrates catalyzed by the functionalized enzymes, namely horseradish peroxidase (HRP) and alkaline phosphatase (ALP), upon complementary target recognition. This method allowed to detect two distinct targets in a one-pot solution with a detection limit of 0.1 and 12 fM using HRP–gold NPs and ALP–gold NPs as labels, respectively. Zhang *et al.* explored anodic stripping voltammetry using a screen-printed carbon electrode chip in combination with bio-barcoded gold NPs, as electrochemical reporters, and magnetic NPs, for easy and clean separation from the sample, to detect multiple pathogens (e.g., *Bacillus anthracis* and *Salmonella enteritidis*) [192]. A multiplex immunoassay was also developed using screen-printed array of carbon electrodes and gold NPs as electrochemical labels [193]. This immunoassay is performed using a sandwich approach between the electrode array probes and gold NPs labeled with antibodies, mediated by the target analytes (*i.e.*, human and goat IgG). Under optimal conditions the method allowed to detect a minimum target concentration of 1.1 and 1.6 ng/mL, respectively, using differential pulse voltammetry.

3. Application in Biosensing Platforms—Future Perspectives

Noble metal NP-based biosensors provide a new horizon for novel functions with a variety of applications in clinical diagnostics and biological research. This review has provided a summary of the various biosensing strategies developed thus far, that explored the unique physicochemical properties of noble metal NPs, towards their potential applications in clinical and point-of-care diagnostics.

Table 2 summarizes the different types of real biological samples that have been tested with these noble metal NP-based biosensors, according to their methodology principle.

Table 2. Summary of real biological samples tested with noble metal NP-based biosensors according to the type of NP and explored methodology principle.

Method	Type of NP	Target/Samples [reference]
Colorimetric/ scanometric	Gold	• SNP (rs2131877) in human DNA [32] • Mutations in EGFR gene in genomic DNA [33] • SNP associated with long QT syndrome in genomic DNA [31] • SNPs in β-thalassemia gene in genomic DNA—mediated by PCR [43,45] • SNPs in MBL2 gene in genomic DNA—mediated by PCR [53,54] • Fusion genes in K562 cell line [55] • Hepatitis C virus RNA [35] • *M. tuberculosis* DNA and associated drug-resistance SNPs in clinical samples [46,48,50] • BCR-ABL fusion transcript in clinical samples [47] • FSY1 mRNA in total RNA [49]
	Gold	• Melamine in whole milk [40] • Prostate specific antigen (PSA) in human serum [63] • CA15-3 breast cancer biomarker in human serum [64] • Genetically modified organisms [52] • Mutations associated to methicillin resistance in S. aureus & Factor V Leiden mutants [58]
	Gold/silver alloy	• TP53 gene [28] • BCR-ABL fusion genes [29]
NIR	Gold	• Prostate cancer cells in mouse [74] • Lymph nodes in mouse [76] • Brain vessels in mouse [77–79] • HER2 cancer biomarker in breast adenocarcinoma cells [80,81]
SERS	Gold	• Nicotinic acid adenine dinucleotide phosphate (NAADP) in cell extracts [88] • Glucose in rat [96] • Multiple pathogen DNA in clinical specimens (cerebrospinal fluid, stool, pus, and sputum) [118] • Feline calicivirus (FCV) antibody from cell culture media [105] • Prostate-specific antigen in human serum [194] • Deep-tissue imaging in living mouse [123]
	Silver	• HIV-1 DNA in genomic DNA - PCR mediated [112] • Glucose in rat [93]
	Gold/silver core/shell	• Phospholipase Cγ1 biomarker protein in cancer cells [122]
Fluorescence-based	Gold	• *Plasmodium falciparum* heat shock protein in infected blood cultures [135]
	Silver	• miRNA-486 expression levels in lung cancer cells [145] • Cell membrane imaging in cell lines [146,147]

Table 2. *Cont.*

Method	Type of NP	Target/Samples [reference]
Electric/ Electrochemical	Gold	• Factor V Leiden DNA mutation in genomic DNA – mediated by PCR [173] • *E. coli* O157:H7 in food samples [152]
	Gold	• Anti-*Toxoplasma gondii* immunoglobulins in rabbit blood and serum [154] • Human and mouse IgG antibody in human and mouse serum [166] • Interleukin-8 (IL-8) cancer biomarker in human serum [177] • Interleukin-6 (IL-6) cancer biomarker in calf serum [178] • Tumor necrosis factor α (TNF-α) in human serum [179] • *Plasmodium falciparum* histidine-rich protein 2 in serum [181] • Anti-hepatitis B virus antibodies and human IgG in human serum [182,183] • HIV-1 protease and inhibitors in human serum [186] • *Salmonella* spp. in pork samples [187] • Human IgG in human serum [188,189] • Human and goat IgG in serum [193]
	Silver	• α-1-Fetoprotein (AFP) in human serum [184]

Noble metal NPs have already proven to be one of the most important groups of nanomaterials for biosensing approaches, as well as in other biomedical applications (e.g., therapy). Highly sensitive and specific biosensors based on noble metal NPs have open up the possibility of creating new diagnostic platforms for disease markers, biological and infectious agents in the early-stage detection of disease and threats. Among the different approaches explored thus far, such as colorimetric, NIR imaging, fluorescence quenching/enhancement, SERS, electric and electrochemical sensing, there are, as always, advantages and disadvantages associated to each approach towards the ultimate diagnostic application in real samples. In most cases, the proof-of-concept for such approaches has been reported using controlled synthetic bioanalytes and/or samples, while validation of these biosensors with a statistically larger population of real samples still remains to be addressed as to further prove the potential application in clinical and point-of-care diagnostics. Apart from that, one key issue to take into consideration in biosensing platform integration is the increasing demand for higher sensitivity and selectivity at minimal costs, and the possibility to monitor biosensing in real-time, especially for point-of-care platforms, for which simplicity should also be considered. Considering this, colorimetric and electrochemical approaches are the most promising due to their simplicity, high sensitivity and specificity, in addition to the fact that in most cases they simply do not require expensive and complex instrumentations to achieve a sample-in/answer-out biosensing platform. Moreover, such approaches allow for multiplexing biosensing enabling their application in a range from low- to high-throughput diagnostics. In fact, some of these approaches have already reached commercialization, as is the case of Verigene® system by Nanosphere, Inc. (Northbrook, IL, USA) which explores the scattering capabilities of gold NPs in a microarray platform providing a diagnostic platform for DNA/RNA and protein sensing.

On the other hand, the use of NIR active noble metal NPs as contrast agents for PAI or PAT is one of the most promising platforms for *in vivo* imaging, provided that aspects concerning the toxicology of such nanomaterials are carefully addressed. Moreover, in most cases, the use of such NP in *in vivo* imaging allows also to simultaneously carry out therapeutic procedures (*i.e.*, theranostics), such as photothermal therapy, enabling a more precise and efficient treatment of diseases, such as cancer. As an example of this potential, Nanospectra Biosciences (Houston, TX, USA) is already carrying out clinical trials for its AuroLase® Therapy approach, which combines gold nanoshells with photothermal ablation technology for *in vivo* imaging and therapy.

Other developed methodologies using noble metal NPs, such as SERS and fluorescent quenching/enhancement approaches, can still find great application in research laboratories, allowing to unveil current paradigms and emerging challenges of biology and medicine. That said, some of the described noble metal NP-based biosensors that are currently under development will most likely revolutionize our understanding of biological mechanisms and push forward the clinical practice through their integration in future diagnostics platforms. As nanotechnology is becoming increasingly accessible to research laboratories and, most recently, to clinical laboratories, significant advances in the area of noble metal NP-based biosensors will certainly occur in the near future, pushed by the intervention of a cross-disciplinary team, consisting of a variety of researchers with diverse backgrounds, that will make the prospect of widespread use of noble metal NPs in clinical and point-of-care diagnostics a reality.

Acknowledgments

The authors acknowledge FCT/MCTES (Portugal) for financial support for CIGMH and PTDC/BIO/66514/2006. João Rosa acknowledges Grant No. SFRH/BD/43320/2008, João Conde SFRH/BD/62957/2009 and Leticia Giestas SFRH/BPD/64505/2009. Nanotruck-Action from NanoSciEra+.

References

1. Jain, K.K. Applications of nanobiotechnology in clinical diagnostics. *Clin. Chem*. **2007**, *53*, 2002–2009.
2. Jain, K.K. Nanomedicine: Application of nanobiotechnology in medical practice. *Med. Princ. Pract.* **2008**, *17*, 89–101.
3. Zhao, W.; Karp, J.M.; Ferrari, M.; Serda, R. Bioengineering nanotechnology: Towards the clinic. *Nanotechnology* **2011**, *22*, doi:10.1088/0957-4484/22/49/490201.
4. Conde, J; Rosa, J.; Lima, J.C.; Baptista, P.V. Nanophotonics for Molecular Diagnostics and Therapy Applications. *Int. J. Photoenergy.* **2011**, *2012*, 619530, doi:10.1155/2012/619530.
5. Baptista, P.V.; Doria, G.; Quaresma, P.; Cavadas, M.; Neves, C.S.; Gomes, I.; Eaton, P.; Pereira, E.; Franco, R. Nanoparticles in molecular diagnostics. *Prog. Mol. Biol. Transl. Sci.* **2011**, *104*, 427-488.
6. Azzazy, H.M.; Mansour, M.M. *In vitro* diagnostic prospects of nanoparticles. *Clin. Chim. Acta* **2009**, *403*, 1-8.
7. Larguinho, M.; Baptista, P.V. Gold and silver nanoparticles for clinical diagnostics—From genomics to proteomics. *J. Proteomics* **2011**, in press.

8. Conde, J.; Doria, G.; Baptista, P. Noble metal nanoparticles applications in cancer. *J. Drug. Deliv.* **2012**, *2012*, doi:10.1155/2012/751075.
9. Dreaden, E.C.; Alkilany, A.M.; Huang, X.; Murphy, C.J.; El-Sayed, M.A. The golden age: Gold nanoparticles for biomedicine. *Chem. Soc. Rev.* **2011**, in press.
10. Sperling, R.A.; Parak, W.J. Surface modification, functionalization and bioconjugation of colloidal inorganic nanoparticles. *Phil. Trans. R. Soc. A* **2010**, *368*, 1333-1383.
11. Baptista, P.; Pereira, E.; Eaton, P.; Doria, G.; Miranda, A.; Gomes, I.; Quaresma, P.; Franco, R. Gold nanoparticles for the development of clinical diagnosis methods. *Anal. Bioanal. Chem.* **2008**, *391*, 943-950.
12. Boisselier, E.; Astruc, D. Gold nanoparticles in nanomedicine: Preparations, imaging, diagnostics, therapies and toxicity. *Chem. Soc. Rev*. **2009**, *38*, 1759-1782.
13. Sperling, R.A.; Gil, P.R.; Zhang, F.; Zanella, M.; Parak, W.J. Biological applications of gold nanoparticles. *Chem. Soc. Rev*. **2008**, *37*, 1896-1908.
14. Turkevich, J.; Garton, G.; Stevenson, P.C. The color of colloidal gold. *J. Colloid Sci.* **1954**, *9*, 26-35.
15. Frens, G. Controlled nucleation for the regulation of the particle size in monodisperse gold suspensions. *Nat. Phys. Sci.* **1973**, *241*, 20-22.
16. Wilcoxon, J.P.; Abrams, B.L. Synthesis, structure and properties of metal nanoclusters. *Chem. Soc. Rev*. **2006**, *35*, 1162-1194.
17. Daniel; M.C.; Astruc, D. Gold nanoparticles: Assembly, supramolecular chemistry, quantum-size-related properties, and applications toward biology, catalysis, and nanotechnology. *Chem. Rev*. **2004**, *104*, 293-346.
18. Kimling, J.; Maier, M.; Okenve, B.; Kotaidis, V.; Ballot, H.; Plech, A. Turkevich method for gold nanoparticle synthesis revisited. *J. Phys. Chem. B* **2006**, *110*, 15700-15707.
19. Tréguer-Delapierre, M.; Majimel, J.; Mornet, S.; Duguet, E.; Ravaine, S. Synthesis of non-spherical gold nanoparticles. *Gold Bull*. **2008**, *41*, 195-207.
20. Yuan, Q.; Wang, X. Aqueous-based route toward noble metal nanocrystals: Morphology-controlled synthesis and their applications. *Nanoscale* **2010**, *2*, 2328-2335.
21. Sau, T.K.; Rogach, A.L. Nonspherical noble metal nanoparticles: Colloid-chemical synthesis and morphology control. *Adv. Mater*. **2010**, *22*, 1781-1804.
22. Murphy, C.J.; Sau, T.K.; Gole, A.M.; Orendorff, C.J.; Gao, J.; Gou, L.; Hunyadi, S.E.; Li, T. Anisotropic metal nanoparticles: Synthesis, assembly, and optical applications. *J. Phys. Chem. B* **2005**, *109*, 13857-13870.
23. Subbiah, R.; Veerapandian, M.; Yun, K.S. Nanoparticles: Functionalization and multifunctional applications in biomedical sciences. *Curr. Med. Chem.* **2010**, *17*, 4559-4577.
24. Barnes, W.L.; Dereux, A., Ebbesen, T.W. Surface plasmon subwavelength optics. *Nature* **2003**, *424*, 824-830.
25. Wilcoxon, J. Optical absorption properties of dispersed gold and silver alloy nanoparticles. *J. Phys. Chem. B* **2009**, *113*, 2647-2656.
26. Jain, P.K.; Lee, K.S.; El-Sayed, I.H.; El-Sayed, M.A. Calculated absorption and scattering properties of gold nanoparticles of different size, shape, and composition: Applications in biological imaging and biomedicine. *J. Phys. Chem. B* **2006**, *110*, 7238-7248.

27. Liz-Marzán, L.M. Tailoring surface plasmons through the morphology and assembly of metal nanoparticles. *Langmuir* **2006**, *22*, 32-41.
28. Doria, G.; Larguinho, M.; Dias, J.T.; Pereira, E.; Franco, R.; Baptista, P.V. Gold-silver-alloy nanoprobes for one-pot multiplex DNA detection. *Nanotechnology* **2010**, *21*, doi:10.1088/0957-4484/21/25/255101.
29. Baptista, P.V.; Doria, G.; Conde, J. Alloy metal nanoparticles for multicolor cancer diagnostics. *Proc. SPIE* **2011**, *7909*, doi:10.1117/12.879025.
30. Jain, P.K.; El-Sayed, M.A. Universal scaling of plasmon coupling in metal nanostructures: Extension from particle pairs to nanoshells. *Nano Lett*. **2007**, *7*, 2854-2858.
31. Li, H.; Rothberg, L.J. Label-free colorimetric detection of specific sequences in genomic DNA amplified by the polymerase chain reaction. *J. Am. Chem. Soc.* **2004**, *126*, 10958-10961.
32. Lee, H.; Joo, S.W.; Lee, S.Y.; Lee, C.H.; Yoon, K.A.; Lee, K. Colorimetric genotyping of single nucleotide polymorphism based on selective aggregation of unmodified gold nanoparticles. *Biosens. Bioelectron.* **2010**, *26*, 730-735.
33. Lee, H.; Kang, T.; Yoon, K.A.; Lee, S.Y.; Joo, S.W.; Lee, K. Colorimetric detection of mutations in epidermal growth factor receptor using gold nanoparticle aggregation. *Biosens. Bioelectron.* **2010**, *25*, 1669-1674.
34. Kim, J.H.; Chung, B.H. Naked eye detection of mutagenic DNA photodimers using gold nanoparticles. *Biosens. Bioelectron.* **2011**, *26*, 2805-2809.
35. Shawky, S.M.; Bald, D.; Azzazy, H.M. Direct detection of unamplified hepatitis C virus RNA using unmodified gold nanoparticles. *Clin. Biochem.* **2010**, *43*, 1163-1168.
36. Xia, F.; Zuo, X.; Yang, R.; Xiao, Y.; Kang, D.; Vallée-Bélisle, A.; Gong, X.; Yuen, J.D.; Hsu, B.B.; Heeger, A.J.; *et al.* Colorimetric detection of DNA, small molecules, proteins, and ions using unmodified gold nanoparticles and conjugated polyelectrolytes. *Proc. Natl. Acad. Sci. USA* **2010**, *107*, 10837-10841.
37. Ma, Z.F.; Tian, L.; Wang, T.T.; Wang, C.G. Optical DNA detection based on gold nanorods aggregation. *Anal. Chim. Acta* **2010**, *673*, 179-184.
38. Kanjanawarut, R.; Su, X.D. Colorimetric detection of DNA using unmodified metallic nanoparticles and peptide nucleic acid probes. *Anal. Chem.* **2009**, *81*, 6122-6129.
39. Wang, G.L.; Dong, Y.M.; Zhu, X.Y.; Zhang, W.J.; Wang, C.; Jiao, H.J. Ultrasensitive and selective colorimetric detection of thiourea using silver nanoprobes. *Analyst* **2011**, *136*, 5256-5260.
40. Wei, F.; Lam, R.; Cheng, S.; Lu, S.; Ho, D.; Li, N. Rapid detection of melamine in whole milk mediated by unmodified gold nanoparticles. *Appl. Phys. Lett*. **2010**, *96*, doi:10.1063/1.3373325.
41. Mirkin, C.A.; Letsinger, R.L.; Mucic, R.C.; Storhoff, J.J. A DNA-based method for rationally assembling nanoparticles into macroscopic materials. *Nature* **1996**, *382*, 607-609.
42. Storhoff, J.J.; Elghanian, R.; Mucic, R.C.; Mirkin, C.A.; Letsinger, R.L. One-pot colorimetric differentiation of polynucleotides with single base imperfections using gold nanoparticle probes. *J. Am. Chem. Soc.* **1998**, *120*, 1959-1964.
43. Li, J.S.; Deng, T.; Chu, X.; Yang, R.H.; Jiang, J.H.; Shen, G.L.; Yu, R. Rolling circle amplification combined with gold nanoparticle aggregates for highly sensitive identification of single-nucleotide polymorphisms. *Anal. Chem*. **2010**, *82*, 2811-2816.

44. Sato, K.; Hosokawa, K.; Maeda, M. Rapid aggregation of gold nanoparticles induced by non-cross-linking DNA hybridization. *J. Am. Chem. Soc*. **2003**, *125*, 8102-8103.
45. Doria, G.; Franco, R.; Baptista, P. Nanodiagnostics: Fast colorimetric method for single nucleotide polymorphism/mutation detection. *IET Nanobiotechnol*. **2007**, *1*, 53-57.
46. Costa, P.; Amaro, A.; Botelho, A.; Inácio, J.; Baptista, P.V. Gold nanoprobe assay for the identification of Mycobacteria of the *Mycobacterium tuberculosis* complex. *Clin. Microbiol. Infect*. **2010**, *16*, 1464-1469.
47. Conde, J.; de la Fuente, J.M.; Baptista, P.V. RNA quantification using gold nanoprobes—Application to cancer diagnostics. *J. Nanobiotechnol.* **2010**, *8*, doi:10.1186/1477-3155-8-5.
48. Baptista, P.V.; Koziol-Montewka, M.; Paluch-Oles, J.; Doria, G.; Franco, R. Gold-nanoparticle-probe-based assay for rapid and direct detection of Mycobacterium tuberculosis DNA in clinical samples. *Clin. Chem.* **2006**, *52*, 1433-1434.
49. Baptista, P.; Doria, G.; Henriques, D.; Pereira, E.; Franco, R. Colorimetric detection of eukaryotic gene expression with DNA-derivatized gold nanoparticles. *J. Biotechnol.* **2005**, *119*, 111-117.
50. Veigas, B.; Machado, D.; Perdigão, J.; Portugal, I.; Couto, I.; Viveiros, M.; Baptista, P.V. Au-nanoprobes for detection of SNPs associated with antibiotic resistance in *Mycobacterium tuberculosis*. *Nanotechnology* **2010**, *21*, doi:10.1088/0957-4484/21/41/415101.
51. Jian, J.W.; Huang, C.C. Colorimetric detection of DNA by modulation of thrombin activity on gold nanoparticles. *Chemistry* **2011**, *17*, 2374-2380.
52. Kalogianni, D.P.; Koraki, T.; Christopoulos, T.K.; Ioannou, P.C. Nanoparticle-based DNA biosensor for visual detection of genetically modified organisms. *Biosens. Bioelectron*. **2006**, *21*, 1069-1076.
53. Litos, I.K.; Ioannou, P.C.; Christopoulos, T.K.; Traeger-Synodinos, J.; Kanavakis, E. Genotyping of single-nucleotide polymorphisms by primer extension reaction in a dry-reagent dipstick format. *Anal. Chem*. **2007**, *79*, 395-402.
54. Litos, I.K.; Ioannou, P.C.; Christopoulos, T.K.; Traeger-Synodinos, J.; Kanavakis, E. Multianalyte, dipstick-type, nanoparticle-based DNA biosensor for visual genotyping of single-nucleotide polymorphisms. *Biosens. Bioelectron*. **2009**, *24*, 3135-3139.
55. Kalogianni, D.P.; Bravou, V.; Christopoulos, T.K.; Ioannou, P.C.; Zoumbos, N.C. Dry-reagent disposable dipstick test for visual screening of seven leukemia-related chromosomal translocations. *Nucleic Acids Res*. **2007**, *35*, doi:10.1093/nar/gkl1097.
56. Fan, M.; Thompson, M.; Andrade, M.L.; Brolo, A.G. Silver nanoparticles on a plastic platform for localized surface plasmon resonance biosensing. *Anal. Chem.* **2010**, *82*, 6350-6352.
57. Taton, T.A.; Mirkin, C.A.; Letsinger, R.L. Scanometric DNA array detection with nanoparticle probes. *Science* **2000**, *289*, 1757-1760.
58. Storhoff, J.J.; Marla, S.S.; Bao, P.; Hagenow, S.; Mehta, H.; Lucas, A.; Garimella, V.; Patno, T.; Buckingham, W.; Cork, W.; Müller, U.R. Gold nanoparticle-based detection of genomic DNA targets on microarrays using a novel optical detection system. *Biosens. Bioelectron*. **2004**, *19*, 875-883.
59. Zhou, X.; Xia, S.; Lu, Z.; Tian, Y.; Yan, Y.; Zhu, J. Biomineralization-assisted ultrasensitive detection of DNA. *J. Am. Chem. Soc*. **2010**, *132*, 6932-6934.

60. Kim, D.; Daniel, W.L.; Mirkin, C.A. Microarray-based multiplexed scanometric immunoassay for protein cancer markers using gold nanoparticle probes. *Anal. Chem*. **2009**, *81*, 9183-9187.
61. Nam, J.M.; Thaxton, C.S.; Mirkin, C.A. Nanoparticle-based bio-bar codes for the ultrasensitive detection of proteins. *Science* **2003**, *301*, 1884-1886.
62. Hill, H.D.; Mirkin, C.A. The bio-barcode assay for the detection of protein and nucleic acid targets using DTT-induced ligand exchange. *Nat. Protoc*. **2006**, *1*, 324-336.
63. Thaxton, C.S.; Elghanian, R.; Thomas, A.D.; Stoeva, S.I.; Lee, J.S.; Smith, N.D.; Schaeffer, A.J.; Klocker, H.; Horninger, W.; Bartsch, G.; *et al.* Nanoparticle based bio-barcode assay redefines ‘‘undetectable’’ PSA and biochemical recurrence after radical prostatectomy. *Proc. Natl. Acad. Sci. USA* **2009**, *106*, 18437-18442.
64. Ambrosi, A.; Airó, F.; Merkoçi, A. Enhanced gold nanoparticle based ELISA for a breast cancer biomarker. *Anal. Chem*. **2010**, *82*, 1151-1156.
65. Zhang, S.-B.; Wu, Z.-S.; Guo, M.-M.; Shen, G.-L.; Yu, R.-Q. A novel immunoassay strategy based on combination of chitosan and a gold nanoparticle label. *Talanta* **2007**, *71*, 1530-1535.
66. Mayer, K.M.; Lee, S.; Liao, H.; Rostro, B.C.; Fuentes, A.; Scully, P.T.; Nehl, C.L.; Hafner, J.H. A label-free immunoassay based upon localized surface plasmon resonance of gold nanorods. *ACS Nano* **2008**, *2*, 687-692.
67. Mayer, K.M.; Hao, F.; Lee, S.; Nordlander, P.; Hafner, J.H. A single molecule immunoassay by localized surface plasmon resonance. *Nanotechnology* **2010**, *21*, doi:10.1088/0957-4484/21/25/255503.
68. Altinoğlu, E.I.; Adair, J.H. Near infrared imaging with nanoparticles. *Wiley Interdiscip. Rev. Nanomed. Nanobiotechnol.* **2010**, *2*, 461-477.
69. He, X.; Wang, K.; Cheng, Z. *In vivo* near-infrared fluorescence imaging of cancer with nanoparticle-based probes. *Wiley Interdiscip. Rev. Nanomed. Nanobiotechnol*. **2010**, *2*, 349-366.
70. Ataka, K.; Heberle, J. Biochemical applications of surface-enhanced infrared absorption spectroscopy. *Anal. Bioanal. Chem*. **2007**, *388*, 47-54.
71. Enders, D.; Ruppa, S.; Küllerc, A.; Puccia, A.Surface enhanced infrared absorption on Au nanoparticle films deposited on SiO2/Si for optical biosensing: Detection of the antibody–antigen reaction. *Surf. Sci*. **2006**, *600*, L305-L308.
72. Chithrani, D.B. Nanoparticles for improved therapeutics and imaging in cancer therapy. *Recent Pat. Nanotechnol*. **2010**, *4*, 171-180.
73. Cho, E.C.; Glaus, C.; Chen, J.; Welch, M.J.; Xia, Y. Inorganic nanoparticle-based contrast agents for molecular imaging. *Trends Mol. Med*. **2010**, *16*, 561-573.
74. Agarwal, A.; Huang, S.W.; O’Donnell, M.; Day, K.C.; Day, M.; Kotov, N.; Ashkenazi, S. Targeted gold nanorod contrast agent for prostate cancer detection by photoacoustic imaging. *J. Appl. Phys*. **2007**, *102*, doi:10.1063/1.2777127.
75. Eghtedari, M.; Oraevsky, A.; Copland, J.A.; Kotov, N.A.; Conjusteau, A.; Motamedi, M. High sensitivity of *in vivo* detection of gold nanorods using a laser optoacoustic imaging system. *Nano Lett.* **2007**, *7*, 1914-1918.
76. Pan, D.; Pramanik, M.; Senpan, A.; Ghosh, S.; Wickline, S.A.; Wang, L.; Lanza, G.M. Near infrared photoacoustic detection of sentinel lymph nodes with gold nanobeacons. *Biomaterials* **2010**, *31*, 4088-4093.

77. Wang, Y.; Xie, X.; Wang, X.; Ku, G.; Gill, K.L.; O'Neal, D.P.; Stoica, G.; Wang, L.V. Photoacoustic tomography of a nanoshell contrast agent in the *in vivo* rat brain. *Nano Lett*. **2004**, *4*, 1689-1692.
78. Yang, X.; Skrabalak, S.E.; Li, Z.Y.; Xia, Y.; Wang, L.V. Photoacoustic tomography of a rat cerebral cortex *in vivo* with Au nanocages as an optical contrast agent. *Nano Lett*. **2007**, *7*, 3798-3802.
79. Lu, W.; Huang, Q.; Ku, G.; Wen, X.; Zhou, M.; Guzatov, D.; Brecht, P.; Su, R.; Oraevsky, A.; Wang, L.V.; Li, C. Photoacoustic imaging of living mouse brain vasculature using hollow gold nanospheres. *Biomaterials* **2010**, *31*, 2617-2626.
80. Loo, C.; Lowery, A.; Halas, N.; West, J.; Drezek, R. Immunotargeted nanoshells for integrated cancer imaging and therapy. *Nano Lett*. **2005**, *5*, 709-711.
81. Bickford, L.; Sun, J.; Fu, K.; Lewinski, N.; Nammalvar, V.; Chang, J.; Drezek, R. Enhanced multi-spectral imaging of live breast cancer cells using immunotargeted gold nanoshells and two-photon excitation microscopy. *Nanotechnology* **2008**, *19*, doi:10.1088/0957-4484/19/31/315102.
82. Johnson, S.A.; Pham, N.-H.; Novick, V.J.; Maroni, V.A. Application of surface-enhanced infrared absorption spectroscopy as a sensor for volatile organic compounds. *Appl. Spectrosc*. **1997**, *51*, 1423-1426.
83. Fleischmann, M.; Hendra, P.J.; McQuillan, A.J. Raman spectra of pyridine adsorbed at a silver *Electrode. Chem. Phys. Lett*. **1974**, *26*, 163-166.
84. Bantz, K.C.; Meyer, A.F.; Wittenberg, N.J.; Im, H.; Kurtuluş, O.; Lee, S.H.; Lindquist, N.C.; Oh, S.H.; Haynes, C.L. Recent progress in SERS biosensing. *Phys. Chem. Chem. Phys*. **2011**, *13*, 11551-11567.
85. Vo-Dinh, T.; Wang, H.N.; Scaffidi, J. Plasmonic nanoprobes for SERS biosensing and bioimaging. *J. Biophotonics*. **2010**, *3*, 89-102.
86. Otto, A.; Mrozek, I.; Grabhorn, H.; Akemann, W. Surface-enhanced Raman scattering. *J. Phys. Condens. Matter* **1992**, *4*, 1143-1212.
87. Michaels, A.M.; Jiang, J.; Brus, L. Ag nanocrystal junctions as the site for surface-enhanced raman scattering of single rhodamine 6G molecules. *J. Phys. Chem. B* **2000**, *104*, 11965-11971.
88. Vitol, E.A.; Brailoiu, E.; Orynbayeva, Z.; Dun, N.J.; Friedman, G.; Gogotsi, Y. Surface-enhanced Raman spectroscopy as a tool for detecting Ca^{2+} mobilizing second messengers in cell extracts. *Anal. Chem*. **2010**, *82*, 6770-6774.
89. Podstawka, E.; Ozaki, Y. Surface-enhanced Raman difference between bombesin and its modified analogues on the colloidal and electrochemically roughen silver surfaces. *Biopolymers* **2008**, *89*, 807-819.
90. Han, X.X.; Kitahama, Y.; Tanaka, Y.; Guo, J.; Xu, W.Q.; Zhao, B.; Ozaki, Y. Simplified protocol for detection of protein-ligand interactions via surface-enhanced resonance Raman scattering and surface-enhanced fluorescence. *Anal. Chem*. **2008**, *80*, 6567-6572.
91. Han, X.X.; Huang, G.G.; Zhao, B.; Ozaki, Y. Label-free highly sensitive detection of proteins in aqueous solutions using surface-enhanced Raman scattering. *Anal. Chem*. **2009**, *81*, 3329-3333.
92. Shafer-Peltier, K.E.; Haynes, C.L.; Glucksberg, M.R.; van Duyne, R.P. Toward a glucose biosensor based on surface-enhanced Raman scattering. *J. Am. Chem. Soc*. **2003**, *125*, 588-593.

93. Yuen, J.M.; Shah, N.C.; Walsh, J.T., Jr.; Glucksberg, M.R.; van Duyne, R.P. Transcutaneous glucose sensing by surface-enhanced spatially offset Raman spectroscopy in a rat model. *Anal. Chem*. **2010**, *82*, 8382-8385.
94. Yonzon, C.R.; Haynes, C.L.; Zhang, X.; Walsh, J.T., Jr.; van Duyne, R.P. A glucose biosensor based on surface-enhanced Raman scattering: Improved partition layer, temporal stability, reversibility, and resistance to serum protein interference. *Anal. Chem*. **2004**, *76*, 78-85.
95. Lyandres, O.; Shah, N.C.; Yonzon, C.R.; Walsh, J.T., Jr.; Glucksberg, M.R.; van Duyne, R.P. Real-time glucose sensing by surface-enhanced Raman spectroscopy in bovine plasma facilitated by a mixed decanethiol/mercaptohexanol partition layer. *Anal. Chem*. **2005**, *77*, 6134-6139.
96. Stuart, D.A.; Yonzon, C.R.; Zhang, X.; Lyandres, O.; Shah, N.C.; Glucksberg, M.R.; Walsh, J.T.; van Duyne, R.P. Glucose sensing using near-infrared surface-enhanced Raman spectroscopy: Gold surfaces, 10-day stability, and improved accuracy. *Anal. Chem*. **2005**, *77*, 4013-4019.
97. Fabris, L.; Dante, M.; Braun, G.; Lee, S.J.; Reich, N.O.; Moskovits, M.; Nguyen, T.Q.; Bazan, G.C. A heterogeneous PNA-based SERS method for DNA detection. *J. Am. Chem. Soc*. **2007**, *129*, 6086-6087.
98. Bonham, A.J.; Braun, G.; Pavel, I.; Moskovits, M.; Reich, N.O. Detection of sequence-specific protein-DNA interactions via surface enhanced resonance Raman scattering. *J. Am. Chem. Soc*. **2007**, *129*, 14572-14573.
99. Ryu, K.; Haes, A.J.; Park, H.Y.; Nah, S.; Kim, J.; Chung, H.; Yoon, M.Y.; Han, S.H. Use of peptide for selective and sensitive detection of an Anthrax biomarker via peptide recognition and surface-enhanced Raman scattering. *J. Raman Spectrosc*. **2010**, *41*, 121-124.
100. Vo-Dinh, T.; Yan, F.; Wabuyele, M. Surface-enhanced Raman scattering for medical diagnostics and biological imaging. *J. Raman Spectrosc*. **2005**, *36*, 640-647.
101. Vo-Dinh, T.; Houck, K.; Stokes, D.L. Surface-enhanced Raman gene probes. *Anal. Chem*. **1994**, *66*, 3379-3383.
102. Vo-Dinh, T.; Allain, L.R.; Stokes, D.L. Cancer gene detection using surface-enhanced Raman scattering (SERS). *J. Raman Spectrosc.* **2002**, *33*, 511-516.
103. Culha, M.; Stokes, D.; Allain, L.R.; Vo-Dinh, T. Surface-enhanced Raman scattering substrate based on a self-assembled monolayer for use in gene diagnostics. *Anal. Chem*. **2003**, *75*, 6196-6201.
104. Xu, S.; Ji, X.; Xu, W.; Li, X., Wang, L.; Bai, Y.; Zhao, B.; Ozaki, Y. Immunoassay using probe-labelling immunogold nanoparticles with silver staining enhancement via surface-enhanced Raman scattering. *Analyst* **2004**, *129*, 63-68.
105. Driskell, J.D.; Kwarta, K.M.; Lipert, R.J.; Porter, M,D., Neill, J.D.; Ridpath, J.F. Low-level detection of viral pathogens by a surface-enhanced Raman scattering based immunoassay. *Anal. Chem.* **2005**, *77*, 6147-6154.
106. Harpster, M.H.; Zhang, H.; Sankara-Warrier, A.K.; Ray, B.H.; Ward, T.R.; Kollmar, J.P.; Carron, K.T.; Mecham, J.O.; Corcoran, R.C.; Wilson, W.C.; Johnson, P.A. SERS detection of indirect viral DNA capture using colloidal gold and methylene blue as a Raman label. *Biosens. Bioelectron*. **2009**, *25*, 674-681.

107. Braun, G.; Lee, S.J.; Dante, M.; Nguyen, T.Q.; Moskovits, M.; Reich, N. Surface-enhanced Raman spectroscopy for DNA detection by nanoparticle assembly onto smooth metal films. *J. Am. Chem. Soc*. **2007**, *129*, 6378-6379.
108. Cao, Y.C.; Jin, R.; Nam, J.M.; Thaxton, C.S.; Mirkin, C.A. Raman dye-labeled nanoparticle probes for proteins. *J. Am. Chem. Soc*. **2003**, *125*, 14676-14677.
109. Graham, D.; Thompson, D.G.; Smith, W.E.; Faulds, K. Control of enhanced Raman scattering using a DNA-based assembly process of dye-coded nanoparticles. *Nat. Nanotechnol*. **2008**, *3*, 548-551.
110. Qian, X.; Zhou, X.; Nie, S. Surface-Enhanced Raman Nanoparticle Beacons Based on Bioconjugated Gold Nanocrystals and Long Range Plasmonic Coupling. *J. Am. Chem. Soc*., **2008**, *130*, 14934-14935.
111. Thuy, N.T.; Yokogawa, R.; Yoshimura, Y.; Fujimoto, K.; Koyano, M.; Maenosono, S. Surface-enhanced Raman spectroscopy for facile DNA detection using gold nanoparticle aggregates formed via photoligation. *Analyst* **2010**, *135*, 595-602.
112. Wabuyele, M.B.; Vo-Dinh, T. Detection of human immunodeficiency virus type 1 DNA sequence using plasmonics nanoprobes. *Anal. Chem*. **2005**, *77*, 7810-7815.
113. Wang, H.N.; Vo-Dinh, T. Multiplex detection of breast cancer biomarkers using plasmonic molecular sentinel nanoprobes. *Nanotechnology* **2009**, *20*, doi:10.1088/0957-4484/20/6/065101.
114. Cao, Y.C.; Jin, R.; Mirkin, C.A. Nanoparticles with Raman spectroscopic fingerprints for DNA and RNA detection. *Science* **2002**, *297*, 1536-1540.
115. Cui, Y.; Ren, B.; Yao, J.; Gu, R.; Tian, Z.J. Multianalyte immunoassay based on surface-enhanced Raman spectroscopy. *Raman Spectrosc*. **2007**, *38*, 896-902.
116. Faulds, K.; McKenzie, F.; Smith, W.E.; Graham, D. Quantitative simultaneous multianalyte detection of DNA by dual-wavelength surface-enhanced resonance Raman scattering. *Angew. Chem. Int. Ed. Engl.* **2007**, *46*, 1829-1831.
117. Jin, R.; Cao, Y.C.; Thaxton, C.S.; Mirkin, C.A. Glass-bead-based parallel detection of DNA using composite Raman labels. *Small* **2006**, *2*, 375-380.
118. Kang, T.; Yoo, S.M.; Yoon, I.; Lee, S.Y.; Kim, B. Patterned multiplex pathogen DNA detection by Au particle-on-wire SERS sensor. *Nano Lett*. **2010**, *10*, 1189-1193.
119. Qin, L.; Banholzer, M.J.; Millstone, J.E.; Mirkin, C.A. Nanodisk codes. *Nano Lett.* **2007**, *7*, 3849-3853.
120. Banholzer, M.J.; Qin, L.; Millstone, J.E.; Osberg, K.D.; Mirkin, C.A. On-wire lithography: Synthesis, encoding and biological applications. *Nat. Protoc*. **2009**, *4*, 838-848.
121. Qian, X.; Peng, X.H.; Ansari, D.O.; Yin-Goen, Q.; Chen, G.Z.; Shin, D.M.; Yang, L.; Young, A.N.; Wang, M.D.; Nie, S. *In vivo* tumor targeting and spectroscopic detection with surface-enhanced Raman nanoparticle tags. *Nat. Biotechnol*. **2008**, *26*, 83-90.
122. Lee, S.; Kim, S.; Choo, J.; Shin, S.Y.; Lee, Y.H.; Choi, H.Y.; Ha, S.; Kang, K.; Oh, C.H. Biological imaging of HEK293 cells expressing PLCgamma1 using surface-enhanced Raman microscopy. *Anal. Chem*. **2007**, *79*, 916-922.
123. Zavaleta, C.L.; Smith, B.R.; Walton, I.; Doering, W.; Davis, G.; Shojaei, B.; Natan, M.J.; Gambhir, S.S. Multiplexed imaging of surface enhanced Raman scattering nanotags in living mice using noninvasive Raman spectroscopy. *Proc. Natl. Acad. Sci. USA* **2009**, *106*, 13511-13516.

124. Jennings, T.L.; Singh, M.P.; Strouse, G.F. Fluorescent lifetime quenching near d = 1.5 nm gold nanoparticles: Probing NSET validity. *J. Am. Chem. Soc.* **2006**, *128*, 5462-5467.
125. Griffin, J.; Singh, A.K.; Senapati, D.; Rhodes, P.; Mitchell, K.; Robinson, B.; Yu, E.; Ray, P.C. Size- and distance-dependent nanoparticle surface-energy transfer (NSET) method for selective sensing of hepatitis C virus RNA. *Chemistry* **2009**, *15*, 342-351.
126. Ray, P.C.; Darbha, G.K.; Ray, A.; Walker, J.; Hardy, W. Gold nanoparticle based FRET for DNA detection. *Plasmonics* **2007**, *2*, 173-183.
127. Dubertret, B.; Calame, M.; Libchaber, A.J. Single-mismatch detection using gold-quenched fluorescent oligonucleotides. *Nat. Biotechnol.* **2001**, *19*, 365-370.
128. Benia, V.; Hayesa, K.; Lerga, M.T.; O'Sullivan, C.K. Development of a gold nano-particle-based fluorescent molecular beacon for detection of cystic fibrosis associated mutation. *Biosen. Bioelectron*. **2010**, *26*, 307-313.
129. Wu, Z.S.; Jiang, J.H.; Fu, L.; Shen, G.L.; Yu, R.Q. Optical detection of DNA hybridization based on Fluorescence quenching of tagged oligonucleotide probes by gold nanoparticles. *Anal. Biochem*. **2006**, *353*, 22-29.
130. Mo, Z.H.; Yang, X.C.; Guo, K.P.; Wen, Z.Y. A nanogold-quenched fluorescence duplex probe for homogeneous DNA detection based on strand displacement. *Anal. Bioanal. Chem.* **2007**, *389*, 493-497.
131. Wang, W.; Chen, C.; Qian, M.; Zhao, X.S. Aptamer biosensor for protein detection using gold nanoparticles. *Anal. Biochem.* **2008**, *373*, 213-219.
132. Ray, P.C.; Fortner, A.; Darbha, G.K. Gold nanoparticle based FRET assay for the detection of DNA cleavage. *J. Phys. Chem. B* **2006**, *110*, 20745-20748.
133. Jennings, T.L.; Schlatterer, J.C.; Singh, M.P.; Greenbaum, N.L.; Strouse, G.F. NSET molecular beacon analysis of hammerhead RNA substrate binding and catalysis. *Nano Lett.* **2006**, *6*, 1318-1324.
134. Mayilo, S.; Kloster, M.A.; Wunderlich, M.; Lutich, A.; Klar, T.A.; Nichtl, A.; Kurzinger, K.; Stefani, F.D.; Feldmann, J. Long-range fluorescence quenching by gold nanoparticles in a sandwich immunoassay for cardiac troponin T. *Nano Lett*. **2009**, *9*, 4558-4563.
135. Guirgis, B.S.; Cunha C.S.; Gomes, I.; Cavadas, M.; Silva, I.; Doria, G.; Blatch, G.L.; Baptista, P.V.; Pereira, E.; Azzazy, H.M.; Mota, M.M.; Prudêncio, M.; Franco, R. Gold nanoparticle-based fluorescence immunoassay for malaria antigen detection. *Anal. Bioanal. Chem.* **2011**, in press.
136. Lacerda, S.H.D.; Park, J.J.; Meuse, C.; Pristinski, D.; Becker, M.L., Karim, A.; Douglas, J.F. Interaction of gold nanoparticles with common human blood proteins. *ACS Nano* **2010**, *4*, 365-379.
137. Dyadyusha, L.; Yin, H.; Jaiswal, S.; Brown, T.; Baumberg, J.J.; Booye, F.P.; Melvin, T. Quenching of CdSe quantum dot emission, a new approach for biosensing. *Chem. Commun.* **2005**, 3201-3203.
138. Oh, E.; Hong, M.Y.; Lee, D.; Nam, S.H.; Yoon, H.C.; Kim, H.S. Inhibition assay of biomolecules based on Fluorescence Resonance Energy Transfer (FRET) between quantum dots and gold nanoparticles. *J. Am. Chem. Soc.* **2005**, *127*, 3270-3271.

139. Chang, E.; Miller, J.S.; Sun, J.; Yu, W.W.; Colvin, V.L.; Drezek, R.; West, J.L. Protease-activated quantum dot probes. *Biochem. Biophys. Res. Commun.* **2005**, *334*, 1317-1321.
140. Song, S.; Liang, Z.; Zhang, J.; Wang, L.; Li, G.; Fan, C. Gold-nanoparticle-based multicolor nanobeacons for sequence-specific DNA analysis. *Angew. Chem. Int. Ed.* **2009**, *48*, 8670-8674.
141. Zhang, Y.; Wang, L.; Tian, J.; Li, H.; Luo, Y.; Sun, X. Ag@poly(m-phenylenediamine) core-shell nanoparticles for highly selective, multiplex nucleic acid detection. *Langmuir* **2011**, *27*, 2170-2175.
142. Huang, Y.; Zhao, S.; Liang, H.; Chen, Z.F.; Liu, Y.M. Multiplex detection of endonucleases by using a multicolor gold nanobeacon. *Chem. Eur. J.* **2011**, *17*, 7313-7319.
143. Zhang, J.; Wang, L.; Zang, H.; Boey, F.; Song, S.; Fan, C. Aptamer-based multicolor fluorescent gold nanoprobes for multiplex detection in homogeneous solution. *Small* **2010**, *6*, 201-204.
144. Dragan, A.I.; Golberg, K.; Elbaz, A.; Marks, R.; Zhang, Y.; Geddes, C.D. Two-color, 30 second microwave-accelerated Metal-Enhanced Fluorescence DNA assays: A new Rapid Catch and Signal (RCS) technology. *J. Immunol. Methods* **2011**, *366*, 1-7.
145. Zhang, J.; Fu, Y.; Mei, Y.; Jiang, F.; Lakowicz, J.R. Fluorescent metal nanoshell probe to detect single miRNA in lung cancer cell. *Anal. Chem.* **2010**, *82*, 4464-4471.
146. Zhang, J.; Fu, Y.; Liang, D.; Zhao, R.Y.; Lakowicz, J.R. Fluorescent avidin-bound silver particle: A strategy for single target molecule detection on a cell membrane. *Anal. Chem.* **2009**, *81*, 883-889.
147. Zhang, J.; Fu, Y.; Li, G.; Nowaczyk, K.; Zhao, R.Y.; Lakowicz, J.R. Direct observation to chemokine receptor 5 on T-lymphocyte cell surface using fluorescent metal nanoprobes. *Biochem. Biophys. Res. Commun.* **2010**, *400*, 111-116.
148. Phillips, R.L.; Miranda, O.R.; You, C.C.; Rotello, V.M.; Bunz, U.H. Rapid and efficient identification of bacteria using gold-nanoparticle-poly(para-phenyleneethynylene) constructs. *Angew. Chem. Int. Ed. Engl*. **2008**, *47*, 2590-2594.
149. Cao, X.; Ye, Y.; Liu, S. Gold nanoparticle-based signal amplification for biosensing. *Anal. Biochem.* **2011**, *417*, 1-16.
150. Wang, J. Nanomaterial-based amplified transduction of biomolecular interactions. *Small* **2005**, *1*, 1036-1043.
151. Wittenberg, N.J.; Haynes, C.L. Using nanoparticles to push the limits of detection. *Wiley Interdiscip. Rev. Nanomed. Nanobiotechnol.* **2009**, *1*, 237-254.
152. Chen, S.H.; Wu, V.C.; Chuang, Y.C.; Lin, C.S. Using oligonucleotide-functionalized Au nanoparticles to rapidly detect foodborne pathogens on a piezoelectric biosensor. *J. Microbiol. Methods* **2008**, *73*, 7-17.
153. Pang, L.; Li, J.; Jiang, J.; Shen, G.; Yu, R. DNA point mutation detection based on DNA ligase reaction and nano-Au amplification: A piezoelectric approach. *Anal. Biochem.* **2006**, *358*, 99-103.
154. Wang, H.; Lei, C.; Li, J.; Wu, Z.; Shen, G.; Yu, R. A piezoelectric immunoagglutination assay for Toxoplasma gondii antibodies using gold nanoparticles. *Biosens. Bioelectron.* **2004**, *19*, 701-709.

155. Jin, X.; Jin, X.; Chen, L.; Jiang, J.; Shen, G.; Yu, R. Piezoelectric immunosensor with gold nanoparticles enhanced competitive immunoreaction technique for quantification of aflatoxin B1. *Biosens. Bioelectron*. **2009**, *24*, 2580-2585.
156. Park, S.J.; Taton, T.A.; Mirkin, C.A. Array-based electrical detection of DNA with nanoparticle probes. *Science* **2002**, *295*, 1503-1506.
157. Li, J.; Xue, M.; Wang, H.; Cheng, L.; Gao, L.; Lu, Z.; Chan, M. Amplifying the electrical hybridization signals of DNA array by multilayer assembly of Au nanoparticle probes. *Analyst* **2003**, *128*, 917-923.
158. Fang, C.; Fan, Y.; Kong, J.; Gao, Z.; Balasubramanian, N. Electrical detection of oligonucleotide using an aggregate of gold nanoparticles as a conductive tag. *Anal. Chem.* **2008**, *80*, 9387-9394.
159. Diessel, E.; Grothe, K.; Siebert, H.M.; Warner, B.D.; Burmeister, J. Online resistance monitoring during autometallographic enhancement of colloidal Au labels for DNA analysis. *Biosens. Bioelectron.* **2004**, *19*, 1229-1235.
160. Sun, Z.; Qiang, W.; Li, H.; Hao, N.; Xu, D.; Chen, H.Y. Electric detection of DNA with PDMS microgap electrodes and silver nanoparticles. *Analyst* **2011**, *136*, 540-544.
161. Kawde, A.N.; Wang, J. Amplified Electrical Transduction of DNA hybridization based on polymeric beads loaded with multiple gold nanoparticle tags. *Electroanalysis* **2004**, *16*, 101-107.
162. Wang, J.; Polsky, R.; Xu, D. Silver-enhanced colloidal gold electrochemical stripping detection of DNA hybridization. *Langmuir* **2001**, *17*, 5739-5741.
163. Wang, J.; Xu, D.; Kawde, A.N.; Polsky, R. Metal nanoparticle-based electrochemical stripping potentiometric detection of DNA hybridization. *Anal. Chem.* **2001**, *73*, 5576-5581.
164. Rochelet-Dequaire, M.; Limoges, B.; Brossier, P. Subfemtomolar electrochemical detection of target DNA by catalytic enlargement of the hybridized gold nanoparticle labels. *Analyst* **2006**, *131*, 923-929.
165. Dequaire, M.; Degrand, C.; Limoges, B. An electrochemical metalloimmunoassay based on a colloidal gold label. *Anal. Chem*. **2000**, *72*, 5521-5528.
166. Lai, G.; Yan, F.; Wu, J.; Leng, C.; Ju, H. Ultrasensitive multiplexed immunoassay with electrochemical stripping analysis of silver nanoparticles catalytically deposited by gold nanoparticles and enzymatic reaction. *Anal. Chem.* **2011**, *83*, 2726-2732.
167. Chumbimuni-Torres, K.Y.; Dai, Z.; Rubinova, N.; Xiang, Y.; Pretsch, E.; Wang, J.; Bakker, E. Potentiometric biosensing of proteins with ultrasensitive ion-selective microelectrodes and nanoparticle labels. *J. Am. Chem. Soc*. **2006**, *128*, 13676-13677.
168. Suprun, E.; Shumyantseva, V.; Bulko, T.; Rachmetova, S.; Rad'ko, S.; Bodoev, N.; Archakov, A. Au-nanoparticles as an electrochemical sensing platform for aptamer-thrombin interaction. *Biosens. Bioelectron*. **2008**, *24*, 831-836.
169. Ting, B.P.; Zhang, J.; Gao, Z.; Ying, J.Y. A DNA biosensor based on the detection of doxorubicin-conjugated Ag nanoparticle labels using solid-state voltammetry. *Biosens. Bioelectron.* **2009**, *25*, 282-287.
170. Tang, D.; Yuan, R.; Chai, Y.; Zhong, X.; Liu, Y.; Dai, J. Electrochemical detection of hepatitis B surface antigen using colloidal gold nanoparticles modified by a sol-gel network interface. *Clin. Biochem.* **2006**, *39*, 309-314.

171. Lokesh, K.S.; Shivaraj, Y.; Dayananda, B.P.; Chandra, S. Synthesis of phthalocyanine stabilized rhodium nanoparticles and their application in biosensing of cytochrome c. *Bioelectrochemistry* **2009**, *75,* 104-109.
172. Wang, Q.; Yang, L.; Yang, X.; Wang, K.; He, L.; Zhu, J. Electrochemical biosensors for detection of point mutation based on surface ligation reaction and oligonucleotides modified gold nanoparticles. *Anal. Chim. Acta* **2011**, *688*, 163-167.
173. Ozsoz, M.; Erdem, A.; Kerman, K.; Ozkan, D.; Tugrul, B.; Topcuoglu, N.; Ekren, H.; Taylan, M. Electrochemical genosensor based on colloidal gold nanoparticles for the detection of Factor V Leiden mutation using disposable pencil graphite electrodes. *Anal. Chem.* **2003**, *75*, 2181-2187.
174. Yu, F.; Li, G.; Qu, B.; Cao, W. Electrochemical detection of DNA hybridization based on signal DNA probe modified with Au and apoferritin nanoparticles. *Biosens. Bioelectron.* **2010**, *26*, 1114-1117.
175. Ghindilis, A.L.; Atanasov, P.; Wilkins, M.; Wilkins, E. Immunosensors: Electrochemical sensing and other engineering approaches. *Biosens. Bioelectron.* **1998**, *13*, 113-131.
176. Polsky, R.; Gill, R.; Kaganovsky, L.; Willner, I. Nucleic acid-functionalized Pt nanoparticles: Catalytic labels for the amplified electrochemical detection of biomolecules. *Anal. Chem.* **2006**, *78*, 2268-2271.
177. Munge, B.S.; Coffey, A.L.; Doucette, J.M.; Somba, B.K.; Malhotra, R.; Patel, V.; Gutkind, J.S.; Rusling, J.F. Nanostructured immunosensor for attomolar detection of cancer biomarker interleukin-8 using massively labeled superparamagnetic particles. *Angew. Chem. Int. Ed. Engl.* **2011**, *50*, 7915-7918.
178. Jensen, G.C.; Krause, C.E.; Sotzing, G.A.; Rusling, J.F. Inkjet-printed gold nanoparticle electrochemical arrays on plastic. Application to immunodetection of a cancer biomarker protein. *Phys. Chem. Chem. Phys*. **2011**, *13*, 4888-4894.
179. Yin, Z.; Liu, Y.; Jiang, L.P.; Zhu, J.J. Electrochemical immunosensor of tumor necrosis factor α based on alkaline phosphatase functionalized nanospheres. *Biosens. Bioelectron.* **2011**, *26*, 1890-1894.
180. Meng, L.; Gan, N.; Li, T.; Cao, Y.; Hu, F.; Zheng, L. A three-dimensional, magnetic and electroactive nanoprobe for amperometric determination of tumor biomarkers. *Int. J. Mol. Sci.* **2011**, *12*, 362-375.
181. Sharma, M.K.; Rao, V.K.; Agarwal, G.S.; Rai, G.P.; Gopalan, N.; Prakash, S.; Sharma, S.K.; Vijayaraghavan, R. Highly sensitive amperometric immunosensor for detection of Plasmodium falciparum histidine-rich protein 2 in serum of humans with malaria: Comparison with a commercial kit. *J. Clin. Microbiol.* **2008**, *46*, 3759-3765.
182. De la Escosura-Muñiz, A.; Maltez-da Costa, M.; Sánchez-Espinel, C.; Díaz-Freitas, B.; Fernández-Suarez, J.; González-Fernández, Á.; Merkoçi, A. Gold nanoparticle-based electrochemical magnetoimmunosensor for rapid detection of anti-hepatitis B virus antibodies in human serum. *Biosens. Bioelectron.* **2010**, *26*, 1710-1714.
183. De la Escosura-Muñiz, A.; Maltez-da Costa, M.; Merkoçi, A. Controlling the electrochemical deposition of silver onto gold nanoparticles: Reducing interferences and increasing the sensitivity of magnetoimmuno assays. *Biosens. Bioelectron.* **2009**, *24*, 2475-2482.

184. Che, X.; Yuan, R.; Chai, Y.; Li, J.; Song, Z.; Wang, J. Amperometric immunosensor for the determination of alpha-1-fetoprotein based on multiwalled carbon nanotube-silver nanoparticle composite. *J. Colloid Interface Sci.* **2010**, *345*, 174-180.
185. Scodeller, P.; Flexer, V.; Szamocki, R.; Calvo, E.J.; Tognalli, N.; Troiani, H.; Fainstein, A. Wired-enzyme core-shell Au nanoparticle biosensor. *J. Am. Chem. Soc.* **2008**, *130*, 12690-12697.
186. Mahmoud, K.A.; Luong, J.H. Impedance method for detecting HIV-1 protease and screening for its inhibitors using ferrocene-peptide conjugate/Au nanoparticle/single-walled carbon nanotube modified electrode. *Anal. Chem.* **2008**, *80*, 7056-7062.
187. Yang, G.J.; Huang, J.L.; Meng, W.J.; Shen, M.; Jiao, X.A. A reusable capacitive immunosensor for detection of Salmonella spp. based on grafted ethylene diamine and self-assembled gold nanoparticle monolayers. *Anal. Chim. Acta.* **2009**, *647*, 159-166.
188. Tian, D.; Duan, C.; Wang, W.; Li, N.; Zhang, H.; Cui, H.; Lu, Y. Sandwich-type electrochemiluminescence immunosensor based on N-(aminobutyl)-N-ethylisoluminol labeling and gold nanoparticle amplification. *Talanta* **2009**, *78*, 399-404.
189. Tian, D.; Duan, C.; Wang, W.; Cui, H. Ultrasensitive electrochemiluminescence immunosensor based on luminol functionalized gold nanoparticle labeling. *Biosens Bioelectron.* **2010**, *25*, 2290-2295.
190. Li, H.; Sun, Z.; Zhong, W.; Hao, N.; Xu, D.; Chen, H.Y. Ultrasensitive electrochemical detection for DNA arrays based on silver nanoparticle aggregates. *Anal. Chem.* **2010**, *82*, 5477-5483.
191. Li, X.M.; Fu, P.Y.; Liu, J.M.; Zhang, S.S. Biosensor for multiplex detection of two DNA target sequences using enzyme-functionalized Au nanoparticles as signal amplification. *Anal. Chim. Acta* **2010**, *673*, 133-138.
192. Zhang, D.; Huarng, M.C.; Alocilja, E.C. A multiplex nanoparticle-based bio-barcoded DNA sensor for the simultaneous detection of multiple pathogens. *Biosens. Bioelectron.* **2010**, *26*, 1736-1742.
193. Leng, C.; Lai, G.; Yan, F.; Ju, H. Gold nanoparticle as an electrochemical label for inherently crosstalk-free multiplexed immunoassay on a disposable chip. *Anal. Chim. Acta* **2010**, *666*, 97-101.
194. Grubisha, D.S.; Lipert, R.J.; Park, H.Y.; Driskell, J.; Porter, M.D. Femtomolar detection of prostate-specific antigen: An immunoassay based on surface-enhanced Raman scattering and immunogold labels. *Anal. Chem*. **2003**, *75*, 5936-5943.

Hindawi Publishing Corporation
International Journal of Photoenergy
Volume 2012, Article ID 619530, 11 pages
doi:10.1155/2012/619530

Review Article

Nanophotonics for Molecular Diagnostics and Therapy Applications

João Conde,[1,2] João Rosa,[1,3] João C. Lima,[3] and Pedro V. Baptista[1]

[1] *CIGMH, Departamento de Ciências da Vida, Faculdade de Ciências e Tecnologia, Universidade Nova de Lisboa, Campus de Caparica, 2829-516 Caparica, Portugal*
[2] *Instituto de Nanociencia de Aragón, Universidad de Zaragoza, Campus Río Ebro, Edifício I+D, Mariano Esquillor s/n, 50018 Zaragoza, Spain*
[3] *REQUIMTE, Departamento de Química, Faculdade de Ciências e Tecnologia, Universidade Nova de Lisboa, Campus de Caparica, 2829-516 Caparica, Portugal*

Correspondence should be addressed to Pedro V. Baptista, pmvb@fct.unl.pt

Received 15 June 2011; Accepted 10 July 2011

Academic Editor: Danuta Wrobel

Light has always fascinated mankind and since the beginning of recorded history it has been both a subject of research and a tool for investigation of other phenomena. Today, with the advent of nanotechnology, the use of light has reached its own dimension where light-matter interactions take place at wavelength and subwavelength scales and where the physical/chemical nature of nanostructures controls the interactions. This is the field of nanophotonics which allows for the exploration and manipulation of light in and around nanostructures, single molecules, and molecular complexes. What is more is the use of nanophotonics in biomolecular interactions—nanobiophotonics—has prompt for a plethora of molecular diagnostics and therapeutics making use of the remarkable nanoscale properties. In this paper, we shall focus on the uses of nanobiophotonics for molecular diagnostics involving specific sequence characterization of nucleic acids and for gene delivery systems of relevance for therapy strategies. The use of nanobiophotonics for the combined diagnostics/therapeutics (theranostics) will also be addressed, with particular focus on those systems enabling the development of safer, more efficient, and specific platforms. Finally, the translation of nanophotonics for theranostics into the clinical setting will be discussed.

1. Introduction

Nanophotonics deals with the interaction of light with matter at a nanometer scale, providing challenges for fundamental research and opportunities for new technologies, encompassing the study of new optical interactions, materials, fabrication techniques, and architectures, including the exploration of natural and synthetic, or artificially engineered, structures such as photonic crystals, holey fibers, quantum dots, subwavelength structures, and plasmonics [1, 2]. The use of photonic nanotechnologies in medicine is a rapidly emerging and potentially powerful approach for disease protection, detection, and treatment. The high speed of light manipulation and the remote nature of optical methods suggest that light may successfully connect diagnostics, treatment, and even the guidance of the treatment in one theranostic procedure combination of therapeutics with diagnostics (including patient prescreening and therapy monitoring).

Limitations in medical practice are closely associated with the fact that diagnostics, therapy, and therapy guidance are three discrete and isolated stages. In order to overcome some of the sensitivity and specificity of current medicines, theranostics unites the three above stages in one single process, supporting early-stage diagnosis and treatment [3, 4]. Nowadays, there is an ever increasing need to enhance the capability of theranostics procedures where nanophotonics-based sensors may provide for the simultaneous detection of several gene-associated conditions and nanodevices utilizing light-guided and light-activated therapy with the ability to monitor real-time drug action (see Figure 1).

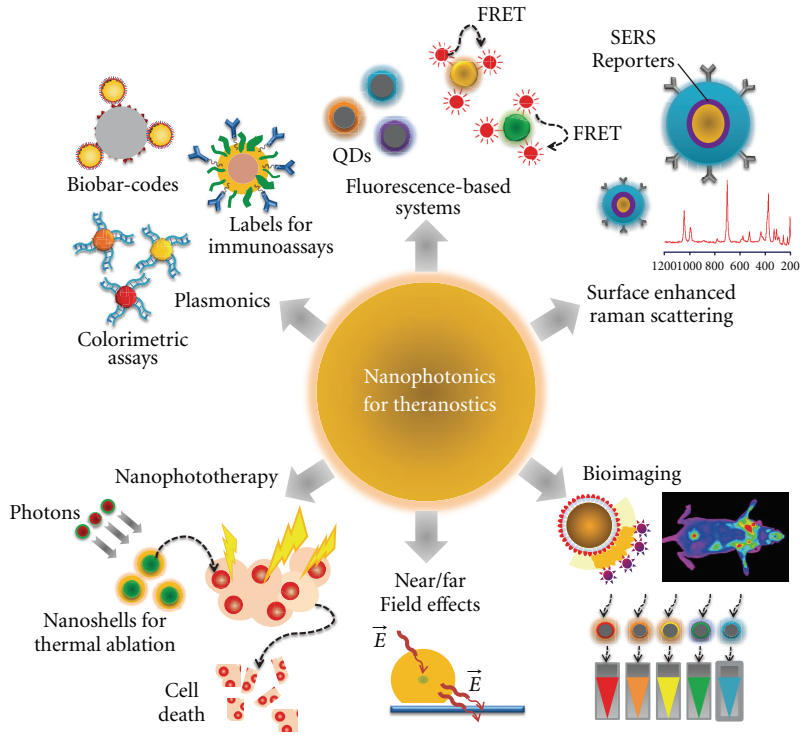

FIGURE 1: *Nanophotonics for theranostics.* Nanoparticles-based strategies can be used for biosensing using *plasmonic nanosensors*, such as metal nanoparticles functionalized with nucleic acid strand for colorimetric assays and biobar codes for protein detection or intense labels for immunoassays. Some nanoparticle systems can also be used for sensing by exploring a typical *FRET system* or can be surrounded with *Raman reporters* in order to provide *in vivo* detection and tumour targeting. In fact, NPs symbolize an important class of materials with unique features suitable for *biomedical imaging* applications such as increased sensitivity in detection and high quantum yields for fluorescence. Alternatively, NPs can survey *near/far field* enhancing qualities that hold promise for a bounty of novel applications in optics and photonics. Engineered NPs can also act as *phototherapeutic agents* that can be attached to specific targets for selective damage to cancer cells.

2. Nanophotonics For Diagnostics

2.1. Surface Plasmons on Nanoparticles and Surfaces. Surface plasmons are collective charge oscillations that occur at the interface between conductors and dielectrics. They can take various forms, ranging from freely propagating electron density waves along metal surfaces to localized electron oscillations on metal nanoparticles (NPs) [5, 6]. When light passes through a metal nanoparticle, it induces dipole moments that oscillate at the respective frequency of the incident wave, consequently dispersing secondary radiation in all directions. This collective oscillation of the free conduction electrons is called localized surface plasmon resonance (LSPR). Light on NP induces the conduction electrons to oscillate collectively with a resonant frequency that depends on the nanoparticles' size, shape, composition, interparticle distance, and environment (dielectric properties) [7–10]. As a result of these SPR modes, the nanoparticles absorb and scatter light so intensely that single NPs are easily observed by eye using dark-field (optical scattering) microscopy. Plasmonic NPs provide a nearly unlimited photon resource for observing molecular binding for longer periods of time, once they do not blink or bleach like fluorophores [11].

Nanoparticle-based colorimetric assays for diagnostics have been a subject of intensive research, where LSPR can be used to detect DNA or proteins by the changes in the local index of refraction upon adsorption of the target molecule to the metal surface. Due to the intense SPR in the visible yielding extremely bright colors, gold nanoparticle colloids have been widely used of molecular diagnostics. In fact, gold nanoparticles (AuNPs) functionalized with ssDNA capable of specifically hybridizing to a complementary target for the detection of specific nucleic acid sequences in biological samples have been extensively used [12–27]. Other approaches use the AuNPs' plasmonic as a core/seed that can be tailored with a wide variety of surface functionalities to provide highly selective nanoprobes for diagnostics [28] or the SPR scattering imaging or SPR absorption spectroscopy generated from antibody-conjugated AuNPs in molecular biosensor techniques for the diagnosis of oral epithelial living cancer cells *in vivo* and *in vitro* [29] and the use of multifunctional AuNPs which incorporate both cytosolic delivery and targeting moieties on the same particle functioning as intracellular sensors to monitor actin rearrangement in live fibroblasts [30].

Plasmonic NPs have also been used as extremely intense labels for immunoassays [31–34] and biochemical sensors [19, 35–37]. Also, the use of colloidal silver plasmon resonant particles (PRPs) coated with standard ligands as target-specific labels has been reported for *in situ* hybridization and

immunocytology assays [34]. Most notably, a nanoparticle-based Biobar code has been developed for the detection of proteins that relies on magnetic microparticle probes with antibodies that specifically bind a target of interest and nanoparticle probes that are encoded with DNA that is unique to the protein target of interest and antibodies that can sandwich the target captured by the microparticle probes [33]. Haes and coworkers have reported on an optical biosensor based on localized surface plasmon resonance spectroscopy developed to monitor the interaction between the antigen, amyloid-β-derived diffusible ligands (ADDLs), and specific anti-ADDL antibodies, used in the detection of a biomarker for Alzheimer's Disease [35].

2.2. Raman-Spectroscopy-Based Systems. When light interacts with a substance, it can be absorbed, transmitted, or scattered. Scattered radiation can result from an elastic collision (Rayleigh scattering) or inelastic (Raman scattering). Raman spectroscopy is based on a change of frequency when light is inelastically scattered by molecules or atoms resulting in a molecular fingerprint information on molecular structure or intermolecular interaction of a specific process or molecule. The potential of Raman spectroscopy as biomedical diagnostics tool is rather low due to its low cross-section ($\sim 10^{-30}\,\mathrm{cm}^2$) that results in low sensitivity [38]. However, in 1977, two groups independently described the use of noble metal surfaces to enhance the Raman scattering signal of target molecules [39, 40]—Surface enhancement raman spectroscopy (SERS). Jeanmaire and Van Duyne proposed a twofold electromagnetic field enhancement that was later associated with the interaction between the incident and scattered photons with the nanostructure's LSPR [41]. Simultaneously, Albrecht and Creighton suggested the source of the enhancement to be caused by a specific interaction between an adsorbate and the nanoparticle surface, briefly, a charge transfer from the adsorbate into the empty energetic levels on the metal surface or from the occupied levels of the nanoparticle's surface to the adsorbate [42–44].

Generally, SERS requires that the biological analyte reaches a suitable surface where the substrates are treated as two-dimensional macroscopic surfaces onto which adsorbed molecules suffer a local-field enhancement. Despite direct adsorption not being a good solution because of its dependence on the affinity between substrate and analyte, a method to identify and distinguish different strains of virus based on signal differences generated by the surface amino-acids using silver nanorods has been successfully developed [45]. Using a similar approach of direct adsorption, Pînzary et al. used naked silver nanoparticles to differentiate *in situ* healthy colon from carcinoma colon tissue [46]. Nanotags have been widely employed to address the lack of specificity [47, 48]. These nanotags usually possess a metallic colloidal core functionalized with a Raman reporting molecule and the specific molecule used to capture the analyte and have been used to directly detect DNA sequences [49, 50] and amplified DNA products of epizootic pathogens using complementary DNA strands so that only the complementary target hybridizes with the probes [51]. Using a similar system, but exploring the distance-dependent enhancement of the electromagnetic field with a hairpin probe molecule, Wabuyele has also been used to distinguish single nucleotide polymorphisms in cancer-related genes [52]. Combining nanotags with other nanoparticles or binding surfaces that target the same analyte in a sandwich conformation proved useful to detect antibodies in serum [53]. A similar approach using a flat substrate instead of NPs had already been proposed to detect DNA, RNA, and proteins [54, 55]. However, in this approach, the substrate is used only to immobilize the analyte; a gold-nanoparticle-based nanotag is used to identify the analyte and the surface enhancement is obtained by silver coating of the nanotag. miRNA profiling has also been pursued via a slightly different approach based on the hybridization of the target molecules with a thiolated oligonucleotide and subsequent functionalization on a silver substrate [56]. SERS have also been explored to identify changes in the analyzed system such as interaction between DNA and xenobiotic molecules like cisplatin [57] or DNA-binding proteins [58, 59]. The combination of magnetic iron/gold core-shell nanoparticles with gold nanorods has also been used to specifically enumerate *E. coli* in water samples in a rapid and sensitive test [60]. In this case, the magnetic nanoparticles are used to concentrate the bacteria, improving the Raman signal by concentration and the posteriorly added gold nanorods serve as Raman signal enhancers.

SERS can also be used in conjunction with colloidal gold to detect and target tumors *in vivo*, where the AuNPs are surrounded with Raman reporters that provide light emission 200 times brighter than quantum dots [61, 62]. It was also found that the Raman reporters became more stable and yielded larger optical enhancements when NPs were encapsulated with a thiol-modified polyethylene glycol coat, which also allows for increased biocompatibility and circulation times *in vivo*. When conjugated to tumor-targeting ligands, these conjugated SERS-NPs were able to target tumor markers at surface of malignant cells, such as epidermal growth factor receptor (EGFR) that is sometimes overexpressed in cells of certain cancer types [29] and used to locate the tumor in xenograft tumor models [50].

2.3. Fluorescence-Based Systems. Quantum dots (QDs) are semiconductor nanoparticles with narrow, tunable, symmetrical emission spectra, and high quantum yields [63–65], and together with compatibility with DNA and proteins, make QDs exceptional substitutes as fluorescence labels. The use of QDs for nucleic acid characterization has long been proposed, for example, CdSe/ZnS QDs for SNP identification on human TP53 gene, multiallele detection of hepatitis B and C viruses [66], and *in situ* detection of chromosome abnormalities and mutations [67]. QDs have also been used as chemical sensors by exploring a typical FRET system where a dark quencher is placed at a protein-binding site attached to a QD surface. The quantum dots emission is quenched in presence of the analyte and upon analyte displacement the emission is restored [68]. A simpler approach was used to detect adenine using fluorescent ZnS nanoparticles at pH7, making use of capability of

adenine itself to quench emission of the quantum-dot-like nanoparticles [69].

Several studies report on the modulation of fluorophores at the vicinity of nanoparticles (e.g., gold, silver, and quantum dots) [70, 71], an interaction that has found application in a variety of systems to detect biologically relevant targets with particular focus upon AuNPs due to their ease in functionalization with biomolecules [72–75]. Several methods based on the quenching of fluorescence have been proposed for DNA detection consisting of fluorophore-labeled ssDNA electrostatically adsorbed onto gold nanoparticles [76], carbon nanotubes [77], and carbon nanoclots [78], where the presence of a complementary target triggers desadsorption of the newly formed dsDNA from the nanostructures due to the electrostatic variation between ssDNA and dsDNA, and fluorescence emission is restored. Also, fluorescence quenching of fluorophores close to metal nanoparticles functionalized with thiol-modified oligonucleotides has been explored in different conformations. Tang and co-workers proposed a method to probe hydroxyl radicals using an AuNP-oligonucleotide-FAM system where the hydroxyl radical promotes strand breakage and consequent release of FAM, restoring the previously quenched fluorescence [79]. The same quenching mechanism was used to detect specific DNA strands using two probes (one with an AuNP label and another labeled with TAMRA) that hybridize to two DNA sequences near each other [80], bringing the fluorophore and AuNP close enough to quench fluorescence emission.

Proteins have also been probed through nanoparticle-fluorescence-mediated systems, for example, human blood proteins have been let to interact with fluorescent AuNPs and detected through quenching [81]. In another example, a sandwich immunoassay using AuNPs quenching has been proposed for the detection of the protein cardiac troponin T by its interaction with two different antibodies, one attached to AuNPs and the other labeled with fluorescent dyes [82]. By means of an opposite modulation, infrared fluorescent nanoparticles showed enhanced fluorescence when interacting with protein [83].

A popular application of fluorescence modulation by nanoparticles has been specific ion sensing. Su and coworkers developed a copper sensor by covering fluorescent DNA-Cu/Ag nanoclusters with mercaptopropionic acid which quenches the intrinsic fluorescence of the nanoparticle; in the presence of Cu^{2+}, the capping agent is oxidized to form a disulfide compound resulting in release of the nanoparticle and restoration of emission suitable for quantification between 5 and 200 nM [84]. A very specific colorimetric and fluorimetric method to detect Hg^{2+} ions was developed with porphyrin-modified $Au@SiO_2$ nanoparticles, where the intensively fluorescent red complex turns green and weakly fluorescent in presence of Hg^{2+} [85]. Another examples include sensing of Pb^{2+} and adenosine by combining an adenosine aptamer and a DNAzyme with an abasic site where 2-amino-5,6,7-trimethyl-1,8-naphthyridine is trapped to quench its fluorescence [86]. When in solution, Pb^{2+} enables the DNAzyme to cleave its substrate thus removing the fluorescent compound from the abasic site restoring its fluorescence. Similarly, the presence of adenosine induces structural change of the aptamer, resulting in the release of the fluorescent molecule from the DNA duplex and a subsequent fluorescence enhancement.

2.4. Nanophotonics Bioimaging. Nanoparticles show unique features suitable for biomedical imaging applications, such as an increased sensitivity in detection through amplification of signal changes (e.g., magnetic resonance imaging); high fluorescence quantum yields and large magnetic moments; properties that induce phagocytosis and selective uptake by macrophages (e.g., liposomes); physicochemical manipulations of energy (i.e., quantum dots); among others [87]. Because light absorption from biologic tissue components is minimized at near infrared (NIR) wavelengths, most nanoparticles (e.g., noble metal and magnetic NPs, nanoshells, nanoclusters, nanocages, nanorods and quantum dots) for *in vivo* imaging and therapy have been designed to strongly absorb in the NIR and used for *in vivo* diagnostics [83, 88, 89]. Ex vivo and *in vivo* imaging applications of nanoparticles have included their use as contrast agents for magnetic resonance imaging (MRI) [90], optical coherence tomography (OCT) [91–93], photoacoustic imaging (PAI) [94], and two-photon luminescence (TPL) spectroscopy [95].

2.4.1. Magnetic Resonance Imaging. Magnetic resonance imaging (MRI) is based heavily on nuclear magnetic resonance (NMR), first described by R. Damadian. Magnetic resonance measurements cause no obvious deleterious effects on biological tissue, and the incident radiation consists of common radio frequencies at right angles to a static magnetic field [96]. Iron oxide nanoparticles show superparamagnetism, allowing for the facile alignment of the magnetic moments to an applied magnetic field, thus of great interest as contrast agents for MRI [97]. Presently, magnetic iron oxide nanoparticles are routinely used as contrast agents to enhance an MRI image, providing sharper contrast between soft and hard tissue in the body (e.g. liver and spleen or lymph nodes) [98]. Jun et al. presented a synthetically controlled magnetic nanocrystal model system that led to the improvement of high-performance nanocrystal—antibody probe systems for the diagnosis of breast cancer cells via magnetic resonance imaging [99]. Also, $MnFe_2O_4$ nanocrystals *functionalized* with an antibody conjugate (herceptin) capable of specific targeting of cancerous cells was successfully used for *in vivo* MRI in mice [88]. Driehuysb et al. developed an imaging method to detect submillimeter-sized metastases with molecular specificity by targeting cancer cells with iron oxide nanoparticles functionalized with cancer-binding ligands, demonstrating *in vivo* detection of pulmonary micrometastases in mice injected with breast adenocarcinoma cells [100]. Hybrid NPs with a superparamagnetic iron oxide/silica core and a gold nanoshell, with significant absorbance and scattering in the NIR region, have been used *in vivo* as contrast agents for MRI presenting a good MR signal in hepatoma, each moiety providing for a distinct signal that enhanced detection [101].

2.4.2. Optical Coherence Tomography. Optical Coherence Tomography (OCT) is an imaging modality that provides cross-sectional subsurface imaging of biological tissue with micrometer scale resolution which is based on a broadband light source and a fiber-optic interferometer. It captures three-dimensional images from within optical scattering media, typically employing near-infrared light. The use of relatively long wavelength light allows it to penetrate into the scattering medium [102–104]. The extra scattering provided by Au-nanoshells enhances optical contrast and brightness for improved diagnostic imaging of tumors in mice due to the preferential accumulation of the nanoshells in the tumor [105]. Tseng et al. developed nanorings with a localized surface plasmon resonance covering a spectral range of 1300 nm that produced both photothermal and image contrast enhancement effects in OCT when delivered into pig adipose samples [106]. Additionally, the image contrast enhancement effect could be isolated by continuously scanning the sample with a lower scan frequency, allowing to effectively control the therapeutic modality. In the same way, gold capped nanoroses have been used in photothermal OCT to detect macrophages in *ex vivo* rabbit arteries [107].

2.4.3. Photoacoustic Imaging. In photoacoustic imaging (PAI) and photoacoustic tomography (PAT), a pulse of NIR laser light, typically 757 nm, is used in resonance with the surface plasmon instead of a continuous NIR source. With this technique causing rapid thermal expansion of the surrounding media, the generated sound wave can be detected on the surface of the subject. NIR reduces the amount of absorption that occurs, but absorption of light by various other organs is unavoidable [108, 109]. Yang et al. demonstrated the feasibility of using poly(ethylene glycol)-coated Au nanocages as a new *in vivo* NIR contrast-enhancing agent for photoacoustic tomography and image their distribution in the vasculature of rat brain. These Au-nanocages enhanced the contrast between blood and the surrounding tissues by up to 81%, achieving a more detailed image of vascular structures at greater depths. Additionally, they were shown to present slight advantages over Au-nanoshells, being better suited for *in vivo* applications, specially due to their more compact size (<50 nm compared to >100 nm for Au-nanoshells) and larger optical absorption cross-sections [110]. Due to the ability of gold-nanorods to have the maximum of the plasmon resonance tuned further into the NIR, Motamedi et al. reported a contrast agent for a laser optoacoustic imaging system for *in vivo* detection of gold nanorods and to enhance the diagnostic power of optoacoustic imaging [111]. Song et al. proposed a noninvasive *in vivo* spectroscopic photoacoustic sentinel lymph node mapping in a rat model using gold nanorods as lymph node tracers [112].

2.4.4. Two-Photon Luminescence. In two-photon luminescence (TPL) spectroscopy, an electron is excited from the conductance band to the valence band of the metal nanoparticles using two photons. As the electron relaxes to the conductance band, light is released and amplified due to a resonant coupling with localized surface plasmons, enhancing a variety of linear and nonlinear optical properties [113, 114]. TPL was first described by Boyd et al. that found that roughened metal surfaces exhibited much higher induced luminescence efficiency than smooth surfaces [115]. In fact, TPL is a potentially powerful technique for noninvasive imaging at the micron scale hundreds of microns deep into scattering tissue. This way, it ought to be possible to discriminate cancerous and healthy tissue based on two-photon imaging from endogenous fluorophores. For enhanced imaging, two-photon contrast agents have been developed showing the ability to increase signal-to-noise ratio and targeted to molecular signatures of interest that are not fluorescent. Because imaging of intrinsic fluorophores is often difficult due to their relatively weak signals, the use of such a bright contrast agent holds the promise to enable *in vivo* applications of two photon imaging in a clinical setting [113, 116, 117]. Wang et al. collected images of single gold nanorods flowing in the mouse ear blood vessels with luminescence three times stronger than background [114]. It is worth mentioning that the TPL signal from a single nanorod is 58 times that of the two-photon fluorescence signal from a single rhodamine molecule.

2.4.5. QDs for In Vivo Imaging. In the last decade, water soluble bioconjugated QDs have been increasingly applied for imaging [63, 64, 118] However, QD probes for imaging show poor stability once inside cytosolic environment and reduced biocompatibility in living organisms [119], which constitutes a serious drawback for widespread *in vivo* application.

Despite the serious concerns related to the *in vivo* use of QDs, these nanocrystals show remarkable imaging properties that may be judged of value for improved diagnostics. In fact, QDs have proven of great value when imaging vascular networks of mammals such as lymphatic and cardiovascular systems [120–124]. Also, Kim et al. demonstrated that quantum dots allowed a major cancer surgery to be performed in large animals (mice and pigs) under complete image guidance, by locating the position of sentinel lymph nodes [125]. With similar potential to that observed when imaging the lymph system, the imaging of cardiovascular systems has also been achieved using QDs [126, 127]. Larson et al. demonstrated that QDs retained their fluorescence after injection and could be detected in the capillaries of skin and adipose tissue of a mouse [128]. The fluorescent emission and multiplexing capabilities of QDs are being exploited to improve the sensitivity and selectivity in the early detection of tumors [61, 129, 130]. Åkerman et al. described for the first time the application of targeted cancer imaging by using ZnS-capped CdSe QDs coated with a lung-targeting peptide that accumulate in the lungs of mice, whereas two other peptides specifically direct QDs to blood vessels or lymphatic vessels in tumors [131]. Later, Gao et al. described the development of multifunctional nanoparticle probes based on QDs with a copolymer linked to tumor-targeting ligands and drug-delivery functionalities for cancer targeting and imaging in living animals [132]. Once the toxicological aspects associated with QDs have been clarified, such studies

demonstrate the potential of QDs for ultrasensitive and multiplexed imaging of molecular targets *in vivo*.

3. Nanophotonics for Therapy

Nanophototerapy uses pulsed lasers and absorbing nanoparticles attached to specific targets for selective damage to cancer cells. Plasmonic photothermal therapy (PPTT) and photodynamic therapy (PDT) are two of the main techniques that take advantage of the selective absorbance of the surface plasmon resonance and the fact that the nanoparticles relax by liberating heat into their surrounding environment.

3.1. Plasmonic Photothermal Therapy. Plasmonic photothermal therapy is a less invasive experimental technique that holds great promise for the treatment of cell malignancies and, in particular, of cancer. It combines two key components: (i) light source, specifically lasers with a spectral range of 650–900 nm for deep tissue penetration and (ii) optical absorption of AuNPs which release the optical irradiation as heat in the picoseconds time scale, thereby inducing photothermal ablation [133–135]. Kirui et al. reported the use of gold and iron oxide hybrid nanoparticles in targeting, imaging, and selective thermal killing of colorectal cancer cells [136]. Huang and colleagues have demonstrated that gold nanorods have a longitudinal absorption band in the NIR on account of SPR oscillations and are effective as photothermal agents [137]. Gold nanorods aspect ratios allow tuning the SPR band from the visible to the NIR (transmits readily through human skin and tissue), making them suitable for photothermal converters of near infrared light for in vivo applications [138, 139]. Effective photothermal destruction of cancer cells and tissue have been demonstrated for other gold nanostructures, such as branched gold nanoparticles [140], gold nanoshells [141–143], gold nanocages [134], and gold nanospheres [144].

3.2. Photodynamic Therapy. Photodynamic therapy employs chemical photosensitizers that generate reactive oxygen species (ROS), such as a singlet oxygen ($^1O_2$), capable of tumor destruction [145, 146]. This technique is noninvasive and can be applied locally or systemically without noticeable cumulative toxicity effects without high costs. To attain maximal killing efficiency of tumor cells, the photosensitizer must be in close proximity to the tumor cells, thus requiring specific targeting when administered systemically. One of the major limitations is the poor tissue penetration of high-energy light and the systemic dispersal of the photosensitizer [147, 148].

Aiming at circumventing some of the limitations of photodynamic therapy, Zhang et al. reported a new type of photosensitizers based on photon upconverting nanoparticles (a process where low energy light, usually near-infrared (NIR) or infrared (IR), is converted to higher energies, ultraviolet (UV), or visible, via multiple absorptions or energy transfer steps) [149, 150]. One year later, Yong et al. reported the use of NPs modified with zinc phthalocyanin photosensitizer that produce green/red emission on near-infrared (NIR) excitation and is capable of singlet oxygen sensitization; upon targeted binding to cancer cells, significant cell destruction was induced [151]. Recently, Qian et al. published similar results with the use of zinc phthalocyanine nanocrystals coated with a uniform layer of mesoporous silica [152].

4. Conclusions

Light is an amazing intermediate with a gargantuan capacity for carrying multiple information and functions. Instinctively, we view light as rays, which propagate in a single direction, either being absorbed or reflected to some extent by any object on which it impinges. However, the propagation of light through a material is itself a quantum effect, involving the excitation and relaxation of electrons in the material. It is well known that light has the facility to act through biological, chemical, mechanical, and thermal pathways at molecular/cellular levels in diagnostic and therapeutic applications.

Currently, we are in the dawn of a new age in therapy driven by nanotechnology vehicles. Although there are technical challenges associated with the therapeutic application of nanodevices, the integration of therapy with diagnostic profiling has accelerated the pace of discovery of new nanotechnology methods. In addition to continuing to push forward on the above challenges, nanotechnology together with photonics can be used both for identifying useful target candidates and for validating their importance in disease states. Nanophotonics may present new opportunities for personalized medicine in which diagnosis and treatment are based on each individual's molecular profile. Further research into the fundamental mechanisms that efficiently control light using nanodevices could unveil new dimensions of nanoparticle-mediated theranostic systems.

Here, we have attempted to give the reader a limited overview of some aspects of the current state of research into the fascinating aspects and control over nanophotonics in molecular diagnostics and therapy applications.

Acknowledgment

The authors acknowledge FCT/MCTES—CIGMH(Portugal) for financial support.

References

[1] M. Ohtsu, K. Kobayashi, T. Kawazoe, T. Yatsui, and M. Naruse, *Principles of Nanophotonics*, Series in Optics and Optoelectronics, Taylor & Francis, CRC Press, 2008.

[2] Y. Shen and P. N. Prasad, "Nanophotonics: a new multidisciplinary frontier," *Applied Physics B*, vol. 74, no. 7-8, pp. 641–645, 2002.

[3] T. Lammers, S. Aime, W. E. Hennink, G. Storm, and F. Kiessling, "Theranostic nanomedicines," *Accounts of Chemical Research*. In press.

[4] F. Pene, E. Courtine, A. Cariou, and J. P. Mira, "Toward theragnostics," *Critical Care Medicine*, vol. 37, no. 1, pp. S50–S58, 2009.

[5] W. L. Barnes, A. Dereux, and T. W. Ebbesen, "Surface plasmon subwavelength optics," *Nature*, vol. 424, no. 6950, pp. 824–830, 2003.

[6] U. Kreibig and M. Vollmer, *Optical Properties of Metal Clusters*, vol. 25 of *Springer Series in Materials Science*, Springer, Berlin, Germany, 1995.

[7] M. C. Daniel and D. Astruc, "Gold nanoparticles: assembly, supramolecular chemistry, quantum-size-related properties, and applications toward biology, catalysis, and nanotechnology," *Chemical Reviews*, vol. 104, no. 1, pp. 293–346, 2004.

[8] S. Eustis and M. A. El-Sayed, "Why gold nanoparticles are more precious than pretty gold: Noble metal surface plasmon resonance and its enhancement of the radiative and nonradiative properties of nanocrystals of different shapes," *Chemical Society Reviews*, vol. 35, no. 3, pp. 209–217, 2006.

[9] S. K. Ghosh and T. Pal, "Interparticle coupling effect on the surface plasmon resonance of gold nanoparticles: from theory to applications," *Chemical Reviews*, vol. 107, no. 11, pp. 4797–4862, 2007.

[10] W. Zhao, M. A. Brook, and Y. Li, "Design of gold nanoparticle-based colorimetric biosensing assays," *ChemBioChem*, vol. 9, no. 15, pp. 2363–2371, 2008.

[11] J. N. Anker, W. P. Hall, O. Lyandres, N. C. Shah, J. Zhao, and R. P. Van Duyne, "Biosensing with plasmonic nanosensors," *Nature Materials*, vol. 7, no. 6, pp. 442–453, 2008.

[12] P. Baptista, G. Doria, D. Henriques, E. Pereira, and R. Franco, "Colorimetric detection of eukaryotic gene expression with DNA-derivatized gold nanoparticles," *Journal of Biotechnology*, vol. 119, no. 2, pp. 111–117, 2005.

[13] P. Baptista, E. Pereira, P. Eaton et al., "Gold nanoparticles for the development of clinical diagnosis methods," *Analytical and Bioanalytical Chemistry*, vol. 391, no. 3, pp. 943–950, 2008.

[14] Y. C. Cao, R. Jin, C. S. Thaxton, and C. A. Mirkin, "A two-color-change, nanoparticle-based method for DNA detection," *Talanta*, vol. 67, no. 3, pp. 449–455, 2005.

[15] M. M. C. Cheng, G. Cuda, Y. L. Bunimovich et al., "Nanotechnologies for biomolecular detection and medical diagnostics," *Current Opinion in Chemical Biology*, vol. 10, no. 1, pp. 11–19, 2006.

[16] J. Conde, J. M. de la Fuente, and P. V. Baptista, "RNA quantification using gold nanoprobes - application to cancer diagnostics," *Journal of Nanobiotechnology*, vol. 8, article no. 5, 2010.

[17] P. Costa, A. Amaro, A. Botelho, J. Inácio, and P. V. Baptista, "Gold nanoprobe assay for the identification of mycobacteria of the Mycobacterium tuberculosis complex," *Clinical Microbiology and Infection*, vol. 16, no. 9, pp. 1464–1469, 2010.

[18] G. Doria, R. Franco, and P. Baptista, "Nanodiagnostics: fast colorimetric method for single nucleotide polymorphism/mutation detection," *IET Nanobiotechnology*, vol. 1, no. 4, pp. 53–57, 2007.

[19] R. Elghanian, J. J. Storhoff, R. C. Mucic, R. L. Letsinger, and C. A. Mirkin, "Selective colorimetric detection of polynucleotides based on the distance-dependent optical properties of gold nanoparticles," *Science*, vol. 277, no. 5329, pp. 1078–1081, 1997.

[20] H. Li and L. Rothberg, "Colorimetric detection of DNA sequences based on electrostatic interactions with unmodified gold nanoparticles," *Proceedings of the National Academy of Sciences of the United States of America*, vol. 101, no. 39, pp. 14036–14039, 2004.

[21] C. A. Mirkin, R. L. Letsinger, R. C. Mucic, and J. J. Storhoff, "A DNA-based method for rationally assembling nanoparticles into macroscopic materials," *Nature*, vol. 382, no. 6592, pp. 607–609, 1996.

[22] W. J. Qin and L. Y. L. Yung, "Nanoparticle-based detection and quantification of DNA with single nucleotide polymorphism (SNP) discrimination selectivity," *Nucleic Acids Research*, vol. 35, no. 17, article no. e111, 2007.

[23] K. Sato, K. Hosokawa, and M. Maeda, "Rapid aggregation of gold nanoparticles induced by non-cross-linking DNA hybridization," *Journal of the American Chemical Society*, vol. 125, no. 27, pp. 8102–8103, 2003.

[24] K. Sato, K. Hosokawa, and M. Maeda, "Non-cross-linking gold nanoparticle aggregation as a detection method for single-base substitutions," *Nucleic Acids Research*, vol. 33, no. 1, article e4, 2005.

[25] J. J. Storhoff, A. D. Lucas, V. Garimella, Y. P. Bao, and U. R. Müller, "Homogeneous detection of unamplified genomic DNA sequences based on colorimetric scatter of gold nanoparticle probes," *Nature Biotechnology*, vol. 22, no. 7, pp. 883–887, 2004.

[26] T. A. Taton, C. A. Mirkin, and R. L. Letsinger, "Scanometric DNA array detection with nanoparticle probes," *Science*, vol. 289, no. 5485, pp. 1757–1760, 2000.

[27] C. S. Thaxton, D. G. Georganopoulou, and C. A. Mirkin, "Gold nanoparticle probes for the detection of nucleic acid targets," *Clinica Chimica Acta*, vol. 363, no. 1-2, pp. 120–126, 2006.

[28] C. C. You, O. R. Miranda, B. Gider et al., "Detection and identification of proteins using nanoparticle-fluorescent polymer 'chemical nose' sensors," *Nature Nanotechnology*, vol. 2, no. 5, pp. 318–323, 2007.

[29] I. H. El-Sayed, X. Huang, and M. A. El-Sayed, "Surface plasmon resonance scattering and absorption of anti-EGFR antibody conjugated gold nanoparticles in cancer diagnostics: applications in oral cancer," *Nano Letters*, vol. 5, no. 5, pp. 829–834, 2005.

[30] S. Kumar, N. Harrison, R. Richards-Kortum, and K. Sokolov, "Plasmonic nanosensors for imaging intracellular biomarkers in live cells," *Nano Letters*, vol. 7, no. 5, pp. 1338–1343, 2007.

[31] W.-C. Law, K.-T. Yong, A. Baev, and P. N. Prasad, "Sensitivity improved surface plasmon resonance biosensor for cancer biomarker detection based on plasmonic enhancement," *ACS Nano*, vol. 5, no. 6, pp. 4858–4864, 2011.

[32] J. S. Mitchell and T. E. Lowe, "Ultrasensitive detection of testosterone using conjugate linker technology in a nanoparticle-enhanced surface plasmon resonance biosensor," *Biosensors and Bioelectronics*, vol. 24, no. 7, pp. 2177–2183, 2009.

[33] J. M. Nam, C. S. Thaxton, and C. A. Mirkin, "Nanoparticle-based bio-bar codes for the ultrasensitive detection of proteins," *Science*, vol. 301, no. 5641, pp. 1884–1886, 2003.

[34] S. Schultz, D. R. Smith, J. J. Mock, and D. A. Schultz, "Single-target molecule detection with nonbleaching multicolor optical immunolabels," *Proceedings of the National Academy of Sciences of the United States of America*, vol. 97, no. 3, pp. 996–1001, 2000.

[35] A. J. Haes, L. Chang, W. L. Klein, and R. P. Van Duyne, "Detection of a biomarker for Alzheimer's disease from synthetic and clinical samples using a nanoscale optical biosensor," *Journal of the American Chemical Society*, vol. 127, no. 7, pp. 2264–2271, 2005.

[36] A. D. McFarland and R. P. Van Duyne, "Single silver nanoparticles as real-time optical sensors with zeptomole sensitivity," *Nano Letters*, vol. 3, no. 8, pp. 1057–1062, 2003.

[37] G. Raschke, S. Kowarik, T. Franzl et al., "Biomolecular recognition based on single gold nanoparticle light scattering," *Nano Letters*, vol. 3, no. 7, pp. 935–938, 2003.

[38] M. K. Hossain and Y. Ozaki, "Surface-enhanced Raman scattering: facts and inline trends," *Current Science*, vol. 97, no. 2, pp. 192–201, 2009.

[39] D. L. Jeanmaire and R. P. Van Duyne, "Surface Raman spectroelectrochemistry Part I. Heterocyclic, aromatic, and aliphatic amines adsorbed on the anodized silver electrode," *Journal of Electroanalytical Chemistry*, vol. 84, no. 1, pp. 1–20, 1977.

[40] M. G. Albrecht and J. A. Creighton, "Anomalously intense Raman spectra of pyridine at a silver electrode," *Journal of the American Chemical Society*, vol. 99, no. 15, pp. 5215–5217, 1977.

[41] B. Pettinger, "Light scattering by adsorbates at Ag particles: quantum-mechanical approach for energy transfer induced interfacial optical processes involving surface plasmons, multipoles, and electron-hole pairs," *The Journal of Chemical Physics*, vol. 85, no. 12, pp. 7442–7451, 1986.

[42] A. M. Michaels, M. Nirmal, and L. E. Brus, "Surface enhanced Raman spectroscopy of individual rhodamine 6G molecules on large Ag nanocrystals," *Journal of the American Chemical Society*, vol. 121, no. 43, pp. 9932–9939, 1999.

[43] P. Etchegoin, H. Liem, R. C. Maher et al., "A novel amplification mechanism for surface enhanced Raman scattering," *Chemical Physics Letters*, vol. 366, no. 1-2, pp. 115–121, 2002.

[44] A. Otto, "On the electronic contribution to single molecule surface enhanced Raman spectroscopy," *Indian Journal of Physics*, vol. 77B, pp. 63–73, 2003.

[45] S. Shanmukh, L. Jones, J. Driskell, Y. Zhao, R. Dluhy, and R. A. Tripp, "Rapid and sensitive detection of respiratory virus molecular signatures using a silver nanorod array SERS substrate," *Nano Letters*, vol. 6, no. 11, pp. 2630–2636, 2006.

[46] S. C. Pînzaru, L. M. Andronie, I. Domsa, O. Cozar, and S. Astilean, "Bridging biomolecules with nanoparticles: surface-enhanced Raman scattering from colon carcinoma and normal tissue," *Journal of Raman Spectroscopy*, vol. 39, no. 3, pp. 331–334, 2008.

[47] S. P. Mulvaney, M. D. Musick, C. D. Keating, and M. J. Natan, "Glass-coated, analyte-tagged nanoparticles: a new tagging system based on detection with surface-enhanced Raman scattering," *Langmuir*, vol. 19, no. 11, pp. 4784–4790, 2003.

[48] W. E. Doering, M. E. Piotti, M. J. Natan, and R. G. Freeman, "SERS as a foundation for nanoscale, optically detected biological labels," *Advanced Materials*, vol. 19, no. 20, pp. 3100–3108, 2007.

[49] L. Sun, C. Yu, and J. Irudayaraj, "Surface-enhanced Raman scattering based nonfluorescent probe for multiplex DNA detection," *Analytical Chemistry*, vol. 79, no. 11, pp. 3981–3988, 2007.

[50] X. Qian, X. Zhou, and S. Nie, "Surface-enhanced raman nanoparticle beacons based on bioconjugated gold nanocrystals and long range plasmonic coupling," *Journal of the American Chemical Society*, vol. 130, no. 45, pp. 14934–14935, 2008.

[51] K. K. Strelau, A. Brinker, C. Schnee, K. Weber, R. Möller, and J. Popp, "Detection of PCR products amplified from DNA of epizootic pathogens using magnetic nanoparticles and SERS," *Journal of Raman Spectroscopy*, vol. 42, no. 3, pp. 243–250, 2011.

[52] M. B. Wabuyele, F. Yan, and T. Vo-Dinh, "Plasmonics nanoprobes: detection of single-nucleotide polymorphisms in the breast cancer BRCA1 gene," *Analytical and Bioanalytical Chemistry*, vol. 398, no. 2, pp. 729–736, 2010.

[53] J. Neng, M. H. Harpster, H. Zhang, J. O. Mecham, W. C. Wilson, and P. A. Johnson, "A versatile SERS-based immunoassay for immunoglobulin detection using antigen-coated gold nanoparticles and malachite green-conjugated protein A/G," *Biosensors and Bioelectronics*, vol. 26, no. 3, pp. 1009–1015, 2010.

[54] Y. C. Cao, R. Jin, and C. A. Mirkin, "Nanoparticles with Raman spectroscopic fingerprints for DNA and RNA detection," *Science*, vol. 297, no. 5586, pp. 1536–1540, 2002.

[55] Y. C. Cao, R. Jin, J. M. Nam, C. S. Thaxton, and C. A. Mirkin, "Raman dye-labeled nanoparticle probes for proteins," *Journal of the American Chemical Society*, vol. 125, no. 48, pp. 14676–14677, 2003.

[56] J. D. Driskell and R. A. Tripp, "Label-free SERS detection of microRNA based on affinity for an unmodified silver nanorod array substrate," *Chemical Communications*, vol. 46, no. 19, pp. 3298–3300, 2010.

[57] A. Barhoumi, D. Zhang, F. Tam, and N. J. Halas, "Surface-enhanced raman spectroscopy of DNA," *Journal of the American Chemical Society*, vol. 130, no. 16, pp. 5523–5529, 2008.

[58] D. Graham, R. Stevenson, D. G. Thompson, L. Barrett, C. Dalton, and K. Faulds, "Combining functionalised nanoparticles and SERS for the detection of DNA relating to disease," *Faraday Discussions*, vol. 149, pp. 291–299, 2011.

[59] C. V. Pagba, S. M. Lane, H. Cho, and S. Wachsmann-Hogiu, "Direct detection of aptamer-thrombin binding via surface-enhanced Raman spectroscopy," *Journal of Biomedical Optics*, vol. 15, no. 4, Article ID 047006, 2010.

[60] B. Guven, N. Basaran-Akgul, E. Temur, U. Tamer, and I. H. Boyaci, "SERS-based sandwich immunoassay using antibody coated magnetic nanoparticles for Escherichia coli enumeration," *Analyst*, vol. 136, no. 4, pp. 740–748, 2011.

[61] W. Cai, D. W. Shin, K. Chen et al., "Peptide-labeled near-infrared quantum dots for imaging tumor vasculature in living subjects," *Nano Letters*, vol. 6, no. 4, pp. 669–676, 2006.

[62] J. Kneipp, H. Kneipp, M. McLaughlin, D. Brown, and K. Kneipp, "In vivo molecular probing of cellular compartments with gold nanoparticles and nanoaggregates," *Nano Letters*, vol. 6, no. 10, pp. 2225–2231, 2006.

[63] W. C. W. Chan and S. Nie, "Quantum dot bioconjugates for ultrasensitive nonisotopic detection," *Science*, vol. 281, no. 5385, pp. 2016–2018, 1998.

[64] M. Bruchez Jr., M. Moronne, P. Gin, S. Weiss, and A. P. Alivisatos, "Semiconductor nanocrystals as fluorescent biological labels," *Science*, vol. 281, no. 5385, pp. 2013–2016, 1998.

[65] H. Weller, "Colloidal semiconductor Q-particles: chemistry in the transition region between solid state and molecules," *Angewandte Chemie - International Edition*, vol. 32, no. 1, pp. 41–53, 1993.

[66] D. Gerion, F. Chen, B. Kannan et al., "Room-temperature single-nucleotide polymorphism and multiallele DNA detection using fluorescent nanocrystals and microarrays," *Analytical Chemistry*, vol. 75, no. 18, pp. 4766–4772, 2003.

[67] S. Pathak, S. K. Choi, N. Arnheim, and M. E. Thompson, "Hydroxylated quantum dots as luminescent probes for in situ hybridization," *Journal of the American Chemical Society*, vol. 123, no. 17, pp. 4103–4104, 2001.

[68] I. L. Medintz, A. R. Clapp, H. Mattoussi, E. R. Goldman, B. Fisher, and J. M. Mauro, "Self-assembled nanoscale biosensors based on quantum dot FRET donors," *Nature Materials*, vol. 2, no. 9, pp. 630–638, 2003.

[69] L. M. Devi and D. P. S. Negi, "Sensitive and selective detection of adenine using fluorescent ZnS nanoparticles," *Nanotechnology*, vol. 22, no. 24, Article ID 245502, 2011.

[70] J. Gersten and A. Nitzan, "Spectroscopic properties of molecules interacting with small dielectric particles," *The Journal of Chemical Physics*, vol. 75, no. 3, pp. 1139–1152, 1981.

[71] K. A. Kang, J. Wang, J. B. Jasinski, and S. Achilefu, "Fluorescence manipulation by gold nanoparticles: from complete quenching to extensive enhancement," *Journal of Nanobiotechnology*, vol. 9, article 16, 2011.

[72] A. Quarta, R. D. Corato, L. Manna, A. Ragusa, and T. Pellegrino, "Fluorescent-magnetic hybrid nanostructures: preparation, properties, and applications in biology," *IEEE Transactions on Nanobioscience*, vol. 6, no. 4, pp. 298–308, 2007.

[73] J. R. Lakowicz, J. Malicka, E. Matveeva, I. Gryczynski, and Z. Gryczynski, "Plasmonic technology: novel approach to ultrasensitive immunoassays," *Clinical Chemistry*, vol. 51, no. 10, pp. 1914–1922, 2005.

[74] J. R. Lakowicz, "Plasmonics in biology and plasmon-controlled fluorescence," *Plasmonics*, vol. 1, no. 1, pp. 5–33, 2006.

[75] I. L. Medintz and H. Mattoussi, "Quantum dot-based resonance energy transfer and its growing application in biology," *Physical Chemistry Chemical Physics*, vol. 11, no. 1, pp. 17–45, 2009.

[76] P. C. Ray, G. K. Darbha, A. Ray, J. Walker, and W. Hardy, "Gold nanoparticle based FRET for DNA detection," *Plasmonics*, vol. 2, no. 4, pp. 173–183, 2007.

[77] Y. Liu, Y. Wang, J. Jin, H. Wang, R. Yang, and W. Tan, "Fluorescent assay of DNA hybridization with label-free molecular switch: reducing background-signal and improving specificity by using carbon nanotubes," *Chemical Communications*, no. 6, pp. 665–667, 2009.

[78] W. Bai, H. Zheng, Y. Long, X. Mao, M. Gao, and L. Zhang, "A carbon dots-based fluorescence turn-on method for DNA determination," *Analytical Sciences*, vol. 27, no. 3, pp. 243–246, 2011.

[79] B. Tang, N. Zhang, Z. Chen et al., "Probing hydroxyl radicals and their imaging in living cells by use of FAM-DNA-Au nanoparticles," *Chemistry*, vol. 14, no. 2, pp. 522–528, 2008.

[80] Z. S. Wu, J. H. Jiang, L. Fu, G. L. Shen, and R. Q. Yu, "Optical detection of DNA hybridization based on fluorescence quenching of tagged oligonucleotide probes by gold nanoparticles," *Analytical Biochemistry*, vol. 353, no. 1, pp. 22–29, 2006.

[81] S. H. De Paoli Lacerda, J. J. Park, C. Meuse et al., "Interaction of gold nanoparticles with common human blood proteins," *ACS Nano*, vol. 4, no. 1, pp. 365–379, 2010.

[82] S. Mayilo, M. A. Kloster, M. Wunderlich et al., "Long-range fluorescence quenching by gold nanoparticles in a sandwich immunoassay for cardiac troponin T," *Nano Letters*, vol. 9, no. 12, pp. 4558–4563, 2009.

[83] X. He, J. Gao, S. S. Gambhir, and Z. Cheng, "Near-infrared fluorescent nanoprobes for cancer molecular imaging: status and challenges," *Trends in Molecular Medicine*, vol. 16, no. 12, pp. 574–583, 2010.

[84] Y. T. Su, G. Y. Lan, W. Y. Chen, and H. T. Chang, "Detection of copper ions through recovery of the fluorescence of DNA-templated copper/silver nanoclusters in the presence of mercaptopropionic acid," *Analytical Chemistry*, vol. 82, no. 20, pp. 8566–8572, 2010.

[85] Y. Cho, S. S. Lee, and J. H. Jung, "Recyclable fluorimetric and colorimetric mercury-specific sensor using porphyrin-functionalized Au@SiO_2 core/shell nanoparticles," *Analyst*, vol. 135, no. 7, pp. 1551–1555, 2010.

[86] Y. Xiang, A. Tong, and Y. Lu, "Abasic site-containing DNAzyme and aptamer for label-free fluorescent detection of Pb^{2+} and adenosine with high sensitivity, selectivity, and tunable dynamic range," *Journal of the American Chemical Society*, vol. 131, no. 42, pp. 15352–15357, 2009.

[87] R. Gill, M. Zayats, and I. Willner, "Semiconductor quantum dots for bioanalysis," *Angewandte Chemie - International Edition*, vol. 47, no. 40, pp. 7602–7625, 2008.

[88] J. H. Lee, Y. M. Huh, Y. W. Jun et al., "Artificially engineered magnetic nanoparticles for ultra-sensitive molecular imaging," *Nature Medicine*, vol. 13, no. 1, pp. 95–99, 2007.

[89] E. I. Altinoğlu and J. H. Adair, "Near infrared imaging with nanoparticles," *Wiley Interdisciplinary Reviews: Nanomedicine and Nanobiotechnology*, vol. 2, no. 5, pp. 461–477, 2010.

[90] P. Vartholomeos, M. Fruchard, A. Ferreira, and C. Mavroidis, "MRI-guided nanorobotic systems for therapeutic and diagnostic applications," *Annual Review of Biomedical Engineering*, vol. 13, pp. 157–184, 2011.

[91] E. V. Zagaynova, M. V. Shirmanova, M. Y. Kirillin et al., "Contrasting properties of gold nanoparticles for optical coherence tomography: phantom, in vivo studies and Monte Carlo simulation," *Physics in Medicine and Biology*, vol. 53, no. 18, pp. 4995–5009, 2008.

[92] J. C. Kah, M. Olivo, T. H. Chow et al., "Control of optical contrast using gold nanoshells for optical coherence tomography imaging of mouse xenograft tumor model in vivo," *Journal of Biomedical Optics*, vol. 14, no. 5, Article ID 054015, 2009.

[93] A. L. Oldenburg, M. N. Hansen, T. S. Ralston, A. Wei, and S. A. Boppart, "Imaging gold nanorods in excised human breast carcinoma by spectroscopic optical coherence tomography," *Journal of Materials Chemistry*, vol. 19, no. 35, pp. 6407–6411, 2009.

[94] X. Yang, E. W. Stein, S. Ashkenazi, and L. V. Wang, "Nanoparticles for photoacoustic imaging," *Wiley Interdisciplinary Reviews. Nanomedicine and nanobiotechnology*, vol. 1, no. 4, pp. 360–368, 2009.

[95] M. B. Mohamed, V. Volkov, S. Link, and M. A. El-Sayed, "The 'lightning' gold nanorods: fluorescence enhancement of over a million compared to the gold metal," *Chemical Physics Letters*, vol. 317, no. 6, pp. 517–523, 2000.

[96] R. Damadian, "Tumor detection by nuclear magnetic resonance," *Science*, vol. 171, no. 3976, pp. 1151–1153, 1971.

[97] D. S. Mathew and R. S. Juang, "An overview of the structure and magnetism of spinel ferrite nanoparticles and their synthesis in microemulsions," *Chemical Engineering Journal*, vol. 129, no. 1–3, pp. 51–65, 2007.

[98] S. Laurent, D. Forge, M. Port et al., "Magnetic iron oxide nanoparticles: synthesis, stabilization, vectorization, physicochemical characterizations and biological applications," *Chemical Reviews*, vol. 108, no. 6, pp. 2064–2110, 2008.

[99] Y. W. Jun, Y. M. Huh, J. S. Choi et al., "Nanoscale size effect of magnetic nanocrystals and their utilisation for cancer diagnosis via magnetic resonance imaging," *Journal of the American Chemical Society*, vol. 127, no. 16, pp. 5732–5733, 2005.

[100] R. T. Branca, Z. I. Cleveland, B. Fubara et al., "Molecular MRI for sensitive and specific detection of lung metastases," *Proceedings of the National Academy of Sciences of the United States of America*, vol. 107, no. 8, pp. 3693–3697, 2010.

[101] D. Kim, M. K. Yu, T. S. Lee, J. J. Park, Y. Y. Jeong, and S. Jon, "Amphiphilic polymer-coated hybrid nanoparticles as CT/MRI dual contrast agents," *Nanotechnology*, vol. 22, no. 15, Article ID 155101, 2011.

[102] D. Huang, E. A. Swanson, C. P. Lin et al., "Optical coherence tomography," *Science*, vol. 254, no. 5035, pp. 1178–1181, 1991.

[103] J. M. Schmitt, "Optical Coherence Tomography (OCT): a review," *IEEE Journal on Selected Topics in Quantum Electronics*, vol. 5, no. 4, pp. 1205–1215, 1999.

[104] H. G. Bezerra, M. A. Costa, G. Guagliumi, A. M. Rollins, and D. I. Simon, "Intracoronary optical coherence tomography: a comprehensive review. Clinical and research applications," *JACC: Cardiovascular Interventions*, vol. 2, no. 11, pp. 1035–1046, 2009.

[105] A. M. Gobin, M. H. Lee, N. J. Halas, W. D. James, R. A. Drezek, and J. L. West, "Near-infrared resonant nanoshells for combined optical imaging and photothermal cancer therapy," *Nano Letters*, vol. 7, no. 7, pp. 1929–1934, 2007.

[106] H. Y. Tseng, C. K. Lee, S. Y. Wu et al., "Au nanorings for enhancing absorption and backscattering monitored with optical coherence tomography," *Nanotechnology*, vol. 21, no. 29, Article ID 295102, 2010.

[107] A. S. Paranjape, R. Kuranov, S. Baranov et al., "Depth resolved photothermal OCT detection of macrophages in tissue using nanorose," *Biomedical Optics Express*, vol. 1, no. 1, pp. 2–16, 2010.

[108] Y. Su, F. Zhang, K. Xu, J. Yao, and R. K. Wang, "A photoacoustic tomography system for imaging of biological tissues," *Journal of Physics D*, vol. 38, no. 15, pp. 2640–2644, 2005.

[109] K. S. Valluru, B. K. Chinni, and N. A. Rao, "Photoacoustic imaging: opening new frontiers in medical imaging," *Journal of Clinical Imaging Science*, vol. 1, article 24, 2011.

[110] X. Yang, S. E. Skrabalak, Z. Y. Li, Y. Xia, and L. V. Wang, "Photoacoustic tomography of a rat cerebral cortex in vivo with Au nanocages as an optical contrast agent," *Nano Letters*, vol. 7, no. 12, pp. 3798–3802, 2007.

[111] M. Eghtedari, A. Oraevsky, J. A. Copland, N. A. Kotov, A. Conjusteau, and M. Motamedi, "High sensitivity of in vivo detection of gold nanorods using a laser optoacoustic imaging system," *Nano Letters*, vol. 7, no. 7, pp. 1914–1918, 2007.

[112] K. H. Song, C. Kim, K. Maslov, and L. V. Wang, "Noninvasive in vivo spectroscopic nanorod-contrast photoacoustic mapping of sentinel lymph nodes," *European Journal of Radiology*, vol. 70, no. 2, pp. 227–231, 2009.

[113] M. B. Mohamed, V. Volkov, S. Link, and M. A. El-Sayed, "The 'lightning' gold nanorods: fluorescence enhancement of over a million compared to the gold metal," *Chemical Physics Letters*, vol. 317, no. 6, pp. 517–523, 2000.

[114] H. Wang, T. B. Huff, D. A. Zweifel et al., "In vitro and in vivo two-photon luminescence imaging of single gold nanorods," *Proceedings of the National Academy of Sciences of the United States of America*, vol. 102, no. 44, pp. 15752–15756, 2005.

[115] G. T. Boyd, Z. H. Yu, and Y. R. Shen, "Photoinduced luminescence from the noble metals and its enhancement on roughened surfaces," *Physical Review B*, vol. 33, no. 12, pp. 7923–7936, 1986.

[116] N. J. Durr, T. Larson, D. K. Smith, B. A. Korgel, K. Sokolov, and A. Ben-Yakar, "Two-photon luminescence imaging of cancer cells using molecularly targeted gold nanorods," *Nano Letters*, vol. 7, no. 4, pp. 941–945, 2007.

[117] K. Imura, T. Nagahara, and H. Okamoto, "Plasmon mode imaging of single gold nanorods," *Journal of the American Chemical Society*, vol. 126, no. 40, pp. 12730–12731, 2004.

[118] K. T. Yong, I. Roy, H. Ding, E. J. Bergey, and P. N. Prasad, "Biocompatible near-infrared quantum dots as ultrasensitive probes for long-term in vivo imaging applications," *Small*, vol. 5, no. 17, pp. 1997–2004, 2009.

[119] A. M. Smith, H. Duan, A. M. Mohs, and S. Nie, "Bioconjugated quantum dots for in vivo molecular and cellular imaging," *Advanced Drug Delivery Reviews*, vol. 60, no. 11, pp. 1226–1240, 2008.

[120] E. G. Soltesz, S. Kim, R. G. Laurence et al., "Intraoperative sentinel lymph node mapping of the lung using near-infrared fluorescent quantum dots," *Annals of Thoracic Surgery*, vol. 79, no. 1, pp. 269–277, 2005.

[121] C. P. Parungo, Y. L. Colson, S. W. Kim et al., "Sentinel lymph node mapping of the pleural space," *Chest*, vol. 127, no. 5, pp. 1799–1804, 2005.

[122] J. P. Zimmer, S. W. Kim, S. Ohnishi, E. Tanaka, J. V. Frangioni, and M. G. Bawendi, "Size series of small indium arsenide-zinc selenide core-shell nanocrystals and their application to in vivo imaging," *Journal of the American Chemical Society*, vol. 128, no. 8, pp. 2526–2527, 2006.

[123] H. Kobayashi, Y. Hama, Y. Koyama et al., "Simultaneous multicolor imaging of five different lymphatic basins using quantum dots," *Nano Letters*, vol. 7, no. 6, pp. 1711–1716, 2007.

[124] Y. Hama, Y. Koyama, Y. Urano, P. L. Choyke, and H. Kobayashi, "Simultaneous two-color spectral fluorescence lymphangiography with near infrared quantum dots to map two lymphatic flows from the breast and the upper extremity," *Breast Cancer Research and Treatment*, vol. 103, no. 1, pp. 23–28, 2007.

[125] S. Kim, Y. T. Lim, E. G. Soltesz et al., "Near-infrared fluorescent type II quantum dots for sentinel lymph node mapping," *Nature Biotechnology*, vol. 22, no. 1, pp. 93–97, 2004.

[126] Y. T. Lim, S. Kim, A. Nakayama, N. E. Stott, M. G. Bawendi, and J. V. Frangioni, "Selection of quantum dot wavelengths for biomedical assays and imaging," *Molecular Imaging*, vol. 2, no. 1, pp. 50–64, 2003.

[127] J. D. Smith, G. W. Fisher, A. S. Waggoner, and P. G. Campbell, "The use of quantum dots for analysis of chick CAM vasculature," *Microvascular Research*, vol. 73, no. 2, pp. 75–83, 2007.

[128] D. R. Larson, W. R. Zipfel, R. M. Williams et al., "Water-soluble quantum dots for multiphoton fluorescence imaging in vivo," *Science*, vol. 300, no. 5624, pp. 1434–1436, 2003.

[129] X. Yu, L. Chen, K. Li et al., "Immunofluorescence detection with quantum dot bioconjugates for hepatoma in vivo," *Journal of Biomedical Optics*, vol. 12, no. 1, Article ID 014008, 2007.

[130] H. Tada, H. Higuchi, T. M. Wanatabe, and N. Ohuchi, "In vivo real-time tracking of single quantum dots conjugated with monoclonal anti-HER2 antibody in tumors of mice," *Cancer Research*, vol. 67, no. 3, pp. 1138–1144, 2007.

[131] M. E. Åkerman, W. C. W. Chan, P. Laakkonen, S. N. Bhatia, and E. Ruoslahti, "Nanocrystal targeting in vivo," *Proceedings*

of the National Academy of Sciences of the United States of America, vol. 99, no. 20, pp. 12617–12621, 2002.

[132] X. Gao, Y. Cui, R. M. Levenson, L. W. K. Chung, and S. Nie, "In vivo cancer targeting and imaging with semiconductor quantum dots," *Nature Biotechnology*, vol. 22, no. 8, pp. 969–976, 2004.

[133] X. Huang, P. K. Jain, I. H. El-Sayed, and M. A. El-Sayed, "Determination of the minimum temperature required for selective photothermal destruction of cancer cells with the use of immunotargeted gold nanoparticles," *Photochemistry and Photobiology*, vol. 82, no. 2, pp. 412–417, 2006.

[134] J. Chen, D. Wang, J. Xi et al., "Immuno gold nanocages with tailored optical properties for targeted photothermal destruction of cancer cells," *Nano Letters*, vol. 7, no. 5, pp. 1318–1322, 2007.

[135] Y. Haba, C. Kojima, A. Harada, T. Ura, H. Horinaka, and K. Kono, "Preparation of poly(ethylene glycol)-modified poly(amido amine) dendrimers encapsulating gold nanoparticles and their heat-generating ability," *Langmuir*, vol. 23, no. 10, pp. 5243–5246, 2007.

[136] D. K. Kirui, D. A. Rey, and C. A. Batt, "Gold hybrid nanoparticles for targeted phototherapy and cancer imaging," *Nanotechnology*, vol. 21, no. 10, Article ID 105105, 2010.

[137] X. Huang, I. H. El-Sayed, W. Qian, and M. A. El-Sayed, "Cancer cell imaging and photothermal therapy in the near-infrared region by using gold nanorods," *Journal of the American Chemical Society*, vol. 128, no. 6, pp. 2115–2120, 2006.

[138] X. Huang, I. H. El-Sayed, and M. A. El-Sayed, "Applications of gold nanorods for cancer imaging and photothermal therapy," *Methods in Molecular Biology*, vol. 624, pp. 343–357, 2010.

[139] W. S. Kuo, C. N. Chang, Y. T. Chang et al., "Gold nanorods in photodynamic therapy, as hyperthermia agents, and in near-infrared optical imaging," *Angewandte Chemie - International Edition*, vol. 49, no. 15, pp. 2711–2715, 2010.

[140] B. Van De Broek, N. Devoogdt, A. Dhollander et al., "Specific cell targeting with nanobody conjugated branched gold nanoparticles for photothermal therapy," *ACS Nano*, vol. 5, no. 6, pp. 4319–4328, 2011.

[141] L. R. Hirsch, R. J. Stafford, J. A. Bankson et al., "Nanoshell-mediated near-infrared thermal therapy of tumors under magnetic resonance guidance," *Proceedings of the National Academy of Sciences of the United States of America*, vol. 100, no. 23, pp. 13549–13554, 2003.

[142] C. Loo, L. Hirsch, M. H. Lee et al., "Gold nanoshell bioconjugates for molecular imaging in living cells," *Optics Letters*, vol. 30, no. 9, pp. 1012–1014, 2005.

[143] C. Loo, A. Lowery, N. Halas, J. West, and R. Drezek, "Immunotargeted nanoshells for integrated cancer imaging and therapy," *Nano Letters*, vol. 5, no. 4, pp. 709–711, 2005.

[144] X. Huang, P. K. Jain, I. H. El-Sayed, and M. A. El-Sayed, "Plasmonic photothermal therapy (PPTT) using gold nanoparticles," *Lasers in Medical Science*, vol. 23, no. 3, pp. 217–228, 2008.

[145] S. B. Brown and S. H. Ibbotson, "Photodynamic therapy and cancer," *BMJ*, vol. 339, Article ID b2459, 2009.

[146] J. Cadet, "The photodynamic therapy of cancer cells," *Photochemistry and photobiology*, vol. 87, no. 1, p. 1, 2011.

[147] A. Lin and S. M. Hahn, "Photodynamic therapy: a light in the darkness?" *Clinical Cancer Research*, vol. 15, no. 13, pp. 4252–4253, 2009.

[148] M. A. MacCormack, "Photodynamic therapy," *Advances in Dermatology*, vol. 22, pp. 219–258, 2006.

[149] P. Zhang, W. Steelant, M. Kumar, and M. Scholfield, "Versatile photosensitizers for photodynamic therapy at infrared excitation," *Journal of the American Chemical Society*, vol. 129, no. 15, pp. 4526–4527, 2007.

[150] B. Ungun, R. K. Prud'homme, S. J. Budijono et al., "Nanofabricated upconversion nanoparticles for photodynamic therapy," *Optics Express*, vol. 17, no. 1, pp. 80–86, 2009.

[151] D. K. Chatterjee and Z. Yong, "Upconverting nanoparticles as nanotransducers for photodynamic therapy in cancer cells," *Nanomedicine*, vol. 3, no. 1, pp. 73–82, 2008.

[152] H. S. Qian, H. C. Guo, P. C. L. Ho, R. Mahendran, and Y. Zhang, "Mesoporous-silica-coated up-conversion fluorescent nanoparticles for photodynamic therapy," *Small*, vol. 5, no. 20, pp. 2285–2290, 2009.

6. GENERAL OBJECTIVES

The studies presented in this Thesis aim to optimise an Au-nanoprobe based technique for the detection of oncogenes' transcripts (*c-Myc* and *BCR-ABL*) that can be used for the evaluation of the expression profile in cancer cells, while simultaneously developing an innovative platform of multifunctional gold nanoparticles loaded with, cell penetrating peptides, tumoral marker, polymers and siRNA capable of silencing the selected proto-oncogenes, which can be used to evaluate the level of expression and determine the efficiency of silencing.

This work is a part of an ongoing collaboration between Faculdade de Ciência e Technologia-Universidade Nova de Lisboa and IUI of Nanoscience of Aragon at the University of Zaragoza within a European project [NanoScieE+ - Nanotruck].
The NANOTRUCK project intends to develop an innovative kind of multifunctional gold nanoparticles loaded with fluorescent, tumoral markers, cell penetrating peptides and RNAi complementary to the proto-oncogene *c-Myc* for cancer diagnosis and treatment. The fellow worked on the synthesis and functionalization of the multifunctional gold nanoparticles and on the in vitro studies for the silencing of *c-Myc* gene in human cells. From this work, he has broadened his experience in techniques in the molecular genetics field such as the cloning of constructs for applications in gene therapy and techniques related with the small interfering RNA approach for gene silencing.

This project implies the collaboration with different groups in Europe with expertise in different subfields: Centre for Cell Engineering (University of Glasgow, UK), Instituto di Cibernetica "E. Caianiello" (Pozzuoli, Italy), Helmholtz Zentrum München (München, Germany), Science and Technology Faculty, New University of Lisbon (Lisbon, Portugal) and IUI of Nanoscience of Aragon at the University of Zaragoza (Zaragoza, Spain). Thanks to these collaborations, the interaction between nanoparticles and biological systems, ranging from in vitro cultured human cells to in vivo animal models (primitive Hydra and complex vertebrate mouse) were studied. From this work, the fellow acquired experience in the diagnostics and therapy fields, as can be seen from his publications on the development of nanosystems for the combined diagnostics/therapeutics (theranostics) involving DNA/RNA detection with strong impact in genetic diagnostics and for gene delivery and silencing systems of relevance for therapy strategies, with particular focus on enabling the development of safer, more efficient, and specific platforms to human disease.

Overall, the objectives of this Thesis are:

- Synthesis and characterisation of thiol-modified ssDNA gold nanoparticles – Au-nanoprobes suitable for the specific detection of the oncogenes' mRNA sequences via non-cross-linking method.

- Optimisation of the Au-nanoprobe system for evaluation of levels of expression – quantitative and/or semi-quantitative.

- Evaluate efficiency of ssDNA-gold nanoparticles for the inhibition of *in vitro* transcription and *in vitro* translation.

- To use multifunctional gold nanoparticles (tumour markers, cell penetrating peptides, polymers) as vectors for siRNA delivery into tumour cells - evaluation of siRNA load by means of standard spectrophotometry and fluorescence labelled oligonucleotides.

- To evaluate the transfection level of siRNA-nanoconjugates by fluorescence techniques (i.e. fluorescence and confocal microscopy)

- To evaluate the silencing efficiency by the previously optimised siRNA-nanoconjugates system in comparison to qRT-PCR.

For this, we used several molecular biology techniques useful for the biomedical applications of nanoparticles (Human Cell culture, Microbiology, Confocal Microscopy, Electrophoresis, Real-Time PCR, etc), and skills useful in the development of applications of nanoparticles in gene therapy (plasmid DNA cloning, Antisense and RNA interference methodologies, work with reporter vectors such as EGFP and luciferase gene expression) and different techniques for nanoparticle characterization (Atomic Force Microscopy, Scanning Electron Microscopy, Transmission Electron Microscopy, Light-Scattering microscopy, FT-IR, Zeta potential, Dynamic Light Scattering, Fluorescence, UV-VIS molecular absorption, etc).

❷

Gold Nanoparticles as Nanosensors for Diagnostics

OVERVIEW

This section presents 3 articles related to the studies on noble metal nanoparticles as nanosensors for cancer diagnostics.

Article A describes the detection and quantification of the *BCR-ABL* gene fusion using DNA thiol-modified gold nanoparticles. In a proof-of-concept experiment we developed an Au-nanoprobe based approach for the molecular recognition of *BCR-ABL* b3a2 fusion that constitute a promising tool in early diagnosis of chronic myelogenous leukemia (CML). The detection procedure is an application of the non-cross-linking Au-nanoprobe method that makes use of the gold nanoparticles' optical properties.

These studies were extended to the simultaneous identification of different mRNA targets in CML using colour multiplexing with other noble metal nanoparticles like gold-silver alloy nanoparticles in **Article B** and **Article C**. In **Article B** we extensively described the protocol for synthesis and functionalization of gold and gold-silver alloy nanoparticles for diagnostic applications.

All these studies were performed at the Research Centre for Human Molecular Genetics, Dept. of Life Sciences at Science and Technology Faculty, New University of Lisbon.

Article A

"RNA Quantification using Gold Nanoprobes - application to Cancer Diagnostics." **João Conde**, J.M. de la Fuente and P.V. Baptista. **Journal of Nanobiotechnology** (2010), Vol. 8, pp. 1-8. *Research article* IF=not yet determined by ISI (unofficial=5.09)

Article B

"RNA Quantification Using Noble Metal Nanoprobes: Simultaneous Identification of Several Different mRNA Targets Using Colour Multiplexing and Application to Cancer Diagnostics." **João Conde**, G. Doria, J.M. de la Fuente and P.V. Baptista. Nanoparticles in Biology and Medicine: Methods and Protocols Series. **Methods in Molecular Biology** (2012), Vol. 906, pp. 71-87. Humana Press, Springer Protocols.

Article C

"Alloy Metal Nanoparticles for Multicolour Cancer Diagnostics." P.V. Baptista, G. Doria, **João Conde**. **Proceedings of SPIE** (2011), Vol. 7909, 79090K-1, Colloidal Quantum Dots/Nanocrystals for Biomedical Applications VI. *Proceedings article*

Articles A, B, C

Declaration of authorship

I, João Diogo Osório de Castro Conde, declare that the manuscripts preparation and writing was carried out by me, Prof. Pedro V. Baptista, Prof. Jesus M. de la Fuente, and all the associated co-authors.

João Conde contributions:

Article A – JC participated in the sequence alignment and design of all the nanoprobes, carried out all the nanoprobe synthesis, and performed all the detection assays. JC also drafted the manuscript and designed all the figures.

Article B – JC designed all the gold nanoprobes and carried out all the gold nanoprobe synthesis. JC also drafted some of the manuscript protocols and figures.

Article C – JC helped in the design of some of the *BCR-ABL* related detection assays.

We, Pedro V. Baptista and Jesus M. De la Fuente, as supervisors of João Conde hereby acknowledge and confirm that the information above is correct.

João Conde

Pedro V. Baptista

Jesus M. de la Fuente

JOURNAL OF NANOBIOTECHNOLOGY

RESEARCH Open Access

RNA quantification using gold nanoprobes - application to cancer diagnostics

João Conde[1], Jesús M de la Fuente[2], Pedro V Baptista[1*]

Abstract

Molecular nanodiagnostics applied to cancer may provide rapid and sensitive detection of cancer related molecular alterations, which would enable early detection even when those alterations occur only in a small percentage of cells. The use of gold nanoparticles derivatized with thiol modified oligonucleotides (Au-nanoprobes) for the detection of specific nucleic acid targets has been gaining momentum as an alternative to more traditional methodologies. Here, we present an Au-nanoparticles based approach for the molecular recognition and quantification of the *BCR-ABL* fusion transcript (mRNA), which is responsible for chronic myeloid leukemia (CML), and to the best of our knowledge it is the first time quantification of a specific mRNA directly in cancer cells is reported. This inexpensive and very easy to perform Au-nanoprobe based method allows quantification of unamplified total human RNA and specific detection of the oncogene transcript. The sensitivity settled by the Au-nanoprobes allows differential gene expression from 10 ng/μl of total RNA and takes less than 30 min to complete after total RNA extraction, minimizing RNA degradation. Also, at later stages, accumulation of malignant mutations may lead to resistance to chemotherapy and consequently poor outcome. Such a method, allowing for fast and direct detection and quantification of the chimeric *BCR-ABL* mRNA, could speed up diagnostics and, if appropriate, revision of therapy. This assay may constitute a promising tool in early diagnosis of CML and could easily be extended to further target genes with proven involvement in cancer development.

Background

The National Cancer Institute envisions that over the next years, nanotechnology will result in significant advances in early detection, molecular imaging, targeted and multifunctional therapeutics, prevention and control of cancer [1]. Nanodiagnostics is a burgeoning field as more and improved techniques are becoming available for clinical diagnostics with increased sensitivity at lower costs [2-10]. Due to their optical properties, gold nanoparticles (AuNPs) have been used for DNA/RNA screening approaches, namely via functionalization with thiolated oligonucleotides (Au-nanoprobes), capable of specifically hybridizing with a complementary oligonucleotide sequence [9].

The surface plasmon resonance (SPR) of AuNPs is responsible for the intense colors - monodisperse Au-nanoprobes (≈ 13 nm) appear red and exhibit a narrow SPR band centered around 520 nm; a solution containing aggregated Au-nanoprobes appears blue, due to a red shift of the SPR. Our method relies on visual and/or spectroscopy comparison of solutions before and after salt induced Au-nanoprobe aggregation -presence of complementary target prevents aggregation and the solution remains red (SPR peak at ± 520 nm); non-complementary targets do not prevent Au-nanoprobe aggregation, resulting in a visible change of color from red to blue (red-shift of the SPR peak to 600-650 nm) [5-7]. The principle of gold nanoparticles assay method detection of RNA hybridization is depicted in Figure 1. This non-cross-linking method has already been successfully applied for detection of eukaryotic gene expression without reverse transcription or PCR amplification steps [6], and for *Mycobacterium tuberculosis* detection [7,8].

Chronic myeloid leukemia (CML) is a clonal neoplastic disease of the hematopoietic stem cell, whose hallmark molecular event is the genetic t(9;22)(q34;q11) translocation known as the Philadelphia (Ph) chromosome [11,12]. This translocation - *ABL* gene (chromosome 9) and *BCR* gene (chromosome 22) - originates a *BCR-ABL* fusion gene, leading to the expression of a

* Correspondence: pmvb@fct.unl.pt
[1]CIGMH, Departamento de Ciências da Vida, Faculdade de Ciências e Tecnologia, Universidade Nova de Lisboa, Campus de Caparica, 2829-516 Caparica, Portugal

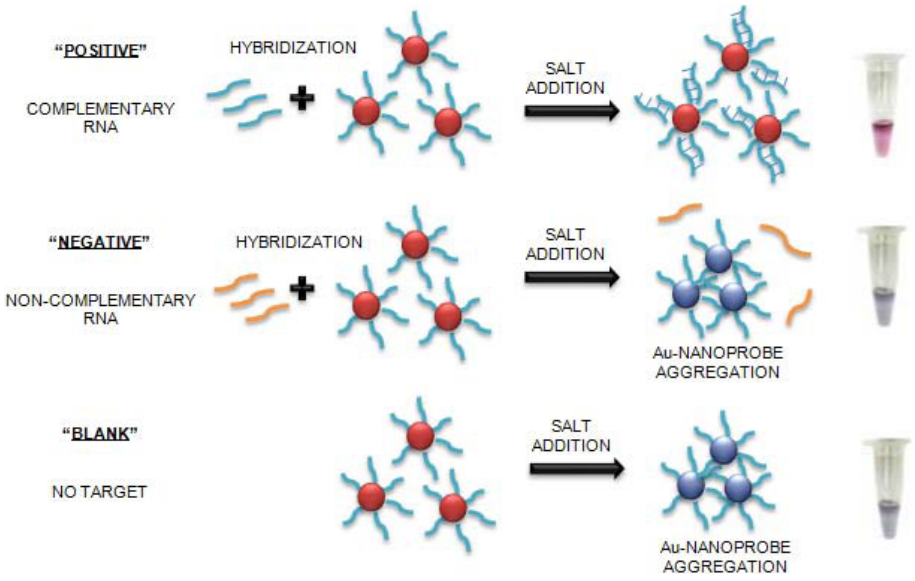

Figure 1 Schematic representation of Au-nanoprobe assay method. The assay is based on the increased stability of the Au-nanoprobes upon hybridization with the complementary RNA target in solution, while non-hybridized Au-nanoprobes easily aggregate once the solution's ionic strength is increased. Positive: sample in the presence of complementary RNA; Negative: sample in the presence of non-complementary RNA; Blank: Au-nanoprobe alone (no target).

chimeric BCR-ABL protein with tyrosine-kinase activity [13-15]. The most commonly used procedures for the initial diagnosis and management of CML patients are expensive and time consuming, e.g karyotype analysis, reverse transcriptase polymerase chain reaction analyses (RT-PCR) and fluorescence in-situ hybridization (FISH) [16-18]. Therefore, there is a need for molecular methods able to detect and quantify the *BCR-ABL* fusion transcripts, which is of paramount relevance when monitoring minimal residual disease and genetic recurrence in patients known to harbor the translocation [19,20].

Here we present an Au-nanoprobe based approach for the molecular recognition and quantification of *BCR-ABL* b3a2 (e14a2) fusion for the early diagnosis of CML, which is inexpensive very easy to perform and uses total human RNA as target without reverse transcription and/or amplification.

Methods

Probe design and Au-nanoprobe synthesis

The probe sequence 5'-thiol-CGCTGAAGGGCTTTTGAACT-3' and the complementary target derive from the *BCR-ABL* b3a2 (e14a2) chimeric protein mRNA (Gene-Bank accession no. AJ 131466.1: 5'-TGGATTTAAGCAGAGTTCAAAAGCCCTTCAGCGGCCAGTA-3'), and the control oligonucleotide target sequences: *BCR* (Gene-Bank accession no. NM 021574.2: 5'-TGGATTTAAGCAGAGTTCAAATCTGTACTGCACCCTGGAG-3'), *ABL* (Gene-Bank accession no. NM 005157.3: 5'-CTCCAGCTGTTATCTGGAAGAAGCCCTTCAGCGGCCAGTA-3') and an unrelated target (5'-AGGAAAACGATTCCTTCTAACAGAAATGTCCTGAGCAATC-3'). The way these sequences relate to each other is illustrated in Figure 2.

The 13 nm gold nanoparticles were prepared by the citrate reduction method described by Lee and Meisel [21]. The thiolated oligonucleotide was dissolved in 1 ml of 0.1 M DTT, extracted three times with ethyl acetate, and further purified through a desalting NAP-5 column (Pharmacia Biotech, Sweden) according to the manufacturer's instructions. The Au-nanoprobe was prepared as described in Baptista et al [5]. Briefly, 500 μl of 10 μM thiol modified oligonucleotide was initially incubated with 6 ml of an aqueous solution of AuNPs (≈8.55 nM) for at least 16 h. After centrifugation (20 min at 14500 G), the oily precipitate was washed with 5 ml of 10 mM phosphate buffer (pH 8.0), 0.1 M NaCl, recentrifuged and redispersed in 5 ml of the same buffer to a final concentration in AuNPs of 8.5 nM. The resulting Au-nanoprobe was stored in the dark at 4°C.

Cell culture and total RNA isolation

K562 erythroleukemic cells (*BCR-ABL* positive cell line derived from CML patients in blast crisis) and HL-60 cell line, a human leukemic promyelocytic cell line (*BCR-ABL* negative) were cultured in 90% RPMI 1640 and 10% FBS at 37°C with 5% CO_2. *Saccharomyces cerevisae* cells were grown in YPD medium at 30°C

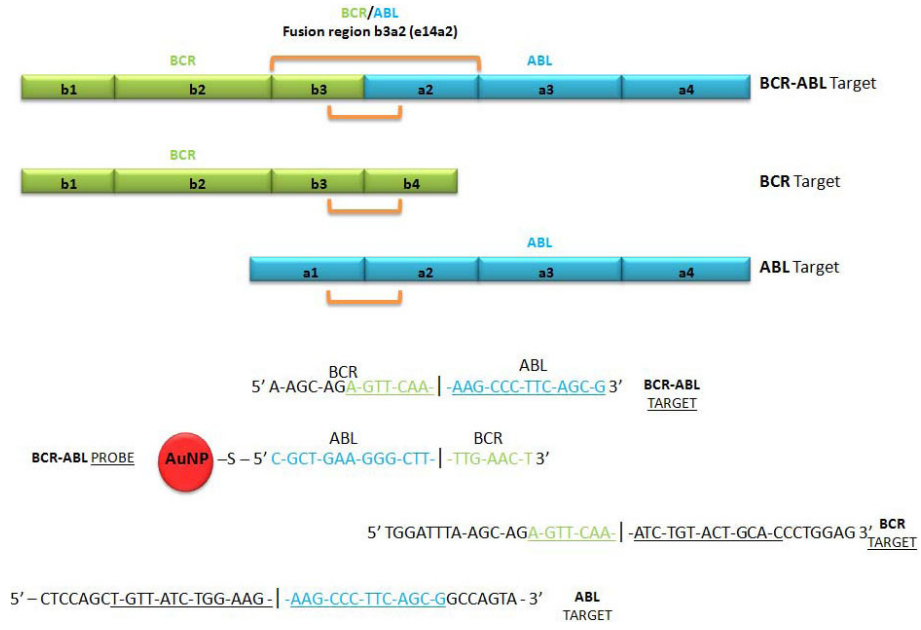

Figure 2 Oligonucleotide probe and target sequences designed for *BCR-ABL* b3a2 (e14a2) junction and for *BCR* and *ABL* genes. Complementary and non-complementary target sequences were used to study the level of specific interaction between the target and the Au-nanoprobes. *BCR-ABL* fusion positive (100% complementary); *BCR* and *ABL* gene sequences were used as controls (50% non-complementary); and a completely unrelated sequence (100% non-complementary) was used as negative control.

overnight. Human peripheral blood mononuclear cells (PBMC) from control individuals were separated from 3 ml of heparinized peripheral venous blood by Ficoll gradient (Histopaque®-1077, Sigma-Aldrich, St. Louis, USA) according to manufacturer's specifications. Isolation of total RNA was performed using a High Pure RNA Isolation Kit (Roche Applied Science) according to the manufacturer's protocol. RNA concentration was determined by UV photometry and the RNA was stored at -80°C until use. RNA integrity was evaluated on a 1% agarose gel stained by GelRed™.

Reverse transcription (RT) and PCR amplification

Total RNA extracted from K562 cells was subjected to RT with Revert-AidTM M-MuLV Reverse Transcriptase (Fermentas, Vilnius, Lithuania) according to the manufacturer's specifications, using 20 μM of BCR-ABLreverse primer, annealing at 42°C for 1 h and 70°C for 10 min to inactivate the reverse transcriptase. The reverse transcription reaction product, a 273-bp fragment of the human *BCR-ABL* fusion gene (b3a2 junction), was PCR amplified using primers BCR-ABLforward (18 nt): 5'-AGTCTCCGGGGCTCTATG-3' and BCR-ABLreverse (20 nt): 5'-GATTATAGCCTAAGACCCGG-3'. PCR amplification of the b3a2 region was carried out in 25 μl using 0.25 μM of primers, 0.2 mM dNTPs with 1 U Taq DNA polymerase (Amersham Biosciences, GE Healthcare, Europe, GmbH). The PCR reactions were performed in duplicate on a MyCycler Thermocycler (Bio-rad). Thermal cycling conditions consisted of denaturation at 95°C for 5 min and 30 cycles of amplification, each cycle consisting of denaturation of 95°C for 30 s, annealing at 52°C for 30 s, elongation was at 72°C for 30 s and final elongation at 72°C for 5 min and cooling at 4°C. The sequence of the PCR products was confirmed by sequencing.

Real-Time RT-PCR assay

The Real-Time PCR amplification was performed in a Corbett Research Rotor-Gene RG3000 using SYBR GreenER Real-Time PCR Kit (Invitrogen, Karlsbad, CA, USA) according to manufacturer's specifications in 50 μl reactions containing cDNA from K562 and HL-60 cell-lines, 1× SYBR Green SuperMix and 200 nM of BCR-ABLforward and BCR-ABLreverse. The amplification conditions consisted of 50°C for 2 min hold, 95°C during 10 min hold, followed by 40 cycles consisting of denaturation at 95°C for 30 s, annealing at 52°C for 30 s, extension at 72°C for 30 s, with a final extension step at 72°C for 5 min. All the results were originated from three independent experiments.

Au-nanoprobe hybridization and color detection

The Au-nanoprobe assay was performed in a total volume of 30 μl containing the Au-nanoprobe at a final concentration of 2.5 nM, the appropriate targets

at a final concentration of 100 fmol/μl (100% complementary *BCR-ABL* target; 50% complementary *BCR* and *ABL* targets, and 100% non-complementary target) in 10 mM phosphate buffer (pH 8.0). Total RNA was used at a final concentration 10-60 ng/μl [100% complementary K562 cells RNA (*BCR-ABL* Positive); non-complementary HL-60 cells RNA (*BCR-ABL* Negative)]. Blank measurements were made in exactly the same conditions but replacing target or total RNA for an equivalent volume of 10 mM phosphate buffer (pH 8.0).

Following 5 min of denaturation at 95°C, the mixtures were allowed to stand for 30 min at 25°C and 0.3 M $MgCl_2$ was added at a final concentration of 0.16 M. After 15 min at room temperature for color development, photographs were taken and assayed by UV-visible spectroscopic measurements of the SPR band. Absorption spectra were performed in a UNICAM, model UV2, UV-visible spectrophotometer with Ultra-Micro quartz cells (Hellma, Germany), using 10 mM phosphate buffer (pH 8.0), 0.1 M NaCl as reference. The areas under the curve ($AUC_{500\ nm\text{-}560\ nm}/AUC_{570\ nm\text{-}630\ nm}$) were calculated with the values for absorbance for 500 nm-600 nm/570 nm-630 nm using the trapezoidal rule.

Results and Discussion

Gold nanoprobe assay for target detection

First, we used thiolated ssDNA, complementary to the fusion site of the *BCR-ABL* mRNA, to functionalize gold nanoparticles and produce specific Au-nanoprobes. These nanoprobes were assessed in terms of specificity by means of total RNA mixtures spiked in with synthetic oligonucleotides harboring the fusion site *BCR-ABL* b3a2. It should be noted that, in reality, patients may only harbor one copy of the fusion gene and the remaining copies of normal *ABL* and *BCR* should be still functional, thus expressing the normal mRNA sequence. Two oligonucleotides, each harboring the normal sequence of the *BCR* and *ABL* genes respectively, were used to evaluate the probe's capability to discriminate from similar sequences. Following salt addition, the presence of the respective complementary synthesized target, protected the Au-nanoprobes from aggregation and the solution remained red; whereas the presence of non-complementary targets does not protect from aggregation and the solution turned blue (*BCR* and *ABL* controls only 50% complementary to the Au-nanoprobe) - Figure 3A. Absence of any target results in extensive aggregation (Blank). Only full hybridization of the Au-nanoprobe to a fully complementary synthetic sequence (*BCR-ABL* fusion sequence) avoids aggregation, whereas semi-complementary targets (normal *ABL* and *BCR* gene sequence) do not show the same capability.

Based on the UV/Vis spectra (see Figure 4) obtained after inducing aggregation, Au-nanoprobe aggregation was evaluated in terms of SPR variation, i.e. a ratio between the free and aggregated fractions after 15 min incubation with [$MgCl_2$] = 0.16 M. The ratio between the areas under the curve of the SPR was calculated using the trapezoidal rule - $AUC_{500\ nm\text{-}560\ nm}/AUC_{570\ nm\text{-}630\ nm}$. A ratio of 1 may be considered as the point of equilibrium between non-aggregated and aggregated nanoprobe, hence the threshold to respectively consider the positive and negative discrimination of sequences (positive identification of complementary target ratio >1). Commonly, for discriminating between two significantly different aggregation levels, as for example in a YES/NO for identification of a given target, the ratio between the peaks at 520 nm and 600 nm is usually used. However, for identifying small differences in aggregation levels between two quantities for the same target, there is a need to decrease the noise level in the spectra. When establishing a ratio between two absorbance values, the error increases mainly due the noise in the spectra, which can be overcome (i.e. strongly reduced) by using an integral of the signal, i.e. the area under the curve.

The Au-nanoprobes were then used for the detection of the *BCR-ABL* b3a2 fusion mRNA in total RNA extracted from K562 cells (*BCR-ABL* positive cell line), HL-60 cells (*BCR-ABL* negative cell line), human peripheral blood mononuclear cells (PBMC) and *S. cerevisiae* cells - Figure 3B. Total RNA from HL-60 cell line and PBMC only express the normal *BCR* and *ABL* transcripts, which are 50% complementary to the probe sequence. Total RNA from an unrelated organism (*S. cerevisae*) was used to confirm specificity of the detection method. The results originate from a minimum of three individual parallel hybridization experiments. *BCR-ABL* fusion discrimination was observed only for samples containing the complementary RNA target (K562 cells). Samples containing the normal *BCR* and *ABL* genes showed a minor stabilization of the Au-nanoprobe, yet below the threshold for positive identification of the target (ratio <1).

Gold nanoprobe assay for RNA quantification

Once the specific identification of the target sequence was achieved, the Au-nanoprobes were used to evaluate both the limit of detection and quantification potential. For this purpose, different concentrations of the specific synthetic oligonucleotide target were used to spike in 20 ng/μl of total RNA extracted from the *BCR-ABL* negative cell line HL-60. Our data indicate a linear correlation (R^2 = 0.9966) between the $AUC_{500\ nm\text{-}560\ nm}/AUC_{570\ nm\text{-}630\ nm}$ for target concentration range between 33 and 133 fmol/μl (Figure 5). A non-complementary target was used in a parallel spike in

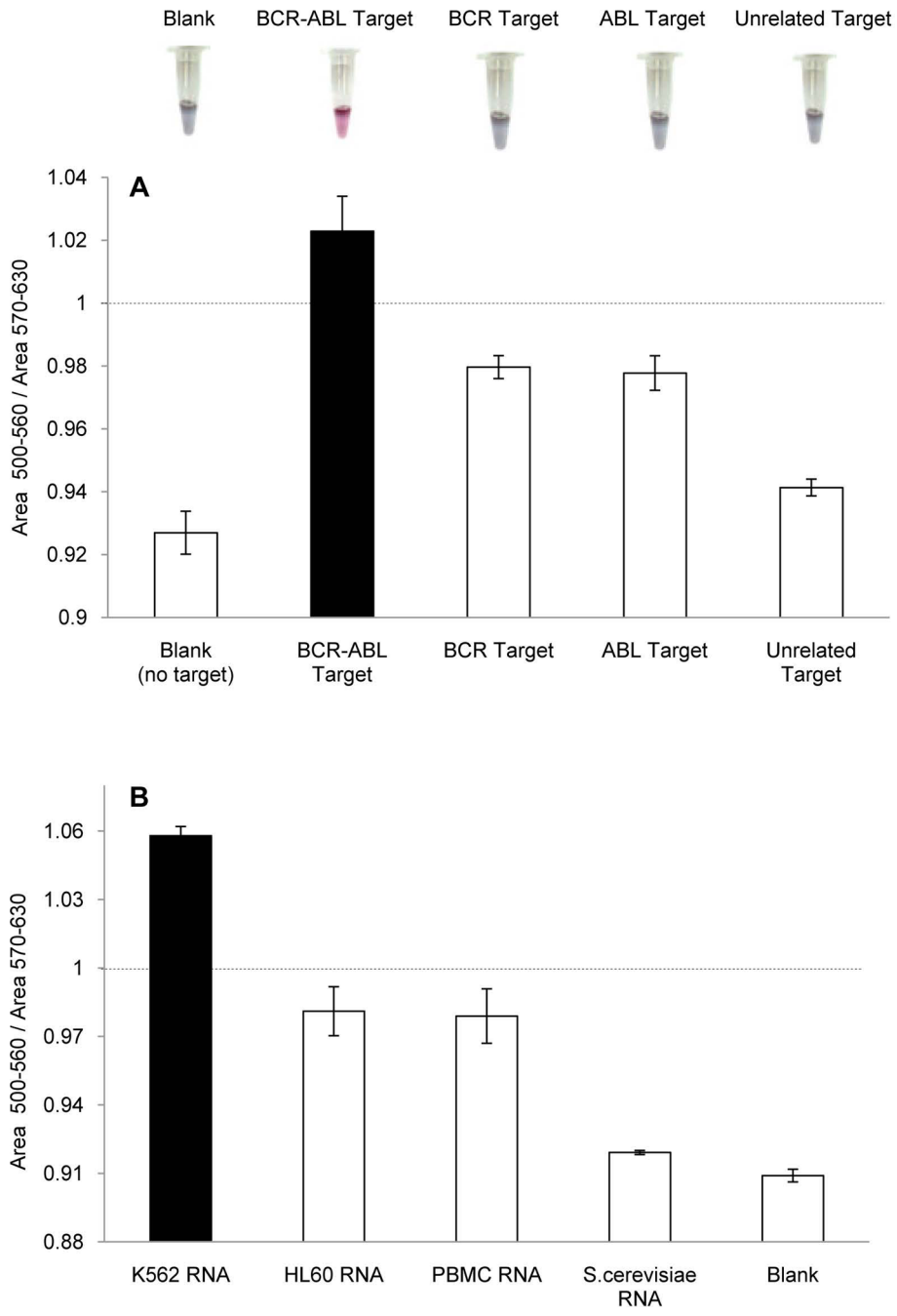

Figure 3 Au-nanoprobe detection of the *BCR-ABL* fusion gene sequence. (**A**) Colorimetric assay (above) and respective spectrophotometry (below) relative to the detection of synthetic *BCR-ABL* oligonucleotide target. Oligonucleotides with *BCR* or *ABL* sequence only (showing 50% complementarity) were used as controls and an unrelated target (showing 100% non-complementarity to the Au-nanoprobe) as negative control. (**B**) Detection of *BCR-ABL* in total RNA from K562 cell line, HL-60 cell line and human PBMC (harboring 50% complementary targets to the nanoprobe) and *S. cerevisiae* cells (100% non-complementary). Nanoprobe aggregation as measured by ratio of $AUC_{500\ nm\text{-}560\ nm}/AUC_{570\ nm\text{-}630\ nm}$. The dashed line represents the threshold of 1 considered for discrimination between Positive and Negative. The error bars represent the standard deviation from three independent assays.

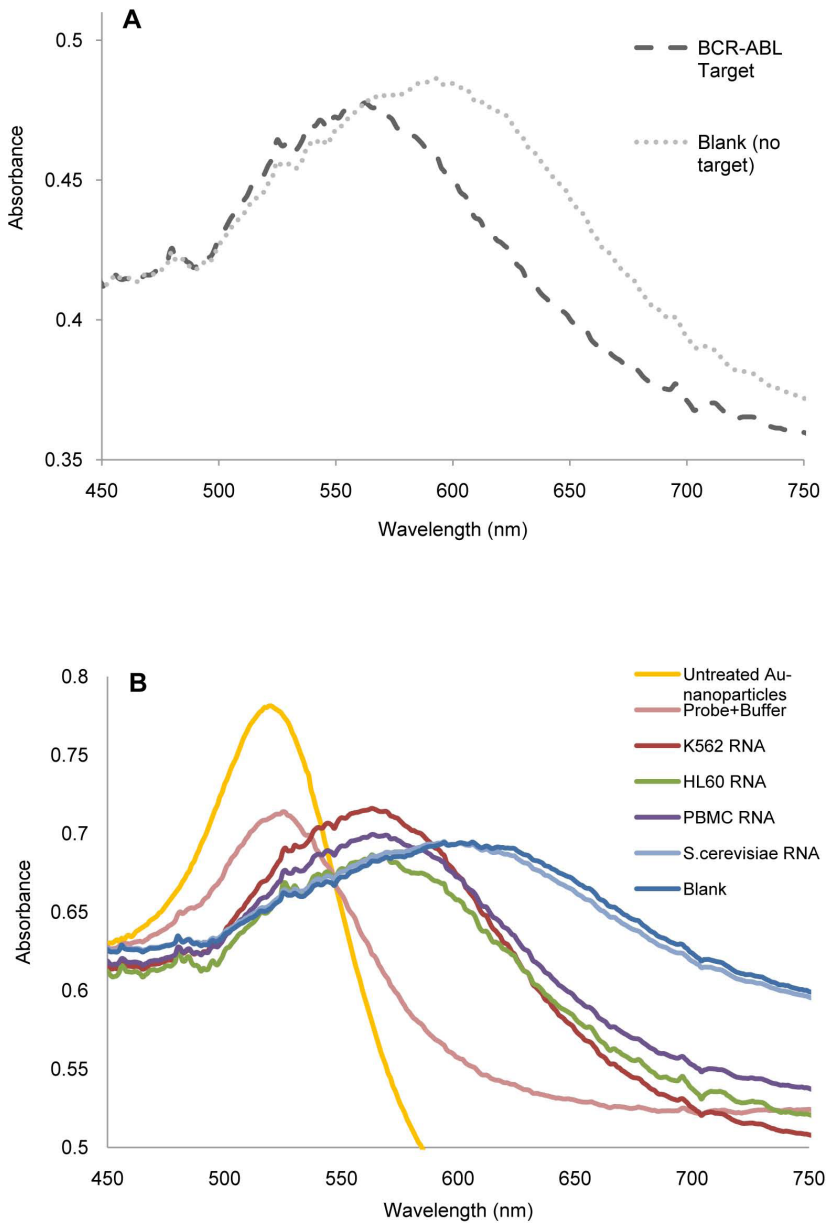

Figure 4 Au-nanoprobe UV/Vis spectra obtained after inducing aggregation. (**A**) UV/Vis spectra in absence (Blank) and in presence of target (*BCR-ABL* target). (**B**) UV/Vis spectra for the detection of the *BCR-ABL* b3a2 fusion mRNA in total RNA from K562 cells (*BCR-ABL* positive cell line), HL-60 cells (*BCR-ABL* negative cell line), human PBMC and *S. cerevisiae* cells; Au-nanoprobe alone before (Au-nanoprobe + buffer) and after (Blank) salt addition. All samples in 10 mM phosphate buffer (pH 8.0). Also, spectral data from untreated Au-nanoparticles in sodium citrate.

experiment, where extensive aggregation of the Au-nanoprobe was observed for all tested concentrations.

In order to validate the detection and quantification potential of the Au-nanoprobes in the positive cell line (K562), Real-time RT-PCR was used. Our method showed a linear correlation for *BCR-ABL* detection within the range of 10-60 ng/μl of total RNA (see Figure 6). A linear association (R^2 = 0.9171) was found between the two methods, Real-Time RT-PCR and Au-nanoprobe, for *BCR-ABL* detection (**inset in Figure** 6). Real-Time RT-PCR is a more robust and sensitive technique but time consuming, more expensive and requiring expensive equipment and highly trained personnel.

Conclusions

In conclusion, we demonstrated the potential of an Au-nanoprobe based assay for the specific identification and quantification of aberrant expression of genes involved

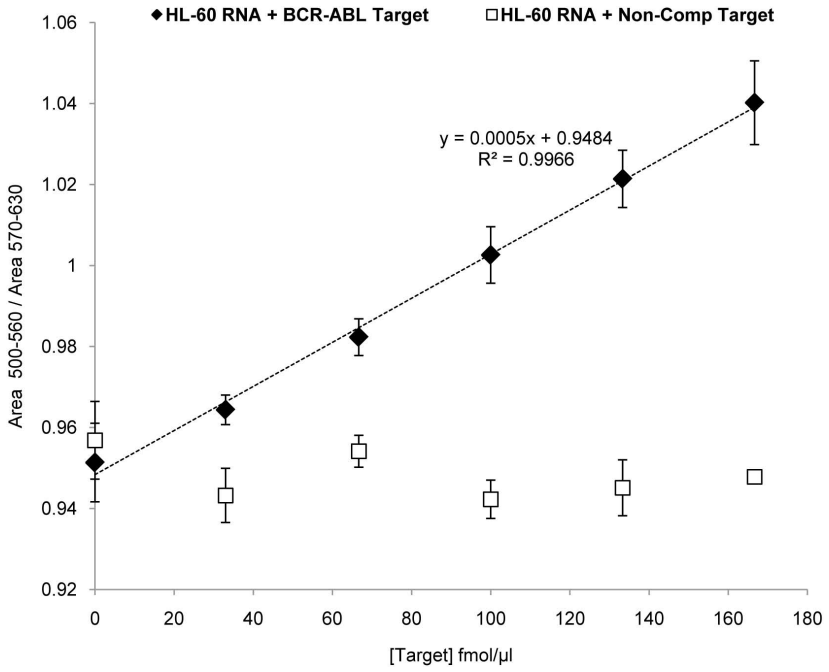

Figure 5 Quantification of *BCR-ABL* by Au-nanoprobe. Ratio $AUC_{500\ nm-560\ nm}/AUC_{570\ nm-630\ nm}$ as function of specific target concentration in mixtures of 20 ng/µl total RNA from *BCR-ABL* negative cell line HL-60 spiked in with increasing concentrations of the synthetic oligonucleotide (black diamond's - complementary target; blank squares - non-complementary target). The error bars represent the standard deviation from three independent assays.

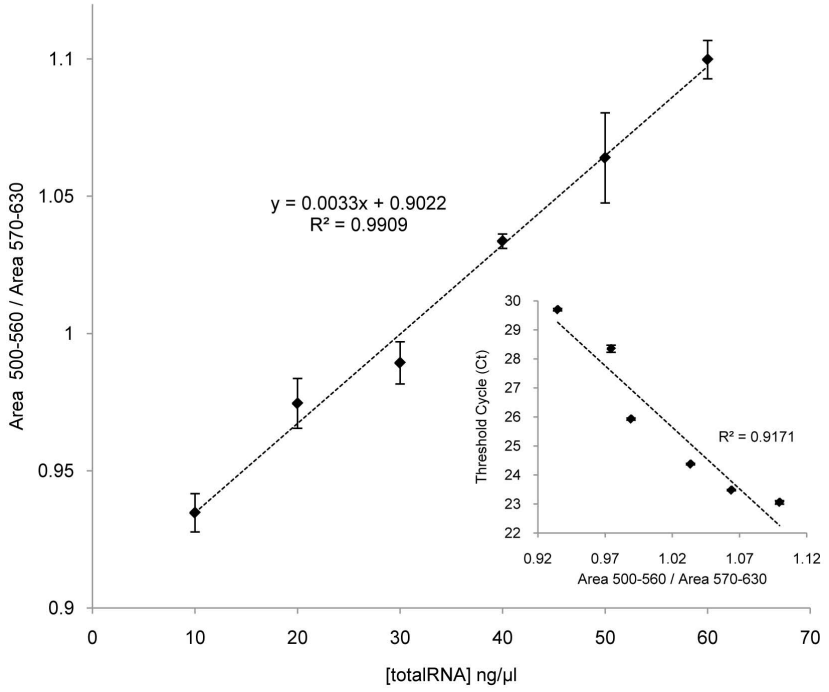

Figure 6 Au-nanoprobe based quantification of *BRC-ABL* fusion mRNA directly in total RNA extracted from K562 cell line. Nanoprobe aggregation as measured by ratio of $AUC_{500\ nm-560\ nm}/AUC_{570\ nm-630\ nm}$ for increasing concentrations of total RNA from a *BCR-ABL* positive cell line (K562) - 10 to 60 ng/µl. (**Inset**) Real-Time RT-PCR *vs.* Au-Nanoprobe Assays. A linear association (R^2 = 0.9171) was found between the two methods. The error bars represent the standard deviation from three independent assays.

in cancer development. This Au-nanoprobe strategy allowed for detection of less than 100 fmol/μl of a specific RNA target, with the possibility of discriminating between a positive and negative from as little as 10 ng/μl of total RNA. As proof-of-concept we used the *BCR-ABL* fusion product that is of paramount importance in chronic myeloid leukemia, showing the application potential in cancer diagnosis. To our knowledge, this is the first report on quantification of human mRNA directly from total RNA without reverse transcription or amplification. The assay has a total work-up time of less than 45 minutes with comparable sensitivity to those demonstrated by traditional molecular biology methodologies.

List of Abbreviations

(CML): Chronic myeloid leukemia; (AuNPs): Gold nanoparticles; (Au-nanoprobes): Gold nanoprobes; (SPR): Surface plasmon resonance; (Ph) chromosome: Philadelphia; (PBMC): Peripheral blood mononuclear cells; (AUC): Area under the curve.

Acknowledgements

This work received the financial support of FCT/MCES through grants to CIGMH-FCT/UNL, PTDC/BIO/66514/2006 and PTDC/SAU-BEB/66511/2006. We thank Dr. A.S. Rodrigues for the human cell lines (K562 and HL-60) and M. Mateus for blood samples.

Author details

[1]CIGMH, Departamento de Ciências da Vida, Faculdade de Ciências e Tecnologia, Universidade Nova de Lisboa, Campus de Caparica, 2829-516 Caparica, Portugal. [2]Instituto de Nanociencia de Aragón, Universidad de Zaragoza, Pedro Cerbuna 12, 50009, Zaragoza, Spain.

Authors' contributions

JC participated in the sequence alignment and design of the nanoprobe, carried out the nanoprobe synthesis, and performed the detection assays. JF participated in the design of the study. PB conceived the study, participated in its design and coordination, and drafted the manuscript. All authors read and approved the final manuscript.

Competing interests

The authors declare that they have no competing interests.

Received: 23 November 2009 Accepted: 24 February 2010
Published: 24 February 2010

References

1. National Cancer Institute: [http://nano.cancer.gov/].
2. Mirkin CA, Letsinger RL, Mucic RC, Storhoff JJ: **A DNA-based method for rationally assembling nanoparticles into macroscopic materials.** *Nature* 1996, **382(6592)**:607-609.
3. Storhoff JJ, Lucas AD, Garimella V, Bao YP, Muller UR: **Homogeneous detection of unamplified genomic DNA sequences based on colorimetric scatter of gold nanoparticle probes.** *Nat Biotechnol* 2004, **22(7)**:883-887.
4. Thaxton CS, Georganopoulou DG, Mirkin CA: **Gold nanoparticle probes for the detection of nucleic acid targets.** *Clin Chim Acta* 2006, **363(1-2)**:120-126.
5. Baptista P, Pereira E, Eaton P, Doria G, Miranda A, Gomes I, Quaresma P, Franco R: **Gold nanoparticles for the development of clinical diagnosis methods.** *Anal Bioanal Chem* 2008, **391(3)**:943-950.
6. Baptista P, Doria G, Henriques D, Pereira E, Franco R: **Colorimetric detection of eukaryotic gene expression with DNA-derivatized gold nanoparticles.** *J Biotechnol* 2005, **119(2)**:111-117.
7. Baptista PV, Koziol-Montewka M, Paluch-Oles J, Doria G, Franco R: **Gold-nanoparticle-probe-based assay for rapid and direct detection of Mycobacterium tuberculosis DNA in clinical samples.** *Clin Chem* 2006, **52(7)**:1433-1434.
8. Costa P, Amaro A, Botelho A, Inácio J, Baptista PV: **Gold nanoprobes assay for identification of mycobacteria from the Mycobacterium tuberculosis complex.** *Clin Microbiol Infect* 2009.
9. Doria G, Franco R, Baptista P: **Nanodiagnostics: fast colorimetric method for single nucleotide polymorphism/mutation detection.** *IET Nanobiotechnol* 2007, **1(4)**:53-57.
10. Griffin J, Singh AK, Senapati D, Lee E, Gaylor K, Jones-Boone J, Ray PC: **Sequence-specific HCV RNA quantification using the size-dependent nonlinear optical properties of gold nanoparticles.** *Small* 2009, **5(7)**:839-845.
11. Hehlmann R, Hochhaus A, Baccarani M: **Chronic myeloid leukaemia.** *Lancet* 2007, **370(9584)**:342-350.
12. Shet AS, Jahagirdar BN, Verfaillie CM: **Chronic myelogenous leukemia: mechanisms underlying disease progression.** *Leukemia* 2002, **16(8)**:1402-1411.
13. Ren R: **Mechanisms of BCR-ABL in the pathogenesis of chronic myelogenous leukaemia.** *Nat Rev Cancer* 2005, **5(3)**:172-183.
14. Wong S, Witte ON: **The BCR-ABL story: bench to bedside and back.** *Annu Rev Immunol* 2004, **22**:247-306.
15. Melo J: **Inviting leukemic cells to waltz with the devil.** *Nat Med* 2001, **7(2)**:156-157.
16. Ou J, Vergilio JA, Bagg A: **Molecular diagnosis and monitoring in the clinical management of patients with chronic myelogenous leukemia treated with tyrosine kinase inhibitors.** *Am J Hematol* 2008, **83(4)**:296-302.
17. Apperley JF: **Part I: mechanisms of resistance to imatinib in chronic myeloid leukaemia.** *Lancet Oncol* 2007, **8(11)**:1018-1029.
18. Burmeister T, Maurer J, Aivado M, Elmaagacli AH, Grunebach F, Held KR, Hess G, Hochhaus A, Hoppner W, Lentes KU, Lubbert M, Schafer KL, Schafhausen P, Schmidt CA, Schuler F, Seeger K, Seelig R, Thiede C, Viehmann S, Weber C, Wilhelm S, Christmann A, Clement JH, Ebener U, Enczmann J, Leo R, Schleuning M, Schoch R, Thiel E: **Quality assurance in RT-PCR-based BCR/ABL diagnostics–results of an interlaboratory test and a standardization approach.** *Leukemia* 2000, **14(10)**:1850-1856.
19. Beillard E, Pallisgaard N, van dVV, Bi W, Dee R, van der SE, Delabesse E, Macintyre E, Gottardi E, Saglio G, Watzinger F, Lion T, van Dongen JJ, Hokland P, Gabert J: **Evaluation of candidate control genes for diagnosis and residual disease detection in leukemic patients using 'real-time' quantitative reverse-transcriptase polymerase chain reaction (RQ-PCR) - a Europe against cancer program.** *Leukemia* 2003, **17(12)**:2474-2486.
20. Gabert J, Beillard E, van dVV, Bi W, Grimwade D, Pallisgaard N, Barbany G, Cazzaniga G, Cayuela JM, Cave H, Pane F, Aerts JL, De MD, Thirion X, Pradel V, Gonzalez M, Viehmann S, Malec M, Saglio G, van Dongen JJ: **Standardization and quality control studies of 'real-time' quantitative reverse transcriptase polymerase chain reaction of fusion gene transcripts for residual disease detection in leukemia - a Europe Against Cancer program.** *Leukemia* 2003, **17(12)**:2318-2357.
21. Lee PC, Meisel D: **Adsorption and surface-enhanced Raman of dyes on silver and gold sols.** *J Phys Chem* 1982, **86(17)**:3391-3395.

doi:10.1186/1477-3155-8-5
Cite this article as: Conde *et al.*: RNA quantification using gold nanoprobes - application to cancer diagnostics. *Journal of Nanobiotechnology* 2010 **8**:5.

Chapter 6

RNA Quantification Using Noble Metal Nanoprobes: Simultaneous Identification of Several Different mRNA Targets Using Color Multiplexing and Application to Cancer Diagnostics

João Conde, Gonçalo Doria, Jesus M. de la Fuente, and Pedro Viana Baptista

Abstract

Nanotechnology provides new tools for gene expression analysis that allow for sensitive and specific characterization of prognostic signatures related to cancer. Cancer is a multigenic complex disease where multiple gene *loci* contribute to the phenotype. The ability to simultaneously monitor differential expression originating from each *locus* allows for a more accurate indication of degree of cancerous activity than either *locus* alone. Metal nanoparticles have been widely used as labels for in vitro identification and quantification of target sequences.

Here we describe the synthesis of nanoparticles with different noble metal compositions in an alloy format that are then functionalized with thiol-modified ssDNA (nanoprobes). We also show how to use such nanoprobes in a non-cross-linking colorimetric method for the direct detection and quantification of specific mRNA targets, without the need for enzymatic amplification or reverse transcription steps. The different metals in the alloy provide for distinct absorption spectra due to their characteristic plasmon resonance peaks. The color multiplexing allows for simultaneous identification of several different mRNA targets involved in cancer development. Comparison of the absorption spectra of the nanoprobes mixtures taken before and after induced aggregation of metal nanoparticles allows to both identify and quantify each mRNA target. We describe the use of gold and gold:silver-alloy nanoprobes for the development of the non-cross-linking method to detect a specific *BCR–ABL* fusion gene (e.g., e1a2 and e14a2) mRNA target associated with chronic myeloid leukemia (CML) using 10 ng μL^{-1} of unamplified total human RNA. This simple methodology takes less than 50 min to complete after total RNA extraction with comparable specificity and sensitivity to the more commonly used methods.

Key words: Gold nanoparticles, Gold:silver alloy nanoparticles, Nanoprobes, Colorimetric method, mRNA detection, Gene expression, Cancer

Mikhail Soloviev (ed.), *Nanoparticles in Biology and Medicine: Methods and Protocols*, Methods in Molecular Biology, vol. 906,
DOI 10.1007/978-1-61779-953-2_6, © Springer Science+Business Media, LLC 2012

1. Introduction

Gene expression detection can provide powerful insights into the chemistry and physiology of biological systems. Cancer cells exhibit deregulation of the cell cycle resulting in uncontrolled growth and they are resistant to programmed death as a result of abnormalities in one or more proteins that inhibit apoptosis. Moreover, alternatively and abnormally expressed mRNAs (e.g., alternatively spliced mRNAs, fusion gene products) are considered as triggers of tumor development. Better understanding of the molecular mechanisms underlying biological processes can be achieved by comparing gene expression between cells in different states or between cells from different tissues, using techniques such as reverse transcription-polymerase chain reaction (RT-PCR) (1–3). However, methods based on reverse transcription are actually based on detection of amplified cDNAs instead of the RNA itself. Direct detection of RNA, especially mRNA, has remained a challenge.

The National Cancer Institute envisions that over the next years, nanotechnology will result in significant advances in early detection, molecular imaging, targeted and multifunctional therapeutics, prevention and control of cancer (4). The use of nanotechnology (materials, devices, or systems) for diagnostics purposes, i.e., nanodiagnostics, has delivered improved techniques for clinical diagnostics with increased sensitivity at lower costs. Due to their optical properties, gold nanoparticles (AuNPs) have been used for DNA/RNA screening approaches, namely via functionalization with thiolated oligonucleotides (Au-nanoprobes), capable of specifically hybridizing with a complementary oligonucleotide sequence (5–12). These optical properties derive from the characteristic surface plasmon resonance (SPR) band that can be easily tailored through the synthesis of NPs with different metal composition, either in an alloy or core–shell structure, e.g., different gold:silver ratios (13, 14).

Baptista and co-workers (15) developed a colorimetric non-cross-linking method where Au-nanoprobes are used to detect the presence of specific DNA and/or mRNA target sequence, which was successfully applied to tuberculosis diagnostics, gene expression studies, and cancer diagnostics (16–20). The method consists in a visual and/or spectrophotometric comparison of solutions before and after salt induced Au-nanoprobe aggregation and the method is outlined in Fig. 1. The presence of a complementary target prevents aggregation and the solution remains red with a strong surface plasmon absorbance peak at ±520 nm. Noncomplementary/mismatched targets do not prevent Au-nanoprobe aggregation, resulting in a visible change of color from red to blue characterized by a concomitant shift in the surface plasmon absorbance from 520 to 600–650 nm. More recently, the same group has developed an

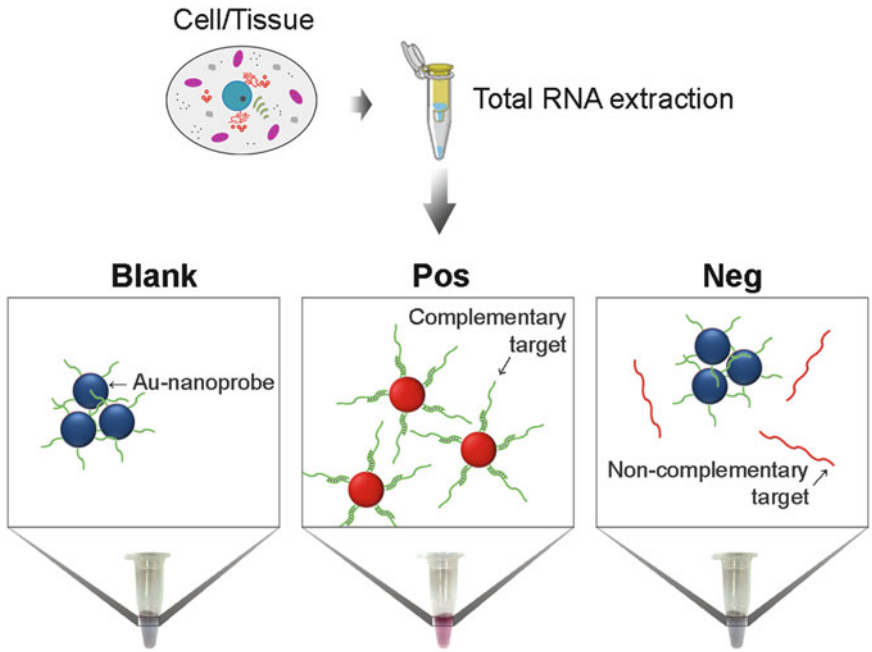

Fig. 1. Schematic of the non-cross-linking assay for RNA quantification. The assay relies on visual comparison of test solutions before and after salt-induced nanoprobe aggregation. "Blank" denotes nanoprobe alone; "Pos" denotes a Positive sample containing complementary mRNA target; "Neg" denotes a Negative sample, where a noncomplementary mRNA is added to the nanoprobe.

one-pot multiplex detection assay by using gold:silver-alloy nanoprobes in conjugation with the Au-nanoprobes (21).

Chronic myeloid leukemia (CML) is a clonal neoplastic disease of the hematopoietic stem cell, and the hallmark molecular event of CML is the genetic t(9;22)(q34;q11) translocation known as the Philadelphia chromosome that is present in >90 % of CML patients (22, 23). This translocation of ABL (chromosome 9) and BCR (chromosome 22) sequences form a BCR–ABL fusion gene, leading to the expression of a chimeric BCR–ABL protein with tyrosine-kinase activity (24). The BCR–ABL abnormal kinase activity is characterized by deregulation of cellular proliferation, decreased adherence of leukemic cells to the bone marrow stroma, and reduced apoptotic activity (25).

Here, we report on the use of gold and gold:silver-alloy nanoprobes for the development of the non-cross-linking method to detect a specific *BCR–ABL* fusion gene (e.g., e1a2 and e14a2) mRNA target associated with CML using 10 ng μL^{-1} of unamplified total human RNA. This simple methodology takes less than 50 min to complete after total RNA extraction with comparable specificity and sensitivity to the more commonly used methods.

2. Materials

2.1. Noble Metal Nanoparticle Synthesis Components

Prepare all solutions using ultrapure grade water, e.g., Milli-Q water (18.2 MΩ-cm at 25 °C) and use analytical grade reagents.

1. Gold(III) chloride trihydrate ($HAuCl_4 \cdot 3H_2O$, ≥49.0 % Au basis).
2. Silver nitrate ($AgNO_3$, ≥99.0 %).
3. Sodium citrate tribasic dihydrate ($HOC(COONa)(CH_2COONa)_2 \cdot 2H_2O$, ≥99.0 %).
4. 4,500 and 250 mL two-neck round bottom flasks equipped with a water-cooled Liebig condenser.
5. Hot plate with magnetic stirrer.
6. 100 and 250 mL Erlenmeyer amber flask with a ground glass cap.
7. *Aqua regia*: Mix three volumes of hydrochloric acid (37 % HCl) with one volume of nitric acid (70 % HNO_3).

2.2. Noble Metal Nanoprobes Synthesis Components

1. 1 M DL-Dithiothreitol (DTT) solution, molecular biology grade. Store at 4 °C until use.
2. Thiol-modified oligonucleotides (5′-thiol-$(CH_2)_6$-ssDNA oligo) containing a complementary sequence to the target(s) of interest (see Note 1 for sequence design tips). The probes given in Table 1 are used to exemplify the specific detection of BCR–ABL fusion gene (e14a2) mRNA, BCR–ABL fusion gene (e1a2) mRNA, and normal ABL gene mRNA. Resuspend the lyophilized thiol-modified oligonucleotides in 100 μL of 1 M DTT and incubate at room temperature for 1 h. Add 900 μL of ultrapure sterile water and mix gently. Store at −20 °C until use.
3. 10 mM phosphate buffer (pH8): 9.32 mM Na_2HPO_4, 0.68 mM NaH_2PO_4. Sterilize by autoclaving and store at 4 °C until use.

Table 1
Oligonucleotide probes

Probes	Sequence (5′-3′)	Gene-Bank acc. number
BCR–ABL (e14a2)	HS-$(CH_2)_6$-CGCTGAAGGGCTTTTGAACT	AJ131466.1
BCR–ABL (e1a2)	HS-$(CH_2)_6$-CGCTGAAGGGCTTCTGCGTC	AF113911.1
ABL (a1a2)	HS-$(CH_2)_6$-CGCTGAAGGGCTTCTTCCAG	NM 005157.3

4. AGEI solution: 2 % (w/v) SDS, 10 mM phosphate buffer (pH 8). Sterilize by filtration (0.22 μm) and store at 4 °C until use. Warm up to 25 °C before use.
5. AGEII solution: 1.5 M NaCl, 0.01 % (w/v) SDS, 10 mM phosphate buffer (pH 8). Sterilize by filtration (0.22 μm) and store at 4 °C until use. Warm up to 25 °C before use.
6. PBS solution: 0.1 M NaCl, 10 mM phosphate buffer (pH 8).
7. Ethyl acetate ($CH_3COOC_2H_5$, ≥99.5 %).
8. NAP-5 columns (GE Healthcare, Sweden).
9. Ultrasound bath S10H (Elma, Germany) or equivalent sonicator (ultrasonic effective power: 30 W; Ultrasonic frequency: 37 kHz).

2.3. Cell Culture Components

1. DMEM: Dulbecco's modified eagle medium.
2. Fetal bovine serum: Heat inactivated. Store at −20 °C until use.
3. CO_2 incubator MCO-96 (Sanyo, UK).

2.4. Total RNA Isolation Components

1. TRIsure® (Bioline, UK).
2. DEPC-treated water: Add 0.1 mL Diethyl Pyrocarbonate (DEPC) for each 100 mL of water to be treated (i.e., 0.1 % (v/v) DEPC) and shake vigorously to bring the DEPC into solution. Incubate the solution at least 1 hour at 37 °C. Autoclave at least 15 min to inactivate any traces of DEPC. Store at 4 °C until use.
3. 75 % ethanol: Add 75 volumes of absolute ethanol to 25 volumes of DEPC-treated water (see Note 2). Store at −20 °C until use.
4. Chloroform.
5. Isopropyl alcohol.

2.5. Non-Cross-Linking Assay Components

1. $MgCl_2$ solution: 0.3 M $MgCl_2$ in deionized water. Store at room temperature.
2. 2.10 mM phosphate buffer (pH 8): as described in Subheading 2.2, step 3.
3. Ultra-Micro quartz cells (Hëllma, Germany) or 384 well small volume, LoBase Polystyrene microplates, black (Greiner Bio-One, Germany).
4. UV–Vis Spectrophotometer UV2 (UNICAM, UK) or Microplate reader Infinite M200 with Absorbance module (Tecan, Switzerland) or equivalent instrument capable of scanning wavelength range 400–800 nm.

Table 2
Control targets

Targets	Sequence (5′-3′)	Gene-Bank acc. number
BCR–ABL (e14a2) gene fusion	TGGATTTAAGCAGAGTTCAAAAGCCCTTCA GCGGCCAGTA	AJ131466.1
BCR–ABL (e1a2) gene fusion	TCCATGGAGACGCAGAAGCCCTTCAGCGGC CAGTAGCATC	AF113911.1
ABL gene	CTCCAGCTGTTATCTGGAAGAAGCCCTTCAG CGGCCAGTA	NM 005157.3
BCR gene	TGGATTTAAGCAGAGTTCAAATCTGTACTGC ACCCTGGAG	NM021574.2
Unrelated	GGCCGCTGCGGCGGGGCTCAGGGCACAAATT GGAACGTTC	n.a.

2.6. RNA and Control Samples (See Note 3)

1. K562 erythroleukemic cells (BCR–ABL positive cell line derived from CML patients in blast crisis, expressing the BCR–ABL gene fusion e1a2 and e14a2 transcripts).
2. 2.HL-60cell line, a human leukemic promyelocytic cell line (BCR–ABL negative).
3. Control oligonucleotide samples—see Table 2. “BCR–ABL (e14a2) gene fusion” and “BCR–ABL (e1a2) gene fusion” oligonucleotide control targets are derived from the reference sequences deposited in Gene Bank with accession no. AJ131466.1 and AF113911.1, respectively. “ABL gene” and “BCR gene” oligonucleotide control targets are derived from the reference sequences Gene Bank accession no. NM 005157.3 and NM021574.2, respectively. The “Unrelated” oligonucleotide control target was randomly generated and checked to present no complementarity to the nanoprobes. The BCR–ABL probes span over the region of fusion, i.e., breakpoint that is present in more than 90 % of CML patients.

3. Methods

3.1. Noble Metal Nanoparticle Synthesis

Treat all glass materials with freshly prepared *aqua regia* (see Note 4) by immersion for at least 1 h and wash vigorously afterwards with ultrapure water. Cover all metal materials used during synthesis (e.g., metallic spatulas) with Teflon to avoid metal corrosion and contamination.

3.1.1. 13 nm Gold Nanoparticle Synthesis

1. In a 500 mL round bottom flask, boil 225 mL of 1 mM $HAuCl_4$ (88.61 mg) until reflux with vigorous stirring.
2. While in reflux, quickly add 25 mL of 38.8 mM sodium citrate (285 mg) and keep reflux for 15 min with vigorous stirring (see Note 5).
3. Stop reflux maintaining the stirring and leave the colloidal solution to cool down to room temperature.
4. Transfer the colloidal solution to a 250 mL Erlenmeyer amber flask with a ground glass cap and store in the dark at room temperature until further use (see Note 6).
5. The colloidal gold concentration should be determined by measuring the absorption (see Note 7) assuming a molar absorptivity for the plasmon resonance band maximum (520 nm) of 2.33×10^8 $M^{-1} cm^{-1}$. The expected typical yield (concentration) should be ~14 nM AuNPs (see Note 8).

3.1.2. Alloy Gold:Silver Nanoparticles Synthesis

1. In a 250 mL round bottom flask, boil 95 mL of 0.126 mM $HAuCl_4$ (4.71 mg) and 0.127 mM $AgNO_3$ (2.04 mg) (see Note 9) until reflux with vigorous stirring.
2. While in reflux, quickly add 5 mL of 34 mM sodium citrate (50 mg) and keep reflux for 15 min with vigorous stirring.
3. Stop reflux maintaining the stirring and leave the colloidal solution to cool down to room temperature.
4. Centrifuge the colloidal solution at $233 \times g$ for 20 min and decant the supernatant to a 100 mL Erlenmeyer amber flask with a ground glass cap, to remove any silver precipitate that may have formed.
5. Store in the dark at room temperature until further use.
6. The colloidal alloy nanoparticle concentration can be determined by measuring the absorption (see Note 7) assuming a molar absorptivity 1.19×10^{10} $M^{-1} cm^{-1}$ for the typical plasmon resonance band maximum at 460 nm (see Note 9). The expected typical yield (concentration) should be ~0.1 nM alloy nanoparticles (50 % Ag: 50 % Au) (see Note 10).

3.2. Noble Metal Nanoprobe Synthesis

1. Extract one volume (100–500 µL) of thiol-modified oligonucleotide resuspended in 0.1 M DTT with 2 volumes of ethyl acetate. Mix thoroughly.
2. Centrifuge for 5 min at $21{,}460 \times g$ and discard the organic phase (i.e., upper phase).
3. Repeat the extraction of the aqueous phase 2 more times.
4. Purify the remaining aqueous phase using a desalting NAP-5 column, following the manufacturer's instructions and using 10 mM phosphate buffer (pH 8) as eluent. Typically, after column equilibration with the eluent, 500 µL of the aqueous

phase is added and let to enter the column. Afterwards, 1,000 μL of purified thiol-modified oligonucleotide can be collected by adding 1,000 μL of the eluent to the column.

5. Quantify the purified thiol-modified oligonucleotide by UV/Vis spectroscopy using the extinction coefficient at 260 nm provided by the oligonucleotide manufacturer. An online Oligonucleotide Properties Calculator (e.g., http://www.basic.northwestern.edu/biotools/oligocalc.html) can be used if the extinction values are not known.
6. Mix the purified thiol-modified oligonucleotide with the colloidal solution in a 1:200 [AuNPs]: oligonucleotide or 1:62,000 [AuAg-alloy-NPs]:oligonucleotide ratio for the alloy nanoparticles.
7. Add AGE I solution to achieve a final concentration of 10 mM phosphate buffer (pH 8), 0.01 % (w/v) SDS. Typically, 15.1 μL of AGE I solution is added to a volume of 3 mL of the solution prepared in previous step.
8. Sonicate the solution for 10 s using an ultrasound bath and incubate at room temperature for 20 min.
9. Afterwards, sequentially increase the ionic strength of the solution by adding the respective volume of AGE II solution up to a final concentration of 10 mM phosphate buffer (pH 8), 0.3 M NaCl, 0.01 % (w/v) SDS (see Note 11). Typically, 104.1, 111.6, 119.8, 129.1, 139.4, and 151 μL of AGE II solution is added sequentially to the 3,015.1 μL of the solution prepared in step 7 to achieve 50 mM incremental increase in NaCl concentration. After each increment, sonicate the solution for 10 s and incubate at room temperature for 20 min before the next increment.
10. Incubate the solution overnight at room temperature.
11. Distribute the functionalized nanoparticles in 1.5 mL microcentrifuge tube and centrifuge for 20 min at 21,460 × *g*, discard the supernatant.
12. Wash the resulting oily pellet in microcentrifuge tubes by adding 1 mL of 10 mM phosphate buffer (pH 8), centrifuge for 20 min at 21,460 × *g*, discard the supernatant.
13. Repeat the above washing step (two washes in total).
14. Wash the pellet in microcentrifuge tubes by adding 1 mL of PBS solution and centrifuge for 20 min at 21,460 × *g*, discard the supernatant.
15. Resuspend the pellet in 500 μL of PBS solution. Transfer the resulting solutions of each microcentrifuge tube into a single polypropylene or glass vial with a conical skirted base.
16. Determine the nanoprobe concentration via Lambert–Beer equation, using the absorbance (see Note 7) and the molar

absorptivity of the respective nanoparticles. Prepare aliquots of 15 or 0.3 nM of Au- or AuAg-alloy-nanoprobes, respectively, using PBS as eluent. Normally, aliquots of 1,300 µL should be sufficient.

17. Store the nanoprobe stock solutions in the dark at 4 °C until further use.

3.3. Cell Culture

1. Grow K562 and HL-60 cells in Dulbecco's modified Eagle's medium (DMEM) with 10 % heat inactivated fetal bovine serum and maintain at 37 °C in 5 % CO_2.
2. After cells reach >80 % confluence level, collect 10^6 cells by centrifugation (1,500 rpm, 5 min at 4 °C).

3.4. Total RNA Isolation

Any suitable method can be used for total RNA extraction and purification. We have tried several commercially available purification kits with equivalent results. Currently, we are using a protocol based on the single step method developed by Chomczynski and Sacchi (26, 27).

1. Isolate Total RNA from K562 and HL-60 cell lines using TRIsure® (use 1 mL of TRIsure per 5×10^6 cells).
2. Lyse cells with 1 mL of TRIsure® and pass the lysate several times through a pipette tip and vortex.
3. Incubate samples for 5 min at room temperature.
4. Add 0.2 mL of chloroform per 1 mL of TRIsure® used. Cap tubes securely and shake vigorously by hand for 15 s.
5. Incubate samples for 2–3 min at room temperature. Centrifuge samples at $12{,}000 \times g$ for 15 min at 4 °C. The sample will separate into a pale green, phenol–chloroform phase, an interphase, and a colorless upper aqueous phase that contains the RNA.
6. Transfer the aqueous phase to another tube. Precipitate the RNA by mixing with 0.5 mL of isopropyl alcohol per 1 mL of TRIsure® used.
7. Incubate samples for 10 min at room temperature then centrifuge at $12{,}000 \times g$ for 10 min at 4 °C.
8. Remove the supernatant and wash the pellet once with 75 % ethanol, adding at least 1 mL of ethanol per 1 mL of TRIsure® used. Vortex samples and centrifuge at $7{,}500 \times g$ for 5 min at 4 °C.
9. Air-dry the pellet for 10 min and dissolve in 25–50 µL of DEPC-treated water (use 25 µL per 10^6 cells) by pipetting the solution up and down, and incubating for 10 min at 55 °C.
10. Store RNA at –80 °C.

3.5. Colorimetric Non-Cross-Linking Assay

3.5.1. Noble Metal Nanoprobes Characterization

1. Prepare six solutions in 200 μL polypropylene thermal-resistant reaction tubes by only mixing the nanoprobe stock solution with the 10 mM phosphate buffer, see Table 3. Do not add $MgCl_2$ at this point!
2. Incubate the solutions for 10 min at 95 °C.
3. Allow the solutions to cool down at room temperature for 30 min.
4. Add the 0.3 M $MgCl_2$ according to Table 3, mix well and spin down the solutions.
5. Incubate the solutions for 15 min at room temperature and register their absorption spectra (350–800 nm) using a UV–visible spectrophotometer or microplate reader.
6. Plot Abs_{peak}/Abs_{600nm} vs. $[MgCl_2]_{final}$ to determine the minimum salt concentration needed for a complete nanoprobe aggregation, where Abs_{peak} is the absorbance peak of the initial dispersed nanoprobe (see Note 12). For Abs_{peak}/Abs_{600nm} ratios below 1, the nanoprobe is considered to be fully aggregated (see Note 13).

3.5.2. mRNA Detection and Quantification

1. In 200 μL polypropylene thermal-resistant reaction tubes, prepare at least four assay solutions (Blank, Positive and Negative control, and sample) by mixing the total RNA sample (final concentration 10–60 ng μL^{-1}) with the BCR–ABL (e14a2) Au-nanoprobe solution (final concentration of 2.5 nM) and an appropriate volume of 10 mM phosphate buffer (pH 8) to make up the total volume (total volume of 60 μL, considering the volume of salt that will be added in step 5). If more than one sample is to be analyzed, more assay solutions can be prepared accordingly.

Table 3
Setup for characterization of nanoprobe aggregation

Tube	Nanoprobe[a] (μL)	10 mM phosphate buffer (pH 8) (μL)	300 mM $MgCl_2$ (μL)	$MgCl_2$ concentration (mM)
1	10	50	–	0
2	10	48	2	10
3	10	46	4	20
4	10	44	6	30
5	10	42	8	40
6	10	40	10	50

[a]Nanoprobe stock solutions: 15 nM Au-nanoprobe or 0.3 nM alloy-nanoprobe (50 % Ag: 50 % Au)

2. As a Positive control use the complementary oligonucleotide BCR–ABL (e14a2) and as a Negative control use the BCR or ABL oligonucleotides (final concentration of 100 fmol μL^{-1})—see Table 1 for sequences. Additionally, prepare the blank solution by replacing the total RNA with an equivalent volume of 10 mM phosphate buffer (pH 8).

   For mRNA quantification, prepare five reference standard solutions using the complementary target ranging in concentration from 0 to 100 fmol μL^{-1}.

3. Incubate the solutions for 10 min at 95 °C.
4. Allow the solutions to cool down for 30 min at room temperature.
5. Add a predetermined volume of the concentrated $MgCl_2$ solution to attain the final concentration needed for aggregation of the nanoprobe as determined in Subheading 3.5.1, step 6, Mix well.
6. Spin down and incubate the solutions for 15 min at room temperature.
7. Register the absorption spectra (350–800 nm) using a UV–visible spectrophotometer or a microplate reader.
8. Determine the Abs_{peak}/Abs_{600nm} ratio (for the described 13 nm gold nanoparticles, Abs_{peak} is typically measured at 520 nm). Compare the ratios of the blank, positive and negative control with the ratios of the sample solutions. Typically, the blank sample, negative control, and negative samples yield ratios below 1, while positive control and positive samples yield ratios above 1 (see Fig. 2).

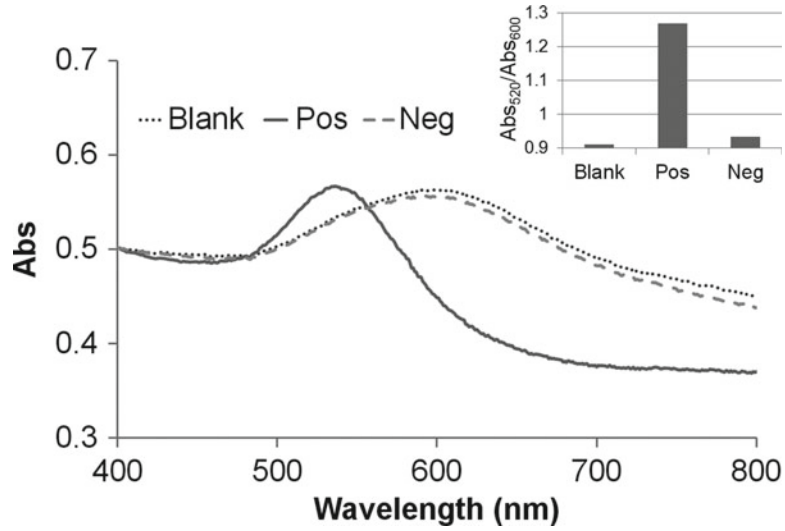

Fig. 2. Characteristic detection assay results. UV/visible spectra of Au-nanoprobe alone (Blank); in the presence of a complementary target (Pos); and in the presence of a non-complementary target (Neg), taken after 15 min incubation with salt. Inlet represents the Abs_{520nm}/Abs_{600nm} ratios of the presented UV/visible spectra.

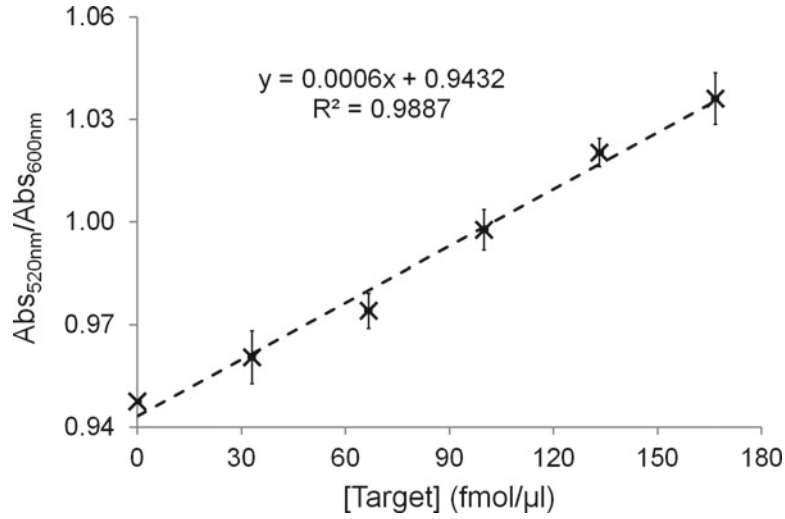

Fig. 3. Characteristic quantification assay results. Typical Abs_{520nm}/Abs_{600nm} ratios obtained for a range of complementary target concentrations. Dashed line represents a linear fit of the experimental data points and the error bars represent the standard deviation ($n = 3$).

9. For quantification, plot the Abs_{520nm}/Abs_{600nm} vs. mRNA concentration of the reference standard solutions and compare with the samples' Abs_{520nm}/Abs_{600nm} ratio to determine their mRNA concentration (see Fig. 3) (see Note 14).

3.5.3. One-Pot Multiplex Detection

1. In 200 µL polypropylene thermal-resistant reaction tubes, prepare at least six assay solutions (blank, three positive and one negative control, and sample) by mixing the total RNA sample (final concentration 10–60 ng μl^{-1}) with the ABL Au-nanoprobe solution (final concentration of 2.5 nM), the BCR–ABL (e1a2) AuAg-alloy-nanoprobe solution (final concentration of 0.05 nM), and an appropriate volume of 10 mM phosphate buffer (pH 8) to make up the total volume (total volume of 60 µL, considering the volume of salt that will be added in step 5). If more than one sample is to be analyzed, more assay solutions can be prepared accordingly.
2. Use the complementary oligonucleotides as Positive controls for each nanoprobe ABL (ABL Au-nanoprobe) and BCR–ABL (e1a2) (BCR–ABL (e1a2) AuAg-alloy-nanoprobe), both separately and mixed. Use the unrelated oligonucleotide sequence as a negative control (final concentration of oligonucleotides at 100 fmol μL^{-1})—see Table 2 for sequences. Additionally, prepare the blank solution by replacing the total RNA with equivalent volume of 10 mM phosphate buffer (pH 8).
3. Incubate all solutions for 10 min at 95 °C.

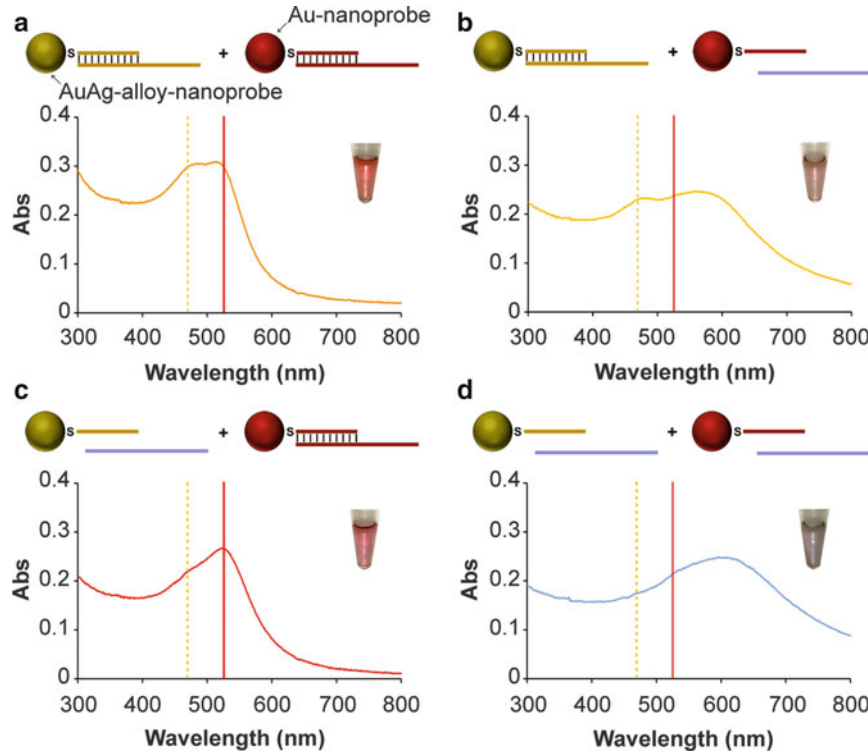

Fig. 4. Representative one-pot assay results. UV/visible spectra and digital photography of AuAg-alloy- and Au-nanoprobe mix in the presence of a complementary targets to both the AuAg-alloy- and Au-nanoprobe – the solution retains the initial orange color (**a**), a complementary target to the AuAg-alloy-nanoprobe – the solution changes from orange to yellow (**b**), a complementary target to the Au-nanoprobe – the solution changes from orange to red (**c**) or a noncomplementary target to both AuAg-alloy- and Au-nanoprobes – the solution changes from orange to blue (**d**). Vertical dashed and solid lines represent the position of absorption peak of the AuAg-alloy-nanoprobes (460 nm) and Au-nanoprobe (520 nm), respectively, when dispersed in solution. Schematics represent each nanoprobe and their complementary or noncomplementary targets. Reproduced from (16) with permission from IOP.

4. Allow the solutions to cool down for 30 min at room temperature.
5. Add a predetermined volume of the concentrated $MgCl_2$ solution to attain the final concentration needed for aggregation of the nanoprobes as determined in Subheading 3.5.1, step 6 (see Note 15).
6. Mix well, spin down, and incubate the solutions for 15 min at room temperature.
7. Measure the absorption spectra (350–800 nm) using a UV–visible spectrophotometer or a microplate reader.
8. Compare the spectra of the blank, positive and negative controls with the spectra of the sample(s)—as an example of typical multiplex results, see Fig. 4. Typically, if only the complementary target to the Au-nanoprobe is present an

absorbance peak at 520 and 600 nm can be observed. If only the complementary target to the AuAg-alloy-nanoprobe is present absorbance peaks at 460 and 600 nm can be observed. If both complementary targets are present absorbance peaks at 460 and 520 nm can be observed. If only one absorbance peak at 600 nm can be observed, the target is either noncomplementary or specific RNA target concentration is below the method's detection limit.

4. Notes

1. Typical thiol-modified oligonucleotide probe sequences range between 15 and 25 nucleotides, according to specificity requirements. Check probe sequence specificity using NCBI nucleotide BLAST tool (http://blast.ncbi.nlm.nih.gov/Blast.cgi). Increased nanoprobe specificity is achieved at the oligonucleotide's 3′ end, so consider any single nucleotide polymorphism at this position when designing the probe (28).
2. Always measure the volume of ethanol and water separately and mix them subsequently. Do not prepare ethanol dilutions based on volumetric flasks, as the total volume of ethanol/water will drop after mixing, leading to an erroneous dilution if the volumetric flask mark is used as reference (29).
3. Thiol-modified ssDNA, complementary to the fusion region of the BCR–ABL mRNA is used to functionalize the gold nanoparticles and produce specific Au-nanoprobes to detect the fusion gene. These nanoprobes are assessed in terms of specificity by means of total RNA mixtures spiked in with synthetic oligonucleotides (complementary target) harboring the fusion site BCR–ABL e14a2. It should be noted that, in reality, patients may only harbor one copy of the fusion gene and the remaining copies of normal ABL and BCR should be still functional, thus expressing the normal mRNA sequence. Two oligonucleotides harboring the normal sequence of the BCR or of the ABL genes are used to evaluate the probe's capability to discriminate from similar sequences.
4. Warning: *aqua regia* is potentially hazardous and highly corrosive. Always wear appropriate personal protective equipment (i.e., safety goggles, gloves, and laboratory coat) and work in a clean, well-ventilated chemical fume hood. Never store *aqua regia* in a sealed container, as pressure may escalate and the container may burst or explode. Dispose *aqua regia* adequately by dilution and neutralization.

5. After adding the citrate solution, the initial pale yellow color of the Au(III) solution should become instantly colorless and then gradually change to deep red due to the nanoparticle formation. The reduction process usually takes a few minutes to occur. During this process, a precursor called acetone dicarboxylic acid is formed as a result of the citrate oxidation. This precursor plays the roles of precursor, reducing and nucleating agents. The Au(III) ions are then reduced to Au(I) and when the solution becomes saturated of Au(I) atoms, they start to precipitate in the form of nanoparticles. The citrate acts as capping and stabilizing agent that sticks to the nanoparticle surface avoiding the aggregation of the nanoparticles.
6. The prepared nanoparticles are stable for months when stored in a clean container (glass or plastic) at room temperature. Do not freeze the nanoparticles as this may cause aggregation.
7. The Lambert–Beer law states that the absorbance of a homogeneous substance becomes linear with its concentration according to formula $A = \varepsilon \times l \times C$, where A is the substance absorbance typically at its wavelength peak, ε is the molar absorptivity for the wavelength of A, l is the optical path length, and C is the substance concentration. Care should be taken not to exceed an absorbance of 2 so as to avoid deviations to the Lambert–Beer law. In case the measured absorbance exceeds this value, dilute the sample and consider the dilution factor when calculating the original stock concentration.
8. Optionally, morphological characterization of the AuNPs can be performed by transmission electron microscopy (TEM) and dynamic light scattering (DLS).
9. To obtain different AuAg alloy nanoparticles with different plasmon resonance peaks, the ratio of $HAuCl_4$ and $AgNO_3$ can be varied (e.g., the molar concentrations presented in the protocol refers to a 50%Au:50%Ag ratio, with a typical SRP band peak at 460 nm and a molar absorptivity of $1.19 \times 10^{10}\ M^{-1}\ cm^{-1}$). See Fig. 5 for typical SPR peak variation as function of the Au:Ag metal ratio. Nanoparticle size may also vary with the Au:Ag metal ratio.
10. Optionally, morphological characterization of the alloy nanoparticles can be performed by TEM and DLS; the Au:Ag ratio can be determined by inductively coupled plasma (ICP) and/or Energy-dispersive X-ray spectroscopy (EDX).
11. Different degrees of nanoprobe functionalization (i.e., oligonucleotide density) are attained by varying the final NaCl concentration during the aging process (e.g., 0.1, 0.5, 0.7 M). Be aware that nanoprobe hybridization efficiency may decrease with increasing density due to steric hindrance. For further information, consult Doria et al. (28).

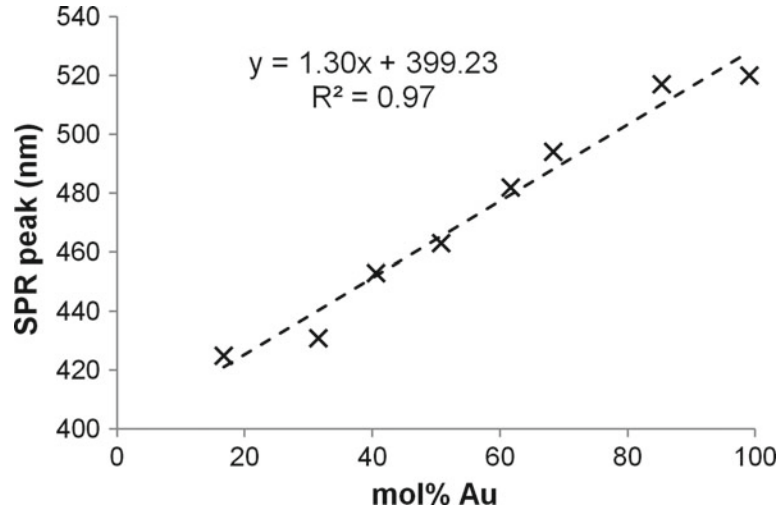

Fig. 5. SPR absorption band peak of alloy-nanoparticles as function of the gold:silver ratio. *Dashed line* represents a linear fit of the experimental data points.

12. Abs_{peak} is the absorbance maximum determined earlier for the particular nanoprobe peak of the initial dispersed nanoprobe. Typical values are 520 nm for Au-nanoprobes or 460 nm for alloy-nanoprobes: (50 % Ag: 50 % Au).
13. If the nanoprobes do not completely aggregate and change color within the suggested concentrations of $MgCl_2$, use higher concentrations of $MgCl_2$ If the nanoprobe changes color and fully aggregates at a final $MgCl_2$ concentration of 10 mM, then derivatization of the nanoparticles with the thiol-modified oligonucleotides may have not been effective. If so happens, repeat nanoprobe synthesis.
14. To discriminate between two significantly different aggregation levels, as for example in a YES/NO identification of a given target, the ratio between the peaks at 520 and 600 nm is usually used for Au-nanoprobes. However, for identifying small differences in aggregation levels between two quantities for the same target, there is a need to decrease the background noise in the spectra. Such background noise may be strongly reduced and even solved if an integral of the signal is used, i.e., the area under the curve (AUC).
15. In order for the one-pot assay to work, both nanoprobes must aggregate at similar minimum salt concentration. If the minimum salt concentration for aggregation varies slightly between nanoprobes, use the highest determined concentration of salt for the one-pot assay.

References

1. Bustin SA (2000) Absolute quantification of mRNA using real-time reverse transcription polymerase chain reaction assays. J Mol Endocrinol 25:169–193
2. Weis JH et al (1992) Detection of rare mRNAs via quantitative RT-PCR. Trends Genet 8:263–264
3. Freeman WM, Walker SJ, Vrana KE (1999) Quantitative RT-PCR: pitfalls and potential. Biotechniques 26:112–115
4. http://nano.cancer.gov/about/plan/ Accessed 11 May 2012
5. Baptista P et al (2008) Gold nanoparticles for the development of clinical diagnosis methods. Anal Bioanal Chem 391:943–950
6. Sato K, Hosokawa K, Maeda M (2005) Non-cross-linking gold nanoparticle aggregation as a detection method for single-base substitutions. Nucleic Acids Res 33:e4
7. Mirkin CA et al (1996) A DNA-based method for rationally assembling nanoparticles into macroscopic materials. Nature 382:607–609
8. Taton TA, Mirkin CA, Letsinger RL (2000) Scanometric DNA array detection with nanoparticle probes. Science 289:1757–1760
9. Qin WJ, Yung LY (2007) Nanoparticle-based detection and quantification of DNA with single nucleotide polymorphism (SNP) discrimination selectivity. Nucleic Acids Res 35:e111
10. Elghanian R et al (1997) Selective colorimetric detection of polynucleotides based on the distance-dependent optical properties of gold nanoparticles. Science 277:1078–1081
11. Sato K, Hosokawa K, Maeda M (2003) Rapid aggregation of gold nanoparticles induced by non-cross-linking DNA hybridization. J Am Chem Soc 125:8102–8103
12. Storhoff JJ et al (2004) Homogeneous detection of unamplified genomic DNA sequences based on colorimetric scatter of gold nanoparticle probes. Nat Biotechnol 22:883–887
13. Wilcoxon J (2009) Optical absorption properties of dispersed gold and silver alloy nanoparticles. J Phys Chem B 113:2647–2656
14. Liz-Marzan LM (2006) Tailoring surface plasmons through the morphology and assembly of metal nanoparticles. Langmuir 22:32–41
15. Baptista P et al (2005) Colorimetric detection of eukaryotic gene expression with DNA-derivatized gold nanoparticles. J Biotechnol 119:111–117
16. Doria G, Franco R, Baptista P (2007) Nanodiagnostics: fast colorimetric method for single nucleotide polymorphism/mutation detection. IET Nanobiotechnol 1:53–57
17. Conde J, de la Fuente JM, Baptista PV (2010) RNA quantification using gold nanoprobes—application to cancer diagnostics. J Nanobiotechnology 8:5
18. Veigas B et al (2010) Au-nanoprobes for detection of SNPs associated with antibiotic resistance in *Mycobacterium tuberculosis*. Nanotechnology 21:415101
19. Baptista PV et al (2006) Gold-nanoparticle-probe-based assay for rapid and direct detection of *Mycobacterium tuberculosis* DNA in clinical samples. Clin Chem 52:1433–1434
20. Costa P et al (2010) Gold nanoprobes assay for identification of mycobacteria from the *Mycobacterium tuberculosis* complex. Clin Microbiol Infect 16:1464–1469
21. Doria G et al (2010) Gold-silver-alloy nanoprobes for one-pot multiplex DNA detection. Nanotechnology 21:255101
22. Hehlmann R, Hochhaus A, Baccarani M (2007) Chronic myeloid leukaemia. Lancet 370:342–350
23. Shet AS, Jahagirdar BN, Verfaillie CM (2002) Chronic myelogenous leukemia: mechanisms underlying disease progression. Leukemia 16: 1402–1411
24. Ren R (2005) Mechanisms of BCR-ABL in the pathogenesis of chronic myelogenous leukaemia. Nat Rev Cancer 5:172–183
25. Melo JV, Hughes TP, Apperley JF (2003) Chronic myeloid leukemia. Hematology Am Soc Hematol Educ Program 132–152
26. Chomczynski P, Sacchi N (1987) Single step method of RNA isolation by acid guanidinum thiocyanate-phenol-chloroform extraction. Anal Biochem 162:156–159
27. Chomczynski P (1993) A reagent for the single-step simultaneous isolation of RNA, DNA and proteins from cell and tissue samples. Biotechniques 15:532–537
28. Doria G et al (2010) Optimizing Au-nanoprobes for specific sequence discrimination. Colloids Surf B 77:122–124
29. Parsons PW, Estrada FJ (1942) Changes in volume on mixing solutions. Ind Eng Chem 34:949–952

Alloy metal nanoparticles for multicolor cancer diagnostics

Pedro V. Baptista*[a], Gonçalo Doria[a], João Conde[a,b]

[a]CIGMH, Departamento de Ciências da Vida, Faculdade de Ciências e Tecnologia, Universidade Nova de Lisboa, 2829-516 Caparica, Portugal
[b]Instituto de Nanociencia de Aragón, Universidad de Zaragoza, Pedro Cerbuna 12, 50009, Zaragoza, Spain

ABSTRACT

Cancer is a multigenic complex disease where multiple gene loci contribute to the phenotype. The ability to simultaneously monitor differential expression originating from each locus results in a more accurate indicator of degree of cancerous activity than either locus alone. Metal nanoparticles have been thoroughly used as labels for in vitro identification and quantification of target sequences. We have synthesized nanoparticles with assorted noble metal compositions in an alloy format and functionalized them with thiol-modified ssDNA (nanoprobes). These nanoprobes were then used for the simultaneous specific identification of several mRNA targets involved in cancer development - one pot multicolor detection of cancer expression. The different metal composition in the alloy yield different "colors" that can be used as tags for identification of a given target. Following a non-cross-linking hybridization procedure previously developed in our group for gold nanoprobes, these multicolor nanoprobes were used for the molecular recognition of several different targets including differently spliced variants of relevant genes (e.g. gene products involved in chronic myeloid leukemia BCR, ABL, BCR-ABL fusion product). Based on the spectral signature of mixtures, before and after induced aggregation of metal nanoparticles, the correct identification could be made. Further application to differentially quantify expression of each locus in relation to another will be presented. The differences in nanoparticle stability and labeling efficiency for each metal combination composing the colloids, as well as detection capability for each nanoprobe will be discussed. Additional studies will be conducted towards allele specific expression studies.

Keywords: gold nanoparticles, alloy nanoparticles, gene expression, cancer, splice variants, multicolor nanoparticles, gene characterization, chronic myeloid leukemia, mRNA

1. INTRODUCTION

Cancer cells exhibit deregulation of the cell cycle resulting in uncontrolled growth and they are resistant to programmed death as result of abnormalities in one or more proteins that inhibit apoptosis. Moreover, alternatively and abnormally expressed mRNAs (e.g. alternatively spliced mRNAs, fusion gene products) are considered as triggers of tumor development. The National Cancer Institute envisions that over the next years, nanotechnology will result in significant advances in early detection, molecular imaging, targeted and multifunctional therapeutics, prevention and control of cancer[1]. Among these advances, nanodiagnostics has been providing for improved techniques for clinical diagnostics with increased sensitivity at lower costs[2-10]. Due to their optical properties, gold nanoparticles (AuNPs) have been used for DNA/RNA screening approaches, namely via functionalization with thiolated oligonucleotides (Au-nanoprobes), capable of specifically hybridizing with a complementary oligonucleotide sequence. These optical properties derive from the characteristic surface plasmon resonance (SPR) band that can be easily tailored through the synthesis of nanoparticles (NPs) with different metal composition, either in an alloy or core-shell structure, e.g. different gold:silver ratios[11,12].

*pmvb@fct.unl.pt; phone/fax: +351 21 2948530

Colloidal Quantum Dots/Nanocrystals for Biomedical Applications VI, edited by Wolfgang J. Parak, Kenji Yamamoto, Marek Osinski, Proc. of SPIE Vol. 7909, 79090K · © 2011 SPIE · CCC code: 1605-7422/11/$18 · doi: 10.1117/12.879025

For the past years we have been developing nanodiagnostics systems based on noble metal NPs in a non-cross linking approach, where an increase of the ionic strength of the surrounding media leads to selective aggregation of nanoprobes: absence of complementary target allows extensive aggregation with concomitant spectral change of the colloidal solution, whereas presence of a complementary target stabilizes the nanoprobe, thus preventing aggregation and colorimetric changes[6-9]. We have recently reported on a highly selective colorimetric detection method for DNA sequences based on AuAg-alloy-NPs functionalized with thiol-modified oligonucleotides, i.e. AuAg-alloy-nanoprobes, and the use of these alloy-nanoprobes together with more common Au-nanoprobes in a one-pot colorimetric assay for the simultaneous differential detection of two gene sequences[13]. Simultaneously, we have shown that the Au-nanoprobe assay could be used for mRNA quantification and used this strategy to quantify gene expression of an aberrant BCR-ABL fusion gene involved in the development of chronic myeloid leukemia[14].

Chronic myeloid leukemia (CML) is a clonal neoplastic disease of the hematopoietic stem cell, whose hallmark molecular event is the genetic t(9;22)(q34;q11) translocation known as the Philadelphia (Ph) chromosome. This translocation - ABL gene (chromosome 9) and BCR gene (chromosome 22) - originates a BCR-ABL fusion gene, leading to the expression of a chimeric BCR-ABL protein with tyrosine-kinase activity[15-20]. Because the translocation can result in distinct breakpoints and, thus, fusion genes, these constitute an interesting model to study splice variants and their expression in cancer development. Furthermore, several other genes may be implicated in the development of the cancer, such as tumor suppressor genes whose expression prevents cell transformation (e.g. p53) or proto-oncogenes, which tend to be upregulated and promote neoplastic events (e.g. C-MYC).

Here, we report the synthesis of AuAg-alloy-NPs with different noble metal molar fractions, and their derivatization with thiol-modified ssDNA oligonucleotides for application in molecular diagnostics. Using the BCR-ABL fusion products as a model, we demonstrate the use of these AuAg-alloy nanoprobes for the quantitative analysis of targets in complex mixtures, and for the differential expression analysis of two genes in relation to each other. Because the assay is performed on total RNA, this approach avoids the need for retrotranscription and/or nucleic acid amplification.

2. MATERIALS AND METHODS

All chemicals were from Sigma-Aldrich and of the highest purity available. All thiol-modified oligonucleotides were purchased from STAB Vida, Lda (Portugal).

2.1 Au- and AuAg-alloy nanoparticles syntheses

AuNPs were prepared by the citrate reduction method described by Lee and Meisel[21]. The AuAg-alloy-NPs were prepared following a similar method by co-reducing $AgNO_3$ and $HAuCl_4$ with sodium citrate described in [13]. Briefly, 12.5 mg of $HAuCl_4 \bullet 3H_2O$ and 16.2 mg of $AgNO_3$ (for a 25:75 Au:Ag ratio); or 25 mg of $HAuCl_4 \bullet 3H_2O$ and 10.8 mg of $AgNO_3$ (for Au:Ag ratio 50:50); or 37.5 mg of $HAuCl_4 \bullet 3H_2O$ and 5.4 mg of $AgNO_3$ (for Au:Ag 75:25 ratio) - were dissolved in 250 mL of milli-Q H_2O and brought to a boil while stirring in a 500 ml round-bottom flask. Twenty-five millilitres of sodium citrate 34 mM were quickly added and the mixture was refluxed for 15 min with continuous stirring. The flask was left to cool down to room temperature and the solution was later centrifuged at 233 g for 20 minutes to remove any silver precipitate, and further filtered using 0.2 μm nylon filters (Whatman, UK). Both Au- and AuAg-alloy-NPs were characterized by Transmission Electron Microscopy (TEM) and UV-visible spectroscopy. The elemental composition (i.e. Au:Ag ratio) of AuAg-alloy-NPs was determined by Inductively Coupled Plasma (ICP) upon dissolving the nanoparticles in freshly prepared *aqua regia*. Solutions containing NPs were kept in the dark at room temperature until further use.

2.2 Au- and AuAg-alloy-nanoprobes syntheses

The sequence of the thiolated oligonucleotides sued for nanoparticle functionalization are indicated in Table 1 together with the synthetic oligos used as complementary and non-complementary targets.

Oligo #	Probe/target	Sequence 5'-3'	Modification
1p	ABL probe	CGCTGAAGGGCTTCTTCCAG	5'-$(CH_2)_6$-SH
1t	ABL target	CTCCAGCTGTTATCTGGAAGAAGCCCTTCAGCGGCCAGTA	
2p	C-MYC probe	GATTGCTCAGGACATTTCTG	5'-$(CH_2)_6$-SH
2t	C-MYC target	TTCCTTCTAACAGAAATGTCCTGAGCAATCACCTATGAAC	
3p	BCR-ABL_e1a2 probe	CGCTGAAGGGCTTCTGCGTC	5'-$(CH_2)_6$-SH
3t	BCR-ABL_e1a2 target	TCCATGGAGACGCAGAAGCCCTTCAGCGGCCAGTAGCATC	
4	Non-complementary target	GGCCGCTGCGGCGGGGCTCAGGGCACAAATTGGAACGTTC	

Both Au- and AuAg-alloy-nanoprobes were synthesized following a previously described protocol[13]. The Au-NPs were functionalized with a thiol-modified 20mer oligonucleotide derived from the junction of exon 1 and 2 of ABL gene (i.e. oligo#1p) or a 20mer oligonucleotide derived from human v-myc myelocytomatosis viral oncogene homolog (C-MYC) gene (i.e. oligo#2p). The AuAg-alloy-NPs (25%Au:75%Ag) were functionalized with a thiol-modified 20mer oligonucleotide derived from the BCR-ABL fusion gene involving the isoform e1a2 (oligo#3p). Briefly, 10μM thiol-modified oligonucleotide was added to NPs in a ratio of 1:200 Au-NPs or 1:3500 AuAg-alloy-NPs per oligonucleotide, in phosphate buffer 10 mM (pH8) with 0.01% sodium dodecyl sulfate (SDS). The solution was incubated at room temperature for 20 min and the concentration of NaCl increased to 0.05 M using phosphate buffer 10 mM (pH8), 1.5 M NaCl, 0.01% SDS. The solution was then submitted to ultrasounds for 10 sec. This salt aging process was repeated three times with increments of 0.1 M NaCl until a concentration of 0.3 M NaCl was reached. After a final incubation over-night at room temperature, the solution was washed three times and ressuspended in phosphate buffer 10 mM (pH8), 0.1 M NaCl. Functionalization was assessed by evaluation of the UV/visible spectra upon increasing concentrations of $MgCl_2$.

2.3 Total RNA purification

Escherichia coli cells were grown in standard Luria-Bertani (LB) broth overnight at 37°C. Isolation of total RNA was performed using a High Pure RNA Isolation Kit (Roche Applied Science) or GeneJET™ RNA Purification Kit (Fermentas) according to the manufacturer's protocol for the human cell lines and for E. coli, respectively. Total RNA concentration was determined by UV photometry and its integrity evaluated on a 2% agarose gel stained with GelRed™ dye (Biotium, USA), and it was stored at -80 ºC until further use.

2.4 Detection/quantification assay

Target detection was carried out via the previously described non-cross-linking protocol[13]. Hybridizations were carried out in 10 mM phosphate buffer (pH 8) by mixing up to 2μM target with either 2.5 nM Au-nanoprobe or 72 pM AuAg-alloy-nanoprobe. Forty-mer ssDNA oligonucleotides were used as targets: complementary to the BCR-ABL_e1a2 AuAg-alloy-nanoprobe (probe's oligo#3p) - oligo#3t derived from BCR-ABL fusion gene, isoform e1a2; complementary to the ABL Au-nanoprobe (probe's oligo#1p) – oligo#1t, derived from ABL gene; complementary to the C-MYC Au-nanoprobe (probe's oligo#2p)– oligo#2t derived from C-MYC gene; non-complementary to either nanoprobes – oligo#4 harboring an unrelated sequence. For each probe assay, at least three solutions were prepared: one with the complementary target (Comp), one with the unrelated sequence (Non-comp) and a Blank to confirm aggregation. Following 10 min of denaturation at 95 ºC, solutions were allowed to stand for 30 min at room temperature, and then $MgCl_2$ was added to a final concentration of 20 mM (for BCR-ABL_e1a2 AuAg-alloy-nanoprobe) or 40 mM (for ABL Au-nanoprobe and One-pot assay), or 0.95M of NaCl for the C-MYC probe. UV/visible spectra of solutions were registered 15 minutes upon salt addition using a UV-Vis Spectrophotometer Evolution 300 (Thermo, USA) and an Ultra-

Micro quartz cell (Hëllma, Germany). Digital photographs were taken using a Canon Rebel Xsi SLR digital camera (Canon, USA).

For the differential quantification assays, the final concentration of BCR-ABL_e1a2 target varied between 0 and 2 μM; ABL target was set at a fixed concentration of 2 μM; the final total ssDNA concentration was kept at 4 μM and total RNA at 20 ng/μL. The c-MYC spike in assays were achieved as a function of specific target concentration in mixtures of 20 ng/μl total RNA from *E.coli* spiked in with increasing concentrations of the synthetic c-MYC oligonucleotide, with final concentration from 33 to 133 nM. For c-MYC quantification the final concentrations of total RNA from a c-MYC positive cell line (HL-60) differed between 10 and 80 ng/μl. All experiments were done with c-MYC-nanoprobe at a final concentration of 2.5 nM.

For the one-pot spiking assay, both nanoprobes were mixed - 72 pM BCR-ABL_e1a2 AuAg-alloy-nanoprobe and 2.5 nM ABL Au-nanoprobe, and the assay carried out as above setting the ABL target (oligo#1t) concentration at 0.2μM and varying the concentration of BCR-ABL_e1a2 target (oligo#3t) between 0 and 2μM, always in a fixed final concentration of 20 ng/μL of *E.coli* total RNA.

3. RESULTS AND DISCUSSION

Regulation of gene expression is fundamental in all living organisms and is essential for the correct development and for the tight control over cell proliferation and physiology. Alterations to the expression of certain genes have strong implications on the development of aberrant phenotypes that can lead to cell cycle deregulation and to cancer. Most of these alterations involve sequence mutations to DNA (e.g. single point mutations, translocations, inversions, etc.) and/or to the way RNA is processed and its expression levels (e.g. splicing, multiple isoforms, etc.). As an example, Chronic myeloid leukemia (CML) is generally associated with the genetic t(9;22)(q34;q11) translocation, originating an aberrant BCR-ABL fusion gene that can differ from one another by the exact localization of the beak-point and which exons are involved in the fusion transcript. As mentioned earlier, other genes may also be deregulated and implicated in disease development, such as p53 and C-MYC. The most commonly used procedures for the initial diagnosis and management of CML patients are expensive and time consuming, e.g. karyotype analysis, reverse transcriptase polymerase chain reaction analyses (RT-PCR) and fluorescence in-situ hybridization (FISH)[20,22]. Molecular methods able to detect and quantify the BCR-ABL fusion transcripts are of paramount relevance when monitoring minimal residual disease and genetic recurrence in patients known to harbor the translocation. There is, therefore, a strong demand for new and improved strategies for the detection of these alterations with increased sensitivity and specificity.

Metal nanoparticles that differ in size and composition can be fabricated to scatter light of different wavelengths according to their distinct SPR. The optical properties from noble metal NPs with different sizes, shapes and composition has been extensively explored, with focus on application to biomolecular detection and characterization. Gold-silver alloy NPs can be synthesized with different ratios of each metal, where increasing molar fractions of silver leads to a typical blue-shift of the SPR absorption band peak. We have previously demonstrated that the use of AuAg-alloy-NPs (50%Au:50%Ag) allowed to modulate the characteristic SPR band of silver NPs, while retaining the ease of functionalization via thiol-modified oligonucleotides conferred by the gold surface[13]. The alloy-nanoprobes thus created were used in a two color one-pot detection scheme based on the non-cross-linking systems developed for Au-nanoprobes. Here, we tuned the SPR band of the alloy-NPs so as to allow better discrimination from the typical AuNPs' SPR band, and evaluated their use as nanoprobes for the differential quantification of specific gene sequences.

3.1 Au and AuAg-alloy-nanoprobes syntheses and characterization

First, we synthesized Au-NPs with 13 nm diameter and functionalized them with the suitable thiol-ssDNA oligonucleotide according to a well-established protocol. Then, we also effectively synthesized stable gold:silver alloy nanoparticles with varying ratios of each metal. Because we aim at using these NPs in conjunction with the AuNPs, the proportion of each metal was chosen so as to allow for an increased difference between the peak of non-aggregated nanoprobes, which, once aggregation takes place, would allow better color discrimination between alloys and gold NPs. AuAg-alloy-NPs with 25% gold and 75% silver were selected due to their SPR peak being located farther away from the

typical peak for pure AuNPs (Figure 1 – inlet). This way, better spectral discrimination can be attained and the simultaneous use of the respective nanoprobes in a one-pot is more effective. So, 29±13 nm AuAg-alloy NPs (25%Au:75%Ag) showing a SPR band peak circa 442 nm were synthesized. Similarly to what is observed with AuNPs, aggregation of the NPs can be achieved by increasing ionic strength, i.e. salt addition. These novel alloy NPs were then successfully functionalized with thiol-modified oligonucleotides via a similar procedure of that described for the synthesis of Au-nanoprobes. These AuAg-alloy-nanoprobes presented an increased stability to salt-induced aggregation when compared to the AuAg-alloy-NPs alone, withstanding a saline concentration up to 20mM $MgCl_2$. In the presence of 20 mM $MgCl_2$, the AuAg-alloy-nanoprobes aggregated and their initial yellow color changed to blue due to a red-shift from 442 nm to >600 nm of the SPR absorbance band (see Figure 1).

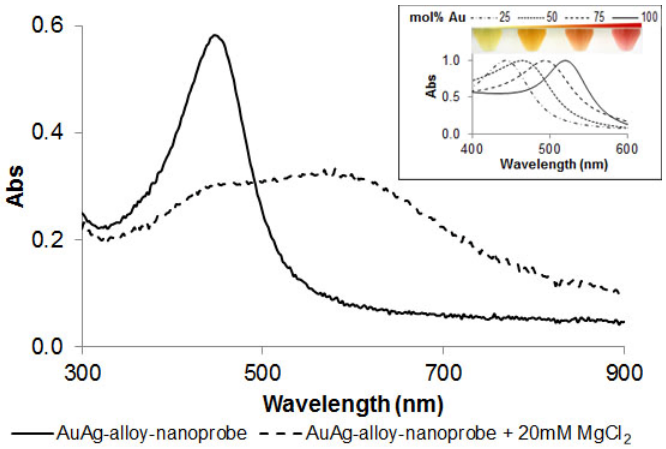

Figure 1 - UV/visible spectrum of AuAg-alloy-nanoprobes (25%Au:75%Ag) alone and in presence of 20mM $MgCl_2$ (dashed line). Inlet: UV/vis spectrum and digital photography of pure Au- and AuAg-alloy-NPs with different metal ratios.

These nanoprobes were assessed in terms of specificity via hybridization to a specific synthetic oligonucleotide complementary to the sequence of the nanoprobe. A non-complementary target in the same conditions was also used to confirm specificity of the reaction. In the case of BCR-ABL fusion product (corresponding to e1a2 fusion product), it should be noted that, in reality, patients may only harbor one copy of the fusion gene and the remaining copies of normal ABL and BCR should be still functional, thus expressing the normal mRNA sequence. Therefore, an oligonucleotide harboring the normal sequence of ABL genes was used to evaluate the probe's capability to discriminate from similar sequences. Following salt addition, the presence of the respective complementary synthesized target, protected the AuAg-alloy-nanoprobes from aggregation and the solution remained yellow; whereas the presence of non-complementary targets did not prevent aggregation and the solution changed color to blue – Figure 2.

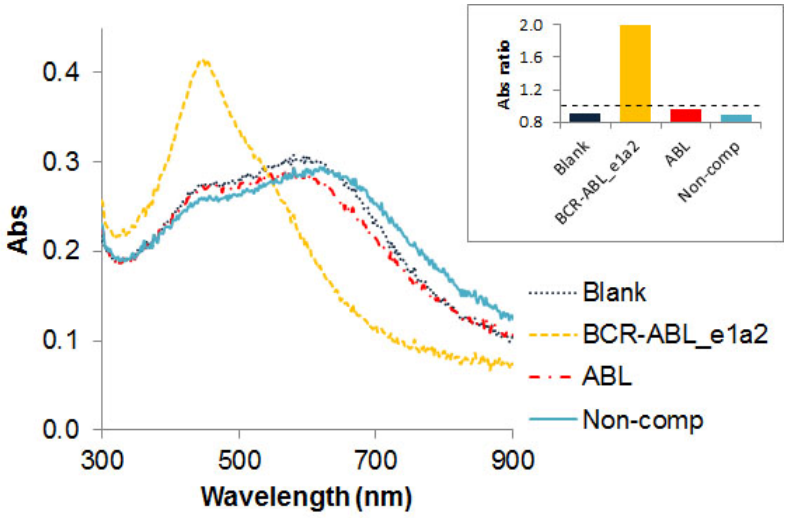

Figure 2 - UV/visible spectrum of BCR-ABL_e1a2 AuAg-alloy-nanoprobe alone (Blank) and in presence of a complementary target (BCR-ABL_e1a2); a semi-complementary target harboring the ABL gene sequence (ABL) and a non-complementary target with a non-related sequence. Inlet shows the ratio Abs_{442nm}/Abs_{600nm} with a dashed line positioned at a ratio equal to 1.

Absence of any target results in extensive aggregation (Blank). Only full hybridization of the AuAg-alloy-nanoprobe to a fully complementary synthetic sequence (BCR-ABL fusion sequence) avoids aggregation, whereas a semi-complementary target (normal ABL gene sequence) did not show the same capability. Based on the UV/Vis spectra, the extension of AuAg-alloy-nanoprobe aggregation was evaluated in terms of SPR variation, i.e. a ratio between the free and aggregated fractions after 15 min incubation with $MgCl_2$. The ratio between the peaks of the SPR characteristic of non-aggregated (Abs_{442nm}) and aggregated (Abs_{600nm}) nanoprobe was calculated. A ratio of 1 was considered as the point of equilibrium between non-aggregated and aggregated nanoprobe, hence the threshold to respectively consider the positive and negative discrimination of sequences (i.e. positive identification of complementary target for ratios greater than 1).

3.2 Au-nanoprobes for quantification of gene expression

Once the specific identification of the target sequence was achieved, the Au-nanoprobes were used to evaluate the quantification potential using an ABL gene specific sequence – Figure 3A. For this purpose, a complementary synthetic target was used in a spike in experiment using a non-complementary target to keep a constant total concentration of nucleic acids in solution. Aggregation of the Au-nanoprobe varied linearly for complementary target concentrations between 0.1 and 0.8 µM. Below 0.1 µM, full aggregation occurred. Above 0.8 µM of ABL target, the stability of ABL Au-nanoprobe remained unaltered. Additionally, a parallel experiment using different concentrations of the specific synthetic oligonucleotide target was performed by spiking in 20 ng/µl of total RNA extracted from an unrelated organism (i.e. *E. coli*). In this case, the ABL Au-nanoprobe no longer fully aggregated although a linear variation in Au-nanoprobe stability could still be observed for different concentrations of complementary target (see Figure 3A inlet). This residual stability could be due to some stabilization derived from partial sequence homology between the human ABL gene and an *E.coli* transposase.

Because C-MYC overexpression has been implicated in CML development[23], we then assessed whether the Au-nanoprobes were suitable for C-MYC expression analysis. Following the same approach as before, and using a C-MYC Au-nanoprobe, our data indicate a linear correlation ($R^2 = 0.96$) between the $Abs_{526nm}/Abs_{600nm}$for target concentration range between 33 and 133 nM (Figure 3B). Then, to show that this nanoprobe approach was suitable for mRNA quantitation in cells, we quantified the amount of C-MYC in total RNA extracted from a HL-60 cell line (an acute myeloid leukemia cell line where C-MYC is over expressed, where a similar linearity was attained (see Figure 3B inlet).

These results show that gene expression analysis is possible directly on total RNA extracted from cells, without the need for retrotranscription and/or amplification via PCR.

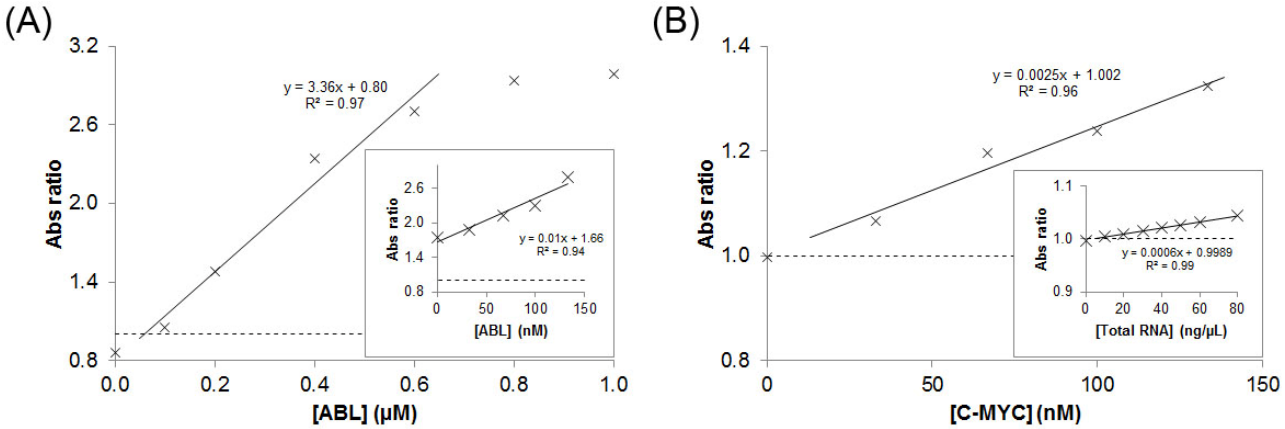

Figure 3 - Absorption ratios of (A) ABL and (B) C-MYC Au-nanoprobes for different concentrations of complementary targets. For (A), (B) and inlet (A) the absorption ratio - Abs526nm/Abs600nm – was considered. In the case of (B) and inlet (A) the complementary targets were spiked in total RNA *E.coli* (20ng/μL). Inlet (B) represents quantification ($AUC_{500nm-560nm}/AUC_{570nm-630nm}$) of C-MYC mRNA in total RNA extracted from HL-60 cell lines. Dashed lines represent a ratio equal to 1 and solid lines represent the trendline for ratios above 1 and up to a saturation point.

3.3 AuAg-alloy-nanoprobes for quantification of gene expression

A similar approach to that described above was followed to assess the potential of AuAg-alloy-nanoprobes (25%Au:75%Ag) for quantification purposes. Total RNA mixtures spiked in with synthetic oligonucleotides harboring the fusion site BCR-ABL_e1a2 – Figure 4.

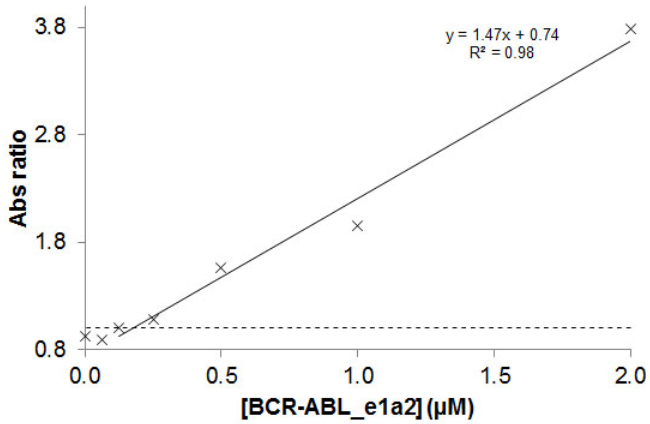

Figure 4 – Absorption ratio (Abs_{442nm}/Abs_{600nm}) of BCR-ABL_e1a2 AuAg-alloy-nanoprobe for different concentrations of complementary target. Total oligonucleotide concentration was kept constant at 4μM. Dashed line represents a ratio equal to1 and the solid line represent a trendline for data points with a ratio greater than 1.

The level of aggregation can be given by the absorption ratio Abs_{442nm}/Abs_{600nm}. Data show a linear correlation between the amount of specific target in the mixture and stability of the alloy-nanoprobe for target concentration range of 125 nM and 2 µM. This quantification capability is in good agreement with what has been demonstrated for Au-nanoprobes.

3.3 Au- and AuAg-alloy-nanoprobes for differential gene expression analysis – *proof-of-concept*

The analysis of differential gene expression is of utmost importance to assess the involvement of a specific gene product in a given phenotype. In CML, it is expected that the normal gene (i.e. ABL) maintains its levels of expression while the BCR-ABL fusion product, because it functions as an oncogene, sees its expression increased. To evaluate the potential of Au- and AuAg-alloy-nanoprobes for the quantification of two sequences in relation to each other, total RNA was spiked in with both targets - ABL and BCR-ABL_e1a2. Keeping the concentration of ABL constant, we added increasing amounts of the BCR-ABL_e1a2 target sequence and quantified it via the nanoprobe system – Figure 5. Despite the overall stabilization effect of the fragments in total RNA, it is clearly visible a concentration dependence of the level of aggregation of the alloy nanoprobe (complementary to the BCR-ABL fusion sequence) while the Au-nanoprobe shows that the levels of its complementary sequence (ABL) are constant.

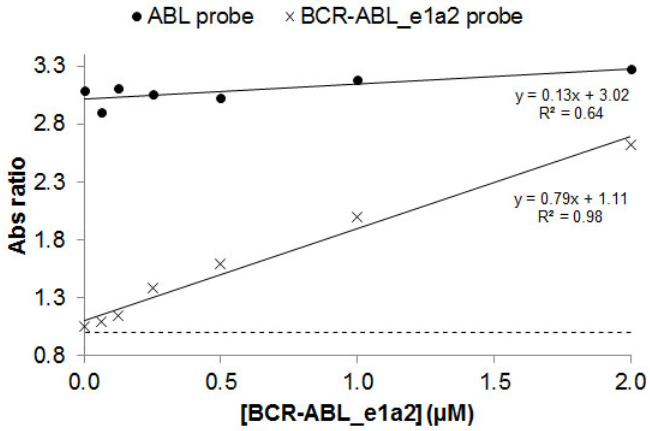

Figure 5- Absorption ratios (Abs_{526nm}/Abs_{600nm} and Abs_{442nm}/Abs_{600nm}, respectively) of ABL Au- and BCR-ABL_e1a2 AuAg-alloy-nanoprobes for different concentrations of BCR-ABL_e1a2 target, keeping the concentration of ABL target (2µM) and total RNA (20ng/µL) constant. Dashed black line represents a ratio equal to 1. Solid lines represent trendline for data points with a ratio greater than1.

The next step was to evaluate the possibility to quantify the BCR-ABL fusion product in a mixture containing constant concentrations of ABL in a one-pot assay – Figure 6. As seen above, aggregation of the AuAg-alloy-nanoprobe causes a red-shift of the SPR peak, with concomitant decrease of the peak intensity at 442 nm that can be easily observed and used for quantitation. Additionally, when the AuAg-alloy-nanoprobe and the Au-nanoprobe are joined together in the same solution, aggregation of the alloy nanoprobe leads to an increase of absorbance in the 500-600 nm region. This originates a small change of the SPR peak of the Au-nanoprobe. To facilitate analysis of the spectral changes as function of target concentration, the UV/visible spectra were normalized. Similarly to what is observed for each nanoprobe in separate, results show that it is possible to quantify the specific BCR-ABL target in solution, whilst keeping ABL constant. In fact, this is exactly what is observed in CML patients, where the BCR-ABL gene expression is induced while the normal ABL gene is under normal regulation and, thus, with constant levels of mRNA expression.

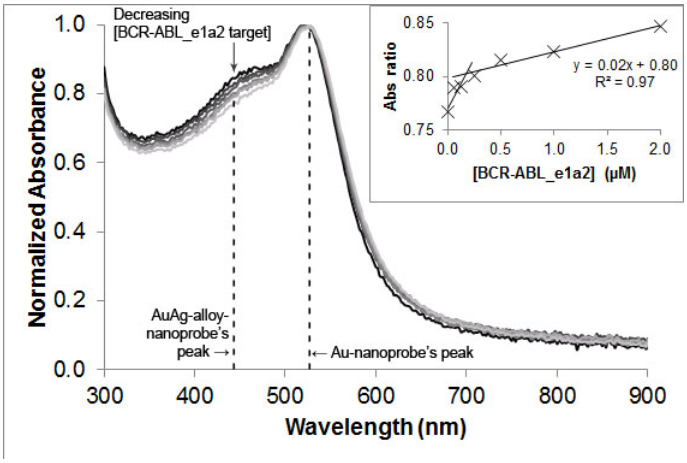

Figure 6 - Normalized UV/visible spectra of binary mixture (one-pot assay) of ABL Au- and BCR-ABL_e1a2 AuAg-alloy-nanoprobes for different concentrations of BCR-ABL_e1a2 target, keeping the concentration of ABL target (2μM) and total RNA (20ng/μL) constant. Dashed lines represent the characteristic SPR peak of each nanoprobe in a non-aggregated state. Inlet: Absorption ratio (Abs_{442nm}/Abs_{526nm}) of normalized data. Solid lines represents trendlines for data points.

4. CONCLUSIONS

We have demonstrated the functionalization of AuAg-alloy-NPs with ssDNA and the use of the resulting alloy nanoprobes for the specific detection of a target of interest. The attained AuAg-alloy-nanoprobes show a combination of the optical properties of Ag nanoparticles (high extinction coefficient) with the ease of functionalization via a thiol bond provided by the gold. Similarly to what is observed for Au-nanoprobes alone, these alloy nanoprobes are sensitive to variations in the quantity of target in solution and can, thus, be used for quantification assays. AuAg-alloy-nanoprobes with 25% gold and 75% silver were successfully synthesized and functionalized to produce nanoprobes that exhibit an SPR peak away from that of the Au-nanoprobes. This way, it is possible to better discriminate the aggregation profiles of both types of nanoprobes once they are used in a one-pot assay. Based on the combination of AuAg-alloy- and Au-nanoprobes, it was possible to develop a differential gene expression assay using the BCR-ABL fusion product involved in chronic myeloid leukemia as a model. We further demonstrated that this *dual-color* nanoparticle approach can be used as sensitive, selective, one-pot multicolor method for the simultaneous quantification of multiple RNA targets in a single reaction. The simultaneous differential quantification of two (or more) sequences is of utmost importance when performing genome based screening, where there is a mandatory need to assess whether a given transcript is present in a homo- or heterozygous form. This approach should be easily extendable to additional colors using the remarkable optical properties of nanoparticles of different sizes and compositions, i.e. different Au:Ag ratios, other metals may provide a multicolor homogenous system for application in array strategies and to rival fluorescence based assays.

ACKNOWLEGDMENTS

Work supported by FCT/MCTES (CIGMH); PTDC/SAU-BEB/66511/2006; SFRH/BD/62957/2009 for J. Conde. Nanotruck-Action NanoSciEra+ for G.Doria.

REFERENCES

[1] http://nano.cancer.gov
[2] Mirkin, C. A., Letsinger, R. L., Mucic, R. C., Storhoff, J. J., "A DNA-based method for rationally assembling nanoparticles into macroscopic materials", Nature 382 (6592), 607-609 (1996).

[3] Storhoff, J. J., Lucas, A. D., Garimella, V., Bao, Y. P., Muller, U. R., "Homogeneous detection of unamplified genomic DNA sequences based on colorimetric scatter of gold nanoparticle probes", Nat. Biotechnol. 22 (7), 883-887 (2004).
[4] Thaxton, C. S., Georganopoulou, D. G., Mirkin, C. A., "Gold nanoparticle probes for the detection of nucleic acid targets". Clin. Chim. Acta 363 (1-2), 120-126 (2006).
[5] Baptista, P., Pereira, E., Eaton, P., Doria, G., Miranda, A., Gomes, I., Quaresma, P., Franco, R., "Gold nanoparticles for the development of clinical diagnosis methods", Anal. Bioanal. Chem. 391 (3), 943-950 (2008).
[6] Baptista, P., Doria, G., Henriques, D., Pereira, E., Franco, R., "Colorimetric detection of eukaryotic gene expression with DNA-derivatized gold nanoparticles". J. Biotechnol. 119 (2), 111-117 (2005).
[7] Baptista, P. V., Koziol-Montewka, M., Paluch-Oles, J., Doria, G., Franco, R., "Gold-nanoparticle-probe-based assay for rapid and direct detection of Mycobacterium tuberculosis DNA in clinical samples", Clin. Chem. 52 (7), 1433-1434 (2006).
[8] Costa, P., Amaro, A., Botelho, A., Inácio, J., Baptista, P.V., "Gold nanoprobes assay for identification of mycobacteria from the Mycobacterium tuberculosis complex", Clin Microbiol Infect., 16, 1464–1469 (2010)
[9] Doria, G., Franco, R., Baptista, P., "Nanodiagnostics: fast colorimetric method for single nucleotide polymorphism/mutation detection", IET. Nanobiotechnol. 1 (4), 53-57 (2007).
[10] Griffin, J., Singh, A. K., Senapati, D., Lee, E., Gaylor, K., Jones-Boone, J., Ray, P. C., "Sequence-specific HCV RNA quantification using the size-dependent nonlinear optical properties of gold nanoparticles", Small 5 (7), 839-845 (2009).
[11] Wilcoxon, J., "Optical absorption properties of dispersed gold and silver alloy nanoparticles", J. Phys. Chem. B 113 (9), 2647-2656 (2009)
[12] Liz-Marzan, L. M., "Tailoring Surface Plasmons through the Morphology and Assembly of Metal Nanoparticles", Langmuir 22, 32-41 (2006)
[13] Doria, G., Larguinho, M., Dias, J. T., Pereira, E., Franco, R., Baptista, P. V., "Gold-silver-alloy nanoprobes for one-pot multiplex DNA detection", Nanotechnology 21(25),255101 (2010)
[14] Conde, J., de la Fuente, J. M., Baptista, P. V., "RNA quantification using gold nanoprobes - application to cancer diagnostics", J. Nanobiotechnol 8(1), 5 (2010)
[15] Hehlmann, R., Hochhaus, A., Baccarani, M., "Chronic myeloid leukaemia", Lancet 370 (9584), 342-350 (2007).
[16] Shet, A. S., Jahagirdar, B. N., Verfaillie, C. M., "Chronic myelogenous leukemia: mechanisms underlying disease progression", Leukemia 16 (8), 1402-1411 (2002).
[17] Ren, R., "Mechanisms of BCR-ABL in the pathogenesis of chronic myelogenous leukaemia", Nat. Rev. Cancer 5 (3), 172-183 (2005).
[18] Wong, S., Witte, O. N., "The BCR-ABL story: bench to bedside and back", Annu. Rev. Immunol. 22, 247-306 (2004).
[19] Melo, J. "Inviting leukemic cells to waltz with the devil", Nat. Med. 7 (2), 156-157 (2001).
[20] Ou, J., Vergilio, J. A., Bagg, A., "Molecular diagnosis and monitoring in the clinical management of patients with chronic myelogenous leukemia treated with tyrosine kinase inhibitors", Am. J. Hematol. 83 (4), 296-302 (2008).
[21] Lee, P. C., Meisel, D., "Adsorption and surface-enhanced Raman of dyes on silver and gold sols", J. Phys. Chem. 86 (17), 3391-3395 (1982).
[22] Burmeister, T., Maurer, J., Aivado, M., Elmaagacli, A. H., Grunebach, F., Held, K. R., Hess, G., Hochhaus, A., Hoppner, W., Lentes, K. U., Lubbert, M., Schafer, K. L., Schafhausen, P., Schmidt, C. A., Schuler, F., Seeger, K., Seelig, R., Thiede, C., Viehmann, S., Weber, C., Wilhelm, S., Christmann, A., Clement, J. H., Ebener, U., Enczmann, J., Leo, R., Schleuning, M., Schoch, R., Thiel, E., "Quality assurance in RT-PCR-based BCR/ABL diagnostics - results of an interlaboratory test and a standardization approach", Leukemia 14 (10), 1850-1856 (2000).
[23] Karakosta, A., Golias, Ch., Charalabopoulos, A., Peschos, D., Batistatou, A., Charalabopoulos, K., "Genetic models of human cancer as a multistep process. Paradigm models of colorectal cancer, breast cancer, and chronic myelogenous and acute lymphoblastic leukaemia", J Exp Clin Cancer Res 24 (4), 505-14 (2005).

❸

Gold Nanoparticles as Nanovectors for Therapy

OVERVIEW

This section presents 5 articles related to the studies on gold nanoparticles as nanovectors for therapy applications, using several strategies of biofunctionalization.

Article D describes the development of a dual pathway silencing of gene expression via ssDNA functionalized gold nanoparticles. In this study, gold nanoparticles modified with single-stranded thiolated-oligonucleotides have been evaluated as a two-way inhibition system that operates towards the suppression of in vitro transcription and translation. AuNPs functionalized with thiolated oligonucleotides to specifically inhibit transcription in vitro, demonstrating the synergetic effect between AuNP and a specific antisense sequence that blocks the T7 promoter region. In addition, we demonstrate that AuNPs functionalized with a thiolated oligonucleotide complementary to the ribosome binding site and the start codon, effectively shuts down in vitro translation. In this important study we also demonstrated that AuNPs efficiently protect the antisense oligonucleotide against nuclease degradation, which can thus retain its inhibitory potential.

Article **E** and **F** describes several strategies for functionalizing AuNPs with different biomolecules, such as proteins, peptides, polymers and RNA molecules. **Article E** describes the synergetic effect of Poly(ethylene glycol) biofunctional spacers and a peptide in dsRNA loading on the surface of AuNPs. This effect was found to be spatially and charged specific once the RNA loading was shaped by the electrostatic interactions between the peptide and the different charged PEG spacers. The peptide could approach the RNA to the gold surface arranging the entry of the oligo through the polyethyleneglycol layer with a positively polarized behaviour enhancing the oligo loading on the nanoparticle. In Article F we study the interaction between AuNPs functionalized with a protein (histone like) and circular DNA molecules. Our aim was to investigate whether or not these AuNP conjugates modified DNA condensation, altering plasmid DNA conformation and inducing structural changes.

These studies from **Articles E** and **F** were an important background for the development of the following studies. **Article G** describes the development of smart multifunctional gold nanoparticles for gene silencing. This study intends to develop an innovative kind of multifunctional gold nanoparticles loaded with polymers, cell penetrating and cell adhesion peptides and RNAi complementary to the proto-oncogene myc. The c-myc gene encodes a transcription factor that is critical for progression through the cell cycle, and mutations that misregulate *c-Myc* are frequently found in human and animal cancers. Thus the main rationale for selecting *c-Myc* as a target for cancer therapy is twofold; (i) the gene is involved in a wide

variety of human tumours and thus therapies could potentially have an impact on the treatment of a broader range of malignancies; (ii) *c-Myc* is involved in both proliferation and apoptosis, thus strategies aimed at targeting *c-Myc* might lead to either inhibition of tumour cell proliferation and/or increase in cell apoptosis. *c-Myc* could be targeted at different biological levels using various techniques, however using specifically designed cell targeting nanoparticles as a mean of intracellular delivery and self-tracking will provide a novel end product.

This biofunctionalization allowed the interaction between NPs and biological systems, ranging from *in vitro* cultured human cells (*HeLa* cells) to *in vivo* animal models (primitive *Hydra* and complex vertebrate mouse – C57BL/6j mice).

These studies were extended to the evaluation of the inflammatory response and therapeutic siRNA silencing via RGD-nanoparticles (the most efficient NPs produced in **Article G**) in a lung cancer mouse model – **Article H**. This article reported the use of siRNA/RGD gold nanoparticles capable of targeting tumour cells in two lung cancer xenograft mouse models, resulting in successful and significant *c-Myc* oncogene downregulation followed by tumour growth inhibition and prolonged survival of the animals.

All these studies were performed at the Research Centre for Human Molecular Genetics, Dept. of Life Sciences at Science and Technology Faculty, New University of Lisbon; IUI of Nanoscience of Aragon at the University of Zaragoza (Zaragoza, Spain); Centre for Cell Engineering (University of Glasgow, UK); Instituto di Cibernetica "E. Caianiello" (Pozzuoli, Italy); and Helmholtz Zentrum München (München, Germany).

Article D

"*In vitro* Transcription and Translation Inhibition via DNA functionalized Gold-Nanoparticles." **João Conde**, J.M. de la Fuente and P.V. Baptista. **Nanotechnology** (2010), Vol. 21, 505101. *Research article (IF= 3.842)*

Article E

"Effect of PEG biofunctional spacers and TAT peptide on dsRNA loading on Gold Nanoparticles." V. Sanz, **João Conde**, Y. Hernández, P.V. Baptista, M.R. Ibarra and J.M. de la Fuente. **Journal of Nanoparticle Research** (2012), Vol. 14, pp. 1-9. *Research article (IF=3.287)*

Article F

"Modification of Plasmid DNA Topology by Histone-Mimetic Gold Nanoparticles." **João Conde**, P.V. Baptista, Y. Hernández, V. Sanz and J.M. de la Fuente. **Nanomedicine (Lond).** (2012), Vol. 7, pp. 1657-1666. *Research article (IF=5.260)*

Article G

"Design of Multifunctional Gold Nanoparticles for In vitro and In vivo Gene Silencing." **João Conde***, A. Ambrosone*, V. Sanz, Y. Hernández, V. Marchesano, F. Tian, H. Child, C.C. Berry, M.R. Ibarra, P.V. Baptista, C. Tortiglione and J.M. de la Fuente. (* Co-first authors). **ACS Nano** (2012), Vol. 6, pp. 8316–8324. *Research article (IF=12.062)*

Article H

"*In vivo* tumour targeting via nanoparticle-mediated therapeutic siRNA coupled to inflammatory response in lung cancer mouse models." **João Conde***, F. Tian*, Y. Hernández, C. Bao, D. Cui, K.P. Janssene, M.R. Ibarra, P.V. Baptista, T. Stoëger and J.M. de la Fuente. (* Co-first authors). **Biomaterials** (2013), Vol. 34, pp. 7744–7753. *Research article (IF=7.604)*

Articles D, E, F, G and **H**

Declaration of authorship

I, João Diogo Osório de Castro Conde, declare that the manuscripts preparation and writing was carried out by me, Prof. Pedro V. Baptista, Prof. Jesus M. de la Fuente, and all the associated co-authors.

João Conde contributions:

Article D – JC designed all the methods, generated the ssDNA-AuNPs, and calibrated, carried out characterization and performed the in vitro assays. JC also drafted the manuscript protocols and all the figures.

Article E – JC carried out the characterization and quantification assays concerning the functionalization of AuNPs with the polymers, peptide and dsRNA molecules. JC also drafted some of the manuscript sections and figures.

Article F – JC conceived the project. JC designed the plasmid-AuNPs interaction and kinetic assays. JC also drafted the manuscript protocols and all the figures.

Article G – JC carried out all the synthesis and functionalization methods regarding the production of all nanoformulations in this study. JC also performed all cell studies. JC also drafted some of the manuscript sections and figures.

Article H – JC carried out all the synthesis and functionalization methods regarding the production of all nanoformulations in this study. JC analysed all the data and wrote the manuscript.

We, Pedro V. Baptista and Jesus M. De la Fuente, as supervisors of João Conde hereby acknowledge and confirm that the information above is correct.

João Conde

Pedro V. Baptista

Jesus M. de la Fuente

Nanotechnology **21** (2010) 505101 (6pp) doi:10.1088/0957-4484/21/50/505101

In vitro transcription and translation inhibition via DNA functionalized gold nanoparticles

J Conde[1,2], J M de la Fuente[2] and P V Baptista[1]

[1] Centro de Investigação em Genética Molecular Humana (CIGMH), Departamento de Ciências da Vida, Faculdade de Ciências e Tecnologia, Universidade Nova de Lisboa, 2829-516 Caparica, Portugal
[2] Instituto de Nanociencia de Aragón, Universidad de Zaragoza, Pedro Cerbuna 12, 50009 Zaragoza, Spain

E-mail: pmvb@fct.unl.pt

Received 1 September 2010, in final form 15 October 2010
Published 22 November 2010
Online at stacks.iop.org/Nano/21/505101

Abstract
The use of gold nanoparticles (AuNPs) has been gaining momentum as vectors for gene silencing strategies, combining the AuNPs' ease of functionalization with DNA and/or siRNA, high loading capacity and fast uptake by target cells. Here, we used AuNP functionalized with thiolated oligonucleotides to specifically inhibit transcription *in vitro*, demonstrating the synergetic effect between AuNPs and a specific antisense sequence that blocks the T7 promoter region. Also, AuNPs efficiently protect the antisense oligonucleotide against nuclease degradation, which can thus retain its inhibitory potential. In addition, we demonstrate that AuNPs functionalized with a thiolated oligonucleotide complementary to the ribosome binding site and the start codon, effectively shut down *in vitro* translation. Together, these two approaches can provide for a simple yet robust experimental set up to test for efficient gene silencing of AuNP–DNA conjugates. What is more, these results show that appropriate functionalization of AuNPs can be used as a dual targeting approach to an enhanced control of gene expression—inhibition of both transcription and translation.

S Online supplementary data available from stacks.iop.org/Nano/21/505101/mmedia

(Some figures in this article are in colour only in the electronic version)

1. Introduction

The unique physico-chemical properties of metal nanoparticles (NPs), and in particular gold NPs, show great potential of application in biomedicine for the development of sensing platforms and therapeutics [1, 2]. Recent advances in approaches using AuNPs functionalized with oligonucleotides have made them an attractive tool for DNA based therapy [3–7], where antisense DNA technology in particular shows a significant potential for gene regulation in therapeutics [8–11]. These approaches rely on the use of nucleic acids that bind to specific targets following cellular uptake, either by blocking the RNA polymerase promoter preventing transcription into mRNA and/or of protein production via impediment of association of the protein production facilities—the ribosome. However, a major problem is the poor stability of nucleic acids in biological media, as unmodified phosphodiester oligonucleotides are rapidly degraded in most biological systems [12]. Protection against degradation by nucleases can be circumvented through the use of AuNPs [13, 14]. Also, AuNPs have been shown to interfere with protein binding, thus strongly modulating the resulting effect [15]. Recently, the effect of non-specific binding of AuNP–DNA nanoconjugates in protein production has been elegantly demonstrated [16]. Therefore, precise assessment of the selected sequence on gene silencing mediated by AuNP–DNA conjugates is of utmost importance when developing efficient antisense therapeutic vectors.

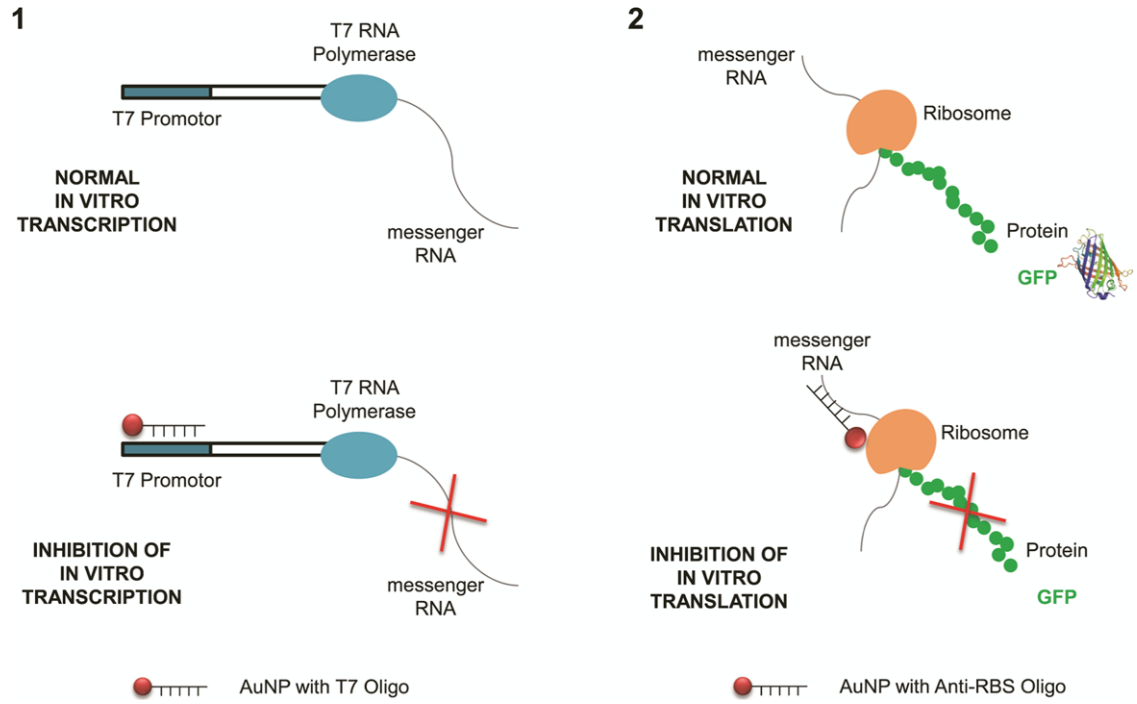

Figure 1. Silencing gene expression using targeted AuNP–DNA conjugates. AuNP–DNA conjugates specifically block (**1**) *in vitro* transcription via binding to the T7 RNA polymerase promoter, and (**2**) *in vitro* translation by suppressing the ribosome binding site (RBS).

We used *in vitro* transcription and *in vitro* translation assays to demonstrate the potential use of specific AuNP–DNA conjugates to silence gene expression. These *in vitro* approaches show some advantages over *in vivo* gene expression as there is no need to support processes required for cell viability, or when the over-expressed product is toxic or insoluble [17, 18]. As a result we can produce a two-way inhibition system (see figure 1) using AuNP–DNA conjugates to specifically block *in vitro* transcription by binding the RNA polymerase promoter and *in vitro* translation by suppressing the ribosome.

We evaluate the use of AuNPs functionalized with thiol-modified single-stranded oligonucleotides to block the transcriptional machinery at the specific promoter site and to repress gene translation by blocking the ribosome binding site. We also evaluate the protection conveyed by the AuNPs against the destructive effect of cellular nucleases on naked oligonucleotides. As the DNA bound to AuNP is efficiently protected from nuclease digestion it is thus expected that these AuNP conjugates might also provide a shield for the entrapped DNA during gene delivery. The proposed system could be of great interest when assessing the gene therapy potential of a given AuNP–DNA conjugate.

2. Experimental procedure

All synthesized unmodified and thiol-modified oligonucleotides were purchased from STAB Vida, Lda. (Portugal). All chemicals were from Sigma-Aldrich and of the highest purity available.

2.1. AuNP synthesis

Gold NPs were prepared by the citrate reduction method described by Lee and Meisel [19]. Briefly, 250 ml of 1 mM $HAuCl_4$ was brought to a boil while stirring in a 500 ml round-bottom flask. Twenty-five milliliters of 38.8 mM sodium citrate was quickly added and the mixture was refluxed for 15 min with continuous stirring. The flask was left to cool to room temperature and stored in the dark until use. The average size of the particles was obtained by analysis of TEM images.

2.2. AuNP–DNA conjugate synthesis

All oligonucleotides used are listed in table 1. Thiolated oligonucleotides were suspended in 1 ml of 0.1 M dithiothreitol (DTT), extracted three times with ethyl acetate and further purified through a desalting NAP-5 column (Pharmacia Biotech, Sweden).

AuNP–DNA conjugates were prepared as previously described [20, 21]. Briefly, an appropriate volume of 10 μM thiol-modified T7 or antisense oligonucleotide was initially incubated with 6 ml of an aqueous solution of AuNPs ($\approx$8.55 nM) for at least 16 h. After centrifugation (20 min at 14 500g), the oily precipitate was washed with 5 ml of 10 mM phosphate buffer (pH 8.0), 0.1 M NaCl, recentrifuged and redispersed in 5 ml of the same buffer to a final concentration in AuNPs of 8.5 nM. The resulting AuNP–DNA conjugate was stored in the dark at 4 °C.

2.3. Quantitation of thiol-oligonucleotides loaded on AuNPs

Coverage (average number of ssDNA strands per particle) was measured by completely displacing the DNA from the AuNPs

Table 1. ssDNA sequences used for *in vitro* transcription and translation assays.

Assay	Oligonucleotide	Sequence
In vitro transcription	AuNP–T7	5′-HS-$(CH_2)_6$-TCTCCCTATAGTGAGTCGTATTA-3′
	T7 oligo	5′-TCTCCCTATAGTGAGTCGTATTA-3′
In vitro translation	AuNP–antisense	5′-HS-$(CH_2)_6$-CATGGTATATCTCCTTCTTA-3′
	AuNP–nonsense	5′-HS-$(CH_2)_6$-CGCTGAAGGGCTTTTGAACT-3′

in 1 M DTT for 48 h. After 48 h at room temperature, the solutions containing the displaced oligonucleotides were removed from the AuNPs by centrifugation at 14 500*g* for 20 min. The concentration of oligonucleotides in the supernatant was measured using an OliGreen ssDNA Quantitation Kit® (Molecular Probes) according to the manufacturer's guidelines in a PerkinElmer LS45 Fluorescence Spectrometer (USA) using an Ultra-Micro quartz cell (Hëllma, Germany). The concentration of DNA was calculated from fluorescence intensity of DNA solutions with known concentration. All the AuNPs samples and the standard solutions of the thiol-oligonucleotide were kept at the same pH and ionic strength and calibration for all measurements due to the sensitivity of the optical properties of the OliGreen® to these conditions. Fluorescence emission was converted to molar concentrations of the thiol-modified oligonucleotide by interpolation from a standard linear calibration curve. Standard curves were prepared with known concentrations of thiol-oligonucleotide using the same buffer pH, salt, and DTT concentrations. The average number of oligonucleotides per particle was obtained by dividing the measured oligonucleotide molar concentration by the original Au nanoparticle concentration.

2.4. Reverse transcription and PCR amplification

The total RNA extracted from HL-60 cells was subjected to reverse transcription (RT) for cDNA synthesis. The RT reaction was performed with Revert-AidTM M-MuLV Reverse Transcriptase (Fermentas, Vilnius, Lithuania) according to the manufacturer's specifications, using 20 μM of MYCreverse primer, annealing at 42 °C for 1 h and 70 °C for 10 min to reverse transcriptase inactivation. The resulting 229 bp fragment of the human v-myc myelocytomatosis viral oncogene homolog (MYC) gene was PCR amplified using the primers MYCforward: 5′-GCTCATTTCTGAAGAGGACTTGT-3′ and MYCreverse: 5′-AGGCAGTTTACATTATGGCTAAATC-3′. PCR amplification was performed in duplicate on a MyCycler Thermocycler (Biorad) in 25 μl using 1 μM of primers, 2.5 mM dNTPs with 1 U Taq DNA Polymerase (GE Healthcare Europe GmbH, Freiburg, Germany), with the following thermal cycling conditions: initial 5 min denaturation at 95 °C, followed by 30 amplification cycles of denaturation at 95 °C for 30 s, annealing at 62 °C for 30 s, elongation at 72 °C for 30 s, and a final elongation at 72 °C for 5 min. The RT-PCR product was re-amplified using a T7 promoter–MYCforward primer (5′-TAATACGACTCACTATAGGGAGAGCTCATTTCTGAAGAGGACTTGT-3′). The resulting 252 bp T7-cMYC-fusion fragment was PCR amplified using the primers MYCreverse and T7 primer (5′-TAATACGACTCACTATAGGGAGA-3′) as described above and purified through an NZYGelpure purification kit (NZYtech genes & enzymes, Portugal). Confirmation of correct PCR products was performed by 2% agarose gel electrophoresis stained with GelRed™. This product was used as template for *in vitro* transcription reactions.

2.5. In vitro transcription

Standard *in vitro* transcription was performed in a volume of 50 μl containing *in vitro* transcription buffer, 10 mM of each NTP, 500 ng of the 252 bp DNA template and with 30 U of T7 RNA polymerase (Fermentas, Vilnius, Lithuania) according to the manufacturer's protocol. Reactions were incubated for 2 h at 37 °C, followed by heat inactivation of enzyme for 15 min at 75 °C and cooling to −20 °C. All transcription reaction products were centrifuged at 14 500*g* for 20 min to pellet the AuNPs and 27 μl of the supernatant was evaluated on a 3% agarose gel electrophoresis with GelRed™ staining. Product quantity determination was performed by pixel intensity/counting using ImageJ™ imaging software as previously described [22, 23]. Determination of the degree of inhibition was performed after normalizing to the intensity of the positive control (100%) of the *in vitro* transcription reaction.

2.6. Nuclease digestion

In order to evaluate nuclease resistance the functionalized AuNP–DNA conjugate and the naked T7 oligonucleotide were subjected to DNase I digestion, performed with 10 U of DNase I (Invitrogen, Karlsbad, CA, USA) in DNase I buffer (100 mM Tris-HCl, 25 mM $MgCl_2$, 1 mM $CaCl_2$, pH 7.5 at 25 °C) for 30, 90 and 180 min at 37 °C, which was subsequently heat inactivated for 10 min at 65 °C. The molar concentration of the naked T7 oligonucleotide was the matched to that of the number of oligonucleotides per particle. The molar concentration of the oligonucleotide bound to AuNP was determined as previously described and the naked T7 oligonucleotide quantified by optical absorbance at 260 nm. Samples containing the AuNP–DNA conjugates were centrifuged at 14 500*g* for 20 min, and those containing the naked T7 oligonucleotide were ethanol precipitated. The resulting pellets were resuspended in DEPC–H_2O and used in transcription reactions as described above.

2.7. In vitro translation

The pGFP vector (4235 bp), which encodes the native (i.e., non-fusion) GFP protein, was transformed into *E. coli* DH5α as described previously [24]. The pGFP (5Prime, GmbH,

VWR International) used as template for *in vitro* protein synthesis reactions contains the GFP gene under control of T7 promoter (TAATACGACTCACTATAGGGAGA) upstream of the ribosome binding site (RBS) with the 'epsilon sequence' (TTAACTTTA) derived from gene 10 of bacteriophage T7 [25] followed by a Shine–Dalgarno sequence (AAGGAG) and a T7 terminator (TAGCATAACCCCTTGGGGCCTC-TAAACGGGTCTTGAGGGGTTTTTTG) at the 3′ end of the GFP gene.

The coupled *in vitro* transcription/translation reactions were performed in a Rapid Translation System RTS 100 *E. coli* HY Kit (5Prime, GmbH, VWR International). GFP protein was synthesized for 6 h at 30 °C followed by incubation at 4 °C for 24 h to GFP maturation. GFP protein levels were measured using fluorescence spectroscopy (λ excitation = 395 nm, λ emission = 510 nm) in a PerkinElmer LS45 Fluorescence Spectrometer (USA) using an Ultra-Micro quartz cell (Hëllma, Germany). Assessment of AuNP–DNA conjugate influence in translation was performed by adding 1 μg of GFP vector and crescent concentrations of the AuNP–DNA conjugates to the standard reaction mixture. After 24 h storage at 4 °C, the reactions were centrifuged at 14 500g for 20 min to pellet AuNP–DNA conjugates. The translation levels were measured as fluorescence of GFP.

3. Results and discussion

AuNPs of 14 nm (D = 14.07 nm, see supplementary information S1 available at stacks.iop.org/Nano/21/505101/mmedia) were synthesized via the citrate reduction method and, in a first set of experiments, functionalized with a thiol-modified 23-mer complementary to the promoter region recognized by T7 RNA polymerase (T7 oligo). We report that the affinity between specific T7 promoter gold nanoparticles and DNA is strong enough to completely inhibit transcription of DNA by T7 RNA polymerase and, as a consequence, decrease the levels of mRNA produced. These AuNP–T7 conjugates, together with the naked AuNPs and oligonucleotide, were used in standard *in vitro* transcription assays, and the level of transcription determined. Direct comparison between T7 oligo and AuNP–T7 conjugates is feasible via utilization of naked T7 at the same concentration as the T7 concentration calculated to be covering the AuNP. When the T7 oligo was added to the reaction, 27% inhibition of transcription was attained, at 0.06 nM (figure 2). Addition of the AuNP–T7 conjugates (70 ± 3 oligos/NP) originated a decrease in the level of transcription of 60%. For higher concentrations of the AuNP–DNA conjugates, the level of transcription quickly reached background levels (>0.64 nM). However, those levels of transcription were impossible to attain with free T7. It should be noted that naked AuNPs can achieve almost total inhibition of transcription at concentrations higher that 2.5 nM, i.e. four times the concentration of AuNP–DNA conjugates needed for comparable inhibition. Results also show that the inhibitory effect of AuNP–DNA conjugates strongly depends on concentration, being exceptionally effective for very low amounts of these conjugates. AuNP–DNA conjugates with half the amount of oligonucleotides

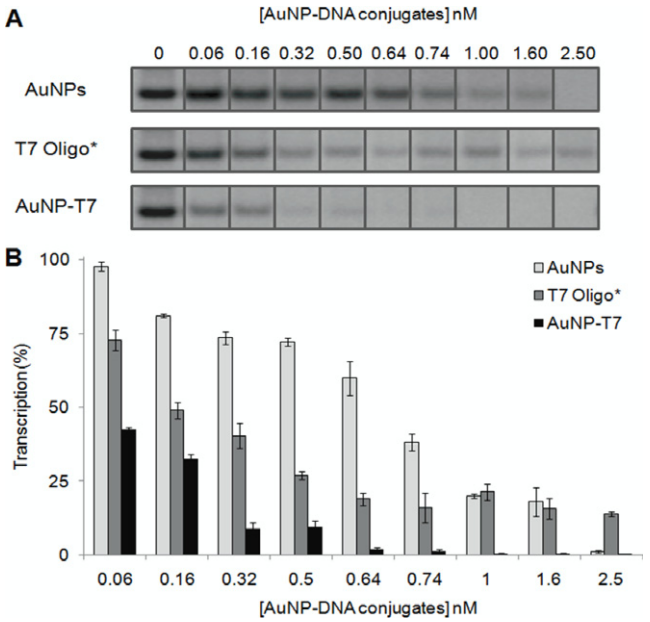

Figure 2. Inhibition of *in vitro* transcription via AuNP–DNA conjugates. (A) Agarose gel electrophoresis of *in vitro* transcription reactions in the presence of increasing AuNP–DNA conjugate concentration. The bands in the gel represent the mRNA product produced by *in vitro* transcription. Increasing concentrations of AuNP–DNA conjugates correspond to decreasing amounts of mRNA. (B) Transcription levels as function of increasing AuNP–DNA conjugates. Determination of the degree of inhibition was performed after normalizing to the intensity of the positive control (100%) of the *in vitro* transcription reaction. Error bars correspond to average and standard deviation of two independent assays. * Direct comparison between free T7 oligonucleotide and AuNP–T7 conjugates is feasible via utilization of naked T7 at the same concentration as the T7 concentration determined at the surface of the AuNP–DNA conjugate.

at the NPs' surface (44 ± 2 oligos/NP), showed comparable inhibitory effect (see supplementary information S2 available at stacks.iop.org/Nano/21/505101/mmedia). Naked AuNPs also demonstrate an inhibitory effect on transcription, maybe due to unspecific adsorption of proteins (i.e. polymerase) to the AuNPs' surface [26, 27]. These results seem to indicate the existence of a synergic effect between the AuNP and the T7 oligonucleotide sequence. Specific sequence inhibition of the promoter region is achieved via the T7 oligonucleotide and localization of the AuNP on the same recognition sequence seriously hampers enzymatic activity, probably due to steric hindrance [28]. In fact, the T7 RNA polymerase exhibits extreme specificity for its own promoter and will only transcribe the DNA harboring the T7 promoter sequence. The steric block is caused by the T7 oligo hybridization to the promoter region compromising the recognition by the polymerase [29].

DNA vectorization into cells is frequently hampered by the degradation of the DNA load by cell nucleases and, therefore, on the inhibition potential of a gene therapy vector. To assess the protective effect of AuNP against nuclease digestion and its repercussion in the inhibition potential of the AuNP–DNA conjugates, we submitted the AuNP–T7

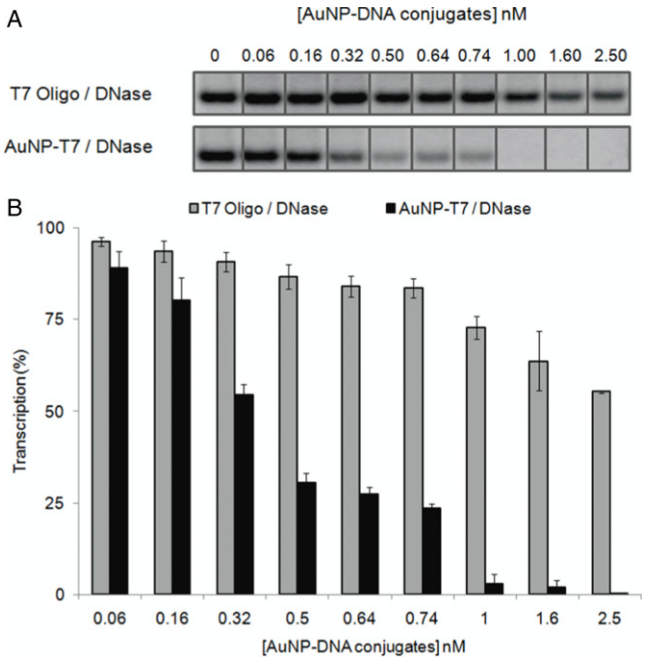

Figure 3. AuNP–DNA conjugates' resistance to nuclease attack. (A) Agarose gel electrophoresis of *in vitro* transcription reactions after 90 min nuclease digestion for AuNP–T7 and free T7 oligonucleotide. The bands in the gel represent the mRNA product produced by *in vitro* transcription. (B) Product quantification performed as described above. Error bars correspond to average and standard deviation of two independent assays. * Direct comparison between T7 oligo alone and AuNP–T7 conjugates is feasible via utilization of naked T7 at the same concentration as the T7 concentration calculated to be covering the AuNP–DNA conjugate.

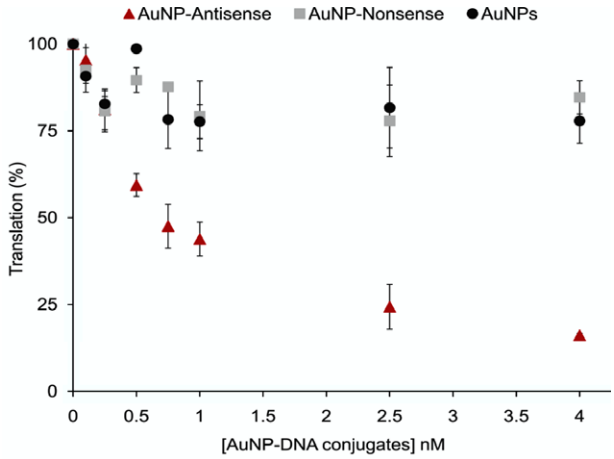

Figure 4. Inhibition of *in vitro* translation by AuNP–DNA conjugates. *In vitro* translation levels, measured as fluorescence of GFP, after incubation with AuNP–antisense conjugates (red triangles), AuNP–nonsense (filled squares) and unmodified AuNPs (filled circles). Error bars correspond to average and standard deviation of two independent assays.

conjugates and the naked T7 oligonucleotide to digestion with DNase I. We then assessed the effect on *in vitro* transcription of the 'digested' AuNP–T7 and naked T7 in a similar way as described above. After 90 min of DNase I digestion, the naked T7 oligonucleotide had minimal influence on the rate of transcription, showing that it had been completely degraded. Conversely, the AuNP–T7 conjugates showed that, even after extensive nuclease activity, they retain the capability to inhibit transcription (figure 3). When compared to the results attained without digestion, where only 0.64 nM of AuNP–DNA conjugate was needed to completely inhibit transcription (see figure 2), following nuclease action the same effect is only attained at 1 nM, i.e. nuclease activity is responsible for a 56% loss of inhibition potential. These results demonstrate the greatly enhanced stability to nuclease attack of single-stranded oligonucleotides functionalized on the surface of gold nanoparticles. The extent of DNA degradation on the AuNP surface was also evaluated through the aggregation profiles of the AuNP–DNA conjugates to increasing salt concentrations, as cleavage of DNA strands in the surface of nanoparticles by DNase I ought to decrease stability to increasing ionic strength and cause AuNP to aggregate. In fact, the 'digested' AuNP–T7 showed only a slight shift in surface plasmon band peak from 520 to 550 nm (see supplementary information S3 available at stacks.iop.org/Nano/21/505101/mmedia) whereas the 'naked' AuNPs show extensive aggregation (red-shift to 700 nm), upon addition of 30 mM $MgCl_2$. The protection provided by the AuNPs also depends on the time of exposure to nucleases (see supplementary information S4 available at stacks.iop.org/Nano/21/505101/mmedia). These results suggest that the AuNP–DNA conjugates' resistance to nuclease degradation ought to increase the lifetime of the oligonucleotide within the cell and, therefore, constitutes a great advantage for antisense oligonucleotide delivery.

We then evaluated the efficiency of AuNP–DNA conjugates to suppress *in vitro* translation. The same AuNPs used for the *in vitro* transcription assays were functionalized with a thiolated 20-mer oligonucleotide (AuNP–antisense) whose sequence is complementary to the Shine–Dalgarno sequence (i.e. the ribosome binding site) and to the start codon. In this way, effective silencing of expression is achieved by simultaneously blocking ribosome access and initiation of translation. Fluorescence measured from green fluorescent protein (GFP) decreased by about 80% after incubation with the AuNP–antisense conjugates—red triangles in figure 4. No significant change to fluorescence measurements was noted for naked AuNPs or AuNP functionalized with an unrelated sequence to that of the target mRNA (AuNP–nonsense)—filled circles and filled squares in figure 4, respectively. Antisense inhibition by AuNP–DNA conjugates has been previously reported [30], even though the antisense mechanism is not clearly understood [31–33]. Recently, enhancement of *in vitro* translation by AuNP–DNA conjugates was demonstrated to occur via a combination of non-specific adsorption of translation-related molecules and the ribosome to the AuNP–DNA conjugate and specific binding to the mRNA of interest; whereas strong binding of AuNP–DNA to mRNA results only in inhibition, as it probably sterically hinders the ribosome from reading the mRNA [15]. Here we showed that combination of AuNP with a specific oligonucleotide that simultaneously blocks the ribosome binding site and the start codon strongly inhibits *in vitro* translation, probably due to the synergetic effect of the sequence unavailability due to the

antisense oligonucleotide and steric hindrance of the binding site essential for recognition by the ribosome.

4. Conclusions

Here we show that gold nanoparticles functionalized with promoter specific oligonucleotides strongly disrupt transcription even after extensive nuclease digestion, indicating the proficiency of these AuNP–DNA conjugates for application as gene silencing vectors. We also demonstrate that enhanced specific *in vitro* translation inhibition is achieved by means of the antisense oligonucleotides on the AuNP surface. These AuNP–DNA conjugates seem to profit from the synergy between the specific sequence blocking and the steric hindrance provided by the AuNPs.

The described experimental setup can provide researchers with a simple yet robust means to assess the gene silencing potential of nanoparticle–DNA conjugates being developed for gene expression silencing purposes. These results show that a dual targeting approach for gene silencing could be explored—blocking transcription and translation, which can be achieved via combination of different oligonucleotide sequences on one or more nanoparticle vectors.

Acknowledgments

The authors thank Fundação para a Ciência e Tecnologia (CIGMH, PTDC/SAU-BEB/66511/2006), Nanotruck-Action NanoSciEra+ and ARAID for funding. J Conde acknowledges grant number (SFRH/BD/62957/2009). Dr G Doria is also acknowledged for valuable discussions and TEM analysis.

References

[1] Baptista P, Pereira E, Eaton P, Doria G, Miranda A, Gomes I, Quaresma P and Franco R 2008 *Anal. Bioanal. Chem.* **391** 943–50
[2] Giljohann D A, Seferos D S, Daniel W L, Massich M D, Patel P C and Mirkin C A 2010 *Angew Chem. Int. Edn.* **49** 3280–94
[3] Peer D, Karp J M, Hong S, Farokhzad O C, Margalit R and Langer R 2007 *Nat. Nanotechnol.* **2** 751–60
[4] Sanvicens N and Marco M P 2008 *Trends Biotechnol.* **26** 425–33
[5] Gil P R and Parak W J 2008 *ACS Nano* **2** 2200–5
[6] Ferrari M 2005 *Nat. Rev. Cancer* **5** 161–71
[7] Braun G B, Pallaoro A, Wu G, Missirlis D, Zasadzinski J A, Tirrell M and Reich N O 2009 *ACS Nano* **3** 2007–15
[8] Davis M E, Zuckerman J E, Choi C H, Seligson D, Tolcher A, Alabi C A, Yen Y, Heidel J D and Ribas A 2010 *Nature* **464** 1067–70
[9] Tamm I, Dorken B and Hartmann G 2001 *Lancet* **358** 489–97
[10] Toub N, Malvy C, Fattal E and Couvreur P 2006 *Biomed. Pharmacother.* **60** 607–20
[11] Fichou Y and Ferec C 2006 *Trends Biotechnol.* **24** 563–70
[12] Cooper S R, Taylor J K, Miraglia L J and Dean N M 1999 *Pharmacol. Ther.* **82** 427–35
[13] Guo P 2005 *J. Nanosci. Nanotechnol.* **5** 1964–82
[14] Ghosh P, Han G, De M, Kim C K and Rotello V M 2008 *Adv. Drug Deliv. Rev.* **60** 1307–15
[15] Park S and Hamad-Schifferli K 2010 *ACS Nano* **4** 2555–60
[16] Agbasi-Porter C, Ryman-Rasmussen J, Franzen S and Feldheim D 2006 *Bioconjug. Chem.* **17** 1178–83
[17] Swartz J R and Spirin A S 2007 *Cell-free Protein Synthesis: Methods and Protocols* (New York: Wiley)
[18] Iskakova M B, Szaflarski W, Dreyfus M, Remme J and Nierhaus K H 2006 *Nucleic Acids Res.* **34** e135
[19] Lee P C and Meisel D 1982 *J. Phys. Chem.* **86** 3391–5
[20] Baptista P, Doria G, Henriques D, Pereira E and Franco R 2005 *J. Biotechnol.* **119** 111–7
[21] Doria G, Baumgartner B G, Franco R and Baptista P V 2010 *Colloids Surf.* B **77** 122–4
[22] Luhtala N and Parker R 2009 *Nucleic Acids Res.* **37** 5529–36
[23] https://www.lukemiller.org/journal/2007/08/quantifying-western-blots-without.html
[24] Ausubel F M, Brent R, Kingston R E, Moore D D, Seidman J G, Smith J A and Struhl K 1987 *Current Protocols in Molecular Biology* (New York: Greene publishing Associates and Wiley–Interscience)
[25] Olins P O and Rangwala S H 1989 *J. Biol. Chem.* **264** 16973–6
[26] Vu B V, Litvinov D and Willson R C 2008 *Anal. Chem.* **80** 5462–7
[27] Giljohann D A, Seferos D S, Patel P C, Millstone J E, Rosi N L and Mirkin C A 2007 *Nano Lett.* **7** 3818–21
[28] Li H and Rothberg L J 2004 *J. Am. Chem. Soc.* **126** 10958–61
[29] Durniak K J, Bailey S and Steitz T A 2008 *Science* **322** 553–7
[30] Rosi N L, Giljohann D A, Thaxton C S, Lytton-Jean A K, Han M S and Mirkin C A 2006 *Science* **312** 1027–30
[31] Jason T L, Koropatnick J and Berg R W 2004 *Toxicol. Appl. Pharmacol.* **201** 66–83
[32] Patil S D, Rhodes D G and Burgess D J 2005 *AAPS J* **7** E61–77
[33] Walton S P, Stephanopoulos G N, Yarmush M L and Roth C M 2002 *Biophys. J.* **82** 366–77

Supporting Information

In vitro transcription and translation inhibition via DNA functionalized gold-nanoparticles

J Conde [1,2], J M. de la Fuente [2] and P V Baptista [1,*]

[1] *CIGMH, Departamento de Ciências da Vida, Faculdade de Ciências e Tecnologia, Universidade Nova de Lisboa, Campus de Caparica, 2829-516 Caparica, Portugal.*

[2] *Instituto de Nanociencia de Aragón, Universidad de Zaragoza, Pedro Cerbuna 12, 50009, Zaragoza, Spain.*

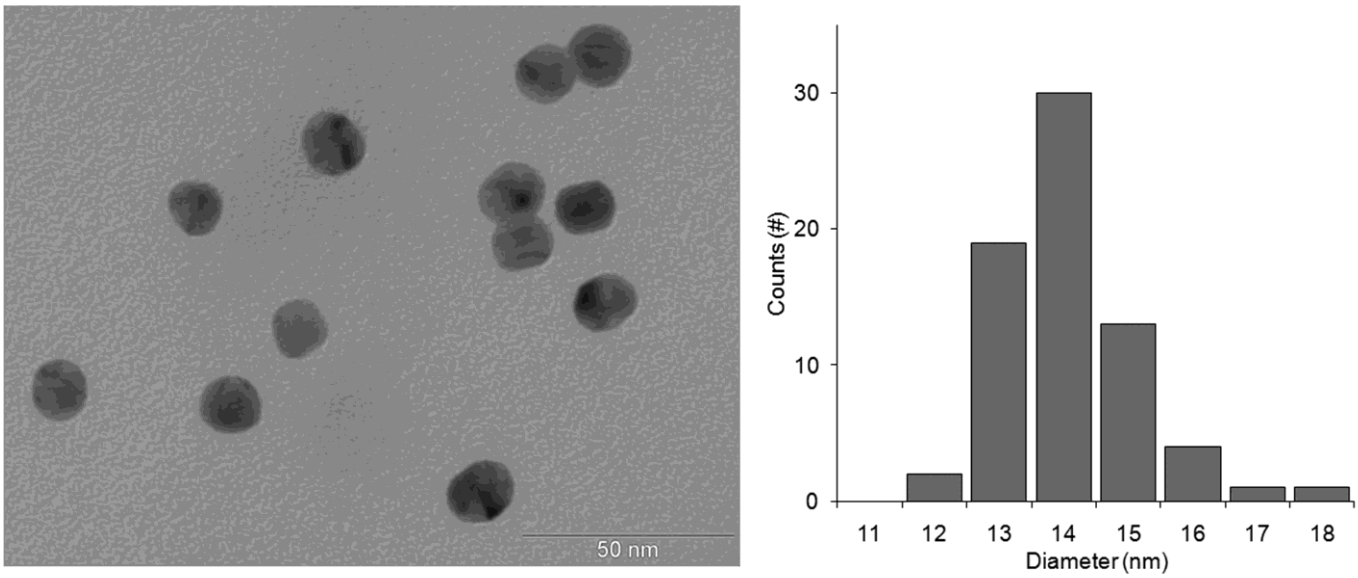

Figure S1. Gold nanoparticles size distribution. TEM images (Left, scale bar = 50 nm) and sizing histogram (Right, average diameter = 14.07 nm) of AuNPs.

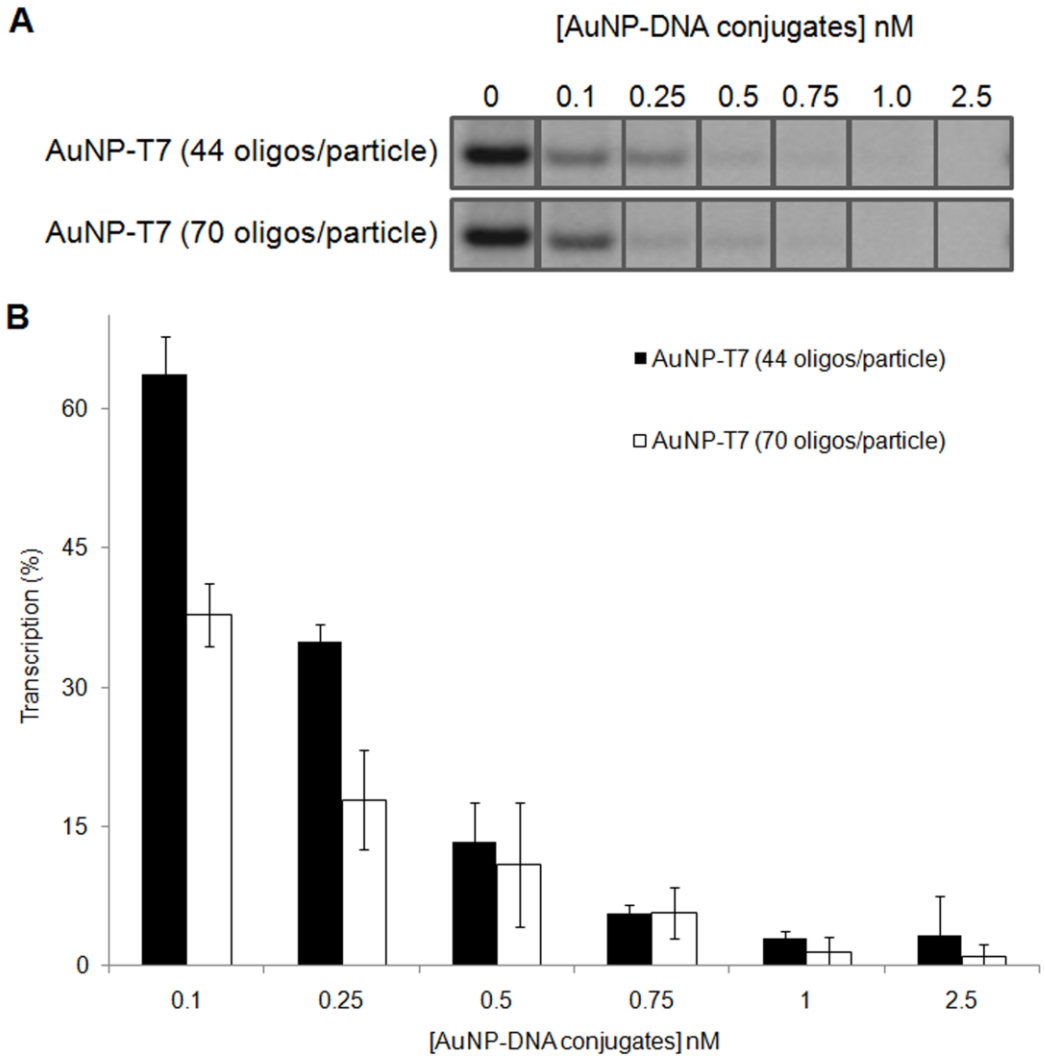

Figure S2. Inhibition of *in vitro* transcription via AuNP-DNA conjugates. Influence of DNA coverage of AuNPs, AuNP-T7 (44 ± 2) and (70 ± 3) oligonucleotides/particle. (**A**) Agarose gel electrophoresis of *in vitro* transcription reactions in the presence of increasing AuNP-DNA conjugates concentration. (**B**) Transcription levels as function of increasing AuNP-DNA conjugates. Determination of the degree of inhibition was performed after normalizing to the intensity of the positive control (100%) of the *in vitro* transcription reaction. Error bars correspond to average and standard deviation of two independent assays.

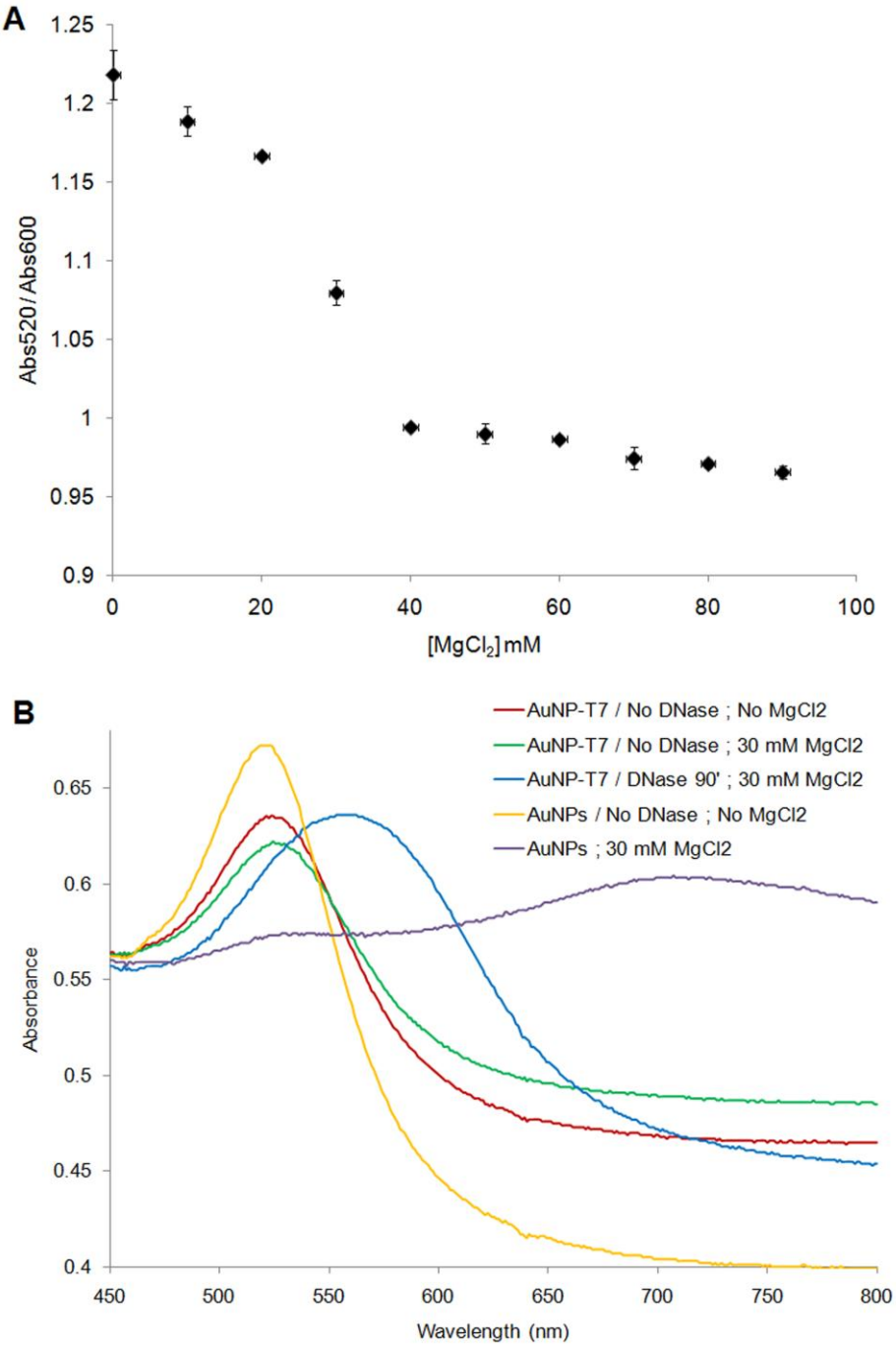

Figure S3. (**A**) **Stability of AuNP-T7 conjugates against salt-induced aggregation.** AuNP-T7 conjugates aggregation as measured by the ratio A_{520nm}/A_{600nm} for increasing concentrations of $MgCl_2$. (**B**) **Stability of AuNP-T7 after nuclease digestion.** DNase I effect on the stability of the AuNP-T7 conjugate and AuNPs after salt (30 mM $MgCl_2$) addition. Error bars correspond to average and standard deviation of two independent assays.

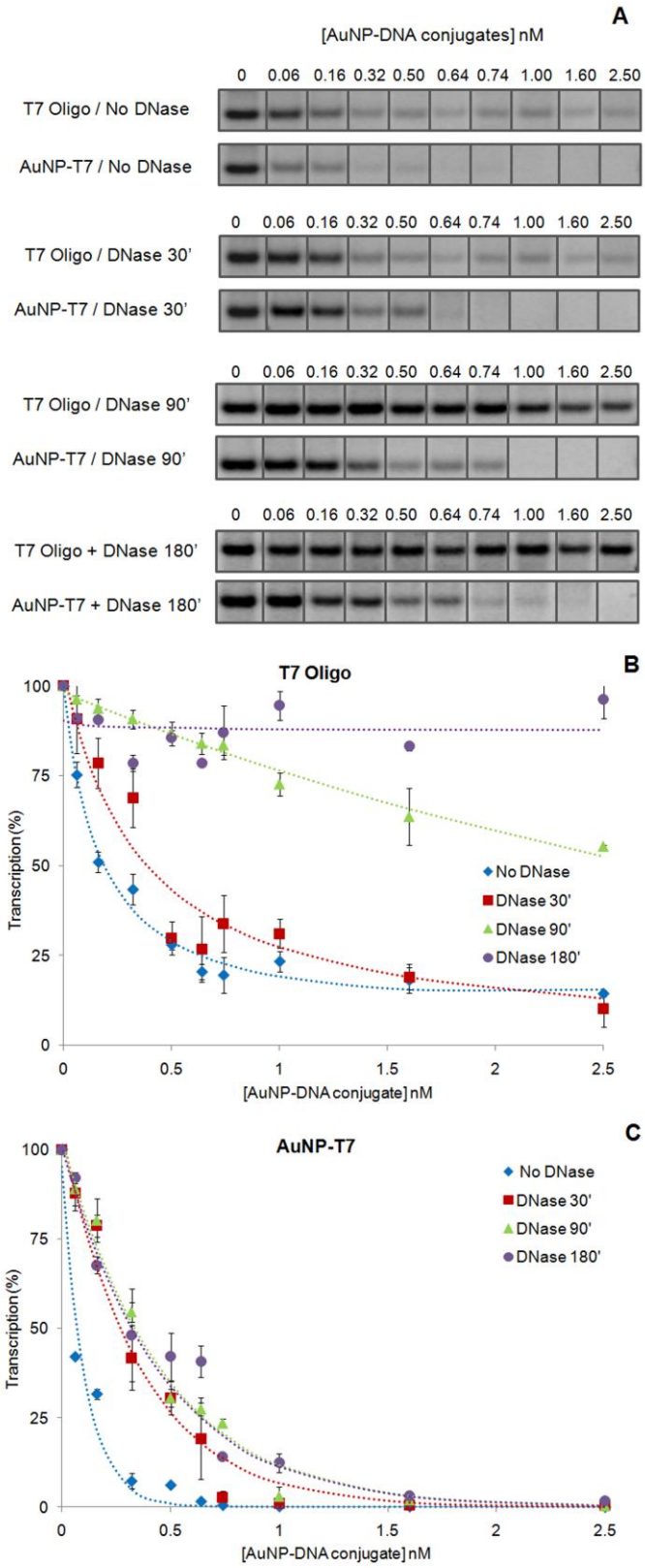

Figure S4. AuNP-DNA conjugates resistance to nuclease activity at several times of exposure. (**A**) Agarose gel electrophoresis of the nuclease digestion for 30, 90 and 180 min of the free T7 oligonucleotide and the AuNP-T7. Transcription product quantification of (**B**) free T7 oligonucleotide and (**C**) AuNP-T7 conjugate at 30 (red squares), 90 (green triangles) and 180 min (purple circles) of digestion. Error bars correspond to average and standard deviation of two independent assays.

J Nanopart Res (2012) 14:917
DOI 10.1007/s11051-012-0917-2

RESEARCH PAPER

Effect of PEG biofunctional spacers and TAT peptide on dsRNA loading on gold nanoparticles

Vanesa Sanz · João Conde · Yulán Hernández · Pedro V. Baptista · M. R. Ibarra · Jesús M. de la Fuente

Received: 21 December 2011 / Accepted: 10 May 2012

Abstract The surface chemistry of gold nanoparticles (AuNPs) plays a critical role in the self-assembly of thiolated molecules and in retaining the biological function of the conjugated biomolecules. According to the well-established gold–thiol interaction the undefined ionic species on citrate-reduced gold nanoparticle surface can be replaced with a self-assembled monolayer of certain thiolate derivatives and other biomolecules. Understanding the effect of such derivatives in the functionalization of several types of biomolecules, such as PEGs, peptides or nucleic acids, has become a significant challenge. Here, an approach to attach specific biomolecules to the AuNPs ($\sim$14 nm) surface is presented together with a study of their effect in the functionalization with other specific derivatives. The effect of biofunctional spacers such as thiolated poly(ethylene glycol) (PEG) chains and a positive peptide, TAT, in dsRNA loading on AuNPs is reported. Based on the obtained data, we hypothesize that loading of oligonucleotides onto the AuNP surface may be controlled by ionic and weak interactions positioning the entry of the oligo through the PEG layer. We demonstrate that there is a synergistic effect of the TAT peptide and PEG chains with specific functional groups on the enhancement of dsRNA loading onto AuNPs.

Keywords Gold nanoparticles · PEG biofunctional spacers · TAT peptide · dsRNA oligonucleotide · Surface science

Introduction

Nanotechnology has entered the fray in the technological leap of controlling materials at nanoscale and offering a "big revolution" in medical and healthcare treatments and therapies (Sanvicens and Marco 2008). Nanotechnology offers a wealth of tools to diagnose and treat cancer—new imaging agents; multifunctional, targeted devices capable of bypassing biological barriers to deliver therapeutic agents directly to cells and tissues involved in cancer growth and metastasis; monitor predictive molecular changes allowing preventive action against precancerous cells; minimizing costs (Baptista 2009).

AuNPs have gained increasing interest due to their special features, such as extraordinary optical

Electronic supplementary material The online version of this article (doi:10.1007/s11051-012-0917-2) contains supplementary material, which is available to authorized users.

V. Sanz · J. Conde · Y. Hernández · M. R. Ibarra · J. M. de la Fuente (✉)
Instituto de Nanociencia de Aragón, Universidad de Zaragoza, Mariano Esquillor s/n 50018, Zaragoza, Spain
e-mail: jmfuente@unizar.es

J. Conde · P. V. Baptista
Departamento de Ciências da Vida, Faculdade de Ciências e Tecnologia, Centro de Investigação em Genética Molecular Humana, Universidade Nova de Lisboa, 2829-516 Caparica, Portugal

Published online: 06 June 2012

and electronic properties, high stability and biological compatibility, controllable morphology and size dispersion, and easy surface functionalization (El-Sayed 2001; Daniel and Astruc 2004). The unique characteristics of these particles, such as high surface-to-volume ratio or size-dependent optical properties, are drastically different from those of their bulk materials and hold pledge in the clinical field for therapy (Kim 2007). This has encouraged the development of new forms and modifications of AuNPs for biomedical applications, as well as the use of these nanoparticles in self-assembly of biomolecules such as DNA/RNA, oligonucleotides, PEGs, and various proteins, that are easily attached to the AuNP surface (Sperling and Parak 2010; Han et al. 2007). On the surface of an AuNP the presence of negative electronic shielding provides a Coulomb force sufficient to bind different molecules, and constitutes a suitable system to adjust the surface properties (El-Sayed 2001; Link and El-Sayed 2003).

In recent years, biodegradable polymeric nanoparticles, particularly those coated with hydrophilic polymer such as PEG, have been used as potential delivery devices. These complexes have the ability to avoid the immune system and circulate for a prolonged time in the blood stream and target a particular organ, consequently they may act as carriers of DNA in gene therapy and to deliver proteins, peptides, and drugs (Kommareddy et al. 2005). For systemic applications the development of surface functionalized and long-circulating AuNPs as cellular probes and delivery agents are desired for passive targeting to tumors and inflammatory sites. PEG-modification of nanoparticles affords long-circulating property by evading macrophage-mediated uptake and removal from the systemic circulation. Owing to its simple structure and chemical stability, it is a prototype of an inert, biocompatible polymer (Sperling and Parak 2010; Verma and Stellacci 2010). Surface modification of AuNPs through the PEG spacers would, therefore, allow the modified nanoparticles to remain in the systemic circulation for the prolonged period and provide flexibility to the attached ligand for efficient interaction with its target (Yu et al. 2007). Using the PEG spacer, gold nano-platform can be conjugated with a variety of biologically-relevant ligands such as peptides and RNAs.

When bound to surfaces, PEG prevents other molecules to bind by steric effects. In fact, the molecules are not attracted by electrostatic forces and cannot penetrate the hydrated PEG layer, producing an inert hydrophilic surface. Nanoparticles modified by PEGs are more stable at high salt concentrations and in biological environments, avoiding non-specific binding to proteins and cells (Liu et al. 2007). On the other hand, the activation of PEG with appropriate functional groups (such as carboxyl and azide) which specifically react with other functional groups (amino and cysteine) of protein can be achieved by 1-ethyl-3-(3-dimethylaminopropyl)-carbodiimide (EDC) reactions. EDC is a zero-length crosslinking agent used to couple carboxyl groups to primary amines. This crosslinker has been used in diverse applications, such as forming amide bonds in peptide synthesis, attaching haptens to carrier proteins to form immunogens, labeling nucleic acids through 5' phosphate groups, and creating amine-reactive NHS-esters of biomolecules (Grabarek and Gergely 1990).

In order to study the self-assembly of certain thiolated components (thiol-PEG and thiol-dsRNA) and positive peptides on the surface of AuNPs we conducted a bioconjugation study of the surface-modified AuNPs with different PEG layer composition and several amounts of TAT peptide and dsRNA. We developed an effective strategy to combine, in a highly controlled way, specific biomolecules to the surface of AuNPs and study their synergetic or antagonistic effect in the functionalization of the specific components. Here, we present the effect of biofunctional spacers such as PEG spacers (with a thiol end to bond covalently to the gold nanoparticle and carboxylic acid (SH–EG(7)–CH_2–COOH) and azide (SH–$(CH_2)_3$–CONH–EG(6)–CH_2–N_3) functional groups in the other end) and TAT peptide in the efficiency of RNA loading into the surface of AuNPs (see Scheme 1).

Materials and methods

Synthesis of citrate-AuNPs

The citrate capped AuNPs were synthesized by the reduction of tetrachloroaurate (III) trihydrate with

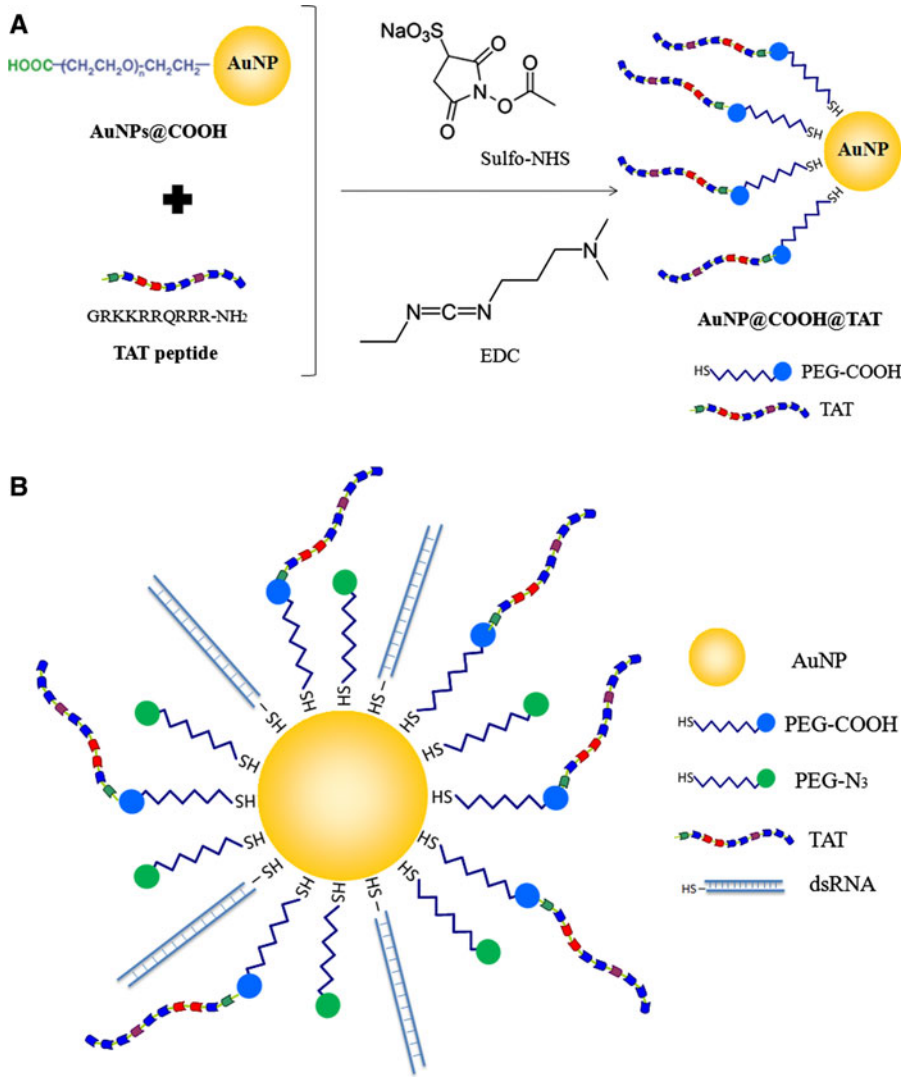

Scheme 1 EDC functionalized polyvalent gold nanoparticles. **a** EDC coupling reaction. 1-Ethyl-3-(3-dimethylaminopropyl)-carbodiimide (EDC), a zero-length crosslinking agent, was used to couple carboxyl groups from PEG to the primary amines of the TAT peptide. In the presence of *N*-hydroxysulfosuccinimide (sulfo-NHS), EDC can be used to convert carboxyl groups to amine-reactive sulfo-NHS esters. The addition of sulfo-NHS stabilizes the amine-reactive intermediate by converting it to an amine-reactive sulfo-NHS ester, thus increasing the efficiency of EDC-mediated coupling reactions. The amine-reactive sulfo-NHS ester intermediate has sufficient stability to permit two-step crosslinking procedures, which allows the PEG with carboxyl groups on one peptide to remain unaltered. **b** Polyvalent gold nanoparticles. Bioconjugation of the surface-modified gold nanoparticles with different thiol-PEG layer composition (SH–EG(7)–CH_2–COOH and SH–$(CH_2)_3$–CONH–EG(6)–CH_2–N_3), TAT peptide and thiol-dsRNA oligonucleotide

sodium citrate described elsewhere (Lee and Meisel 1982). In brief, in this method a mixture of the gold salt (0.2 mg) and sodium citrate (0.57 g) in 500 mL of distilled water is heated under reflux. The pale yellow-colored solution turned to deep red as the AuNPs were formed and stabilized by adsorbed citrate ions. The nanoparticles suspension was observed with a transmission electron microscope (TEM) obtaining an average diameter of 14.47 nm (see Fig. S1, electronic supplementary material).

Synthesis of PEG heterofunctional surfaces on citrate-AuNPs

The synthesis of heterofunctional surfaces was accomplished with bifunctional spacers (PEG) with a thiol end to bond covalently to the AuNP and other functional group in the other end (azide and carboxylic acid groups) which can act as a flexible spacer and as substrates for EDC/NHS coupling reactions. Two kinds of nanoparticles with distinct PEG surfaces were synthesized—one functionalized with only PEG with carboxylic groups (SH–EG(7)–CH_2–COOH) and other with both PEG-azide and PEG with carboxylic groups (SH–$(CH_2)_3$–CONH–EG(6)–CH_2–N_3 and SH–EG(7)–CH_2–COOH, respectively). Both kinds of the nanoparticles were functionalized with 15 % of saturated PEG layer to allow the incorporation of other thiolated components such as the thiolated RNA. Thereafter AuNPs@COOH were functionalized with 100 % of SH–EG(7)–CH_2–COOH and the AuNPs@COOH@N_3 with a mixture of 50 % of SH–EG(7)–CH_2–COOH and 50 % of SH–$(CH_2)_3$–CONH–EG(6)–CH_2–N_3 (see Determination of the degree of saturation of gold nanoparticles functionalized with thiolated polyethylene glycol chains, in Supplementary Information).

TAT functionalization by EDC/NHS coupling reaction

The synthesis of AuNPs functionalized with increasing amounts of TAT peptide was based on an EDC/NHS coupling reaction (Grabarek and Gergely 1990) between the amine-containing peptide and carboxyl-functionalized AuNPs. In the presence of *N*-hydroxysulfosuccinimide (sulfo-NHS), 1-ethyl-3-(3-dimethylaminopropyl)-carbodiimide (EDC) can be used to convert carboxyl groups to amine-reactive sulfo-NHS esters (Staros et al. 1986). In brief, 1 mg/mL AuNPs@PEG were incubated in 1.25 mg/mL sulfo-NHS and in 25 mM MES (2-(*N*-morpholino)ethanesulfonic acid) buffer pH 6.1. Then, TAT peptide was added to the mixture at a final concentration from 0.1 to 0.8 μg/mL and allowed to stabilize for 5 min. After this period of time, EDC was added at a final concentration of 150 μg/mL and the mixture was incubated at room temperature for 16 h. Then, AuNP@PEGs were centrifuged at 14.000 rpm for 30 min at 4 °C to remove the excess of peptide, the supernatants were recovered and tested for protein concentration by the Bradford assay.

AuNPs functionalization with RNA

Thiolated dsRNA (Quiagen) was dissolved in 1 mL of 0.1 M DTT, extracted three times with ethyl acetate, and further purified through a desalting NAP-5 column (Pharmacia Biotech) according to the manufacturer's instructions. The purified dsRNAs, at a constant concentration of 0.035 nmol, in with RNase-free solution were incubated with the AuNP@PEG@TAT (0.45 mg/mL) and sonicated to increase the coverage of oligoribonucleotides on the surface. After incubation during 16 h at 4 °C, the particles were purified by centrifugation at 13.000 rpm for 20 min at 4 °C, and re-suspended in DEPC-water. This process was repeated 3 times. The number of dsRNA per AuNP was determined using the nucleic acid intercalator GelRed. In this procedure, the supernatants were incubated with GelRed ×100 and TBE ×0.5, the fluorescence was measured using a fluorimeter Perkin Elmer LS50B (excitation and emission slits 7.5 nm) and interpolated in the calibration curve.

Characterization of the functionalized AuNPs

Characterization of the nanoparticles was performed by Dynamic Light Scatter (DLS) and UV/Vis Spectroscopy. Size increase shown by DLS and shifts in UV/Vis spectra also confirmed the peptide and the dsRNA functionalization (see Fig. 6). Zeta-potential studies were also carried out for the AuNPs@COOH and AuNPs@COOH@N_3 with increasing amounts of the TAT peptide and with a constant concentration of dsRNA (see Fig. 5).

Results and discussion

The most common and efficient method in terms of stability and strength of the interaction for the binding of oligonucleotides to AuNPs is the use of the bond gold–thiol—a quasi-covalent bond between the thiol group and the gold surface. When other groups or molecules are or have to be attached to the AuNP depending on the final application of the complex it is important that the availability of the gold surface for the effectiveness of the binding of the thiolated oligonucleotide. In this situation, a non-saturated AuNP with available and enough binding points for the interaction gold–thiol is needed. In this work, we

study the effect of other groups or molecules co-immobilized with thiolated dsRNA on AuNPs on the loading yield of these oligos. For this purpose, we first studied the effect of the degree of saturation of a thiolated layer already attached to the AuNP on the binding of other thiolated molecules, in our case the thiolated PEG and dsRNA, respectively. In this way, it is possible to obtain the conditions at which it is feasible for the approach and binding of a thiolated molecule to an AuNP already functionalized with a layer of thiolated chains. The AuNPs show an average diameter of 14.47 nm (Fig. S1, electronic supplementary material). These nanoparticles were functionalized with two kinds of thiolated PEG chains: a) a PEG chain containing a carboxylic group (SH–EG(7)–CH_2–COOH), and b) a PEG chain containing an azide group (SH–$(CH_2)_3$–CONH–EG(6)–CH_2–N_3). As it will be shown below, both carboxyl and azide groups make possible a chemical functionality to the AuNP to be able to bind other molecules to the nanoparticle through common coupling reactions. The best conditions for obtaining AuNPs with a non-saturated thiolated PEG layer were obtained (see Supplementary Information). It was observed that AuNPs are able to bind around 5,000 thiolated chains until their complete saturation with a thiolated PEG layer. It was also observed that it is possible to control the degree of saturation of the thiolated layer (see Figs. S3 and S4, electronic supplementary material). Thiolated layers with a degree of saturation below 10 % lead to non-stable nanoparticles that tend to aggregate, whereas AuNPs with thiolated layers with a degree of saturation above 10 % are stable and allow further studies for the purposes of this work: first, they allow the modeling of the entrance and binding of another thiolated molecule, and second, they are stable enough to perform coupling reactions for the binding of other molecules. As it was stated above, the purpose of this work is to study the binding of thiolated oligonucleotides to AuNPs carrying different groups and molecules. For this study, AuNP@COOH and AuNP@COOH@N_3 complexes were prepared from a starting thiolated PEG layer of around 15 % of saturation. Under these conditions, it is possible to allow the entrance and binding of thiolated oligonucleotides on the non-saturated surface of the AuNPs and to perform coupling reactions, thanks to the chemical functionality imparted by the pegylated chains. This will allow us to investigate the effect that other molecules bound to the AuNPs have on the further loading of the oligonucleotides. The binding of thiolated oligonucleotides to these non-saturated AuNPs was confirmed to be the proof of concept of the described model. A constant amount of thiolated oligonucleotide was incubated with the same concentration of the two kinds of AuNPs, AuNP@COOH, and AuNP@COOH@N_3. It was observed that the thiolated oligonucleotide was able to bind to both functionalized AuNPs, as expected. However, the degree of binding was about twice for AuNP@COOH@N_3 (19 ± 0.4 oligonucleotides per AuNP) than for AuNP@COOH (9 ± 2 oligonucleotides per AuNP) showing that the spacer plays an important role on the loading yield of the thiolated oligonucleotide (see Fig. S6, electronic supplementary material). AuNP@N_3 are not stable enough in suspension after synthesis. In fact, following functionalization with only the azide-containing PEG, nanoparticles aggregate, making it impossible to study the effect on dsRNA loading.

At this point, we have created AuNPs with a non-saturated thiolated layer composed of two kinds of spacers that allow the binding of thiolated oligonucleotides. Furthermore, the two kinds of thiolated PEG chains produce a chemically functional surface around the AuNP. As it was stated above, the loading of thiolated oligonucleotide was different depending on the composition of the PEG layer on the non-saturated AuNPs. The functional groups that the thiolated chains carry, allow the binding of other molecules or groups to the AuNPs given their chemical reactivity. The question that arises now is what would be the role of a further binding of other molecules on the oligonucleotide loading yield.

As a model example we have bound amine-containing molecules to carboxyl groups by the EDC coupling reaction. This methodology makes possible to bind other molecules to the carboxyl groups and study the effect of these molecules on the oligonucleotide loading yield. With this aim in mind we selected a cationic peptide (TAT). The optimal conditions for the binding of this peptide through the EDC reaction were obtained. The procedure used was based on the stability assays of the AuNPs that were carried out to determine the range of peptide concentrations available for the EDC reaction. In Fig. 1, the stability of AuNP@COOH and AuNP@COOH@N_3 nanoparticles as a function of the peptide concentration in the EDC reaction conditions is represented. It

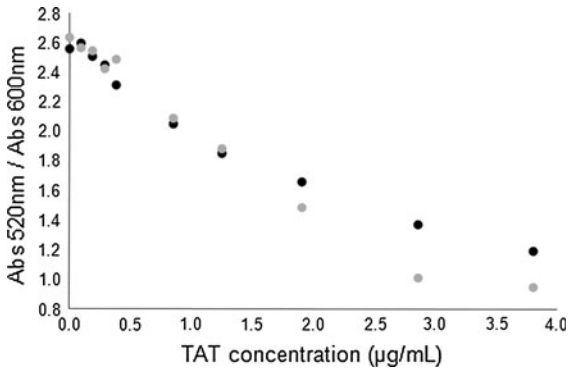

Fig. 1 Stability of AuNPs as a function of TAT concentration in the EDC coupling reaction conditions. The stability is given as the ratio between the absorbance values at 520 and 600 nm. A ratio Abs520/Abs600 of 1 may be considered as the point of equilibrium between non-aggregated and aggregated nanoparticles. Black points AuNP@COOH and gray points AuNP@COOH@N_3

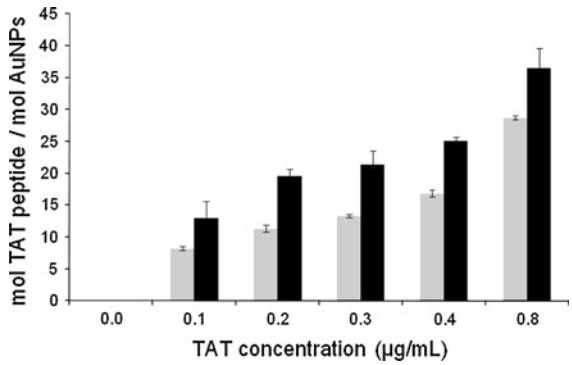

Fig. 2 Determination of the number of TAT chains bound to AuNPs by the EDC reaction as a function of the initial peptide concentration in the reaction mixture. *Black bars* AuNP@COOH@N_3 and *grey bars* AuNP@COOH

can be seen that a slight aggregation of the AuNPs is observed only for TAT concentrations higher than 2 μg/mL, which is more pronounced for AuNP@COOH@N_3 nanoparticles than for AuNP@COOH. This decrease in stability can be explained by the ionic interaction between the peptide, which is cationic, and the nanoparticles which are negatively charged because of their functionalization with the carboxylated chain. As the peptide concentration increases, this ionic interaction takes place in a higher extent triggering the aggregation of the nanoparticles. AuNP@COOH@N_3 nanoparticles showed a slightly lower stability owing to the fact that they are a bit less stable themselves because of the azide-containing chain which is nonionic and impairs a lower stability to the nanoparticles (Fig. 1). Peptide concentrations lower than 3 μg/mL lead to the covalent coupling of the peptide to the carboxylated chain without causing any aggregation of the nanoparticles. For this reason, the TAT concentration in the EDC coupling reaction was varied between 0.1 and 0.8 μg/mL. In the optimal conditions for the binding, a method for the quantification of the bound peptide was developed (see Fig. S5, electronic supplementary material). In Fig. 2, the number of TAT chains bound to AuNP as a function of the initial concentration of peptide in the reaction mixture is shown. As it can be seen, the amount of bound peptide is proportional to the initial concentration of peptide and, therefore, it is possible to control the number of peptide chains per AuNP. As expected, the amount of peptide bound to the nanoparticles is higher for AuNP@COOH@N_3 than for AuNP@COOH because of the higher amount of carboxylated chains available for the EDC reaction. From these coupling reactions, two other kinds of functionalized AuNPs were obtained, both AuNP@COOH and AuNP@COOH@N_3 carrying the peptide: AuNP@COOH@TAT and AuNP@COOH@N_3@TAT, respectively. For all kinds of nanoparticles the loading of the peptide can be varied and controlled.

Once the procedure for the binding of the TAT to the functionalized AuNPs had been optimized, a study of the thiolated oligonucleotide loading was carried out. Interestingly, as it can be seen in Fig. 3, the loading yield of the oligonucleotide was much higher for AuNP@COOH@N_3@TAT than AuNP@COOH @TAT as the peptide concentration increases. The dsRNA loading on AuNP@COOH@TAT remains constant, while there is an increase on the RNA loading on AuNP@COOH@N_3@TAT with increasing concentration of bound peptide. This is very important, as it establishes the conditions at which the loading yield of thiolated oligonucleotides shows a clear enhancement. The explanation for this phenomenon cannot be understood by the pure effect of the peptide chain itself. As we can see in Fig. 3, AuNP@COOH@TAT and AuNP@COOH@N_3@TAT nanoparticles (containing the same number of peptide chains—see Fig. 2) do not lead to the same oligonucleotide loading. Therefore, just an increase on the peptide loading on the AuNP does not lead to an increase on the oligonucleotide loading. As a consequence, an increase of the thiolated oligonucleotide loading because

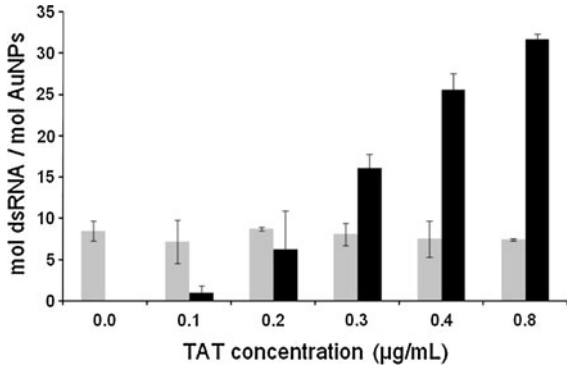

Fig. 3 Loading of thiolated oligonucleotide (HS-dsRNA) on AuNPs functionalized with TAT peptide and with both PEG-azide and PEG–COOH and only with PEG–COOH. *Black bars* AuNP@COOH@N_3@TAT, and gray bars AuNP@COOH @TAT

of an ionic interaction and not by the expected thiol–gold interaction should be discarded. To confirm this hypothesis, AuNPs already loaded with the thiolated oligonucleotide were incubated with sodium chloride at a final concentration of 0.3 M to detach any oligonucleotide that would have been bound by an ionic interaction. The addition of salt do not cause any release of the bound thiolated oligonucleotide (data not shown). Therefore, it is confirmed the quasi-covalent bound of the thiolated oligonucleotide to the functionalized AuNPs and that a pure ionic interaction of the oligo with the peptide is not responsible for the enhancement of the oligo loading on the nanoparticles. Our hypothesis is that there is a synergetic effect of the peptide and the azide-containing chain on the enhancement of the oligonucleotide loading. This synergistic effect can be explained by the approaching effect of the azide-containing chain to the gold surface. The azide group has a resonant structure with a positively polarized behavior. This structure can attach the negatively charged thiolated oligo to the gold surface. On the other hand, the azide-containing chain contains an amide group near the gold surface that could play a role in approaching the thiol group of the oligonucleotide to the gold surface. This amide group could form a hydrogen bond with one of the hydroxyl groups of the ribose group near the thiol group on the oligo. This hydrogen bond could approach the oligo to the gold surface steering its entry through the PEG layer enhancing the oligo loading on the nanoparticle (see Fig. 4).

For the complete characterization of the functionalized AuNPs Z potential studies were carried out. In Fig. 5a, b, the Z potential values for AuNP@COOH and AuNP@COOH@N_3 nanoparticles as a function of peptide and oligonucleotide loading is represented. It can be observed that for AuNP@COOH@TAT and AuNP@COOH@N_3@TAT the Z potential values change toward more positive values as the load of

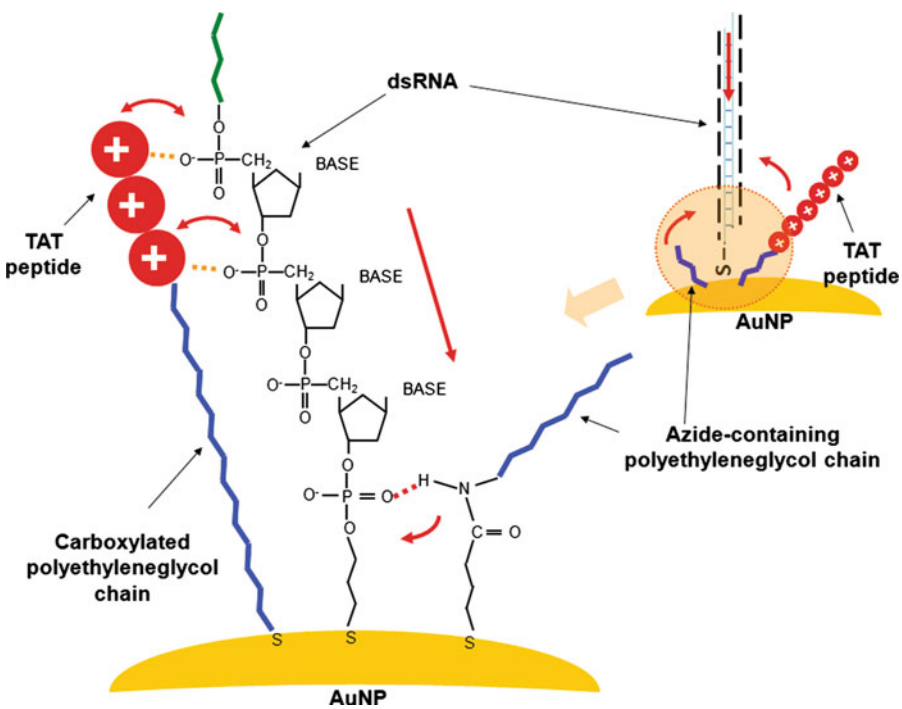

Fig. 4 Mechanism for the enhancement of the dsRNA loading on AuNP functionalized with PEG chains and TAT peptide. The azide group has a resonant structure with a positively polarized behavior that can attach the negatively charged thiolated oligo to the gold surface. The azide-containing chain also encloses an amide group near the gold surface that could play a role in approaching the thiol group of the oligonucleotide to the gold surface. This amide group could form a hydrogen bond with one of the hydroxyl groups of the ribose group near the thiol group on the oligo

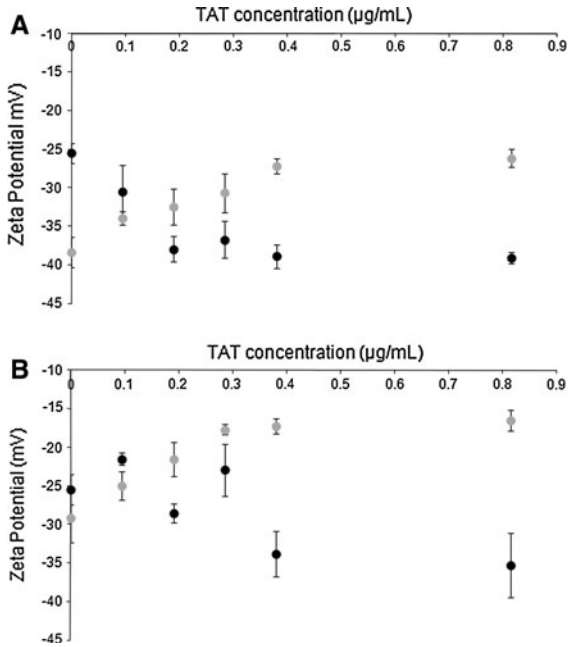

Fig. 5 Zeta-Potential measurements for AuNPs@COOH **a** (*gray points* AuNP@COOH@TAT, *black points* AuNP@-COOH@TAT@dsRNA), and AuNPs@COOH@N_3 **b** (*gray points* AuNP@COOH@N_3@TAT, *black points* AuNP@-COOH@N_3@TAT@dsRNA) incubated with increasing amounts of the TAT and with a constant concentration of dsRNA

the peptide increases. This is expected for the negatively charged nanoparticles AuNP@COOH and AuNP@COOH@N_3 that after increasing the amount of the cationic peptide bound to the nanoparticle they become more positively charged. Besides, the binding of the thiolated oligonucleotide to the AuNP@-COOH@TAT and AuNP@COOH@N_3@TAT nanoparticles shifts again the Z potentials toward more negative values, as expected. DLS measurements were also performed on the functionalized AuNPs. As it can be seen in Fig. 6, the binding of the peptide and the oligonucleotide produces a shift on the size of the nanoparticles toward higher values as expected. This is a confirmation of the binding of the peptide and the oligonucleotide on the AuNPs. This binding was also confirmed by the shift in the SPR of the AuNPs when functionalized with the PEG chains, the TAT peptide and the dsRNA. As it can be seen in Fig. 7, there is a 3 nm shift of the SPR when the peptide is bound to the nanoparticles whereas the shift is higher (5 nm) after RNA binding.

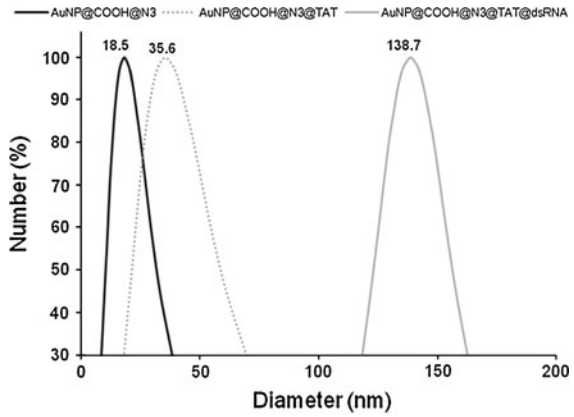

Fig. 6 Dynamic light scattering (DLS) measurements with diameter distribution of AuNPs@COOH@N_3, AuNPs@COOH @N_3@TAT and AuNPs@COOH@N_3@TAT@dsRNA

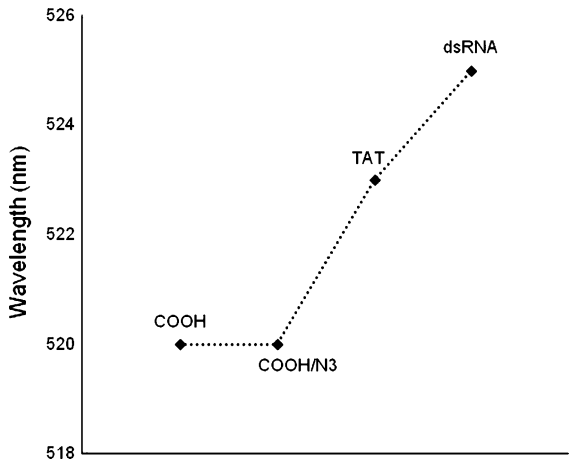

Fig. 7 Surface plasmon resonance (SPR) shift for the functionalization of PEG chains, TAT peptide, and dsRNA. The spatial arrangement of gold nanoparticles can be inferred by measuring the shift of a characteristic surface plasmon band that is influenced by their size, shape, aggregation state, and surrounding medium polarity

Conclusions

In this study, an approach to bind specific biomolecules to the surface of AuNPs and study the effects in the combined functionalization is developed. The effect of thiolated PEG (PEG) spacers carrying different functional groups (carboxyl and azide) and the positively charged TAT peptide on the dsRNA loading into the surface of AuNPs was studied. We demonstrated that there is a synergetic effect of the TAT peptide and the azide-containing PEG chain on

the enhancement of the dsRNA loading into AuNPs. Based on the obtained data, we hypothesize that loading of oligonucleotides onto the AuNP surface may be controlled by ionic and weak interactions, such as the TAT peptide and the polarized azide group on one of the PEG chains, thus positioning the entry of the oligo through the PEG layer,. It was also demonstrated that the weak interactions, e.g., hydrogen bounds, between PEG chains spacers and dsRNA enhance the loading of the dsRNA onto the AuNPs by steering its entry through the PEG layer.

Acknowledgments This study has been funded by CTQ2008-03739/PPQ, NanoSciERA Grant-NANOTRUCK, and ERC-Starting Grant 239931-NANOPUZZLE. J. Conde thanks FCT/MCTES (SFRH/BD/62957/2009). P.V. Baptista thanks CIG MH-FCT/MCTES and JM de la Fuente thanks ARAID for financial support. Authors also thank I. Echaniz and S. Rivera for technical support.

References

Baptista PV (2009) Cancer nanotechnology—prospects for cancer diagnostics and therapy. Curr Cancer Therapy Rev 5:80–88

Daniel MC, Astruc D (2004) Gold nanoparticles: assembly, supramolecular chemistry, quantum-size-related properties, and applications toward biology, catalysis, and nanotechnology. Chem Rev 104:293–346

El-Sayed MA (2001) Some interesting properties of metals confined in time and nanometer space of different shapes. Acc Chem Res 34:257–264

Grabarek Z, Gergely J (1990) Zero-length crosslinking procedure with the use of active esters. Anal Biochem 185:131–135

Han G, Ghosh P, Rotello VM (2007) Multi-functional gold nanoparticles for drug delivery. Adv Exp Med Biol 620:48–56

Kim KY (2007) Nanotechnology platforms and physiological challenges for cancer therapeutics. Nanomedicine 3:103–110

Kommareddy S, Tiwari S, Amiji MM (2005) Long-circulating nanovectors for tumor-specific gene delivery. Technol Cancer Res Treat 4:615–626

Lee PC, Meisel D (1982) Adsorption and surface-enhanced Raman of dyes on silver and gold sols. J Phys Chem 86:3391–3395

Link S, El-Sayed MA (2003) Optical properties and ultrafast dynamics of metallic nanocrystals. Annu Rev Phys Chem 54:331–366

Liu Y, Shipton MK, Ryan J et al (2007) Synthesis, stability, and cellular internalization of gold nanoparticles containing mixed peptide-poly(ethylene glycol) monolayers. Anal Chem 79:2221–2229

Sanvicens N, Marco MP (2008) Multifunctional nanoparticles—properties and prospects for their use in human medicine. Trends Biotechnol 26:425–433

Sperling RA, Parak W (2010) Surface modification, functionalization and bioconjugation of colloidal inorganic nanoparticles. Phil Trans A Math Phys Eng Sci 368:1333–1383

Staros JV, Wright RW, Swingle DM (1986) Enhancement by N-hydroxysulfosuccinimide of water-soluble carbodiimide-mediated coupling reactions. Anal Biochem 156:220–222

Verma A, Stellacci F (2010) Effect of surface properties on nanoparticle-cell interactions. Small 6:12–21

Yu WW, Chang E, Falkner JC et al (2007) Forming biocompatible and nonaggregated nanocrystals in water using amphiphilic polymers. J Am Chem Soc 129:2871–2879

SUPPLEMENTARY INFORMATION

Effect of PEG biofunctional spacers and TAT peptide on dsRNA loading on gold nanoparticles

Vanesa Sanz[1], João Conde[2,1], Yulán Hernández[1], Pedro V. Baptista[2], M.R. Ibarra[1] and Jesús M. de la Fuente[1*]

[1] Instituto de Nanociencia de Aragón, Universidad de Zaragoza, Mariano Esquillor s/n 50018, Zaragoza, Spain.

[2] Centro de Investigação em Genética Molecular Humana (CIGMH), Departamento de Ciências da Vida, Faculdade de Ciências e Tecnologia, Universidade Nova de Lisboa, 2829-516 Caparica, Portugal.

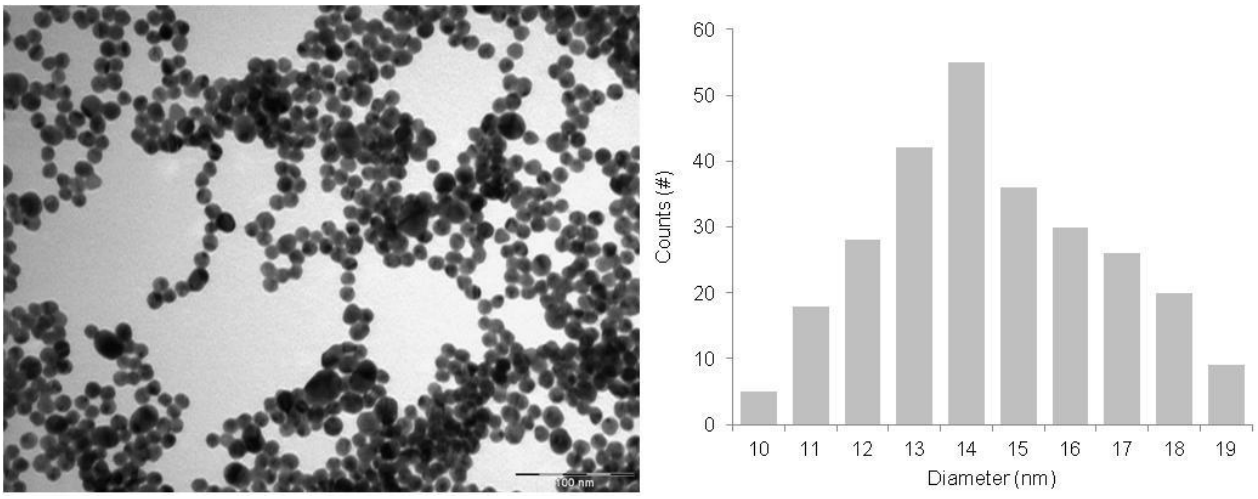

Figure S1 – Citrate-Gold nanoparticle characterization. TEM images (left, scale bar = 100 nm), size distribution histogram (right) showing an average diameter of 14.47 nm.

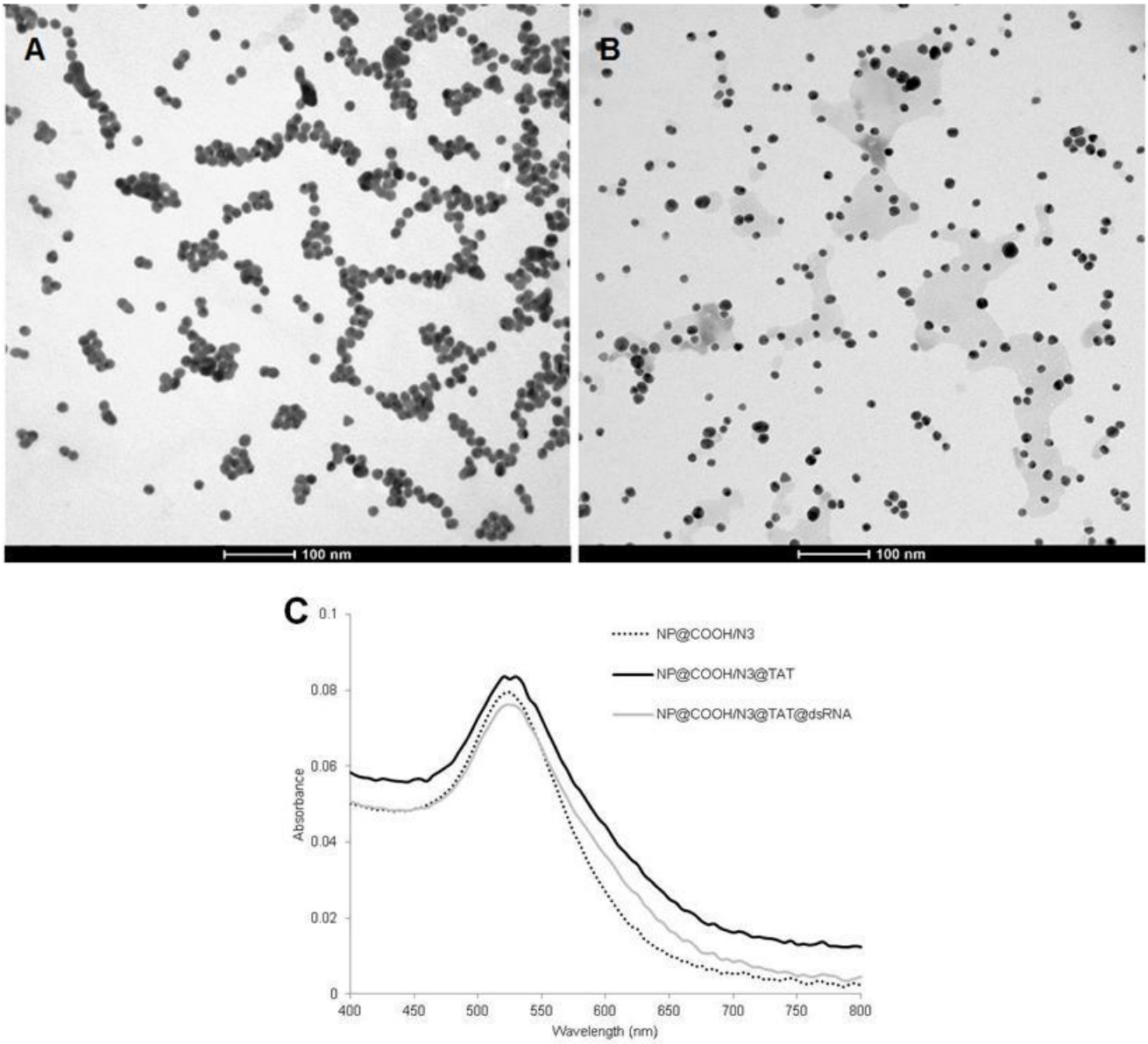

Figure S2 – **A.** TEM image of AuNPs@COOH (scale bar: 100 nm). **B.** TEM image of AuNPs@COOH/N_3 (scale bar: 100 nm). C. UV/Vis Spectroscopy of AuNPs@COOH/N_3, AuNPs@COOH/N_3@TAT and AuNPs@COOH/N_3@TAT@dsRNA.

1. Determination of the degree of saturation of gold nanoparticles functionalized with thiolated polyethyleneglycol chains.

For the determination of the degree of saturation of gold nanoparticles functionalized with thiolated polyethyleneglycol chains we developed and optimized a procedure based on the Ellman's assay. With this procedure it is possible to determine the number of thiolated chains that have been bound to gold nanoparticles. After the incubation of the gold nanoparticles with the thiolated chains, the nanoparticles are functionalized with a defined number of chains being the excess of thiolated chains free in solution. In order to determine the number of bound chains, this suspension is centrifuged and the supernatant with the excess of thiolated chains is kept to perform the quantification assay. The number of exchanged chains is given by the difference between the amount determined by this assay and the initial amount of chains in the incubation mixture with the nanoparticles. As it was stated above, the free thiolated chains are determined by a procedure based on the Ellman's assay. In this assay, the supernatant, containing the spacer with thiol groups on its structure, reacts with DTNB (5,5'-dithio-bis(2-nitrobenzoic) acid) to give a colored product that can be measured spectrophotometrically. In the optimal conditions, 200 µL of stock solution of the thiolated chain or the sample containing the supernatant are mixed with 100 µL of phosphate buffer 0.5 M pH 7 and 7 µL of DTNB 5 mg/mL in phosphate buffer 0.5 M pH 7. The mixture is made to react for 10 minutes and the absorbance at 412 nm is measured. The linear range for the thiolated chain is 0.5-30 µg/mL (Abs_{412} = 0.0229[chain, µg/mL] + 0.0587).

The total number of thiolated chains that can be attached per gold nanoparticle were calculated. As it is shown in **Figure S3**, the excess of thiolated chain versus the initial concentration of thiolated chain in an incubation mixture with a constant concentration of gold nanoparticles is represented. As the initial concentration of thiolated chain increases, the excess of free chain increases in an equilibrium dependent way (equilibrium constant [bound chain]/[free chain]=0.76). There is a point at which the

nanoparticle becomes saturated with a thiolated layer and is not able to uptake more thiolated chains. At this point it is possible to calculate the maximum number of thiolated chains that it is possible to bind per gold nanoparticle being estimated a number of around 5000 chains per nanoparticle.

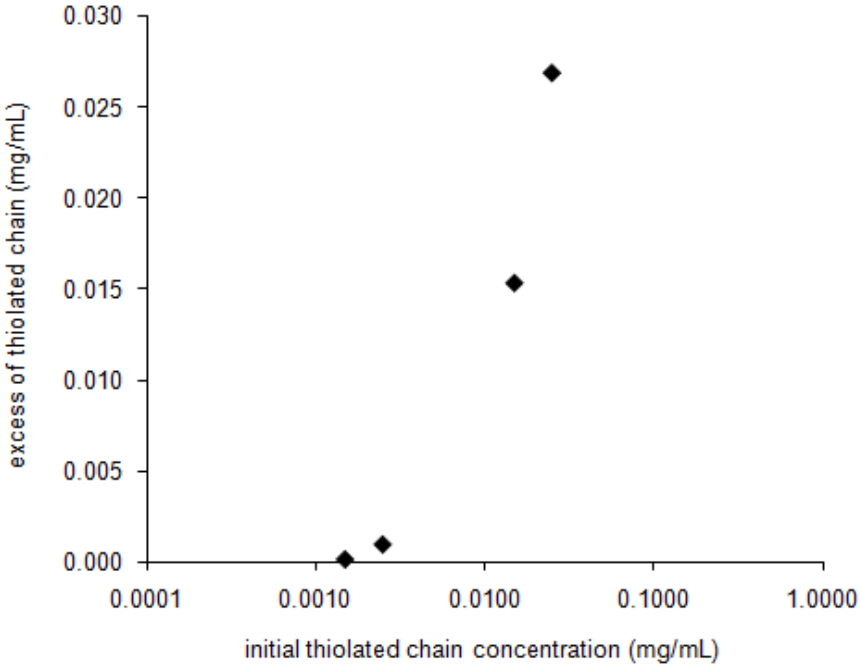

Figure S3. Variation of the excess of thiolated chain as a function of the initial concentration in the incubation mixture with gold nanoparticles. Initial concentration of gold nanoparticles 0.5 mg/mL.

Therefore, it is possible to prepare gold nanoparticles with a controlled degree of saturation if an initial thiolated chain concentration below the saturation conditions is used (below 0.05 mg/mL of thiolated chain per 0.5 mg/mL of gold nanoparticles). In order to determine the degree of saturation at which gold nanoparticles are stable enough and allow the binding of additional thiolated chains we performed the following assay. Gold nanoparticles were functionalized with a controlled amount of thiolated chains in order to obtain nanoparticles with different degrees of saturation. After this, a fixed amount of a thiolated chain was added and incubated with the gold nanoparticles. The

concentration of thiolated chain that was bound to the non-saturated gold nanoparticles was determined by the Ellman's assay. As it is shown in **Figure S4**, as the initial percentage of saturation of the thiolated layer decreases the gold nanoparticles are able to bind a higher amount of thiolated chain added on this second addition. The best conditions for the binding by a second addition of a thiolated molecule are to work with gold nanoparticles with a degree of saturation below 35 %. However, gold nanoparticles with a degree of saturation below 10 % are less stable. For these reasons, the best conditions for study the binding of thiolated molecules on gold nanoparticles functionalized with a non-saturated thiolated chain layer is between 10 and 35 %.

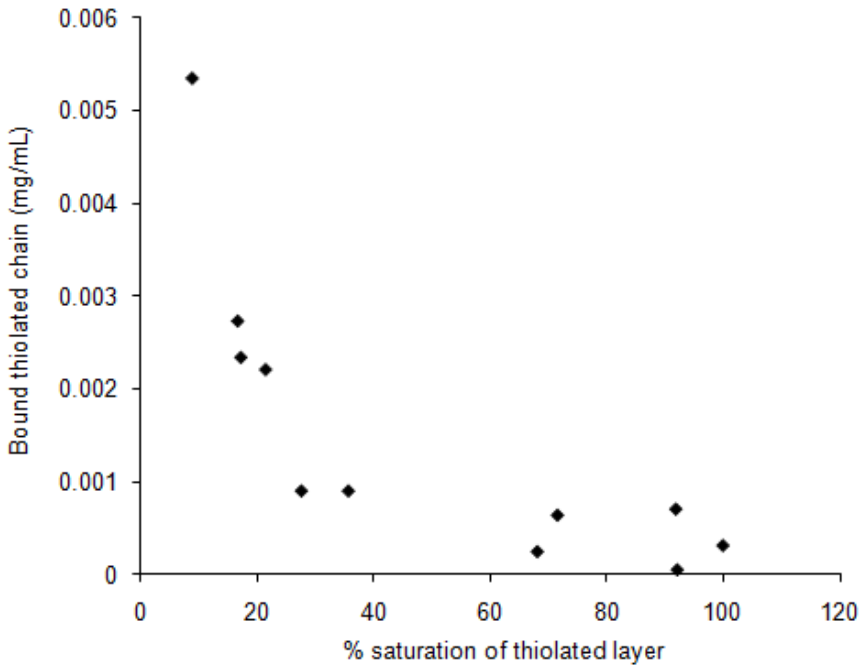

Figure S4. Determination of the amount of thiolated chain bound to gold nanoparticles already functionalized with a thiolated chain layer with different degree of saturation. The initial concentration of gold nanoparticles is 0.5 mg/mL.

2. Procedure for the determination of the bound TAT peptide by the EDC coupling reaction to functionalized gold nanoparticles.

As it was stated in method section, a procedure for the determination of the peptide that was bound to gold nanoparticles through the EDC coupling reaction was developed. This assay was based on the Bradford method. Given that the reagents for the EDC reaction (sulfo-NHS, EDC) interferes with the assay an standard addition calibration curve for the TAT peptide in the EDC reaction conditions was obtained (see **Figure S5**). This calibration curve was used for the interpolation of the samples containing the excess of peptide that was not bound to gold nanoparticles.

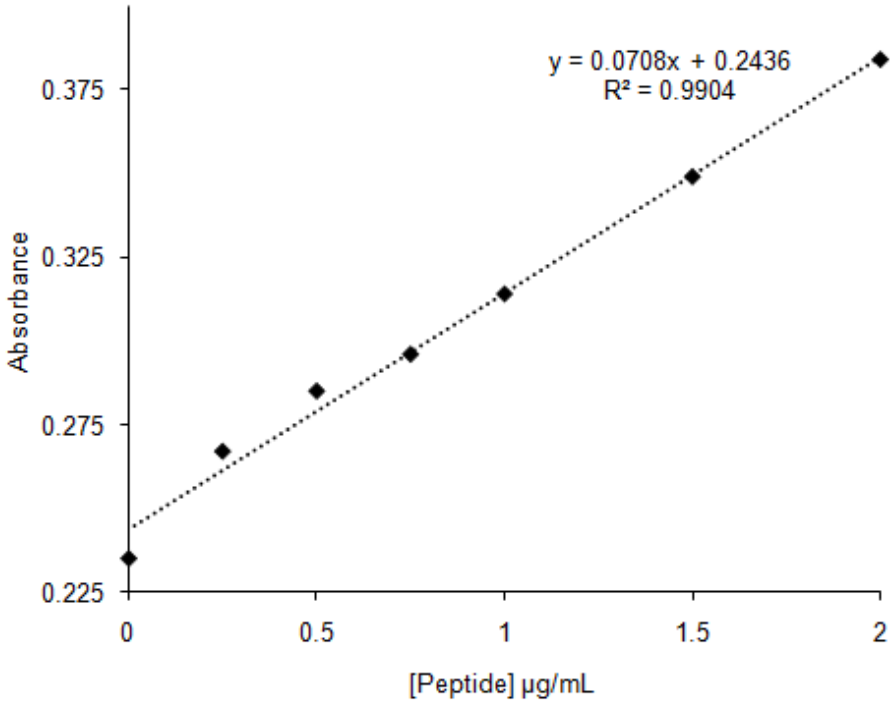

Figure S5. Standard addition calibration curve for the TAT peptide in the conditions of the EDC coupling reaction. In the linear range the calibration curve is given by the following equation Abs570 = 0.071[peptide, µg/mL] + 0.24.

3. Quantification of the dsRNA strand loaded into gold nanoparticles

In order to carry out the dsRNA quantification we used the GelRed™ dye as a nucleic acid intercalator. The GelRed™ is a sensitive, stable fluorescent nucleic acid dye commonly designed to stain dsDNA, ssDNA as well as ds and ssRNA. Here, we had developed an analytical method to quantify the amount of dsRNA that was lost during the functionalization. We measured the dsRNA concentration in the supernatants after incubation, which is measuring the dsRNA in excess, that hadn't bound to gold surface. Briefly, the supernatants were incubated with GelRed 100× and TBE 0.5× and fluorescence was measured with emission at 602 nm. A Correlation to a standard curve of known dsRNA concentrations allows accurate measurement of dsRNA in unknown samples. In Figure S6A we can see the fluorescence spectra of the GelRed only and when it is bound to dsRNA. Figure S6B presents the calibration curve for the thiolated dsRNA used in the experiments.

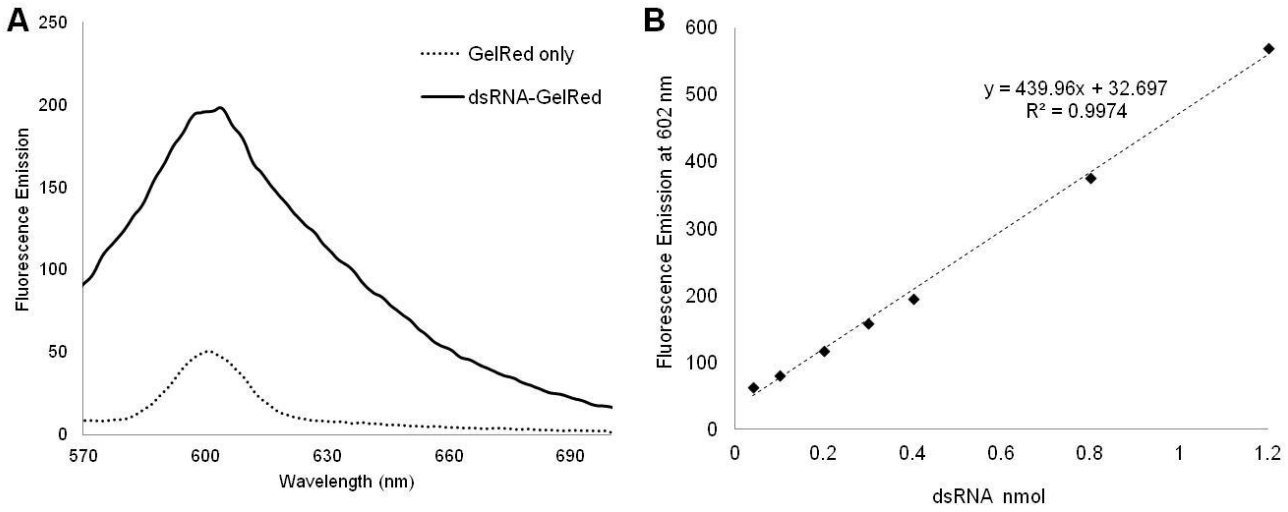

Figure S6. A. Fluorescence spectra of the GelRed only and dsRNA-GelRed. **B.** Calibration curve for the thiolated dsRNA. In the linear range the calibration curve is given by the following equation: Emission at 602nm = 439.96[dsRNA, nmol] + 32.697.

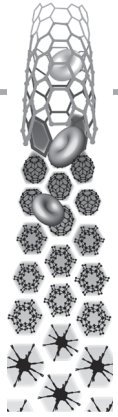

Modification of plasmid DNA topology by 'histone-mimetic' gold nanoparticles

Aims: Our aim is to explore whether gold nanoparticles (AuNPs) functionalized with a carboxylated polyethylene glycol (PEG) and protamine (AuNP@PEG@Prot) can modulate – enhance or restrain – DNA condensation, altering DNA conformation and inducing structural changes. Understanding how these nanoconjugates modulate DNA structure, size and shape of DNA condensates, and enable control over the resulting 3D structures is of major biological and therapeutic importance. **Materials & methods:** Citrate-AuNPs were covered with a dense layer of a hetero-functional octa(ethylene glycol) (SH-EG(8)-COOH). Conjugation of protamine to the AuNP@PEG was achieved by taking advantage of the carboxylated surface previously generated on the surface of the NP and the remaining amino groups from the protamine, using carbodiimide and *N*-hydroxysulfosuccinimide coupling reactions. **Results & conclusion:** AuNP@PEG@Prot modulates the structure and topology of DNA, not only for condensation, but also for decondensation, via formation of higher quantities of dimers and multimers, when compared with AuNP@PEG and free protamine.

Original submitted 16 July 2011; Revised submitted 9 January 2012; Published online 14 May 2012

KEYWORDS: DNA integrity ■ DNA topology ■ gold nanoparticles ■ histones ■ plasmid DNA conformations ■ protamine ■ sperm chromatin

João Conde[1,2], Pedro V Baptista[2], Yulan Hernández[1], Vanesa Sanz[‡1] & Jesus M de la Fuente*[‡1]

[1]Instituto de Nanociencia de Aragón, Universidad de Zaragoza, Mariano Esquillor s/n 50018, Zaragoza, Spain
[2]Centro de Investigação em Genética Molecular Humana (CIGMH), Departamento de Ciências da Vida, Faculdade de Ciências e Tecnologia, Universidade Nova de Lisboa, 2829-516 Caparica, Portugal
**Author for correspondence: jmfuente@unizar.es*
‡Authors contributed equally

Nanotechnology-based systems have shown the potential to provide effective therapies with minimal side effects and high specificity [1–3], where the use of gold (Au) nanoparticles (NPs) as nontoxic carriers for drug and gene delivery [4–6] has been widely reported. Gold nanoparticles (AuNPs) have emerged as an attractive tool for biomedical applications due to their unique features, such as quantum properties, biocompatibility, high stability and a relatively large functional surface [2,7–10]. Many of these platforms rely on the functionalization and/or interaction of a particular biomolecule of interest and the surface of the NP, and in particular several studies of DNA and protein interactions with NPs by noncovalent interactions have been reported [11–14]. Despite the wide application of these nanosystems, the effect on DNA structure and topology of interactions between the dielectric environment of AuNPs and DNA has not been extensively studied.

Watson and Crick first described DNA to be composed of two helical chains each coiled round the same axis, consisting of simple and repeating units called nucleotides, with backbones made of sugars and phosphate groups joined by ester bonds that run in opposite directions to each other [15]. It was initially believed that all DNAs were linear with two free ends, but the existence of closed-circular duplex structures were soon confirmed by naturally occurring circular DNAs, such as plasmids [16,17]. Plasmids are small autonomous replicating genetic elements that provide a means for horizontal genetic transfer and can be used for transient or sustained expression of foreign genes in a given cell, and are often applied to gene therapy. Histones and protamine can improve the intranuclear disposition of plasmid DNA and are capable of modulating transgene expression. These DNA complexes are expected to penetrate the cell membrane by a nonendocytotic pathway and enter the nucleus through nuclear pores. Furthermore, plasmids provide excellent molecular models to study DNA topology. In solution, plasmids adopt three main types of circular molecules – relaxed, supercoiled (Sc) and nicked circle (Nc). Although the relaxed and Sc forms are not restricted to plasmid DNA, it provides the best model to study DNA molecules with different levels of topology and condensation [18]. The flexible structure of DNA is a function of both the surrounding ionic environment and the nature of DNA-binding proteins [17,19]. Changes to DNA topology are of utmost importance as they mediate gene expression and silencing, while allowing packaging into the cell nucleus, which is mediated by histones that coil the DNA into small nucleosomal units organized

Future Medicine part of fsg

in chromatin fibers [20,21]. Histones are relatively small proteins, whose high content of lysine and arginine provides a strong cationic effect, capable of stabilizing the DNA by ionic/electrostatic bonds. Condensation of rigid and highly charged DNA molecules into compact structures can also be achieved by small cationic proteins such as protamine [22–24]. In gametogenesis, these small arginine-rich proteins bind to the entire length of the haploid genome in sperm cells, causing the DNA to coil into toroidal (50–60 kb of DNA) structures, thus inactivating the entire genome [25]. Protamine's arginine-rich anchoring domains bind to the negatively charged phosphodiester backbone of DNA in a base sequence-independent fashion leading to neutralization of the negative charge, inducing both condensation and decondensation of sperm chromatin during fertilization [26]. Protamine is the histone substitute in sperm chromatin during the haploid phase of spermatogenesis [27], where the proper replacement of histones by transition proteins followed by the more basic protamine, constitutes the main event in sperm maturation that affects chromatin structure [28]. Several studies have shown that male factor infertility patients possess anomalies in the composition of their sperm nuclei, displaying damaged DNA and higher levels of loosely packaged chromatin, probably due to protamine deficiency [29–31]. Also, it has been shown that approximately 85% of the DNA in the sperm nucleus is associated with protamines and that 15% remains associated with histones or other proteins [32].

Owing to their ultra small size and unique physico-chemical properties, AuNPs are capable of permeating easily inside the cell and nucleus and interacting with DNA, which may induce changes to chromatin condensation and/or decondensation processes and nuclear structure. This interaction can be strongly enhanced via conjugation with protamine. Free protamine molecules have been used for gene and macromolecule delivery into cells [33] due to their cell penetrating activity [34]. Changes to DNA conformation and topology can produce important effects on the transfection efficiency, as they can promote or disrupt the expression of the genes encoded by the plasmid. The efficiency and strength of plasmid DNA binding to AuNPs can also be affected by DNA conformation on the NP surface. This binding has important implications in gene delivery as it will determine the ability of the NP to carry and deliver the plasmid (i.e., binding has to be strong enough to carry the plasmid to the target, yet loose enough to deliver it with efficiency into the cell for effective expression).

Recently, functionalized AuNPs were used as novel markers for sex-sorting of mammalian sperm and for the selection of sperm with heritable DNA sequences interesting for animal breeding [35]. However, protamine's role in controlling plasmid DNA structure, topology and levels of condensation and decondensation when complexed with polyethylene glycol (PEG)ylated AuNPs has not been described.

Here, we report the use of AuNPs functionalized with PEG carboxylated and protamine (AuNP@PEG@Prot) to modulate plasmid DNA topology in a histone-mimetic way. Our main goal is to study the influence of AuNP@PEG@Prot conjugates on plasmid DNA condensation, and to develop a method to control plasmid DNA topology for downstream cellular applications that avoids the use of histones (Figure 1).

Materials & methods

Synthesis of citrate-AuNPs

The citrate-AuNPs were synthesized by the reduction of tetrachloroaurate ($HAuCl_4$) with sodium citrate, described elsewhere [36]. Briefly, hydrogen tetrachloroaurate (III) hydrate (Strem Chemicals, MA, USA; 0.2 g; 0.589 mmol) was dissolved in 500 ml of distilled water, heated and stirred under reflux. Upon boiling, the sodium citrate dihydrate (0.57 g; 1.94 mmol) is added and the solution is kept under reflux for 30 min, turning the color of the solution to red due to the synthesis of the NPs. In this process, the Au^{3+} ions are reduced by citrate to neutral Au atoms. When the solution becomes saturated with Au atoms, they start to precipitate in the form of NPs. The citrate acts as a stabilizing agent that sticks to the NP surface avoiding the aggregation of the NPs. When the process finished, we cooled the reaction mixture and kept it protected from light. The NP suspension was observed with a transmission electron microscope (TEM) (T20, 200 KeV; FEI) to determine Au core size, dynamic light scattering (DLS; Brookhaven ZetaPALS) and Fourier transform infrared spectroscopy (FTIR; JASCO FT/IR 4100).

Synthesis of PEGylated AuNPs (AuNP@PEG)

Functionalization of PEGylated AuNPs was carried out using commercial hetero-functional PEG functionalized with a thiol and a carboxylated group (SH-EG(8)-COOH, 450 Da; Iris-Biotech). 0.5 mg/ml of the citrate-AuNPs was mixed with 0.03 mg/ml of SH-EG(8)-COOH

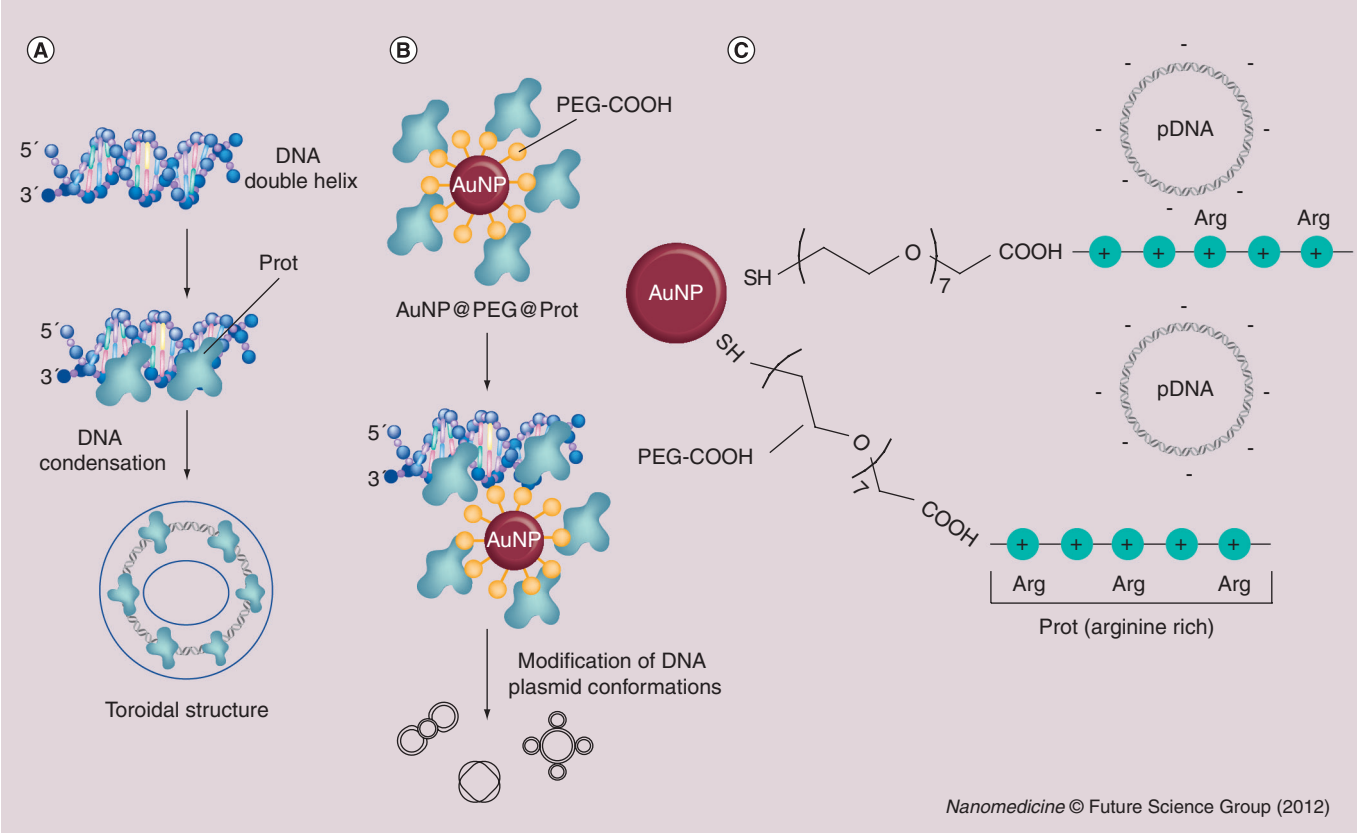

Figure 1. The effect of protamine on DNA topology. (A) Formation of toroidal structures (50–60 kb DNA) by free Prot. **(B)** Conformational changes of plasmid DNA mediated by AuNP@PEG@Prot. **(C)** Electrostatic interactions between AuNP@PEG@Prot and plasmid DNA. Prot possesses large tracts of positively charged arginine residues that neutralize the negative phosphodiester backbone of the DNA.
AuNP: Gold nanoparticle; PEG: Polyethylene glycol; Prot: Protamine.

in an aqueous solution of SDS (0.028%). Following this, NaOH was added to a final concentration of 25 mM and the mixture was incubated for 16 h at room temperature.

Excess PEG was removed by centrifugation (14,000 rpm, 30 min, 4°C) and quantified by the Ellman's Assay. The Ellman's Assay is suitable for sulfhydryl group determination. 0.05 mg/ml of 5,5′-dithio-bis-(2-nitrobenzoic acid) reacts with sulfhydryls under slightly alkaline conditions (0.5 M phosphate buffer, pH 7–8), to release the highly cromogenic compound (412 nm) 5-thio-2-nitrobenzoic acid after 15 min at room temperature. A linear standard curve was prepared in the range of 0.5–30 µg/ml of SH-EG(8)-COOH. The excess SH-EG(8)-COOH was determined after interpolation in this curve (Supplementary figure 1A; see online www.future-medicine.com/doi/suppl/10.2217/nnm.12.21). The linear range for the thiolated chain is 0.5–30 µg/ml (Abs_{412} = 0.0248 × [SH-EG(8)-COOH, µg/ml] + 0.0645). The total number of thiolated-PEG chains that can be attached per AuNP was determined to be 5624.4 ± 456.8 chains per NP (Supplementary figure 1).

AuNP@PEG were analyzed by TEM, DLS and FTIR confirming the presence of PEG on the NPs.

Functionalization of histone-mimetic AuNPs (AuNP@PEG@Prot)

The process for producing the histone-mimetic AuNPs was based on a carbodiimide (EDC)/*N*-hydroxysuccinimide (NHS) coupling reaction [37] of protamine and carboxyl-functionalized AuNPs. A commercial hetero-functional PEG with a thiol group on one terminus and a carboxylic acid functional group on the other (SH-EG(8)-COOH) was used for the carboxyl functionalization of AuNPs. Briefly, 1 mg/ml Au@PEG and 1.25 mg/ml *N*-hydroxysulfosuccinimide (sulfo-NHS) were incubated in 25 mM MES (2-(N-morpholino) ethanesulfonic acid) at pH 6.1. After this, protamine sulfate from salmon sperm (SIGMA; molecular weight of 5000–10000 Da) was added to the mixture at a final concentration of 0.5 µg/ml and allowed to stabilize for 5 min. After this period of time, EDC was added at a final concentration of 150 µg/ml and the mixture

incubated at room temperature for 16 h. Then, the AuNP@PEG@Prot were centrifuged at 14,000 rpm for 30 min at 4ºC to remove the excess protamine, and supernatants were recovered and tested for protein concentration by the Bradford assay. The Bradford assay, a colorimetric protein assay, is based on an absorbance shift of the dye Coomassie Brilliant Blue in which under acidic conditions the red form of the dye is converted into its bluer form to bind to the protein being assayed. After interpolation in a standard curve for protamine concentration (Supplementary figure 2) AuNP@PEG@Prot were determined to have 4.8 ± 0.34 molecules of protamine per AuNP.

Characterization of the NPs was performed by DLS ζ-potential (Brookhaven ZetaPALS), UV/Vis Spectroscopy (Varian Cary50 Probe) and FTIR. Size increase shown by DLS and ζ-potential values also confirmed protamine functionalization.

Plasmid DNA conformation studies

Evaluation of plasmid (psiCHECK™-2; Promega) conformations (Supplementary figure 3) was confirmed by linearizing the plasmid with 20 U of HindIII (Fermentas), incubating at 37°C for 1 h and 80ºC for 20 min for inactivation. The plasmid was also nicked with 10U of S1 nuclease (Fermentas), incubating the mixture at room temperature for 30 min. To stop the reaction, 2 µl of 0.5 M EDTA was added and the reaction heated at 70°C for 10 min. Confirmation of proper conformations was performed by 0.8% agarose gel, at 70 V during 100 min.

Plasmid DNA conformation quantification was performed by pixel intensity/counting using ImageJ™ imaging software.

Atomic force microscopy studies

For atomic force microscopy (AFM) analysis, an atomic force microscope (Nanotec) and noncontact cantilever (SuperSharpSilicon; Nanosensors) (fo = 190 kHz) probes were used to image the DNA topology when incubated with AuNPs functionalized with protamine. Samples were deposited from water solution. Samples were deposited onto freshly cleaved mica sheets, left for 20 min and then air dried. Images were collected in air at room temperature. The raw data images were rendered using Nanotec WSxM software (version v5.0 Develop 3.1).

Results & discussion

AuNPs were synthesized by the reduction of tetrachloroaurate acid with sodium citrate. NPs were 14.47 nm in size as determined by TEM (Supplementary figure 4). Chemical functionalization was incorporated into the NPs by substitution of citrate with a hetero-functional octa(ethylene glycol) (SH-EG(8)-COOH) with a thiol group at one end to be linked to the Au core and a carboxylic group at the other end to incorporate chemical functionality onto the NPs. AuNPs were covered with a dense layer of SH-EG(8)-COOH and functionalized NPs (AuNP@PEG) were obtained. The excess SH-EG(8)-COOH was removed by centrifugation at 4°C, and evaluated by the Ellman's method (see Material & methods section), retrieving a PEG:AuNP ratio of 5624:1. Conjugation of protamine to AuNP@PEG was achieved by taking advantage of the carboxylated surface previously generated on the NP and the remaining amino groups from the protamine. Using EDC and sulfo-NHS, protamine was covalently conjugated to the NP surface yielding AuNP@PEG@Prot. Determination of the amount of protamine per NP was achieved by quantification of supernatants using the Bradford assay, and a final protamine:AuNP ratio of 4.8 ± 0.34 was obtained. UV/Vis and DLS were also used to confirm protamine conjugation (Figure 2) as well as FTIR (Supplementary figure 5). ζ-potential values are -29.10 ± 0.83 for AuNP@PEG and -17.24 ± 0.64 for AuNP@PEG@Prot. Au@PEG is negatively charged, whereas AuNP@PEG@Prot is slightly more positive, which could be explained by the differences in ratio of PEGs (5624:1) and protamine (5:1) per AuNP. Interaction between AuNP@PEG@Prot and DNA is driven by the nature of the ligand protamine, which is selective for DNA binding, when bound to AuNPs. Alteration of DNA conformation is driven by the specific binding to protamine molecules arranged on the surface of AuNPs, associated with a local ionic interaction between the DNA-binding site on protamine and the DNA itself.

After functionalization of the Au conjugates, we performed the plasmid DNA conformation studies. The free plasmid DNA (control) presents several distinct conformations that can be identified through the electrophoretic profile of the uncut plasmid in an agarose gel (0.6% – TBE 1x, 70 V for 100 min) (Figure 3B). Plasmid DNA shows two distinct conformations: Sc, where DNA is wound up into a compact structure; and Nc, where one strand is a covalently continuous circle and the other has been cut; either in the form of monomers or dimers. In the Sc structure (or covalently closed-circular structure), DNA is fully intact with

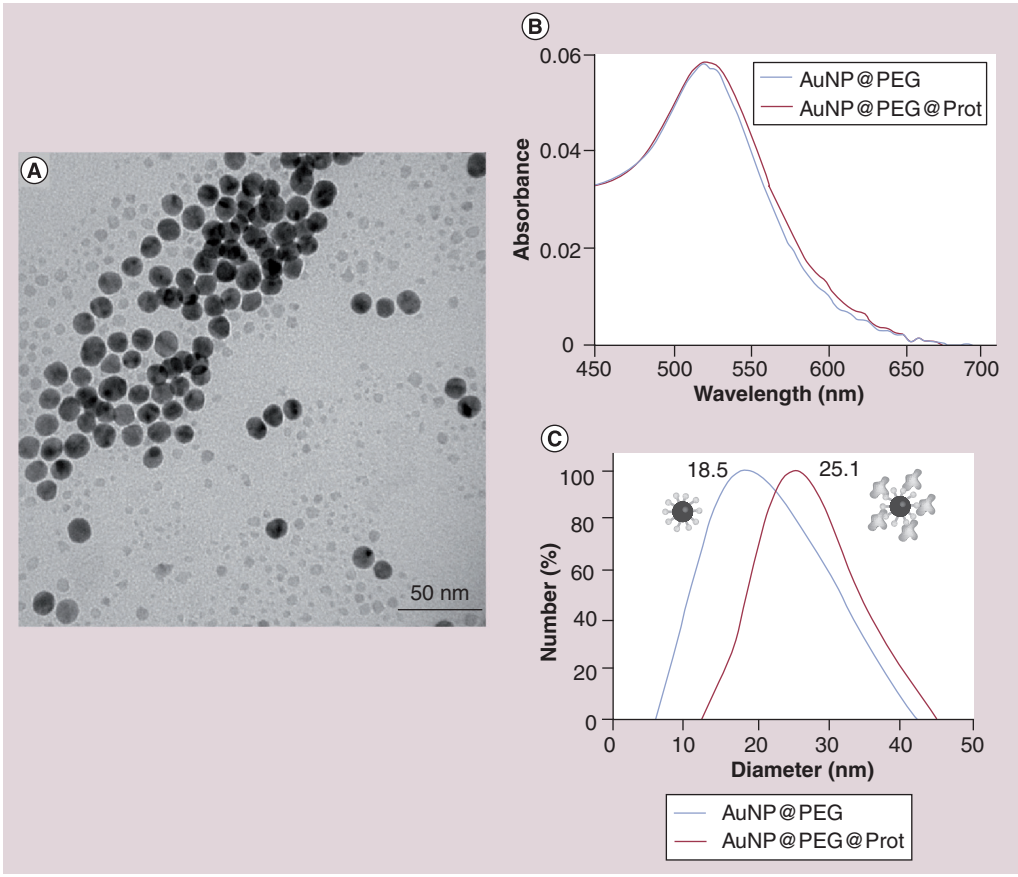

Figure 2. Characterization of gold nanoparticle conjugates by (A) transmission electron microscopy, (B) UV/Vis and (C) dynamic light scattering. The polydispersity index is 0.265 for AuNP@PEG and 0.091 for AuNP@PEG@Prot. The size increase shown by dynamic light scattering confirmed Prot functionalization.
AuNP: Gold nanoparticle; PEG: Polyethylene glycol; Prot: Protamine.

both strands uncut with a built in twist, resulting in a twisted compact form where the strands may become more tightly or more loosely wound together accommodating one too many or one too few helical twists. Once one of the strands has been cut, the superhelical tension relaxes and the tightly wound ball becomes a floppy circle. This Nc form is one of the most relaxed and unstressed states of a closed-circular DNA and shows the slowest electrophoretic mobility for uncut plasmid DNA. The Sc DNA shows the highest electrophoretic mobility in an agarose gel and represents 95% of all plasmid DNA conformations. The Sc and Nc conformations are the two main conformational structures of a single plasmid molecule (monomer). Nevertheless, two plasmid molecules can join to form a dimer with twice the molecular weight of that of the monomer. This way, a dimer will show a decreased electrophoretic mobility and becomes visible in the gel above the monomeric form. As for the monomeric plasmid, Sc shows the highest mobility and Nc the lowest.

Regarding the effect of free protamine in plasmid conformation, we demonstrate that protamine allows plasmid DNA condensation (Supplementary figure 6). The quantity of unbound plasmid DNA could easily be assayed by a gel shift assay, and shows plasmid binding to protamine at a range of 10^{-4}–0.1 mg/ml at a constant plasmid concentration (4.4 ng/µl). The binding of plasmid to protamine is apparent at protamine concentrations from 2×10^{-3} to 0.1 mg/ml. The significant decrease in DNA mobility is associated with the formation of extremely dense clumps of plasmid DNA and protein. For lower concentrations of protamine, it is still possible to observe the monomeric and dimeric, both Sc and Nc, forms of the plasmid. In fact, no change in Sc and Nc conformations is observed for 10^{-4} to 2×10^{-3} mg/ml of protamine.

Following demonstration of the potential for DNA condensation and complexation, we then evaluated protamine function when functionalized on AuNP@PEG. Protamine effect on plasmid conformation when bound to AuNP@PEG

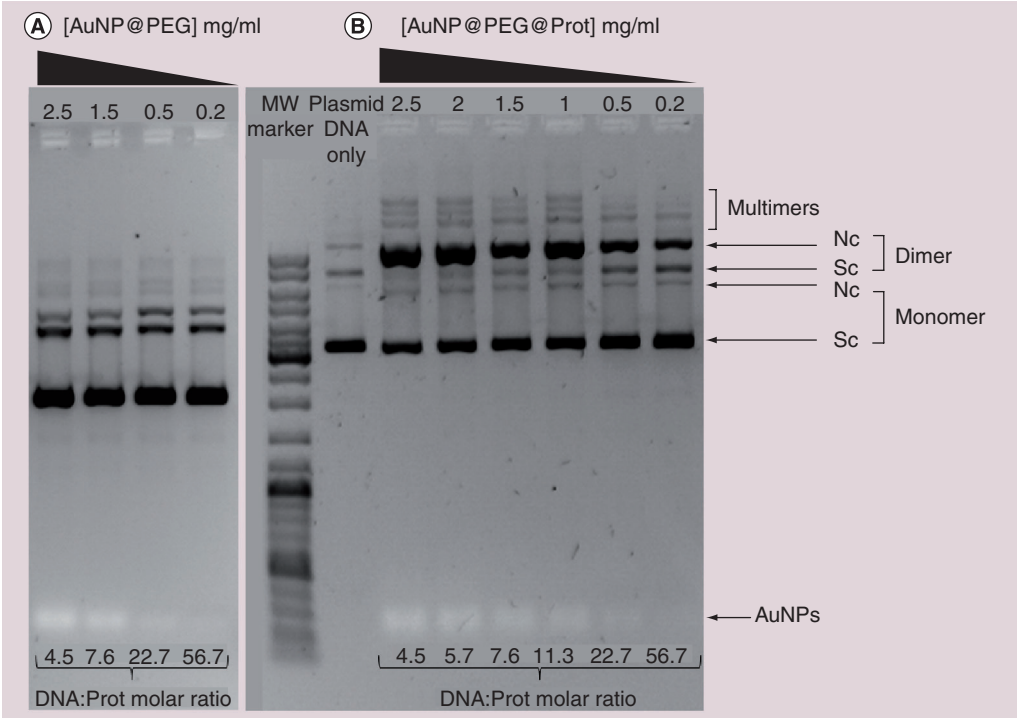

Figure 3. Comparison of DNA topology changes between gold nanoparticles functionalized with (A) polyethylene glycol or (B) polyethylene glycol and protamine. AuNP@PEG@Prot concentration varies from 2.5 to 0.2 mg/ml and plasmid concentration was kept constant (2.5 ng/µl). The stoichiometric ratio between Prot and DNA molecules to obtain different topologies are shown. The quantity of the Sc conformation of the monomer decreases at the same time the Nc conformation of the dimer increases in an AuNP@PEG@Prot concentration-dependent manner. AuNP@PEG did not show the same effect as AuNP@PEG@Prot in changing plasmid conformation. Both Sc and Nc conformations maintain almost the same quantities as the control (plasmid DNA only). Agarose gel electrophoresis was carried out at 70 V for 100 min.
AuNP: Gold nanoparticle; Nc: Nicked circle; PEG: Polyethylene glycol; Prot: Protamine; Sc: Supercoiled.

can easily be observed in Figure 3A. In contrast to the effect of AuNP@PEG, AuNP@PEG@Prot (Figure 3B) greatly influences plasmid DNA topology. In a concentration-dependent manner, for higher concentrations of the AuNP conjugates, the quantity of the Sc conformation of the monomer decreases at the same time the Nc conformation of the dimer increases. Also, for higher concentrations of AuNP conjugates more than two plasmid molecules join together and create high-molecular-weight multimers. It is usually difficult to distinguish conformations of multimers but, in Figure 3B, the three conformations of the multimers can be easily seen. Similar to the Nc conformation of the dimer, with a high concentration of AuNP conjugates an increase in multimer quantity can be seen. As revealed in Figure 3B, DNA condensation by AuNP@PEG@Prot results in the formation of DNA condensates with a wider diversity of plasmid morphologies and with great potential for formation of greater quantity of dimers and multimers. The Nc conformations of plasmid dimers were still the predominant morphology; however, the multimers (probably representing toroidal condensates of 50–60 kb of DNA) were also observed. For higher AuNP@PEG@Prot concentrations, there is an increase in the Nc conformation and a decrease in Sc form, both for monomers and dimers. It seems that when protamine is associated with AuNPs, it favors the most relaxed forms of plasmid DNA, instead of supporting the most condensed conformations. Conversely, there is an increasing formation of DNA multimers, most likely toroidal structures, with increasing concentrations of Au@PEG@Prot. This proves that protamine is capable of inducing both condensation and decondensation of DNA. In fact, protamine, when complexed to AuNPs, plays an active role in controlling plasmid DNA structure and quantity, not only for condensation but also for decondensation of DNA, as demonstrated by the increase in the Nc conformation, the most relaxed and unstressed state of plasmid DNA. Furthermore, this behavior was observed to be general and not dependent on plasmid

size. The pattern of the conformational changes mediated by AuNP@PEG@Prot on plasmids of different sizes presents a similar tendency (data not shown). AFM was also carried out to confirm the results obtained by gel electrophoresis (FIGURE 4). FIGURE 4A depicts the AFM images of the DNA alone (plasmid with 6273 bp) with condensed and decondensed strands. The condensed DNA molecules have significantly more nodes (the number of visible crossover points in AFM images) than the relaxed forms. FIGURE 4C shows the effect of AuNP@PEG without protamine on DNA condensation: the NPs are present with circular semi-decondensed DNA in their vicinity. In the case of AuNP@PEG@Prot (FIGURE 4D), the DNA structures are even less condensed (i.e., decondensed). We can see that AuNP@PEG@Prot binds to DNA, stretching the plasmid strands. This effect is due to the conjugated effect of AuNPs and protamine, as protamine alone induces the high level of condensation seen in FIGURE 4B. DNA condenses into distinct toroid structures and highly condensed particles when protamine alone is added. In fact, the positively charged guanidinium groups of arginine residues of the protamine bind electrostatically to the negatively charged phosphate groups of DNA. These effects are observed in gel electrophoresis (SUPPLEMENTARY FIGURE 1) and in the band gel quantification (FIGURE 5).

A time-dependence study of plasmid conformation changes mediated by AuNP@PEG@Prot was also performed in order to calculate the kinetic constants for DNA topology modification via histone-mimetic AuNPs. The concentration of Sc monomers and dimers decreases in a similar fashion, with Nc dimers being the conformational product of the former species (SUPPLEMENTARY FIGURE 7). A theoretical equation that relates the variation of the conformational species as a function of time was developed (SUPPLEMENTARY MATERIAL 1, theoretical model for kinetic constant calculation):

$$\ln\left[1-\frac{[Nd]t}{[P]_0-[Nm]_0}\right]=\ln\left[1-\frac{[Nd]_0}{[P]_0-[Nm]_0}\right]-kft$$

The main conformation transitions are from Sc for monomer and dimer forms to Nc for dimer forms. The relative concentration of the Sc conformations (Sm: Sc monomer; Sd: Sc dimer) decrease as a function of time with a similar tendency. Therefore, both species decrease in concentration with the same kinetic constant (kinetic constant of formation of Nc dimer, kf). From adjustment of the theoretical equation, a kinetic constant (kf) of 1152 M/s was calculated.

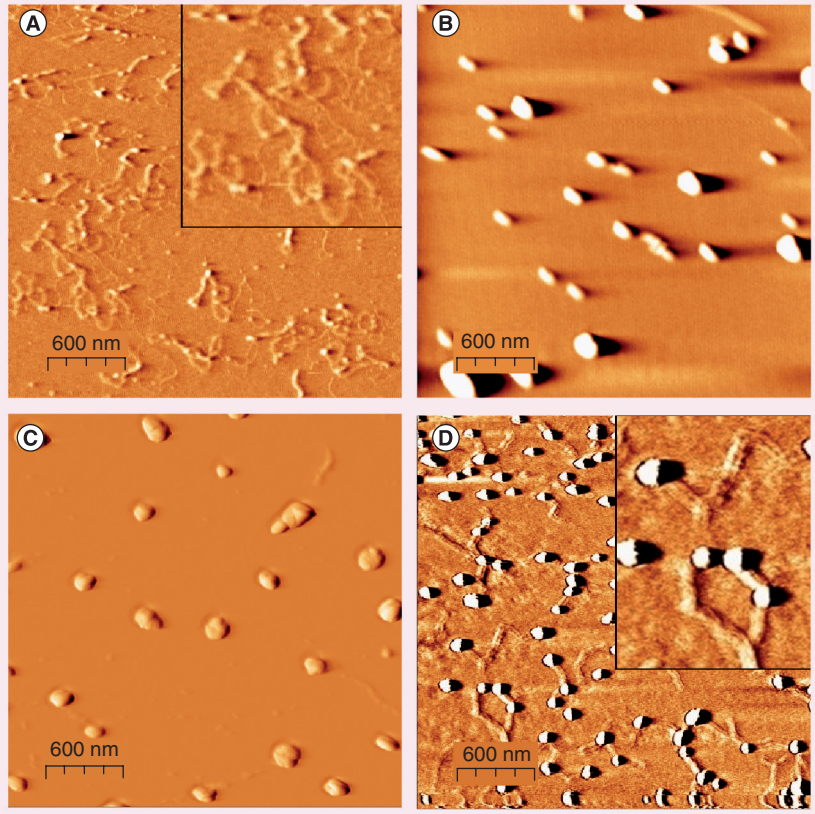

Figure 4. Atomic force microscopy images. (A) Plasmid DNA, **(B)** protamine–DNA complex, **(C)** gold nanoparticles functionalized with a carboxylated polyethylene glycol plus plasmid DNA and **(D)** gold nanoparticles functionalized with polyethylene glycol and protamine–DNA complex, showing an increase in diameter to approximately 54 nm confirming PEG and protamine functionalization. The 14-nm particles refer to the citrate-gold nanoparticles without any functionalization.

Conclusion

We successfully report the use of AuNPs functionalized with PEG-carboxylated and protamine to modify plasmid DNA topology. We demonstrate that AuNP@PEG@Prot plays an active role in controlling plasmid DNA structure, topology and levels of condensation and decondensation. Conversely to what occurs when using free protamine, AuNP@PEG@Prot may allow control of the levels of condensation and decondensation of DNA molecules in a stable and organized manner. By means of a theoretical equation, it is possible to exert control over the amount of each plasmid DNA conformation by constraining the initial conditions and the incubation time of AuNPs with plasmid DNA. Although the functionalized AuNPs show an opposite effect on DNA structure, plasmid DNA conformations could be selectively extracted to shift the equilibrium of the reaction towards the desired conformation.

We hypothesize that the effect of AuNP@PEG@Prot on plasmid DNA conformations probably mimics the interactions between AuNPs and

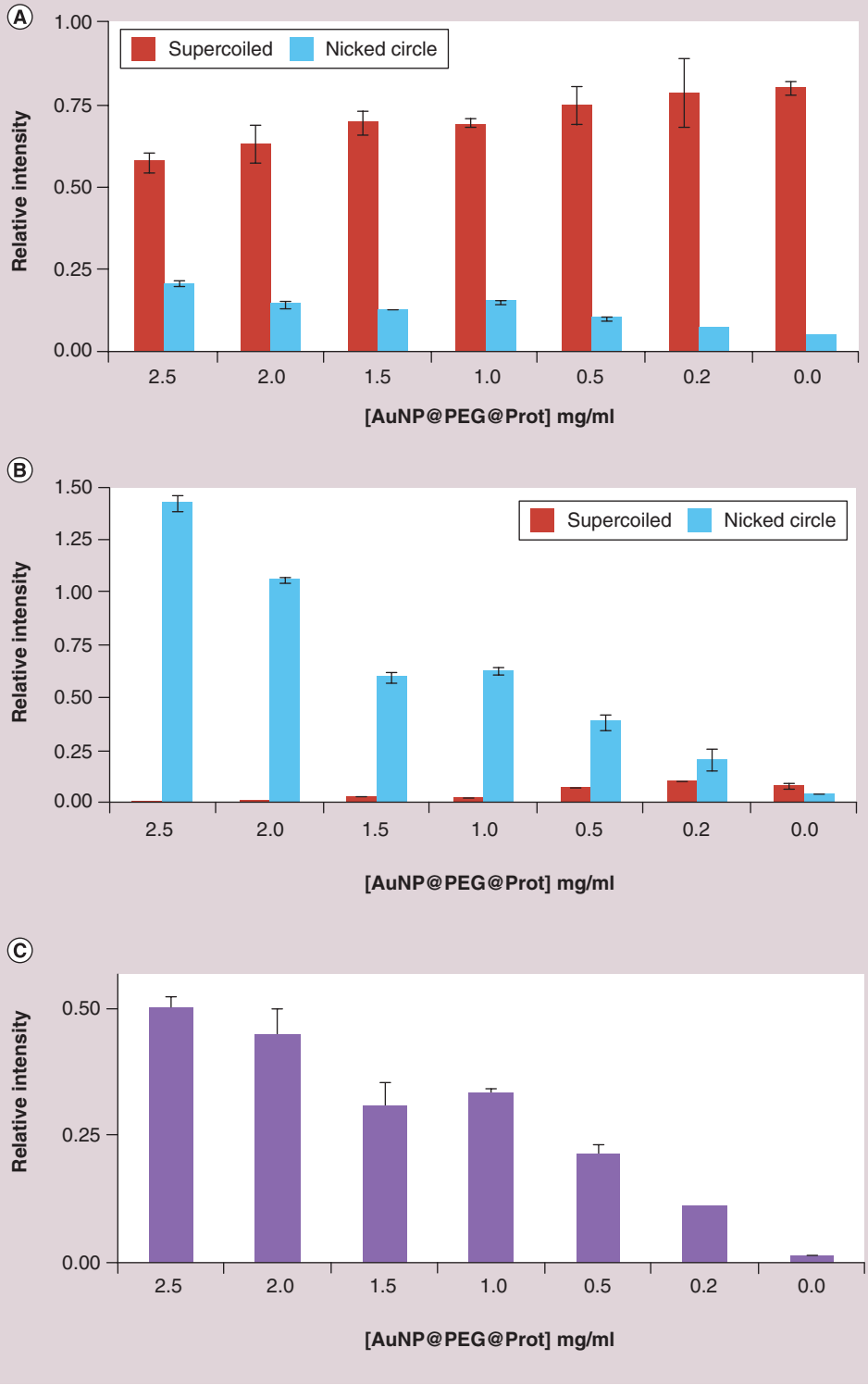

Figure 5. Relative quantification of the main plasmid conformations for the (A) monomers, (B) dimers and (C) multimers after incubation of 2.5 ng/µl of plasmid DNA with increasing amounts of gold nanoparticles functionalized with polyethylene glycol and protamine.
Error bars correspond to the average and standard deviation of three independent measurements.
AuNP: Gold nanoparticle; PEG: Polyethylene glycol; Prot: Protamine.

the DNA double helix in sperm chromatin. This hypothesis is supported by the fact that protamine proteins play an important role in condensation and stabilization of spermatic nuclear chromatin and that when combined with AuNPs of this particular size they may locate within the wide

groove of the DNA molecule, thus disturbing the structure of liquid crystals of DNA, changing its topology [38]. Although plasmid DNA is different from genomic and sperm DNA, it can be used as a valuable model to study DNA topology.

Several studies have shown that aberrant protamine content results in human male infertility due to diminished parameters of semen quality, such as sperm count, motility and morphology [30,39]. In fact, sperm chromatin/DNA integrity is essential for the accurate transmission of paternal genetic information. In addition, a deficient function in protamine may also predispose DNA to damages and fragmentation characterized by both single and double DNA strand breaks, and this characteristic is particularly frequent in infertile men. With this in mind, the present report may constitute a good model study and to evaluate application of histone-mimetic AuNPs – AuNP@PEG@Prot. If proven effective in cell models and on genomic DNA, such a system may be considered for therapy and/or infertility procedures, for example, in protamine-deficient sperm individuals. For this, further studies of *in vitro* experiments with intact nuclear membrane and nuclear core complexes, and with a relevant *in vivo* model of spermatogenesis will be needed to support this hypothesis.

Acknowledgements

The authors would like to thank JL Diez for atomic force microscopy analysis and I Echaniz for technical support.

Financial & competing interests disclosure

This work has been funded by the Spanish Ministry of Science and Innovation (CTQ2008-03739/PPQ), NanoSciERA Grant-NANOTRUCK and ERC-Starting Grant 239931-NANOPUZZLE. J Conde thanks FCT/MCTES (SFRH/BD/62957/2009). PV Baptista thanks CIGMH-FCT/MCTES and JM de la Fuente thanks ARAID for financial support. The authors have no other relevant affiliations or financial involvement with any organization or entity with a financial interest in or financial conflict with the subject matter or materials discussed in the manuscript apart from those disclosed.

No writing assistance was utilized in the production of this manuscript.

Ethical conduct of research

The authors state that they have obtained appropriate institutional review board approval or have followed the principles outlined in the Declaration of Helsinki for all human or animal experimental investigations. In addition, for investigations involving human subjects, informed consent has been obtained from the participants involved.

Executive summary

Synthesis of gold nanoconjugates

- Gold nanoparticles (AuNPs; ~14 nm) were synthesized by the reduction of tetrachloroaurate acid with sodium citrate.
- Chemical functionalization was incorporated into the nanoparticles by substitution of citrate by a hetero-functional octa(ethylene glycol) with a thiol group at one end to be linked to the gold core and a carboxylic group at the other end to incorporate chemical functionality onto the nanoparticles.
- Using carbodiimide and *N*-hydroxysulfosuccinimide, protamine was covalently conjugated to the nanoparticles' surface, yielding AuNP@PEG@Prot.

Effect of free protamine on DNA topology

- We demonstrate that the significant decrease of DNA mobility is associated with the formation of extremely dense clumps of plasmid DNA and protein.
- Protamine alone induces high levels of condensation of DNA (formation of toroidal structures: 50–60 kb of DNA).

Effect of AuNP@PEG & AuNP@PEG@Prot on DNA topology

- In contrast to the effect of AuNP@PEG, AuNP@PEG@Prot greatly influences plasmid DNA topology.
- DNA condensation by AuNP@PEG@Prot results in the formation of DNA condensates with a wider diversity of plasmid morphologies and with a great potential for formation of higher quantities of dimers and multimers.
- When protamine is associated with gold nanoparticles, it favors the most relaxed forms of plasmid DNA, instead of supporting the most condensed conformations.

Conclusion

- Protamine, when complexed to AuNPs, plays an active role in controlling plasmid DNA structure and quantity, not only for condensation of DNA, but also for decondensation of DNA as demonstrated by the increase in the nicked circular conformation, the most relaxed and unstressed state of plasmid DNA.
- AuNP@PEG@Prot presents a tool to control, in a stable and organized approach, the levels of condensation and decondensation of DNA molecules.

References

1 Heath JR, Davis ME. Nanotechnology and cancer. *Annu. Rev. Med.* 59, 251–265 (2008).

2 Peer D, Karp JM, Hong S, Farokhzad OC, Margalit R, Langer R. Nanocarriers as an emerging platform for cancer therapy. *Nat. Nanotechnol.* 2(12), 751–760 (2007).

3 Ferrari M. Cancer nanotechnology: opportunities and challenges. *Nat. Rev. Cancer* 5, 161–171 (2005).

4 Cai W, Gao T, Hong H, Sun J. Applications of gold nanoparticles in cancer nanotechnology. *Nanotechnol. Sci. Appl.* 1, 17–32 (2008).

5 Ghosh P, Han G, De M, Kim CK, Rotello VM. Gold nanoparticles in delivery applications. *Adv. Drug Deliv. Rev.* 60(11), 1307–1315 (2008).

6 Nishiyama N. Nanomedicine: nanocarriers shape up for long life. *Nat. Nanotechnol.* 2(4), 203–204 (2007).

7 Baptista PV. Cancer Nanotechnology – prospects for cancer diagnostics and therapy. *Curr. Cancer Ther. Rev.* 5(5), 80–88 (2009).

8 Rosi NL, Mirkin CA. Nanostructures in biodiagnostics. *Chem. Rev.* 105(4), 1547–1562 (2005).

9 Conde J, de la Fuente JM, Baptista PV. RNA quantification using gold nanoprobes – application to cancer diagnostics. *J. Nanobiotechnol.* 8, 5 (2010).

10 Han G, Ghosh P, Rotello VM. Multifunctional gold nanoparticles for drug delivery. *Adv. Exp. Med. Biol.* 620, 48–56 (2007).

11 Han G, Chari NS, Verma A *et al.* Controlled recovery of the transcription of nanoparticle-bound DNA by intracellular concentrations of glutathione. *Bioconjugate Chem.* 16(6), 1356–1359 (2005).

12 Chen C, Lin Y, Wang C *et al.* DNA – gold nanorod conjugates for remote control of localized gene expression by near infrared irradiation. *J. Am. Chem. Soc.* 128(11), 3709–3715 (2006).

13 Park S, Hamad-Schifferli K. Enhancement of *in vitro* translation by gold nanoparticle – DNA conjugates. *ACS Nano.* 4(5), 2555–2560 (2010).

14 Zanchet D, Micheel CM, Parak WJ *et al.* Electrophoretic isolation of discrete au nanocrystal/DNA conjugates. *Nano Lett.* 1(1), 32–35 (2001).

15 Watson JD, Crick FH. The structure of DNA. *Cold Spring Harb. Symp. Quant. Biol.* 18, 123–131 (1953).

16 Vologodskii AV, Lukashin AV, Anshelevich VV, Frank-Kamenetskii MD. Fluctuations in superhelical DNA. *Nucleic Acids Res.* 6(3), 967–982 (1979).

17 Benham CJ, Mielke SP. DNA mechanics. *Annu. Rev. Biomed. Eng.* 7, 21–53 (2005).

18 Sambrook J, Russell WD. *Molecular Cloning – a Laboratory Manual. Third Edition.* Cold Spring Harbor Laboratory Press, Cold Spring Harbor, NY, USA (2001).

19 Murray AW. How to compact DNA. *Science* 282(5388), 425, 427 (1998).

20 Braun RE. Packaging paternal chromosomes with protamine. *Nat. Genet.* 28(1), 10–12 (2001).

21 Brewer L, Corzett M, Lau EY, Balhorn R. Dynamics of protamine 1 binding to single DNA molecules. *J. Biol. Chem.* 278(43), 42403–42408 (2003).

22 Brewer L, Corzett M, Balhorn R. Condensation of DNA by spermatid basic nuclear proteins. *J. Biol. Chem.* 277(41), 38895–38900 (2002).

23 Hud NV, Milanovich FP, Balhorn R. Evidence of novel secondary structure in DNA-bound protamine is revealed by Raman spectroscopy. *Biochemistry* 33(24), 7528–7535 (1994).

24 Toma AC, de FM, Livolant F, Raspaud E. DNA condensed by protamine: a 'short' or 'long' polycation behavior. *Biomacromolecules* 10(8), 2129–2134 (2009).

25 Balhorn R. The protamine family of sperm nuclear proteins. *Genome Biol.* 8(9), 227 (2007).

26 Brewer LR, Corzett M, Balhorn R. Protamine-induced condensation and decondensation of the same DNA molecule. *Science* 286(5437), 120–123 (1999).

27 Oliva R, Goren R, Dixon GH. Quail (Coturnix japonica) protamine, full-length cDNA sequence, and the function and evolution of vertebrate protamines. *J. Biol. Chem.* 264(30), 17627–17630 (1989).

28 Erenpreiss J, Bars J, Lipatnikova V, Erenpreisa J, Zalkalns J. Comparative study of cytochemical tests for sperm chromatin integrity. *J. Androl.* 22(1), 45–53 (2001).

29 Carrell DT, Emery BR, Hammoud S. Altered protamine expression and diminished spermatogenesis: what is the link? *Hum. Reprod. Update* 13(3), 313–327 (2007).

30 Steger K, Fink L, Failing K *et al.* Decreased protamine-1 transcript levels in testes from infertile men. *Mol. Hum. Reprod.* 9(6), 331–336 (2003).

31 Zini A, Libman J. Sperm DNA damage: clinical significance in the era of assisted reproduction. *CMAJ* 175(5), 495–500 (2006).

32 Oliva R. Protamines and male infertility. *Hum. Reprod. Update* 12(4), 417–435 (2006).

33 Mayer G, Vogel V, Weyermann J *et al.* Oligonucleotide–protamine–albumin nanoparticles: protamine sulfate causes drastic size reduction. *J. Control Release* 106(1–2), 181–187 (2005).

34 Reynolds F, Weissleder R, Josephson L. Protamine as an efficient membrane translocating peptide. *Bioconjugate Chem.* 16(5), 1240–1245 (2005).

35 Barchanski A, Taylor U, Klein S, Petersen S, Rath D, Barcikowski S. Golden perspective: application of laser-generated gold nanoparticle conjugates in reproductive biology. *Reprod. Dom. Anim.* 46(3), 42–52 (2011).

36 Lee PC, Meisel D. Adsorption and surface-enhanced Raman of dyes on silver and gold sols. *J. Phys. Chem.* 86(17), 3391–3395 (1982).

37 Grabarek Z, Gergely J. Zero-length crosslinking procedure with the use of active esters. *Anal. Biochem.* 185(1), 131–135 (1990).

38 Hunt RA, Munde M, Kumar A *et al.* Induced topological changes in DNA complexes: influence of DNA sequences and small molecule structures. *Nucleic Acids Res.* 39(10), 4265–4274 (2011).

39 Aoki VW, Carrell DT. Human protamines and the developing spermatid: their structure, function, expression and relationship with male infertility. *Asian J. Androl.* 5(4), 315–324 (2003).

Modification of plasmid DNA Topology by "Histone-Mimetic" Gold Nanoparticles

João Conde[1,2], Pedro V. Baptista[2], Yulan Hernández[1], Vanesa Sanz[1*] and Jesus M. de la Fuente[1*]

[1] Instituto de Nanociencia de Aragón, Universidad de Zaragoza, Mariano Esquillor s/n 50018, Zaragoza, Spain.

[2] Centro de Investigação em Genética Molecular Humana (CIGMH), Departamento de Ciências da Vida, Faculdade de Ciências e Tecnologia, Universidade Nova de Lisboa, 2829-516 Caparica, Portugal.

CORRESPONDING AUTHORS EMAIL ADDRESS

jmfuente@unizar.es

vasanz@unizar.es

Supplementary figure 1. Determination of the degree of saturation of gold nanoparticles functionalized with hetero-functional octa(ethylene glycol) (SH-EG(8)-COOH).

For the determination of the degree of saturation of gold nanoparticles functionalized with thiolatedpoly(ethylene glycol) chains, we developed and optimized a procedure based on the Ellman's assay. With this procedure it is possible to determine the number of thiolated chains that bound to the gold nanoparticles. Following incubation of the AuNPs with the thiolated chains the thiolated PEG chains bind to the nanoparticle surface. The excess of thiolated chains not bound to the AuNP surface, i.e. free in solution, can then be experimentally determined via the optimized protocol described.

In order to determine the number of bound chains, the suspension is centrifuged and the supernatant with the excess of thiolated chains is used for the quantification assay. The free thiolated chains are quantified by a procedure based on the Ellman's assay, where the supernatant, containing the spacer with thiol groups on its structure, reacts with DTNB (5,5'-dithio-bis(2-nitrobenzoic) acid) to give a coloured product that can be measured spectrophotometrically. A stock solution of the thiolated chain is used for constructing a calibration curve from which the number of chains of any given sample can be interpolated. The number of bound chains to the AuNPs' surface is given by the difference between the amount determined by this assay and the initial amount of chains in the incubation mixture.

In the present case, 200 μL of stock solution (of different concentrations) and of the sample containing the supernatant are mixed with 100 μL of phosphate buffer 0.5 M pH 7 and 7 μL of DTNB 5 mg/mL in phosphate buffer 0.5 M pH 7. The mixture is made to react for 10 minutes and the absorbance at 412 nm is measured. A linear standard curve was prepared in the range of 0.5–30 μg/mL of SH-EG(8)-COOH (see Figure S1A). The excess of SH-EG(8)-COOH was determined after interpolation in this curve. The linear range for the PEG

thiolated chain is given by the Abs412nm = 0.0248×[SH-EG(8)-COOH chain, µg/mL] + 0.0645.

Following experimental determination of the total number of SH-EG(8)-COOH chains attached per gold nanoparticle via interpolation of a calibration curve, the level of saturation on the surface of the NP can also be calculated. Figure S1Bshows the excess of SH-EG(8)-COOH chains versus the initial concentration of SH-EG(8)-COOH chains in an incubation mixture with a constant concentration of gold nanoparticles is represented. As the initial concentration of SH-EG(8)-COOH chains increases, the excess of free SH-EG(8)-COOH chains increases in an equilibrium dependent way (equilibrium constant [bound chain]/[free chain]=0.76). There is a point at which the nanoparticle becomes saturated with a SH-EG(8)-COOH layer and is not able to uptake more PEG chains. It is then possible to calculate the average number of SH-EG(8)-COOH chains bound to each gold nanoparticle, which was 5624.4±456.8 chains per nanoparticle.

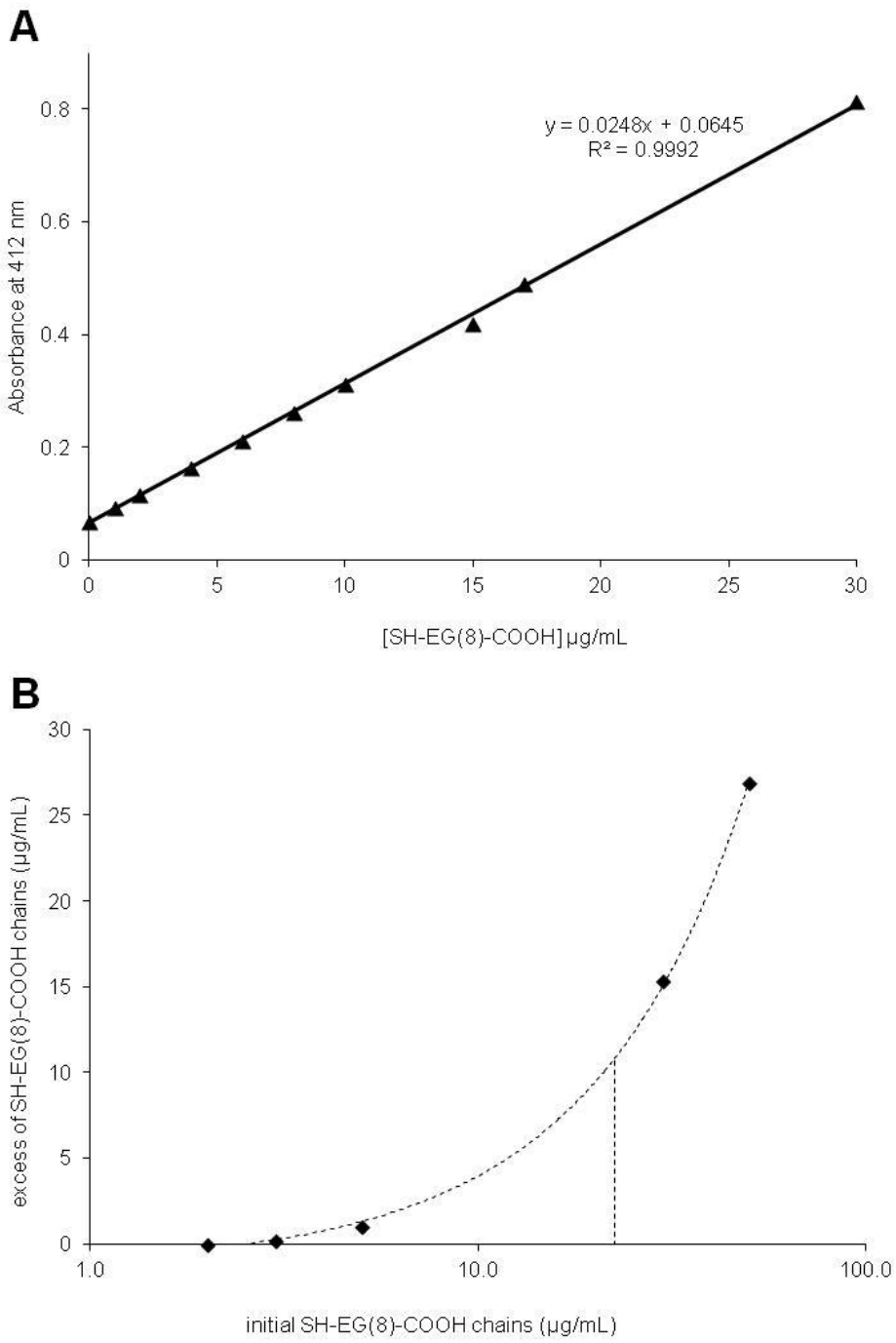

(A) Standard addition calibration curve for the SH-EG(8)-COOH chains. In the linear range the calibration curve is given by the following equation Abs412nm = 0.0248×[SH-EG(8)-COOH, µg/mL] + 0.0645. **(B)** Variation of the excess of thiolated SH-EG(8)-COOH chains as a function of the initial concentration in the incubation mixture with gold nanoparticles. Initial concentration of gold nanoparticles is0.5 mg/mL.

Supplementary figure 2. Determination of the Protamine peptide bound by the EDC coupling reaction to functionalized gold nanoparticles.

As it was stated in materials and methods section, a procedure for the determination of the Protamine peptide that was bound to gold nanoparticles through the EDC coupling reaction was developed. This assay was based on the Bradford method. Given that the reagents for the EDC reaction (sulfo-NHS, EDC) interferes with the assay an standard addition calibration curve for the Protamine peptide in the EDC reaction conditions was obtained (see Figure S2). This calibration curve was used for the interpolation of the samples containing the excess of peptide that was not bound to gold nanoparticles.

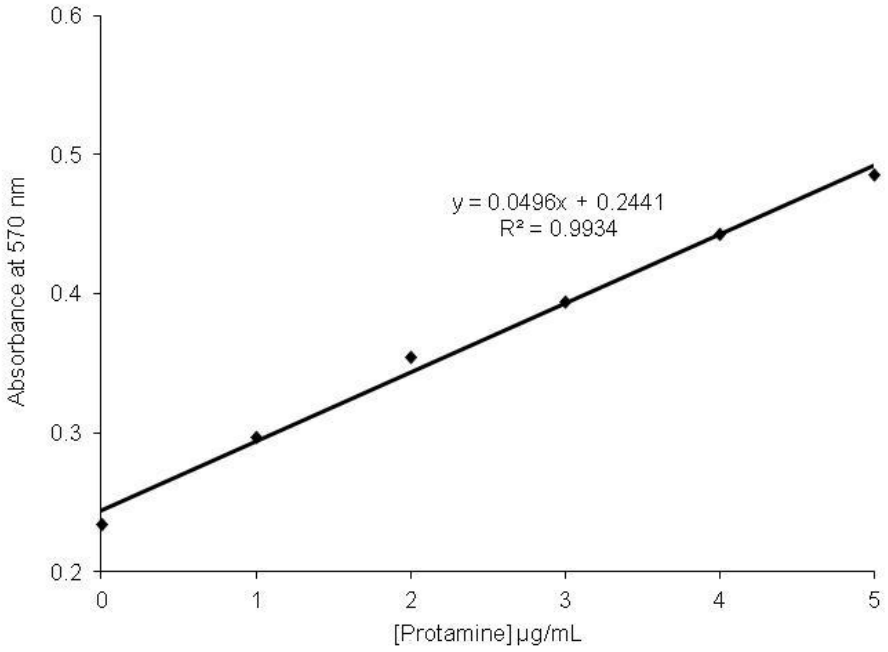

Standard addition calibration curve for the Protamine peptide in the conditions of the EDC/NHS coupling reaction. In the linear range the calibration curve is given by the following equation Abs570nm = 0.0496×[Protamine peptide, µg/mL] + 0.2441.

Supplementary figure 3.Plasmid DNA conformations.

Plasmid DNA conformations: circular, linear (digested with Hind III) and nicked (digested with nuclease S1).

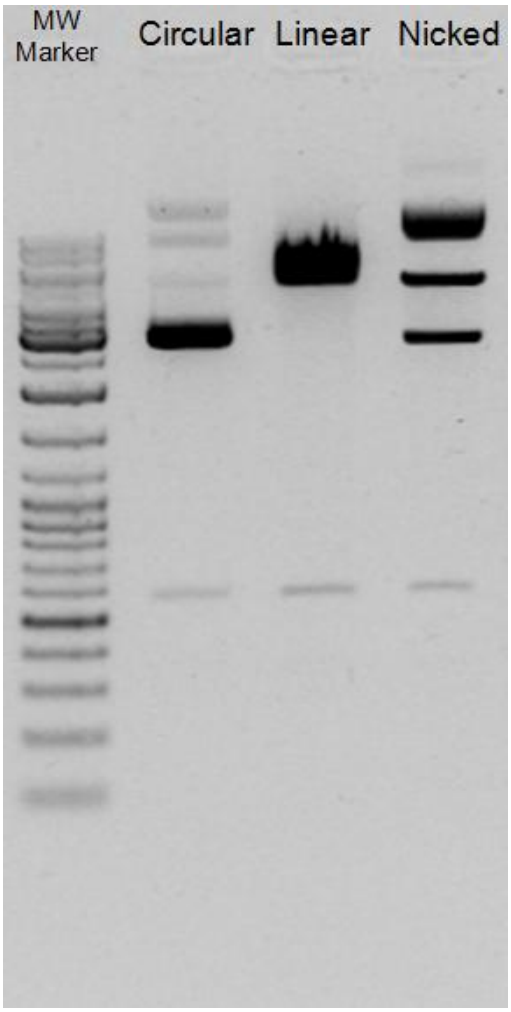

Supplementary figure 4: Citrate-Gold Nanoparticle Characterization.

Citrate-Gold nanoparticle characterization.**(A)** TEM images (scale bar = 100 nm). **(B)** Size distribution histogram showing an average diameter of 14.47 nm. **(C)** TEM micrograph of AuNP@PEG@Prot, where PEG and protamine layer can be observed.

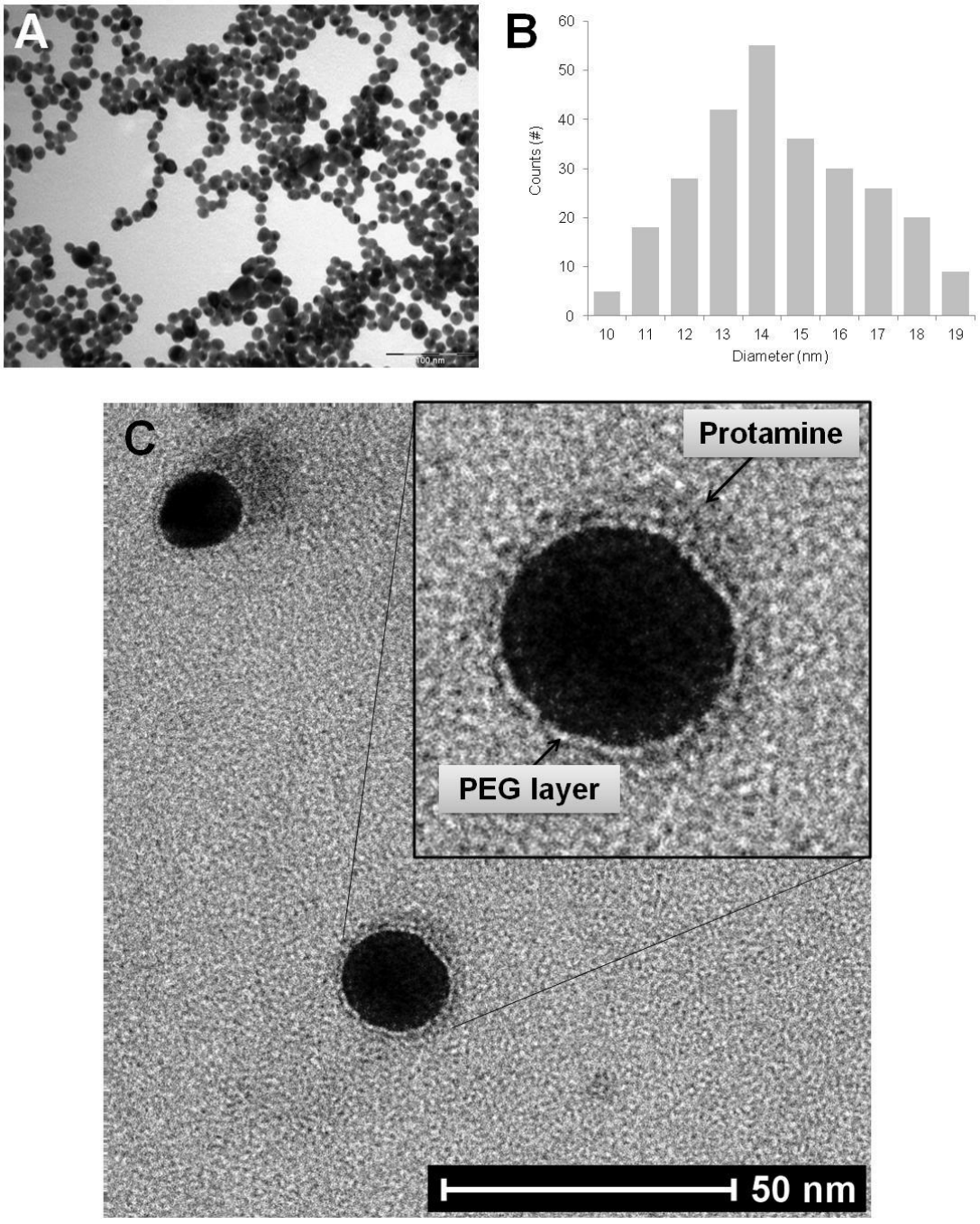

Supplementary figure 5: Infra-red (FT-IR) spectra of AuNP's conjugates.

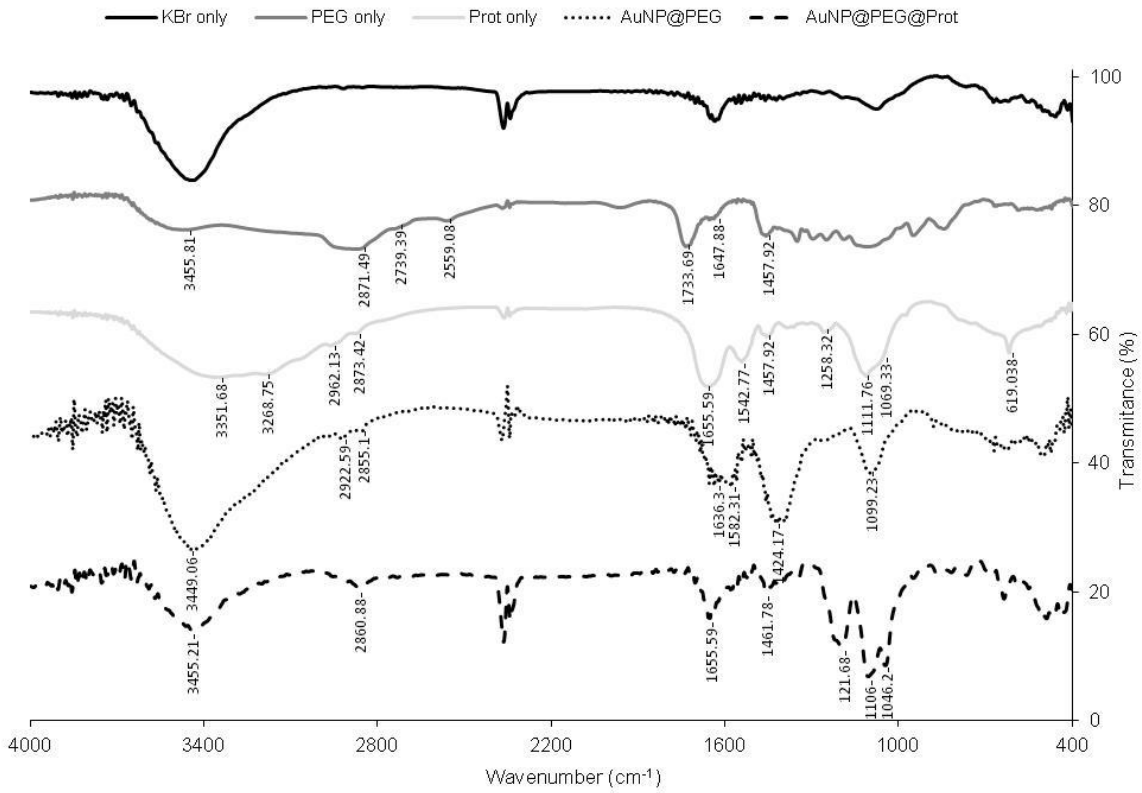

Infra-red (FT-IR) spectra of PEG, Protamine, AuNP@PEG and AuNP@PEG@Prot. **PEG FT-IR peaks:** 3456 cm^{-1} (OH st), 2871 cm^{-1} (-CH st), 2739 cm^{-1}, 2599 cm^{-1}, 1734 cm^{-1}, 1648 cm^{-1} (C=O st), 1458 cm^{-1}; **Protamine FT-IR peaks:** 3352 cm^{-1}, 3269 cm^{-1}, 2962 cm^{-1}, 2873 cm^{-1} (-CH st), 1656 cm^{-1} (amide I, α-helix), 1543 cm^{-1} (Amide II vibration C–N–H), 1458 cm^{-1} (amide II), 1258 cm^{-1} (amide III band), 1112 cm^{-1}, 1069 cm^{-1}; **AuNP@PEG FT-IR peaks:** 3449 cm^{-1} (NH st), 2855 cm^{-1} (-CH st), 1636 cm^{-1} (C=O st); **AuNP@PEG@Prot FT-IR peaks:** 3455 cm^{-1} (NH st), 2860 cm^{-1} (-CH st), 1655 cm^{-1} (amide I, α-helix), 1461 cm^{-1} (amide II).

The characteristic amide I and II peaks of protamine is found on AuNP@PEG@Prot showing that protamine is conjugated to gold nanoparticles. The Amide I band is due to carbonyl stretching vibrations while the Amide II is due primarily to NH bending vibrations.

Supplementary figure 6. Effect of free protamine in plasmid conformation.

Effect of free protamine in plasmid conformation. Free protamine shows plasmid binding at a range of 10^{-4}–0.1 mg/mL), with a constant plasmid concentration (4.4 ng/µL). The binding of plasmid to the protamine is apparent at protamine concentrations from 2×10^{-3} to 0.1 mg/mL. For lower concentrations of protamine it is still possible to observe the monomeric and dimeric, both Sc and Nc, forms of the plasmid DNA. No change in Sc and Nc conformations is observed for 10^{-4} to 2×10^{-3} mg/mL of protamine.

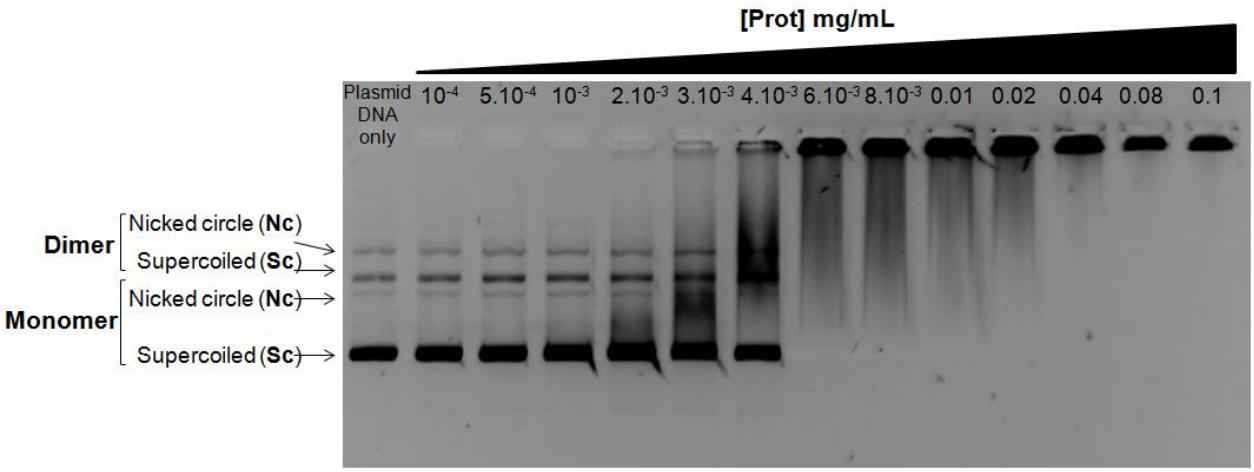

Supplementary figure 7.Kinetic study of plasmid conformation changes.

Kinetic study of plasmid conformation changes mediated by AuNP@PEG@Prot.**(A)** Variation of relative quantification of the main plasmid conformation for the monomers and dimers in a time dependence way. **(B)** Adjustment by the theoretical model for kinetic constant calculations ($\ln (1–[Nd]/[P]_0 – [Nm]_0)= -0.0036t – 0.4855$, $R^2= 0.99$)

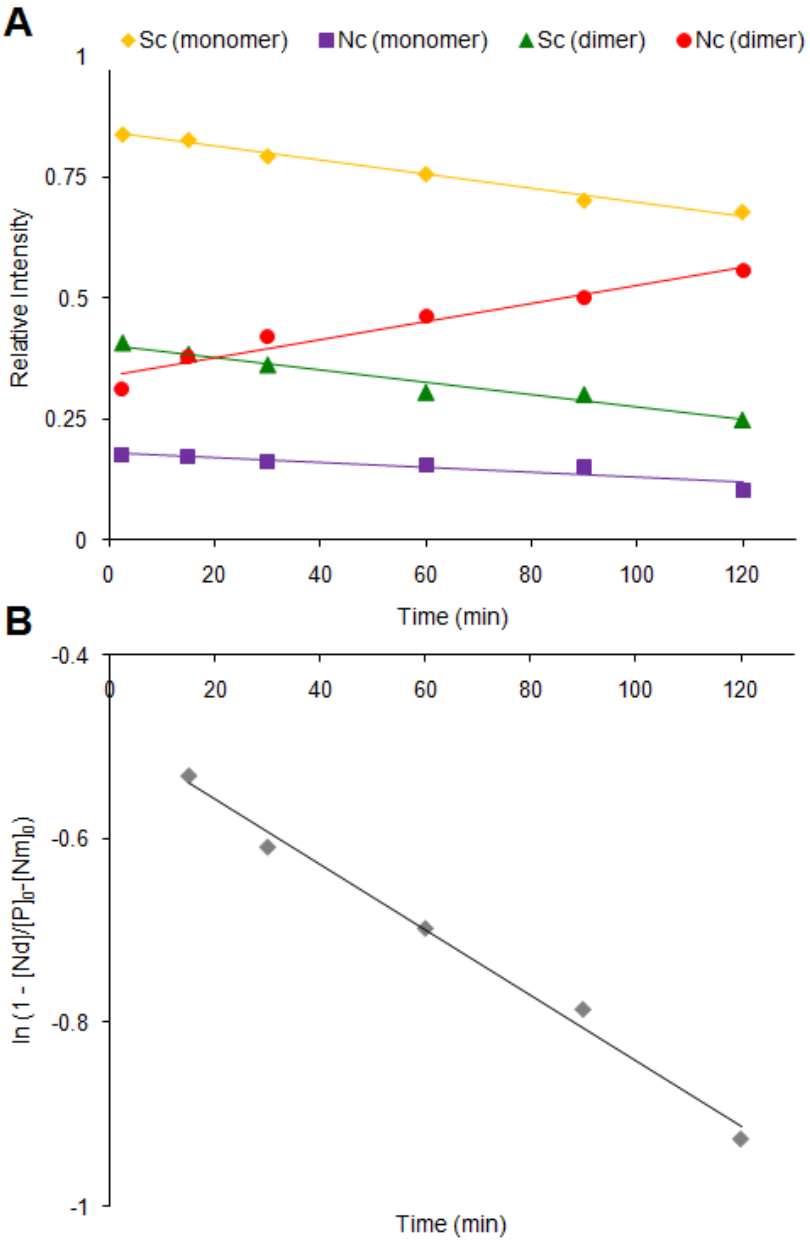

Supplementary material 8. Theoretical model for kinetic constant calculation

The kinetics data was obtained from the line scans of the bands in the gel mobility shifts (see Figure 3 from the manuscript). From Figure S7A the main conformation transitions are from Supercoiled for monomer and dimer forms to the Nicked circle for dimer (Nd). The relative concentration of the Sc conformations (Sm – supercoiled for monomer; Sd – supercoiled for dimer) decrease as a function of time with a similar tendency. Therefore both species decrease in concentration with the same kinetic constant (kinetic constant of formation of Nc dimer, kf). From this hypothesis the kinetic equation for the formation of the Nc dimer form is as follows:

$$\frac{d[Nd]t}{dt} = kf \times ([Sm]t + [Sd]t) \qquad eq.1$$

The mass balance for total plasmid concentration ($[P]_0$) is given by equation 2:

$$[P]0 = [Sm]t + [Sd]t + [Nd]t + [Sd]t + [M]t \qquad eq.2$$

From Figure S7A it is possible to see that the concentration of the supercoiled for dimer [Sd] and for multimers [M] are negligible and remain as constant during the kinetic process. Consequently can be group as a constant:

$$[Sd]0 + [M]0 = [Sd]t + [M]t \qquad eq.3$$

From equation 1 to 3 the follow deferential equation has to be solved:

$$\left[\frac{d[Nd]}{\left(kf\left([P]0 - [Sd]0 - [M]0 - [Nd]\right) = \int_0^t dt \qquad eq.4\right]}\right]$$

Where $[Nd]_0$ is the initial concentration of the nicked circle form for dimer and $[Nd]_t$ is the nicked circle form for dimer at *t* time.

The equation 4 solution is:

$$\ln\left[1 - \frac{[Nd]t}{[P]0 - [Nm]0}\right] = \ln\left[1 - \frac{[Nd]0}{[P]0 - [Nm]0}\right] - kf\,t \qquad eq.5$$

As the concentration of plasmid conformations is proportional to gel band intensity (I) it leads to:

$$\ln\left[1 - \frac{I\mathrm{Nd},t}{I\mathrm{P},0 - I\mathrm{Nm},0}\right] = \ln\left[1 - \frac{I\mathrm{Nd},0}{I\mathrm{P},0 - I\mathrm{Nm},0}\right] - kf\,t \qquad eq.6$$

As the experimental data fit the equation 6 (see Figure S7B) it confirms the proposed hypothesis validating the theoretical model presented.

Design of Multifunctional Gold Nanoparticles for *In Vitro* and *In Vivo* Gene Silencing

João Conde,[†,‡,¶] Alfredo Ambrosone,[§,¶] Vanesa Sanz,[†] Yulan Hernandez,[†] Valentina Marchesano,[§] Furong Tian,[⊥] Hannah Child,[∥] Catherine C. Berry,[∥] M. Ricardo Ibarra,[†] Pedro V. Baptista,[‡] Claudia Tortiglione,[§,*] and Jesus M. de la Fuente[†,*]

[†]Instituto de Nanociencia de Aragon, University of Zaragoza, C/Mariano Esquillor s/n Zaragoza, Spain, [‡]CIGMH, Departamento de Ciências da Vida, Faculdade de Ciências e Tecnologia, Universidade Nova de Lisboa, Campus de Caparica, 2829-516 Caparica, Portugal, [§]Istituto di Cibernetica "E. Caianiello", Consiglio Nazionale delle Ricerche (CNR), Via Campi Flegrei 34, Pozzuoli, Italy, [⊥]Comprehensive Pneumology Center, Institute of Lung Biology and Disease, Helmholtz Zentrum München, Munich, Germany, and [∥]Centre for Cell Engineering, University of Glasgow, Joseph Black Building, University Place, Glasgow, United Kingdom. [¶]These authors contributed equally to this work.

ABSTRACT Over the past decade, the capability of double-stranded RNAs to interfere with gene expression has driven new therapeutic approaches. Since small interfering RNA (siRNAs, 21 base pair double-stranded RNA) was shown to be able to elicit RNA interference (RNAi), efforts were directed toward the development of efficient delivery systems to preserve siRNA bioactivity throughout the delivery route, from the administration site to the target cell. Here we provide evidence of RNAi triggering, specifically silencing c-myc protooncogene, *via* the synthesis of a library of novel multifunctional gold nanoparticles (AuNPs). The efficiency of the AuNPs is demonstrated using a hierarchical approach including three biological systems of increasing complexity: *in vitro* cultured human cells, *in vivo* invertebrate (freshwater polyp, *Hydra*), and *in vivo* vertebrate (mouse) models. Our synthetic methodology involved fine-tuning of multiple structural and functional moieties. Selection of the most active functionalities was assisted step-by-step through functional testing that adopted this hierarchical strategy. Merging these chemical and biological approaches led to a safe, nonpathogenic, self-tracking, and universally valid nanocarrier that could be exploited for therapeutic RNAi.

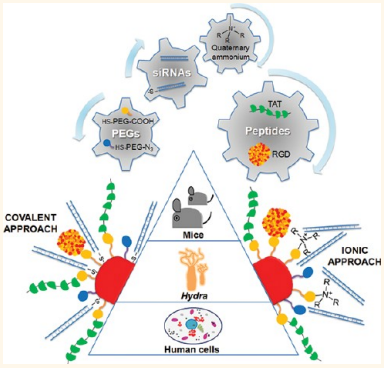

KEYWORDS: gold nanoparticles · RNA interference · animal models · biofunctionalization · c-myc · cancer

Nanoparticles exhibit excellent physicochemical properties for application in drug delivery, namely, their reduced sizes, rendering them capable of interacting with biomolecules in a one-to-one scale, and the high surface-to-volume ratio allowing for surface functionalization with a plethora of molecules for specific targeting and drug payloads.[1,2] Among the numerous nanoparticle formulations designed to improve siRNA[3,4] delivery and efficiency, those based on gold nanoparticles (AuNPs) have been extensively investigated without undesirable immune response or off-target effects.[5−15] To our knowledge, with the exception of one report on AuNPs for systemic administration of siRNA in humans,[16] over the last 6 years, formulations using AuNP-siRNA have solely been tested in cell cultures targeting reporter genes, such as luciferase or green fluorescence protein.[17] However, as with any drug treatment, gene therapy vehicles need extensive testing in archetypal animal models before translation into the clinics, and this requires the coordinated effort of interdisciplinary research groups.[18]

Here we used a functional comparative approach to assist the smart design, synthesis, and testing of a library of multifunctional nanodevices for RNAi, resulting in a nanocarrier based on AuNPs as the delivery system, with demonstrated functionality both *in vitro* and *in vivo* for RNAi-based therapy. Several biochemical moieties, cell penetrating and cell adhesion peptides were selected to enhance cellular recognition and uptake and confer specific downregulation of gene expression. The c-myc protooncogene, a key gene playing a pivotal role in cell cycle and tissue homeostasis,[19] was selected as RNAi target; poly(ethylene glycol) (PEG) molecules were incorporated to guarantee nanoparticle stability and avoid unspecific interactions, and three *in vitro*/*in vivo* model systems were selected: human cells (HeLa), freshwater polyps (*Hydra vulgaris*), and

* Address correspondence to c.tortiglione@cib.na.cnr.it, jmfuente@unizar.es.

Received for review July 6, 2012 and accepted August 12, 2012.

Published online August 12, 2012
10.1021/nn3030223

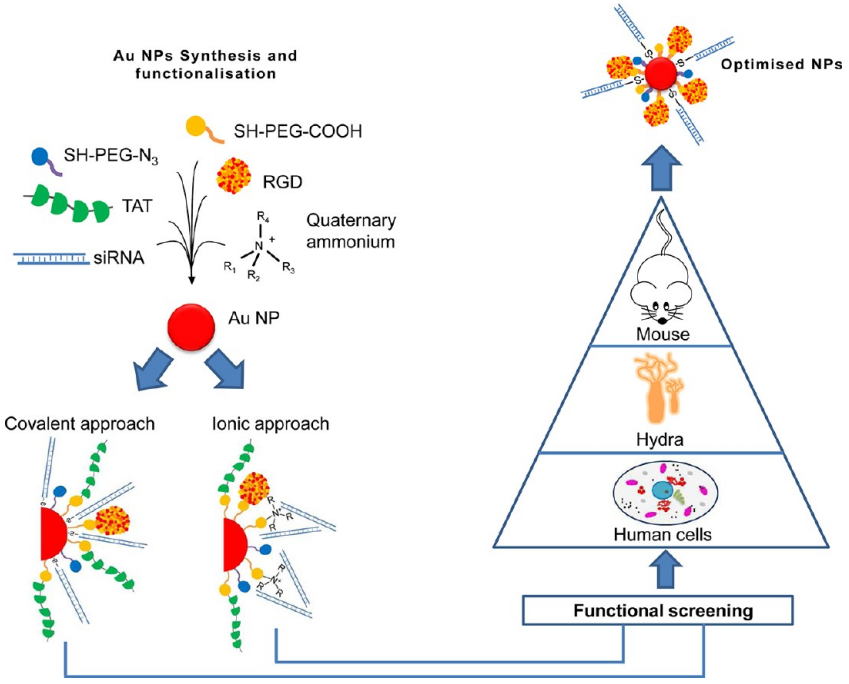

Figure 1. *In vivo* **gene silencing through nanoparticle-mediated RNAi. The nanocarrier is a AuNP functionalized with multiple biomolecules: PEG, cell penetration and cell adhesion peptides, and siRNA. Two different approaches were employed to conjugate the siRNA to the AuNP: (1) covalent approach, use of thiolated siRNA for gold−thiol binding to the nanoparticle; (2) ionic approach, interaction of the negatively charged siRNA to the modified surface of the AuNP through ionic interactions. A hierarchical scheme employed three biological systems of increasing complexity: cultured cells (HeLa), freshwater polyp (Hydra vulgaris), and mouse (C57BL/6j) to screen the synthesized nanocarrier library and select the ideal engineered AuNP for the delivery of siRNA to block gene function.**

mouse (C57BL/6j) (Figure 1). This chemical and biological strategy allowed us to compare the effect of the siRNA linkage to the NPs and the effect of cell penetration and adhesion peptides, finally leading to an optimally designed nanocarrier for RNAi therapeutic purposes.

RESULTS AND DISCUSSION

Stable AuNPs with an average diameter of 14 ± 1 nm were synthesized by reduction of sodium tetrachloroaurate(III) hydrate with sodium citrate dehydrate (Figure S1 of Supporting Information). To increase the stability, biocompatibility, and grant chemical functionality, AuNPs were functionalized with two types of thiolated poly(ethylene glycol) (PEG) spacers: a commercial carboxylated spacer, SH-EG(8)-$(CH_2)_2$-COOH, and an azide-containing spacer custom synthesized in our lab, SH-$(CH_2)_3$-CONH-EG(6)-$(CH_2)_2$-N_3. The carboxylated spacer provides the anchoring moieties for the covalent binding of amine-containing molecules through carbodiimide chemistry, while the azide-containing spacer confers positive *Z*-potential values, which is a crucial factor for cell uptake. Combined functionalization of the AuNPs with both spacers was finely tuned by controlling both specific spacer composition and degree of saturation (Figure S2). In order to elucidate the most efficient strategy to bond siRNA to AuNPs, two types of AuNPs stabilized by different degrees of PEG saturation were selected: (i) NP-ion with 100% coverage (25% azide-containing spacer and 75% carboxylated spacer); (ii) NP-cov with 25% coverage (50% of either spacer). These AuNP formulations represented the basic nanoparticles for downstream functionalization with c-myc siRNA, using either ionic interaction (ION) or covalent binding (COV). Both were initially tested for biocompatibility and toxicity in two human cancer cell lines (MCF-7 and HeLa). Cell survival rates following AuNP exposure were determined *via* MTT, with no cytotoxicity detected up to 48 h of incubation with either NP-ion or NP-cov (Figure S5). Further functionalization of these nontoxic AuNPs with c-myc siRNA and the HIV-derived TAT peptide was performed.[20] In the ION method, quaternary ammonium groups (R_4N^+) were bound to AuNPs through carbodiimide chemistry between the carboxylated spacer and (2-aminoethyl)trimethylammonium hydrochloride. Ionic interactions between the negatively charged siRNA backbone and both the azide and quaternary ammonium positively charged groups ensured binding of siRNA onto the NP surface for the whole pH range. In the COV method, thiolated siRNA was bound *via* a thiol bond to AuNPs with a nonsaturated PEG layer. The TAT peptide was bound to NP-ion and NP-cov by EDC/NHS coupling between the carboxylated spacer and the amine terminal group of the KKKGRKKRRQRRR (KKK-TAT) peptide. The binding efficiency of each functional group was determined by Bradford assay, alongside detailed

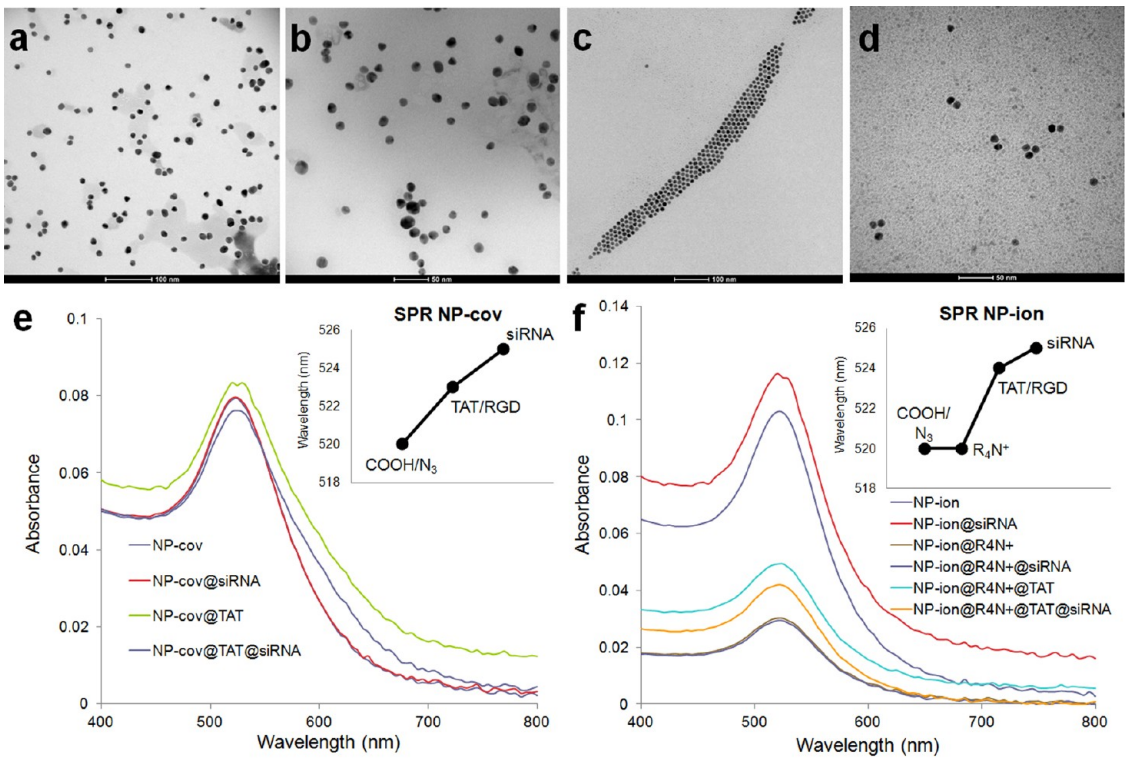

g AuNP conjugates	PEG chains/NP	TAT peptides/NP	RGD peptides/NP	siRNA strands/NP	Zeta Potential (mV)
NP-cov	1250.5±279.8	–	–	–	-38.3±3.5
NP-cov@siRNA	1250.5±279.8	–	–	41.3±0.8	-25.5±1.2
NP-cov@TAT@siRNA	1250.5±279.8	22.5±1.2	–	46.5±0.9	-39.1±0.7
NP-cov@TAT	1250.5±279.8	22.5±1.2	–	–	-26.1±0.9
NP-cov@RGD@siRNA	1250.5±279.8	–	20.6±0.7	62.9±0.8	-32.3±2.1
NP-ion	4783.8±349	–	–	–	-21.2±0.7
NP-ion@siRNA	4783.8±349	–	–	107.1±2.0	-14.5±0.9
NP-ion@R_4N^+@siRNA	4783.8±349	–	–	78.5±1.1	-7.7±1.0
NP-ion@R_4N^+	4783.8±349	–	–	–	4.3±1.1
NP-ion@ R_4N^+@TAT	4783.8±349	38.5±1.4	–	–	18.3±0.6
NP-ion@R_4N^+@TAT@siRNA	4783.8±349	38.5±1.4	–	76.1±2.1	-25.1±2.7
NP-ion@R_4N^+@RGD@siRNA	4783.8±349	–	12.7±1.1	45.6±1.4	-26.8±1.5

Figure 2. Physicochemical characterization of AuNPs. TEM analysis of (a) NP-cov@myc-siRNA, (b) NP-cov@TAT@myc-siRNA, (c) NP-ion@R_4N^+@myc-siRNA, (d) NP-ion@R_4N^+@TAT@myc-siRNA. The stabilization effect of the different functional groups on the multifunctional AuNPs can be observed *via* examination of the optical properties by UV−vis spectroscopy (e,f): absorption band of the resulting AuNPs appeared at ±520 nm due to the surface plasmon resonance (SPR) of the AuNPs. The spatial arrangement of AuNP can be inferred by measuring the shift of a characteristic SPR band dependent from size, shape, aggregation state, and medium polarity. The SPR of the AuNPs shown in e and f insets exhibited a red shift from 520 to 525 nm: a 3 nm shift for TAT/RGD peptides binding and a 5 nm shift for siRNA binding indicating successful binding of several groups. (g) Quantification of the PEG chains, TAT and RGD peptides, and siRNA strands is shown for all bioconjugates, together with the *Z*-potential measurements.

AuNP assay characterization (Supporting Information). All AuNP bioconjugates presenting at the surface siRNA and/or TAT/RGD and/or quaternary ammonium groups (R_4N^+) in various combinations were characterized by transmission electron microscopy (TEM), UV/vis spectroscopy, surface plasmon resonance (SPR) shift, and zeta-potential (see Figure 2). To determine cell uptake and intracellular fate, HeLa cells were incubated with the functionalized AuNPs for 18 h and processed for TEM analysis. Results show that both NP-ion and NP-cov conjugates were found isolated or as small aggregates in the cytoplasm (Figure 3b,c).

To permit rapid screening of the large variety of functionalized AuNPs in terms of c-myc RNAi, the c-myc gene sequence was cloned into a psiCHECK-2 vector downstream of the Renilla luciferase reporter (Figure S4). This construct was stably expressed in HeLa cells, and the decrease in luciferase activity, as consequence of RNAi, was quantified by a luminescence assay. Figure 3d shows normalized luciferase activity of each AuNP conjugate, where both synthetic approaches used to bind siRNA onto the AuNP (ION *versus* COV) show comparable silencing efficiency, matching that attained *via* the transfection of naked siRNA with lipofectamine. Control experiments utilized

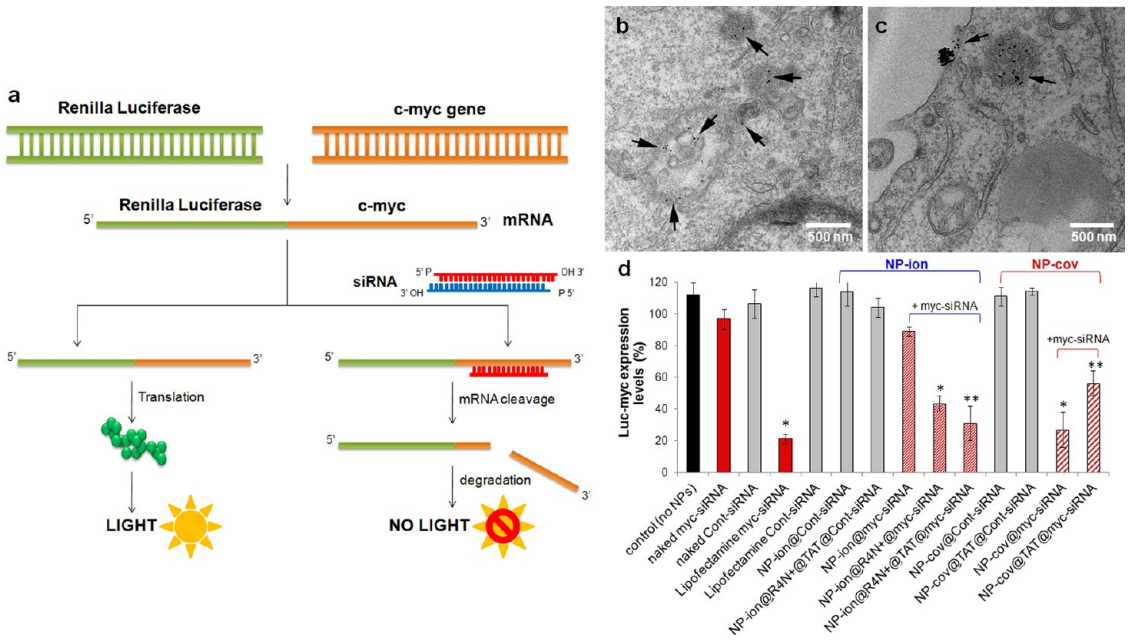

Figure 3. Internalization and efficiency of c-myc RNAi induced by functionalized AuNP in HeLa cells. (a) Renilla luciferase was used as the primary reporter gene, and the c-myc gene was cloned into a multiple cloning region located downstream of the Renilla gene. Initiation of the RNAi process by synthetic myc-siRNAs results in cleavage and subsequent degradation of the fusion mRNA. Measuring decreases in Renilla activity provides a convenient way of monitoring the RNAi effect. This vector also contains a second reporter gene, Firefly luciferase, which functions as an internal control for reporter gene activity (scheme adapted from Promega psiCHECK vectors). (b,c) TEM images of cells treated with NP-cov@myc-siRNA (b) and NP-ion@myc-siRNA (c) show NPs present in the cytoplasm as single units, supporting the correct delivery of siRNA to initiate RNAi. (d) Quantitative assessment of RNAi efficiency. HeLa cells were transfected with the recombinant vector psiCHECK-2, encoding for the fusion protein Renilla luciferase-myc. Decrease of Renilla luciferase activity induced by c-myc-siRNA was expressed as percentage of normal luciferase activity. Unrelated siRNA (cont-siRNA) bound on the AuNPs; naked or lipofectamine delivered siRNA were included as negative and positive RNAi controls, respectively. Data marked with asterisks are statistically significant relative to the corresponding NP-ion/cov with control siRNA as calculated by paired Sample *t* test (, $P \leq 0.0001$; *, $P \leq 0.001$).**

a nonrelated siRNA (cont-siRNA) that does not induce downregulation of luciferase or c-myc. These results clearly show the effective capability of the functionalized AuNPs to specifically and selectively silence c-myc gene expression. With regard to NP-ion design, Figure 3d depicts the importance of including R_4N^+ moiety to introduce ionic interactions between the positively charged NPs and the negatively charged siRNA. Absence of R_4N^+ did not induce any silencing, suggesting a possible proton-sponge effect played by the carboxylic and quaternary ammonium groups, which could be responsible for endosome rupture and release of the trapped materials (siRNA) into the cytoplasm.[21] Also, addition of the TAT peptide branched on NP-ion@R_4N^+@myc-siRNA showed negligible effects when compared to the same NP without TAT, probably due to steric hindrance of siRNA. Concerning the NP-cov@myc-siRNA, their efficiency in achieving RNAi might result from increased stability of the siRNA covalently bound to the gold core compared to their stability when adsorbed by electrostatic interaction on the NP surface. However, the possibility that the strong efficiency of this adduct might depend on cytoplasmic release of the siRNA (due to the reducing environment of the cytoplasm acting on the thiol bonds) and prompt availability to trigger the RNAi machinery cannot be excluded. When branched on NP-cov@myc-siRNA, the TAT peptide again decreased the RNAi efficiency from 73 ± 11 to 43 ± 7%. These data support the hypothesis that the TAT peptide may act as a suppressor of the RNAi response, as previously reported,[22] which might be related to the fact that this virally derived peptide has evolved to naturally bypass cell defense mechanisms. In summary, despite the low AuNP concentration used (2.1 nM AuNPs, 2 pM siRNA), following confirmed cell uptake *via* TEM (Figure 3b,c), it was able to trigger a very efficient RNAi, likely due to the amplification of the siRNA signal *in vivo*, as elsewhere reported.[23]

Prior to testing the efficiency of the multifunctional nanocarrier for c-myc RNAi on an archetypal animal model, we used a simpler and more singular invertebrate model, *Hydra vulgaris* (Cnidaria, Hydrozoa), to allow for further fine-tuning of the nanocarrier. Thus, following successful silencing in the cell model, the efficiency of both NP-ion and NP-cov were evaluated in the *Hydra in vivo* model. The increase in complexity of the animal model, in fact, could enable us to select the more appropriate nanocarrier to test in mouse. *Hydra* is a freshwater polyp whose structural anatomy reflects a tissue grade of organization (body composed of two cell layers; absence of either proper organs, or central

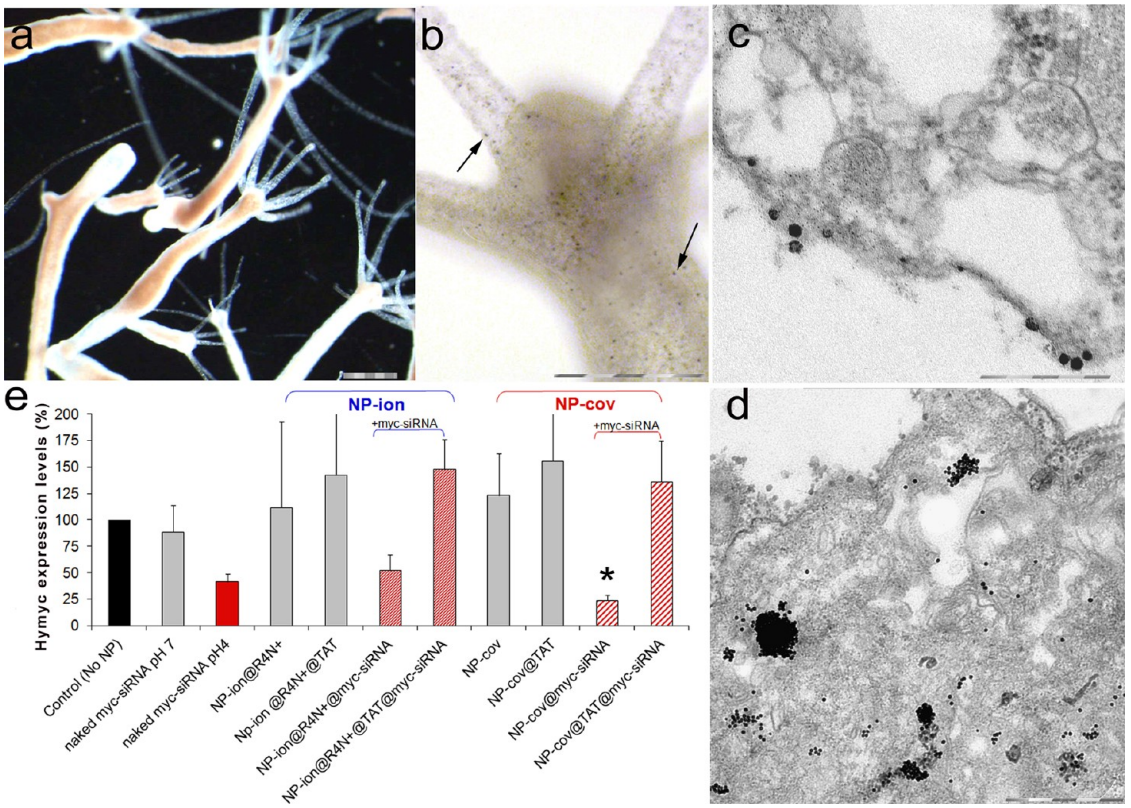

Figure 4. Hymyc RNAi in Hydra vulgaris. (a) Representative images of living polyps of Hydra vulgaris (scale bar 0.5 mm). (b) Bright-field image of Hydra treated 24 h with NP-cov@myc-siRNA (scale bar 200 μm). Nanoparticles appear as dark spots on the Hydra ectodermal cells. Same uptake was observed for NP-ion@myc-siRNA (Supporting Information Figure S3). (c,d) TEM images of Hydra tissues, prepared from polyps treated with 15 nM of NP-cov@myc-siRNA for 30 min (c) and 24 h (d). NPs are detected as single unit or small clusters into the cytoplasm for correct delivery of siRNA. Scale bar: 0.2 μm (c) and 0.5 μm (d). (e) Molecular assessment of RNAi efficiency by qRT-PCR using 15 nM AuNPs and 25 polyps in 100 μL of Hydra medium. Hymyc relative expression upon incubation with NP-ion and NP-cov was compared to naked siRNA. Relative gene expression changes from NPs not carrying c-myc siRNA are shown as gray bars, while those induced by Hymyc siRNA functionalized NPs are colored red. Data are means of three independent experiments from three biological replicates; error bars show standard deviation. Data marked with asterisk are statistically significant relative to the corresponding NP-ion/cov without siRNA as calculated by paired sample *t* test (*, $P \leq 0.005$).

nervous system), but exhibiting behavior and physiology proper of animals (Figure 4a and Figure S6 of Supporting Information). Reliable methods have been developed for a comprehensive analysis of nanoparticle impact in *Hydra*, spanning from *in vivo* analysis induced by nanoparticle treatments (structural morphological changes, impact on reproductive rate, efficiency of regeneration) to *in vitro* approaches of cell biology, microscopy, and molecular biology to investigate the internalization routes and the genotoxic effects.[24,25]

Moreover, the *Hydra c-myc* (Hymyc) homologue gene function has been recently identified,[26,27] allowing to functionally test the RNAi efficiency. NP-ion and NP-cov were initially tested for biocompatibility and toxicity by measuring the impact on population growth rate,[25] showing the absence of toxic effects (Figure S7). Optical microscopy showed that both NP-ion and NP-cov were internalized at low rate by ectodermal cells, facing the animal outer plane (Figure 4b and Figure S3), and TEM analysis was necessary for subcellular localization of AuNPs. In Figure 4c, TEM images on thin sections from animals incubated 30 min with NP-cov@myc-siRNA show nanoparticles bound to the membrane glycocalix, as single units or small clusters passing through the bilayer structure of the cell membrane. After 24 h of incubation, AuNPs were found in the cytoplasm, clustered or monodispersed, demonstrating their capability to cross biological membranes and shuttle siRNA into the cytoplasm (Figure 4d). Hymyc silencing efficiency was assessed using the AuNPs recommended following HeLa silencing (NP-ion@R_4N^+@myc-siRNA, NP-ion@R_4N^+@TAT@myc-siRNA, NP-cov@TAT@myc-siRNA, NP-cov@myc-siRNA). The qRT-PCR results in *Hydra* further restricted the selection of bioactive AuNP conjugates previously identified in HeLa cells: only two of those nanoparticles induced Hymyc gene silencing, NP-ion@R_4N^+@myc-siRNA and NP-cov@myc-siRNA, which rise up to 80% of gene downregulation in the case of the covalent conjugate (Figure 4e). TAT peptide (initially employed to enhance the cell permeability), but causing a decrease in the RNAi efficiency of the NP-cov conjugates in HeLa cells, completely inhibited

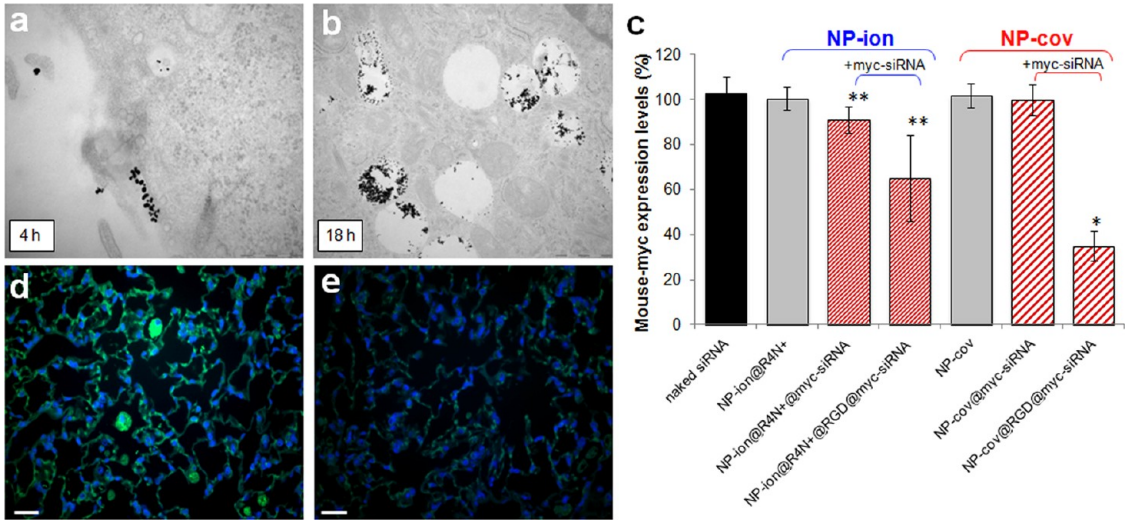

Figure 5. c-myc RNAi in mouse. (a,b) TEM images of lung epithelial cells. Mice (C57BL/6j strain) were treated with 16 nM of NP-cov@RGD@myc-siRNA by intratracheal instillation. At 4 h (a) after instillation, NPs are located in ruffles of lung epithelial cell membranes and a few NPs are in the vesicles. At 18 h (b), huge amounts of NPs are found in vesicles or free in cytoplasm (scale bars 500 nm). (c) Molecular assessment of RNAi efficiency. To quantify efficiency of silencing, total RNAs from lung tissue (four mice treated with each NP type) were extracted after 48 h and analyzed by qRT-PCR. The c-myc expression levels were determined using β-actin as reference gene. Data marked with asterisks are statistically significant relative to the corresponding NP-ion/cov without siRNA as calculated by paired sample *t* test (*, $P \leq 0.001$; **, $P \leq 0.01$). (d,e) c-myc protein expression on alveolar epithelial cells in lung tissue after 48 h treatment. (d) Mice instillated with 16 nM NP-cov@RGD, (e) mice instillated with 16 nM NP-cov@RGD@myc-siRNA. The c-myc protein was detected by Alexa-488-conjugated anti-c-myc antibody (green), and cell nuclei were DAPI stained (blue). Scale bars 200 μm.

the RNAi process in *Hydra*, further suggesting that TAT RNAi suppressor activity may be conserved throughout the animal kingdom.[22] Those AuNPs unable to induce gene silencing in cells were also ineffective in *Hydra*, confirmed by analysis of gene expression (Figure 4e).

Finally, the two AuNPs identified as inducing c-myc silencing in both HeLa and *Hydra*, NP-ion@R_4N^+@myc-siRNA and NP-cov@myc-siRNA, were tested in the more complex *in vivo* mouse model. Both AuNPs were administered to 10−12 week aged female mice (n = 6−8 animals) by intratracheal instillation. While intravenous administration is the most popular choice in clinical studies, an oral route inhalation or intratracheal instillation mode, together with intranasal drug delivery, convection-enhanced diffusion, and intrathecal/intraventricular drug delivery systems has been gaining considerable attention. Intratracheal instillation of nanoparticles becomes an important criterion of consideration to overcome the physiological barriers of the lung and to achieve locally high drug concentrations for pulmonary diseases. In our case, the choice was also dictated by the siRNA loaded on the AuNP, targeting the c-myc gene. As this oncogene is deregulated in lung cancer, in a future study of lung cancer treatment, this administration mode might allow proper deliver of therapeutic siRNA to the target organ. After 7 days from instillation, mice were dissected for bronchoalveolar lavage (BAL cells) and lung tissue extraction. In general, NPs of size <100 nm and different zeta-potential display toxic effects, due to trade-off between drug potency and immunologic surveillance.[28,29] In fact, the influence of size, solubility, and surface modification on the biocompatibility of nanoparticles and their use in biological applications is well-known. NPs have a proclivity *in vivo* and *in vitro* to bioaccumulate within various types of cells with a special affinity for macrophage-type cells and reticuloendothelial cells throughout the body. In order to select safe material for drug delivery, toxicity studies of both NP-cov and NP-ion sets were performed in mice following 1, 3, and 14 days of treatment by the evaluation of the number of macrophages, neutrophils, and lymphocytes, in which an increase indicates an inflammation process. Results showed negligible adverse effects using a low instillation dose (16 nM) (Supporting Information, Figure S8). However, the qRT-PCR performed on four lung samples of each groups, instilled with this dose of NPs, showed very low gene downregulation (Figure 5c), probably due to a lack of NPs' selectivity to the target cells. The functional studies performed in *in vitro* cell culture and in living *Hydra* provided feedback for improving the design and synthesis of AuNPs@siRNA targeting mouse. To this aim, the cell adhesion peptide RGD was incorporated on the AuNP to reinforce cell−NP interaction and drive lung-specific uptake. RGD integrin ligand is well-known for its capability to bind to the integrin $\alpha_v\beta_3$ receptor family,[30] involved in a wide range of cell−extracellular matrix and cell−cell interactions. Previous studies have demonstrated RGD efficiency to promote NP−cell adhesion events.[31] RGD-containing peptides were conjugated to both NP-ion and NP-cov,

in the presence or absence of c-myc siRNA, by EDC/NHS coupling between the carboxylated spacer and the primary amine in the RGD peptide (Supporting Information). Mice were treated as previously indicated. TEM analysis on lung epithelial cells revealed the efficient uptake of NPs conjugated with RGD with sufficient cytoplasmic availability (Figure 5a,b) to initiate RNAi. The qRT-PCR results showed a 65.2 ± 6.7% c-myc downregulation induced by NP-cov@RGD@myc-siRNA and 34.9 ± 19% c-myc silencing by NP-ion@R_4N^+@RGD@myc-siRNA. These results confirm the specificity of the RNAi approach. Immunolocalization of the MYC protein on alveolar epithelial cells in lung tissue from mice treated with NP-cov@RGD@myc-siRNA confirmed decreased MYC protein accumulation in lung tissue, unequivocally demonstrating the bioactivity of the multifunctional NP (Figure 5d,e).

Remarkably, the same NP-cov@siRNA adduct was shown to elicit highest RNAi in HeLa cells, *Hydra vulgaris*, and mouse, with the only exception of the RGD presence when testing on mouse, as it is not expressed in *Hydra*. From an evolutionary point of view, having found that gene silencing in this primitive animal is accomplished by the same nanocarrier working on human cell cultures and mouse, underlines not only the conservation of key molecular pathways throughout animal evolution but also the conservation of the basic chemicophysical interactions between nanoparticle and the living world, *Hydra* bridging the gap between cell cultures and complex models.

CONCLUSION

In this study, we show that two balanced formulations (ionic and covalent approaches), in terms of stability/electrostatic interactions, designed to produce smart multifunctional nanostructures succeeded to generate new innovative and versatile tools for efficient RNA interference in eukaryotic systems. Using three biological models of increasing complexity (cultured cells, invertebrate, and mammal), both design and validation of multifunctional nanocarriers capable of selectively and specifically delivering siRNA *in vivo* were demonstrated. This functional screening approach allowed us to finely tune concentrations, bonding, and the combination of different chemical groups on the nanoparticle surface, addressing current ethical issues on unnecessary, cost-effective, and time-consuming vertebrate testing. These multifunctional nanocarriers are robust enough to preserve stability without showing acute toxicity or cell viability impairment while simultaneously able to bypass biological barriers to perform RNAi activity without off-target effects. Our universal nanocarrier represents a valid gene delivery platform that can be exploited for clinical application in the near future. While treatment of a lung cancer mouse model might represent the first therapeutic test of the nanocarrier developed here, the simple change of the siRNA sequence might target the same device to a huge range of diseases, strengthening the way to clinical application of RNAi.

METHODS

We divided the methods into similar parts for each system (except for the synthesis). Full description of methods can be found in Supporting Information.

Synthesis and Functionalization of Gold Nanoparticles. AuNPs with a diameter of 14 ± 1 nm were synthesized by the citrate reduction method described by Lee and Meisel.[32] A mixture of AuNPs, 0.028% SDS, and SH-EG(8)-$(CH_2)_2$-COOH (Iris-Biotech) and SH-$(CH_2)_3$-CONH-EG(6)-$(CH_2)_2$-N_3 in the adequate ratio for NP-ion and NP-cov was mixed under basic conditions for 16 h. PEGylated AuNPs were obtained after purification by centrifugation. Number of PEG molecules was carried out by Ellman's method. Further chemical functionalization with quaternary ammonium ((2-aminoethyl)trimethylammonium chloride hydrochloride), TAT, and RGD peptides was carried out by EDC (1-ethyl-3-(3-dimethylaminopropyl)carbodiimide) (Sigma) and sulfo-NHS (sulfo-hydroxysuccinimide) (Sigma) chemistry at pH 6.1 (25 mM MES). Quantification of TAT peptides was obtained by Bradford assay (CA). AuNP functionalization with siRNA (Thermo Scientific Dharmacon) was taking place using unmodified siRNA for NP-ion by mixing them with NP-ion@R_4N^+@TAT during 16 h at 4 °C. For NP-cov, thiolated siRNA was incubated with NP-cov@TAT containing 0.028% SDS and 0.1 M NaCl. Excess siRNA was removed by centrifugation at 4 °C. siRNA quantification was carried out by fluorescence measurement (Perkin-Elmer LS55) using a GelRed (Biotium) acid nucleic intercalator (see Supporting Information, Table 1, for siRNA sequences).

Hydra Culturing. *Hydra vulgaris* (strain Zurich, originally obtained by P. Tardent) were asexually cultured in Hydra medium (1 mM $CaCl_2$, 0.1 mM $NaHCO_3$, pH 7). The animals were kept at 18 ± 1 °C and fed three times per week with freshly hatched *Artemia salina* nauplii. *In vivo* imaging was accomplished at several magnifications by using both a stereomicroscope and an inverted microscope (Axiovert 100, Zeiss).

Transmission Electron Microscopy. To visualize the cellular uptake of NPs, HeLa cells were incubated with all NPs for 18 h. Mice were treated with NPs for 4 and 18 h. Mice were sacrificed and mice lungs fixed in 2.5% glutaraldehyde for TEM. For *Hydra*, polyps were treated with 2% urethane in Hydra medium and then fixed for 2 h in 2% glutaraldehyde in Hydra medium. Samples were postfixed in 1% buffered OsO_4 followed by 0.5% uranyl acetate for 1 h and then taken through alcohol dehydration increments and left in resin (propylene oxide Epon 812 resin mix (1:1) for cells and propylene oxide/Epon 12 resin mix (1:1) for *Hydra*) overnight. Cell layers were captured in pure resin and cured overnight in an oven. *Hydra* were incubated 2 × 2 h in Epon 12 resin. Blocks were then cut into ultrathin sections, stained with 2% methanolic uranyl acetate and Reynolds lead citrate, and viewed under a Leo 912 AB TEM (120 kV for cells and 80 kV for *Hydra*).

Toxicity. Cellular cytotoxicity was assessed by standard MTT assay (Invitrogen). *Hydra* growth rate was calculated to monitor NP toxicity, as previously described.[25] Toxicity in mice was assessed by enumeration of total differential cells in bronchoalveolar lavage cells. Several nanomaterials studied in the size range from *ca.* 5 to 20 nm (TiO_2, Fe, Cu, Ag) induced higher neutrophil recruitment in BAL fluid, compared to control.[33] Low amounts of neutrophiles and lymphocytes indicate minimal inflammatory response or toxicity.

Assessment of RNAi in HeLa Cells. c-myc RNAi was evaluated by using the psiCHECK Vector system (Promega), which allows one to monitor change in expression of a reporter gene (Luciferase) fused to a target gene. **MYC-Luciferase vector construction:** the whole human v-myc myelocytomatosis viral oncogene homologue (c-myc) gene was PCR amplified from cDNA retrotranscribed from HeLa cells total RNA (see Supporting Information) and the resulting product cloned in frame with Luciferase reporter gene contained into the vector psiCHECK-2, and maintained in *Escherichia coli* DH5α strains. **Cell culture:** HeLa cells were grown in Dulbecco's modified Eagle's medium (DMEM, Lonza) with 10% heat inactivated fetal bovine serum, 2 mM glutamine, 100 U/mL penicillin, and 100 μg/mL streptomycin and maintained at 37 °C in 5% CO_2. Cells were seeded at a density of 5×10^3 cells/well in 96-well plates and grown for 1 day prior to transfection of the MYC-Luciferase vector (0.125 μg per well) using Lipofectamine 2000 (Invitrogen) and Opti-MEM reduced serum medium (Invitrogen) according to the manufacturer's recommendations. RNAi efficiency of different NP conjugates (2.1 nM AuNPs, 2 nM siRNA) was tested by treating the cells for 48 h and by quantification of luciferase expression using a dual-luciferase reporter assay (Promega) assay according to the manufacturer's protocols. Data are average (±SD) of three experiments.

RNAi Experiments in Hydra. Groups of 10 animals, collected in plastic multiwells, were incubated in 100 μL of Hydra medium in the presence of AuNPs (15 nM), and the treatment was renewed after 24 h to account for possible siRNA degradation. At 48 h, animals were washed and processed for RNA extraction and qRT-PCR. Animals interfered by naked siRNA, nonfunctionalized NP, or untreated were used as controls. Briefly, total RNAs were purified using Trizol (Invitrogen), retrotranscribed using SuperScript II retrotranscriptase (Invitrogen), and used for qRT-PCR analysis (see Supporting Information for detailed methods and primers employed).

RNAi Experiments in Mouse. C57BL/6J mice were anesthetised by intraperitoneal injection of a mixture of Medetomidin (0.5 mg/kg body mass), Midazolam (5.0 mg/kg body mass), and Fentanyl (0.05 mg/kg body mass). The animals were then intubated by a nonsurgical technique. Using a cannula inserted 10 mm into the trachea, a suspension containing 16 nM AuNP in 50 μL of pyrogene-free distilled water was instilled, followed by 100 μL of air. After instillation, animals were antagonized by subcutaneous injection of a mixture of Atipamezol (2.5 mg/kg body mass), Flumazenil (0.5 mg/kg body mass), and Naloxon (1.2 mg/kg body mass) to guarantee their awakening and well-being. Animals were treated humanely and with regard for alleviation of suffering; experimental protocols were reviewed and approved by the Bavarian Animal Research Authority.

Preparation of BAL Cells/Fluid. BAL fluid was obtained by injecting and recovering of two 0.5 mL aliquots of PBS *via* a tracheal cannula. Cells in the lavage fluids were counted using a hemocytometer, and the differentials were determined by utilizing light microscopy to count 200 cells on cytospin preparations.

Molecular Analyses of Gene Expression in Mouse. Immunolocalization: Lung tissues were sliced and blocked by adding 1% BSA in PBS for 30 min. Mouse anti-c-myc (Molecular Probes) was added (dilution 1:1000) for 1 h, washed in PBS with agitation for 5 min three times, and incubated with goat anti-mouse IgG coupled with Alexa-488 (Molecular Probes) at 2 μg/mL for 30 min. Nuclei were DAPI stained before slide mounting with 50 μL of fluormount mounting medium. Total RNAs were extracted from mouse lungs, retrotranscribed, and analyzed by qRT-PCR (see Supporting Information for detailed methods and primers employed).

Conflict of Interest: The authors declare no competing financial interest.

Acknowledgment. Authors thank ERANET-NANOSCIERA NANOTRUCK project for financial support. We thank A. Tino, G. Estrada, V. Grazu, and P. del Pino for fruitful discussions. Authors thank I. Echaniz, S. Rivera, and G. Marino for technical support. J.M.F. thanks ARAID for financial support. P.V.B. thanks CIGMH. J.C. acknowledges FCT Grant SFRH/BD/62957/2009. A.A., V.M., and F.T. were granted by NANOTRUCK.

Supporting Information Available: Synthesis, physicochemical characterization, and functionalization of AuNPs; internalization of AuNP conjugates; evaluation of RNAi efficiency by functional reporter gene assay; evaluation of toxicity. This material is available free of charge *via* the Internet at http://pubs.acs.org.

REFERENCES AND NOTES

1. Sperling, R. A.; Parak, W. J. Surface Modification, Functionalization and Bioconjugation of Colloidal Inorganic Nanoparticles. *Philos. Trans. R. Soc, A* **2010**, *368*, 1333–1383.
2. Dreaden, E. C.; Alkilany, A. M.; Huang, X.; Murphy, C. J.; El-Sayed, M. A. The Golden Age: Gold Nanoparticles for Biomedicine. *Chem. Soc. Rev.* **2012**, *41*, 2740–2779.
3. Fire, A.; Xu, S.; Montgomery, M. K.; Kostas, S. A.; Driver, S. E.; Mello, C. C. Potent and Specific Genetic Interference by Double-Stranded RNA in *Caenorhabditis elegans*. *Nature* **1998**, *391*, 806–811.
4. Elbashir, S. M.; Harborth, J.; Lendeckel, W.; Yalcin, A.; Weber, K.; Tuschl, T. Duplexes of 21-Nucleotide RNAs Mediate RNA Interference in Cultured Mammalian Cells. *Nature* **2001**, *411*, 494–498.
5. Pecot, C. V.; Calin, G. A.; Coleman, R. L.; Lopez-Berestein, G.; Sood, A. K. RNA Interference in the Clinic: Challenges and Future Directions. *Nat. Rev. Cancer* **2011**, *11*, 59–67.
6. Shahzad, M. M.; Mangala, L. S.; Han, H. D.; Lu, C.; Bottsford-Miller, J.; Nishimura, M.; Mora, E. M.; Lee, J. W.; Stone, R. L.; Pecot, C. V.; *et al.* Targeted Delivery of Small Interfering RNA Using Reconstituted High-Density Lipoprotein Nanoparticles. *Neoplasia* **2011**, *13*, 309–319.
7. Giljohann, D. A.; Seferos, D. S.; Daniel, W. L.; Massich, M. D.; Patel, P. C.; Mirkin, C. A. Gold Nanoparticles for Biology and Medicine. *Angew. Chem., Int. Ed.* **2010**, *49*, 3280–3294.
8. Giljohann, D. A.; Seferos, D. S.; Prigodich, A. E.; Patel, P. C.; Mirkin, C. A. Gene Regulation with Polyvalent siRNA Nanoparticle Conjugates. *J. Am. Chem. Soc.* **2009**, *131*, 2072–2073.
9. Guo, S.; Huang, Y.; Jiang, Q.; Sun, Y.; Deng, L.; Liang, Z.; Du, Q.; Xing, J.; Zhao, Y.; Wang, P. C.; *et al.* Enhanced Gene Delivery and siRNA Silencing by Gold Nanoparticles Coated with Charge Reversal Polyelectrolyte. *ACS Nano* **2010**, *4*, 5505–5511.
10. Lee, Y.; Lee, S. H.; Kim, J. S.; Maruyama, A.; Chen, X.; Park, T. G. Controlled Synthesis of PEI-Coated Gold Nanoparticles Using Reductive Catechol Chemistry for siRNA Delivery. *J. Controlled Release* **2011**, *155*, 3–10.
11. Song, W. J.; Du, J. Z.; Sun, T. M.; Zhang, P. Z.; Wang, J. Gold Nanoparticles Capped with Polyethyleneimine for Enhanced siRNA Delivery. *Small* **2010**, *6*, 239–246.
12. Oishi, M.; Nakaogami, J.; Ishii, T.; Nagasaki, Y. Smart PEGylated Gold Nanoparticles for the Cytoplasmic Delivery of siRNA To Induce Enhanced Gene Silencing. *Chem. Lett.* **2006**, *35*, 1046–1047.
13. Moon, J. H.; Mendez, E.; Kim, Y.; Kaur, A. Conjugated Polymer Nanoparticles for Small Interfering RNA Delivery. *Chem. Commun.* **2011**, *47*, 8370–8372.
14. Lee, S. H.; Bae, K. H.; Kim, S. H.; Lee, K. R.; Park, T. G. Amine-Functionalized Gold Nanoparticles as Noncytotoxic and Efficient Intracellular siRNA Delivery Carriers. *Int. J. Pharm.* **2008**, *364*, 94–101.
15. Lee, J. S.; Green, J. J.; Love, K. T.; Sunshine, J.; Langer, R.; Anderson, D. G. Gold, Poly(β-amino ester) Nanoparticles for Small Interfering RNA Delivery. *Nano Lett.* **2009**, *9*, 2402–2406.
16. Davis, M. E.; Zuckerman, J. E.; Choi, C. H.; Seligson, D.; Tolcher, A.; Alabi, C. A.; Yen, Y.; Heidel, J. D.; Ribas, A. Evidence of RNAi in Humans from Systemically Administered siRNA *via* Targeted Nanoparticles. *Nature* **2010**, *464*, 1067–1070.
17. Lytton-Jean, A. K.; Langer, R.; Anderson, D. G. Five Years of siRNA Delivery: Spotlight on Gold Nanoparticles. *Small* **2011**, *7*, 1932–1937.
18. Lares, M. R.; Rossi, J. J.; Ouellet, D. L. RNAi and Small Interfering RNAs in Human Disease Therapeutic Applications. *Trends Biotechnol.* **2010**, *28*, 570–579.

19. Vita, M.; Henriksson, M. The Myc Oncoprotein as a Therapeutic Target for Human Cancer. *Semin. Cancer Biol.* **2006**, *16*, 318–330.
20. de la Fuente, J. M.; Berry, C. C. Tat Peptide as an Efficient Molecule To Translocate Gold Nanoparticles into the Cell Nucleus. *Bioconjugate Chem.* **2005**, *16*, 1176–1180.
21. Yezhelyev, M. V.; Qi, L.; O'Regan, R. M.; Nie, S.; Gao, X. Proton-Sponge Coated Quantum Dots for siRNA Delivery and Intracellular Imaging. *J. Am. Chem. Soc.* **2008**, *130*, 9006–9012.
22. Qian, S.; Zhong, X.; Yu, L.; Ding, B.; de Haan, P.; Boris-Lawrie, K. HIV-1 Tat RNA Silencing Suppressor Activity Is Conserved Across Kingdoms and Counteracts Translational Repression of HIV-1. *Proc. Natl. Acad. Sci. U.S.A.* **2009**, *106*, 605–610.
23. Sijen, T.; Fleenor, J.; Simmer, F.; Thijssen, K. L; Parrish, S.; Timmons, L.; Plasterk, R. H.; Fire, A. On the Role of RNA Amplification in dsRNA Triggered Gene Silencing. *Cell* **2001**, *107*, 465–476.
24. Tortiglione, C. An Ancient Model Organism to Test *In Vivo* Novel Functional Nanocrystals. In *Biomedical Engineering: From Theory to Application*: Fazel-Rezai, R., Ed.; InTech Publisher, 2011; pp 225−252.
25. Ambrosone, A.; Mattera, L.; Marchesano, V.; Quarta, A.; Susha, A. S.; Tino, A.; Rogach, A. L.; Tortiglione, C. Mechanisms Underlying Toxicity Induced by CdTe Quantum Dots Determined in an Invertebrate Model Organism. *Biomaterials* **2012**, *33*, 1991–2000.
26. Hartl, M.; Mitterstiller, A. M.; Valovka, T.; Breuker, K.; Hobmayer, B.; Bister, K. Stem Cell-Specific Activation of an Ancestral myc Protooncogene with Conserved Basic Functions in the Early Metazoan Hydra. *Proc. Natl. Acad. Sci. U.S.A.* **2010**, *107*, 4051–4056.
27. Ambrosone, A.; Marchesano, V.; Tino, A.; Hobmayer, B.; Tortiglione, C. Hymyc1 Downregulation Promotes Stem Cell Proliferation in *Hydra vulgaris*. *PLoS One* **2012**, *7*, e30660.
28. Semmler-Behnke, M.; Kreyling, W. G.; Lipka, J.; Fertsch, S.; Wenk, A.; Takenaka, S.; Schmid, G.; Brandau, W. Biodistribution of 1.4- and 18-nm Gold Particles in Rats. *Small* **2008**, *4*, 2108–2111.
29. Bhaskar, S.; Tian, F.; Stoeger, T.; Kreyling, W.; de la Fuente, J. M.; Grazú, V.; Borm, P.; Estrada, G.; Ntziachristos, V.; Razansky, D. Multifunctional Nanocarriers for Diagnostics, Drug Delivery and Targeted Treatment Across Blood-Brain Barrier: Perspectives on Tracking and Neuroimaging. *Part. Fibre Toxicol.* **2010**, *7*, 1–25.
30. Brooks, P. C.; Montgomery, A. M.; Rosenfeld, M.; Reisfeld, R. A.; Hu, T.; Klier, G.; Cheresh, D. A. Integrin $\alpha_v\beta_3$ Antagonists Promote Tumour Regression By Inducing Apoptosis of Angiogenic Blood Vessels. *Cell* **1994**, *79*, 1157–1164.
31. de la Fuente, J. M.; Berry, C. C.; Riehle, M. O.; Curtis, A. S. G. Nanoparticle Targeting at Cells. *Langmuir* **2006**, *22*, 3286–3293.
32. Lee, P. C.; Meisel, D. Adsorption and Surface-Enhanced Raman of Dyes on Silver and Gold Sols. *J. Phys. Chem.* **1982**, *86*, 3391–3395.
33. Adamcakova-Dodd, A.; Thorne, P. S.; Grassian, V. H. *In Vivo* Toxicity Studies of Metal and Metal Oxide Nanoparticles. In *Handbook of Systems Toxicology*; Cascinao, D. A., Sahu, S. C., Eds.; John Wiley & Sons, Ltd.: New York, 2011; pp 803−834.

SUPPORTING INFORMATION

Design of Multifunctional Gold Nanoparticles for *in vitro* and *in vivo* Gene Silencing

João Conde,[1,2]♯ Alfredo Ambrosone,[3]♯ Vanesa Sanz,[1] Yulan Hernandez,[1] Valentina Marchesano,[3] Furong Tian,[4] Hannah Child,[5] Catherine C. Berry,[5] M. Ricardo Ibarra,[1] Pedro V. Baptista,[2] Claudia Tortiglione,[3]* Jesus M. de la Fuente[1]*

[1] Instituto de Nanociencia de Aragon, University of Zaragoza. C/ Mariano Esquillor s/n Zaragoza, Spain
[2] CIGMH, Departamento de Ciências da Vida, Faculdade de Ciências e Tecnologia, Universidade Nova de Lisboa, Campus de Caparica, 2829-516 Caparica, Portugal.UNL
[3] Istituto di Cibernetica "E. Caianiello", Consiglio Nazionale delle Ricerche (CNR), Via Campi Flegrei 34, Pozzuoli, Italy.CNR
[4] Comprehensive Pneumology Center, Institute of Lung Biology and Disease, Helmholtz Zentrum München, Germany Munich.Munich
[5] Centre for Cell Engineering, University of Glasgow. Joseph Black Building, University Place, Glasgow UK.

♯ Both authors have contributed equally
* Corresponding authors: c.tortiglione@cib.na.cnr.it & jmfuente@unizar.es

This file includes additional information for the following sections:

S1: Synthesis, physicochemical characterisation and functionalisation of AuNPs

S2: Internalisation of AuNPs conjugates

S3: Evaluation of RNAi efficiency by functional reporter gene assay

S4: Evaluation of Toxicity

Additional Figures

Additional references

S1: Synthesis, physicochemical characterisation and functionalisation of AuNPs

Synthesis of citrate-gold nanoparticles

Gold nanoparticles with an average diameter of ~14 nm were synthesised by the citrate reduction method described by Lee and Meisel[1]. Briefly, hydrogen tetrachloroaureate (III) hydrate (Strem Chemicals) (0.2 g; 0.589 mmol) was solved in 500 ml of distilled water, heated and stirred under reflux. When the solution boils, sodium citrate dihydrate (0.57 g; 1.94 mmol) was added resulting in a red solution. The solution is kept under ebullition and protected from light for 30 min, whereby it is cooled down and kept protected from light.

Synthesis of PEG heterofunctional surfaces in citrate-gold nanoparticles

Two types of NPs with distinct surfaces were prepared 1) 100% saturated PEG layer (NP-ion) functionalised with 75% carboxylic groups (SH-EG(8)-$(CH_2)_2$-COOH) and 25% of azide groups (SH-$(CH_2)_3$-CONH-EG(6)-$(CH_2)_2$-N_3); 2) 25% saturated PEG layer (NP-cov) functionalised with 50% carboxylic groups (SH-EG(8)-$(CH_2)_2$-COOH) and 50% of azide groups (SH-$(CH_2)_3$-CONH-EG(6)-$(CH_2)_2$-N_3). This PEG saturation allows the incorporation of further thiolated components, such as the SH-siRNA.

Briefly, a mixture of 10 nM of the citrate-gold nanoparticles, 0.028 % SDS and 39 μM SH-EG(8)-$(CH_2)_2$-COOH (Iris-Biotech) and 13 μM SH-$(CH_2)_3$-CONH-EG(6)-$(CH_2)_2$-N_3 for NP-ion and 7 μM SH-EG(8)-$(CH_2)_2$-COOH (Iris-Biotech) and 7 μM SH-$(CH_2)_3$-CONH-EG(6)-$(CH_2)_2$-N_3 for NP-cov were prepared. NaOH was further added to a final concentration of 25 mM and the mixture was incubated for 16 hr at room temperature. The excess PEG chains were removed by centrifugation at 14.000 rpm for 30 min at 4°C and the supernatant was discarded. This washing process was repeated three times and the pellet with AuNPs was dissolved in pure water.

AuNP functionalisation with TAT peptides and Quaternary Ammonium groups by EDC/NHS coupling reactions

For NP-ion AuNPs 26 nM were incubated in 13 mM sulfo-NHS and 50 mM MES (2-(N-morpholino)ethanesulfonic acid) buffer pH 6.1. Then, 38 mM of (2-aminoethyl)trimethylammonium chloride hydrochloride (R_4N^+) were added to the mixture, EDC (1-Ethyl-3-(3-dimethylaminopropyl)-carbodiimide) was added at a final concentration of 3 mM and the mixture incubated for 20 min. TAT peptide (H-KKK-GRKKRRQRRR-OH) was added at a final concentration of 1 μM. For NP-cov AuNPs 20 nM were incubated

in 6 mM sulfo-NHS and 25 mM MES buffer pH 6.1. Then TAT peptide was added to a final concentration of 0.5 μM followed by 0.8 mM of EDC. In both approaches, the mixture was incubated at room temperature for 16 hr, at which point the AuNP were centrifuged at 14000 rpm for 30 min at 4ºC to remove excess TAT peptide and the supernatants were recovered and tested for protein concentration by the Bradford assay (BioRad, CA).

AuNP functionalisation with RGD peptides.

The Arginine-Glycine-Aspartic Acid (G-RGD-S)-Peptide (Sigma, MW 490.47 Da) functionalisation was done in the same step as for the TAT and R_4N^+. Briefly, all the reagents were used in the same conditions previously described and the RGD was added at a final concentration of 0.5 μM for NP-cov and 2 μM for NP-ion. The mixture was incubated at room temperature for 16 hr. Then the AuNPs were centrifuged at 14000 rpm for 30 min at 4ºC to remove excess RGD peptide and the supernatants were recovered and tested for protein concentration using a BCA Protein Assay Kit (Thermo Scientific).

Characterisation of citrate-gold nanoparticles

AuNPs were characterised by different techniques (Figure S1). The high monodispersity of the gold core was confirmed by Transmission Electron Microscopy (TEM, T20 200KeV; FEI) showing an average size of 14 nm. Infrared spectra (FTIR, JASCO FT/IR 4100) confirmed the presence of the citrate groups covering the gold cores. The UV-Vis molecular absorption spectra of the AuNPs show the characteristic surface plasmon resonant peak at 519 nm. They present at pH 7 with a negative Z-potential value of -12.32 mV.

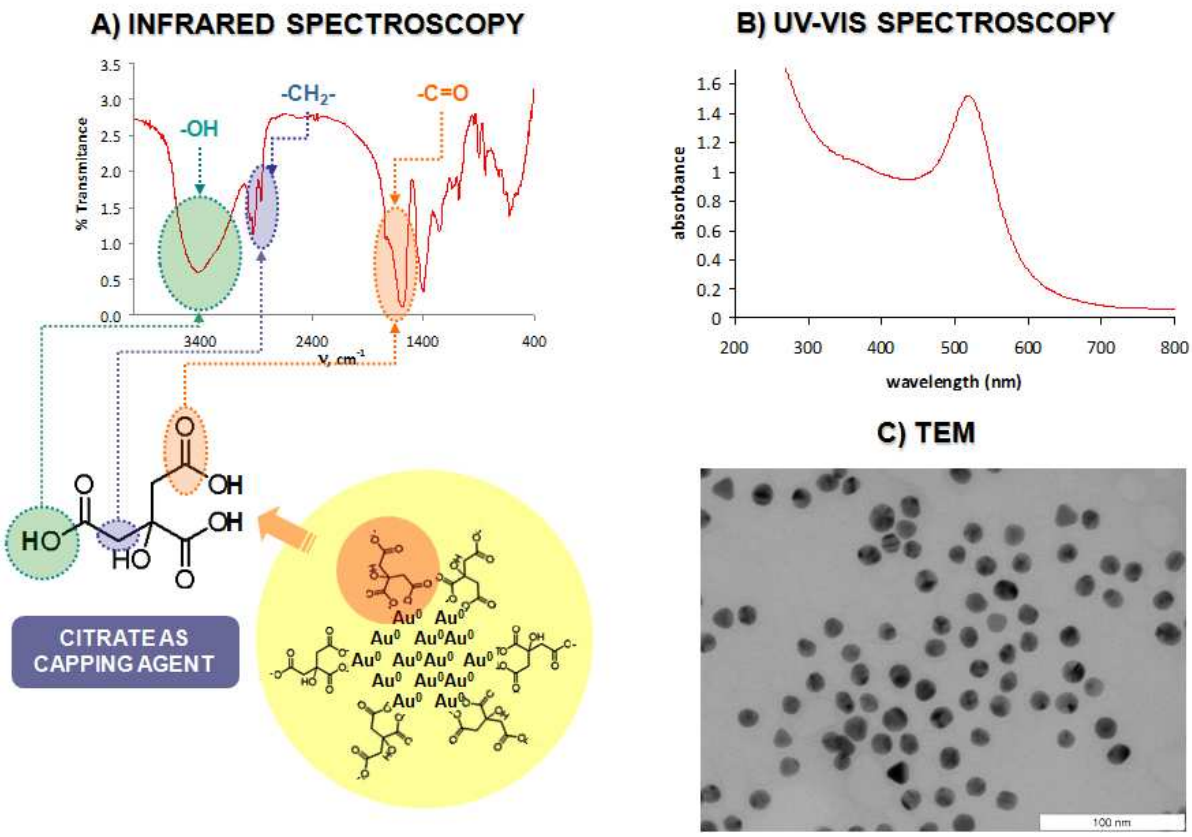

Figure S1. Characterisation of citrate-AuNPs **A)** Infrared spectra, peaks appear at 3422.06 cm^{-1}, 2957.30 cm^{-1}, 2925.48 cm^{-1}, 2854.13 cm^{-1}, 1584.23 cm^{-1}, 1400.07 cm^{-1}, 1253.50 cm^{-1}, 1080.90 cm^{-1}; **B)** UV-Vis molecular absorption spectra (Absorbance peak at 520 nm) **C)** Transmission Electron Microscopy, scale bar 100 nm.

Synthesis of N-(20-azido-3,6,9,12,15,18-hexaoxoicosane)-4-mercaptobutanamide ($HS-(CH_2)_3-CONH-EG(6)-(CH_2)_2-N_3$)

For the synthesis, 0.6 mmoles of α-Amine-ω-azido hepta(ethylene glycol) were added to 12.5 mL of dimethylsulfoxide under argon atmosphere in a poly(ethylene glycol) bath at 50°C and under continuous stirring. Subsequently, 0.63 mmol of γ-tiobutirolactone and 5.7 mmol of triethylamine were added. After 5 hr, the mixture was cooled down and lyophilised obtaining a yellow oil. The yield of the reaction was 93%, without any further purification step. The product was characterised by: FT-IR: 3301 cm^{-1} (NH st), 2870 cm^{-1} (-CH st), 2530 cm^{-1} (SH st), 2106 cm^{-1} (N_3 st), 1663 cm^{-1} (C=O st); ^{1}H-RMN 300 MHz (δ): 2,00 (m, 2H);

2,25 (t, 2H, *J*=7,30 Hz); 2,65 (t, 2H, *J*=7,00 Hz); 3,01 (s, 1H, SH); 3,32 (t, 4H, *J* = 5,00 Hz); 3,37 (t, 2H, *J* = 5,22 Hz); 3,59 (s, 22H); 6,60 (t, 1H, *J* = 4,76 Hz) and mass spectroscopy [M-H^+] 451.1.

Quantification of SH-EG(8)-$(CH_2)_2$-COOH bound to AuNPs

To estimate the degree of saturation of AuNPs functionalised with thiolated PEG chains (SH-EG(8)-$(CH_2)_2$-COOH) we developed and optimised a procedure based on the Ellman's assay. In this assay, the supernatant, containing the spacer with thiol groups on its structure, reacts with 5,5'-dithio-bis(2-nitrobenzoic) acid (DTNB) to give a coloured product that can be measured by spectrometry. With this procedure it is possible to determine the number of thiolated chains that have bound to the AuNP. After the incubation of the AuNP with the thiolated chains, the suspension was centrifuged at 14000 rpm for 30 min at 4°C and the supernatant retained for quantification assay: 400 µL of either the stock solution of PEG-COOH or the supernatant are mixed with 100 µL of TRIS buffer 1M pH 8 and 50 µL of DTNB 2 mM in sodium acetate (NaAc) buffer 50 mM. After 10 min of incubation the absorbance at 412 nm is measured. The linear range for the PEG-COOH chain obtained by this method is 1-100 µM (Abs_{412} = 0.006·[PEG-COOH, µM] + 0.1764)). The number of exchanged chains is given by the difference between the amount determined by this assay and the initial amount of chains in the incubation mixture with the NPs.

Quantification of SH-$(CH_2)_3$-CONH-EG(6)-$(CH_2)_2$-N_3 bound to AuNPs

At the end of SH-$(CH_2)_3$-CONH-EG(6)-$(CH_2)_2$-N_3 synthesis, the compound was obtained as a disulphide (N_3-$(CH_2)_2$-EG(6)-NHCO-$(CH_2)_3$-S-S-$(CH_2)_3$-CONH-EG(6)-$(CH_2)_2$-N_3). In order to determine the number of azide-containing chains bound to the AuNPs by the Ellman's assay, a reduction step of the disulphide compound was necessary. One of the simplest methods to reduce disulphide groups is the use of sodium borohydride ($NaBH_4$) under anaerobic conditions. This common reducing agent is able to specifically reduce disulphides to free thiols without affecting any of the other major functional groups and without any secondary reactions with Ellman's reagent. Briefly, the sample containing the disulphide was dissolved in phosphate buffer 0.05M pH 8. Sodium borohydride was added at final concentration of 0.12M and incubated 90 min. The pH of the reaction was acidified using HCl 3M:Acetone (1:1) (v/v) and incubated 10 min to guarantee the complete elimination of excess borohydride. NaOH 3M was added in order to neutralize the

reaction. The neutralised solution was buffered at pH 7 with phosphate buffer 0.2M and immediately analysed by the Ellman's assay to prevent re-oxidation of the thiols to disulphides. The linear range was 0.022-2.2 mM (Abs_{412} = 0.5 [PEG-N_3, nM] + 0.1215).

As the sensitivity of this method was shown low for the quantification of PEG-N_3 bound to AuNPs an indirect method using a second addition of PEG-COOH (see below) was employed, while the presence of PEG-N_3 chain on the AuNPs was confirmed by FTIR (2106 cm^{-1}, N_3 st).

The PEG chains loaded on the AuNPs were quantified by using the PEG-COOH chain as a model. PEG-COOH was added to AuNPs until a complete saturation (0.1 mM of thiolated chain per 10 nM of gold nanoparticles). AuNPs were functionalised with a controlled amount of thiolated chains in order to obtain NPs with different degrees of saturation – Figure S2A (increasing amount of PEG-N_3 at a constant PEG-COOH chains bound to AuNPs) and Figure S2B (increasing amount of PEG-COOH at a constant PEG-N_3 chains bound to AuNPs). After this, a fixed amount of a PEG-COOH chain was added and incubated with the AuNPs. The concentration of thiolated chains bound to non-saturated AuNPs was determined by the Ellman's assay. As illustrated in Figure S2A-B, when the initial percentage of saturation of the thiolated layer decreases the AuNPs are able to bind a higher amount of thiolated chains further added. The best condition to bind further thiolated molecules was to work with AuNPs with a degree of saturation below 47%, but higher than 20% to guarantee stability, corresponding to a range from 37 μM to 11 μM of total PEG chains per 10 nM of gold (see Figure S2C). This model was used to determine the optimum degree of saturation of AuNPs for the loading of thiolated siRNA by the covalent approach.

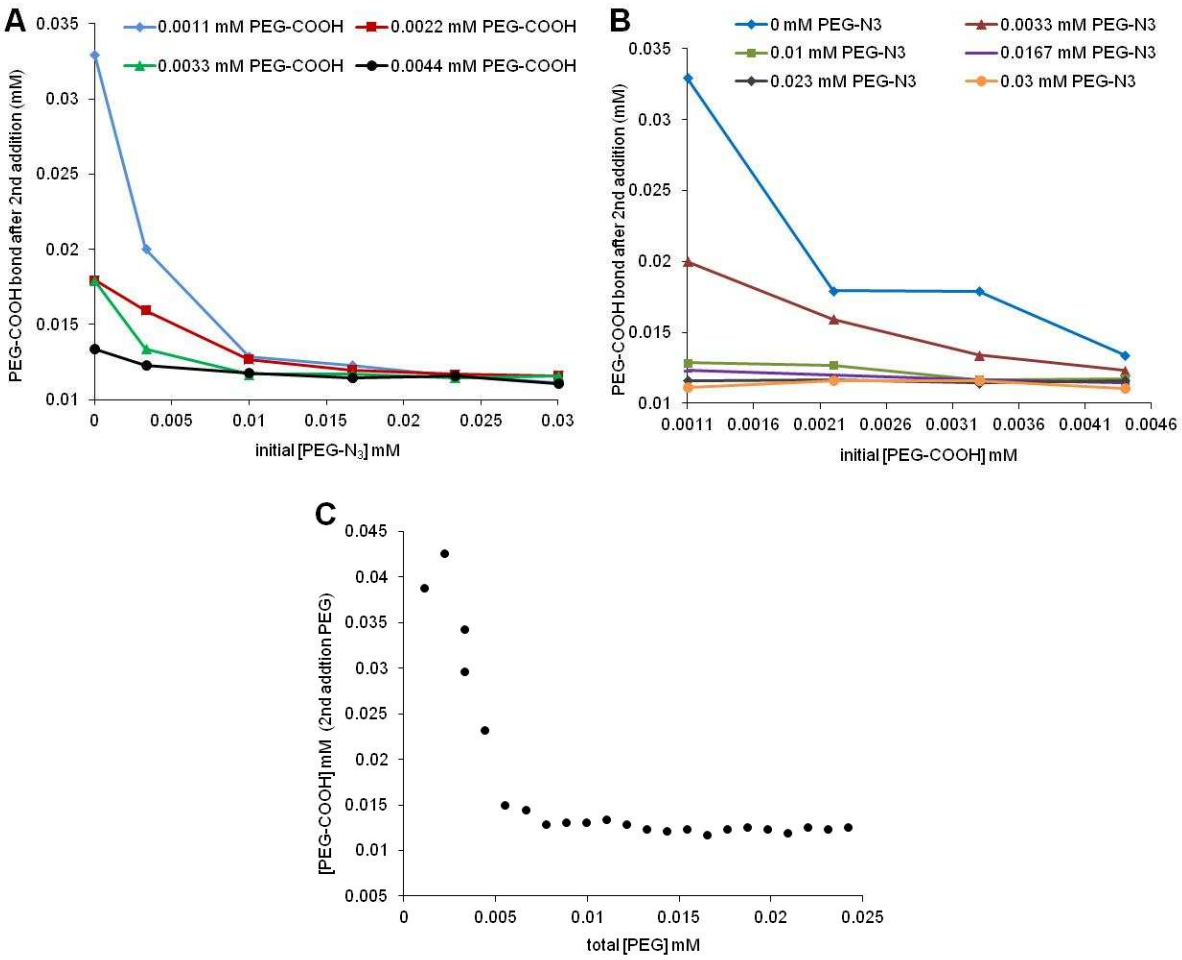

Figure S2. Quantification of degree of saturation for the PEG chains. **A)** Increasing amount of PEG-N_3 at a constant PEG-COOH chains bound to AuNPs. **B)** Increasing amount of PEG-COOH at a constant PEG-N_3 chains bound to AuNPs. **C)** Optimum degree of saturation of AuNPs for the entrance of a third thiolated chain.

Determination of the bound TAT peptide by the EDC coupling reaction to functionalised AuNPs

As was stated in the methods section, a procedure for the determination of the bound TAT peptide was developed based on Bradford method. Given that the reagents for the EDC reaction (sulfo-NHS, EDC) interfere with the assay a standard addition calibration curve for the TAT peptide in the EDC reaction conditions was obtained (Abs570 = 0.1265 [TAT peptide, μM] + 0.24). This calibration curve was used for the interpolation of the samples containing the excess peptide that was not bound to AuNPs.

Quantification of the RGD peptide

The RGD quantification was achieved using the BCA Protein Assay (Thermo Scientific) according to manufactures' instructions. This assay is a detergent-compatible formulation based on bicinchoninic acid (BCA) for the colorimetric detection and quantification of total protein. This method combines the well-known reduction of Cu^{+2} to Cu^{+1} by protein in an alkaline medium (the biuret reaction) with the highly sensitive and selective colorimetric detection of the cuprous cation (Cu^{+1}) using a unique reagent containing bicinchoninic acid. The purple-colored reaction product of this assay is formed by the chelation of two molecules of BCA with one cuprous ion. This water-soluble complex exhibits a strong absorbance at 562 nm in a near linear relationship with increasing protein concentrations. Briefly, 0.1 mL of each standard and unknown sample (the supernatants) was mixed with 2.0 mL of the BCA™ Working Reagent to each tube. The reaction mixture was incubated at 60°C for 2 hr. After this period the tubes were cooled down to room temperature and the absorbance measured at 562 nm. The standard curve was used to determine the RGD concentration of each unknown sample (supernatant). The calibration curve for a working range (0–18 μg/ml) is given by the following equation $Abs562nm = -0.0001x^2 + 0.0081x + 0.0017$.

Quantification of the siRNA strands loaded onto AuNPs

In order to carry out the siRNA duplexes quantification, we used the GelRed™ (Biotium) dye as a nucleic acid intercalator. An analytical method to quantify the amount of siRNA in excess during the functionalisation was developed. Briefly, the supernatants were incubated with GelRed 100× and TBE 0.5× and fluorescence was measured with emission at 602 nm. A Correlation to a standard curve of known siRNA concentrations allowed accurate measurement of siRNA in unknown samples (Emission at 602nm = 439.96·[siRNA, nmol] + 32.697)**.**

siRNAs used for NP functionalisation

Thiolated siRNA (Thermo Scientific Dharmacon) was dissolved in 1 ml of 0.1 M DTT, extracted three times with ethyl acetate, and further purified through a desalting NAP-5 column (Pharmacia Biotech) according to the manufacturer's instructions. The unmodified siRNA used for the ionic approach was only resuspended in DEPC-water. The sequences of human, mouse and hydra c-myc siRNAs (Thermo Scientific, Dharmacon) are depicted in table 1.

c-myc siRNA	siRNA sequence
Human	Sense: 5'-Thiol-GCGAGGAUAUCUGGAAGAAAUUU-3'
	Antisense: 5'-AUUUCUUCCAGAUAUCCUCGCUU-3'
Mouse	Sense: 5'-Thiol-GUGAGGAUAUCUGGAAGAAAUUU-3'
	Antisense: 5'-AUUUCUUCCAGAUAUCCUCACUU-3'
Hydra	Sense: 5'-Thiol-AAGAUGCUCACGCGUCAAGAAUU-3'
	Antisense: 5'-UUCUUGACGCGUGAGCAUCUU-3'
Nonsense control	Sense: 5'-Thiol-AAUUCUCCGAACGUGUCACGUUU-3'
	Antisense: 5'- ACGUGACACGUUCGGAGAAUUUU -3'

Table 1. The siRNA sequences designed on human, mouse and hydra c-myc genes.

For NP-ion, the unmodified siRNAs, at a constant concentration of 5 nmol/mL, were incubated with RNase-free solution of the NP-ion@R_4N^+@TAT (10 nM) for 16 hr at 4ºC. With regards non-saturated AuNPs, the purified SH-siRNAs, at a constant concentration of 5 nmol/mL, were incubated with RNase-free solution of the NP-ion@TAT (10 nM) containing 0.028 % SDS. Subsequently, the salt concentration was increased to 0.1M NaCl with brief ultrasonication following each addition to increase the coverage of oligonucleotides on the nanoparticle surface.

Following 16 hr incubation at 4ºC, the particles were purified by centrifugation at 14000 rpm, 20 min at 4°C, and re-suspended in DEPC-water. This process was repeated 3 times.

The number of siRNA per gold nanoparticle was determined by using an acid nucleic intercalator – GelRed. Briefly, the supernatants were incubated with GelRed 100× and TBE 0.5× and fluorescence was measured using a fluorometer Perkin Elmer LS55 with emission at 602 nm and compared to a standard curve.

S2: Internalisation of AuNPs conjugates

Uptake of AuNP by living *Hydra* polyps

Polyps were incubated for 24 h with NP-ion and NP-cov and their corresponding siRNA functionalised NP, at 15 nM, and the uptake of AuNP monitored by optical microscopy.

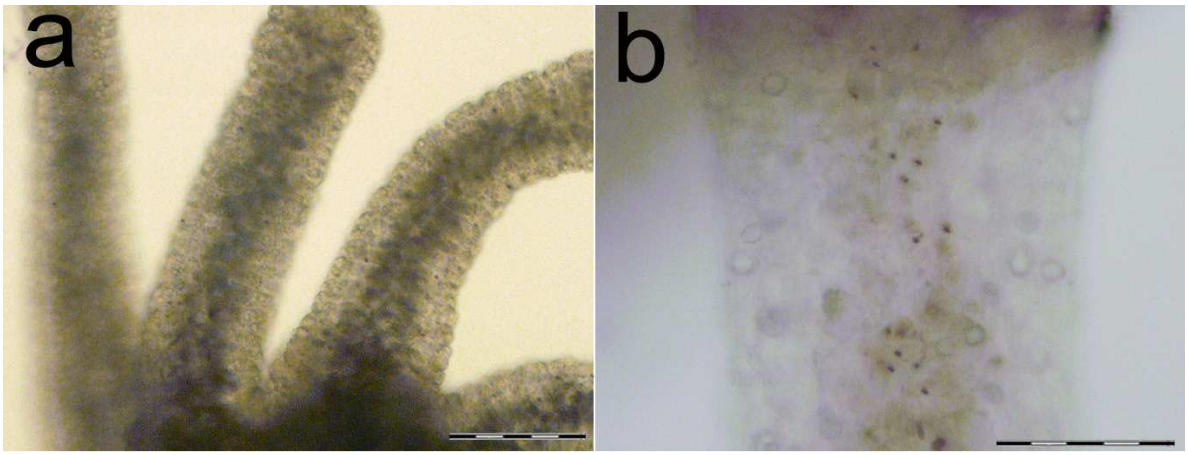

Figure S3. AuNP uptake in *Hydra vulgaris*.

In vivo imaging of *Hydra vulgaris* treated with NP-ion@myc-siRNA. Low level of uptake was observed with both NP-cov@myc-siRNA and NP-ion@myc-siRNA. The image (**a**) shows NP-ion@myc-siRNA as small violet vesicle-like structures present over the tentacles (**b**) and the body. This lower rate of internalisation compared to AuNPs coated with 100% PEG azide (data not shown) is due to the siRNA functionalisation, which causes a decrease of the Zeta Potential value. Scale bars: A, 200 μm; B, 100 μm.

S3: Evaluation of RNAi efficiency by functional reporter gene assay

1. **MYC-Luciferase vector construction**

Total RNA extracted from HeLa cells was subjected to Reverse Transcriptase (RT) for cDNA synthesis. Isolation of total RNA was performed using Trisure (Bioline) according to the manufacturer's protocol. The total RNA was subjected to DNase I digestion to ensure absence of DNA after the extraction and was performed with 2U of DNase I (Fermentas) for 1 h at 37ºC, which was subsequently inactivated by adding 50 mM EDTA and incubated for 10 min at 65ºC. The RNA concentration was determined by measurement of the optical density at 260nm and the RNA was stored at -80ºC until use. The quality of each RNA sample was controlled on a 1% agarose gel (TBE) stained by GelRedTM. The RT reaction was performed with 200 U of Revert-AidTM M-MuLV Reverse Transcriptase (Fermentas) according to the manufacturer's specifications, using 500 ng of total RNA, 20 µM of MYCreverse primer, 1mM of dNTPs, annealing at 42°C for 1 h and 70°C for 10 min to reverse transcriptase inactivation.

The 1458-bp product, which corresponds to the whole human v-myc myelocytomatosis viral oncogene homolog (MYC) gene, was PCR amplified using primers MYCforward: 5'–CTTCTCTGAAAGGCTCTCC–3′ and MYCreverse: 5'–TCATAGGTGATTGCTCAGGA–3′. PCR amplification were performed in a MasterCycler Personal (Eppendorf) in 50 µl using 0.2 µM of primers, 0.2 mM dNTPs with 2U Taq DNA Polymerase (Fermentas), with the following thermal cycling conditions: initial 5 min denaturation at 95°C, followed by 35 amplification cycles of denaturation at 95 °C for 30 s, annealing at 62 °C for 30 s, elongation at 72 °C for 120 s, and a final elongation at 72 °C for 10 min.

The RT-PCR product was re-amplified using primers containing the specific restriction sites for the multiple cloning region located downstream of the Renilla luciferase translational stop codon of the psiCHECK™-2 Vector (Promega) with 6273bp. The MYC gene was re-amplified with primers for the XhoI (5'–GTTCTCGAGCTCCTTCTCTGAAAGGCTCTCC–3') and NotI (5'–GATGCGGCCGCTCATAGGTGATTGCTCAGGA–3') restriction enzymes as described above and purified through QIAquick PCR Purification Kit (Quiagen). Confirmation of correct PCR products was performed by 2% agarose gel electrophoresis stained with GelRedTM.

The Ligation between the MYC insert (with sticky ends) and the Luciferase vector was carried out in a ligation buffer containing 2U of T4 DNA ligase (Fermentas) at 22ºC for 1 h and at 4ºC overnight. Confirmation of proper ligation products was performed by 2% agarose gel. The ligation mixture was used for transformation of competent E. coli DH5α strains (plated on nutrient agar containing ampicillin (100 µg/ml) as described previously[2]. Confirmation of the correct cloning was performed by sequencing.

2. Myc-psiCHECK2 recombinant vector for assessment of RNAi efficiency in HeLa cells

The whole human v-myc myelocytomatosis viral oncogene homolog (c-myc) gene (NCBI Reference Sequence: *NM_002467.4*) was cloned into a psiCHECK™-2 Vector from Promega as described above. Confirmation of the correct cloning vector was performed by DNA sequencing (see Figure S4). This vector was designed to provide a quantitative and rapid approach for optimisation of RNAi enabling to monitor changes in expression of a target gene (c-myc) fused to a reporter gene (Luciferase). The c-myc PCR product was cloned downstream the Renilla luciferase primary reporter gene. As initiation of the RNAi process by siRNAs results in cleavage and subsequent degradation of the fusion mRNA measuring decreases in Renilla activity provides a quantitative evaluation of RNAi effect. A second reporter gene, the Firefly luciferase, under a different promoter, is present into the cloning vector psiCHECK™-2 as internal control, allowing normalisation of Renilla luciferase expression, robust and reproducible results.

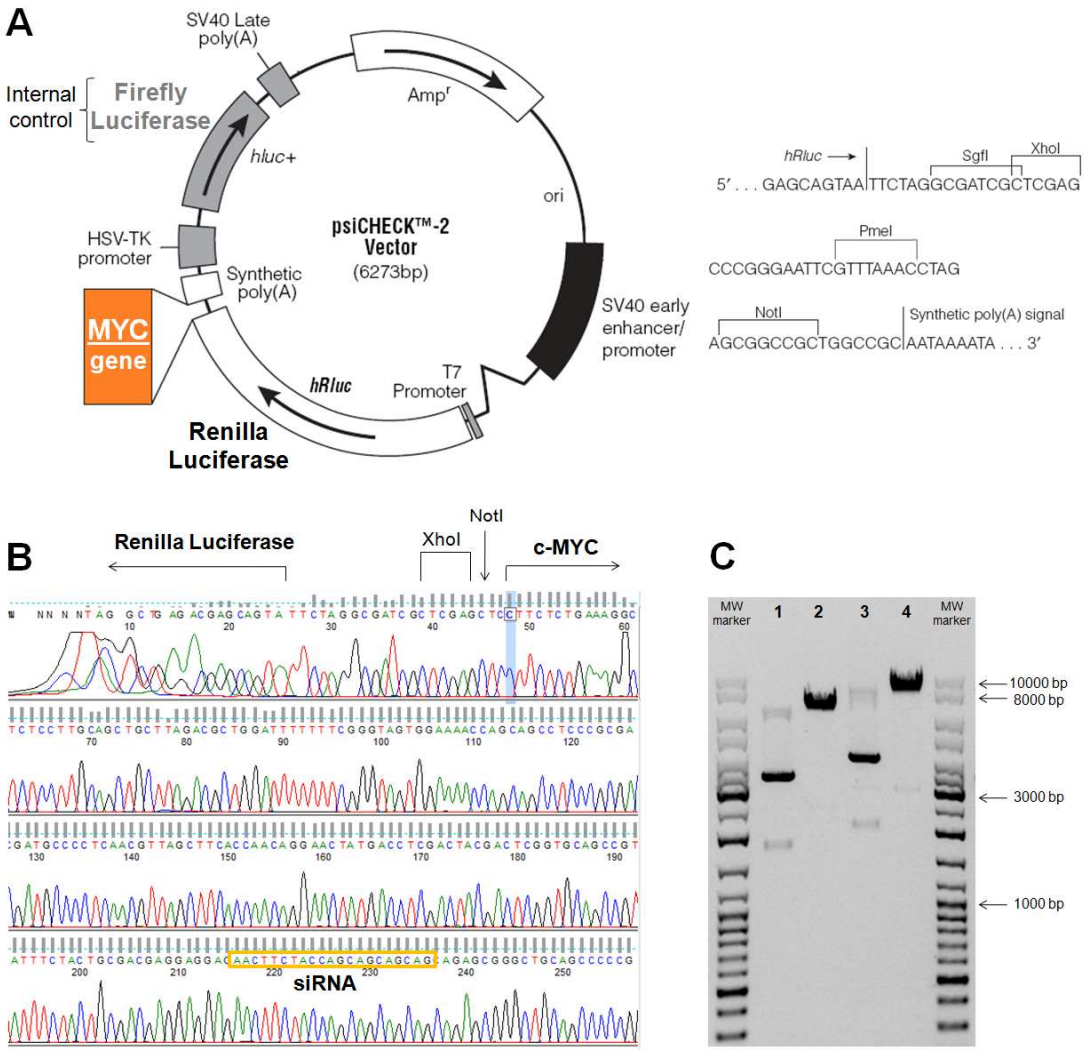

Figure S4. A) Map of the cloning vector psiCHECK™-2 (Promega). In orange the multiple cloning site used for c-myc cloning is shown. A c-myc PCR product (1457 bp) was cloned into the NotI site of the psiCHECK-2 vector (image adapted from Promega psiCHECK™ vectors). **B)** Sequence chromatographs obtained from the Fused Renilla Luciferase-MYC vector are illustrated to confirm the fusion between c-myc and Renilla luciferase genes, and to show the mRNA region targeted by myc-siRNA (yellow squared, siRNA sequence). **C)** Agarose gel electrophoresis (0.8% agarose in TBE 1×) of the luciferase vectors. Lane 1 - psiCHECK™-2 vector (supercoiled); Lane 2 – psiCHECK™-2 (6273 bp), linearised by BamHI digestion; Lane 3 – Recombinant Renilla Luciferase-MYC vector (supercoiled); Lane 4 – recombinant Renilla Luciferase-MYC vector (7730 bp), BamHI digested . The higher molecular weight of the bands on lanes 3 and 4 demonstrate c-myc gene cloning.

3. Molecular analysis of gene expression in *Hydra*

Quantitative Real-Time polymerase chain reaction (qRT-PCR) was performed in 25 µl of reaction mixture consisting of 1x Platinum SYBR green qPCR SuperMix-UDG with ROX (Invitrogen), serial cDNA dilutions and 0.5 µM each primer. The reactions were processed using the StepOne Real-Time PCR system (Applied Biosystem) under the following cycling steps: 10 min at 94°C; 40 cycles at

94°C for 15 s; 58°C for 30 s; 72°C for 30 s, and a 20 min gradient from 55°C to 90°C to obtain a melting curve. To normalize RNA levels, *Hydra* Elongation factor 1alfa gene (HyEf-1α, GenBank Accession no. Z68181.1) was employed as internal calibrator. Gene-specific primers were: HyEf-1α: forward, 5'CCAGGAGACAATGTCGGTTT 3'; reverse, 5'GCTTCAATGGCAGGATCATT 3'; Hy*myc1*: forward, 5' TACAGAAAGCGAGGACGAAGTT 3'; reverse, 5'GCGAAGCAACTTTCAGTATTGTTAC 3'). At least three independent repeats for each experiment were carried out. Herein, the delta–delta Ct ($2^{-\Delta\Delta CT}$) method, for comparing relative expression results between treatments, was applied[3].

4. Molecular analysis of gene expression in mouse lung

PCR was amplified from cDNAs retrotranscribed from mice lung total RNA using the following primers: 5' ATCTGCGACGAGGAAGAGA 3' and 5' AGCGACCGCAACATAGGAT 3'. Quantitative Real-Time polymerase chain reaction (qRT-PCR) was performed in 25 µl of reaction mixture consisting of 1x Platinum SYBR green qPCR SuperMix-UDG with ROX (Invitrogen), serial cDNA dilutions and 0.5 µM each primer. The reactions were processed using the StepOne Real-Time PCR system (Applied Biosystem) under the following cycling steps: 10 min at 94°C; 35 cycles at 94°C for 15 s; 56°C for 30 s; 72°C for 30 s. and a final elongation at 72 °C for 10 min. At least three independent repeats for each experiment were carried out. The delta–delta Ct ($2^{-\Delta\Delta CT}$) method, for comparing relative expression results between treatments, was applied[3].

S4: Evaluation of Toxicity

1. **Toxicity tests on human cell cultures**

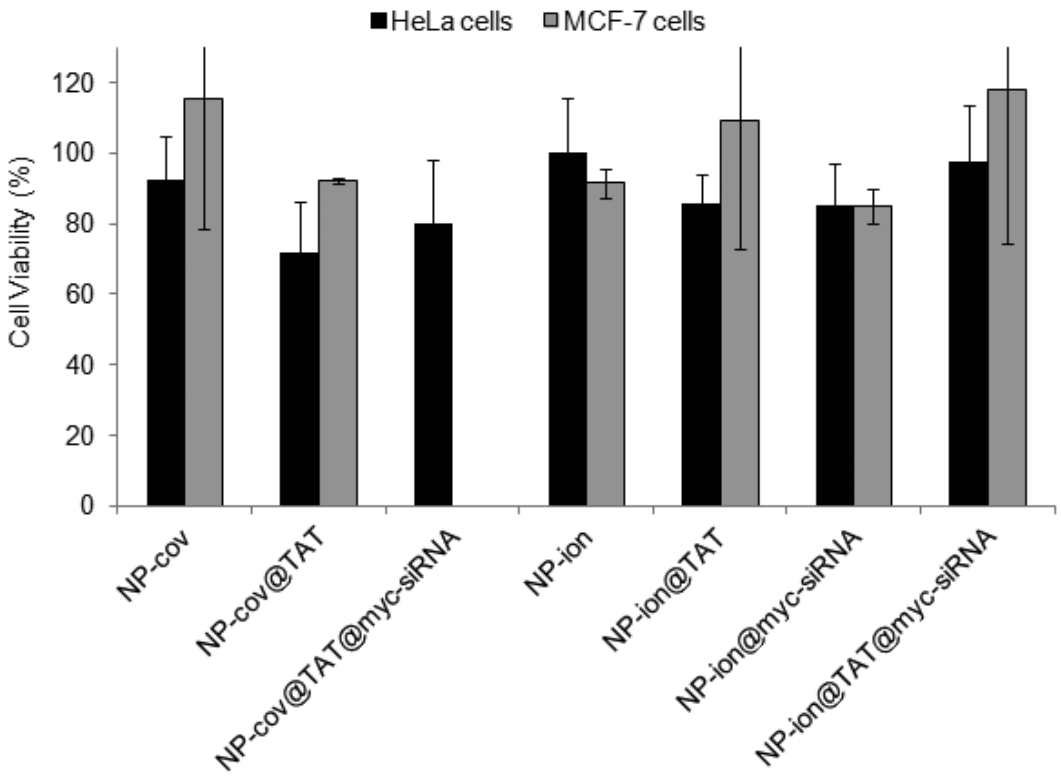

Figure S5. Cytotoxicity of NP-cov and NP-ion in Human cancer cell lines (MCF-7 and HeLa) *via* the MTT assay following 48 hr AuNP exposure. The tetrazolium salts (present in the MTT reagent) are cleaved to formazan by cellular enzymes. An expansion in the number of viable cells results in an increase in the overall activity of mitochondrial dehydrogenases in the sample. This augmentation in enzyme activity leads to an increase in the amount of formazan dye formed, which directly correlates to the number of metabolically active cells in the culture.

2. Acute and long term toxicity effects of AuNP on *Hydra vulgaris*

At the base of metazoan evolution the freshwater polyp *Hydra vulgaris* (Cnidaria; Hydrozoa) has been shown an amenable system to study the interaction between nanoparticles and living systems[4]. Reliable methods have been developed for a comprehensive analysis of the NP impact in *Hydra*, spanning from *in vivo* analysis induced by NP treatments (structural morphological changes, impact on reproductive rate, efficiency of regeneration), to *in vitro* approaches of cell and molecular biology[5,6]. The animal is composed of just two epithelial cell layers (an inner endoderm and an outer ectoderm) with few interspersed specialised cell types and a neuronal net controlling functions and physiology.

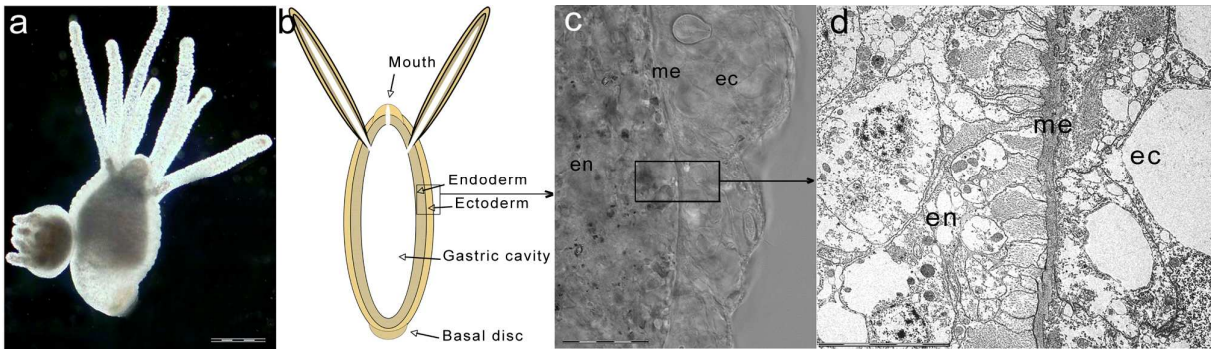

Figure S6. Structural anatomy of *Hydra vulgaris.* **a**) *In vivo* imaging of an adult polyp, showing the simple anatomical structure, shaped as a hollow tube, with a mouth surrounded by crown of 6-8 tentacles, and a foot to anchor to a substrate. The bud on the left side of the animal shows the animal asexual reproduction. **b**) Scheme showing a longitudinal section of the animal. The body is composed of two cell layers, an outer single cell layer, the ectoderm (ec) is separated by an acellular matrix, the mesoglea (me) from the inner cell layer, the endoderm (en) lining the gastric cavity. The bilayered structure is shown in **c**) by confocal and in **d**) by TEM microscopy analysis. Scale bars are 500μm, 50μm and 10 μm, respectively in **a**, **c** and **d**.

We have previously optimised standard toxicity protocols, developed for testing environmental pollutants, for NP toxicity evaluation[7]. With regards identifying potential toxicity of AuNP on Hydra, groups of 20 living animals were soaked in culture medium supplemented with increasing doses of NP-ion and NP-cov (10 nM to 80 nM) and monitored for acute and chronic toxicity by using three different approaches, i.e. presence of morphological changes, impact on regeneration and reproductive rates. No changes in the animal morphology were detected at 24, 48 and 72 h of continuous incubation, neither animals treated 24 h with nanoparticles and

then bisected, were impaired in the capability to regenerate body missing parts. The long term effect was analysed by monitoring the population growth rate, which is an indirect measure of the *Hydra* tissue growth rate and cell viability (see Figure S7). A group of founder animals (n°) either untreated or incubated for 24 h with 80 nM NP-ion or NP-cov, were monitored over two weeks, and the total number of individuals (n) used to calculate the growth rate constant (k) over the duration of the experiment (t), was defined by the equation $\ln(n/n°) = kt$. Control animals at the same developmental stage were not treated. Both experimental and control *Hydra* were fed once daily and monitored for bud formation and detachment. For $n/n_0 = 2$, $t = T_2$, the doubling time of the population. T_2 was determined by linear regression[8]. No significant differences were observed between growth parameters of treated or untreated animals, showing the absence of toxic effects of these NP on Hydra survival and reproductive capabilities.

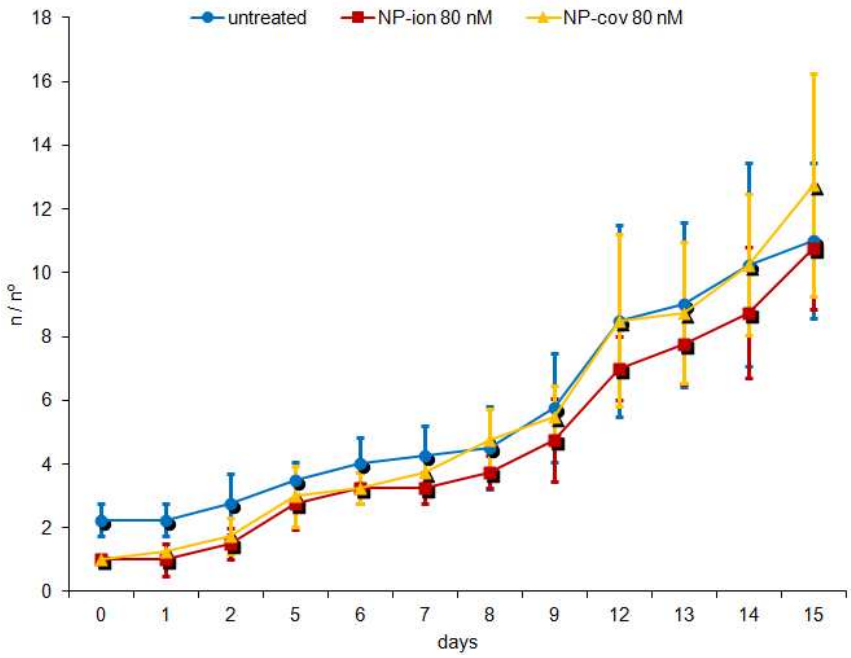

Figure S7. Impact of AuNP treatment on the population growth rate. The ratio between the number *n* of polyps present at a given day and the number *n*° of the founder individuals is reported. 80 nM was the highest possible concentration tested.

3. Toxicity of NP-cov@RGD@myc-siRNA in mice

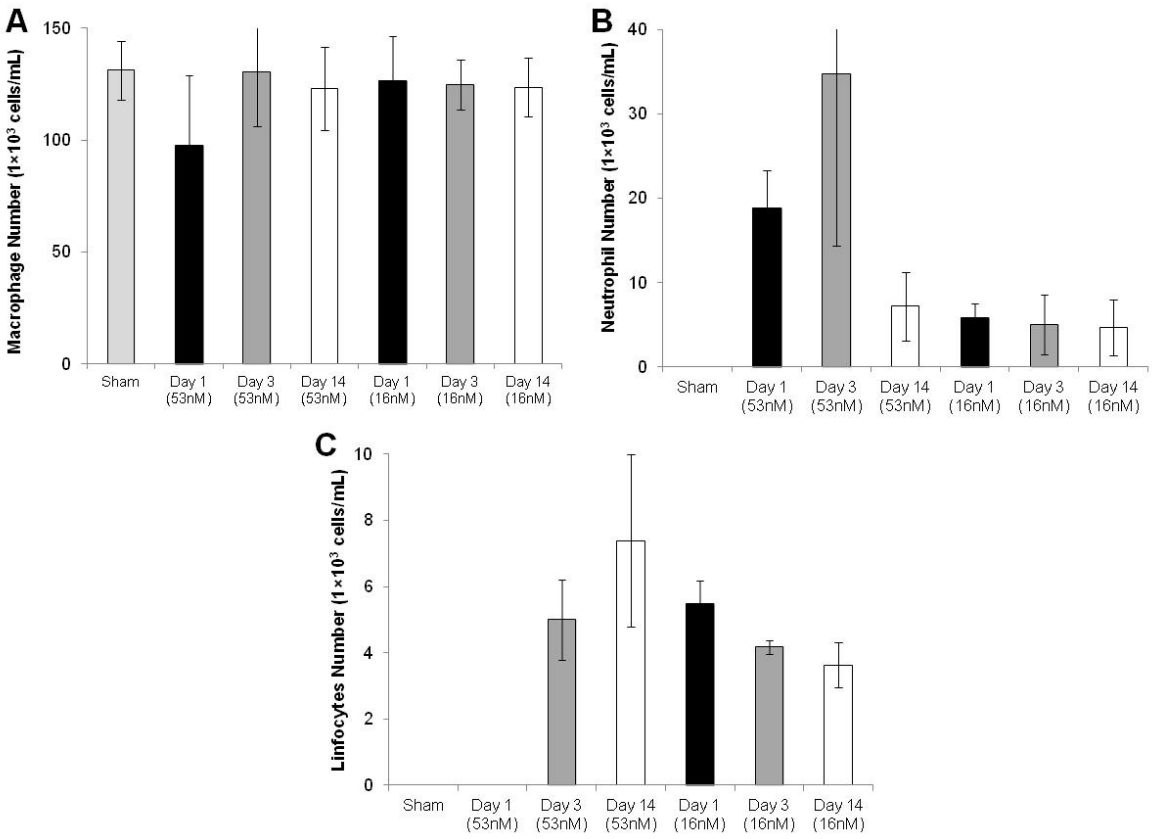

Figure S8. Toxicity study of NP-cov@RGD@myc-siRNA in mice during 1, 3 and 14 days of treatment. Evaluation of the number of Macrophages (**A**), Neutrophils (**B**) and Lymphocytes (**C**) was used to detect inflammation[9]. The increased number of Neutrophils with 53 nM of NP-cov@RGD@myc-siRNA represents inflammation, whereas for 16 nM of NP-cov@RGD@myc-siRNA (concentration used in the mouse silencing studies) the activation of neutrophils is negligible.

Additional references

1. Lee, P. C.; Meisel, D. Adsorption and surface-enhanced Raman of dyes on silver and gold sols. *J. Phys. Chem.* **1982**, 86, 3391-3395.
2. Ausubel, F. M.; Brent, R.; Kingston, R. E.; Moore, D. D.; Seidman, J. G.; Smith, J. A.; Struhl, K. Current Protocols in Molecular Biology, *Greene publishing Associates and Wiley-Interscience*, New York **1987**.
3. Livak, K. J.; Schmittgen, T. D. Analysis of relative gene expression data using real-time quantitative PCR and the 2(-Delta Delta C(T)) Method. *Methods* **2001**, 25, 402-408.
4. Tortiglione, C.; Quarta, A.; Malvindi, M. A.; Tino, A.; Pellegrino, T. Fluorescent nanocrystals reveal regulated portals of entry into and between the cells of Hydra. PLoS One **2009**, 4, e7698.
5. Tortiglione, C. An ancient model organism to test in vivo novel functional nanocrystals, Biomedical Engineering - From Theory to Applications, Reza Fazel-Rezai (Ed.), *InTech Publisher* **2011**.
6. Tino, A.; Ambrosone, A.; Mattera, L.; Marchesano, V.; Susha, A.; Rogach, A.; Tortiglione, C. A new in vivo model system to assess the toxicity of semiconductor nanocrystals. *Int. J. of Biomaterials* **2011**, 2011, 792854.
7. Ambrosone A.; Mattera, L.; Marchesano, V.; Quarta, A.; Susha, A. S.; Tino, A.; Rogach, A. L.; Tortiglione, C. Mechanisms underlying toxicity induced by CdTe quantum dots determined in an invertebrate model organism. Biomaterials **2012**, 33, 1991-2000.
8. Bosch, T. C. G.; David, C. N. Growth regulation in Hydra: relationship between epithelial cell cycle length and growth rate. *Devi. Biol.* **1984**, 104, 161-171.
9. Yin, R.; Tian, F.; Frankenberger, B.; de Angelis, M. H.; Stoeger, T. Selection and evaluation of stable housekeeping genes for gene expression normalization in carbon nanoparticle-induced acute pulmonary inflammation in mice. B*iochem. Biophys. Res. Commun.* **2010**, 399, 531-536.

Biomaterials 34 (2013) 7744–7753

Contents lists available at SciVerse ScienceDirect

Biomaterials

journal homepage: www.elsevier.com/locate/biomaterials

In vivo tumor targeting via nanoparticle-mediated therapeutic siRNA coupled to inflammatory response in lung cancer mouse models

João Conde [a,b,1], Furong Tian [c,1], Yulán Hernández [a], Chenchen Bao [c,d], Daxiang Cui [d], Klaus-Peter Janssen [e], M. Ricardo Ibarra [a], Pedro V. Baptista [b], Tobias Stoeger [c,*], Jesús M. de la Fuente [a,*]

[a] Instituto de Nanociencia de Aragon (INA), Universidad de Zaragoza, Zaragoza 50018, Spain
[b] CIGMH, Departamento de Ciências da Vida, Faculdade de Ciências e Tecnologia, Universidade Nova de Lisboa, Campus de Caparica, 2829-516 Caparica, Portugal
[c] Comprehensive Pneumology Centre, Institute of Lung Biology and Disease, Helmholtz Zentrum München, Neuherberg, Germany
[d] Department of Bio-Nano Science and Engineering, National Key Laboratory of Micro/Nano Fabrication Technology, Institute of Micro&Nano Science and Technology, Shanghai JiaoTong University, P.R.China
[e] Department of Surgery, Klinikum rechts der Isar, Technische Universität München, Ismaninger Strasse 22, Munich, Germany

ARTICLE INFO

Article history:
Received 2 May 2013
Accepted 23 June 2013
Available online 12 July 2013

Keywords:
RGD/siRNA nanoparticles
Gene silencing
Inflammatory response
Mice tumor targeting
Lung cancer therapy

ABSTRACT

Up to now, functionalized gold nanoparticles have been optimized as an effective intracellular *in vitro* delivery vehicle for siRNAs to interfere with the expression of specific genes by selective targeting, and provide protection against nucleases. Few examples however of suchlike *in vivo* applications have been described so far.

In this study, we report the use of siRNA/RGD gold nanoparticles capable of targeting tumor cells in a lung cancer syngeneic orthotopic murine model. Therapeutic RGD-nanoparticle treatment resulted in successful targeting evident from significant c-myc oncogene down-regulation followed by tumor growth inhibition and prolonged survival of lung tumor bearing mice, possibly via αvβ3 integrin interaction. Our results suggest that RGD gold nanoparticles-mediated delivery of siRNA by intratracheal instillation in mice leads to successful suppression of tumor cell proliferation and respective tumor size reduction. These results reiterate the capability of functionalized gold nanoparticles for targeted delivery of siRNA to cancer cells towards effective silencing of the specific target oncogene. What is more, we demonstrate that the gold-nanoconjugates trigger a complex inflammatory and immune response that might promote the therapeutic effect of the RNAi to reduce tumor size with low doses of siRNA.

1. Introduction

RNA interference via the use of small-interfering RNA (siRNA) [1,2] is a powerful and useful tool to block gene function through sequence-specific post-transcriptional gene silencing, playing an important role in the down-regulation of gene expression. siRNAs can be transfected into mammalian cells by a variety of methods [3–5] that influence the strength and duration of the silencing response, which in turn is affected by the amount of siRNA effectively delivered and by the potential of each siRNA to suppress its target. Nevertheless, naked siRNAs show extremely short half-lives due to RNases activity, poor chemical stability, and dissociation from the vector [2]. In fact, the major obstacle to clinical application is the uncertainty about how to deliver siRNA with maximal therapeutic impact.

Nanotechnology in general, and nanoparticles in particular, offer unprecedented opportunities towards effective cancer therapy [6], as multifunctional devices capable of bypassing biological barriers for the specific delivery of therapeutic agents, reducing systemic toxicity and severe adverse side effects avoiding the undesirable distribution to healthy organs and tissues [7,8]. Nowadays the main challenge in therapy is to develop a delivery system capable of circulating in the blood stream undetected by the immune system and capable to recognize a desirable target and signal it for effective drug delivery or gene silencing. Due to their chemical properties and ease of surface modification with a variety of ligands (e.g.

* Corresponding authors.
E-mail addresses: tobias.stoeger@helmholtz-muenchen.de (T. Stoeger), jmfuente@unizar.es (J.M. de la Fuente).
[1] These authors contribute equal to the paper.

0142-9612/$ – see front matter © 2013 Elsevier Ltd. All rights reserved.
http://dx.doi.org/10.1016/j.biomaterials.2013.06.041

targeting moieties, therapeutic loads), gold nanoparticles (AuNPs) are optimal non-toxic carriers for gene therapy [9,10]. In fact, numerous studies using engineered AuNPs modified with siRNA have demonstrated cytoplasmic delivery of siRNA and efficient gene silencing [11–18]. However, almost all nanoconjugates using siRNA have exclusively been tested in cell cultures targeting only reporter genes.

Recently, we provided evidence of a proof-of-concept *in vitro* and *in vivo* RNAi triggering via the synthesis of a library of multifunctional AuNPs. Using a hierarchical approach including three biological systems of increasing complexity: *in vitro* cultured human cells, *in vivo* freshwater polyp (*Hydra vulgaris*), and *in vivo* healthy nude mice, we could identify the most adequate nanoparticles to efficiently transport siRNAs [19]. These previous results evidenced the importance of a correct design in the functionalization of nanoparticles for biological applications, mainly for complex animal systems such as mice. The ionic linkage of siRNA on the AuNPs showed efficiency in cells and in *Hydra*, however only a covalent bond ensured an active RNAi release in mice. This efficiency was reinforced by the addition of RGD peptide to the surface of the nanoparticles. RGD has been extensively investigated as cell adhesion peptide that is recognized by cell-surface receptors, such as integrins, known to mediate cell adhesion and proliferation [20]. These adhesion molecules play a key role in tumor angiogenesis and metastasis, being considerably up-regulated on the endothelium during angiogenesis. The αvβ3 integrin receptor is expressed specifically on proliferating endothelial cells such as those present in tumors, representing a marker for malignancy [21].

Here, we set out for the treatment of lung cancer in two orthograft mouse tumor models. We used female C57BL/6 mice, tumor induced with LA-4 adenocarcinoma cells and to monitoring tumor size a female C57BL/6 albino mice tumor induced with luciferase expressing CMT/167 adenocarcinoma cells. For therapy we used the previously as most active identified AuNPs to drive RNAi release into the cytoplasm of the target cell: AuNPs@PEG@RGD@siRNA. Our results suggest a synergistic effect resulting in delayed tumor growth, and increased tumor mouse survival related to an enhanced inflammatory response in lung tumor tissue when compared to healthy lungs (see Fig. 1).

2. Materials and methods

2.1. Synthesis of RGD/siRNA gold nanoparticles

All gold nanoconjugates used in this study were synthesized and extensively describe elsewhere (Supplementary Information, Figure S1) [19]. Briefly, gold nanoparticles with an average diameter of ~14 nm, were synthesized by the citrate reduction method and functionalized with 25% saturated PEG layer, functionalized with 50% carboxylic groups (SH-EG(8)–$(CH_2)_2$–COOH) and 50% of azide groups (SH–$(CH_2)_3$–CONH-EG(6)–$(CH_2)_2$–N_3). A mixture of 10 nM of the citrate-gold nanoparticles, 0.028% SDS and 7 μM SH-EG(8)–$(CH_2)_2$–COOH (Iris-Biotech) and 7 μM SH–$(CH_2)_3$–CONH-EG(6)–$(CH_2)_2$–N_3, AuNPs@COOH/N_3 was prepared. Then, NaOH was added to a final concentration of 25 mM and the mixture was incubated for 16 h at room temperature. The excess of PEG chains was removed by centrifugation at 14,000 rpm for 30 min at 4 °C and the supernatant was discarded. For functionalization with the Arginine–Glycine–Aspartic Acid (G-RGD-S)-Peptide (Sigma, MW 490.47 Da), 20 nM of AuNPs@COOH/N_3 were incubated in 6 mM sulfo-*N*-hydroxysulfosuccinimide sodium salt and 25 mM MES buffer pH 6.1 followed by the addition of the peptide at a final concentration of 0.5 μM. The mixture was incubated at room temperature for 16 h. Then the AuNPs were centrifuged at 14,000 rpm for 30 min at 4 °C to remove excess RGD peptide and the supernatants were recovered and tested for protein concentration using a BCA Protein Assay Kit (Thermo Scientific). Purified thiolated siRNA (Thermo Scientific Dharmacon) for mouse c-myc (Sense strand: 5′-Thiol GUGAGGAUAUCUGGAAGAAAUUU-3′; Antisense strand: 3′-AUUUCUUCCAGAUAUCCUCACUU-5′) at a constant concentration of 5 nmol/mL, were incubated with RNase-free solution of the AuNPs@COOH/N_3@RGD (10 nM) containing 0.028% SDS. Subsequently, the salt concentration was increased to 0.1 M

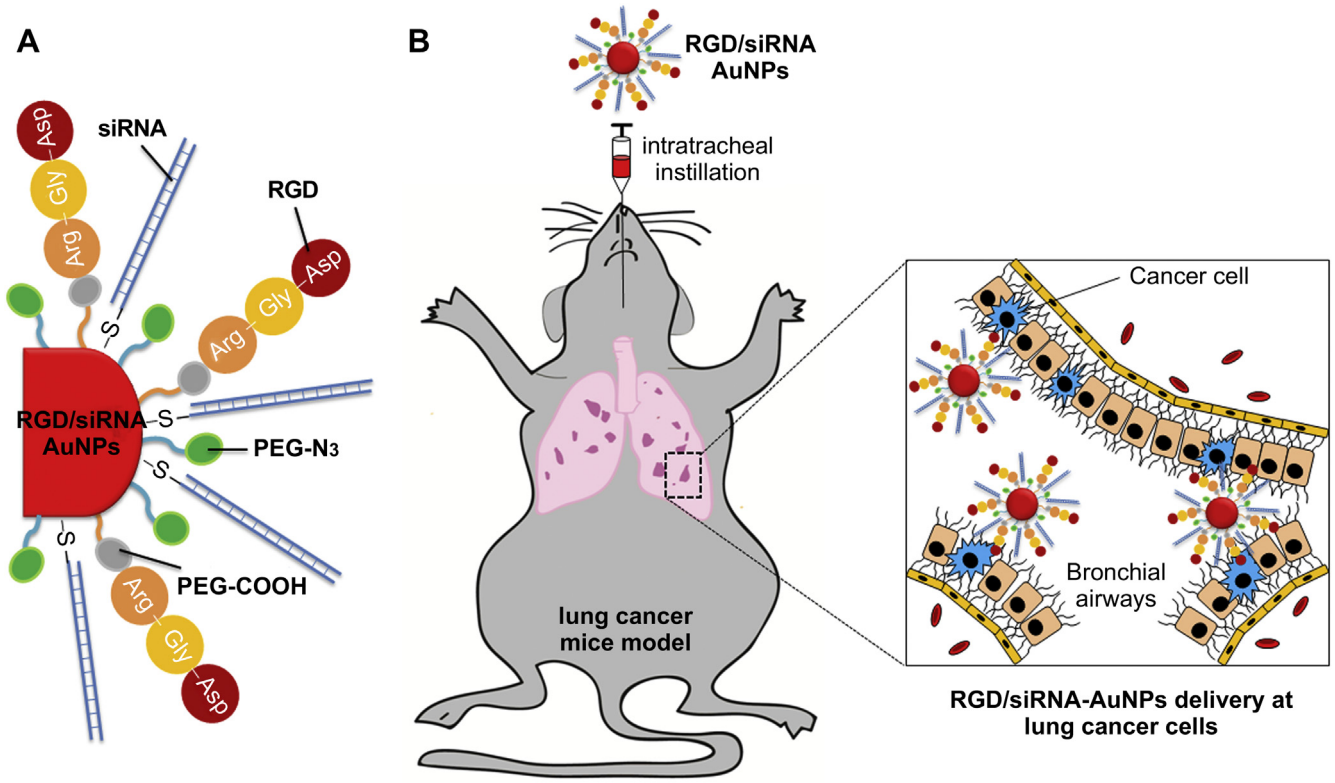

Fig. 1. Inflammatory response and therapeutic siRNA silencing through RGD-nanoparticles in a lung cancer syngeneic orthotopic mouse model. (A) Engineered nanoparticles modified with RGD and siRNA can represent a delivery system of siRNA and a useful tool for sequence-specific post-transcriptional gene silencing in a lung cancer mouse model. (B) AuNPs@PEG@RGD@siRNA are administered by intratracheal instillation and directly delivered to bronchial airways, where the can efficiently target tumor cells. Nanoparticles can passively accumulate or anchor through targeting RGD receptors, such as αvβ3 integrins, expressed in lung tumor cells.

NaCl with brief ultrasonication following each addition to increase the coverage of oligonucleotides on the nanoparticle surface. After functionalization during 16 h at 4 °C, the particles were purified by centrifugation at 14,000 rpm (20 min) at 4 °C, and re-suspended in DEPC-water.

Full characterization for AuNPs@PEG@RGD@siRNA has been reported elsewere [19]. For brief characterization see Supplementary Information S1.

2.2. Inflammatory response in bronchoalveolar lavage (BAL) cells

BAL fluid was obtained by 4 times injecting and recovering 1 mL PBS via a tracheal cannula. Cells recovered with the lavage fluid (lymphocytes and neutrophils accompanying the predominant population of alveolar macrophages) were determined utilizing light microscopic counting of 200 cells on cytospin preparations. Details of the bronchoalveolar lavage (BAL) procedure were described elsewhere [22].

2.3. Assessment of c-myc downregulation

Total RNAs were extracted using the RNA Purification Kit PP-210L (Jena Bioscience) from lung tissue treated for 48 h with 0.3 pmol of different nanoparticles (AuNP@PEG, AuNP@PEG@RGD, AuNP@PEG@siRNA and AuNP@PEG@RGD@siRNA), or dissected lungs, reverse transcribed and analyzed by qRT-PCR. qPCR was performed using the following primers for the amplification of 165 bp c-myc gene (GenBank: BC138931.1): 5′-ATCTGCGACGAGGAAGAGA-3′ and 5′-AGCGACCGCAACATAGGAT-3′. Quantitative Real-Time polymerase chain reaction (qRT-PCR) was performed in 25 μL of reaction mixture consisting of 1× Platinum SYBR green qPCR SuperMix-UDG with ROX (Invitrogen), serial cDNA dilutions and 0.5 μM each primer. The reactions were processed using the StepOne Real-Time PCR system (Applied Biosystem) under the following cycling steps: 10 min at 94 °C; 35 cycles at 94 °C for 15 s; 56 °C for 30 s; 72 °C for 30 s and a final elongation at 72 °C for 10 min. At least three independent repeats for each experiment were carried out. The delta–delta Ct ($2^{-\Delta\Delta CT}$) method, for comparing relative expression results between treatments, was applied.

2.4. Cell lines and flow cytometry

Lung fibroblasts (ATCC® CCL-206™), and two alveolar epithelial type II like adenocarcinoma cell lines LA-4 (ATCC® CCL-196™) and MLE12 (ATCC® CRL-2110™) were grown under standardized conditions as recommended by the manufacturer. 10,000 Cells were used for flow cytometrical analysis of integrin expression using anti αvβ3-integrin antibody (BD Bioscience) and fixed cells were analyzed in BD FACSDiva Software (BD Biosciences) as described by Schiller et al. [23].

2.5. RNAi and tumor targeting experiments in mice

Prior to instillation, mice were anesthetized by intraperitoneal injection of a mixture of Medetomidin (0.5 mg/kg body mass), Midazolam (5.0 mg/kg body mass) and Fentanyl (0.05 mg/kg body mass). The animals were then intubated by a nonsurgical technique. Using a cannula inserted 10 mm into the trachea, a suspension containing 1×10^5 cancer cells in 50 μl pyrogene-free distilled water was instilled, followed by 100 μl of air, at week 8. Four weeks after the lung cancer induction 0.3 pmol AuNPs (at weeks 12, 13, 14 and 15), in 50 μl pyrogene-free distilled water was intratracheally instilled into the mice, followed by 100 μl of air. After instillation animals were antagonized by subcutaneous injection of a mixture of Atipamezol (2.5 mg/kg body mass), Flumazenil (0.5 mg/kg body mass) and Naloxon (1.2 mg/kg body mass) for antagonization and to control awakening of the mice. Animal experiments were carried out according to the German law of protection of animal life and were approved by an external review committee for laboratory animal care (animal approval number: 55.2-1-54-2532-20-11).

2.6. Molecular analyses of MYC expression in mouse

The lung cancer tissues (from C57BL/6 female mice induced with LA-4 adenocarcinoma cells) were embedded and sliced into 3 μm section. A normal Hematoxylin and Eosin (H&E) staining were employed for cancer morphology observation. For immunolocalisation, standard immunohistochemical staining method was employed. The tissue slide was incubated with anti-mouse c-myc and anti-rabbit caspase-3 (Invitrogen) (1:1000) in PBS containing 1% BSA for 60 min, and was washed three times in Tris-buffered saline (TBS). The slide was incubated with 560 nm anti-mouse and FITC anti-rabbit as the secondary antibody (Invitrogen), at the recommended dilution, in TBS containing 1% BSA, for 30 min, and then was washed for three times in PBS. The slides were mounted with 50 μl of mounting medium. The images were taken by Olympus microscopy and the fluorescent density per cell was analyzed by ImageJ. The percentages of MYC expression in each group were compared with cancer cell without treatment. To visualize the particle in cancer cell, mice were treated with 1×10^5 cancer cells and with 0.3 pmol AuNPs. Mice were sacrificed and mice lungs fixed in 2.5% glutaraldehyde for TEM as described elsewhere [19].

2.7. Bioluminescence imaging

Stable clones of CMT64/61 cells, originally derived from a spontaneous lung adenocarcinoma of a C57Bl/ICRF mouse [24] were generated by transfection with pGL3-Control vector (Promega GmbH), and co-transfection for selection with a linear Hygromycin resistance marker (Clontech). A stable clone (CMT/167-luc) expressing high levels of firefly luciferase, constitutively driven by the SV40 promoter and enhancer, was instilled into female C57BL/6 albino mice. Prior to instillation, mice were anesthetized by intraperitoneal injection of a mixture of Medetomidin (0.5 mg/kg body mass), Midazolam (5.0 mg/kg body mass) and Fentanyl (0.05 mg/kg body mass). The animals were then intubated by a nonsurgical technique. Using a cannula inserted 10 mm into the trachea, a suspension containing 1×10^5 CMT/167-luc cells in 50 μl pyrogene-free distilled water was instilled, followed by 100 μl of air, at week 8. Four weeks after orthotropic lung cancer induction mice were treated by instillation of 0.3 pmol AuNP (at weeks 12, 13, 14 and 15), respectively, in 50 μl pyrogene-free distilled water, followed by 100 μl of air. After instillation animals were antagonized by subcutaneous injection of a mixture of Atipamezol (2.5 mg/kg body mass), Flumazenil (0.5 mg/kg body mass) and Naloxon (1.2 mg/kg body mass). Luciferase expression was monitored applying the IVIS® imaging system (Lumina, PerkinElmer) from mice bearing tumors from luciferase-CMT/167 cells ($n = 8$ animals per treated group).

2.8. Statistical analysis

All statistical analysis was performed with SPSS statistical package (version 15, SPSS Inc., Chicago, IL) using a Paired-Sample *t*-test. All experiments, unless otherwise stated, were performed in triplicate. All error bars used in this report are ±s.d of at least three independent experiments.

3. Results and discussion

3.1. Inflammatory response in bronchoalveolar lavage cells

AuNPs have been shown *in vivo* and *in vitro* to accumulate within various types of cells with a special affinity for macrophage-like and reticuloendothelial cells throughout the body, where they bioaccumulate in lymph nodes, bone marrow, spleen, adrenals, liver and kidneys [25]. On the other hand, the influence of size, solubility and surface chemistry on the biocompatibility of nanoparticles is well known and thus impacts their use in biomedical applications [26].

In order to evaluate off-target effects, the inflammatory response to the assembled gold-nanoconjugates (see Supplementary Information S1 for characterization of siRNA/RGD AuNPs) was evaluated as a known sensitive readout for local toxicity by bronchoalveolar lavage (BAL). Analysis of BAL cell counts provides insights into immunologic, inflammatory, neoplastic, and infectious processes occurring at the pulmonary level. BAL may also be helpful to identify alveolar hemorrhage, malignancy, or opportunistic infection. The method represents a valid diagnostic procedure also used to assess interstitial lung disease and the detection of lung tumor infiltrates by washing resident or inflammatory leukocytes as well as mediators from the alveolar and bronchial airspaces. Under healthy conditions alveolar macrophages represent the most frequent cell type recovered in BAL fluid (>95%), but lymphocyte and neutrophil numbers rapidly increase upon inflammation. Consequently, evaluation of the number of macrophages, lymphocytes and neutrophils was used to characterize the inflammatory response (Fig. 2A–C) upon treatment with AuNPs@PEG@RGD@siRNA in healthy mice during 1, 3 and 14 days. As expected, BAL from sham treated lungs reveals healthy conditions with normal alveolar macrophage numbers without any sign for an infection (Fig. 2A). Significant inflammatory neutrophil infiltration is noted for the high dose, 1 pmol AuNPs@PEG@RGD@siRNA treated groups on days 1 and 3 (Fig. 2A–B). In contrast for 0.3 pmol of AuNPs@PEG@RGD@siRNA the neutrophil influx seems negligible (Fig. 2C). During the acute phase of inflammation neutrophils are one of the first-responders to migrate towards the site of inflammation, and transient and over two weeks resolving increases of neutrophils in the lower respiratory tract were observed for AuNP treated mice thus characterizing a

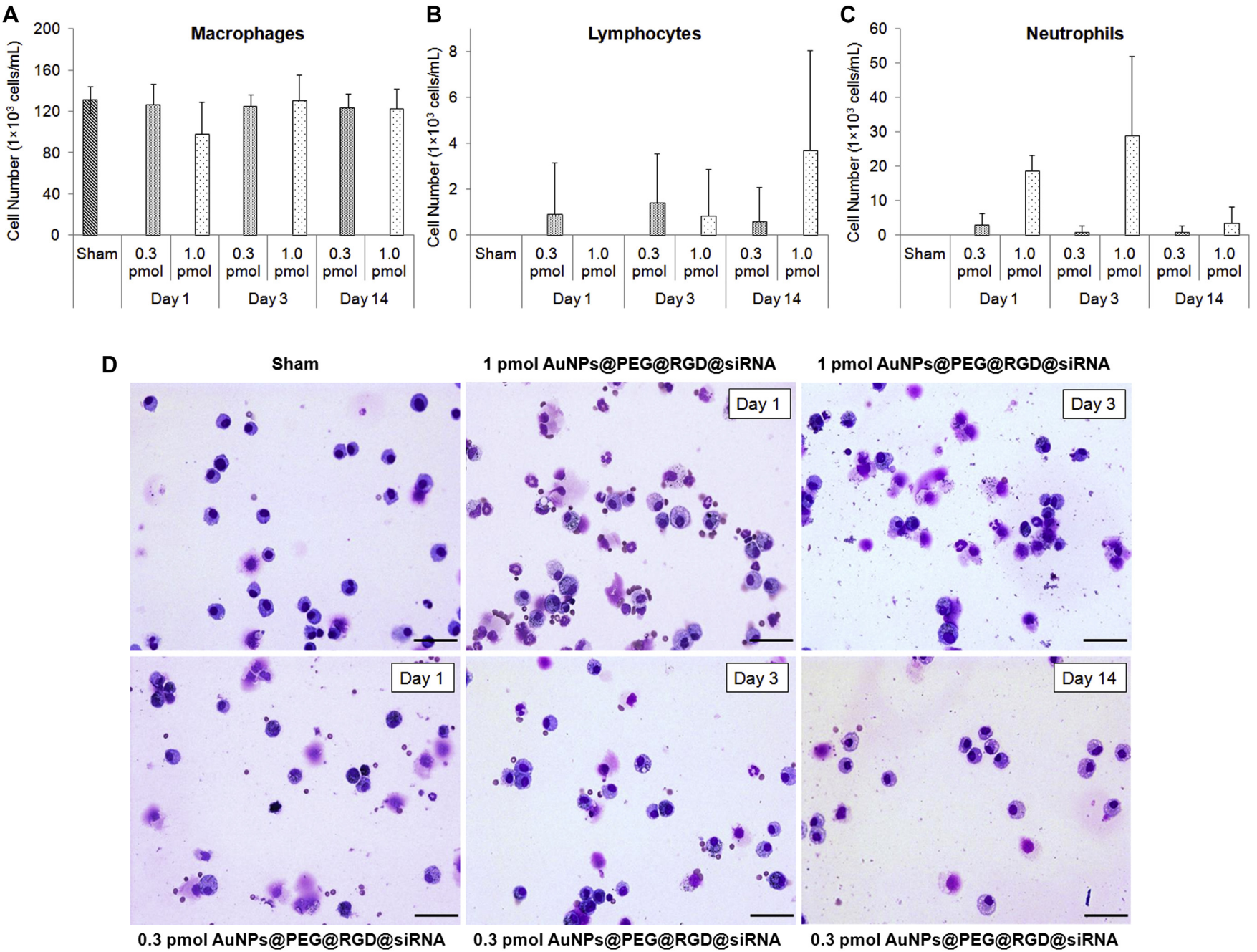

Fig. 2. Inflammatory response assessed by bronchoalveolar lavage (BAL) cell analysis. Inflammatory response to different doses of intratracheal instilled AuNPs@PEG@RGD@siRNA in the lungs of mice after 1, 3 and 14 days of treatment. Evaluation of the number of Macrophages (A), Lymphocytes (B) and Neutrophils (C) was used to characterize the inflammatory response. (D) Representative microscope images of BAL cells (scale bars, 50 μm) at days 1 and 3 for 1 pmol of AuNPs@PEG@RGD@siRNA and upon treatment with 0.3 pmol of AuNPs@PEG@RGD@siRNA in mice during 1, 3 and 14 days after AuNPs instillation.

typical moderate, acute inflammatory response. No significant increases in BAL lymphocyte numbers have been observed except with 1 pmol of AuNPs@PEG@RGD@siRNA 14 days after exposure to NPs (Fig. 2B). Fig. 2D shows representative light microscope images of cytospin preparations from BAL cells at days 1 and 3 for 1 pmol of AuNPs@PEG@RGD@siRNA and upon treatment with 0.3 pmol of AuNPs@PEG@RGD@siRNA in mice during 1, 3 and 14 days. No multinucleated macrophages were detected in all conditions, indicating biocompatibility of the nanomaterials over time.

Based on these data and considering that at a concentration of 0.3 pmol of AuNPs@PEG@RGD@siRNA caused no significant inflammatory response, this concentration was used for subsequent siRNA delivery studies.

3.2. siRNA silencing via RGD/siRNA–AuNPs in murine cell lines

Several reports have shown that therapeutic siRNA silencing is prone to off-target effects leading to cellular and systemic toxicity, which depends on the type of delivery system and commonly associated with lack of siRNA specificity and/or high doses of therapeutic agent. Specific gene knockdown activity is only attained when siRNA binding, internalization, and cytoplasmic release are achieved [2]. Previously we had observed an appreciable effect in the silencing of endogenous c-myc in healthy nude mice [19], which showed some variation between cell types and between different organisms. For that reason, the silencing efficiency was evaluated with other cell lines, and adenocarcinoma cells were selected to act as a proof of concept for subsequent studies and cancer treatment using this strategy.

Consequently, we conducted the molecular assessment of RNAi efficiency in three different murine cell lines (CCL-206 lung fibroblasts, and two alveolar epithelial type II like adenocarcinoma cell lines LA-4 and MLE12). To quantify efficiency of silencing, total RNAs from the three murine cell lines were extracted after 48 h of treating the cells with 0.3 pmol of all AuNPs conjugates and analyzed by qRT-PCR (Fig. 3A). The c-myc expression levels were determined using β-actin as reference gene. Treatment with naked siRNA alone was also analyzed for comparison, once does not freely cross the cell membrane, is relatively unstable in blood and serum and it is rapidly degraded by endo- and exo-nucleases.

Data show that steady state expression of c-myc was substantially inhibited by the specific AuNPs@PEG@RGD@siRNA at 48 h only for alveolar epithelial type II like adenocarcinoma LA-4 cells (78.7 ± 6.5% c-myc downregulation) (Fig. 3A). No significant silencing effect was observed for AuNPs@PEG only, AuNPs@PEG@RGD and AuNPs@PEG@siRNA, probably due to a lack of selectivity of the NPs towards the target cells. These results demonstrate that AuNPs@PEG@RGD@siRNA are potent and specific in c-myc expression silencing.

RGD integrin ligand is well-known for its capability to bind to the integrin αvβ3 receptor family, involved in a wide range of cell extracellular matrix and cell–cell interactions. The cell adhesion molecule αvβ3 integrin is a specific marker of angiogenesis and the expression of αvβ3 integrin correlates with tumor grade [27], suggesting a possible role as marker of malignancy. Therefore, the ability to target tumor cells via αvβ3 integrin in living subjects would allow a better tumor targeting and regression in regions with higher aggressiveness. This might be valuable to improve other anti-angiogenic and noninvasive antitumor therapies. In order to evaluate whether AuNPs@PEG@RGD@siRNA promote siRNA targeting in lung cancer cells via αvβ3 integrin interaction, flow cytometry analysis was performed in CCL-206 lung fibroblasts, LA-4 and MLE12 cells. Flow cytometry analysis (Fig. 3B) revealed highest levels of the RGD motive binding integrin αvβ3 expressed on LA4 cells ($P < 0.05$) compared to CCL-206 and MLE-12 cells. LA4 cells show 84.5% of positive cells for αvβ3 integrin antibody staining, showing that AuNPs@PEG@RGD@siRNA promotes siRNA targeting in LA-4 cancer cell and c-myc downregulation (Fig. 3A) via αvβ3 integrin interaction. The multifunctional arrangement of RGD on AuNPs may enhance the binding affinity to endothelial cells, promoting the delivery of c-myc siRNA to suppress tumor growth and angiogenesis. Moreover, direct conjugate of RGD ligands present in AuNPs@PEG@RGD@siRNA possibly saturates integrin receptors, resulting in inefficient receptor-mediated endocytosis, allowing enhanced cellular uptake. Actually, RGD-surface-modified nanoparticles, including polyplexes and liposomes, have been extensively used to deliver therapeutic genes, confirming the involvement of integrins in transfection [28]. Moreover, cellular uptake efficiency and intracellular distribution of the RGD/siRNA–AuNPs have been evaluated using transmission electron microscopy (see Supplementary Information S2).

These results validated RGD-directed stealth-based siRNA–AuNPs as an effective systemic nucleic acid delivery system. It should be pointed out that delivery targeting via αvβ3 integrin interaction could achieve therapeutic siRNA silencing delivery of nucleic acids to αvβ3 positive lung tumor cells.

3.3. Lung tumor targeting and therapeutic siRNA silencing via RGD/siRNA-AuNPs

Lung cancer is the most common cause of cancer-related death in men and women in the modern world [29] and the selectively reactivated expression of developmental regulator genes, such as c-myc have frequently been associated with lung tumor development and progression, and inhibition of c-myc expression may be sufficient to permanently stop tumor growth and induce regression of tumors [30]. However, ubiquitous inhibition of c-myc expression unavoidable leads to side effects, since regenerating tissue compartments require endogenous expression levels to sustain normal activity. Conversely, Soucek et al. show that c-myc inhibition triggers rapid regression of incipient and established lung tumors, defining an unexpected role for endogenous c-myc function in the maintenance of Ras-dependent tumors *in vivo*. Although systemic suppression of c-myc activity has profound effects on proliferating somatic tissues, these effects are well tolerated, without any discernible negative impact on animal well being and they are completely reversible. Thus, the authors demonstrate the feasibility of targeting c-myc, a common downstream conduit for many oncogenic signals, as an effective, efficient and tumor-specific cancer therapy [30].

With the attempt to translate the concept of gene therapy to clinical cancer therapeutics, the engineering of delivery systems that could achieve translocation of siRNA duplexes directly into the tumor cell cytoplasm and accomplish successful silencing has become essential. To ascertain whether the targeted delivery system can provide effective *in vivo* delivery of functional siRNA to tumors, a lung cancer tumor model in nude mice was established and treated with AuNPs@PEG@RGD@siRNA. Cancer model was achieved by intratracheal instillation of induction LA-4 adenocarcinoma cells (1×10^5 cells) into C57BL/6 mice lung for 4 weeks. After this period, 0.3 pmol of NPs (AuNPs@PEG@RGD and AuNPs@PEG@RGD@siRNA) and Sham (mice without induction of LA-4 adenocarcinoma cells and treated with water) were administrated by intratracheal instillation. After 72 h mice lungs were dissected and prepared for Hematoxylin and Eosin staining (H&E) to verify the extents of tumorigenesis by tissue sections. As expected, Sham tissue staining reveals healthy and normal alveolar architecture without any tumor (Fig. 4A). AuNPs@PEG@RGD treated group demonstrates a cancer lung tissue characterized by hypercellularity and thickened alveolar septa (Fig. 4B). Severe

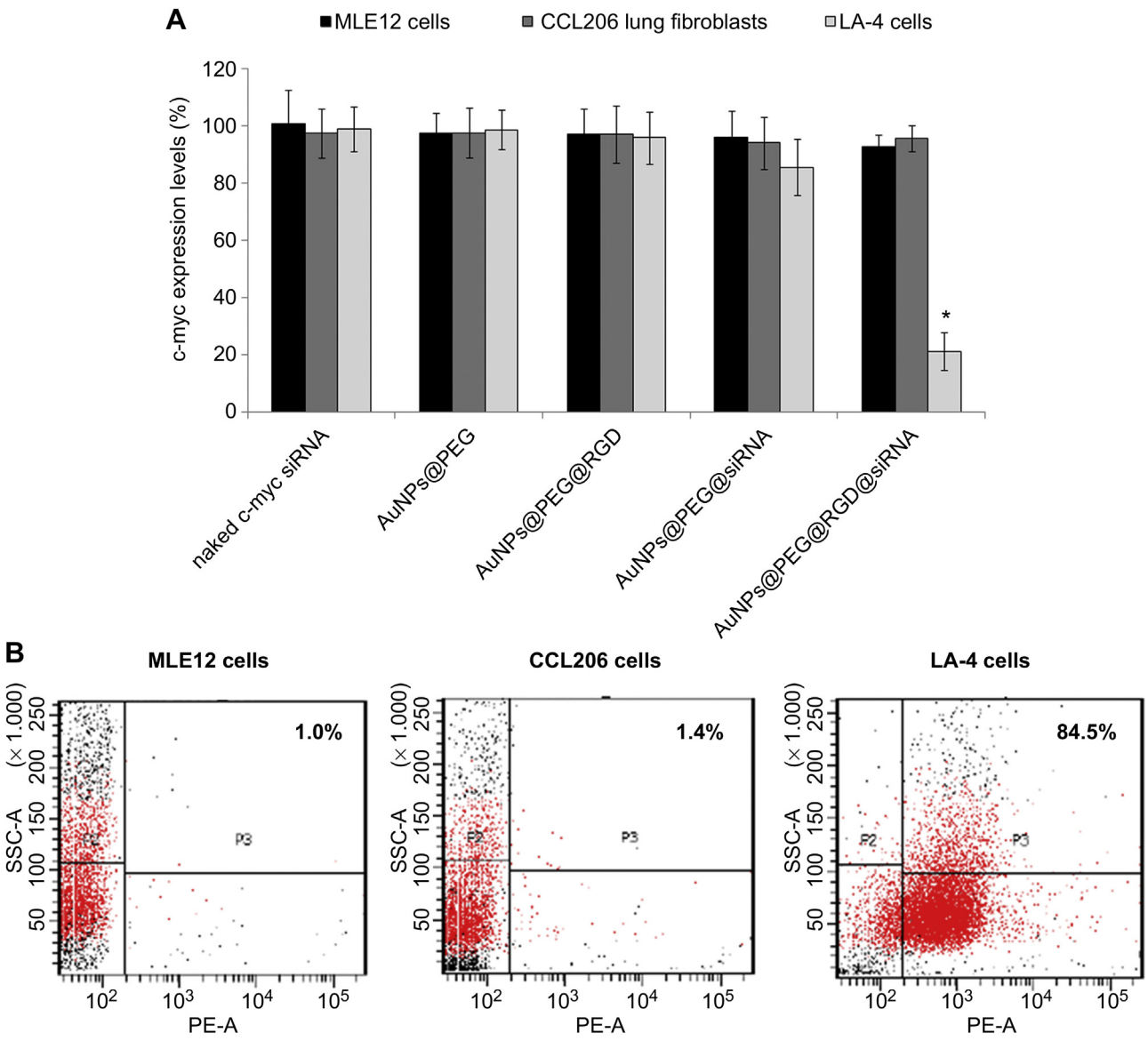

Fig. 3. siRNA mediated c-myc silencing via AuNPs@PEG@RGD@siRNA in murine cell lines. (A) Molecular assessment of RNAi efficiency. To quantify the efficiency of silencing, total RNAs from three different murine cell lines (CCL-206 lung fibroblasts, and two alveolar epithelial type II like adenocarcinoma cell lines LA-4 and MLE12), treated with various NP types was extracted after 48 h and analyzed by qRT-PCR. The c-myc mRNA expression levels were determined using β-actin as reference gene. Data marked with asterisks indicate statistically significant changes relative to the corresponding NP without RGD and siRNA (AuNPs@PEG) as calculated by paired sample *t* test (*, $P < 0.001$). (B) Flow cytometric profiling of αvβ3 integrin surface expression in the three different murine cell lines (CCL-206, LA-4 and MLE12). Within the dot-plots the upper right quadrant (P3) illustrates the fraction of αvβ3 integrin positive cells (84.5% for LA-4 cells, 1.4% for CCL-206 cells and 1.0% for MLE12 cells).

interstitial inflammatory cells infiltration is noted, with predominance of mononuclear cells and perivascular and peribronchiolar edemas as indicated by arrows. In the AuNPs@PEG@RGD-treated groups, no significant effect on tumor regression was obtained when compared to AuNPs@PEG@RGD@siRNA treated group. Essentially, in cancer lung AuNPs@PEG@RGD@siRNA (Fig. 4C) treatment group, there was a significant decrease in the incidence and severity of tumor clones in lung, revealing the capacity of AuNPs@PEG@RGD@siRNA in reducing tumor cells in a lung cancer mice model.

Previous studies with nanosized gold vectors have also proved successful results in lung tumor targeting. Lippard and Mirkin have exploited the rapid intracellular uptake of AuNPs to deliver and activate cisplatin and achieve efficient cytosolic delivery of this prodrug to lung cancer cells [31]. Similarly efficiency has also been demonstrated from AuNP conjugates of oxyplatin [32]. Furthermore, Chen et al. have also studied AuNPs conjugates of methotrexate, a dihydrofolate reductase inhibitor for the treatment of primary lung tumors [33].

However, the AuNPs@PEG@RGD@siRNA described here as targeted therapeutic approach for lung cancer therapy in murine cell lines and in this lung cancer syngenic orthotopic mouse model has not been described so far. In fact, our data suggests that intratracheal administration of AuNPs@PEG@RGD@siRNA leads to successful and statistically significant suppression of tumor cells in lung tissue.

Having determined that AuNPs@PEG@RGD@siRNA is delivered efficiently to cancer mice, we conducted the molecular assessment of c-myc silencing efficiency in the same lung tumor model (C57BL/6 mice induced with LA-4 adenocarcinoma cells). AuNPs@PEG@RGD and AuNPs@PEG@RGD@siRNA were administered (0.3 pmol) to 10–12 week aged mice ($n = 6–8$ animals) by

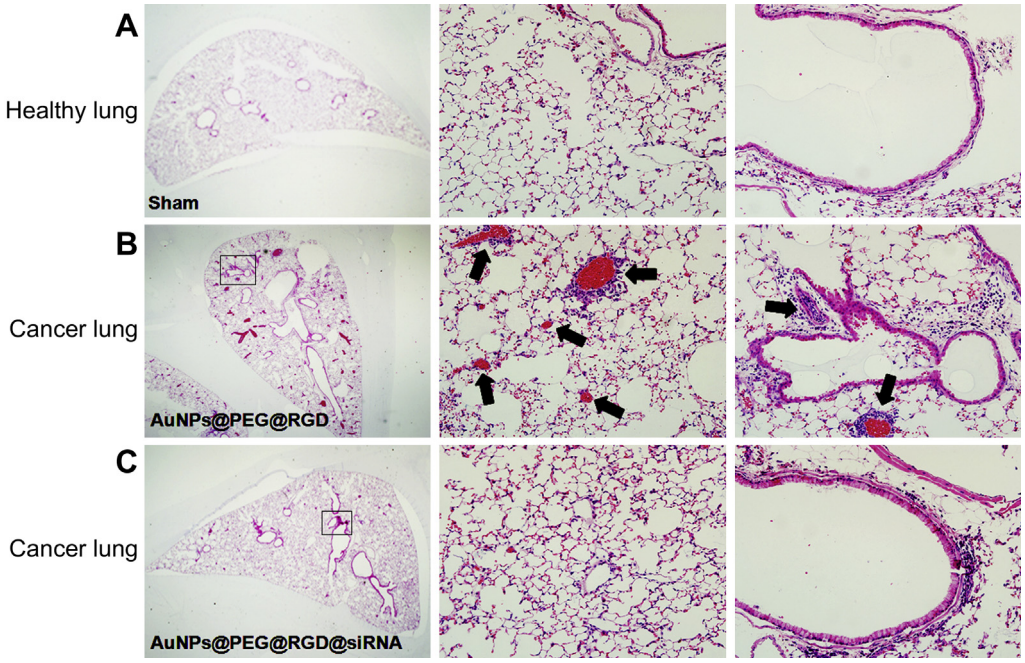

Fig. 4. Lung tumor treatment via AuNPs@PEG@RGD@siRNA. Hematoxylin and eosin (H&E) stains of (A) the Sham treated group (healthy lung tissue from untreated mice), (B) AuNPs@PEG@RGD treated group (LA4 induced lung cancer tissue) and (C) AuNPs@PEG@RGD@siRNA-treated group (LA4 induced lung cancer tissue). Severe interstitial infiltration of inflammatory cells is noted in the AuNPs@PEG@RGD treated group, with a predominance of mononuclear cells and perivascular and peribronchiolar edema (arrows). The lung cancer tissue is characterized by hypercellularity and thickened alveolar septa. In cancer lungs the AuNPs@PEG@RGD@siRNA treatment group, shows a significant decrease in the incidence and severity of inflammation, revealing the capacity of AuNPs@PEG@RGD@siRNA in reducing tumor cells in a lung cancer model on C57BL/6 mice induced with LA-4 adenocarcinoma cells.

intratracheal instillation. Since tumor cell apoptosis is an important indicator of treatment success, tumor cells were also stained for Caspase 3 detection. Fig. 5A,C shows high expression of MYC protein and positive staining of Caspase 3 in cytoplasm of tumor cells after exposure to AuNPs@PEG@RGD. Whereas, Fig. 5B,D illustrate tumor cells treated with AuNPs@PEG@RGD@siRNA and shows downregulation of local MYC expression and high expression of Caspase 3, probably leading tumor cells to apoptosis. On day 27

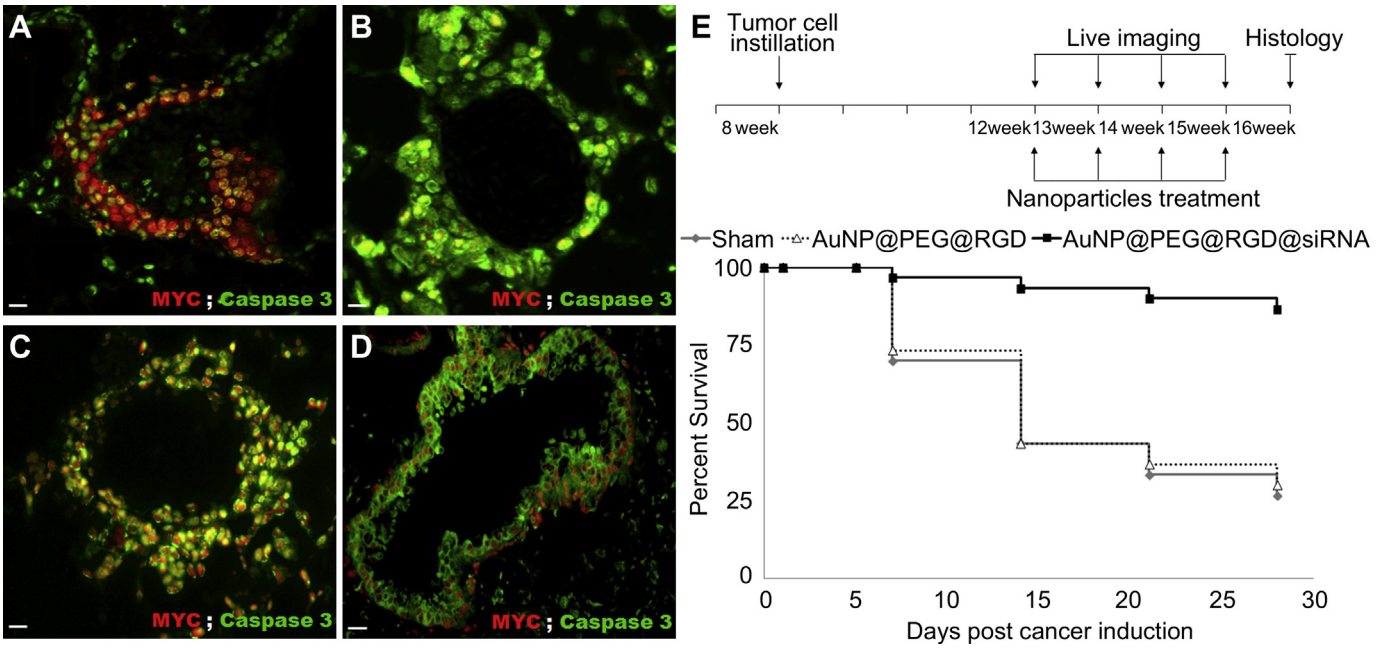

Fig. 5. Therapeutic siRNA silencing in murine lung cancer tissue. (A–D) Immunolocalization of MYC protein in tumor cells from C57BL/6 mice (induced with LA-4 adenocarcinoma cells) after 48 h of AuNPs@PEG@RGD (A,C) and AuNPs@PEG@RGD@siRNA (B,D) treatment. Tumor cells in lung tissue stained for Caspase 3 (green) and c-myc (red) (Scale bars, 50 μm). (E) Time course of tumor model induction, therapy and analysis as well as Kaplan–Meier survival rates for mice ($n = 30$ animals) treated with to AuNPs@PEG@RGD and AuNPs@PEG@RGD@siRNA after lung cancer induction. Sham mice were also inoculated with LA-4 adenocarcinoma cells but were not exposed to any type of nanoparticles. (For interpretation of the references to color in this figure legend, the reader is referred to the web version of this article.)

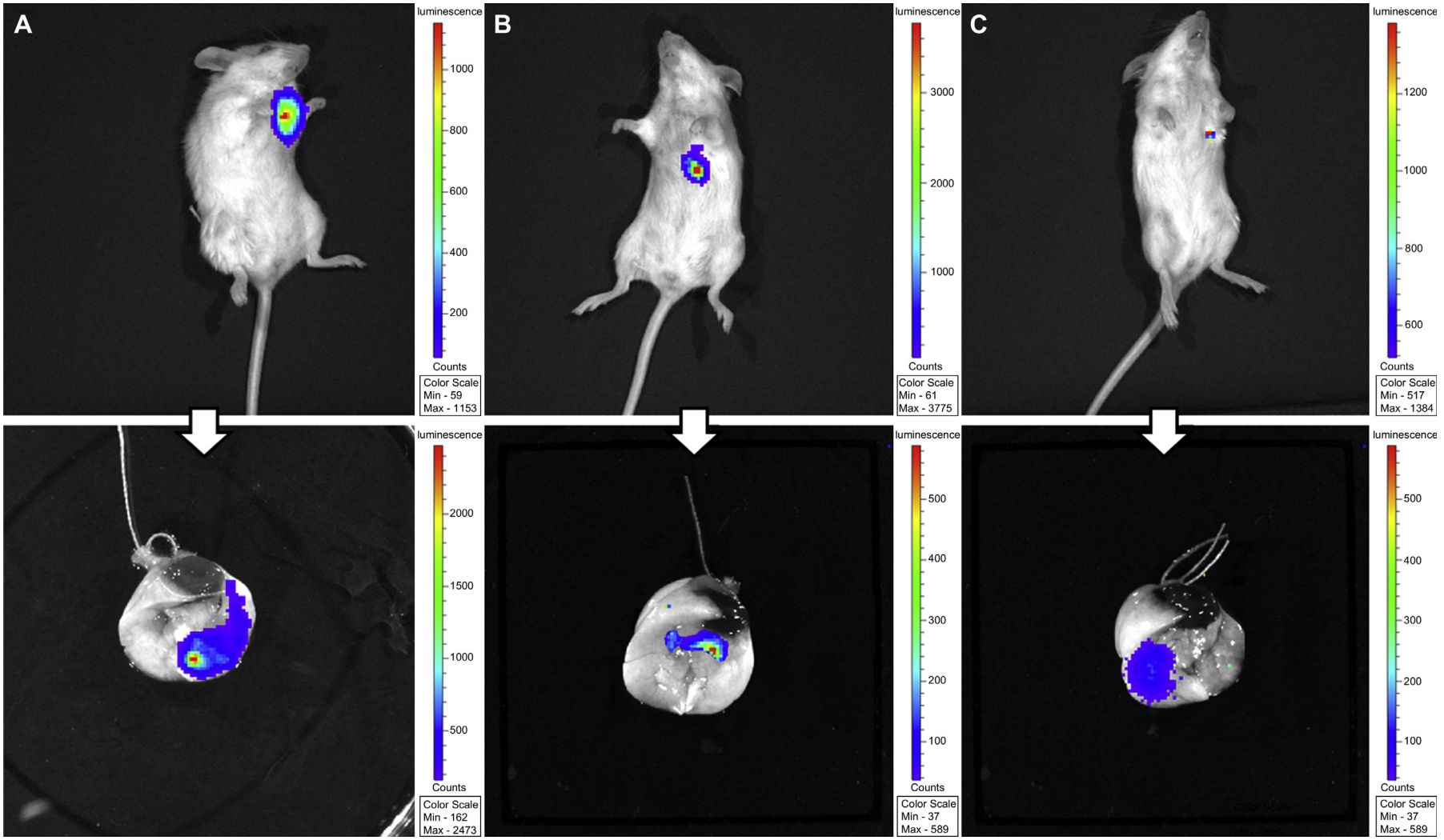

Fig. 6. Bioluminescent imaging of B6 albino mice injected with luciferase-CMT/167 adenocarcinoma cells ($n = 8$ animals per treated group). Bioluminescence imaging was performed to serially assed tumor size in each mouse, with luciferase activity as a measure for the tumor burden. Images show lung cancer mice and respective control lungs with no treatment (A), or with AuNPs@PEG@RGD (B) and AuNPs@PEG@RGD@siRNA (C) treatment. These bioluminescence images clearly depict a tumor regression (decrease of 80–90% related to fluorescence signal) in AuNPs@PEG@RGD@siRNA treated group.

after cancer induction the therapeutic outcome of AuNPs@PEG@RGD and AuNPs@PEG@RGD@siRNA was analyzed in terms of animal survival in a Kaplan–Meier curve (Fig. 5E) ($n = 30$ animals). Animals in the AuNPs@PEG@RGD@siRNA treated group demonstrated tumor growth inhibition, which resulted in significant increase in survival (approximately 80% increase) compared to AuNPs@PEG@RGD and sham mice without nanoparticle treatment (Fig. 5E). AuNPs@PEG@RGD@siRNA leads to a concomitant maintenance of survival of lung tumor-bearing animals. There was no significant increase in survival seen in animals treated only with AuNPs@PEG@RGD.

In order to test changes of lung tumor size in mice, bioluminescence imaging was carried out in a second model to serially assess lung tumor in each mouse (B6 albino female mice injected with luciferase-CMT/167 adenocarcinoma cells), treated with 0.3 pmol of AuNPs@PEG@RGD and 0.3 pmol of AuNPs@PEG@RGD@siRNA, with luciferase activity as a measure for tumor burden (Fig. 6). Briefly, stable clones of CMT/167 cells, derived from a spontaneous lung adenocarcinoma in B6 albino mice expressing high levels of firefly luciferase constitutively driven by an SV40 promoter (CMT/167-luc) as previously described [34]. Representative imaging of individual mice from each treated group ($n = 8$ animals) is shown, with the same scale of photon flux indicating luciferase activity. Fig. 6 shown images of lung cancer mouse with no NP treatment (Fig. 6A), with exposure to AuNPs@PEG@RGD (Fig. 6B) and AuNPs@PEG@RGD@siRNA (Fig. 6C). These bioluminescence images clearly depict tumor size regression (decrease of 80–90%) in AuNPs@PEG@RGD@siRNA treated group. Exposure to AuNPs@PEG@RGD without siRNA shows a negligible decrease of 1–5%.

Based on this data, the systemically delivery of AuNPs@PEG@RGD@siRNA was the only treatment condition that resulted in successful tumor growth inhibition and prolonged survival of the animals, in two lung cancer mice models (C57BL/6 female mice induced with LA-4 adenocarcinoma cells and B6 albino female mice injected with luciferase-CMT/167 adenocarcinoma cells). Using siRNA/RGD gold nanoparticles, targeted gene delivery based on selective expression of αvβ3 integrin in the tumor vasculature might become applicable to lung cancer gene therapy. In reality, the observed *in vivo* gene silencing and tumor regression by siRNA/RGD AuNPs suggests its possible use as a therapeutic agent for lung cancer, as well as opening a new translational avenue to approach the many diseases driven by deregulation of c-myc gene expression.

4. Conclusions

In summary, we report that RGD-functionalization of therapeutic nanoparticles can promote siRNA targeting in LA-4 cancer cell likely via αvβ3 integrin interaction leading to downregulation of c-myc oncogene expression. Moreover we show that, siRNA/RGD gold nanoparticles are capable of targeting tumor cells in two different orthotopic mouse models, resulting in successful and significant c-myc oncogene down-regulation and subsequent by tumor growth inhibition, as well as extended survival of mice bearing tumors.

Our findings pave the way for clinical cancer therapeutics via engineered and fine-tuned AuNPs@PEG@RGD@siRNA capable to deliver siRNA into lung tumor cells and effectively silence a proto-oncogene without side effects or toxicity.

Acknowledgments

Authors thank ERANET-NANOSCIERA NANOTRUCK project for financial support. We thank C. Tortiglione, G. Estrada, V. Grazu and V. Sanz for fruitful discussion. Authors thank I. Echaniz and S. Rivera for technical support. JMF thanks ARAID and Fondo Social Europeo for financial support. PVB thanks CIGMH/FCT/MCES (PEst-OE/SAU/UI0009/2011). JC acknowledges FCT grant (SFRH/BD/62957/2009).

Appendix A. Supplementary data

Supplementary data related to this article can be found at http://dx.doi.org/10.1016/j.biomaterials.2013.06.041.

References

[1] Fire A, Xu S, Montgomery MK, Kostas SA, Driver SE, Mello CC. Potent and specific genetic interference by double-stranded RNA in caenorhabditis elegans. Nature 1998;39:806–11.
[2] Wall NR, Shi Y. Small RNA: can RNA interference be exploited for therapy? The Lancet 2003;362:1401–3.
[3] Lee SH, Mok H, Jo S, Am Hong C, Park TG. Dual gene targeted multimeric siRNA for combinatorial gene silencing. Biomaterials 2011;32:2359–68.
[4] Li X, Xie QR, Zhang J, Xia W, Gu H. The packaging of siRNA within the mesoporous structure of silica nanoparticles. Biomaterials 2011;32:9546–56.
[5] Shrestha R, Elsabahy M, Florez-Malaver S, Samarajeewa S, Wooley KL. Endosomal escape and siRNA delivery with cationic shell crosslinked knedel-like nanoparticles with tunable buffering capacities. Biomaterials 2012;33:8557–68.
[6] Gil PR, Parak WJ. Composite nanoparticles take aim at cancer. ACS Nano 2008;2:2200–5.
[7] Peer D, Karp JM, Hong S, Farokhzad OC, Margalit R, Langer R. Nanocarriers as an emerging platform for cancer therapy. Nat Nanotechnol 2007;2:751–60.
[8] Lammers T, Aime S, Hennink WE, Storm G, Kiessling F. Theranostic nanomedicines. Acc Chem Res 2011;44:1029–38.
[9] Ghosh P, Han G, De M, Kim CK, Rotello VM. Gold nanoparticles in delivery applications. Adv Drug Deliv Rev 2008;60:1307–15.
[10] Conde J, Doria G, Baptista P. Noble metal nanoparticles applications in cancer. J Drug Deliv 2012;2012:751075.
[11] Lee SK, Han MS, Asokan S, Tung CH. Effective gene silencing by multilayered siRNA-coated gold nanoparticles. Small 2011;7:364–70.
[12] Kim ST, Chompoosor A, Yeh YC, Agasti SS, Solfiell DJ, Rotello VM. Dendronized gold nanoparticles for siRNA delivery. Small 2012;8:3253–6.
[13] Giljohann DA, Seferos DS, Prigodich AE, Patel PC, Mirkin CA. Gene regulation with polyvalent siRNA-nanoparticle conjugates. J Am Chem Soc 2009;131:2072–3.
[14] Lee Y, Lee SH, Kim JS, Maruyama A, Chen X, Park TG. Controlled synthesis of PEI-coated gold nanoparticles using reductive catechol chemistry for siRNA delivery. J Control Release 2011;155:3–10.
[15] Song WJ, Du JZ, Sun TM, Zhang PZ, Wang J. Gold nanoparticles capped with polyethyleneimine for enhanced siRNA delivery. Small 2010;6:239–46.
[16] Lee JS, Green JJ, Love KT, Sunshine J, Langer R, Anderson DG. Gold, poly(beta-amino ester) nanoparticles for small interfering RNA delivery. Nano Lett 2009;9:2402–6.
[17] Lee SH, Bae KH, Kim SH, Lee KR, Park TG. Amine-functionalized gold nanoparticles as non-cytotoxic and efficient intracellular siRNA delivery carriers. Int J Pharm 2008;364:94–101.
[18] Guo S, Huang Y, Jiang Q, Sun Y, Deng L, Liang Z, et al. Enhanced gene delivery and siRNA silencing by gold nanoparticles coated with charge-reversal polyelectrolyte. ACS Nano 2010;4:5505–11.
[19] Conde J, Ambrosone A, Sanz V, Hernandez Y, Marchesano V, Tian F, et al. Design of multifunctional gold nanoparticles for *in vitro* and *in vivo* gene silencing. ACS Nano 2012;6:8316–24.
[20] Li B, Chen J, Wang JH. RGD peptide-conjugated poly(dimethylsiloxane) promotes adhesion, proliferation, and collagen secretion of human fibroblasts. J Biomed Mater Res A 2006;79:989–98.
[21] Cai W, Sam Gambhir S, Chen X. Multimodality tumor imaging targeting integrin alphavbeta3. Biotechniques 2005;39:14–25.
[22] Götz AA, Rozman J, Rödel HG, Fuchs H, Gailus-Durner V, Hrabě de Angelis M, et al. Comparison of particle-exposure triggered pulmonary and systemic inflammation in mice fed with three different diets. Part Fibre Toxicol 2011;8:1–13.
[23] Schiller HB, Szekeres A, Binder BR, Stockinger H, Leksa V. Mannose 6-phosphate/insulin-like growth factor 2 receptor limits cell invasion by controlling alphaVbeta3 integrin expression and proteolytic processing of urokinase-type plasminogen activator receptor. Mol Biol Cell 2009;20:745–56.
[24] Steele JG, Rowlatt C, Sandall JK, Franks LM. Cell surface properties of high- and low-metastatic cell lines selected from a spontaneous mouse lung carcinoma. Int J Cancer 1983;32:769–79.
[25] Dobrovolskaia MA, Aggarwal P, Hall JB, McNeil SE. Preclinical studies to understand nanoparticle interaction with the immune system and its potential effects on nanoparticle biodistribution. Mol Pharm 2008;5:487–95.
[26] Lewinski N, Colvin V, Drezek R. Cytotoxicity of nanoparticles. Small 2008;4:26–49.
[27] Brooks PC, Clark RAF, Cheresh DA. Requirement of vascular integrin αvβ3 for angiogenesis. Science 1994;264:569–71.

[28] Erbacher P, Remy JS, Behr JP. Gene transfer with synthetic virus-like particles via the integrin-mediated endocytosis pathway. Gene Ther 1999;6:138–45.
[29] Siegel R, Naishadham D, Jemal A. Cancer statistics, 2012. CA Cancer J Clin 2012;62:10–29.
[30] Soucek L, Whitfield J, Martins CP, Finch AJ, Murphy DJ, Sodir NM, et al. Modelling Myc inhibition as a cancer therapy. Nature 2008;455:679–83.
[31] Dhar S, Daniel WL, Giljohann DA, Mirkin CA, Lippard SJ. Polyvalent oligonucleotide gold nanoparticle conjugates as delivery vehicles for platinum(IV) warheads. J Am Chem Soc 2009;131:14652–3.
[32] Brown SD, Nativo P, Smith JA, Stirling D, Edwards PR, Venugopal B, et al. Gold nanoparticles for the improved anticancer drug delivery of the active component of oxaliplatin. J Am Chem Soc 2010;132:4678–84.
[33] Chen YH, Tsai CY, Huang PY, Chang MY, Cheng PC, Chou CH, et al. Methotrexate conjugated to gold nanoparticles inhibits tumor growth in a syngeneic lung tumor model. Mol Pharmaceutics 2007;4:713–22.
[34] Li H, Sorenson AL, Poczobutt J, Amin J, Joyal T, Sullivan T, et al. Activation of PPARγ in myeloid cells promotes lung cancer progression and metastasis. PLoS One 2011;6:e28133.

SUPPLEMENTARY INFORMATION

In vivo tumor targeting via nanoparticle-mediated therapeutic siRNA coupled to inflammatory response in lung cancer mouse models

João Conde [a, b#], Furong Tian [c#], Yulán Hernández [a], Chenchen Bao [c,d], Daxiang Cui [d], Klaus-Peter Janssen[e], M. Ricardo Ibarra [a], Pedro V. Baptista [b], Tobias Stoeger [c]*, Jesús M. de la Fuente [a]*

[a] Instituto de Nanociencia de Aragon (INA), Universidad de Zaragoza, Zaragoza, 50018, Spain.

[b] CIGMH, Departamento de Ciências da Vida, Faculdade de Ciências e Tecnologia, Universidade Nova de Lisboa, Campus de Caparica, 2829-516 Caparica, Portugal.

[c] Comprehensive Pneumology Centre, Institute of Lung Biology and Disease, Helmholtz Zentrum München, Neuherberg, Germany.

[d] Department of Bio-Nano Science and Engineering, National Key Laboratory of Micro/Nano Fabrication Technology, Institute of Micro&Nano Science and Technology, Shanghai JiaoTong University, P.R.China.

[e] Department of Surgery, Klinikum rechts der Isar, Technische Universität München, Ismaninger Strasse 22, Munich, Germany.

# These authors contribute equal to the paper

[*] Corresponding-Authors

S1. Preparation and characterization of RGD/siRNA-gold nanoparticles

Spherical citrate-AuNPs with an average diameter of 14±1 nm (**Figure S1A Inset**) were functionalized with two kinds of poly(ethylene glycol) (PEG) spacers, a RGD peptide and an siRNA molecule to c-myc gene. The high monodispersity of the gold core was confirmed by Transmission Electron Microscopy (TEM) (**Figure S1A**). The diameter of citrate-AuNPs observed by TEM was in good agreement with the DLS measurement, showing an average diameter of 14.7 nm with relatively narrow distribution (polydispersity index 0.197±1.529). The UV-Vis molecular absorption spectra of the citrate-AuNPs show the characteristic surface plasmon resonant peak at 519 nm, presenting at pH 7 a negative Zeta potential value of -12.32 mV.

PEGylated AuNPs with 15% saturated PEG layer, were functionalized with 50% carboxylic groups (SH-EG(8)-$(CH_2)_2$-COOH) and 50% of azide groups (SH-$(CH_2)_3$-CONH-EG(6)-$(CH_2)_2$-N_3). The 15% of saturated PEG layer (1250.5±279.8 PEG chains per nanoparticle) allows the incorporation of further thiolated components, such as the thiolated siRNA. The carboxylated spacer provides the anchoring moieties for the covalent binding of amine-containing molecules through carbodiimide chemistry. Besides, PEG-carboxylic and PEG-azide were used as opposite polyelectrolytes in order to improve nanoparticle transfection and gene silencing efficiency. PEGylated AuNPs (AuNP@COOH/N_3) were then functionalized with Arg-Gly-Asp (RGD peptide) amino acid sequence by EDC/NHS coupling reaction between the carboxylated spacer and the amine terminal group of the RGD peptide (20.6±0.7 RGD peptides per nanoparticle). Consequently, AuNPs@COOH/N_3@RGD were functionalized with a siRNA molecule (62.9±0.7 RGD peptides per nanoparticle) complementary to a master regulator gene, the proto-oncogene c-myc.

It is known that the solubility of the coated AuNPs is largely affected by size and surface charges. Therefore, the process of AuNPs functionalization was monitored by Dynamic Light

Scattering (DLS) (**Figure S1B**) and Zeta potential (**Figure S1C)** measurements of all AuNPs conjugates. Additionally, the spatial arrangement of AuNPs can be inferred by measuring the shift of a characteristic surface plasmon band. In fact, the Surface Plasmon Resonance (SPR) of the AuNPs shown in **Figure S1B** exhibited a red shift from 519 to 525nm when PEG, RGD and siRNA were bound. SPR peaks showed a 3 nm shift of the SPR when the RGD peptide is bound to the nanoparticles whereas the shift is higher (5 nm) after siRNA binding.

The determination of the degree of saturation of AuNPs functionalized with thiolated poly(ethylene glycol) chains and quantification of RGD peptides and siRNA strands per nanoparticle was extensively described elsewhere [19].

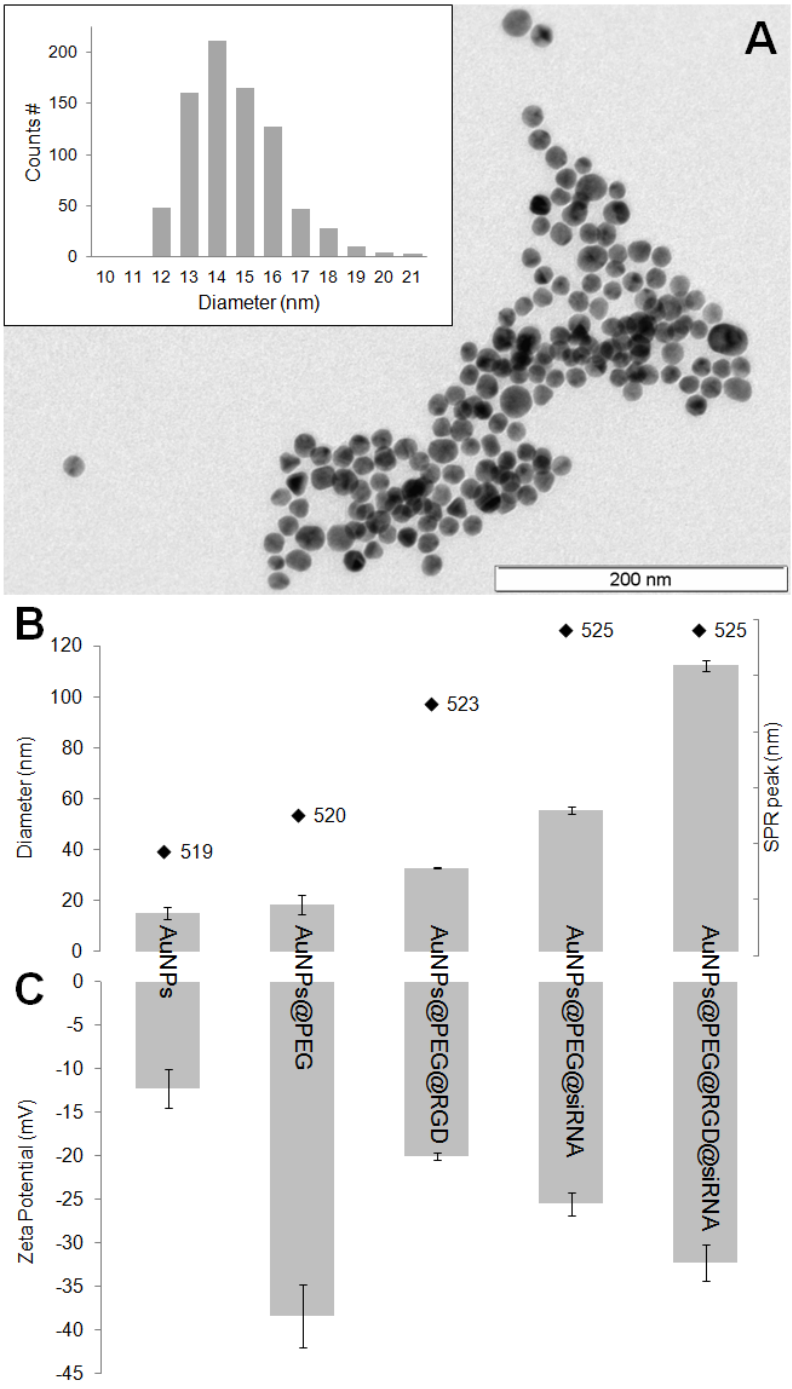

Figure S1. Physical characterization of AuNPs conjugates. (**A**) Transmission Electron Microscopy (TEM) of citrate-AuNPs, **Inset:** size distribution histogram showing an average diameter of 14±1 nm. (**B**) Dynamic Light Scattering (DLS) showing average diameter of AuNPs conjugates and Surface Plasmon Resonance (SPR) shift peaks. (**C**) Surface charge measurements by Zeta Potential at each functionalization step.

S2. RGD/siRNA-gold nanoparticles internalization in lung cells

In order to assess the effectiveness of gene silencing in lung tumor cells, cellular uptake efficiency and intracellular distribution of the RGD/siRNA–AuNPs have been evaluated using transmission electron microscopy (TEM) (see **Figure S2A,B**). TEM images of LA-4 lung epithelial cells treated with 0.3 pmol of RGD/siRNA–AuNPs (AuNP@PEG@RGD@siRNA) show NPs in the cytoplasm as single units, supporting the correct delivery of siRNA to initiate RNAi. LA-4 induced tumor mice were treated with 0.3 pmol of RGD/siRNA–AuNPs by intratracheal instillation. At 24 hours (**Figure S2A**) after instillation, some NPs are located outside of tumor cell membranes and a few NPs are inside vesicles. At 48 hours (**Figure S2B**), bigger amounts of NPs are found in vesicles or free in cytoplasm. RGD/siRNA–AuNPs were exclusively localized in the cytoplasm where siRNA mediates its function, thus demonstrating that these RGD/siRNA capped-AuNPs facilitate the intracellular distribution of siRNA to cytoplasm.

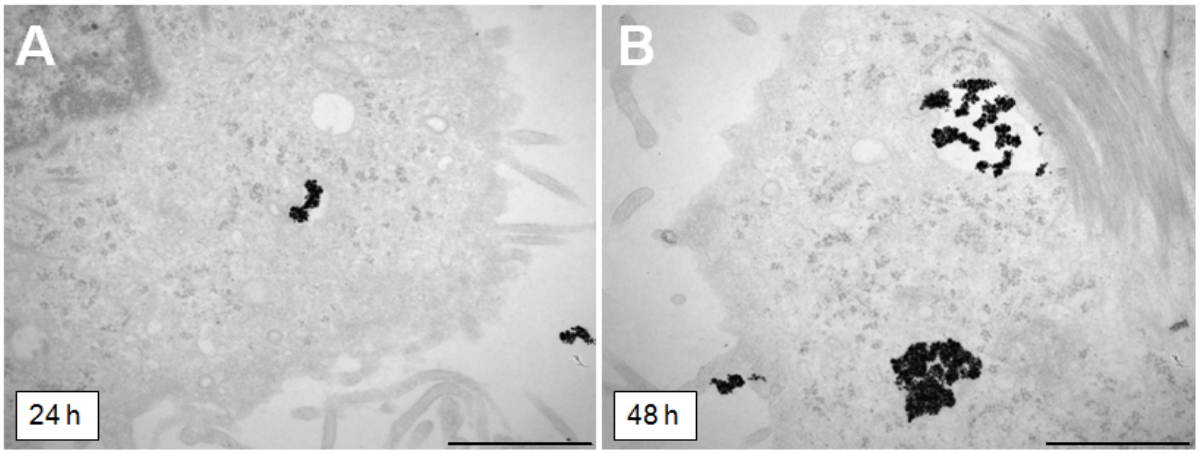

Figure S2. RGD/siRNA-gold nanoparticles internalization in lung cancer cells (**A, B**) TEM images of lung cancer cells. Mice implanted with LA-4 cancer cells were treated with 0.3 pmol of AuNP@PEG@RGD@siRNA by intratracheal instillation. At 24 hours (**A**) after instillation, TEM images show NPs located outside of the cell but a few NPs also located inside cellular vesicles. After 48 hours (**B**), bigger amounts of NPs are found in vesicles or also free in cytoplasm (scale bars, 500 nm).

❹

Gold Nanoparticles for Theranostics

OVERVIEW

This section presents 3 articles related to the studies on gold nanoparticles as nanovectors for both diagnostics and therapy applications – Theranostics.

Article I describes the development of a direct method to follow RNA synthesis in real time based on gold nanoparticles (AuNPs) functionalized with a fluorophore labeled hairpin-DNA, i.e. gold-nanobeacon (Au-nanobeacon). With a reporter Au-nanobeacon we were able to measure the rate of in vitro RNA synthesis. At the same time, we designed a second Au-nanobeacon targeting the promoter sequence (inhibitor) so as to inhibit transcription whilst simultaneously monitor the number of promoters being silenced. Using the two Au-nanobeacons in the same reaction mixture, we are capable of quantitatively assess in real time the synthesis of RNA and the level of inhibition. This strategy defines the way of using these gold nanoconjugates for the detection (diagnostic) and at the same time for the inhibition of specific genes (therapy).

This gold-nanobeacon concept was extended and adapted to a universal tool for RNAi, from gene specific silencing to silence-the-silencers (**Article J**). For the first time, we reported the potential of a single molecular nanoconjugate to intersect all RNA pathways: from gene specific downregulation to silencing the silencers, i.e. siRNA and miRNA pathways. Gold-nanobeacons were capable of efficiently silencing single gene expression, exogenous siRNA and endogenous miRNAs while yielding a quantifiable fluorescence signal directly proportional to the level of silencing.

In **Article K** we evaluate the genotoxicity, cell toxicity and proteome profiling analysis of the previous gold-nanobeacons system for gene therapy. An integrated toxicology evaluation was performed based on acute cell toxicity, genomic DNA damage and proteome profiling showing that the proposed strategy does not exhibit significant toxicity, which is extremely relevant when translating into in vivo systems.

All these studies were performed at the Research Centre for Human Molecular Genetics, Dept. of Life Sciences at Science and Technology Faculty, New University of Lisbon.

Article I

"Gold-Nanobeacons for Real-Time Monitoring of RNA Synthesis." J. Rosa*, **João Conde***, J.M. de la Fuente, J.C. Lima and P.V. Baptista. (* Co-first authors). **Biosensors & Bioelectronics** (2012), Vol. 36, pp. 161-167. *Research article (IF=5.437)*

Article J

"Gold-nanobeacons for simultaneous gene specific silencing and intracellular tracking of the silencing events." **João Conde**, J. Rosa, J.M. de la Fuente and P.V. Baptista. **Biomaterials** (2013), Vol. 34, pp. 2516–2523. *Research article (IF=7.604)*

Article K

"A Gold-nanobeacon system for Gene therapy: evaluation of Genotoxicity, Cell toxicity and Proteome profiling analysis" **João Conde**, M. Larguinho, A. Cordeiro, L.R. Raposo, P.M. Costa, S. Santos, M.S. Diniz, A.R. Fernandes and P.V. Baptista. **Nanotoxicology** (2013). *Research article (IF=7.844)*

Articles I, J and **K**

Declaration of authorship

I, João Diogo Osório de Castro Conde, declare that the manuscripts preparation and writing was carried out by me, Prof. Pedro V. Baptista, Prof. Jesus M. de la Fuente, and all the associated co-authors.

João Conde contributions:

Article I – JC designed the method, generated the Au-nanobeacons, calibrated, carried out characterization and performed the *in vitro* assays. JC also drafted the manuscript and all the figures.

Article J – JC designed the method, generated the Au-nanobeacons, calibrated, carried out characterization and performed the *in vitro* assays. JC performed the cell studies and molecular calibration assays. JC analyzed the data and wrote the manuscript.

Article K – JC carried out all the synthesis and functionalization methods regarding the production of all nanoformulations in this study. JC performed the gene silencing and citotoxicity assays. JC analysed all the data and wrote some sections of the manuscript.

We, Pedro V. Baptista and Jesus M. de la Fuente, as supervisors of João Conde hereby acknowledge and confirm that the information above is correct.

João Conde

Pedro V. Baptista

Jesus M. de la Fuente

Biosensors and Bioelectronics 36 (2012) 161–167

Contents lists available at SciVerse ScienceDirect

Biosensors and Bioelectronics

journal homepage: www.elsevier.com/locate/bios

Gold-nanobeacons for real-time monitoring of RNA synthesis

João Rosa [a,b,1], João Conde [a,c,1], Jesus M. de la Fuente [c], João C. Lima [b], Pedro V. Baptista [a,*]

[a] CIGMH, Departamento de Ciências da Vida, Faculdade de Ciências e Tecnologia, Universidade Nova de Lisboa, Campus de Caparica, 2829-516 Caparica, Portugal
[b] REQUIMTE, Departamento de Química, Faculdade de Ciências e Tecnologia, Universidade Nova de Lisboa, Campus de Caparica, 2829-516 Caparica, Portugal
[c] Instituto de Nanociencia de Aragón, Universidad de Zaragoza, Campus Ri˙o Ebro, Edifi˙cio I+D, Mariano Esquillor, s/n, 50018 Zaragoza, Spain

ARTICLE INFO

Article history:
Received 31 January 2012
Received in revised form
20 March 2012
Accepted 9 April 2012
Available online 20 April 2012

Keywords:
Gold nanoparticles
Fluorophore labeled hairpin-DNA
Gold-nanobecons
RNA synthesis
Inhibition of transcription

ABSTRACT

Measuring RNA synthesis and, when required, the level of inhibition, is crucial towards the development of practical strategies to evaluate silencing efficiency of gene silencing approaches. We developed a direct method to follow RNA synthesis in real time based on gold nanoparticles (AuNPs) functionalized with a fluorophore labeled hairpin-DNA, *i.e.* gold-nanobeacon (Au-nanobeacon). Under hairpin configuration, proximity to gold nanoparticles leads to fluorescence quenching; hybridization to a complementary target restores fluorescence emission due to the Au-nanobeacons' conformational reorganization that causes the fluorophore and the AuNP to part from each other, yielding a quantitative response. With this *reporter* Au-nanobeacon we were able to measure the rate of *in vitro* RNA synthesis (~10.3 fmol of RNA per minute). Then, we designed a second Au-nanobeacon targeting the promoter sequence (*inhibitor*) so as to inhibit transcription whilst simultaneously monitor the number of promoters being silenced. Using the two Au-nanobeacons in the same reaction mixture, we are capable of quantitatively assess in real time the synthesis of RNA and the level of inhibition.

The biosensor concept can easily be extended and adapted to situations when real-time quantitative assessment of RNA synthesis and determination of the level of inhibition are required. In fact, this biosensor may assist the *in vitro* evaluation of silencing potential of a given sequence to be later used for *in vivo* gene silencing.

1. Introduction

Monitoring and controlling RNA synthesis is of great relevance for understanding the cell (and the organism) homeostasis. The ability to scrutinize cellular processes *in vitro* has become an important tool for novel approaches to gene studies and for molecular therapeutics (Agrawal, 1996; Fichou and Ferec, 2006; Tamm et al., 2001; Toub et al., 2006). Several techniques to analyze RNA synthesis *in vitro* have been described, *e.g.* Northern Blot (Bor et al., 2006), RT-PCR (Freeman et al., 1999; Weis et al., 1992) and cDNA microarrays (Schena et al., 1995). In addition, molecular beacons have provided a rapid and sensitive system capable of efficient quantitative monitoring of RNA synthesis and/or inhibition in real-time. A molecular beacon is a stem–loop DNA single-stranded-oligonucleotide that carries a fluorophore and a quencher at both ends: in absence of target, the stem–loop structure is closed forcing the fluorophore and the quencher to close proximity, resulting in fluorescence quenching; upon hybridization to a complementary target the stem–loop sequence opens, the fluorophore and quencher are spatially separated and the fluorescence is restored (Tan et al., 2004; Tyagi and Kramer, 1996). Fluorescence monitoring allows quantitative kinetic analysis of the conformation changes occurring in the molecular beacon under various situations such as real-time monitoring of DNA cleavage caused by enzymes (Li et al., 2000a, 2000b), protein–DNA interaction studies (Li et al., 2000a, 2000b), real-time *in vitro* transcription monitoring (Liu et al., 2002; Marras et al., 2004) and real-time PCR detection (Waltz et al., 2005).

Although robust, traditional molecular beacons can be easily degraded by nucleases that are often residually present in reaction mixtures and/or in cellular extracts, rendering the beacons ineffective. Gold nanoparticles (AuNPs) can overcome this problem by conferring protection against nucleases (Conde et al., 2010; Rosi et al., 2006) whilst maintaining the quenching and sensing properties of the beacon (Baptista et al., 2008; Baptista, 2009; Lakowicz, 2006; Paciotti et al., 2004; Quarta et al., 2007; Saha et al., 2012; Seferos et al., 2007). The combination of the optical properties of AuNPs with fluorophores in a molecular beacon conformation (Au-nanobeacon) have been used to detect sequence-specific DNA targets (Song et al., 2009) and even be more sensitive in detecting single-mismatch than regular molecular beacons (Dubertret et al., 2001).

Recently, we have assisted to a renewed interest in gene silencing strategies that aim to decrease the effective capability

* Corresponding author. Tel./fax: +351 212948530.
E-mail address: pmvb@fct.unl.pt (P.V. Baptista).
[1] These authors contributed equally to the work.

0956-5663/$ - see front matter © 2012 Elsevier B.V. All rights reserved.
http://dx.doi.org/10.1016/j.bios.2012.04.006

of a given gene to express itself, either by an inhibition of transcription or via an increased specific degradation. In fact, ssDNA-functionalized AuNPs have already been used in modulation of *in vitro* transcription and translation (Agbasi-Porter et al., 2006; Conde et al., 2010). Evaluation of transcription inhibition is usually assessed mainly by end-point quantification of RNA synthesis and comparison to transcription levels without silencing. However, when evaluating the effectiveness of inhibition, it is of utmost relevance to ascertain the number of molecules being *de facto* silenced, and correlating the level of inhibition to that of product production (*i.e.* RNA). Doing so in real-time would also provide information on the kinetics involved, thus yielding important information towards optimization of silencing strategy, re-design of target and effector sequences, etc (Rayburn and Zhang, 2008).

Here, we present a two-gold-nanobeacon system for the real-time monitorization of RNA transcription and inhibition: one Au-nanobeacon monitors the transcription level (*reporter*), and a second Au-nanobeacon acts as inhibitor of transcription (*inhibitor*) that quantitatively assesses the number of sequences being inhibited. Because the inhibitor reports on the number of targets it binds to, we attain real time quantification of the number of sequences being silenced at one time, and the consequent effect on transcription is provided by the reporter Au-nanobeacon—Fig. 1. This dual-biosensing system may be a practical and straightforward tool for kinetics and mechanistic studies in gene silencing approaches.

2. Experimental details

2.1. Materials

All chemicals were purchased from Sigma Aldrich in the highest purity available and used without further purification. T7 RNA Polymerase and Revert-Aid™ M-MuLV Reverse Transcriptase were purchased from Fermentas. DNase I and SYBR® GreenER Real-Time PCR Kit purchased from Invitrogen. All oligonucleotides were purchased from STAB Vida, Portugal.

2.2. Synthesis of citrate–gold nanoparticle

Gold nanoparticles with an average diameter of ~14 nm were synthesized by the citrate reduction method described by Lee and Meisel (1982). Briefly, 1 mM hydrogen tetrachloroaureate (III) hydrate (88.61 mg) was dissolved in 500 ml of distilled water, heated and stirred under reflux. Then, 38.8 mM sodium citrate tribasic dihydrate (285 mg) was added resulting in a red solution. The solution is kept under ebullition and protected from light for 30 min. After this, the solution is cooled down to room temperature

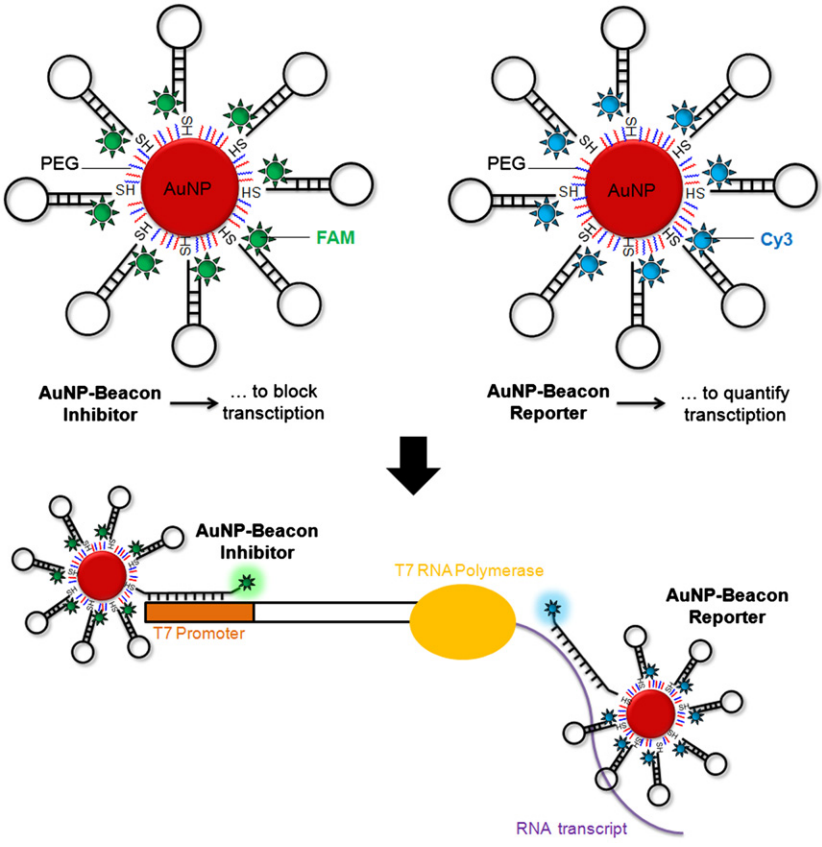

Fig. 1. *Gold-nanobeacons for monitoring and inhibition of real-time RNA synthesis.* An Au-nanobeacon is composed of a hairpin DNA structure with a gold nanoparticle at 5′ and a fluorophore at 3′. When the hairpin has its stem–loop structure formed, the fluorophore is forced to be in close proximity with gold nanoparticles and fluorescence is quenched due to gold nanoparticles modulation properties on standard organic fluorophores. On the other hand, in the presence of a target that can hybridize with the loop sequence of the hairpin the stem–loop structure is opened and the fluorophore is parted from the gold nanoparticles resulting in restoration of fluorescence. A cy3-labeled Au-nanobeacon hybridizes with the RNA transcript as it is formed in an *in vitro* reaction acting as a reporter of the levels of transcription. Simultaneously, a FAM-labeled Au-nanobeacon is used to hybridize with the T7 promoter region of the dsDNA template which results in inhibition of *in vitro* transcription. The fluorescence of both Au-nanobeacons is measured and quantification of both as to how many T7 promoter sites are being blocked and how many RNA products are being formed is retrieved.

and kept protected from light. Citrate–gold nanoparticles were characterized by Transmission Electron Microscopy (TEM) and UV–vis spectroscopy (see Figure S1 in Supplementary Information).

2.3. Gold-nanobeacons syntheses

We prepared two gold-nanobeacons: the inhibitor, a stem–looped oligonucleotide double labeled with 3′-FAM and 5′-Thiol-C6 (5′-TTTGCATCTCCCTATAGTGAGTCGTATTATGCAAA-3′) complementary to the promoter region recognized by T7-RNA polymerase, thus capable of blocking the transcriptional machinery at the specific promoter site; the reporter, a stem–looped oligonucleotide double labeled with 3′-Cy3 and 5′-Thiol-C6 (5′-TTTGCATAGCTGTTCAAGTTTGTGTTTCATGCAAA-3′) complementary to the *c-MYC* transcript produced by *in vitro* transcription—see below. Briefly, the thiolated oligonucleotides (STAB Vida, Portugal) were suspended in 1 mL of 0.1 M dithiothreitol (DTT), extracted three times with ethyl acetate and further purified through a desalting NAP-5 column (Pharmacia Biotech, Sweden) using 10 mM phosphate buffer (pH 8) as eluent. Following oligonucleotide quantification via UV/Vis spectroscopy, each oligomer was added to the AuNP solution in a 50:1 ratio. AGE I solution (2% (w/v) SDS, 10 mM phosphate buffer (pH 8)) was added to the mixture to achieve a final concentration of 10 mM phosphate buffer (pH 8), 0.01% (w/v) SDS. The solution was sonicated for 10 s using an ultrasound bath and incubated at room temperature for 20 min. After this period, 0.045 mg/mL of O-(2-Mercaptoethyl)-O′-methyl-hexa(ethylene glycol), $C_{15}H_{32}O_7S$ was added to the mixture and incubated for another 20 min at room temperature. Afterwards, the ionic strength of the solution was increased sequentially in 50 mM NaCl increments by adding the required volume of AGE II solution (1.5 M NaCl, 0.01% (w/v) SDS, 10 mM phosphate buffer (pH 8)) up to a final concentration of 10 mM phosphate buffer (pH 8), 0.3 M NaCl, 0.01% (w/v) SDS. After each increment, the solution was sonicated for 10 s and incubated at room temperature for 20 min before the next increment. Following the last addition, the solution was left to rest for additional 16 h at room temperature. Then, the functionalized Au-nanobeacons were centrifuged for 20 min at 21,460 × *g*, the oily precipitate washed three times with DEPC-treated H_2O, and redispersed in the same buffer to a final concentration in Au-nanobeacons of 15 nM. The resulting Au-nanobeacons were stored in the dark at 4 °C until further use.

2.4. Quantitation of beacon coverage on AuNPs

Coverage, *i.e.* average number of labeled beacons per nanoparticle was assessed following complete displacement of the thiolated oligonucleotides (beacons) from the AuNP by means of 0.12 mM β-Mercapthoethanol incubation for 48 h. After 48 h at room temperature, the solutions were centrifuged at 14500*g* for 20 min. The concentration of beacon in the supernatant was measured by monitoring the emission spectra of FAM (Exc = 490 nm) or Cy3 (Exc = 530 nm) dyes in a Cary Eclipse (Varian, USA) using an Ultra-Micro quartz cell (Hëllma, Germany). All the AuNPs samples and the standard solutions of the thiol-oligonucleotide beacon were kept at the same pH and ionic strength and calibration for all measurements. Fluorescence emission was converted to molar concentrations of the thiol modified oligonucleotide by interpolation from a standard linear calibration curve. Standard curves were prepared with known concentrations of beacon using the same buffer pH, salt, and β-Mercapthoethanol concentrations. The average number of molecular beacon strands per particle was obtained by dividing the oligonucleotide molar concentration by the AuNP concentration.

2.5. RNA extraction and cDNA production

Total RNA extracted from HL-60 cells was subjected to RT for cDNA synthesis with Revert-AidTM M-MuLV Reverse Transcriptase (Fermentas, Vilnius, Lithuania) according to the manufacturer's specifications, using 20 μM of MYCreverse primer, annealing at 42 °C for 1 h and 70 °C for 10 min to reverse transcriptase inactivation. Gene specific primers MYCforward: 5′-GCTCATTTCTGAAGAGGACTTGT-3′ and MYCreverse: 5 ≤ -AGGCAGTTTACATTATGGCTAAATC-3′ can then be used to PCR amplify a 229-bp fragment of the human v-myc myelocytomatosis viral oncogene homolog (c-MYC) gene (Gene-Bank accession no. NM_002467.4).

2.6. Transcription template preparation and purification

PCR amplification of the c-MYC specific fragment was performed in duplicate on a MyCycler Thermocycler (Biorad) in 25 μL using 1 μM of primers, 2.5 mM dNTPs with 1 U Taq DNA Polymerase (Amersham Biosciences, GE Healthcare, Europe, GmbH), with the following thermal cycling conditions: initial 5 min denaturation at 95 °C, followed by 30 amplification cycles of denaturation at 95 °C for 30 s, annealing at 62 °C for 30 s, elongation at 72 °C for 30 s, and a final elongation at 72 °C for 5 min. This amplification product was re-amplified under the same reaction conditions and thermal cycling as above using a T7 promoter – MYCforward primer (5′-TAATACGACTCACTATAGGGAGAGCTCATTTCTGAAGAGGACTTGT-3′). The resulting 252-bp *T7-MYC*-fusion fragment was then PCR amplified using primers MYCreverse and T7 primer (5′-TAATACGACTCACTATAGGGAGA-3′) as described above and purified through band gel extraction. Confirmation of correct PCR products was performed by 2% agarose gel electrophoresis stained with GelRed™. This amplification product was used as template for *in vitro* transcription reactions.

2.7. Real-time RT-PCR

To evaluate the expression of the *c-MYC* transcript, Real-time RT-PCR was performed. Real-Time PCR amplification was performed in a Corbett Research Rotor-Gene RG3000 using SYBR GreenER Real-Time PCR Kit (Invitrogen) according to manufacturer's specifications in 50 μl reactions containing 6 μl of cDNA from HCT-116 cells, 1 × SYBR Green SuperMix and 200 nM of primers (STAB Vida)—MYCforward and MYCreverse. The amplification conditions consisted of 50 °C for 2 min hold, 95 °C during 10 min hold, followed by 50 cycles consisting of denaturation at 95 °C for 30 s, annealing at 60 °C for 30 s, extension at 72 °C for 30 s, with a final extension step at 72 °C for 10 min. Data were collected from three independent experiments.

2.8. Monitoring RNA synthesis

Standard *in vitro* transcription was performed in 100 μL reaction containing *in vitro* transcription buffer (200 mM Tris-HCl (pH 7.9), 30 mM $MgCl_2$, 50 mM NaCl, 10 mM spermidine), 10 mM of each NTP, 0.6 μg of DNA template, and 30 U of T7 RNA polymerase (Fermentas, Vilnius, Lithuania) according to the manufacturer's protocol. For the real time quantification experiments, 1 nM of the *reporter* Au-nanobeacon (labeled with Cy3) was added to each transcription reaction. When using the *inhibitor* Au-nanobeacon (labeled with FAM), 1 nM was also added to the reaction mixture. All measurements were performed in a PerkinElmer LS45 Fluorescence Spectrometer (USA) using an Ultra-Micro quartz cell (Hëllma, Germany) programmed to incubate the reactions for 120 min at 37 °C while recording the fluorescence intensity of the Au-nanobeacon every 2 min at an excitation wavelength of 490 nm or

530 nm for FAM-labeled or Cy3-labeled Au-nanobeacon, respectively. After the measurements, the enzyme was heat inactivated for 15 min at 75 °C.

All transcription reaction products were also evaluated on a 3% agarose gel electrophoresis with GelRed™ staining. Product quantity determination was performed by pixel intensity/counting using ImageJ™ imaging software as previously described (Luhtala and Parker, 2009).

3. Results and discussion

3.1. Au-nanobeacon design

We demonstrate the use of Au-nanoparticle based molecular beacon structures (Au-nanobeacons) for real time monitoring of RNA synthesis. First, we designed Au-nanobeacons constituted by AuNPs with an average diameter of 14 nm (see Figure S1 in Supplementary Information) that work both as support structure for the thiolated DNA hairpin structure labeled with Cy3 or FAM and as a quencher to these fluorophores. Much like standard molecular beacons, in the native conformation the hairpin structure is closed and the fluorophore (Cy3 or FAM) and AuNP are brought together, and fluorescence is quenched. In one Au-nanobeacon, the loop in the hairpin structure is complementary to a fragment of the *c-MYC* proto-oncogene mRNA produced by *in vitro* transcription (*reporter*); as transcription occurs, the presence of mRNA target induces the opening of the *reporter*'s structure with concomitant fluorescence intensity increment.

Transcription of a gene into mRNA is highly regulated and can be elegantly switched on and off by blocking the respective promoter. The RNA promoter determines the maximal rate of RNA synthesis and is the site of binding or "initiation" for RNA polymerase. To silence gene transcription, we constructed an *inhibitor* Au-nanobeacon complementary to the promoter region recognized by the T7-RNA polymerase, thus capable of blocking the transcriptional machinery at the specific promoter site and impede transcription. However, the same rationale may be used to target any specific gene sequence of choice, thus blocking a specific gene from being transcribed.

3.2. Au-nanobeacon calibration

First, we calibrated the response of the *reporter* Au-nanobeacon to the complementary target using the DNA template that was subsequently used for *in vitro* transcription (see Fig. 2A). A 10-fold increase in fluorescence was detected upon hybridization of the Au-nanobeacon to the complementary target at 37 °C when compared to hybridization to non-related target, showing that the nanobeacon is capable of specific sequence recognition. To ensure that, during transcription, the Au-nanobeacon in solution would not be totally hybridized to the DNA template alone before transcription started, a fixed amount of Au-nanobeacon was added to crescent target concentrations, heated and cooled-down to induce maximum hybridization before transcription.

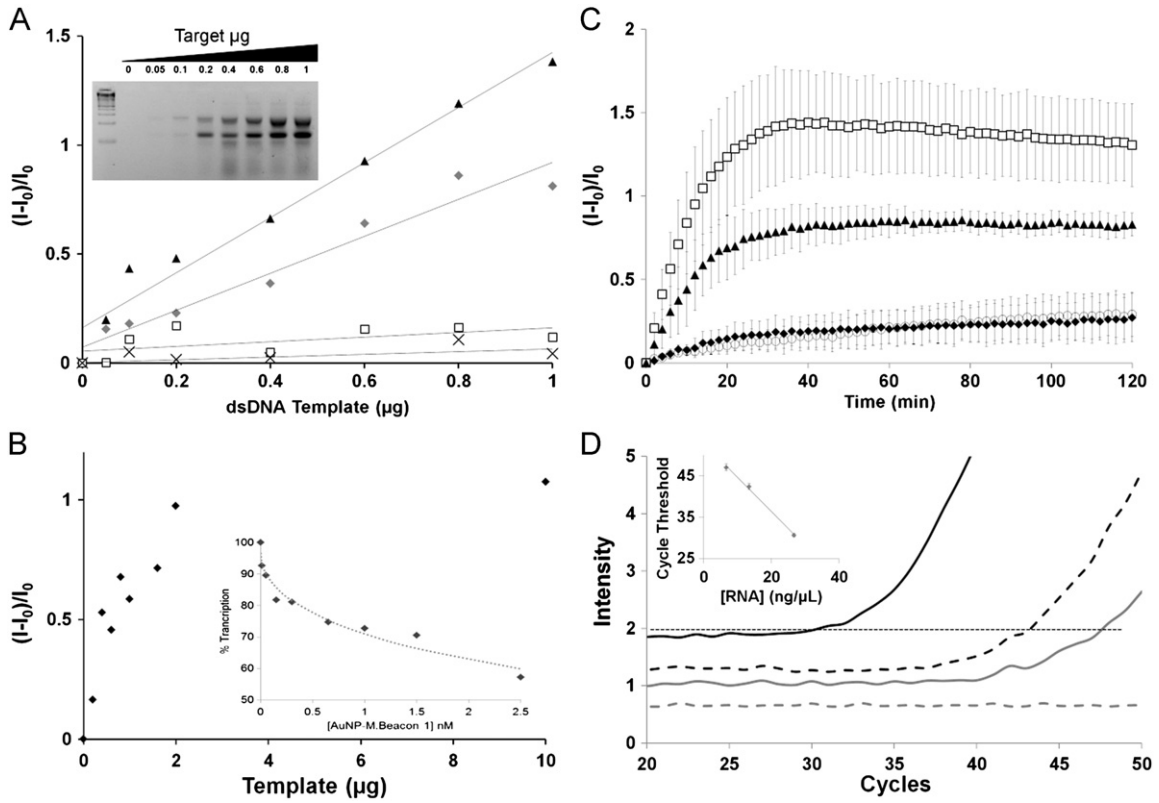

Fig. 2. *Au-nanobeacon calibration.* (A) – *Reporter* Au-nanobeacon normalized emission before and after transcription of dsDNA templates that generate complementary (gray diamonds, $y=0.8482x+0.0719$; and black triangles, $y=1.2634x+0.1614$, respectively) and non-complementary (black crosses, $y=0.0618x+0.0018$; and white squares, $y=0.1076x+0.0539$, respectively) RNA products for increasing transcription template. Inset: Agarose gel demonstrating an increase in the intensity of the band corresponding to the transcript for higher template mass. (B) – *Inhibitor* Au-nanobeacon normalized emission in presence of increasing dsDNA template. Inset: Transcription inhibition with increasing amounts of *inhibitor* Au-nanobeacon. (C) – *Reporter* Au-Nanobeacon normalized emission for 120 min at 37 °C in presence of increasing concentrations of total RNA (0 ng/µL – white circles, 6.7 ng/µL – black diamonds, 13.3 ng/µL – black triangles, 26.7 ng/µL – white squares). Error bars represent at least 3 independent assays. (D) – Real-time PCR of the total RNA samples tested with the *reporter* Au-nanobeacon (0 ng/µL – gray dashed line, 6.7 ng/µL – gray full line, 13.3 ng/µL – black dashed line, 26.7 ng/µL – black full line). Inset: Plot of Cycle Threshold *vs.* [total RNA], $y=-0.8721x+54.1$, $R^2=0.9948$. The Threshold Cycle (Ct) represents the cycle number at which the fluorescence produced within a reaction crosses the threshold line (horizontal dotted line at Intensity=2).

Then, the fluorescence intensity of the total system before and after transcription was measured. The fluorescence intensity consistently increases after transcription indicating that, although higher quantities of template correspond to higher fluorescent intensities, there are still hairpin-structures available for specific hybridization to the newly formed transcript. It should be noted that, when compared to traditional molecular beacons, we have more than one hairpin-oligonucleotide per nanoparticle, which results in better signal to background noise, *i.e.* better capability to detect complementary targets that has also been previously reported by others (Cheng et al., 2011). From these calibrating experiments, a working concentration of 0.6 μg of template for the real-time assay was selected. The reporting signal obtained from the *reporter* Au-nanobeacon was further validated by (i) hybridization to total RNA containing complementary target – Fig. 2C; and (ii) real-time quantitative PCR, the *gold standard* for transcript quantification – Fig. 2D. Results corroborate the quantification capability of the *reporter* Au-nanobeacon.

The *inhibitor* Au-nanobeacon presents an average of 4.95 ± 0.66 oligomer per AuNP (see Figure S4 in Supplementary Information). We first calibrated the *inhibitor* Au-nanobeacon as described above for the reporter Au-nanobeacon, showing its capability to specifically detect its complementary target sequence inducing a 4.3-fold increase in fluorescence, while not hybridizing to a non-complementary target (Figure S5 in Supplementary Information). In a typical inhibition assay, the dsDNA template (*T7-MYC*) is incubated with increasing concentrations of *inhibitor* Au-nanobeacon and then the transcription reaction is carried out. Following agarose gel electrophoresis, quantification of the amount of mRNA produced in each transcription showed a steady decrease with increasing amount of *inhibitor* Au-nanobeacon, as expected – Fig. 2B. It is clear that the *inhibitor* Au-nanobeacon can effectively compete with the template DNA sequence for RNA polymerase and drastically reduce the level of transcription. This is in clear agreement with previous reports that demonstrate that AuNPs enhance the silencing capability of oligonucleotides, while conveying protection against nucleases (Conde et al., 2010). At the same time it blocks transcription, the *inhibitor* Au-nanobeacon simultaneously signals out the amount of target it is binding to, *i.e.* the fraction of promoters being blocked at any given time.

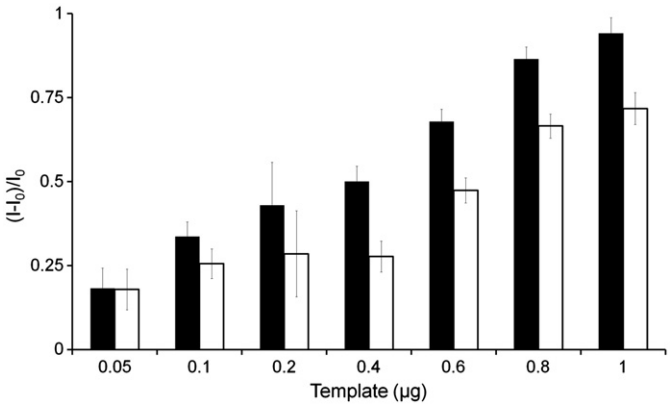

Fig. 3. *Au-nanobeacon effect on in vitro transcription. In vitro* transcription in the presence of the reporter Au-nanobeacon (black bars) and in the presence of both reporter (1 nM) and inhibitor (1 nM) Au-nanobeacons (white bars) with increasing amounts of DNA template, measuring the fluorescent intensity of cy3 (λ=530 nm) for two independent assays (n=2). Full bars correspond to average of the assays and the error bars to the respective standard deviation.

3.3. Monitoring of RNA synthesis inhibition

We then used the *reporter* and the *inhibitor* Au-nanobeacons simultaneously in the same reaction vial so as to assess transcription and transcription inhibition – Fig. 3. Data show increasing fluorescence output from the *reporter* Au-nanobeacon with increasing concentrations of template that correlates with increasing levels of transcription. The presence of the *inhibitor* Au-nanobeacon (1 nM) can be noted by a decrease in fluorescence from the reporter (1 nM) Au-nanobeacon, showing that it is blocking transcription.

As the concentration of template increases, the level of transcription also increases showing that the same amount of *inhibitor* Au-nanobeacon is blocking a smaller percentage of all the available templates present in the reaction medium. In fact, considering that each AuNP of the *inhibitor* Au-nanobeacon possess an average of five hairpins on its surface, one may assume that all the hairpins per AuNP are in the open conformation if each Au-nanobeacon is blocking five promoters. In this situation the *inhibitor* Au-nanobeacon is saturated and ceases to respond to incremental increases in target concentration, which happens for a concentration of target of about 10 μg (6.43×10^{-11} mol) (see Fig. 2B). Taken this into account and retrieving the fluorescence of the *inhibitor* Au-nanobeacon, it is possible to determine the ratio of promoters being effectively blocked – Table 1. The percentage of promoters being blocked is lower for the higher template concentrations, which correlates to lower inhibition and consequent higher levels of transcription. This way, we demonstrate that this system can effectively quantify the level of RNA synthesis and simultaneously assess the ratio of blocked promoters. To the best of our knowledge, this is the first time a DNA-AuNP conjugate is used to simultaneously silence transcription and quantify the percentage of promoters being effectively blocked.

3.4. Real-time assessment of transcription and inhibition – a dual color Au-nanobeacon approach

Based on the previous results, we employed the same approach to follow the *in vitro* transcription in real-time – Fig. 4. We used both Au-nanobeacons in the same RNA synthesis reaction towards a dual-color system for the real time monitoring of both RNA synthesis and level of inhibition. We first measured the fluorescence of the *reporter* Au-nanobeacon for 120 min immediately after the addition of T7 enzyme and NTPs to a previously stabilized solution containing the Au-nanobeacon and template. The reporter Au-nanobeacon signals the continuous synthesis of the complementary mRNA, whilst the production of a non-related transcript induces no changes to the fluorescence intensity. Because of the calibration of the Au-nanobeacon

Table 1
In vitro transcription inhibition *vs. inhibited* Au-nanobeacon hybridization.

Added template ($\text{mol} \times 10^{-12}$)	1.29 (0.2 μg)	2.57 (0.4 μg)	3.86 (0.6 μg)	5.14 (0.8 μg)	6.43 (1 μg)
Inhibited template ($\text{mol} \times 10^{-12}$)	0.23 (17.63%)	0.35 (13.79%)	0.42 (10.79%)	0.36 (6.91%)	0.49 (7.64%)
Inhibition of transcription (%)	96.14	90.69	66.49	62.00	56.39
Inhibitor saturation (%)	45.34	70.95	83.23	71.08	98.28

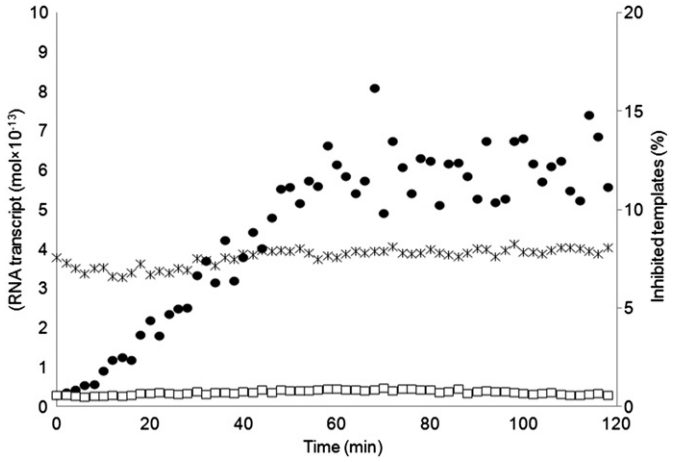

Fig. 4. *Real-time in vitro transcription and inhibition using Au-nanobeacons. In vitro* transcription was measured (excitation wavelength of 530 nm, primary axis) in real-time in presence of the *reporter* Au-nanobeacon (black circles) and in simultaneous presence of the *reporter* and *inhibitor* Au-nanobeacons (white squares). The emission of the *inhibitor* Au-nanobeacon was also measured throughout the experience (black stars, secondary axis, and excitation wavelength 490 nm).

previously described it is possible at any time point to correlate directly to the actual amount of RNA being produced (as number of moles or mass). This is extremely relevant if one is to study the regulatory and controlling elements of transcription of a given gene.

We then combined 1 nM of each Au-nanobeacon in one *in vitro* transcription reaction and measured the fluorescent intensity of both fluorophores with excitation at 490 and 530 nm. During the entire reaction time there was no rise in fluorescence associated with production of transcript (*reporter* Au-nanobeacon), showing that the *inhibitor* Au-nanobeacon is effectively blocking the promoter. The *inhibitor*'s emission is constant throughout the entire time lapse, and the percentage of blocked promoters can be easily determined via the procedure described above (7.61%). The level of inhibition of transcription can be easily calculated for each time point. What is more, as can be seen in Figure S7B in Supplementary Information, a normalized intensity curve can be plotted as function of the resulting transcription product retrieved from the agarose gel electrophoresis (see Figure S7A in Supplementary Information).

Real-time monitoring of RNA transcription reactions gave fluorescence plots with an initial lag phase, followed by a first-order increase. The initial lag may be due to assay sensitivity and kinetics of double-helix formation between the Au-nanobeacon and its RNA target. Comparison between the linear phase of the RNA synthesis for the *reporter* Au-nanobeacon (black circles) and *reporter*+*inhibitor* (white squares) demonstrate that we can achieve a 14.1-fold decrease in RNA synthesis after 60 min of transcription (~618 fmol of RNA and ~43.9 fmol of RNA, respectively). These results were confirmed through quantification of transcription via agarose gel electrophoresis (see Figure S8 in Supplementary Information).

4. Conclusions

Here, we demonstrate the use of Au-nanobeacons capable of recognizing specific complementary sequences that can be easily synthesized by functionalization of gold nanoparticles with thiolated DNA hairpin oligonucleotides. One of the Au-nanobeacons was designed so as to monitor the synthesis of a specific RNA sequence related to the human proto-oncogene *c-MYC – reporter*; whereas the *inhibitor* was designed to specifically recognize the *c-MYC* sequence downstream of the RNA polymerase T7 promoter, thus blocking transcription in a sequence dependent manner. Because of its beacon conformation, the *inhibitor* is able to simultaneously block the promoter and signal out the number of promoters being effectively blocked. Following Au-nanobeacons calibration, we used them to quantitatively monitor RNA synthesis in real-time and for kinetic quantification of RNA transcript synthesized by a RNA polymerase (~10.3 fmol of RNA per minute of reaction). We also demonstrate that by combining the use of a *reporter* and an *inhibitor* Au-nanobeacon, we were able to create a dual color system capable of quantify transcription and the level of inhibition in a single reaction vial. It is possible to quantify the level of inhibition of the RNA synthesis and relate it to the amount of template being effectively silenced, *i.e.* assessing actual silencing capability. Even though some reports can be found on the use of gold nanoparticles for detection of gene expression, to the best of our knowledge, this is the first time an approach for the simultaneous quantitative monitoring of RNA synthesis and inhibition in real-time is reported. The proposed Au-nanobeacon biosensor allows for fast, accurate and sensitive RNA transcript expression profiling. A unique feature of this sensor, compared to conventional measurements of polymerase activities using intercalating dyes, is that the probes do not generate a signal from unrelated nucleic acids and polymerase activities can be distinguished from promoter-specific RNA polymerization. The simplicity and speed of the sensor are also great advantages.

This new Au-nanobeacon sensor allows extending quantification of gene expression to real-time assessment of transcription and inhibition, thus providing means to evaluate the potential of a given sequence to effectively silence a target gene. Also, because the AuNPs confer resistance to nuclease degradation, these sensors may be used to follow gene silencing *in vivo*, thus providing additional information to assist modeling of actual gene therapy protocols. Nevertheless, before *in vivo* utilization, exhaustive studies need to be conducted in situations of increasing complexity, *e.g.* complex reaction mixtures, cell extracts and cell lineages.

Acknowledgments

This work was supported by Fundação para a Ciência e Tecnologia [CIGMH, REQUIMTE, PTDC/QUI-QUI/112597/2009, SFRH/BD/43320/2008 to J.R., SFRH/BD/62957/2009 to J.C.]; Nanotruck-Action from NanoSciEra+; ARAID to J.M.F.

Appendix A. Supporting information

Supplementary data associated with this article can be found in the online version at http://dx.doi.org/10.1016/j.bios.2012.04.006.

References

Agbasi-Porter, C., Ryman-Rasmussen, J., Franzen, S., et al., 2006. Bioconjugate Chemistry 17, 1178–1183.
Agrawal, S., 1996. Trends in Biotechnology 14, 376–387.
Baptista, P., 2009. Current Cancer Therapy Reviews 5, 80–88.
Baptista, P., Pereira, E., Eaton, P., et al., 2008. Analytical and Bioanalytical Chemistry 391, 943–950.
Bor, Y.C., Swartz, J., Li, Y., Coyle, et al., 2006. Nature Protocols.
Cheng, Y., Stakenborg, T., Van Dorpe, P., et al., 2011. Analytical Chemistry 83, 1307–1314.
Conde, J., de la Fuente, J.M., Baptista, P.V., 2010. Nanotechnology 21, 1–6.

Dubertret, B., Calame, M., Libchaber, A.J., 2001. Nature Biotechnology 19, 365–370.
Fichou, Y., Ferec, C., 2006. Trends in Biotechnology 24, 563–570.
Freeman, W.M., Walker, S.J., Vrana, K.E., 1999. Biotechniques 26, 112–115.
Lakowicz, J.R., 2006. Plasmonics 1, 5–33.
Lee, P.C., Meisel, D., 1982. The Journal of Physical Chemistry 86, 3391–3395.
Li, J.J., Fang, X., Schuster, S.M., 2000a. Angewandte Chemie-International Edition 39, 1049–1052.
Li, J.J., Geyer, R., Tan, W., 2000b. Nucleic Acids Research 28, 1–6.
Liu, J., Feldman, P., Chung, T.C., 2002. Analytical Biochemistry 300, 40–45.
Luhtala, N., Parker, R., 2009. Nucleic Acids Research 37, 5529–5536.
Marras, S.A., Gold, B., Kramer, F.R., et al., 2004. Nucleic Acids Research 32, 1–6.
Paciotti, G.F., Myer, L., Weinreich, D., et al., 2004. Drug Delivery 11, 169–183.
Quarta, A., Di Corato, R., Manna, L., et al., 2007. IEEE Transactions on Nano-Bioscience 6, 298–308.
Rayburn, E.R., Zhang, R., 2008. Drug Discovery Today 13, 513–521.
Rosi, N.L., Giljohann, D.A., Thaxton, C.S., et al., 2006. Science (New York, NY) 312, 1027–1030.
Saha, K., Agasti, S.S., Kim, C., et al., 2012. Chemical Reviews. Article ASAP.
Schena, M., Shalon, D., Davis, R.W., et al., 1995. Science (New York, NY) 270, 467–470.
Seferos, D.S., Giljohan, D.A., Hill, H.D., Prigodich, et al., 2007. Journal of the American Chemical Society 129, 15477–15479.
Song, S., Liang, Z., Zhang, J., et al., 2009. Angewandte Chemie-International Edition 48, 8670–8674.
Tamm, I., Dorken, B., Hartmann, G., 2001. Lancet 358, 489–497.
Tan, W., Wang, K., Drake, T.J., 2004. Current Opinion in Chemical Biology 8, 547–553.
Toub, N., Malvy, C., Fattal, E., Couvreur, P., 2006. Biomedicine and Pharmacotherapy—Biomedecine and Pharmacotherapie 60, 607–620.
Tyagi, S., Kramer, F.R., 1996. Nature Biotechnology 14, 303–308.
Waltz, T.L., Marras, S., Rochford, G., et al., 2005. Journal of Clinical Microbiology 43, 254–258.
Weis, J.H., Tan, S.S., Martin, B.K., et al., 1992. Trends in Genetics 8, 263–264.

Supplementary Information

Gold-nanobeacons for real-time monitoring of RNA synthesis

João Rosa[1,2,†], João Conde[1,3,†], Jesus M. de la Fuente[3], João C. Lima[2] and Pedro V. Baptista[1,*]

[1]CIGMH, Departamento de Ciências da Vida, Faculdade de Ciências e Tecnologia, Universidade Nova de Lisboa, Campus de Caparica, 2829-516 Caparica, Portugal.

[2]REQUIMTE, Departamento de Química, Faculdade de Ciências e Tecnologia, Universidade Nova de Lisboa, Campus de Caparica, 2829-516 Caparica, Portugal.

[3]Instituto de Nanociencia de Aragón, Universidad de Zaragoza, Campus Río Ebro, Edifício I+D, Mariano Esquillor, s/n, 50018 Zaragoza, Spain.

*Corresponding author. Email: pmvb@fct.unl.pt. Phone/Fax: +351 212948530

† These authors contributed equally to the work.

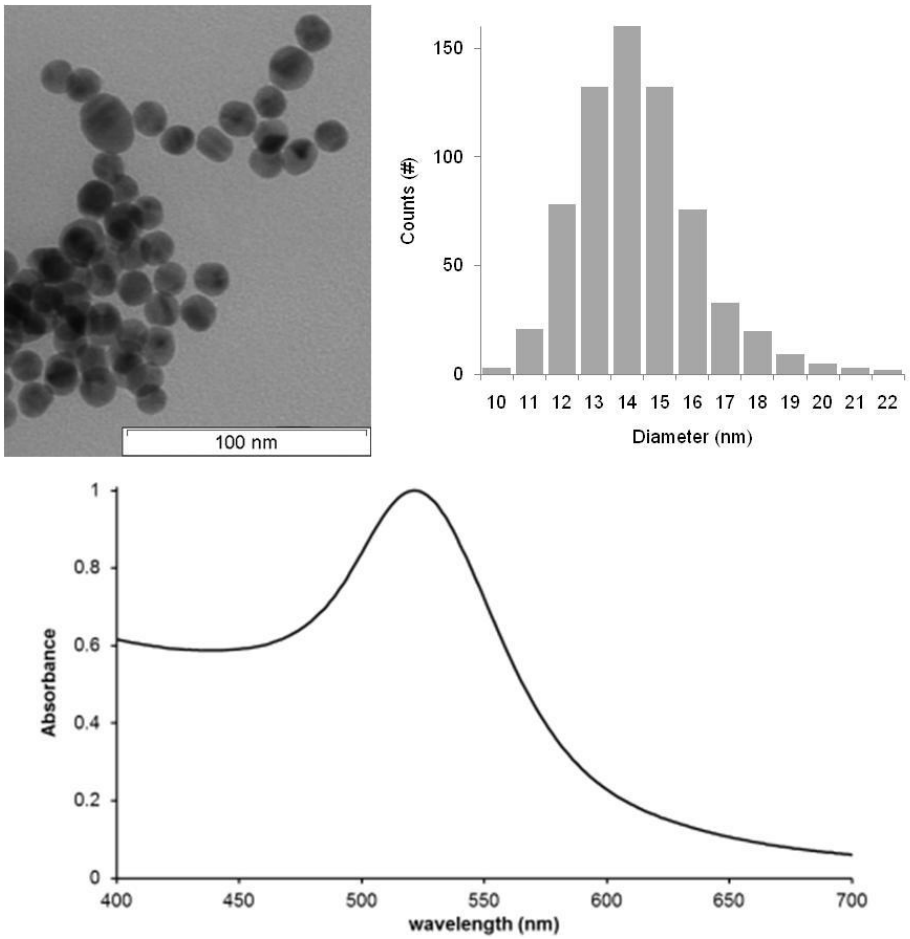

Figure S1. Gold nanoparticle characterization. TEM images (left, scale bar = 100 nm), size distribution histogram (right) showing an average diameter of 14.3 nm; UV-Vis spectra of the synthesized gold nanoparticles (bottom).

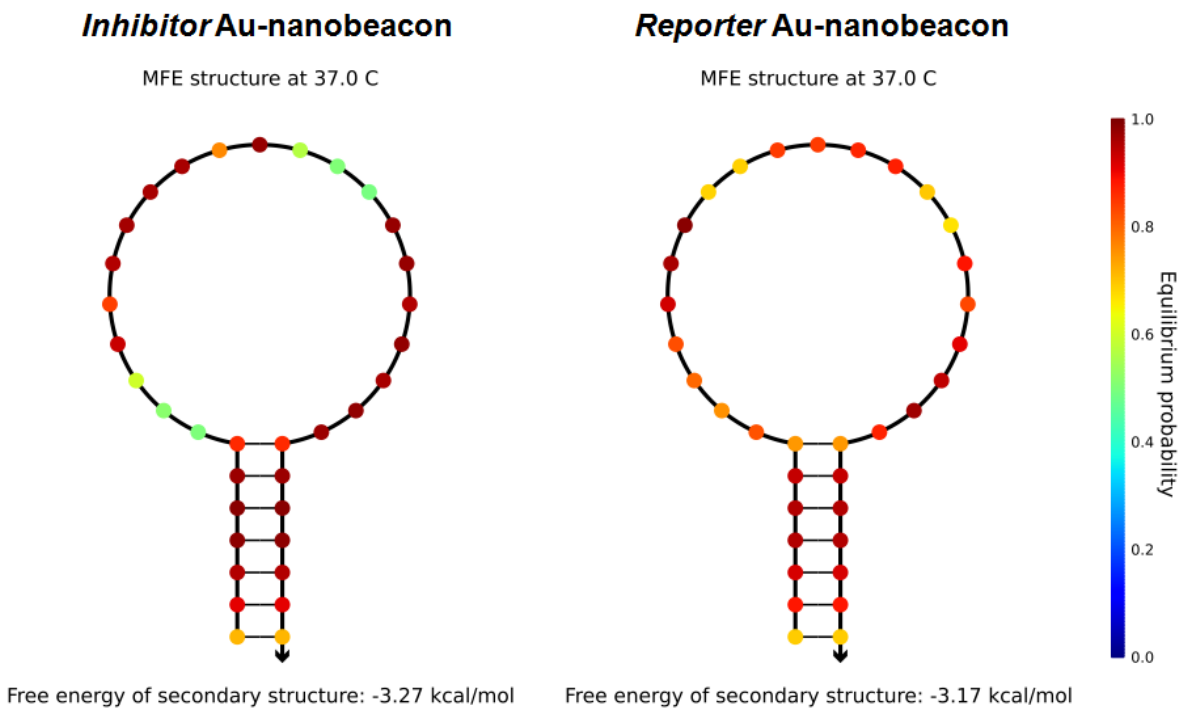

Figure S2. Two-dimensional structures of the *inhibitor* and *reporter* Au-nanobeacons at 37ºC as predicted by NUPACK (Zadeh, J.N., Steenberg, C.D., Bois, J.S., et al., 2011. NUPACK: analysis and design of nucleic acid systems. *J. Comput. Chem*. 32, 170–173.)

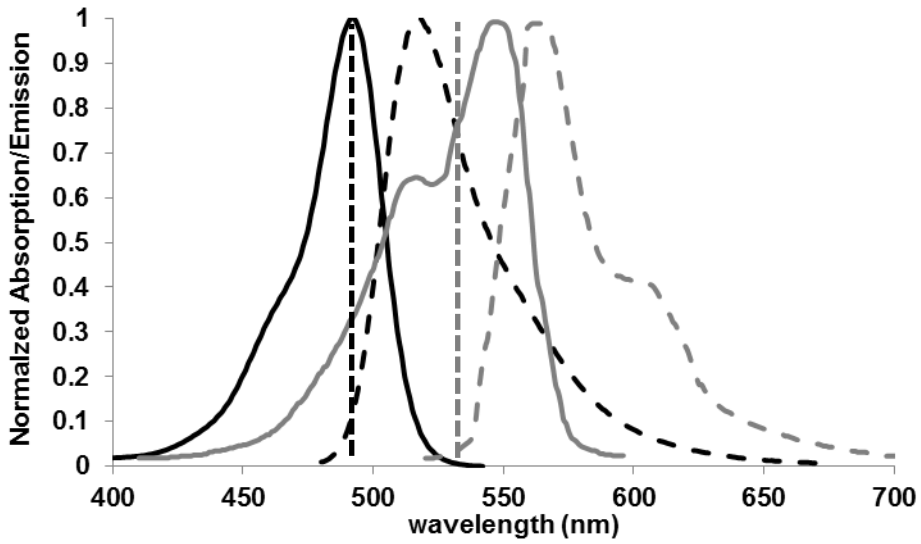

Figure S3. Absorption and emission spectra of the fluorophores. Absorption (full lines) and emission (dashed lines) spectra of FAM (black lines) and cy3 (grey lines). Vertical lines represent the excitation wavelength of each fluorophore. Cy3 was excited at 530 nm to enhance the full emission spectra.

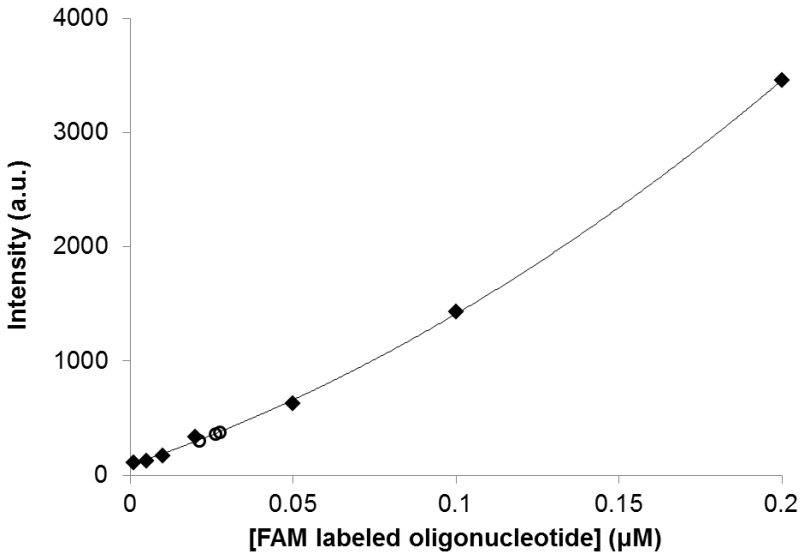

Figure S4. Oligonucleotides density - *inhibitor* Au-nanobeacon. Calibration curve of FAM-labeled oligonucleotide (diamonds, $y=36090.0x^2+9625.8x+89.7$, $R^2=0.9996$) and fluorescence intensities measured in the supernatants of Au-nanobeacon (circles). A ratio of 4.96±0.66 oligonucleotides per gold nanoparticle was calculated.

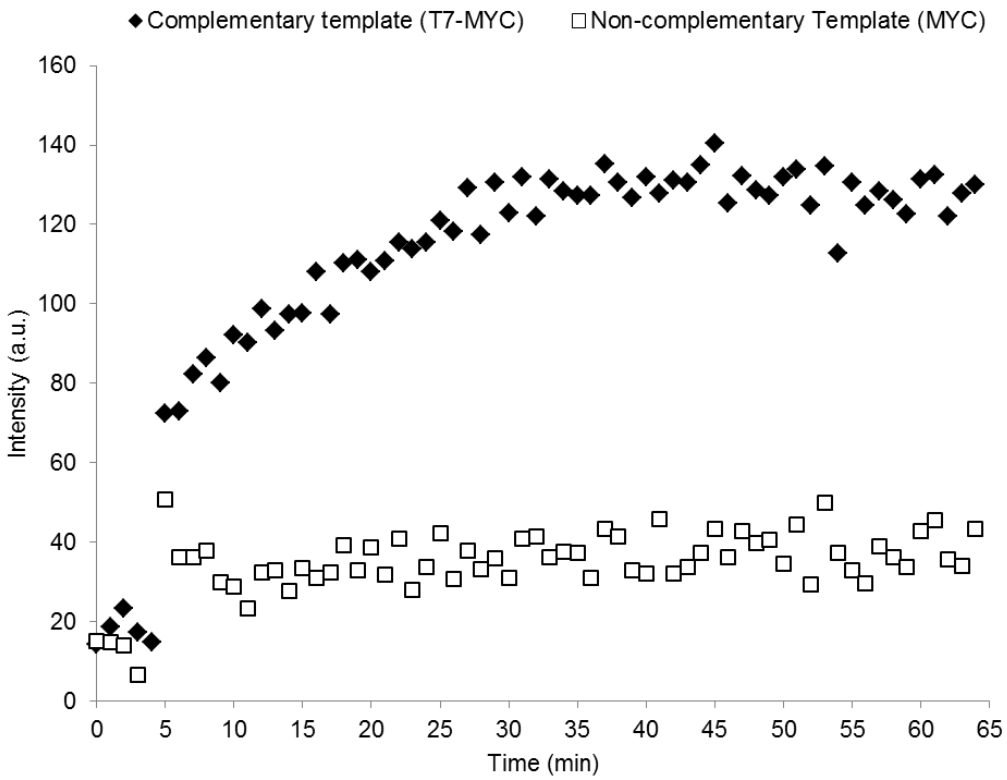

Figure S5. ***Inhibitor*** **Au-nanobeacon specificity.** Hybridization kinetics of the Au-nanobeacon inhibitor at 37º C in presence of the complementary target (black diamonds) and non-complementary target (white squares).

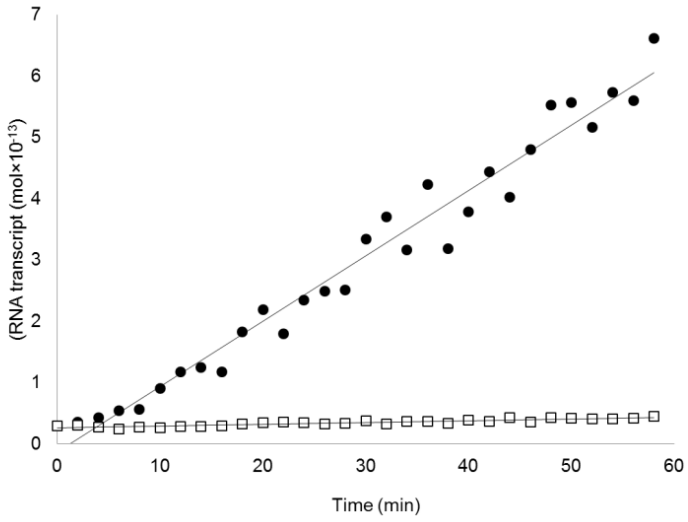

Figure S6. Real-time monitorization with the *reporter* Au-nanobeacon. Real-time measurement of *in vitro* transcription of RNA products showing complementarity to the *reporter* (black circles) and without any complementarity to the *reporter* (white squares). The complementary RNA product caused a linear response (y=0.1066x–0.1336) corresponding to the formation of 10.6 fmol of RNA/min.

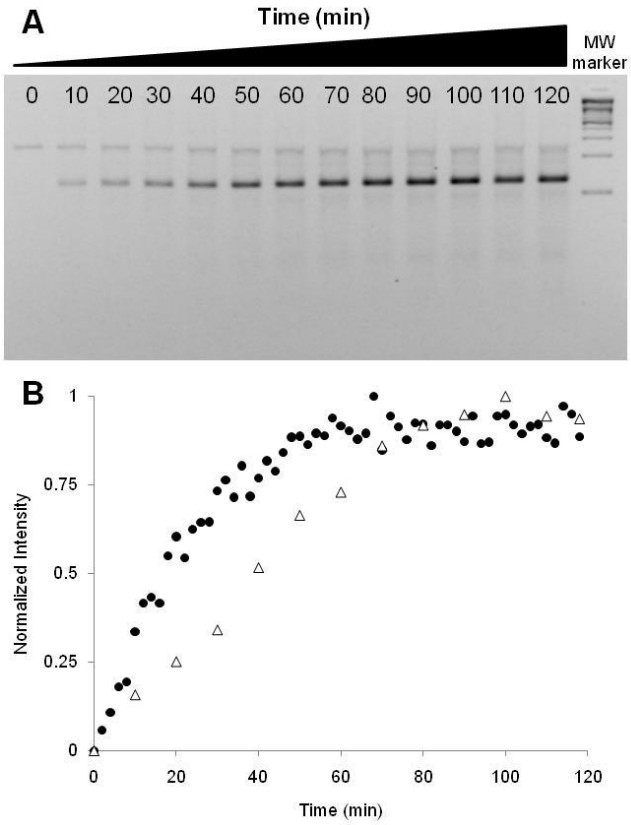

Figure S7. A. Agarose gel electrophoresis of the transcription product as function of time. **B.** Normalized intensity curve plotted as function of the resulting transcription product retrieved from the agarose gel electrophoresis (white triangles) and with the fluorescence intensity measurements of the *reporter* Au-nanobeacon (black circles) for 120 minutes immediately after the addition of T7 enzyme and NTPs to a previously stabilized solution containing the Au-nanobeacon and template**.** All transcription reaction products were also evaluated on a 3% agarose gel electrophoresis with GelRed^{TM} staining. Product quantity determination was performed by pixel intensity/counting using ImageJ^{TM} imaging software as previously described (Luhtala and Parker, 2009).

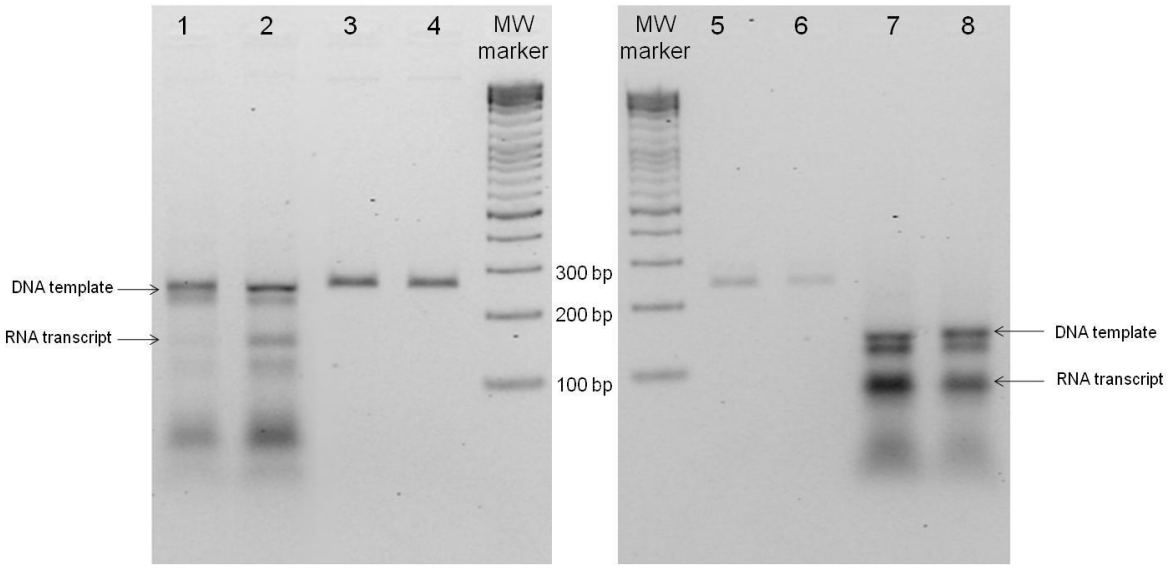

Figure S8. Agarose gel electrophoresis of end-point measurements of RNA synthesis and inhibition using active and non-active (denaturated) T7 RNA polymerase. Data show that fluorescence is strictly dependent of transcription of the added template. Lane 1 – *Reporter* + *Inhibitor* with active T7 Pol., Complementary target (T7-MYC); Lane 2 – *Reporter* with active T7 Pol., Complementary target (T7-MYC); Lane 3 – *Reporter* + *Inhibitor* with non-active T7 Pol., Complementary target (T7-MYC); Lane 4 – *Reporter* with non-active T7 Pol., Complementary target (T7-MYC); Lane 5 – *Reporter* with active T7 Pol., Non-complementary target I (X); Lane 6 – *Reporter* + *Inhibitor* with active T7 Pol., Non-complementary target I (X); Lane 7 – *Reporter* with active T7 Pol., Non-complementary target II (T7-Y); Lane 8 – *Reporter* + *Inhibitor* with active T7 Pol., Non-complementary target II (T7-Y).

Biomaterials 34 (2013) 2516–2523

Contents lists available at SciVerse ScienceDirect

Biomaterials

journal homepage: www.elsevier.com/locate/biomaterials

Gold-nanobeacons for simultaneous gene specific silencing and intracellular tracking of the silencing events

João Conde [a,b], João Rosa [a,c], Jesús M. de la Fuente [b], Pedro V. Baptista [a,*]

[a] CIGMH, Departamento de Ciências da Vida, Faculdade de Ciências e Tecnologia, Universidade Nova de Lisboa, Campus de Caparica, 2829-516 Caparica, Portugal
[b] Instituto de Nanociencia de Aragón, Universidad de Zaragoza, Campus Rio Ebro, Edificio ID, Mariano Esquillor s/n, 50018 Zaragoza, Spain
[c] REQUIMTE, Departamento de Química, Faculdade de Ciências e Tecnologia, Universidade Nova de Lisboa, Campus de Caparica, 2829-516 Caparica, Portugal

ARTICLE INFO

Article history:
Received 18 October 2012
Accepted 15 December 2012
Available online 11 January 2013

Keywords:
RNA interference
MicroRNAs
Gold-nanobeacons
AntimiRs
Gene silencing
Cancer nanotheranostics

ABSTRACT

The potential of a single molecular nanoconjugate to intersect all RNA pathways: from gene specific downregulation to silencing the silencers, i.e. siRNA and miRNA pathways, is demonstrated. Gold-nanobeacons are capable of efficiently silencing single gene expression, exogenous siRNA and endogenous miRNAs while yielding a quantifiable fluorescence signal directly proportional to the level of silencing. The silencing potential is comparable to that of traditional siRNA but the same nanoconjugates structure is also capable of reversing the effect of an exogenous siRNA. We further demonstrate the Gold-nanobeacons' efficiency at targeting and silencing miR-21, an endogenous miRNA involved in cancer development, which could become a valid nanotheranostics approach. Again, expression of miR-21 was inhibited with concomitant increase of the Au-nanobeacons' fluorescence that can be used to assess the silencing effect. This way, a single nanostructure can be used to intersect all RNA regulatory pathways while allowing for direct assessment of effective silencing and cell localization via a quantifiable fluorescence signal, making cancer nanotheranostics possible.

1. Introduction

Antisense DNA [1,2], small interfering RNA (siRNA) [3–5] or microRNA [6] technologies have been widely explored to modulate RNA expression [7–9] and may also be directed towards silencing endogenous miRNAs, whose deregulation is associated with cancer development. Within the intricate network of cell regulation, RNA pathways are key regulatory players of gene expression and cell fate, where deregulation of endogenous miRNAs has been associated with tumor progression and differentiation. Particularly, upregulated miRNAs act as endogenous silencers of crucial pathways and silencing these silencers constitute optimal targets for treatment [8]. The ability of modulating miRNA expression in tumor cells is of paramount relevance and has been drawing increasing interest from researchers that require tools capable of silencing these endogenous silencers while signaling out for evaluation. These silencing tools can be conveyed into mammalian cells by a variety of methods [10–14] that influence the strength and duration of the silencing response, which in turn is affected by the amount of therapeutic agent that is delivered and on the potential of each agent to suppress its target. Thus, one potential drawback of using naked silencing tools is that they show extremely short half-lives, weak protection against action by RNases, poor chemical stability, and common dissociation from vector [15,16]. In fact, the major obstacle to clinical application is the uncertainty about how to deliver therapeutic RNAs (e.g., miRNA and/or siRNA) with maximal therapeutic impact. Nanotechnology offers an unprecedented opportunity to overcome these problems, as nanoscale devices, due to their small size, can readily interact with biomolecules on both the surface of cells and inside of cells for longer periods of time [16].

Gold nanoparticles (AuNPs) are optimal delivery vehicles for antisense and siRNA therapy because they provide enhanced protection against RNases and ease of functionalization with moieties for selective targeting [15]. Engineered AuNPs are effortlessly internalized by cells and they outperform traditional delivery systems leading to effective gene silencing [17–26]. Previous reports show that single-stranded DNA functionalized AuNPs represents a good gene delivery system with greater knockdown of gene expression and lower cell toxicity than antisense DNA delivered by Lipofectamine [17]. Additionally, these AuNPs constructs often have fluorophores on the surface for intra-cellular tracking of the NPs regardless of being actively hybridizing to the target molecules and silencing them. Recently, we provided evidence of *in vitro* and *in vivo*

* Corresponding author. Tel./fax: +351 212948530.
E-mail address: pmvb@fct.unl.pt (P.V. Baptista).

0142-9612/$ – see front matter © 2012 Elsevier Ltd. All rights reserved.
http://dx.doi.org/10.1016/j.biomaterials.2012.12.015

RNAi triggering via the synthesis of a library of multifunctional siRNA–AuNPs, using a hierarchical approach including three biological systems of increasing complexity: *in vitro* cultured human cells, *in vivo* freshwater polyp (*Hydra vulgaris*), and *in vivo* mice models [27]. Nevertheless, a nanoformulation that explores the capacity of silencing any RNA target, be it gene specific mRNA, exogenous (siRNA and antisense oligonucleotides) or endogenous (microRNAs) silencers has not been described so far. To realize the therapeutic potential of blocking crucial silencing pathways, we developed a nanoparticle delivery technology – Gold-nanobeacon – to target and promote silencing of miRNAs involved in the regulation of gene expression while providing means to assess effective binding. The ubiquitous application of this gold-nanobeacon approach for gene silencing was further demonstrated by pursuing an antisense, RNA interference and microRNA approaches and to support the recovery of gene expression in cancer cells.

Recently, we reported a direct method to follow RNA synthesis and inhibition in real time based on the use of AuNPs functionalized with a fluorophore labeled hairpin-DNA, i.e. Gold nanobeacons (Au-nanobeacon) [28]. In these Au-nanobeacons, the fluorescently labeled hairpin DNA brings the fluorophore into close proximity to the AuNP, quenching fluorescence. Hybridization of the Au-nanobeacon to the complementary target restores fluorescence. Here, we propose that a strategy based on Au-nanobeacons is capable of intersecting both pathways of interference RNA regulating gene expression – siRNA and miRNA. Our approach is based on the use of Au-nanobeacons to directly downregulate a specific gene (EGFP) and also to silence the silencers allowing for recovery of previously downregulated gene expression, while simultaneously tracking cell internalization and identifying the cells where silence is occurring. Following proof-of-concept demonstration, we target for silencing an endogenous microRNA (miR-21) commonly upregulated in cancer to illustrate the Au-nanobeacons' potential for anti-cancer therapeutics via the silencing of the silencers pathway in colorectal carcinoma cells (HCT-116) (see Fig. 1).

2. Materials and methods

2.1. Gold nanoparticles synthesis and Au-nanobeacon assembly

Gold nanoparticles, with an average diameter of 14.6 ± 1.7 nm, were synthesized by the citrate reduction method described by Lee and Meisel [29]. AuNPs were then functionalized with polyethylene glycol (PEG) using commercial heterofunctional PEG modified with a thiol group O-(2-Mercaptoethyl)-O′-methyl-hexa(ethylene glycol), $C_{15}H_{32}O_7S$, 356.48 Da. Excess PEG was removed by centrifugation (21.460 × g, 30 min, 4 °C), and the level of PEG coverage on the AuNP evaluated via the Ellman's Assay to be 190 ± 20 chains per nanoparticle, corresponding to 30% of saturation of the gold's surface. For Au-nanobeacon assembly, the stem-looped oligonucleotides modified with 3′-Cy3 and 5′-Thiol-C6 (STABVIDA) were suspended in 1 ml of 0.1 M dithiothreitol (DTT), extracted three times with ethyl acetate and further purified through a desalting NAP-5 column (Pharmacia Biotech) using 10 mM phosphate buffer (pH 8) as eluent. Following oligonucleotide quantification via UV/Vis spectroscopy, each oligomer was added to the AuNP@PEG in a 100:1 ratio and processed as previously described [28]. Finally, the resulting Au-nanobeacons were centrifuged for 20 min at 21.460 × g, the oily precipitate washed three times with DEPC-treated H_2O, and redispersed in 10 mM phosphate buffer (pH 8), 0.3 M NaCl, 0.01% (w/v) SDS at a final concentration of 15 nM. The resulting Au-nanobeacons were stored in the dark at 4 °C until further use. Detailed Au-nanobeacons characterization can be found in Supporting Information Table 1.

2.2. Target specificity of the Au-nanobeacons

The capability to recognize the specific target was evaluated by incubating 1 nM of each Au-nanobeacon in 10 mM phosphate buffer (pH 7) with 5 nM of a complementary and a non-complementary target (see Supporting information, Fig. S4). Cy3 fluorescence intensity as function of incubation time was determined at 2 min intervals in a PerkinElmer LS45 Fluorescence Spectrometer (Cary Eclipse, Varian) using an Ultra-Micro quartz cell (Hëllma) programmed to incubate the reactions for 120 min at 37 °C (excitation/emission, 530 nm/560 nm). Additional information on target recognition can be found in Supporting Information Fig. S3.

2.3. Cell culture and EGFP vector transfection

HCT-116 cells (from colorectal carcinoma) were grown in Dulbecco's modified Eagle's medium with Glutamax (DMEM, Invitrogen) with 10% heat inactivated fetal bovine serum (Invitrogen), 100 U/ml penicillin and 100 μg/ml streptomycin (Invitrogen) and maintained at 37 °C in 5% CO_2. Cells were seeded at a density of 1×10^5 cells/well in 24-well plates and grown for 24 h prior to transfection of the EGFP vector (pVisionGFP-N vector 4.7 kb, Biovision) encoding for green fluorescent protein, VisionGFP, optimized for high expression in mammalian cells. On the day of transfection, EGFP vector (1 μg per well) was added cells at approximately 50% confluence with 2 μg of Lipofectamine 2000® (Invitrogen) and Opti-MEM® Reduced Serum Medium (Invitrogen) according to the manufacturer's recommendations.

2.4. EGFP silencing with antisense Au-nanobeacon

After 24 h of EGFP transfection, cells were treated with 30 nM of Antisense Au-nanobeacons in Opti-MEM® Reduced Serum Medium (Invitrogen). After 48 h, cells were washed with 1 × PBS, lysed in water and collected for analysis of EGFP silencing, RNA extraction and confocal imaging. Fluorescence was measured at least 3 times in a Cary Eclipse spectrofluorimeter (Varian) using an Ultra-Micro quartz cell (Hëllma) by taking the area under the curve from 495 to 650 nm. EGFP fluorescence values were normalized to the bulk protein concentration determined via the Bradford assay (Thermo Scientific), and then normalized against the controls to determine percent knockdown of EGFP.

2.5. EGFP silencing via siRNA and Au-nanobeacon silencing of siRNA pathway

After 24 h of EGFP transfection, cells were treated with 10 nM of siRNA for EGFP using 1.5 μg of Lipofectamine 2000® (Invitrogen) and Opti-MEM® Reduced Serum Medium (Invitrogen) according to the manufacturer's recommendations. EGFP silencing was evaluated as described above. For Au-nanobeacon silencing of siRNA evaluation, 10 nM (concentration of beacon on NP) of Anti-siRNA Au-nanobeacon were added to the media with 10 nM of siRNA with several delays of incubation (0.5, 1, 3, 6 and 24 h). After 48 h, the cells were washed in 1 × PBS, lysed with water and collected for analysis of EGFP recovery as above.

2.6. Silencing the silencer – Au-nanobeacon for endogenous microRNA-21 silencing

Cells were seeded at a density of 1×10^5 cells/well in 24-well plates and grown for 24 h prior to incubation with 10, 30 and 50 nM Anti-miR-21 Au-nanobeacon for 24, 48 and 72 h. After 24, 48 and 72 h, cells were washed with 1 × PBS, lysed and collected for RNA extraction and confocal imaging.

2.7. qRT-PCR

Total RNA was extracted from the cell line using the Trisure reagent (Bioline) according to the manufacturer's protocol, and used for qRT-PCR to evaluate expression of EGFP, miR-21 and β-actin. cDNA was attained by subjecting 1 μg of total RNA to Reverse Trancriptase with 200U of Revert-AidTM M-MuLV Reverse Transcriptase (Fermentas) according to the manufacturer's specifications, using 20 μM of EGFP and β-actin reverse primers and miR-21 loop primer, annealing at 42 °C for 1 h and 70 °C for 10 min to reverse transcriptase inactivation.

Real-Time PCR amplification was performed in a Corbett Research Rotor-Gene RG3000 using SYBR GreenER Real-Time PCR Kit (Invitrogen) according to manufacturer's specifications in 50 μl reactions containing 2 μl of cDNA, 1 × SYBR Green SuperMix and 200 nM of primers (STABVIDA, Portugal). Detailed information on primer sequence, cycling conditions, melting analysis and data processing can be found in Supporting Information Figs. S5, S6 and Table 3.

2.8. Confocal microscopy

All confocal microscopy samples were prepared as described above for EGFP silencing and recovery and miR-21 silencing. Cells were fixed with 4% paraformaldehyde in 1 × PBS for 15 min at 37 °C and mounted in ProLong® Gold Antifade Reagent with DAPI (Invitrogen) to allow for nuclear staining. Images of cells were taken with a Confocal Laser Point-Scanning Microscope Zeiss LSM 510 META. Once optimized, the same microscope settings were used throughout. The laser lines used for excitation were 405 nm for DAPI (nucleus), 480 nm for EGFP, and 561 nm for Cy3 (Au-nanobeacons).

2.9. Cytotoxicity evaluation

Standard MTT [3-(4,5-dimethylthiazol-2-yl)-2,5-diphenyltetrazoliumbromide] reduction assay (Invitrogen) was performed to determine cytotoxicity following transfection with Au-nanobeacons, siRNA and ssRNA complexes as described above. After 24 h, 100 μl of Au-nanobeacons were added to the wells and cells further incubated for 48 and 72 h. Following medium removal, cells were washed twice with sterile 1 × PBS and incubated for 2 h with 300 μl of fresh medium with serum supplemented with 16.7 μl of sterile MTT stock solution (5 mg/ml in 1 × PBS). Next, medium was

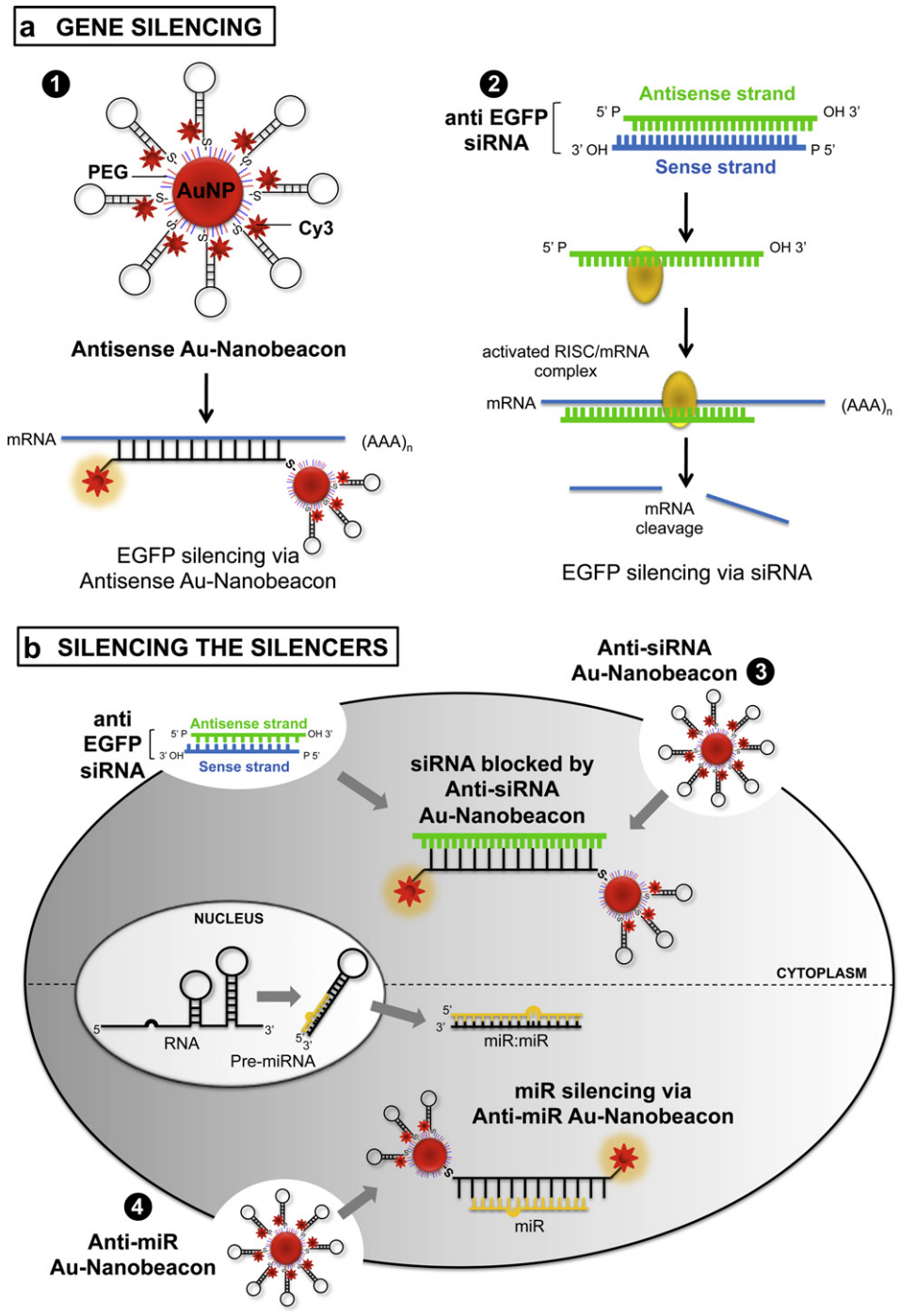

Fig. 1. Au-nanobeacons as multi-targeting tools for RNAi: from specific gene silencing to silencing the silencers. (a) GENE SILENCING – human cancer cells (HCT-116) efficiently transfected with EGFP expression vector were used for assessing the gene silencing potential of Au-nanobeacons – antisense Au-nanobeacon (❶) and by traditional siRNA approach (❷). Upon hybridization to the target sequence, the beacons' conformation change leads to fluorescence emission that signals target recognition and that silencing is occurring. (b) SILENCING THE SILENCERS – specific Au-nanobeacons are capable of intersecting both pathways – siRNA (❸) and miRNA (❹), leading to recovery of previously downregulated gene expression while simultaneously discriminating cells where silencing is occurring. The fluorescence signal may allow for tracking cell internalization and sub-cellular localization. The Au-nanobeacons' potential for anti-cancer therapeutics via the silencing of the silencers is demonstrated by blocking the endogenous microRNA pathway via an Anti-miR Au-nanobeacon complementary to the mature microRNA-21 (miR-21), commonly upregulated in cancer phenotypes [31].

removed, formazan crystals resuspended in 300 μl of dimethyl sulfoxide (Sigma), and absorbance measured at 540 nm as a working wavelength and 630 nm as reference using a Microplate reader Infinite M200 with Absorbance module (Tecan). Cell viability was normalized to that of cells cultured in the culture medium with PBS treatment.

2.10. Statistical analysis

All statistical analysis were performed with SPSS statistical package (version 15, SPSS Inc., Chicago, IL) using a Paired-Sample *T*-test. All experiments, unless otherwise stated, were performed in triplicate. All error bars used in this report are ±s.d. of at least three independent experiments.

3. Results and discussion

To assess the potential of the Au-nanobeacons for gene silencing, we transfected HCT-116 cells with EGFP that was then targeted for silencing by an Au-nanobeacon that contains a stem-looped

oligonucleotide double labeled with 3′-Cy3 and 5′-Thiol-C6 complementary to the Kozak consensus translation initiation site and start codon of the EGFP expression vector, thus capable of blocking the transcriptional machinery in the colorectal cell-line. Stable AuNPs with an average diameter of 14.6 ± 1.7 nm synthesized by reduction of sodium tetrachloroaurate (III) hydrate with sodium citrate dehydrate were functionalized with poly(ethylene glycol) (PEG) spacers to increase stability, biocompatibility and grant chemical functionality as well as avoid opsonization (Supporting Information Figs. S1 and S2) [27,30]. PEGylated AuNPs were then functionalized with a Cy3-labeled hairpin-DNA and calibrated to respond to the specific complementary target (Supporting Information Fig. S3). A substantial increase in fluorescence was detected upon hybridization of the Au-nanobeacon to the complementary target (ssRNA, siRNA and microRNA oligos) at 37 °C, showing that the Au-nanobeacons are capable of specific sequence recognition. The number of beacons per AuNP was determined for all constructs, together with the hydrodynamic diameter by Dynamic light Scattering (DLS), gold core diameter by Transmission Electron Microscopy and surface charge by Zeta-potential (Supporting Information Fig. S2 and Table 2).

We next compared the silencing effect of these antisense Au-nanobeacons (58 ± 4 beacons per nanoparticle) to that of traditional siRNA transfection using lipofectamine. All cellular uptake assays were carried out with serum-free media to avoid unspecific binding of serum proteins to the Au-nanobeacons and compromise cell uptake. Results show that both approaches are effective at blocking EGFP expression. After 24 h of EGFP vector transfection, cells were treated with 30 nM of antisense Au-nanobeacons or 10 nM of siRNA for optimal EGFP silencing (Supporting Information Fig. S7). After 48 h of Au-nanobeacons exposure, the cells were lysed and the bulk fluorescence of the lysate was measured in the emission range of the EGFP protein (Excitation/Emission, 480/510 nm) and collected for total RNA extraction.

Quantification of EGFP expression by direct measurement of EGFP fluorescence levels in bulk cell lysates at 48 h (Fig. 2b)

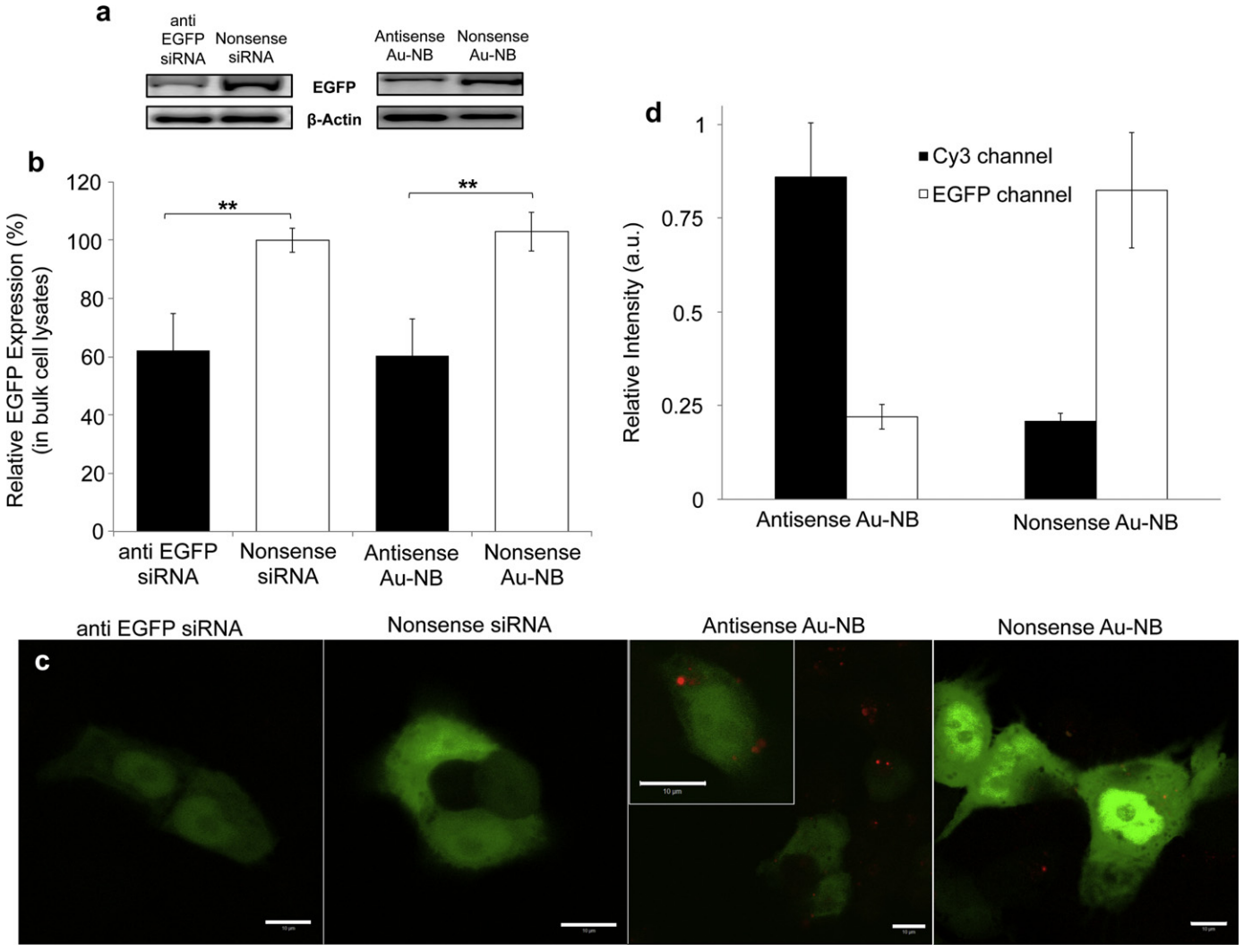

Fig. 2. Au-nanobeacon silencing of specific gene expression in colorectal carcinoma cell line (HCT-116). HCT-116 cells were transfected with EGFP expression vector and mRNA expression confirmed by qRT-PCR before and (a) after siRNA and antisense Au-nanobeacon transfection, using β-actin as reference. (b) EGFP silencing was confirmed by significant fluorescence decrease (**, $P \leq 0.005$) in bulk cell lysates (as percentage of original EGFP fluorescence levels), using an unrelated siRNA (Nonsense siRNA) or unrelated hairpin DNA bound onto AuNPs (Nonsense Au-nanobeacon). Values are means ± s.d. from 6 independent experiments. (c) Confocal imaging (scale bar, 10 μm) show HCT-116 cells expressing EGFP after transfection with siRNA 10 nM, nonsense siRNA 10 nM, antisense Au-nanobeacon 30 nM and nonsense Au-nanobeacon 30 nM. EGFP expression levels can be evaluated by the intensity of its fluorescence (green) and Au-nanobeacons in open conformation (red, Cy3) can be identified as fine punctuation dispersed throughout the cytoplasm. (d) Relative fluorescence intensity of Au-nanobeacons (Cy3, black bars) and EGFP (white bars) obtained after individual color channel analysis of the same confocal images using ImageJ software. (For interpretation of the references to colour in this figure legend, the reader is referred to the web version of this article).

reveals similar silencing for both approaches: 39.7 ± 12.5% and 37.9 ± 12.6% for antisense Au-nanobeacon and siRNA, respectively. These data are corroborated by qRT-PCR (Fig. 2a). EGFP expression is not affected by a nonsense Au-nanobeacon (32 ± 3beacons per NP) or nonsense siRNA indicating that the knockdown is sequence specific. No changes in cell viability that would indicate off-target effects were observed (Supporting Information Fig. S13).

Confocal imaging clearly shows specific EGFP knockdown by siRNA anti EGFP and antisense Au-nanobeacon (Fig. 2c). Cells show a punctuate fluorescence pattern indicating that the antisense Au-nanobeacons are distributed evenly in the cytoplasm (Fig. 2c), and a closer examination revealed more fluorescence in perinuclear regions. It should be noted that Au-nanobeacons require no transfection agent to enter cells. The intensity of fluorescence signals was broken down by specific channels that show striking differences for Cy3 and EGFP emissions related to the antisense and nonsense Au-nanobeacons, i.e. silencing occurs upon hairpin conformational change due to specific hybridization to the target sequence, which can be identified via the fluorescence emission. This way, effective silencing can be evaluated by the beacons' fluorescence (Fig. 2d). Measuring the intensity of the Cy3 and EGFP channels, we observe a decrease in EGFP fluorescence with an increase in antisense Au-nanobeacons signal. The opposite occurs with the respective control, the nonsense Au-nanobeacon. Our data demonstrate that silencing of the silencers is attained only when the Au-nanobeacon opens and emits fluorescence that in turn signals out the localization and effectiveness of silencing (Supporting Information Fig. S10).

Once EGFP expression had been blocked by siRNA, we reversed the silencing effect and regained EGFP expression via an anti-siRNA Au-nanobeacon that blocks siRNA. A specific anti-siRNA Au-nanobeacon was synthesized with 31 ± 5 anti-siRNA beacons per

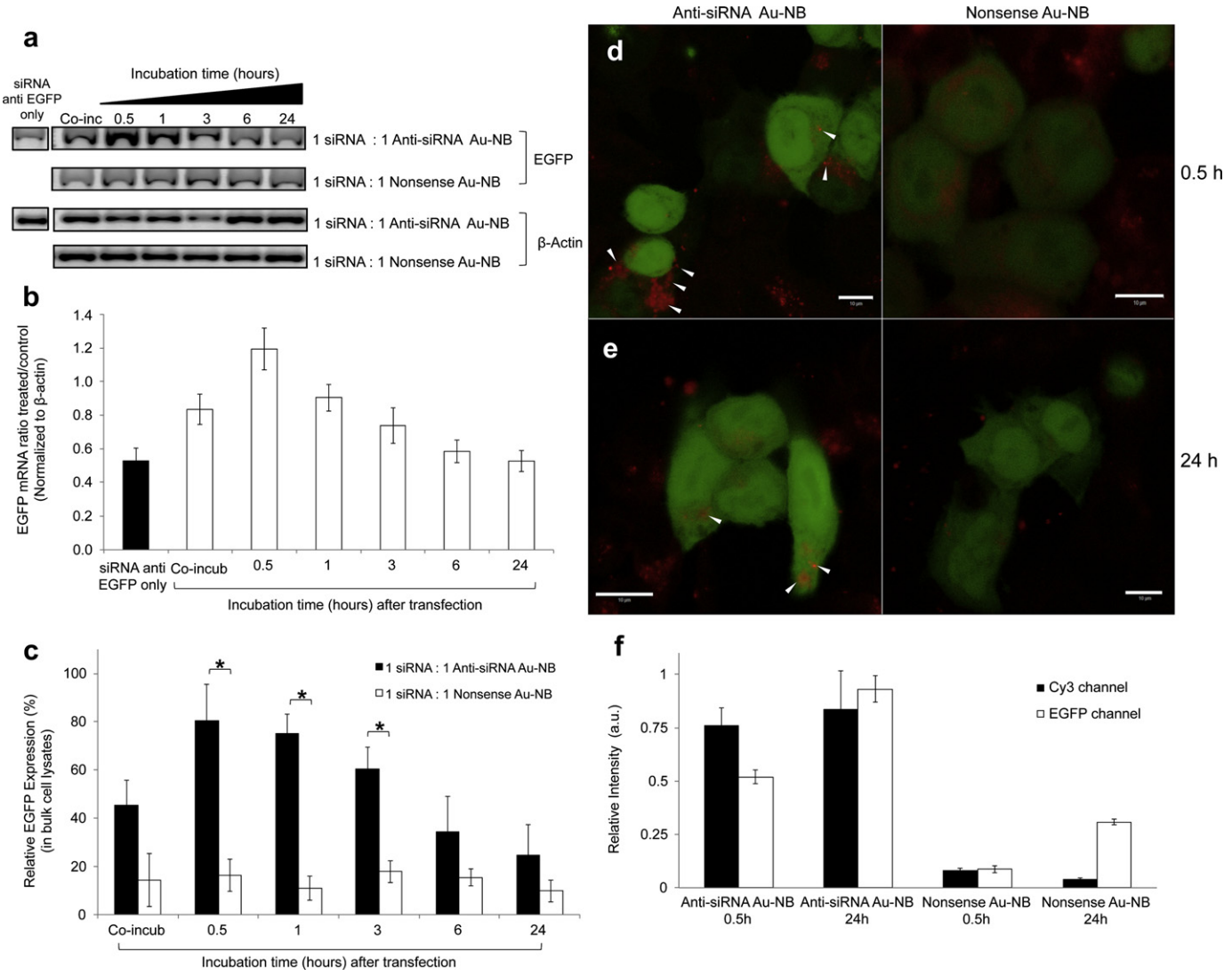

Fig. 3. Au-nanobeacons silencing of siRNA leads to EGFP expression recovery. HCT-116 cells were transfected with EGFP expression vector, followed by co-transfection with 10 mM anti-EGFP siRNA and 10 nM (concentration of beacon on AuNP) Anti-siRNA Au-nanobeacon or nonsense Au-nanobeacon and points measured with several delays of incubation (0.5, 1, 3, 6 and 24 h). (a) EGFP recovery confirmed by qRT-PCR after treatment with Anti-siRNA Au-nanobeacon or nonsense Au-nanobeacon using β-actin as reference. (b) maximal effect of the Au-nanobeacon on siRNA silencing is attained almost immediately (0.5 h), which then decreases leveling at circa 40% EGFP recovery. (c) significant EGFP recovery (asterisk, $P \leq 0.05$) as function of time from incubation with anti-siRNA Au-nanobeacon is corroborated by fluorescence evaluation in bulk cell lysates (as percentage of original EGFP fluorescence levels), using a nonsense Au-nanobeacon as control. Values are means ± s.d. from 3 independent experiments. Confocal imaging (scale bar, 10 μm) show EGFP recovery at (d) 0.5 and (e) 24 h delay incubation. Arrows point to Au-nanobeacons (Cy3) only observable in the cytoplasm of cells with high levels of EGFP recovery. (f) Silencing of silencers effect is corroborated by the relative fluorescence intensity of Au-nanobeacons (Cy3, black bars) and EGFP (white bars) after individual color channel analysis of the same confocal images using ImageJ software.

nanoparticle. Quantification of the number of beacons at the NPs' surface is crucial to match the siRNA being used to silence. Therefore, 10 nM (beacon concentration on AuNP) of anti-siRNA Au-nanobeacon were added to the cell media previously incubated with 10 nM of siRNA at several delays of incubation (0.5 h, 1 h, 3 h, 6 h and 24 h). After 48 h, the cells were lysed and collected for analysis of EGFP recovery (Fig. 3). Silencing of the silencer, i.e. blockage of the siRNA, is most effective for the first 3 h of incubation, where maximum EGFP recovery is accomplished after 0.5 h of siRNA transfection (80.6 ± 14.8% recovery of EGFP expression) and barely detected after 24 h. Expression of the EGFP was also confirmed by qRT-PCR analysis of transfected HCT-116 cells (Fig. 3a,b). Again, confocal imaging (Fig. 3d,e) clearly shows EGFP recovery using an anti-siRNA Au-nanobeacon, particularly when compared with a non-sense Au-nanobeacon for 0.5 and for 24 h. Surprisingly, EGFP recovery decreases in a time dependent manner showing almost no recovery at 24 h of incubation after adding the "silencer". The high levels of expression recovery by silencing the silencer with an anti-siRNA Au-nanobeacon, which successfully blocks the antisense strand of siRNA, together with the persistent recovery of EGFP may be the result of the stabilization of hairpin-DNA on nanoparticle. Gold nanobeacons provide significant protection from nuclease degradation in an extracellular context, probably due to the hairpin configuration and to the proximity of the oligonucleotide to the gold surface, increasing the resistance to nuclease degradation and the oligonucleotide lifetime in the cell [18,22]. Our data shows that the Au-nanobeacon approach uses the beacon's fluorescence to track the silencing inside the cell whilst evaluating whether the target is effectively being silenced. It is clear that the beacon's fluorescence increases for increased levels of silencing (Fig. 3f). Once again, the fluorescence intensity in each channel shows an increase (recovery) in EGFP fluorescence when there is an increase in anti-siRNA Au-nanobeacon signal (Cy3). And that the reverse is also true, i.e. the nonsense Au-nanobeacon that does not silence the siRNA, is not capable to promote EGFP recovery (Fig. 3f, Supporting Information Fig. S11a and b).

We then used ssRNA oligomers to silence the antisense Au-nanobeacon and a 70.3 ± 15.5% of EGFP recovery was attained. Interestingly, for the first hour of incubation, the silencing of the Au-nanobeacon by ssRNA oligomers was more effective than that of the anti-siRNA Au-nanobeacon (Supporting Information Figs. S8 and Fig. S11c and d). However, the recovery of EGFP due to silence of the siRNA seems to last for longer and 10–20% more than that observed when the antisense Au-nanobeacon is silenced

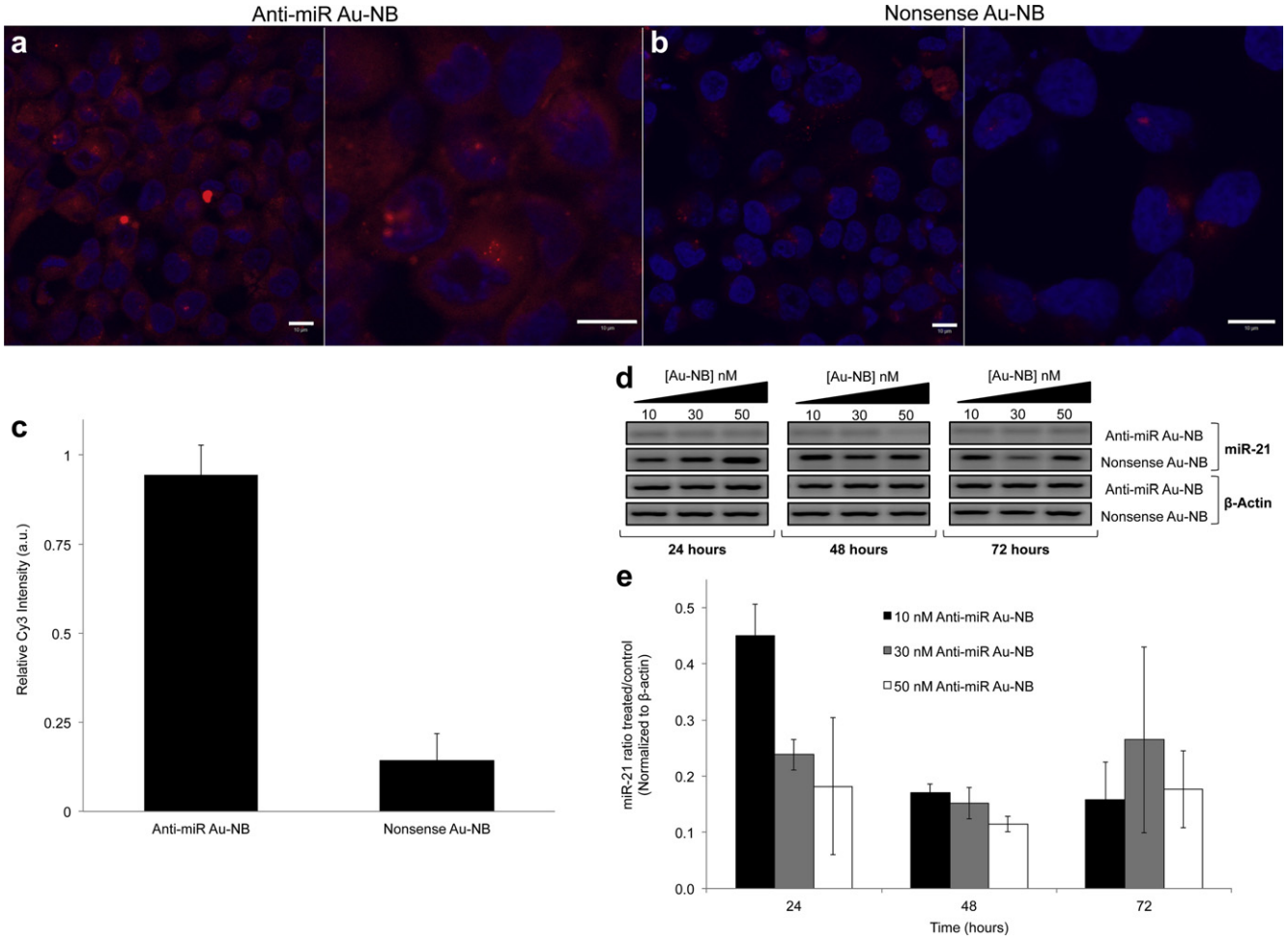

Fig. 4. Au-nanobeacons silencing of endogenous silencers – silencing of miR-21. Confocal imaging (scale bar, 10 μm) shows internalization of 50 nM (a) Anti-miR Au-nanobeacon 50 nM and (b) nonsense Au-nanobeacon. Target (mature miR-21) recognition leads to change of Anti-miR Au-nanobeacon conformation in the cytoplasm with concomitant fluorescence signal (red, Cy3) encircling the cell nuclei (blue, DAPI). (c) Specificity of target recognition is corroborated by the relative fluorescence intensity of Au-nanobeacons reading in the Cy3 channel (black bars). (d) Quantitative assessment of miR-21 silencing in colorectal carcinoma cells (HCT-116) induced by 10, 30 and 50 nM of Anti-miR Au-nanobeacon for 24, 48 and 72 h of incubation using β-actin as reference was confirmed by RT-PCR followed by agarose gel electrophoresis. (e) qRT-PCR analysis of assay versus control normalized for β-actin expression for the same conditions depicted as in (d), error bars indicate ± s.d. from 3 independent experiments. (For interpretation of the references to colour in this figure legend, the reader is referred to the web version of this article).

by the ssRNA, which might be due to increased degradation of naked ssRNA by nucleases [17,22].

Finally, we show that this Au-nanobeacon strategy is effective at targeting and silencing an endogenous miRNA towards modulation of miRNA pathway in a simple and straightforward way, making the Au-nanobeacon a valid therapeutic approach against oncomiRs. An anti-miR-21 Au-nanobeacon (33 ± 3 anti-miR beacons per nanoparticle) was used to block miR-21, which is upregulated in this cell line. The miR-21, referred as an "oncomiR" has been found to be over-expressed in most epithelial cancers and therefore, believed to play a pivotal role in the progression of many malignancies, including colon cancer and in colorectal carcinoma cells [31]. Quantitative expression and silencing efficiency of miR-21 was performed by qRT-PCR31 using 10, 30 and 50 nM of anti-miR-21 Au-nanobeacon during 24, 48 and 72 h of incubation. Data show that steady state expression of miR-21 was transiently but substantially inhibited by the specific Au-nanobeacon at 48 h (88.5 ± 1.4% miR-21 downregulation) and barely reduced at 72 h (Fig. 4d,e). Confocal microscopy (Fig. 4a,b) shows that miR-21 silencing is associated with increased Au-nanobeacon fluorescence that can be used to assess the silencing effect (Supporting Information Fig. S9). Data from the Cy3 channel show that specific target recognition by anti-miR-21 Au-nanobeacon leads to higher signal intensity than that of the nonsense Au-nanobeacon (Fig. 4c), demonstrating that miR-21 silencing is attained only when the anti-miR-21 Au-nanobeacon opens and emits fluorescence (Supporting Information Fig. S12).

To reassure that the Au-nanobeacon fluorescence emission is due to the specific recognition of the target inside cells, thus avoiding false positive signals, the Au-nanobeacons were incubated with increasing concentrations of dithiothreitol (DTT) or glutathione (GST) to mimic the reductive cell milieu (Supporting Information Fig. S4). Incubation of anti-miR Au-nanobeacon with 5 mM (physiological concentration), 10 mM and 100 mM of DTT at 37 °C during 24 h, showed no increase in fluorescence, which demonstrates that, at physiological reductive conditions, the Au-nanobeacons' emission is due to hybridization to the specific target sequence. Data show no increase in fluorescence up to 24 h incubation, which demonstrates that, at physiological reductive conditions, the Au-nanobeacons' emission is due to hybridization to the specific target.

For all experiments, cell survival rates upon siRNA and Au-nanobeacon exposure were determined via the MTT assay on HCT-116 cells, with the same experimental conditions of both silencing and recovery of expression. No cell cytotoxicity was detected up to 48 and 72 h incubation for all Au-nanobeacons and oligomers (Supporting Information Fig. S13).

These *in vitro* results open the path for *in vivo* application in particular the combination of Au-nanobeacons with other chemical functionalisations, e.g. targeting moieties, may enhance the therapeutic potential of our concept. Simultaneous studies of distinct cell populations should also be feasible using multicolor labeling.

4. Conclusions

In this paper, we show that Au-nanobeacons are a versatile concept for gene specific silencing while simultaneously allowing for intracellular tracking of the silencing events. A significant attribute of these Au-nanobeacons is the ability to inhibit the endogenous and exogenous silencers with noticeably small amounts of effector molecule and without chemical co-transfectants. Our approach, combining a fluorescence nanobeacon with silencing capability is simple, inexpensive and straightforward as adjustment to any specific target can be easily made, be it a specific mRNA or an endogenous or exogenous silencing nucleic acid. We demonstrate such potential by specifically silencing the expression of EGFP and overturning the knockdown effect of silencers after a first wave of silencing/delivery. The possibility of silencing the silencers and of discriminating specific cells, where silencing is occurring, may provide an useful tool for studying and modulating cellular mechanisms involved in cancer.

Acknowledgments

The authors thank Dr. J.C. Lima for insightful discussions on fluorescence experiments, Dr. A. Fernandes for HCT-116 cells and Dr. J. Rino and Dr. A. Temudo (BioImaging Unit at Instituto de Medicina Molecular) for assistance in confocal microscopy. This work was supported by Fundação para a Ciência e Tecnologia, Ministry of Science and Education (FCT/MEC): PTDC/BBB-NAN/1812/2012; CIGMH, Strategic Project PEst-OE/SAU/UI0009/2011; J.C. supported by SFRH/BD/62957/2009 and J.R. by SFRH/BD/43320/2008. Additional funding was from the Nanotruck-Action from NanoSciEra+. J.M.F. thanks ARAID for financial support.

Appendix A. Supplementary data

Supplementary data related to this article can be found at http://dx.doi.org/10.1016/j.biomaterials.2012.12.015.

References

[1] Modarresi F, Faghihi MA, Lopez-Toledano MA, Fatemi RP, Magistri M, Brothers SP, et al. Inhibition of natural antisense transcripts in vivo results in gene-specific transcriptional upregulation. Nat Biotechnol 2012;30:453–9.
[2] Fichou Y, Ferec C. The potential of oligonucleotides for therapeutic applications. Trends Biotechnol 2006;24:563–70.
[3] Fire A, Xu S, Montgomery MK, Kostas SA, Driver SE, Mello CC. Potent and specific genetic interference by double-stranded RNA in Caenorhabditis elegans. Nature 1998;391:806–11.
[4] Baker M. RNA interference: from tools to therapies. Nature 2010;464:1225.
[5] Wall NR, Shi Y. Small RNA: can RNA interference be exploited for therapy? Lancet 2003;362:1401–3.
[6] He L, Hannon GJ. MicroRNAs: small RNAs with a big role in gene regulation. Nat Rev Genet 2004;5:522–31.
[7] Pai SI, Lin YY, Macaes B, Meneshian A, Hung CF, Wu TC. Prospects of RNA interference therapy for cancer. Gene Ther 2006;13:464–77.
[8] Obad S, dos Santos CO, Petri A, Heidenblad M, Broom O, Ruse C, et al. Silencing of microRNA families by seed-targeting tiny LNAs. Nat Genet 2011;43:371–8.
[9] Eggleston AK. RNA silencing. Nature 2009;457:395.
[10] Leuschner F, Dutta P, Gorbatov R, Novobrantseva TI, Donahoe JS, Courties G, et al. Therapeutic siRNA silencing in inflammatory monocytes in mice. Nat Biotechnol 2011;29:1005–10.
[11] Cheng D, Cao N, Chen J, Yu X, Shuai X. Multifunctional nanocarrier mediated co-delivery of doxorubicin and siRNA for synergistic enhancement of glioma apoptosis in rat. Biomaterials 2012;33:1170–9.
[12] Chang RS, Suh MS, Kim S, Shim G, Lee S, Han SS, et al. Cationic drug-derived nanoparticles for multifunctional delivery of anticancer siRNA. Biomaterials 2011;32:9785–95.
[13] Li X, Xie QR, Zhang J, Xia W, Gu H. The packaging of siRNA within the mesoporous structure of silica nanoparticles. Biomaterials 2011;32:9546–56.
[14] Hannon GJ, Rossi JJ. Unlocking the potential of the human genome with RNA interference. Nature 2004;431:371–8.
[15] Whitehead KA, Langer R, Anderson DG. Knocking down barriers: advances in siRNA delivery. Nat Rev Drug Discov 2009;8:129–38.
[16] Conde J, Doria G, Baptista P. Noble metal nanoparticles applications in cancer. J Drug Deliv 2012;751075:1–12.
[17] Rosi NL, Giljohann DA, Thaxton CS, Lytton-Jean AK, Han MS, Mirkin CA. Oligonucleotide-modified gold nanoparticles for intracellular gene regulation. Science 2006;312:1027–30.
[18] Giljohann DA, Seferos DS, Prigodich AE, Patel PC, Mirkin CA. Gene regulation with polyvalent siRNA-nanoparticle conjugates. J Am Chem Soc 2009;131:2072–3.
[19] Lee Y, Lee SH, Kim JS, Maruyama A, Chen X, Park TG. Controlled synthesis of PEI-coated gold nanoparticles using reductive catechol chemistry for siRNA delivery. J Control Release 2011;155:3–10.
[20] Song WJ, Du JZ, Sun TM, Zhang PZ, Wang J. Gold nanoparticles capped with polyethyleneimine for enhanced siRNA delivery. Small 2010;6:239–46.
[21] Lee MY, Park SJ, Park K, Kim KS, Lee H, Hahn SK. Target-specific gene silencing of layer-by-layer assembled gold-cysteamine/siRNA/PEI/HA nanocomplex. ACS Nano 2011;5:6138–47.

[22] Conde J, de la Fuente JM, Baptista PV. In vitro transcription and translation inhibition via DNA functionalized gold nanoparticles. Nanotechnology 2010; 21:1–6.
[23] Braun GB, Pallaoro A, Wu G, Missirlis D, Zasadzinski JA, Tirrell M, et al. Laser-activated gene silencing via gold nanoshell-siRNA conjugates. ACS Nano 2009; 3:2007–15.
[24] Lee JS, Green JJ, Love KT, Sunshine J, Langer R, Anderson DG. Gold, poly(beta-amino ester) nanoparticles for small interfering RNA delivery. Nano Lett 2009; 9:2402–6.
[25] Lee SH, Bae KH, Kim SH, Lee KR, Park TG. Amine-functionalized gold nanoparticles as non-cytotoxic and efficient intracellular siRNA delivery carriers. Int J Pharm 2008;364:94–101.
[26] Guo S, Huang Y, Jiang Q, Sun Y, Deng L, Liang Z, et al. Enhanced gene delivery and siRNA silencing by gold nanoparticles coated with charge-reversal polyelectrolyte. ACS Nano 2010;4:5505–11.
[27] Conde J, Ambrosone A, Sanz V, Hernandez Y, Marchesano V, Tian F, et al. Design of multifunctional gold nanoparticles for in vitro and in vivo gene silencing. ACS Nano 2012;6:8316–24.
[28] Rosa J, Conde J, de la Fuente JM, Lima JC, Baptista PV. Gold-nanobeacons for real-time monitoring of RNA synthesis. Biosens Bioelectron 2012;36: 161–7.
[29] Lee PC, Meisel D. Adsorption and surface-enhanced Raman of dyes on silver and gold sols. J Phys Chem 1982;86:3391–5.
[30] Sanz V, Conde J, Hernandez Y, Baptista PV, Ibarra MR, de la Fuente JM. Effect of PEG biofunctional spacers and TAT peptide on dsRNA loading on gold nanoparticles. J Nanopart Res 2012;14:1–9.
[31] Yan LX, Huang XF, Shao Q, Huang MY, Deng L, Wu QL, et al. MicroRNA miR-21 overexpression in human breast cancer is associated with advanced clinical stage, lymph node metastasis and patient poor prognosis. RNA 2008;14: 2348–60.

Supporting Information

Gold-nanobeacons for simultaneous gene specific silencing and intracellular tracking of the silencing events

João Conde[1,2], João Rosa[1,3], Jesús M. de la Fuente[2] and Pedro V. Baptista[1,*]

[1]CIGMH, Departamento de Ciências da Vida, Faculdade de Ciências e Tecnologia, Universidade Nova de Lisboa, Campus de Caparica, 2829-516 Caparica, Portugal.
[2]Instituto de Nanociencia de Aragón, Universidad de Zaragoza, Campus Río Ebro, Edifício I+D, Mariano Esquillor, s/n, 50018 Zaragoza, Spain.
[3]REQUIMTE, Departamento de Química, Faculdade de Ciências e Tecnologia, Universidade Nova de Lisboa, Campus de Caparica, 2829-516 Caparica, Portugal.

*Corresponding author. Email: pmvb@fct.unl.pt. Phone/Fax: +351 212948530

This file includes additional information for the following sections:

A. Physical characterization of Au-nanobeacons

1. Synthesis of citrate-gold nanoparticles (AuNPs)

Gold nanoparticles, with an average diameter of 14.6±1.7 nm, were synthesized by the citrate reduction method. Briefly, 225 mL of 1 mM hydrogen tetrachloroaureate (III) hydrate (Sigma) (88.61 mg) solved in 500 ml of distilled water were heated to reflux while stirring. Then, 25 mL of 38.8 mM sodium citrate dihydrate (285 mg) were added and refluxed for additional 30 minutes with vigorous stirring and protected from light. The resulting red solution is cooled down and kept protected from light. Citrate capped AuNPs were characterized by Transmission Electron Microscopy (TEM) and UV-Vis spectroscopy (see **Figure S2**).

2. Poly(ethylene glycol) functionalization of gold nanoparticles (AuNP@PEG)

Briefly, 10 nM of the AuNP solution were mixed with 0.003 mg/mL of a commercial hetero-functional poly(ethylene glycol) (PEG) [O-(2-Mercaptoethyl)-O'-methyl-hexa(ethylene glycol), $C_{15}H_{32}O_7S$, 356.48 Da] in an aqueous solution of SDS (0.028%). Then, NaOH was added to a final concentration of 25 mM and the mixture incubated for 16 hours at room temperature. Excess PEG was removed by centrifugation (21.460 ×g, 30 min, 4ºC), and quantified by a modification of the Ellman's Assay [29]. The excess of thiolated chains in the supernatants is quantified by interpolating a calibration curve set by reacting 200 μL of stock solution of the O-(2-Mercaptoethyl)-O'-methyl-hexa(ethylene glycol) in 100 μL of phosphate buffer 0.5 M (pH 7) with 7 μL of 5,5'-dithio-bis(2-nitrobenzoic) acid (DTNB) 5 mg/mL in phosphate buffer 0.5 M (pH 7), and measuring the absorbance at 412 nm after 10 minutes. The linear range (see **Figure S1b**) for the O-(2-Mercaptoethyl)-O'-methyl-hexa(ethylene glycol) chain obtained by this method is 0.0002–0.035 mg/mL (Abs412 = 26.034×[PEG, mg/mL] + 0.0627). The number of exchanged chains is given by the difference between the amount determined by this assay and the initial amount incubated with the

AuNPs. There is a point at which the nanoparticle becomes saturated with a thiolated layer and is not able to take up more thiolated chains - maximum coverage per gold nanoparticle, i.e. 0.01 mg/mL of O-(2-Mercaptoethyl)-O'-methyl-hexa(ethylene glycol) (**Figure S1c**). The Au-nanobeacons were functionalized with 0.003 mg/mL of O-(2-Mercaptoethyl)-O'-methyl-hexa(ethylene glycol) corresponding to 30% of PEG saturation of AuNPs' surface (190.29 ± 19.56 chains per nanoparticle).

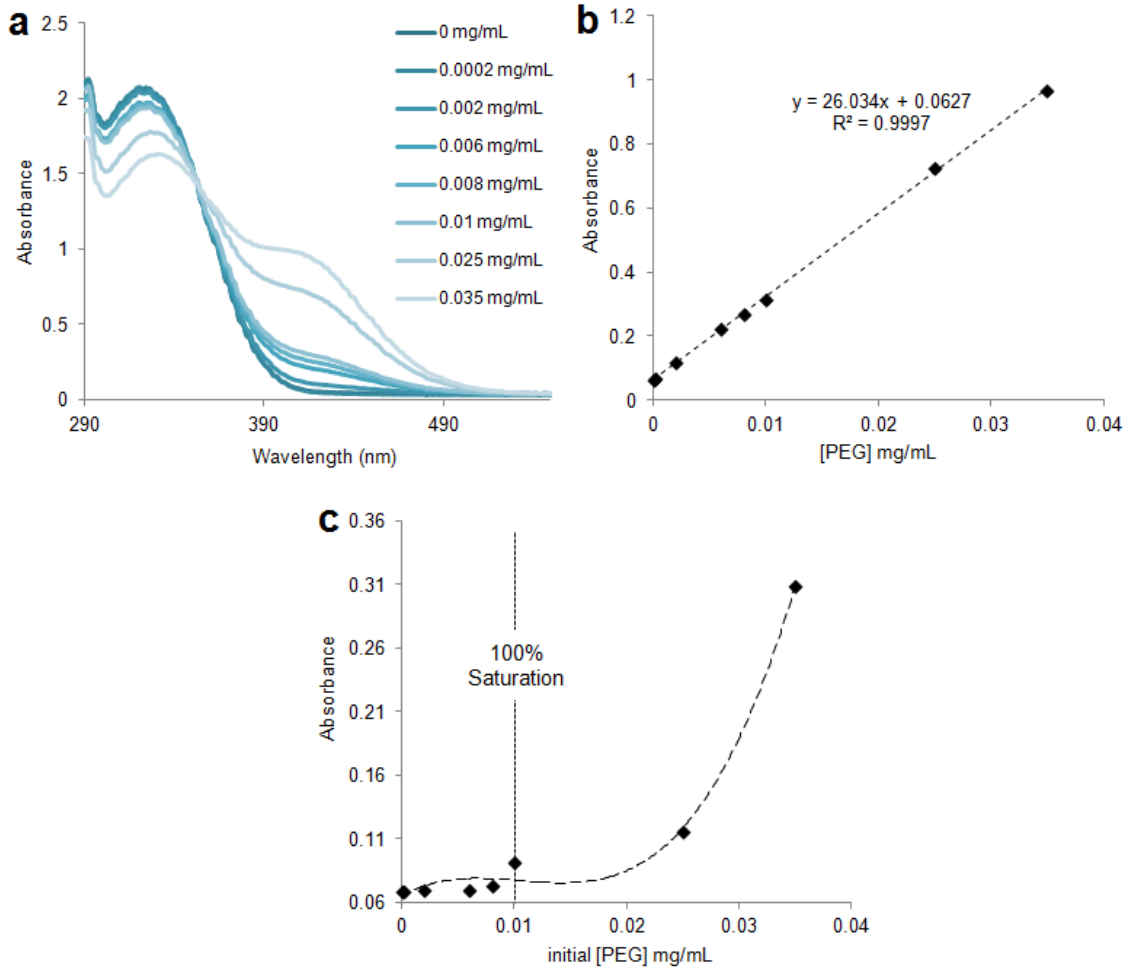

Figure S1. (a) Absorbance spectra of DTNB after reaction with the thiolated PEG. **(b)** Standard calibration curve for PEG chains, whose concentration can be calculated via the following equation Abs412nm = 26.034 × [PEG, mg/mL] + 0.0627. **(c)** Variation of the excess of PEG thiolated chains as a function of the initial concentration in the incubation with 10 mM AuNPs. The dashed vertical line indicates the 100% saturation, i.e. the PEG concentration above which no more PEG can be bonded to the AuNPs' surface.

3. Assembly of Au-nanobeacons (AuNP@PEG@Beacon)

We prepared four sets of Au-nanobeacons using double modified oligonucleotides, 3'-Cy3 and 5'-Thiol-C6, in an hairpin conformation (see **Table 1**): antisense Au-nanobeacon, a stem-looped oligonucleotide complementary to the Kozak consensus translation initiation site and start codon of EGFP (pVisionGFP-N vector 4.7 kb, Biovision), thus capable of blocking the transcriptional machinery; anti-siRNA Au-nanobeacon, a stem-looped oligonucleotide complementary to the siRNA that silences EGFP; nonsense Au-nanobeacon, an unrelated stem-looped oligonucleotide; and anti-miR Au-nanobeacon, a stem-looped oligonucleotide complementary to miR-21. Briefly, the thiolated beacons (STABVIDA) were suspended in 1mL of 0.1M dithiothreitol (DTT), extracted three times with ethyl acetate and further purified through a desalting NAP-5 column (Pharmacia Biotech) using 10 mM phosphate buffer (pH 8) as eluent. Following oligonucleotide quantification via UV/Vis spectroscopy, each beacon was added to the AuNP@PEG in a 100:1 ratio. AGE I solution (2% (w/v) SDS, 10 mM phosphate buffer (pH 8)) was added to the mixture to a final concentration of 10 mM phosphate buffer (pH 8), 0.01% (w/v) SDS, sonicated for 10 seconds using an ultrasound bath and incubated at room temperature for 20 minutes. Afterwards, the ionic strength of the solution was increased sequentially in 50 mM NaCl increments by adding the required volume of AGE II solution (1.5 M NaCl, 0.01% (w/v) SDS, 10 mM phosphate buffer (pH 8)) up to a final concentration of 10 mM phosphate buffer (pH 8), 0.3 M NaCl, 0.01% (w/v) SDS. After each increment, the solution was sonicated for 10 seconds and incubated at room temperature for 20 minutes. The solution was allowed to rest for additional 16 hours at room temperature. Then, the functionalized Au-nanobeacons were centrifuged for 20 minutes at 21.460 ×g, the oily precipitate washed three times with DEPC-treated H_2O, and redispersed in the same buffer to a final concentration in Au-nanobeacons of 15 nM. The resulting Au-nanobeacons were stored in the dark at 4 °C until further use.

Physical characterization of the Au-nanobeacons was performed by Dynamic Light Scattering (Zetasizer, Malvern), Zeta Potential (Zetasizer, Malvern), UV/Vis Spectroscopy and Transmission Electron Microscopy (see **Figure S2** and **Table 2**).

Table 1. Oligomers sequences used in Au-nanobeacons functionalisation and in target specificity.

Oligomers	**Sequences**	**ΔG (kcal/mol) No target**	**ΔG (kcal/mol) With target**
antisense Au-nanobeacon	5'-TTTGCCTCGTCGCTCTCCATGGTGGGCAAA-3'	-3.38	-27.28
anti-siRNA Au-nanobeacon	5'-TTTGCCGCATGACCAACAAGATGAAGGCAAA-3'	-4.71	-25.48
anti-miR Au-nanobeacon	5'-TTTGCCTCAACATCAGTCTGATAAGCTAGGCAAA-3'	-4.74	-27.43
nonsense Au-nanobeacon	5'-TTTGCCCCGTTACTATTTGCACCACGGCAAA-3'	-3.04	N/A
Antisense target	5'-CACCAUGGAGAGCGACGA-3'	N/A	N/A
anti EGFP siRNA	Sense: 5'-GCAUGACCAACAAGAUGAAUU-3' Antisense: 3'-UUCAUCUUGUUGGUCAUGCUU-5'	N/A	N/A
nonsense siRNA	Sense: 5'-AAUUCUCCGAACGUGUCACGUUU-3' Antisense: 3'-UUUUAAGAGGCUUGCACAGUGCA-5'	N/A	N/A
miR-21 target	5'-UAGCUUAUCAGACUGAUGUUGA-3'	N/A	N/A

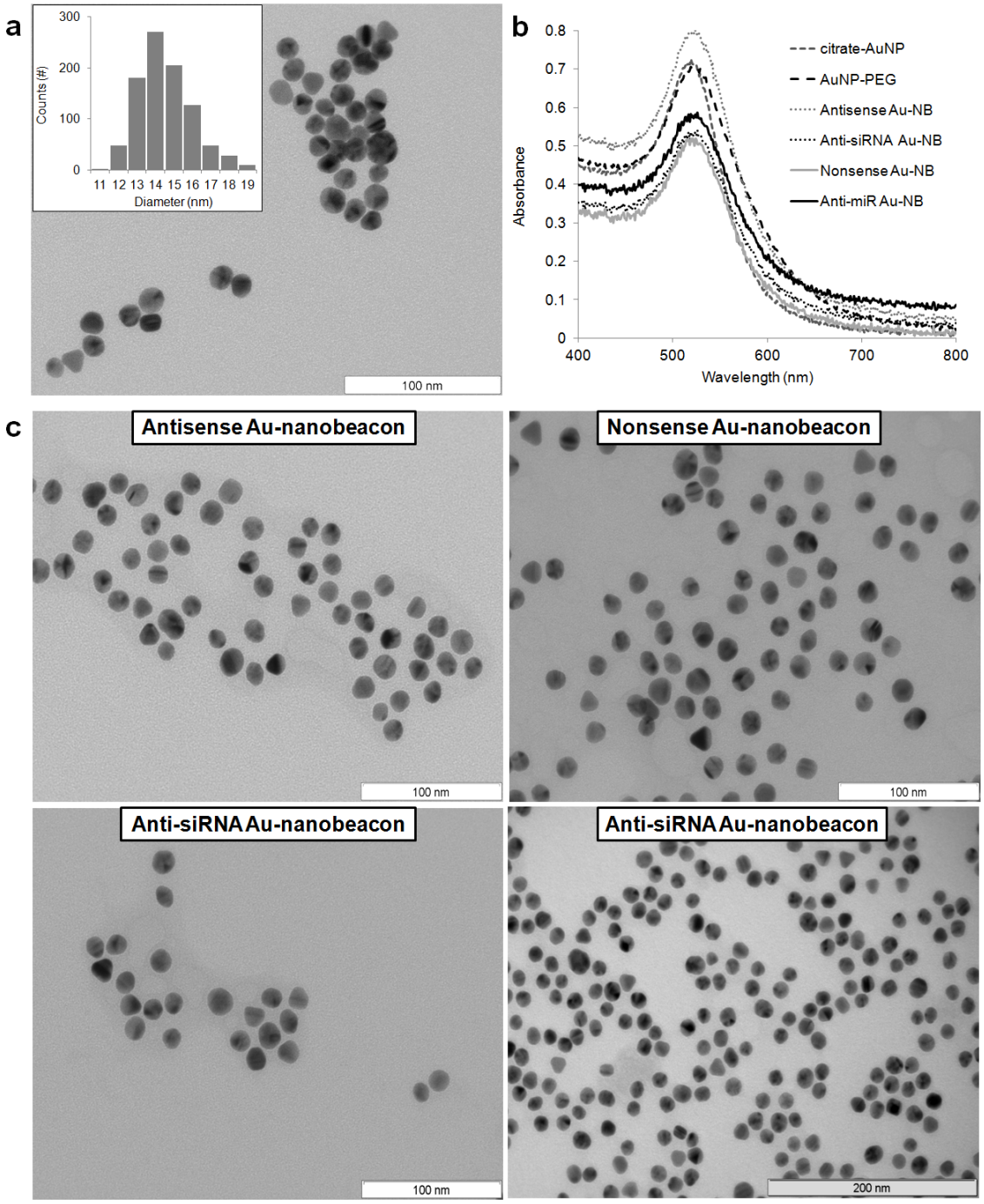

Figure S2. Au-nanoparticle characterization. (**a**) The high monodispersity of the gold cores was confirmed by Transmission Electron Microscopy (TEM) (scale bar, 100 nm). **Inset:** Size distribution histogram showing an average diameter of the AuNPs of 14.6±1.7 nm. (**b**) UV-Vis spectra of the synthesized AuNPs, Au@PEG and Au-nanobeacons showing the characteristic surface plasmon resonant peak shift from 520 to 525 nm due to surface functionalization. (c) TEM images of all Au-nanobeacons.

4. Quantitation of Beacon coverage on AuNP@PEG

Coverage, i.e. number of beacons per nanoparticle, was determined by quantification of the excess beacons in the supernatants collected during synthesis via the emission spectra of Cy3 (excitation/emission, 530 nm/560 nm) dye in a Cary Eclipse (Varian) using an Ultra-Micro quartz cell (Hëllma). All AuNPs samples and standard solutions of the thiolated-beacons were kept at the same pH and ionic strength for all measurements. Fluorescence emission was converted to molar concentrations by interpolation from a standard linear calibration curve prepared with known concentrations of beacon - see **Table 2**.

Table 2. Quantification of the PEG chains and beacon for all Au-nanobeacons, together with DLS and Zeta-potential measurements.

Au-nanobeacons	**PEG chains/NP**	**Hairpin DNA (Beacons)/NP**	**DLS Diameter (nm)**	**Zeta Potential (mV)**
antisense Au-nanobeacon	190.29 ± 19.56	57.87 ± 3.92	33.95 ± 7.10	-36.53 ± 1.24
anti-siRNA Au-nanobeacon	190.29 ± 19.56	30.78 ± 4.84	40.77 ± 4.42	-37.73 ± 1.34
anti-miR Au-nanobeacon	190.29 ± 19.56	33.04 ± 2.99	52.65 ± 8.08	-21.87 ± 1.41
nonsense Au-nanobeacon	190.29 ± 19.56	31.64 ± 3.49	34.86 ± 1.21	-33.76 ± 2.37

5. Au-nanobeacon target recognition

Each Au-nanobeacon capability to specifically recognize the complementary target was assessed by hybridizing 1 nM of Au-nanobeacon to 5 nM of complementary OR non-complementary targets in 10 mM of phosphate buffer (pH 7) (see **Figure S3**). A PerkinElmer LS45 Fluorescence Spectrometer (Varian) using an Ultra-Micro quartz cell (Hëllma) programmed to incubate the

reactions for 120 min at 37°C recoded the fluorescence intensity of the Au-nanobeacon every 2 minutes at an excitation wavelength of 530 nm.

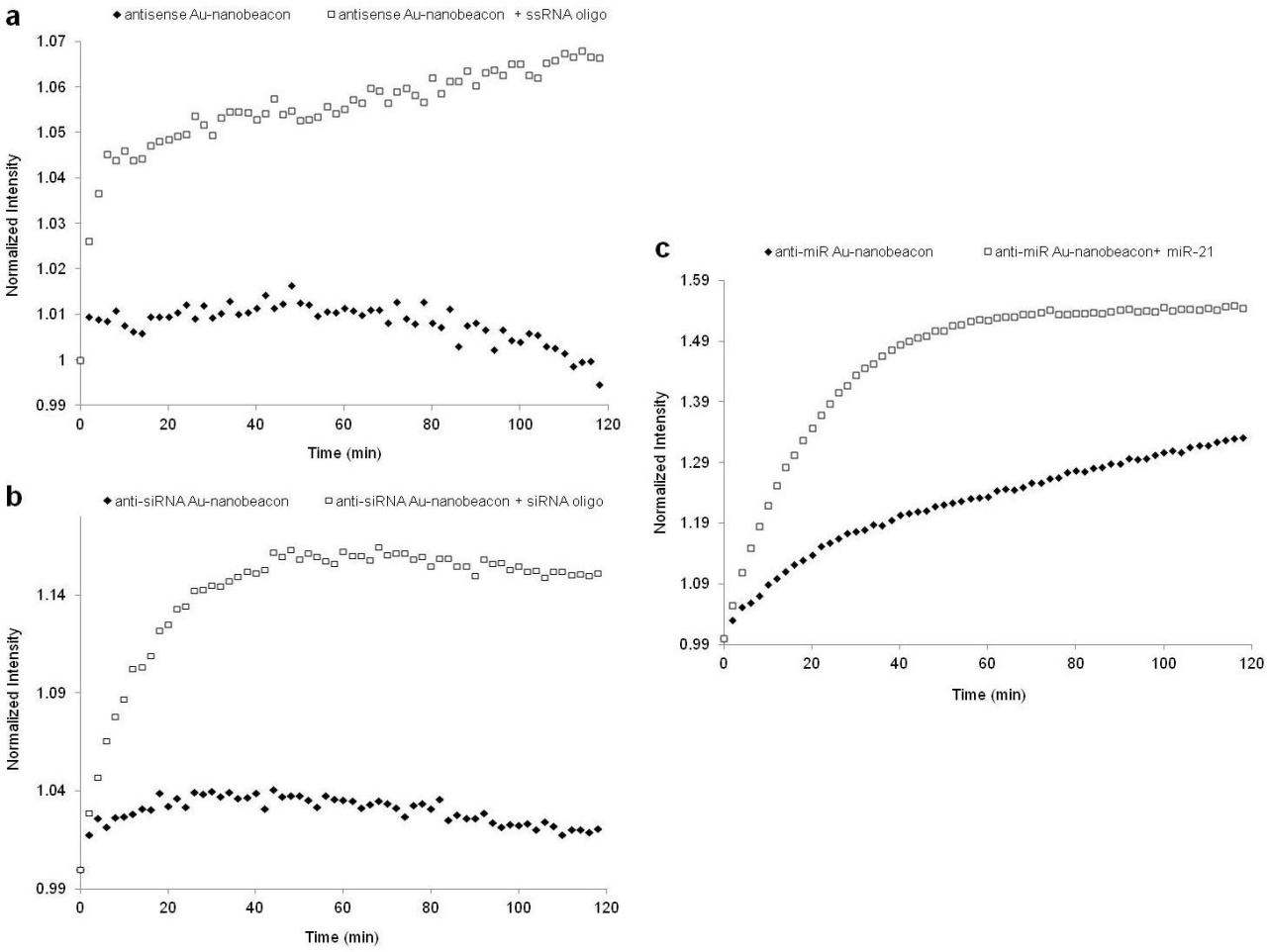

Figure S3. Au-nanobeacons specificity for target. Fluorescence emission as function of hybridization time with (**a**) the antisense Au-nanobeacon, (**b**) anti-siRNA Au-nanobeacon, and (**c**) anti-miR Au-nanobeacon at 37ºC in presence of the complementary target (white squares) or a non-complementary target . Target sequences are depicted in **Table 1**.

6. Au-nanobeacon behaviour in a reductive milieu

To evaluate whether the reductive cell environment would cause detachment of the beacon from the AuNPs' surface, the Au-nanobeacons resistance to DTT or glutathione (GST) was evaluated. To mimic the behaviour in the intra-cellular milieu, 1 nM of the Anti-miR-21 Au-nanobeacon was incubated with 5, 10 and 100 mM of DTT or GST (Sigma-Aldrich) at 37°C for up to 24 h. Fluorescence intensity was measured in a PerkinElmer LS45 Fluorescence Spectrometer (Varian) using an Ultra-Micro quartz cell (Hëllma) programmed to incubate the reactions for 1440 min (24 hours) at 37°C at 15 minutes intervals (excitation/emission, 530 nm/560 nm) (see **Figure S4**). The curves show that for concentrations of reducing agent between 5 and 10 mM, the Au-nanobeacon remains in its closed conformation, which demonstrate that, under physiologic intracellular conditions, observable Au-nanobeacon fluorescence is solely due to hybridization to specific target.

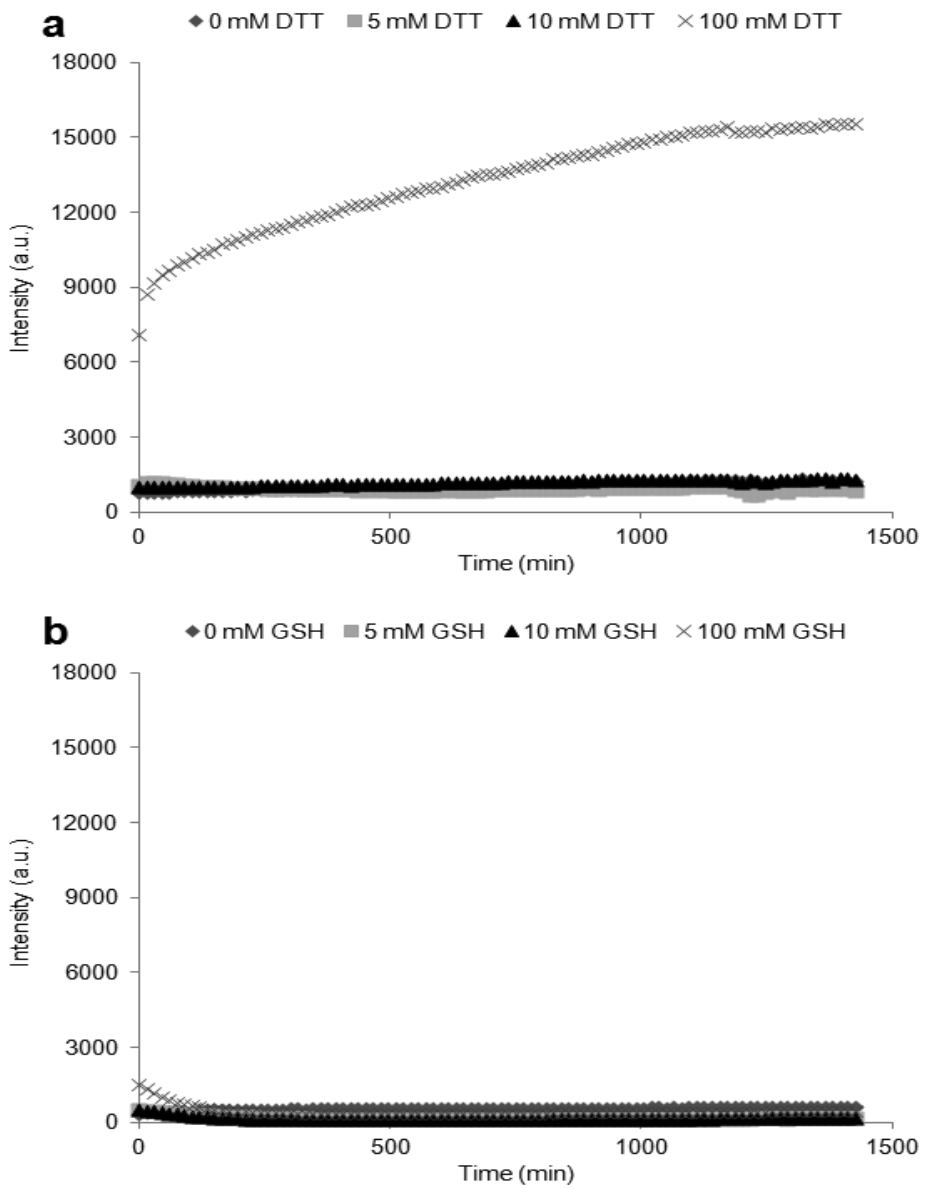

Figure S4. Au-nanobeacon behaviour in presence of increasing concentration of (a) DTT or (b) GST as reducing agent. The anti-miR Au-nanobeacon was incubated with 5 mM (physiological millieu), 10 mM and 100 mM of DTT or GST, at 37ºC during 24 hours, and fluorescence plotted as function of time.

B. Gene expression quantification via Real-time RT-PCR

Real-Time PCR was performed in a Corbett Research Rotor-Gene RG3000 using SYBR GreenER Real-Time PCR Kit (Invitrogen) according to manufacturer's specifications in 50 µl reactions containing 2 µl of cDNA from HCT-116 cells, 1× SYBR Green SuperMix and 200 nM of primers (STABVIDA) - see **Table 3** for primer sequences. The amplification conditions consisted of 50°C for 2 min hold, 95°C during 10 min hold, followed by 40 cycles consisting of denaturation at 95°C for 30 s, annealing at 52°C for 60 s, extension at 72°C for 45 s, with a final extension step at 72°C for 10 min. All data originated from three independent experiments. PCR amplification products were subjected to agarose gel electrophoresis (2% agarose, TBE 1×, 75 minutes at 90V, GelRed staining visualized under UV light) to confirm amplicons' molecular weight: 158 bp (β-actin), 792 bp (EGFP) and 75 bp (miR-21) (see **Figure S5**). As the difference of PCR amplification efficiency of EGFP, miR-21 and β-actin products was less than 5%, qRT-PCR data were derived from $2^{-\Delta\Delta CT}$ using β-actin expression levels as reference [fold-induction was calculated by the Ct method as follows: $\Delta\Delta CT = (Ct\ EGFP(or\ miR\text{-}21) - Ct\ \beta\text{-}actin)_{treated\ for\ EGFP(or\ miR\text{-}21)} - (Ct\ EGFP(or\ miR\text{-}21) - Ct\ \beta\text{-}actin)_{untreated}$] [32].

Table 3. Primer sequences used in qReal-Time PCR.

Primers	Sequences
β-actin forward	5´-ATAGCACAGCCTGGATAGCAAC-3´
β-actin reverse	5´-CACCTTCTACAATGAGCTGCGT-3´
EGFP forward	5´-AGCTTCGAATTCTGCAGTCG-3´
EGFP reverse	5´-GGCTGATTATGATCTAGAGTC-3´
miR-21 loop	5'-TGTTGCCATGAGATTCAACAGTCAACATCAGTCTGATAAGCTACCCGACA-3'
miR-21 forward	5'-GCCGCTAGCTTATCAGACTGATGT-3'

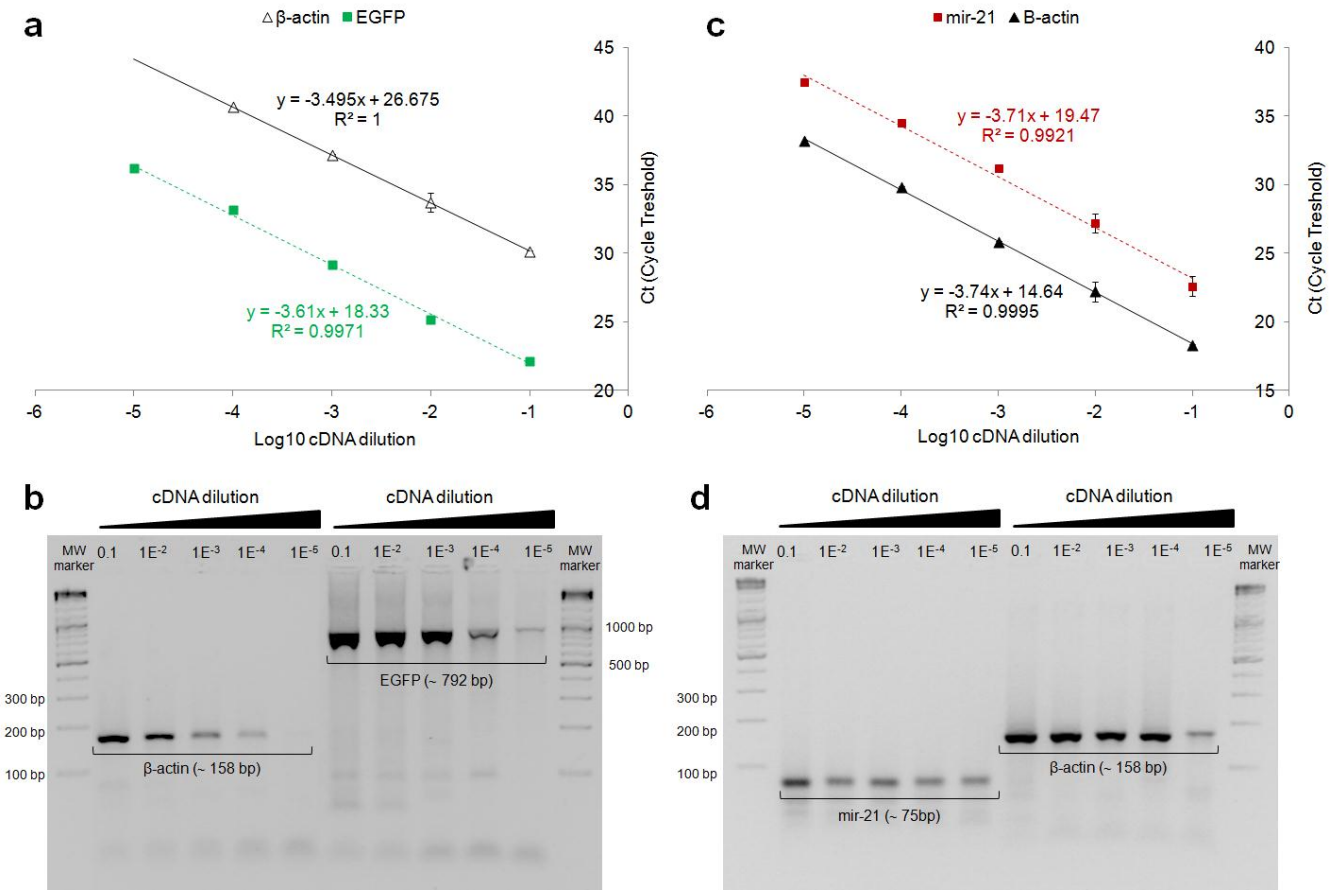

Figure S5. Standard curves for primers in RT-PCR for EGFP (**a**) and miR-21 (**c**) expression profiles used for calculation of primer efficiency (Efficiency = $10^{\wedge(-1/\text{slope})} - 1$). Agarose gel electrophoresis (2% agarose, TBE 1×, 75 minutes at 90V) of the standard curves for primers. The expected sizes of the PCR products are 158 bp (β-actin) and 792 bp (EGFP) (**b**) and 75 bp (miR-21) (**d**).

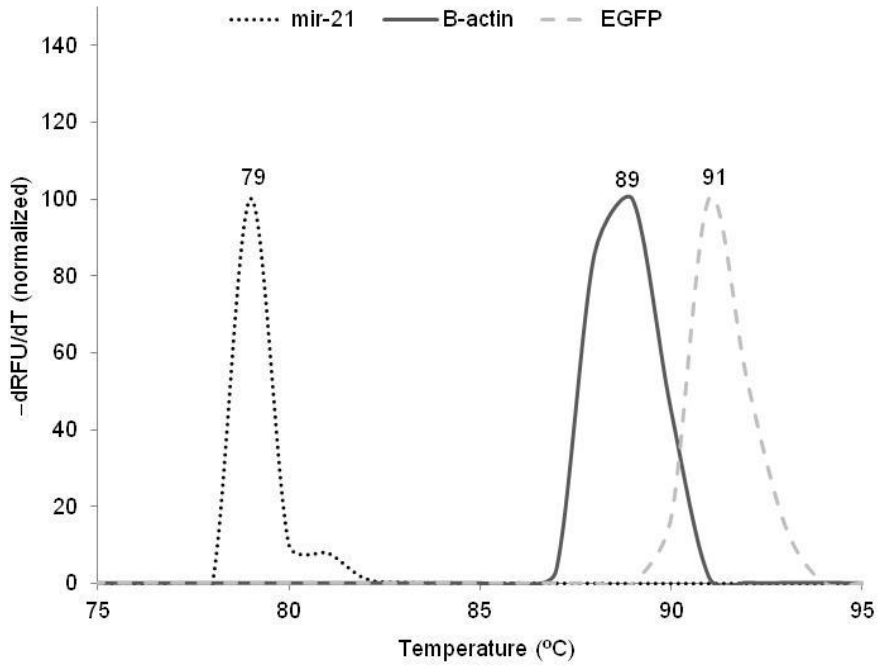

Figure S6. 1st Derivative melting temperature curve of the miR-21, β-actin and EGFP Real-time PCR products. The theoretic melting temperatures of the PCR products were 75.5ºC (miR-21), 84.8ºC (β-actin) and 90.2ºC (EGFP).

C. Silencing of specific gene expression - Optimization

Cells were incubated for 48 hours with increasing concentrations of Anti EGFP siRNA and Antisense Au-nanobeacon, i.e. 10, 20 and 30 nM, so as to ascertain the best silencing conditions for either approach.

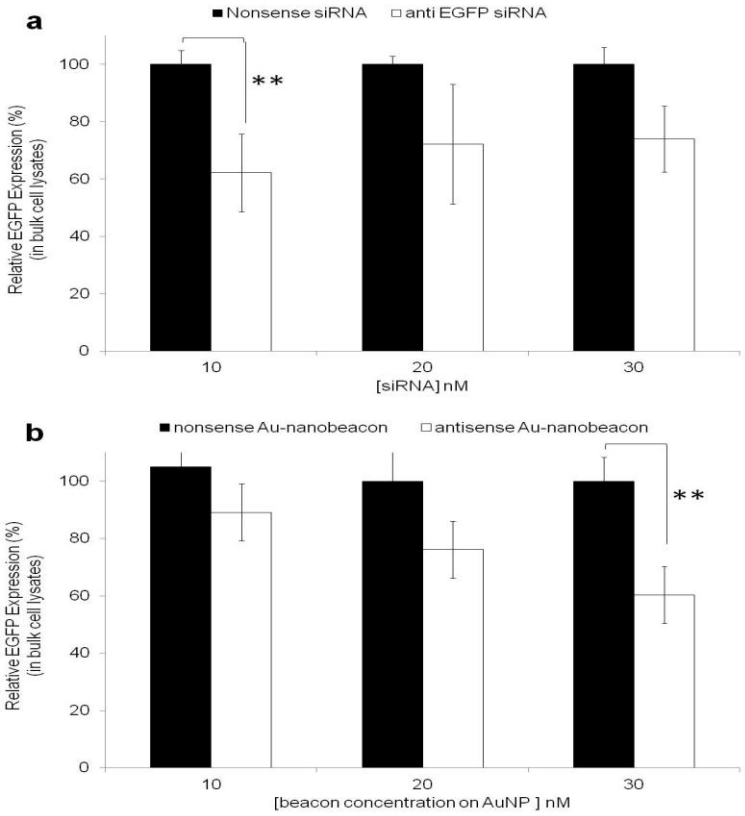

Figure S7. Silencing of specific gene expression.

EGFP expression silencing confirmed by significant fluorescence decrease (**, $P \leq 0.005$) in bulk cell lysates (as percentage of original EGFP fluorescence levels), using an unrelated siRNA (Nonsense siRNA) (**a**) or unrelated hairpin DNA bound onto AuNPs (Nonsense Au-nanobeacon) (**b**). Values are means ± s.d. from 3 independent experiments.

D. Recovery of EGFP expression by ssRNA anti-antisense Au-nanobeacon

To evaluate EGFP recovery, 30 nM of ssRNA complementary to the Antisense Au-nanobeacon was added to the media together with 30 nM of the Au-nanobeacon with several delays of incubation (0.5, 1, 3, 6 and 24 hours). After 48 hours, EGFP fluorescence was evaluated as for the silencing experiments. Expression of the EGFP was confirmed by qRT-PCR analysis of transfected HCT-116 cells using β-actin as reference. Evaluation of EGFP recovery in bulk cell lysates following Antisense Au-nanobeacon silencing was performed by addition of 30 nM of anti-antisense ssRNA to the cell media with 30 nM of antisense Au-Nanobeacon at several delays of incubation

(0.5, 1, 3, 6 and 24 hours). Bioactivity of anti-antisense ssRNA oligo was compared to that of a nonsense ssRNA oligo.

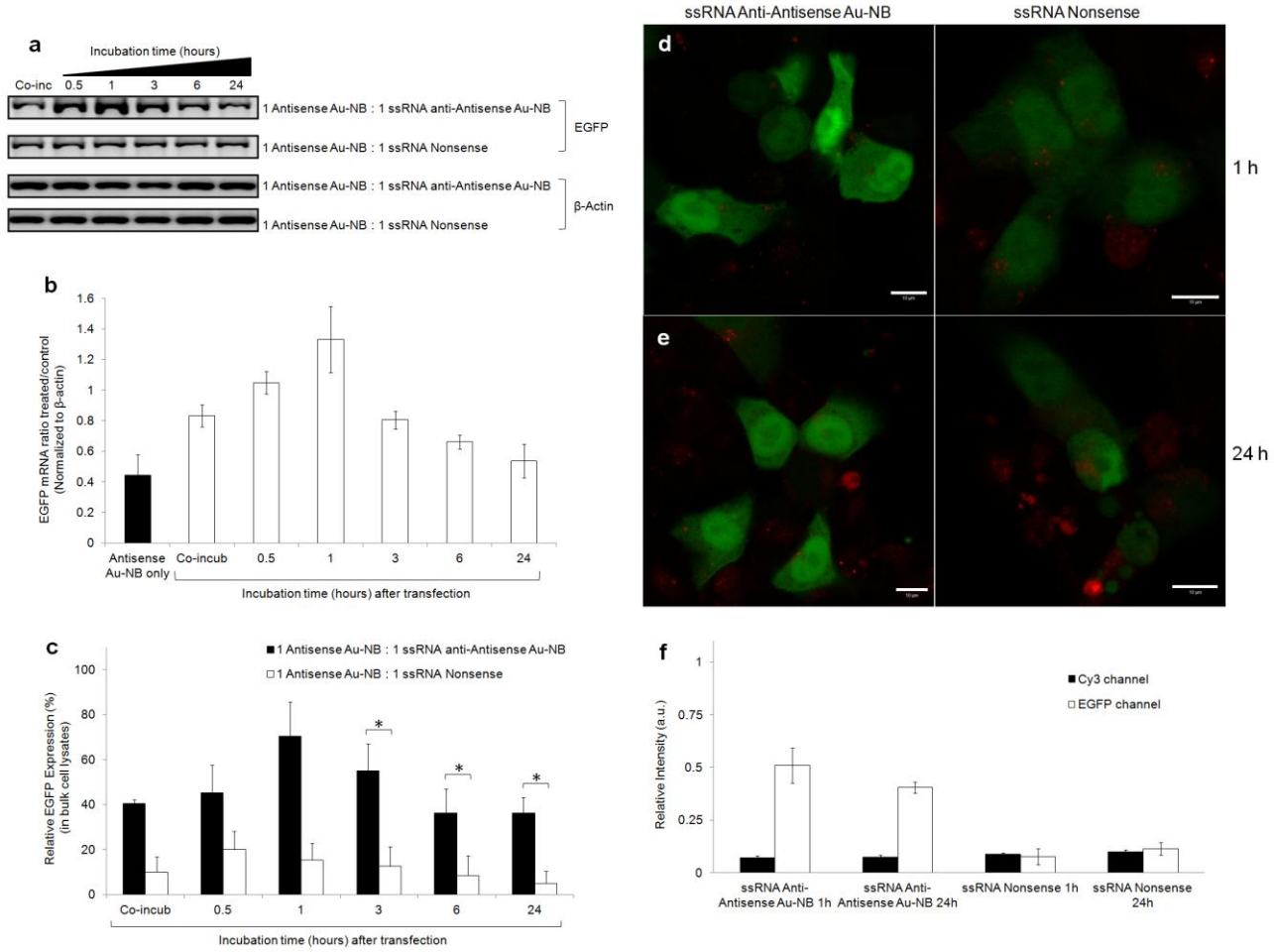

Figure S8. Recovery of EGFP expression by ssRNA anti-antisense Au-nanobeacon. Evaluation of EGFP recovery by (**a**,**b**) qRT-PCR and (**c**) in bulk cell lysates in presence of ssRNA oligo nonsense (grey bars), ssRNA oligo anti-antisense Au-Nanobeacon (black bars) indicating statistically significant difference as calculated by Paired-Sample T-test (asterisk, $P \leq 0.05$). Values are means ± s.d. from 3 independent experiments. Confocal imaging (scale bar, 10 μm) show EGFP recovery at (**d**) 1 and (**e**) 24 hours delay incubation. (**f**) blocking of Antisense Au-nanobeacon by ssRNA oligomer is corroborated by the relative fluorescence intensity of Au-nanobeacons (Cy3, black bars) and EGFP (white bars) after individual colour channel analysis of the same confocal images using ImageJ software.

E. Intracellular localization of Anti-miR-21 Au-nanobeacon

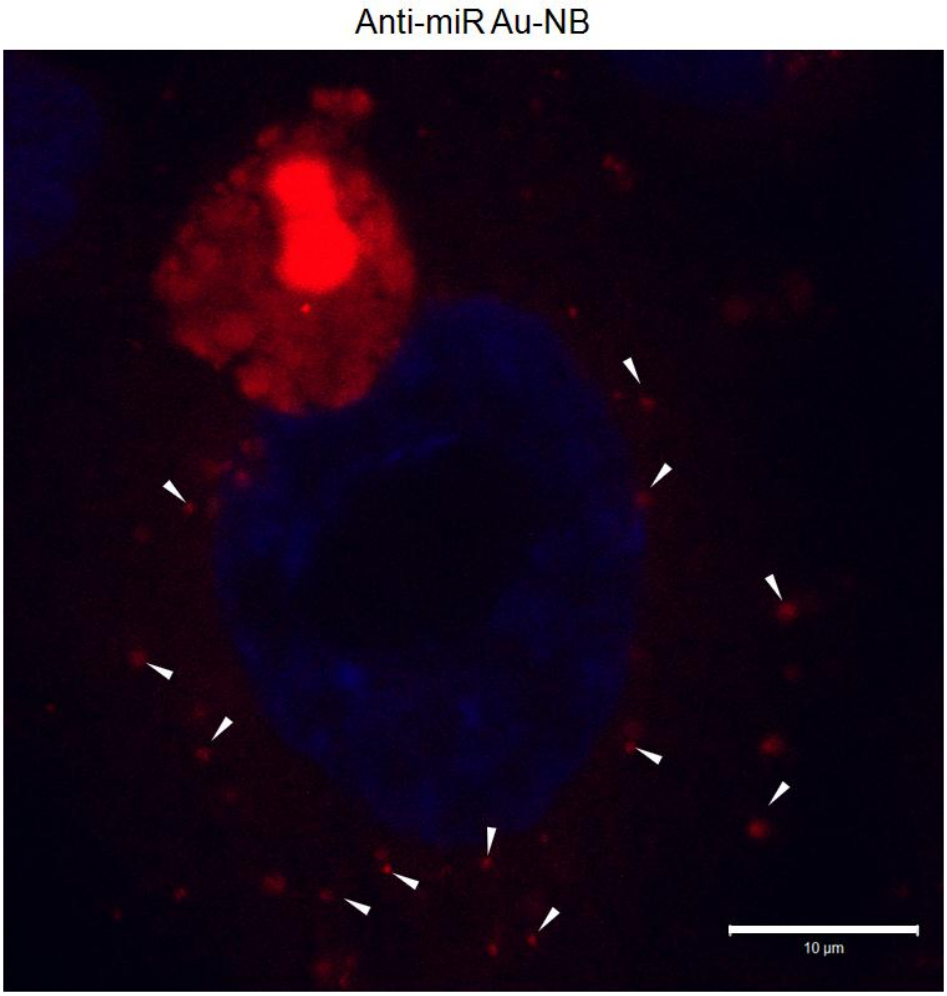

Figure S9. Intracellular localization of the anti-miR-21 Au-nanobeacon. Cell show a punctuate fluorescence pattern indicating that the anti-miR Au-nanobeacons distributed evenly in the cytoplasm (white arrows) following hairpin conformational change due to specific hybridization to the miR-21 target sequence. A large amount of fluorescence seems to be engulfed in a localized compartment above the plan of the nucleus, possibly indicating entrapment in cell vesicle.

F. Individual quantification of Cy3 and EGFP fluorescence signals in confocal images

Confocal images were processed using ImageJ software to break down fluorescence signals into separate channels for Cy3 and EGFP (green), which can be composed into B&W depictions. This way, each signal can be observed separately and, therefore, its origin clearly identified. The

intensity of each individual signal could then be quantified. This process allowed to confirm that only when the Au-nanobeacons are open, due to specific target recognition, their effect on gene expression modulation can be felt.

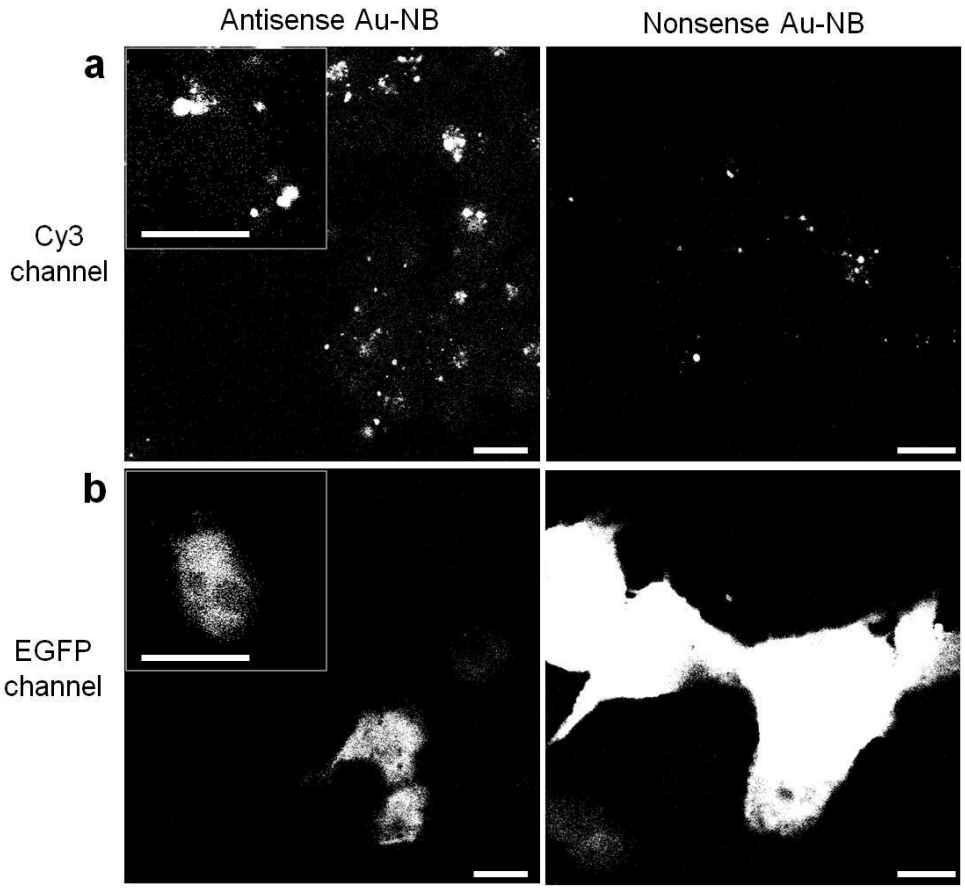

Figure S10. Antisense Au-nanobeacon silencing of EGFP. Striking differences for Cy3 and EGFP emissions related to the antisense and nonsense Au-nanobeacon effect can be observed, thus confirming that silencing occurs upon hairpin conformational change due to specific hybridization to the target sequence. Scale bar, 10 μm.

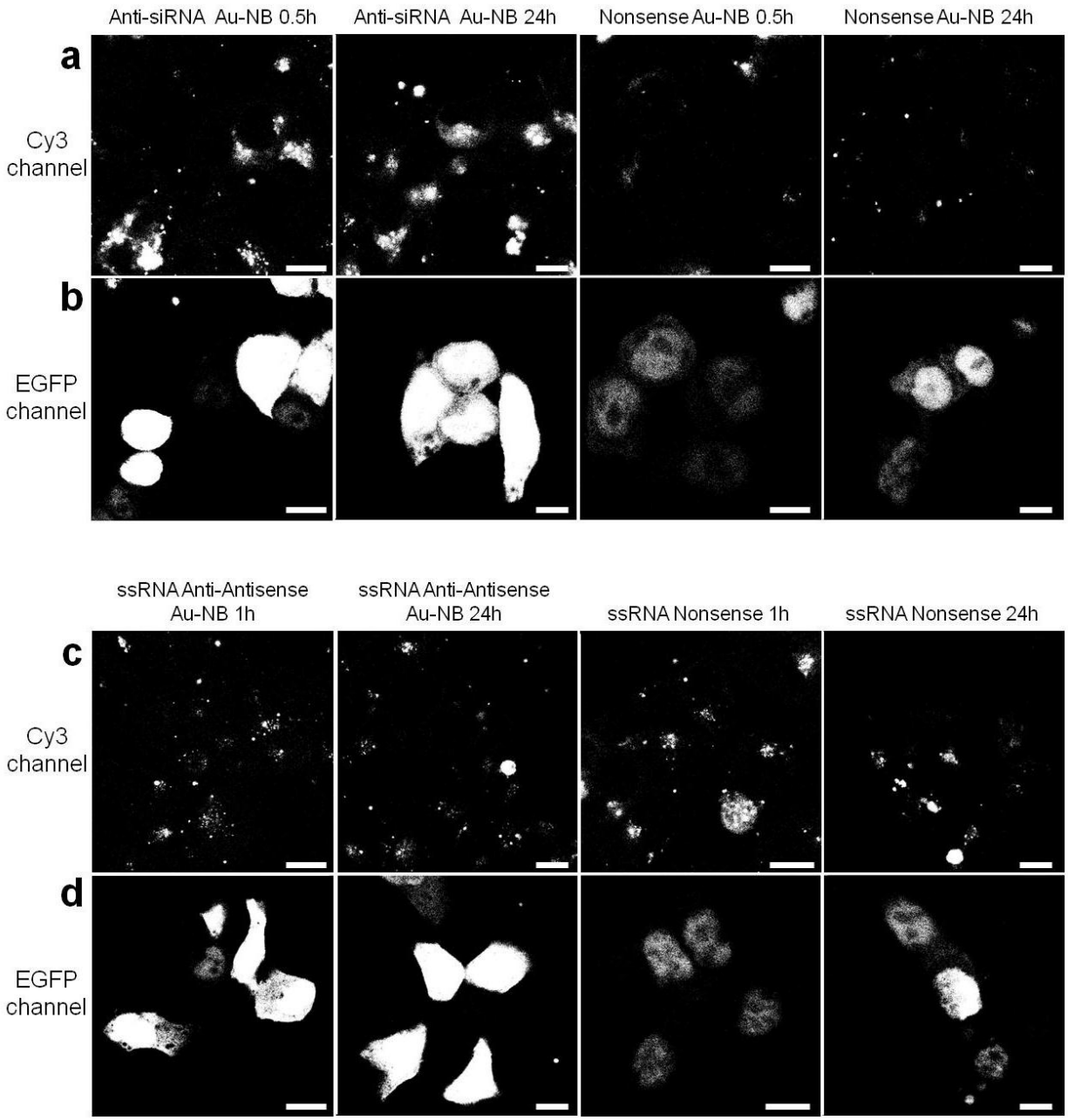

Figure S11. EGFP recovery due to anti-siRNA Au-nanobeacon silencing of siRNA. It can be clearly seen that only when the anti-siRNA Au-nanobeacon is emitting fluorescence, thus silencing siRNA, EGFP recovery is observed. The nonsense Au-nanobeacon shows no effect. Regarding the EGFP recovery by ssRNA oligomers used to silence the antisense Au-nanobeacon, there is no difference in Cy3 channel (**c**) once all cells are incubated with 30 nM of antisense Au-nanobeacon. The EGFP channel (**d**) clear demonstrates that EGFP recovery was attained only by ssRNA oligomers anti-antisense Au-nanobeacon, when compared to ssRNA nonsense. Scale bar, 10 µm.

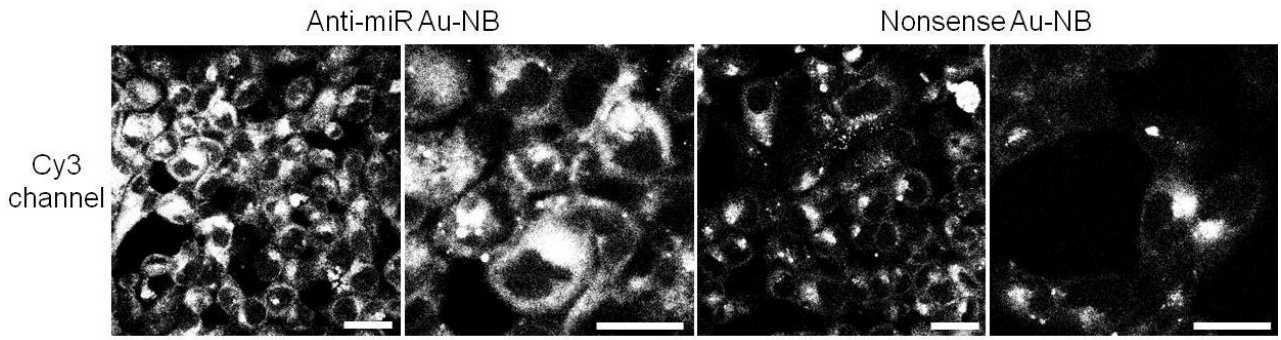

Figure S12. Silencing the silencers via anti-miR Au-nanobeacons. Silencing of miR-21 is clearly observed when the Anti-miR Au-nanobeacon is open due to hybridization to the target, shown by the increased fluorescence intensity in Cy3 channel. These results corroborate what is shown above (Figure S9). The nonsense Au-nanobeacon only shows residual fluorescence hardly observable above background. Scale bar, 10 μm.

G. Acute cytotoxicity evaluation by the MTT assay

Living cells' enzymes cleave the tetrazolium salts from the MTT reagent to yield formazan, which directly correlates to the number of metabolically active cells in culture. An expansion in the number of viable cells results in an increase in the overall activity of mitochondrial dehydrogenases, thus increasing the formation of formazan dye.

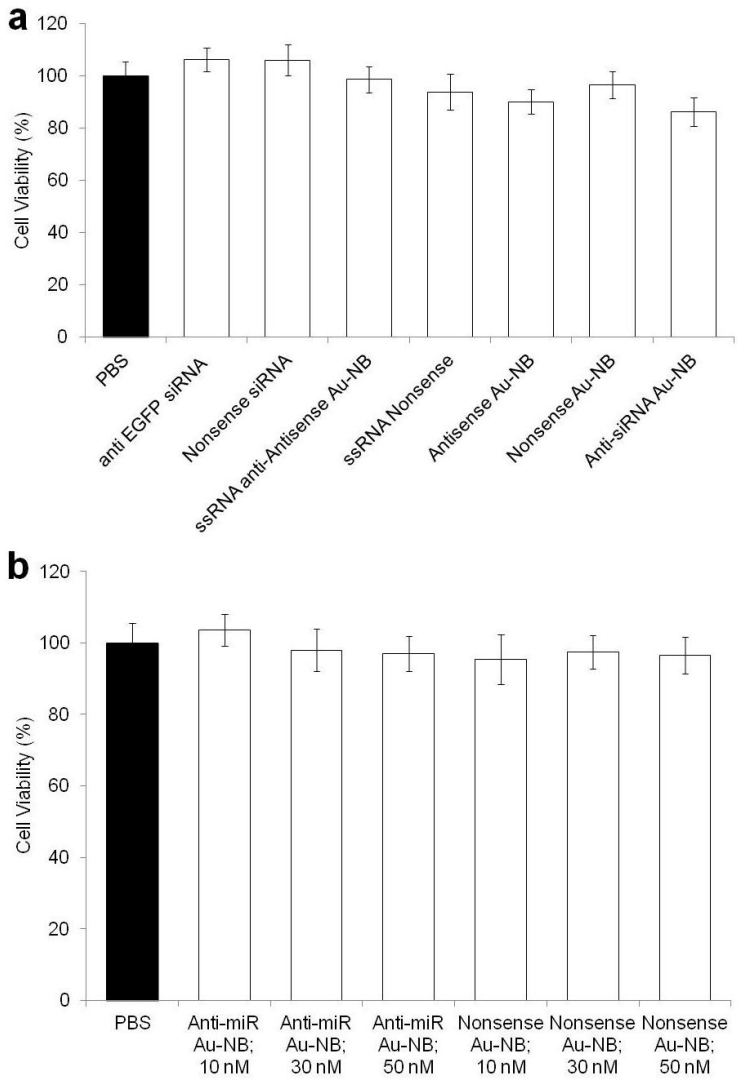

Figure S13. Cytotoxicity evaluation of all biomolecular assemblies administered to human colorectal cancer cells (HCT-116 cell line) in the present study via the MTT assay at 48 (**a**) and 72 hours (**b**) of exposure. Negligible influence in cell viability is observed for all assemblies tested when compared to untreated cells (black bar).

Additional references

(32) Schmittgen TD, Livak KJ. Analyzing real-time PCR data by the comparative CT method. Nat Protocols 2008; 3:1101-08.

Nanotoxicology, 2013; Early Online, 1–12

ISSN: 1743-5390 print / 1743-5404 online
DOI: 10.3109/17435390.2013.802821

informa
healthcare

Gold-nanobeacons for gene therapy: evaluation of genotoxicity, cell toxicity and proteome profiling analysis

João Conde[1,2], Miguel Larguinho[1,3], Ana Cordeiro[1,3], Luís R. Raposo[4,5], Pedro M. Costa[6], Susana Santos[4,5], Mário S. Diniz[3], Alexandra R. Fernandes[4,5,7], & Pedro V. Baptista[1]

[1]CIGMH, DCV, Faculdade de Ciências e Tecnologia, Universidade Nova de Lisboa, Caparica, Portugal, [2]Instituto de Nanociencia de Aragón, Universidad de Zaragoza, Zaragoza, Spain, [3]REQUIMTE, DQ, Faculdade de Ciências e Tecnologia, Universidade Nova de Lisboa, Caparica, Portugal, [4]Centro de Química Estrutural, Instituto Superior Técnico, Lisboa, Portugal, [5]CB3, FECN, Universidade Lusófona de Humanidades e Tecnologias, Lisboa, Portugal, [6]IMAR, DCEA, Faculdade de Ciências e Tecnologia, Universidade Nova de Lisboa, Caparica, Portugal and [7]DCV, Faculdade de Ciências e Tecnologia, Universidade Nova de Lisboa, Caparica, Portugal

Abstract

Antisense therapy is a powerful tool for post-transcriptional gene silencing suitable for down-regulating target genes associated to disease. Gold nanoparticles have been described as effective intracellular delivery vehicles for antisense oligonucleotides providing increased protection against nucleases and targeting capability via simple surface modification. We constructed an antisense gold-nanobeacon consisting of a stem-looped oligonucleotide double-labelled with 3′-Cy3 and 5′-Thiol-C6 and tested for the effective blocking of gene expression in colorectal cancer cells. Due to the beacon conformation, gene silencing was directly detected as fluorescence increases with hybridisation to target, which can be used to assess the level of silencing. Moreover, this system was extensively evaluated for the genotoxic, cytotoxic and proteomic effects of gold-nanobeacon exposure to cancer cells. The exposure was evaluated by two-dimensional protein electrophoresis followed by mass spectrometry to perform a proteomic profile and 3-(4,5-Dimethylthiazol-2-Yl)-2,5-Diphenyltetrazolium Bromide (MTT) assay, glutathione-S-transferase assay, micronucleus test and comet assay to assess the genotoxicity. This integrated toxicology evaluation showed that the proposed nanotheranostics strategy does not exhibit significant toxicity, which is extremely relevant when translating into *in vivo* systems.

Keywords: antisense, gold nanoparticles, gene silencing, DNA damage, cytotoxicity, proteomics

Introduction

The development of a safe, efficient, specific and non-pathogenic vehicle for gene delivery is highly attractive (Kim et al. 2009; Akhtar & Benter 2007). Nanoparticles (NPs), in particular, are expected to provide a range of devices for diagnosis and treatment in cancer as their dimensions are well matched in size to biologic molecules and structures found inside living cells (Conde et al. 2012b). Gold nanoparticles (AuNPs) have been extensively investigated and applied in conjunction with biomolecules due to their ease of synthesis and functionalisation derived from their large surface-to-volume ratio (Conde et al. 2012a; Doria et al. 2012; Daniel & Astruc 2004; Jain 2008; Haglund et al. 2009). This way, several strategies have been proposed based on AuNPs as intracellular delivery vehicles for antisense oligonucleotides by providing protection against intracellular nucleases and ease of functionalisation for selective targeting (Whitehead et al. 2009; Giljohann et al. 2009; Rana et al. 2012; Ghosh et al. 2008a; Ghosh et al. 2008b; Thomas & Klibanov 2003; McIntosh et al. 2001; Conde et al. 2010; Rosi et al. 2006).

In this study, we used a gold-nanobeacon (Au-nanobeacon) to target and silence a specific mRNA while providing means to assess its effectiveness via fluorescence signalling. The antisense Au-nanobeacon consisting of a stem-looped oligonucleotide double-labelled with 3′-Cy3 and 5′-Thiol-C6 bonded to the AuNPs' surface, whose sequence is capable of blocking enhanced green fluorescent protein (EGFP) expression. This nanoconjugate was tested for the effective blocking of EGFP expression in a colorectal cancer cell-line (HCT-116). The beacon's increase in fluorescence upon hybridisation to the specific target was used to evaluate the effective silencing as a higher level of silencing yields a more intense fluorescence signal from the beacon. Previously, we demonstrated that Au-nanobeacons could successfully be used for assessing the effective level of gene silencing *in vitro* (Rosa et al. 2012; Conde et al. 2013).

Correspondence: Pedro V. Baptista, Department of Life Sciences, Faculdade de Ciências e Tecnologia, Universidade Nova de Lisboa, Campus de Caparica, 2829-516 Caparica, Portugal. Tel: +351212948530. Fax: +351212948530. E-mail: pmvb@fct.unl.pt

(Received 19 February 2013; accepted 2 May 2013)

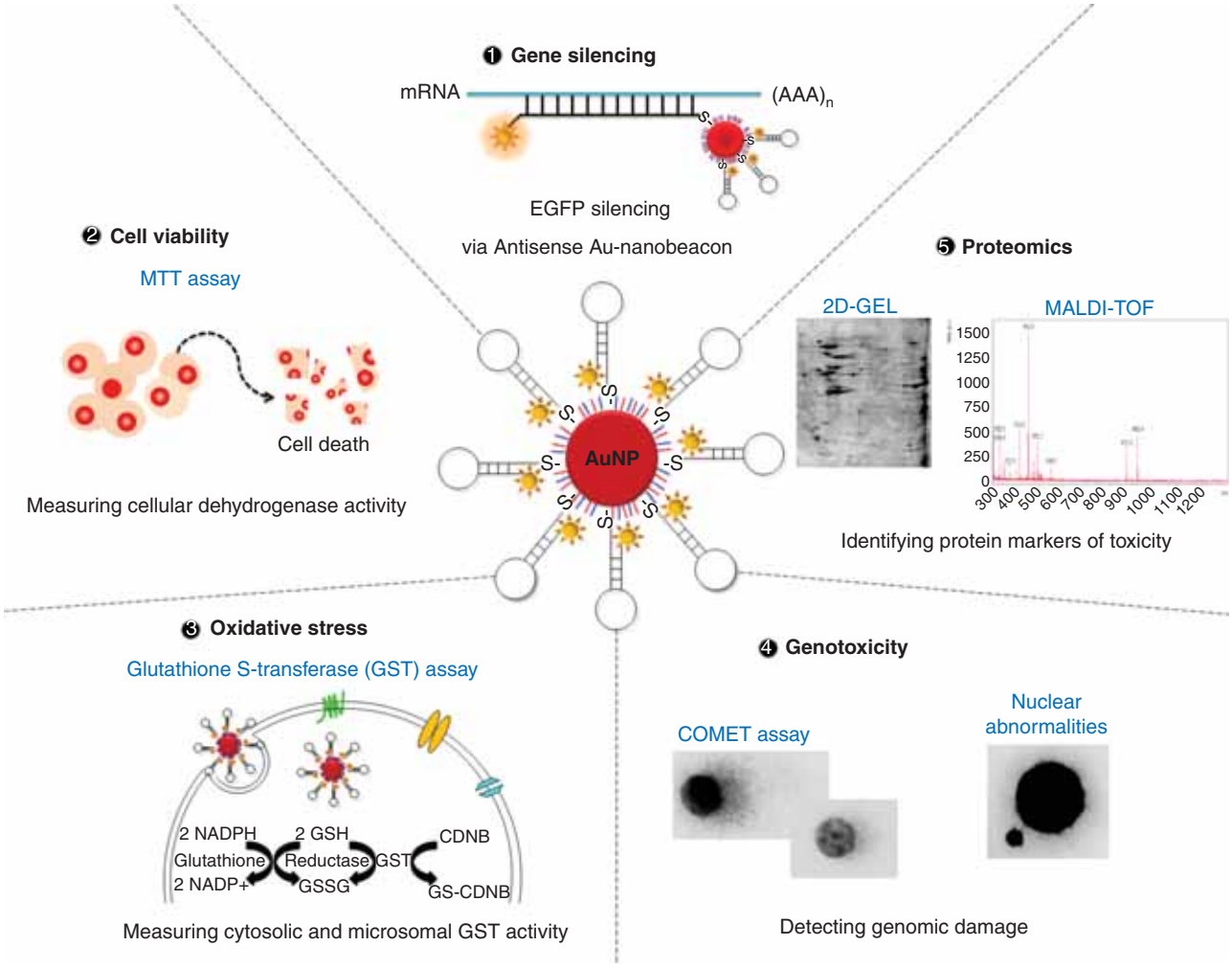

Figure 1. Antisense Au-nanobeacons for gene therapy: from genotoxicity to proteomics. ❶ Gene silencing via antisense Au-nanobeacons; ❷ cell viability (MTT assay); ❸ oxidative stress (glutathione-S-transferase activity); ❹ genotoxicity assessment (NAs and comet assay); and ❺ identifying protein markers by two-dimensional protein electrophoresis followed by peptide mass fingerprinting.

Despite major advances in nanotechnology-based drug delivery, the vast majority of studies merely report on the biocompatibility of nanomaterials relying on cell viability evaluation and cell counting (van et al. 2011; Dobrovolskaia & McNeil 2007; Wall & Shi 2003; Ozpolat et al. 2010). Thus far, little attention has been directed to the detection of genome damage, such as DNA strand breaks and formation of nuclear abnormalities (NAs), characterisation of protein markers of toxicity or measuring the level of oxidative stress. When considering the toxicity of AuNPs, size, concentration and surface coating also play a role in triggering cellular and physiologic response (Alkilany & Murphy 2010). For instance, poly(ethylene glycol) (PEG)-coated AuNPs have been shown to exhibit size-dependent *in vivo* toxicity and PEG alone is known to trigger cellular stress (Zhang et al. 2011). All these markers are of great importance when assessing biocompatibility and safety of the nanomaterials if they are to be used for medical purposes, and ought to be used as primary screen once therapeutic effect is demonstrated (Dobrovolskaia & McNeil 2007). Identification of these disease/toxicity biomarkers may allow improvement of safety assessment of nanomaterials.

Here, following demonstration of the Au-nanobeacons' gene silencing capability, the system was extensively evaluated in terms of cellular toxicity, namely at the proteomic and genomic level. HCT-116 cells were exposed to antisense Au-nanobeacons as putative nanotheranostics tool, and toxicity evaluated using MTT assay, glutathione-S-transferase assay, NAs and comet assay, and two-dimensional protein electrophoresis followed by mass spectrometry for identification of putative stress markers (see Figure 1).

Methods

Synthesis of citrate-AuNPs

AuNPs were synthesised by the citrate reduction method described by Lee and Meisel (1982). Citrate-capped AuNPs were characterised by transmission electron microscopy (TEM) and UV-Vis spectroscopy (seeSupplementary Figure S1A-B).

Synthesis of PEGylated-gold nanoparticles

Functionalisation of PEGylated AuNPs was carried out using commercial hetero-functional PEG functionalised with a thiol group O-(2-Mercaptoethyl)-O′-methyl-hexa(ethylene glycol), $C_{15}H_{32}O_7S$, 356.48 Da (Sigma), as previously

described (Rosa et al. 2012; Conde et al. 2013; Sanz et al. 2012). Excess PEG was removed by centrifugation (21.460 × *g*, 30 min, 4°C), and quantified by the Ellman's Assay suitable for sulfhydryl group determination.

Synthesis of gold nanobeacons (AuNP@PEG@Beacon)

The antisense Au-nanobeacon contains a stem-looped oligonucleotide double-labelled with 3′-Cy3 and 5′-Thiol-C6(5′-TTTGCCTCGTCGCTCTCCATGGTGGGCAAA-3′)complementary to the Kozak consensus translation initiation site and start codon of the EGFP (pVisionGFP-N vector 4.7 kb, Biovision), thus capable of blocking the translational machinery. The nonsense Au-Nanobeacon contains a stem-looped oligonucleotide of unrelated sequence double-labelled with 3′-Cy3 and 5′-Thiol-C6 (5′-TTTGCC CCGTTACTATTTGCACCACGGCAAA-3′). Briefly, the thiolated oligonucleotides (STABVIDA) were suspended in 1 mL of 0.1 M dithiothreitol (DTT), extracted three times with ethyl acetate and further purified through a desalting NAP-5 column (Pharmacia) using 10 mM phosphate buffer (pH 8) as eluent. Following oligonucleotide quantification via UV/Vis spectroscopy, each oligomer was added to the AuNP@PEG solution in a 100:1 ratio. AGE I solution [2% (w/v) sodium dodecyl sulphate (SDS), 10 mM phosphate buffer (pH 8)] was added to the mixture to achieve a final concentration of 10 mM phosphate buffer (pH 8), 0.01% (w/v) SDS. The solution was sonicated for 10 sec using an ultrasound bath and incubated at room temperature for 20 min. Afterwards, the ionic strength of the solution was increased sequentially in 50 mM NaCl increments by adding the required volume of AGE II solution (1.5 M NaCl, 0.01% (w/v) SDS, 10 mM phosphate buffer (pH 8)) up to a final concentration of 10 mM phosphate buffer (pH 8), 0.3 M NaCl, 0.01% (w/v) SDS. After each increment, the solution was sonicated for 10 sec and incubated at room temperature for 20 min before the next increment. Following the last addition, the solution was left to rest for additional 16 h at room temperature. Then, the functionalised Au-nanobeacons were centrifuged for 20 min at 21.460 × *g*, the oily precipitate washed three times with Diethyl Pyrocarbonate (DEPC)-treated H_2O, and redispersed in the same buffer to a final concentration in Au-nanobeacons of 15 nM. The resulting Au-nanobeacons were stored in the dark at 4°C until further use. Au-nanobeacons were characterised by dynamic light scattering (DLS) (Zetasizer, Malvern), Zeta Potential (Zetasizer, Malvern), UV/Vis Spectroscopy and TEM (see Supplementary Figure S1C–F).

Quantitation of beacon coverage on AuNP@PEG

Coverage, i.e. average number of labelled beacons per NP was assessed by quantification of the thiolated oligonucleotides in supernatant from the Au-nanobeacon synthesis. All the three supernatants containing the unbound oligonucleotides were measured by monitoring the emission spectra of Cy3 (Exc = 530 nm) dye in a Cary Eclipse (Varian) using an Ultra-Micro quartz cell (Hëllma). All AuNP samples and standard solutions of the thiol-oligonucleotide beacon were kept at the same pH and ionic strength and calibration for all measurements. Fluorescence emission was converted to molar concentrations by interpolation from a standard linear calibration curve, prepared using the same buffer pH and salt concentrations.

Cell culture and EGFP vector transfection

As a model system, HCT-116 cells (from colorectal carcinoma) were grown in Dulbecco's modified Eagle's medium with Glutamax (DMEM, Invitrogen) with 10% heat-inactivated fetal bovine serum (Invitrogen), 100 U/mL penicillin and 100 μg/mL streptomycin (Invitrogen), and maintained at 37°C in 5% CO_2. Cells were seeded at a density of 1×10^5 cells/well in 24-well plates and grown for 24 h prior to transfection of EGFP vector (pVisionGFP-N vector 4.7 kb, Biovision) encoding green fluorescent protein optimised for high expression in mammalian cells. On the day of transfection, cells were approximately 50% confluent. EGFP vector (1 μg per well) was added with 2 μg of Lipofectamine 2000® (Invitrogen) and Opti-MEM® Reduced Serum Medium (Invitrogen) according to the manufacturer's recommendations (see Supplementary Information S2).

EGFP silencing with antisense Au-nanobeacon

After 24 h of EGFP transfection, cells were treated with 30 nM of antisense Au-nanobeacons in Opti-MEM® reduced serum medium (Invitrogen). After 48 h, cells were washed with 1× PBS, lysed in ultrapure water and collected for analysis of EGFP silencing, RNA extraction and confocal imaging. Fluorescence was measured at least three times in a Cary Eclipse spectrofluorimeter (Varian) using an Ultra-Micro quartz cell (Hëllma) by taking the area under the curve from 495 to 650 nm. EGFP fluorescence values were normalised to the bulk protein concentration determined via the Bradford assay (Thermo Scientific), and then normalised against the controls to determine percent knockdown of EGFP.

qRT-PCR

Total RNA was extracted from the cell line using the Trisure reagent (Bioline) according to the manufacturer's protocol, and used for quantitative real-time polymerase chain reaction (qRT-PCR) to evaluate expressions of EGFP and β-actin. cDNA was obtained by subjecting 1 μg of total RNA to reverse transcription with 200 U of Revert-AidTM M-MuLV reverse transcriptase (Fermentas) according to the manufacturer's specifications, using 20 μM of EGFP and β-actin reverse primers, annealing at 42°C for 1 h and 70°C for 10 min for reverse transcriptase inactivation. Real-time PCR amplification was performed in a Corbett Research Rotor-Gene RG3000 using SYBR GreenER real-time PCR kit (Invitrogen) according to the manufacturer's specifications in 50 μL reactions containing 2 μl of cDNA, 1× SYBR Green SuperMix and 200 nM of primers (STABVIDA). The following primers were employed: β-actin forward 5′-ATAGCACAGCCTGGATAGCAAC-3′; β-actin reverse 5′-CACC TTCTACAATGAGCTGCGT-3′; EGFP forward 5′-AGCTTCG AATTCTGCAGTCG-3′; EGFP reverse 5′-GGCTGATTATGAT CTAGAGTC-3′. The amplification conditions consisted of 50°C for 2 min hold, 95°C during 10 min hold, followed by 40 cycles consisting of denaturation at 95°C for 30 sec,

annealing at 52°C for 60 sec, extension at 72°C for 45 sec, with a final extension step at 72°C for 10 min. All the results were originated from three independent experiments. Threshold cycle values were analysed by the ΔCt method (Livak & Schmittgen 2001; Pfaffl 2001), once the difference of PCR amplification efficiency of EGFP and β-actin products was less than 5% (Efficiency = $10^{(-1/\text{slope})} - 1$). The β-actin expression levels were used as reference, and fold-induction was calculated by the Ct method as follows: $\Delta CT = (Ct\ EGFP - Ct\ \beta\text{-actin})_{\text{treated for EGFP}} - (Ct\ EGFP - Ct\ \beta\text{-actin})_{\text{untreated}}$. The final data were then derived from $2^{-\Delta CT}$. The expected sizes of the PCR products were 158 bp (β-actin) and 792 bp (EGFP). The PCR products were subjected to electrophoresis on a 2% agarose gel (TBE 1×), during 75 min at 90 V, stained with GelRed (Biotium) and visualised under UV light.

Confocal microscopy

HCT-116 cells were seeded at a concentration of 1×10^5 cells/well in 24-well plates on glass slides in 500 μL of DMEM (Invitrogen) with 10% heat-inactivated fetal bovine serum (Invitrogen) and maintained at 37°C in 5% CO_2. All confocal microscopy samples were prepared under the same conditions as described above for GFP silencing and recovery. Cells were fixed with 4% paraformaldehyde in PBS for 15 min at 37°C and mounted in ProLong® Gold Antifade Reagent with DAPI (Invitrogen) to allow for nuclear staining. Images were acquired with a confocal laser point-scanning microscope Zeiss LSM 510 META, with excitation at 405 nm for DAPI (nucleus), 480 nm for EGFP and 561 nm for Cy3 (Au-nanobeacons).

MTT assay

Standard MTT [3-(4,5-dimethylthiazol-2-yl)-2,5-diphenyltetrazoliumbromide] reduction assay (Invitrogen) was performed to determine the cytotoxicity of the functionalised AuNP complexes. Briefly, cells were seeded at a density of 1×10^5 cells per well in 24-well culture plates in complete DMEM (500 μl) with serum. After 24 h, 100 μl of functionalised AuNPs under the same conditions of the EGFP knockdown/recovery experiments were added and cells further incubated for 48 and 72 h. The medium was then removed and cells were washed twice with sterile PBS and 300 μl of fresh medium with serum was added. For the assay, 16.7 μl of sterile MTT stock solution (5 mg/mL in PBS) were added to each well, incubated for 2 h, the medium removed and the formazan crystals resuspended in 300 μl of dimethyl sulphoxide (DMSO) (Sigma). The solution was mixed and its absorbance was measured at 540 nm as working wavelength and 630 nm as reference, using a Microplate reader Infinite M200 with an absorbance module (Tecan). The cell viability was normalised to that of cells cultured in the culture medium with PBS treatment. The experiments were repeated three times.

Genotoxicity assessment

Genotoxic effects were assessed by quantification of DNA strand breakage, through the alkaline version of comet assay (Costa et al. 2008; Singh et al. 1988) and frequency of NAs. Forty-eight hours after treatment with the Au-nanobeacons (with or without Lipofectamine), HCT-116 cells were centrifuged and the pellet resuspended in 50 μL of 1× PBS. From this suspension, a drop containing approximately 2.5×10^5 cells was smeared on glass microscope slides and left to dry at room temperature for subsequent analysis of NAs. Preparations were methanol-fixed (for 15 min), stained with 0.1 g/L acridine orange and mounted using the non-fluorescent DPX resin (from BDH) (Costa & Costa 2007). The frequency of cells with NAs was determined by scoring 1000 cells per preparation, following criteria established elsewhere (Fenech et al. 2003) (see Supplementary Information S3). For the comet assay, glass microscope slides were previously coated with 1% (w/v) agarose (normal melting point) in 1× TAE buffer and left to dry for at least 48 h, at 37°C. Sample preparation was as follows: 2 μL of the cell suspension in 1× PBS was diluted in 310 μL of 1% (w/v) liquid low melting-point agarose (LMPA) in 1× PBS (35–40°C). One hundred and fifty microlitres of cell-containing LMPA were spotted onto the prepared glass slides (1.1×10^4 cells per slide) and covered with a coverslip. Upon agarose solidification, coverslips were removed and the slides dipped into lysis solution (450 mM NaCl; 3.72% EDTA; 5 mM TRIS; to which 10% (v/v) DMSO and 1% (v/v) Triton-X were added just before use) during 1 h at 4°C, followed by 40 min into cold electrophoresis solution (1 mM EDTA; 300 mM NaOH, pH 13) to ensure DNA unwinding and promote expression of alkali-labile sites. Electrophoresis was carried out at 4°C, for 30 min, at 25 V using a Sub-Cell model 96 apparatus (Bio-Rad). Afterwards, slides were placed into 0.1 M Tris–HCl buffer (pH 7.5) during 15 min for neutralisation. All described steps were performed under strictly controlled temperature and light conditions to minimise accessory DNA degradation and gel lifting from slides. Upon staining with ethidium bromide (20 μg/mL), an approximated number of 100 intact nucleoids per slide was analysed, using the CometScore software v.1.5 (TriTek Corp.). The DNA percentage in the comets' tail was employed as metrics for total DNA strand breakage. Both imaging analyses were performed by epi-fluorescence microscopy, on a DLMB microscope equipped with an EL6000 light source (Leica Microsystems), using an I3 filter (for acridine orange staining) and N2.1 filter (for ethidium bromide staining).

Measurement of glutathione-S-transferase activity

After the 48-h treatment, cells were washed with 1× PBS, lysed in ultrapure water and the pellets resuspended in 50 μL ultrapure water. Briefly, glutathione s-transferase (GST) activity was determined based on a procedure described by Habig et al. (1974) by measuring the conjugation of 1-chloro-2,4-dinitro benzene with glutathione (GSH). The enzyme activity was determined by measuring the absorbance at every minute during a maximum of 10 min on a 96-well plate (SPL LifeSciences), using 3 replicas for each sample. The change in absorbance was measured at 340 nm using an Infinite 2000 Microplate reader (Tecan) and values were normalised to total protein concentration determined by the Bradford assay (Thermo Scientific).

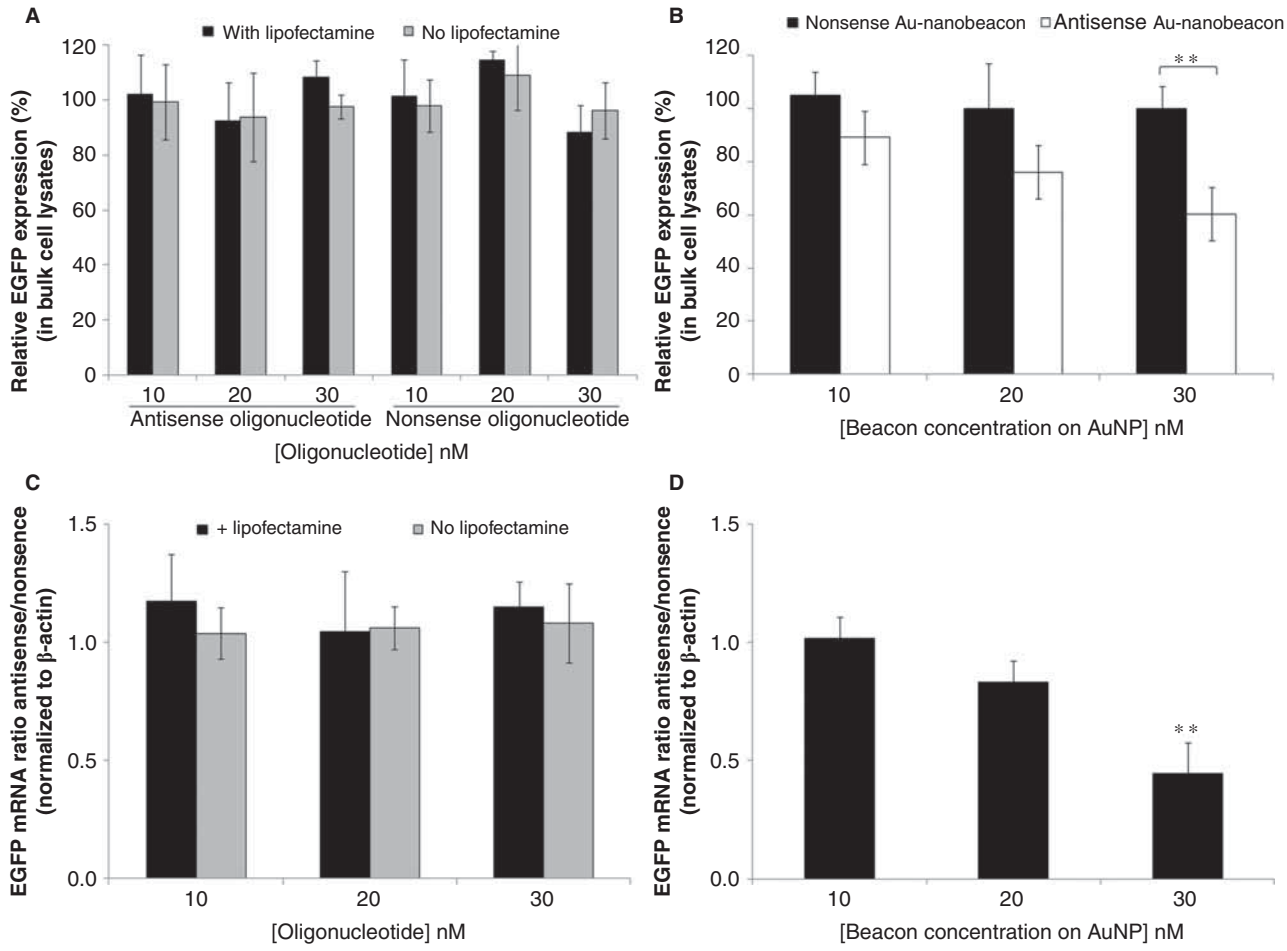

Figure 2. Quantitative assessment of EGFP silencing efficiency via antisense Au-nanobeacons, nonsense Au-nanobeacon and naked oligonucleotides. (A,B) EGFP silencing was confirmed by measurement of EGFP intensity in bulk cell lysates (as percentage of original EGFP fluorescence levels) using an antisense and a nonsense oligonucleotide (without AuNP) (A) and with antisense and nonsense Au-nanobeacons (B). EGFP silencing was confirmed by significant fluorescence decrease when compared to non-treated cells (**, $p \leq 0.005$) in bulk cell lysates at 30 nM of antisense Au-nanobeacon only. EGFR mRNA expression confirmed by qRT-PCR for antisense and nonsense oligonucleotides (C); and with antisense and nonsense Au-nanobeacons (D), using β-actin as reference.

Protein sample preparation

To minimise sample degradation, all solutions for sample preparation contained 1× phosphatase inhibitor (PhosStop, Roche), 1× protease inhibitor (cOmplete Mini, Roche®), 1 mM PMSF and 0.1% (w/v) DTT. After treatment, cells were collected and concentrated in lysis buffer (150 mM NaCl; 50 mM Tris, pH = 8.0; 5 mM EDTA, 2% (w/v) NP-40) by centrifugation at 14,000 × *g* for 30 min at 4°C. Supernatant was collected and samples stored at −80°C.

Two-dimensional gel electrophoresis

Prior to two-dimensional gel electrophoresis, protein concentration was determined via the 2-D Quant kit (GE Healthcare). Isoelectric focusing was performed using immobilised pH gradient strips (GE Healthcare) in an Ettan-nIPGphor 3 focusing unit (GE Healthcare) according to Teixeira et al. (2005) (see Supplementary Information S4). Variation of each protein expression level was calculated as the ratio of the normalised intensity of each protein spot in gels corresponding to each condition compared to those corresponding to control samples. The Mr values for the identified proteins were determined by comparison with the relative positions of the proteins included in the molecular weight protein marker (HyperPAGE, Bioline), which were run for the second dimension with the samples under study. Spots with significantly altered intensities between conditions (up- or down-regulated proteins in comparison to control samples) were selected and picked from gels towards identification via matrix-assisted laser desorption/ionisation-time of flight mass spectrometry.

Statistical analysis

All statistical analyses were performed with SPSS statistical package (version 15, SPSS Inc., Chicago, IL, USA). Data derived from the comet assay, frequencies of cells with NAs and GST activity were analysed using non-parametric statistics, namely the Mann–Whitney *U* tests for pairwise comparisons between experimental conditions. A statistical significance threshold $\alpha = 0.05$ was set for all analyses.

Results

Synthesis and characterisation of Au-nanobeacons

The synthesised citrate-capped AuNPs were characterised by: TEM, showing an average diameter of 14.6 ± 1.7 nm, in good agreement with DLS measurement (average diameter

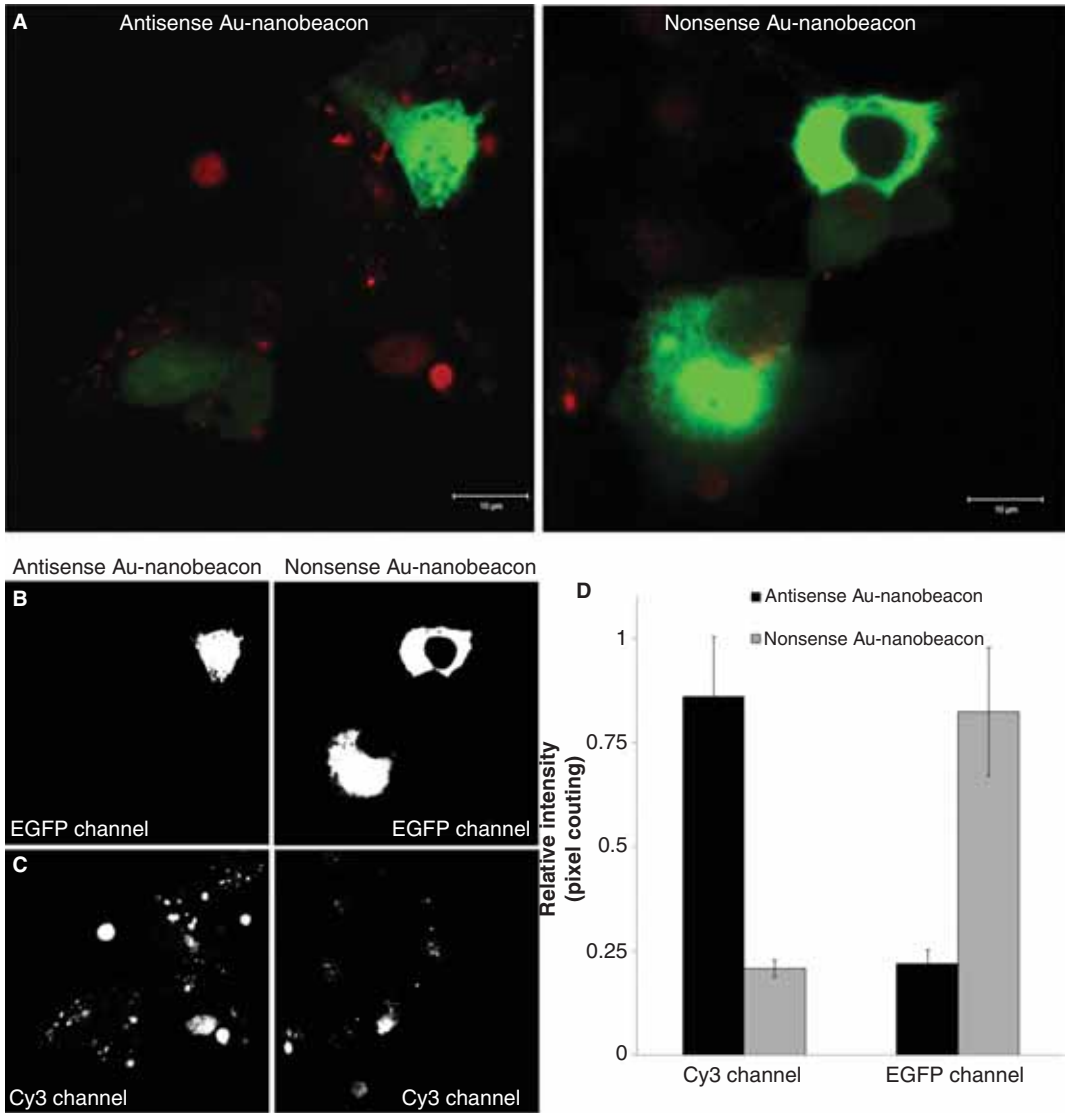

Figure 3. Confocal fluorescence imaging of antisense and nonsense Au-nanobeacons effect in HCT-116 cells. Confocal imaging (scale bar, 10 μm) shows HCT-116 cells expressing EGFP after exposure to 30 nM of antisense and nonsense Au-nanobeacons (A). EGFP expression levels can be evaluated by the intensity of its fluorescence (green, EGFP) (B) and Au-nanobeacons in open conformation (red, Cy3) can be identified as fine punctuation dispersed throughout the cytoplasm (C). Relative fluorescence intensity of Cy3 and EGFP channels for antisense (black bars) and nonsense (grey bars) Au-nanobeacons obtained after individual colour channel analysis of the same confocal images using ImageJ software (D).

of 16.7 ± 5.9 nm) with a relatively narrow distribution with a polydispersity index of 0.294 ± 0.017; a Zeta potential of −28.6 ± 2.4 mV at pH 7; and the characteristic surface plasmon resonant peak at 519 nm (Supplementary Figure S1). These AuNPs were then functionalised with a PEG spacer to increase stability, biocompatibility and grant chemical functionality as well as avoid opsonisation (Liu et al. 2007). The PEGylated AuNPs (AuNP@PEG) showed a 30% saturated PEG layer (190.29 ± 19.56 PEG chains per NP), which allows the incorporation of the thiolated fluorescence-labelled hairpin oligonucleotide capable of blocking the transcriptional machinery – *antisense Au-nanobeacon* (57.87 ± 3.92 hairpins per NP); or an unrelated stem-looped oligonucleotide – *nonsense Au-nanobeacon* (31.64 ± 3.49 hairpins per NP). The determination of the degree of saturation of AuNPs functionalised with thiolated PEG chains and quantification of molecular beacon strands per NP was extensively discussed elsewhere (Rosa et al. 2012; Conde et al. 2013).

Au-nanobeacon for gene silencing – a nanotheranostics tool

EGFP knockdown studies were conducted in colorectal cancer cells (HCT-116 cells) using an EGFP expression plasmid as a target model. Quantification of EGFP expression by direct measurement of EGFP fluorescence levels (Figure 2A and B) reveals that only the antisense Au-nanobeacon at 30 nM down-regulates EGFP expression (Figure 2B). The use of Lipofectamine did not result in EGFP silencing (Figure 2A). These data are corroborated by qRT-PCR (Figure 2C and D). A significant fluorescence decrease (55.57 ± 13.34% EGFP down-regulation) was observed at 30 nM of antisense Au-nanobeacon (Figure 2D).

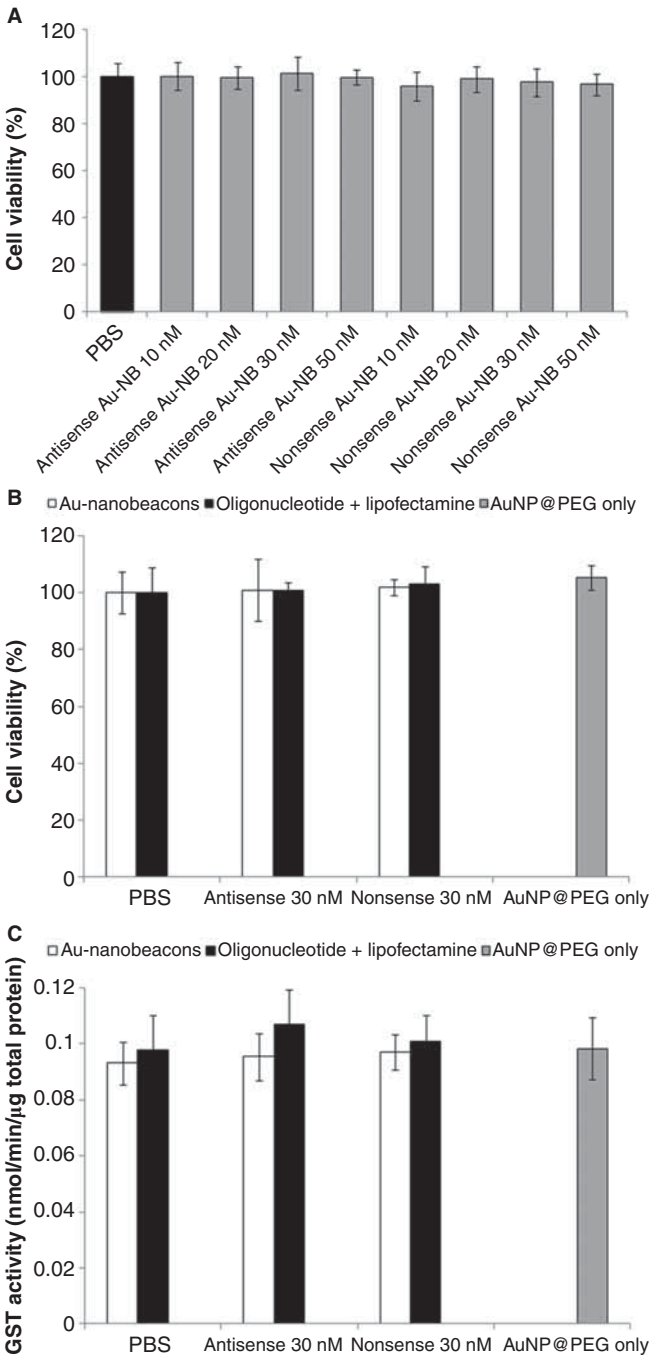

Figure 4. MTT and GST assays in human colorectal cancer cells (HCT-116). (A) Cell viability (MTT assay) with increasing concentrations of the nanoformulations used in this study. Negligible influence is observed for all concentrations tested when compared to untreated cells (black bar). (B) MTT assay for all (nano)biomolecular assemblies (30 nM) administered in the present study at 48 h of exposure. Negligible influence in cell viability is observed for all assemblies tested when compared to untreated cells (PBS). (C) GST activity was measured for both antisense and nonsense Au-nanobeacons and naked oligonucleotides at 30 nM.

Confocal fluorescence imaging shows that cells that internalised the antisense Au-nanobeacon exhibit lower fluorescence compared to those treated with nonsense Au-nanobeacon (Figure 3A). Moreover, cellular distribution of the Au-nanobeacon is observed by the punctuate fluorescence pattern. Data from the Cy3 channel show that antisense Au-nanobeacon leads to higher signal intensity than that of the nonsense Au-nanobeacon (Figure 3B and C). Striking differences for Cy3 and EGFP emissions related to the antisense and nonsense Au-nanobeacon effect can be observed in Figure 3D.

Toxicity assessment of Au-nanobeacons

To characterise the system effects in terms of cell viability, metabolic stress and DNA damage (genotoxicity) and evaluate the potential of the antisense Au-nanobeacon as nanotheranostics tool, we assessed acute toxicity parameters for all tested conditions: cell survival rates (MTT assay), oxidative stress (glutathione-S-transferase assay) and genomic DNA damages (comet assay and frequency of NAs). Regarding the MTT assay, which determines mitochondrial activity in living cells, no cell viability changes were detected up to 48 h incubation for both antisense and nonsense Au-nanobeacons (Figure 4A) and oligonucleotides only at 30 nM (Figure 4B). No major changes in GST activity, which is often used as an oxidative stress biomarker, were observed for antisense and nonsense Au-nanobeacons or for the naked oligonucleotides (Figure 4C) and no significant differences were observed amongst all samples ($p < 0.05$).

Genotoxicity was assessed in cells treated with nanobeacon/oligonucleotide concentrations of 30 nM using two standard techniques: single-cell gel electrophoresis (comet assay) and frequency of NAs. According to the % of DNA in tail, comets were assigned to one of five different classes (0–4, corresponding to <20%, 20–40%, 40–60%, 60–80% and >80% total DNA strand breakage). Reference images for the different classes of comets are shown in Figure 5A. Cells from the control treatment (i.e. cells expressing EGFP) exhibited an average of 46.58 ± 10.36% DNA in tail, similar to that observed in cells treated with AuNP@PEG (45.70 ± 12.58%). Cells treated with antisense (39.66 ± 3.84%) and nonsense (32.28 ± 5.13%) Au-nanobeacons failed to yield any significant differences to that of controls ($p < 0.05$). Additionally, the nucleoid distribution per class is uniform amongst these samples as minor or no alterations are observed (Figure 5B). Significant differences ($p < 0.05$) arise, however, in cells transfected with Lipofectamine and both antisense (23.09 ± 1.63%) or nonsense (25.26 ± 8.15%) oligonucleotides, when compared with the treatment with Lipofectamine alone (43.93 ± 5.05%). Similarly, differences in class distribution are denoted (Figure 5B). Despite these differences, treatment with Lipofectamine alone does not differ significantly from the control experiment. Comparing antisense with nonsense oligonucleotide treatments (Figure 5C), no significant differences were found between Au-nanobeacons or Lipofectamine use for internalisation. DNA tail percentages above 80% have not been observed with our approach. Regarding the NA frequency, different abnormalities, such as micronuclei or nuclear buds, were surveyed to determine the average frequency of abnormalities for each treatment – see Figure 5J (for reference, different scored abnormalities are included in Figure 5D–I). The most frequently observed NAs were micronuclei (>95%). Data show no significant differences between samples ($p < 0.05$): cells expressing EGFP show a frequency of 2.60 ± 1.14%, similar to those treated with AuNP@PEG

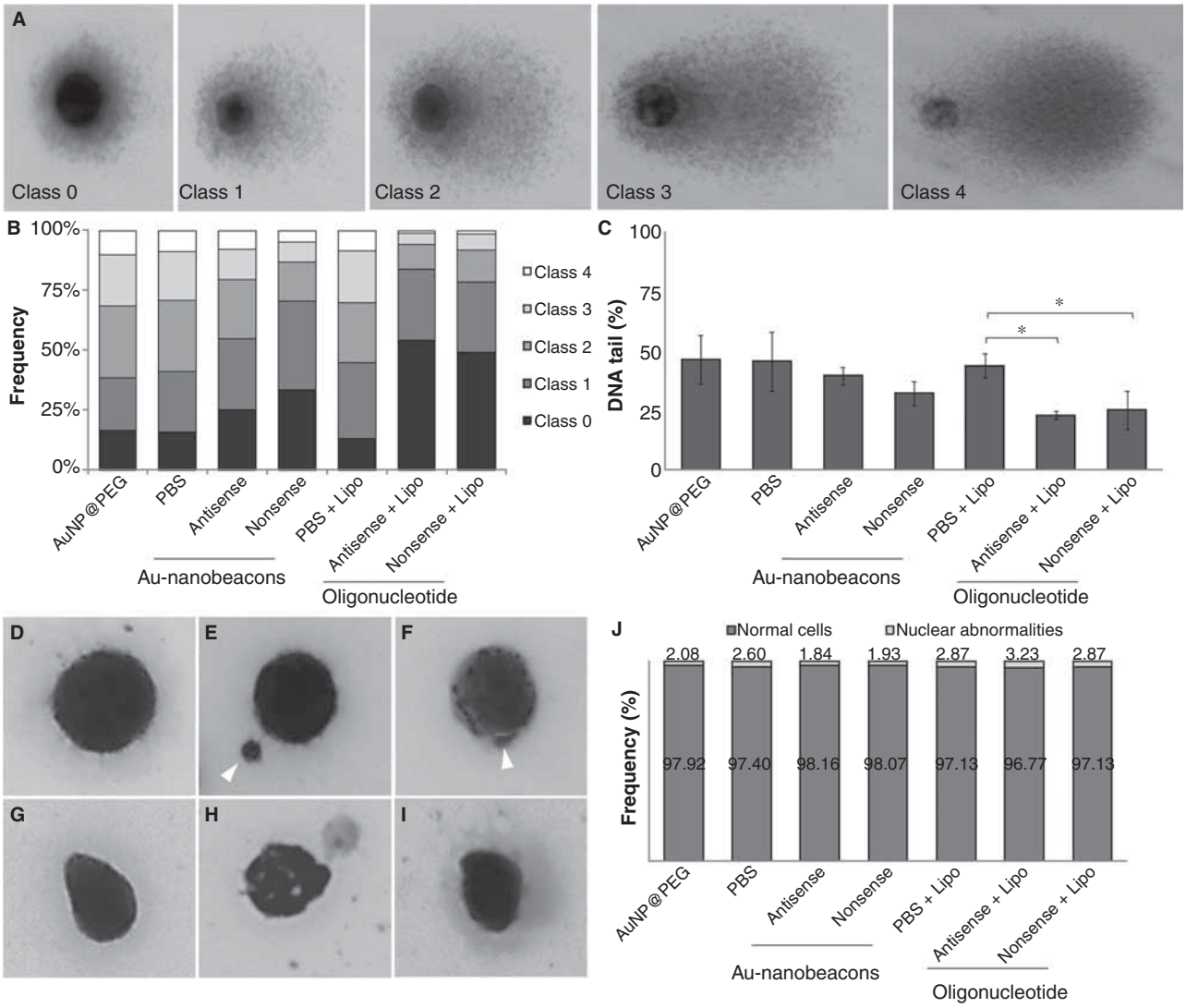

Figure 5. Comet assay and NA frequency for evaluation of genotoxic effects in human colorectal cancer cells (HCT-116). (A) Fluorescent microscopy images of comet classification according to DNA % in tail: class 0 (0–20%); class 1 (20–40%); class 2 (40–60%); class 3 (60–80%); class 4 (80–100%). (B) Relative frequency profile of comet class distribution according to DNA % in tail. (C) Average DNA % in tail assessed for each treatment. (D–I) Fluorescent microscopy reference images of observed NAs: D (normal nucleus); E (single micronucleus, highlighted with an arrow); F (nuclear bud, highlighted with an arrow); G–I (irregular shaped nuclei exhibiting nuclear lobes and buds). (J) NA frequency analysis. Significant differences ($p < 0.05$) marked with *.

(2.08 ± 0.64%), and cells transfected with either the antisense (1.84 ± 0.69%) or the nonsense (1.93 ± 1.10%) Au-nanobeacon. Average frequency of cells transfected with and without Lipofectamine is equivalent ($p < 0.05$).

Proteome profiling

To have additional insights into the cellular toxicity of Au-nanobeacons, colorectal cancer cells (HCT-116) previously transfected with EGFP were used for proteome profiling. Firstly, the effect of Lipofectamine (transfection vehicle; PBS+Lipo) or AuNPs (as vectors for gene silencing; AuNP@PEG) in the proteome of HCT-116 cells was evaluated. A total of five proteins (T-complex protein 1 subunit alpha, 40S ribosomal protein SA and alpha-enolase in Figure 6A-PBS +Lipo and Ezrin and 40S ribosomal protein SA in Figure 6A-AuNP@PEG; Supplementary Figure S4B-C and Table S1) show an increased expression (more than threefold) when compared to control (Figure 6A-PBS; Supplementary Figure S4A; Table S1). Protein 40S ribosomal protein SA was overexpressed (8-fold and 18-fold) in PBS+Lipo and AuNP@PEG, respectively (Figure 6A; Supplementary Figure S4B-C and Table S1). In the presence of Lipofectamine, 19 additional proteins were identified with less than 2-fold overexpression, most of them acting as molecular chaperones that assist protein folding (Figure 6A; Supplementary Figure S3B-C and Table S1). The exposure of EGFP transfected colorectal cancer cells to naked antisense or nonsense oligonucleotides revealed no major toxicity when compared with EGFP transfected cells (PBS+Lipo) (Figure 6A, Supplementary Figure S4-D-E and Table S1). Interestingly, protein 40S ribosomal protein SA and alpha-enolase, which were up-activated in control cells, have an almost normal level of expression in the presence of both oligonucleotides. Also, actin cytoplasmatic 2 was slightly activated (twofold) (Figure 6A, Supplementary Figure S4-D-E and Table S1).

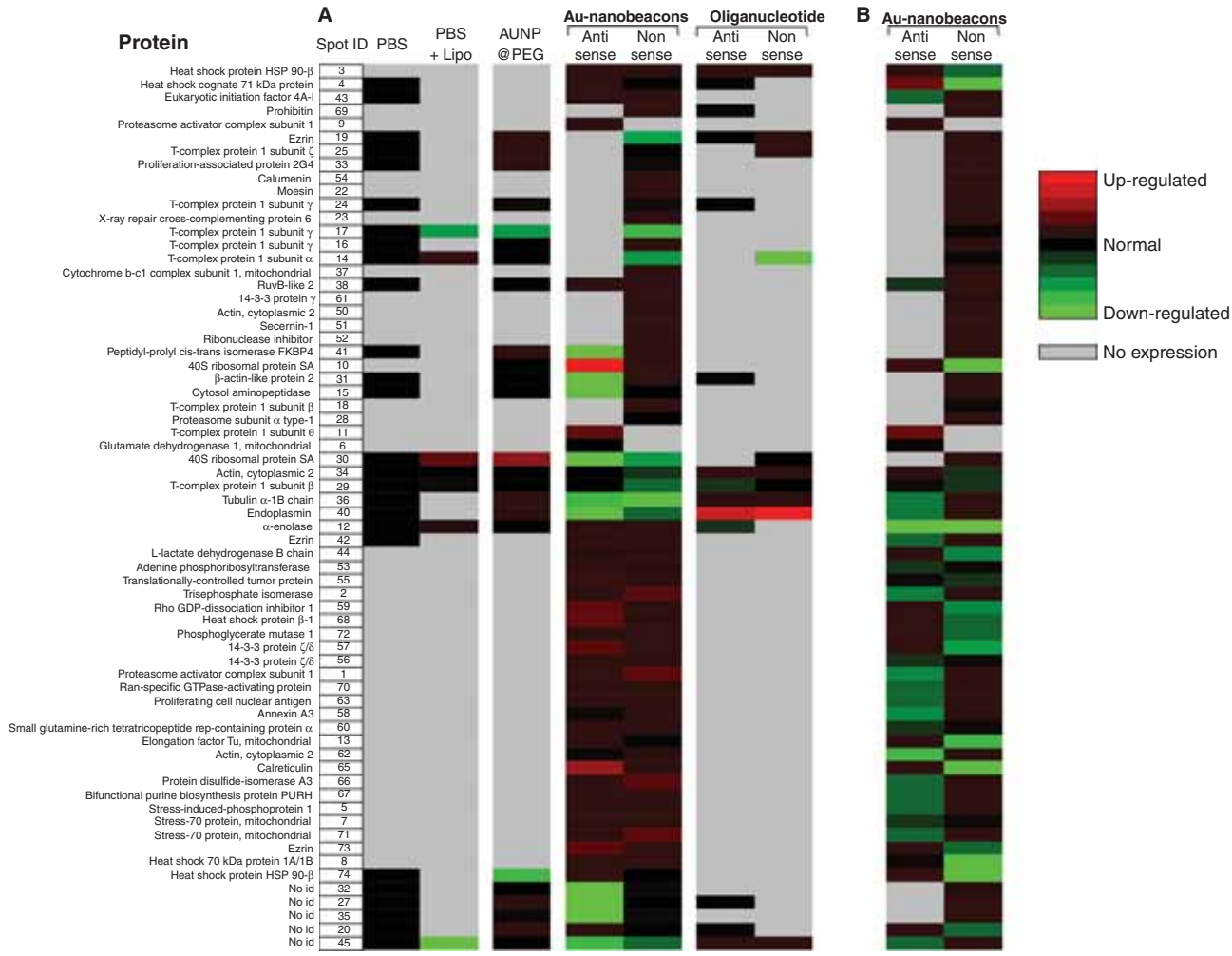

Figure 6. Proteome profiling – comparative levels of protein expression in HCT-116 cells previously transfected with EGFP. Incubated with (A) PBS, PBS + Lipofectamine (PBS + Lipo), AuNPs (AuNP@PEG), antisense Au-nanobeacon, nonsense Au-nanobeacon, naked antisense oligonucleotide, naked nonsense oligonucleotide; and (B) ratios of antisense Au-nanobeacon/nonsense Au-nanobeacon and nonsense Au-nanobeacon/antisense Au-nanobeacon.

To enquire the cellular toxicity of antisense and nonsense Au-nanobeacons, protein expression levels in EGFP-transfected colorectal cancer cell were compared to those of cells treated with antisense or nonsense Au-nanobeacons (Figure 6A, antisense Au-nanobeacon or nonsense Au-nanobeacon, respectively). No significant differences were found between cells treated with Au-nanobeacons and controls. Only one protein alpha-enolase displayed a higher level of expression (threefold) in both conditions (Figure 6A, Supplementary Figure S4-D-E and Table S1). The antisense Au-nanobeacon was responsible for triggering a sevenfold over-expression of the 40S ribosomal protein SA and the heat-shock protein 90-beta relative to the nonsense Au-nanobeacon (Figure 6A, Supplementary Figure S4-D-E and Table S1).

Discussion

To evaluate the full potential of the antisense Au-nanobeacon as nanotheranostics tool, we first discuss the capability of gene silencing via blockage of translation by conducting EGFP knockdown studies in HCT-116 cells using an EGFP expression plasmid as a target model, followed by a characterisation of the system effects in terms of cell viability, metabolic stress and DNA damage (genotoxicity). Additionally, a proteome profiling, for the same experimental conditions as those of EGFP silencing, is presented so as to identify putative protein markers of toxicity on HCT-116 cells.

EGFP fluorescence intensity as a direct indicator of EGFP silencing showed that only the antisense Au-nanobeacon at 30 nM effectively down-regulates EGFP expression (Figure 2). EGFP expression is not affected by either the nonsense Au-nanobeacon or nonsense oligonucleotide indicating that the knockdown is sequence specific. Interestingly, EGFP-targeting using the naked antisense oligonucleotide delivered with or without Lipofectamine did not result in EGFP silencing (Figure 2A). Confocal fluorescence imaging allowed for intracellular localisation pattern of the antisense Au-nanobeacons and direct evaluation of EGFP silencing associated with an increased Au-nanobeacon fluorescence that can be used to assess the silencing effect (Figure 3A). It should be emphasised that Au-nanobeacons require no transfection agent to enter cells. These results show that effective and specific gene silencing can be attained by

means of the proposed antisense Au-nanobeacons. The specificity and level of silencing can be directly correlated to the nanobeacon's fluorescence emission, which demonstrates the possibility of using this nanovectorisation approach as a nanotheranostics tool.

The future use of this system for *in vivo* models, and for clinical applications, clearly depends on the evaluation of its effects in the living system, i.e. toxicity evaluation. Therefore, we characterised the effects in terms of cell viability and metabolic stress, DNA damage (genotoxicity) and profiled the proteome response to the developed gene-silencing vehicle. In the present study HCT-116 was used as model but one should be aware that differences between cell lines do exist and that toxicity may depend on cell types. Moreover, toxicity may be a function of transfection efficiency, which would show a significant cell type-to-cell type variation, and therefore extrapolation to other systems is not straightforward. No cell viability changes and no major changes in GST activity were detected up to 48 h incubation, suggesting that no oxidative status changes occur within the cell following nanobeacon internalisation. These results are supported by the evidence that GST is inducible and its expression is directly modulated by the presence of oxidative radicals that inactivate the Keap repressor, which in turn releases the Nrf2 transcription factor of GST and other antioxidant enzymes (Kobayashi & Yamamoto 2005). The Au-nanobeacon approach may not elicit extensive oxidative damage, contrarily to what has been previously reported on internalisation of AuNPs and subsequent intracellular GSH depletion, promoting oxidative stress in HL7702 cells and lung fibroblasts (Li et al. 2010; Gao et al. 2011). The low oxidative stress induced by our approach, and hence low DNA damage, is in agreement with the genotoxicity assessment, in particular by the comet assay (see below).

In what comet assay is concerned, cells treated with antisense (39.66 ± 3.84%) and nonsense (32.28 ± 5.13%) Au-nanobeacons presented no significant differences to that of controls ($p < 0.05$). The uniform nucleoid distribution per class occurring amongst these samples (Figure 5B) has been previously reported in cultured cell lines not subjected to DNA-damage-inducing agents (Costa et al. 2012). These data show that the proposed antisense Au-nanobeacon strategy for gene silencing does not appear to significantly exhibit genotoxicity, which is in accordance with the expected reduced formation of oxidative radicals, generally regarded as a major cause of direct DNA strand breakage. Regarding samples treated with Lipofectamine (alone, and with both nonsense and antisense oligonucleotides), despite the verified differences in % of DNA in tail and class distribution (Figure 5B), Lipofectamine alone does not differ significantly from the control experiment. It has been previously shown that these cationic liposome-mediated transfection systems present toxic effects at concentrations higher than those used in this study and that liposome:DNA ratio modulates physicochemical properties of this complex and cytotoxic consequences upon its internalisation (Sakurai et al. 2000). Comparing antisense with nonsense oligonucleotide treatments (Figure 5C), no significant differences were found between Au-nanobeacons or Lipofectamine use for internalisation. DNA tail percentages above 80%, indicating extensive DNA damage and necrotic, apoptotic or nearly apoptotic cells (Choucroun et al. 2001; Hao et al. 2010), have not been observed with our approach, suggesting that, despite the observed variations, no severe genotoxic consequences arise from Au-nanobeacon internalisation. The rather elevated DNA % in tail value observed for cells expressing EGFP (46.58 ± 10.36%) might be associated with high mitotic activity of this cell line or to EGFP expression as previously reported (Liu et al. 1999; Chalfie & Kain 2006).

NAs usually arise due to errors during mitosis, essentially consisting of chromosomal aberrations deriving from incorrect segregation, and may translate into different observable abnormalities, such as micronuclei (Fenech et al. 2003). Our data showed no significant differences ($p < 0.05$) between control cells (expressing EGFP, and treated with AuNP@PEG) and cells transfected with either antisense or nonsense Au-nanobeacons. Thus far, such comprehensive evaluation of potential cyto- and/or genotoxic effects to the cell derived from AuNP-based vectorisation of gene-silencing strategies has never been presented. Here, effective gene regulation is attained without significant biological consequences, i.e. no decrease in cell viability, no perceptible oxidative stress and no increase of NA frequency and DNA strand breaks support the idea that the presented methodology bears no critical genotoxic or mutagenic consequences to the cell.

Regarding the proteome profiling, the effect of Lipofectamine as a transfection vehicle versus AuNPs as vectors for gene silencing in HCT-116 cells was firstly evaluated. We highlight the over-expression of protein 40S ribosomal protein SA that is required for the assembly and/or stability of the 40S ribosomal subunit and also functions as a cell surface receptor for laminin, playing a role in cell adhesion to the basal membrane (Venticinque & Meruelo 2012). Moreover, 19 additional proteins with less than 2-fold over-expression were identified in the presence of Lipofectamine, most of them acting as molecular chaperones that assist protein folding. These results indicate that Lipofectamine and AuNPs may induce a slight alteration of protein biosynthesis and folding, and induce cytoskeletal remodelling. Nevertheless, no relevant cellular toxicity is observed, which is in clear agreement with the data from cell viability, absence of oxidative stress and the lack of DNA strand breaks and NAs (see previous sections). Tedesco and co-workers showed similar effects by exposing *Mytilus edulis* to approximately 15 nm AuNPs (same size of our AuNPs), which lead to a small decrease in the levels of thiol proteins that they attributed to light oxidation (Tedesco et al. 2010). However, in our proteomic study we were not able to observe the reduction of thiol-containing proteins (Figure 6A and Supplementary Table S1). Interestingly, these authors were also not able to find lipid peroxidation (as indicator of oxidative damage) or induction of thioredoxin reductase activity (Tedesco et al. 2010). Despite no differences in protein expression levels in EGFP-transfected colorectal cancer cell to those of cells treated with antisense or nonsense Au-nanobeacons, the antisense Au-nanobeacon caused a sevenfold over-expression of the 40S ribosomal protein SA

and the heat-shock protein 90-beta relative to the Nonsense Au-nanobeacon (Figure 6A, Supplementary Figure S4-D-E and Table S1). These over-expression values may result from an alteration of cell homeostasis related with EGFP production, as EGFP silencing by antisense Au-nanobeacon may trigger mechanisms of cellular stress response. In support of this idea, we can observe an increase in the expression levels of cellular chaperones, namely heat-shock proteins encoded by HSP90B, HSP71 and HSP7C genes, different T-complex subunits and calreticulin. Peptidyl-prolylcis-trans isomerase (a component of non-ligated steroid receptors heterocomplexes through interaction with heat-shock protein 90 that may play a role in the intracellular trafficking of heterooligomeric forms of steroid hormone receptors between cytoplasm and nuclear compartments) and peptide 35 (no protein identification) expression levels were reduced (1.5-fold) in the presence of antisense Au-nanobeacon relative to nonsense Au-nanobeacon and with similar expression levels in the other tested conditions (Figure 6A and B, Supplementary Figure S4-D-E and Table S1).

Conclusions

We developed a robust and versatile system with nanotheranostics potential capable of blocking specific gene expression via an antisense Au-nanobeacon. A significant attribute of these Au-nanobeacons is the ability to attain similar levels of inhibition of gene expression with lower amounts than those of free oligonucleotides. This extraordinary efficiency occurs probably due to the large payload capacity of the NPs. The nanobeacon conformation allows for detection of silencing events as it occurs inside cells; thus, our approach becomes simple, inexpensive and straightforward as adjustment to any specific target can be easily made.

Evaluating biocompatibility and safety issues of these nanomaterials is imperative towards its use for medical purposes. However, the vast majority of studies report only on the biocompatibility of nanomaterials through the study of cell viability. Here, we went one step further and provide for the first time an extensive toxicity study of NPs for gene therapy. Modulation of gene expression was successfully attained with 30 nM of antisense Au-nanobeacon, without decreased cell viability or induction of oxidative stress. Moreover, an assessment of genome-related toxicity revealed no significant DNA damage increase, as well as no potential mutagenic or clastogenic consequences to the cell. Proteomics appears to be a relevant approach for mechanistic studies of cellular responses to Au-nanobeacons. The proteome profiling, as presented here, represents a useful tool for systematic analysis of toxicity of nanoconjugates, not only at the molecular level but also for the discovery of biomarkers and pathways towards the understanding of the mechanisms of toxicity. It must be emphasised that such mechanistic studies must be ultimately verified on relevant *in vivo* models. Identification of response pathways to AuNP internalisation may assist in gathering relevant information on acute toxicity so as to optimise systems for translation to *in vivo* models, and eventually to clinical applications.

Acknowledgements

This work was funded by Fundação para a Ciência e Tecnologia, Ministry of Science and Education (FCT/MEC): CIGMH (PEst-OE/SAU/UI0009/2011); REQUIMTE (PEst-C/EQB/LA0006/2011); PTDC/QUI-QUI/112597/2009; PTDC/CTM-NAN/109877/2009; PTDC/BBB-NAN/1812/2012; J.C. for SFRH/BD/62957/2009; ML for SFRH/BD/64026/2009; PC for SFRH/BPD/72564/2010; LRR for SFRH/BD/70202/2010. Additional funding was from the Nanotruck-Action from NanoSciEra^{+}.

Declaration of interest

The authors declare that they have no competing interests.

References

Akhtar S, Benter IF. 2007. Nonviral delivery of synthetic siRNAs in vivo. J Clin Invest 117:3623–3632.

Alkilany AM, Murphy CJ. 2010. Toxicity and cellular uptake of gold nanoparticles: what we have learned so far? J Nanopart Res 12:2313–2333.

Chalfie M, Kain SR. 2006. Green fluorescent protein: properties, applications and protocols. New Jersey, USA: Wiley and Sons, Inc.

Choucroun P, Gillet D, Dorange G, Sawicki B, Dewitte JD. 2001. Comet assay and early apoptosis. Mutat Res 478:89–96.

Conde J, Ambrosone A, Sanz V, Hernandez Y, Marchesano V, Tian F, et al. 2012a. Design of multifunctional gold nanoparticles for in vitro and in vivo gene silencing. ACS Nano 6:8316–8324.

Conde J, de la Fuente JM, Baptista PV. 2010. In vitro transcription and translation inhibition via DNA functionalized gold nanoparticles. Nanotechnology 21:505101.

Conde J, Doria G, Baptista P. 2012b. Noble metal nanoparticles applications in cancer. J Drug Deliv 2012:751075.

Conde J, Rosa J, de la Fuente JM, Baptista PV. 2013. Gold-Nanobeacons for simultaneous gene specific silencing and intracellular tracking of the silencing events Biomaterials. 34:2516–2523.

Costa PM, Costa MH. 2007. Genotoxicity assessment in fish peripheral blood: a method for a more efficient analysis of micronuclei. J Fish Biol 71:148–151.

Costa PM, Lobo J, Caeiro S, Martins M, Ferreira AM, Caetano M, et al. 2008. Genotoxic damage in Soleasenegalensis exposed to sediments from the Sado Estuary (Portugal): effects of metallic and organic contaminants. Mutat Res 654:29–37.

Costa PM, Milhinhos A, Simões M, Marum L, Oliveira AM, Costa MH, et al. 2012. Determining DNA strand breakage from embryogenic cell cultures of a conifer species using the single-cell gel electrophoresis assay. Tree Genet Genomes 8:425–430.

Daniel MC, Astruc D. 2004. Gold nanoparticles: assembly, supramolecular chemistry, quantum-size-related properties, and applications toward biology, catalysis, and nanotechnology. Chem Rev 104:293–346.

Dobrovolskaia MA, McNeil SE. 2007. Immunological properties of engineered nanomaterials. Nat Nanotechnol 2:469–478.

Doria G, Conde J, Veigas B, Giestas L, Almeida C, Assunção M, et al. 2012. Noble metal nanoparticles for biosensing applications. Sensors (Basel) 12:1657–1687.

Fenech M, Chang WP, Kirsch-Volders M, Holland N, Bonassi S, Zeiger E. 2003. HUMN project: detailed description of the scoring criteria for the cytokinesis-block micronucleus assay using isolated human lymphocyte cultures. Mutat Res 534:65–75.

Gao W, Xu K, Ji L, Tang B. 2011. Effect of gold nanoparticles on glutathione depletion-induced hydrogen peroxide generation and apoptosis in HL7702 cells. Toxicol Lett 205:86–95.

Ghosh P, Han G, De M, Kim CK, Rotello VM. 2008a. Gold nanoparticles in delivery applications. Adv Drug Deliv Rev 60:1307–1315.

Ghosh PS, Kim CK, Han G, Forbes NS, Rotello VM. 2008b. Efficient gene delivery vectors by tuning the surface charge density of amino acid-functionalized gold nanoparticles. ACS Nano 2:2213–2218.

Giljohann DA, Seferos DS, Prigodich AE, Patel PC, Mirkin CA. 2009. Gene regulation with polyvalent siRNA-nanoparticle conjugates. J Am Chem Soc 131:2072–2073.

Habig WH, Pabst MJ, Jakoby WB. 1974. Glutathione S-transferases. The first enzymatic step in mercapturic acid formation. J Biol Chem 249:7130–7139.
Haglund E, Seale-Goldsmith MM, Leary JF. 2009. Design of multifunctional nanomedical systems. Ann Biomed Eng 37:2048–2063.
Hao H, Lei F, Nancai Y, Wen S, Xiaojuan Q. 2010. The single-cell gel electrophoresis assay to determine apoptosis induced by siRNA in Colo 320 cells. Afr J Biotechnol 8:3731–3733.
Jain KK. 2008. Nanomedicine: application of nanobiotechnology in medical practice. Med Princ Pract 17:89–101.
Kim SS, Garg H, Joshi A, Manjunath N. 2009. Strategies for targeted nonviral delivery of siRNAs in vivo. Trends Mol Med 15:491–500.
Kobayashi M, Yamamoto M. 2005. Molecular mechanisms activating the Nrf2–Keap1 pathway of antioxidant gene regulation. Antioxid Redox Signal 7:385–394.
Lee PC, Meisel D. 1982. Adsorption and surface-enhanced Raman of dyes on silver and gold sols. J Phys Chem 86:3391–3395.
Li JJ, Hartono D, Ong CN, Bay BH, Yung LY. 2010. Autophagy and oxidative stress associated with gold nanoparticles. Biomaterials 31:5996–6003.
Liu HS, Jan MS, Chou CK, Chen PH, Ke NJ. 1999. Is green fluorescent protein toxic to the living cells? Biochem. Biophys Res Commun 260:712–717.
Liu Y, Shipton MK, Ryan J, Kaufman ED, Franzen S, Feldheim DL. 2007. Synthesis, stability, and cellular internalization of gold nanoparticles containing mixed peptide-poly(ethylene glycol) monolayers. Anal Chem 79:2221–2229.
Livak KJ, Schmittgen TD. 2001. Analysis of relative gene expression data using real-time quantitative PCR and the 2(-Delta DeltaC(T)) method. Methods 25:402–408.
McIntosh CM, Esposito EA, III Boal AK, Simard JM, Martin CT, Rotello VM. 2001. Inhibition of DNA transcription using cationic mixed monolayer protected gold clusters. J Am Chem Soc 123:7626–7629.
Ozpolat B, Sood AK, Lopez-Berestein G. 2010. Nanomedicine based approaches for the delivery of siRNA in cancer. J Intern Med 267:44–53.
Pfaffl MW. 2001. A new mathematical model for relative quantification in real-time RT-PCR. Nucleic Acids Res 29:e45.
Rana S, Bajaj A, Mout R, Rotello VM. 2012. Monolayer coated gold nanoparticles for delivery applications. Adv Drug Deliv Rev 64:200–216.
Rosa J, Conde J, de la Fuente JM, Lima JC, Baptista PV. 2012. Gold-nanobeacons for real-time monitoring of RNA synthesis. Biosens Bioelectron 36:161–167.
Rosi NL, Giljohann DA, Thaxton CS, Lytton-Jean AK, Han MS, Mirkin CA. 2006. Oligonucleotide-modified gold nanoparticles for intracellular gene regulation. Science 312:1027–1030.
Sakurai F, Inoue R, Nishino Y, Okuda A, Matsumoto O, Taga T, et al. 2000. Effect of DNA/liposome mixing ratio on the physicochemical characteristics, cellular uptake and intracellular trafficking of plasmid DNA/cationic liposome complexes and subsequent gene expression. J Control Release 66:255–269.
Sanz V, Conde J, Hernandez Y, Baptista PV, Ibarra MR, de la Fuente JM. 2012. Effect of PEG biofunctional spacers and TAT peptide on dsRNA loading on gold nanoparticles. J Nanopart Res 14:1–9.
Singh NP, McCoy MT, Tice RR, Schneider EL. 1988. A simple technique for quantitation of low levels of DNA damage in individual cells. Exp Cell Res 175:184–191.
Tedesco S, Doyle H, Blasco J, Redmond G, Sheehan D. 2010. Exposure of the blue mussel, Mytilus edulis, to gold nanoparticles and the pro-oxidant menadione. Comp Biochem Physiol C Toxicol Pharmacol 151:167–174.
Teixeira MC, Santos PM, Fernandes AR, Sá-Correia I. 2005. A proteome analysis of the yeast response to the herbicide 2,4-dichlorophenoxyacetic acid. Proteomics 5:1889–1901.
Thomas M, Klibanov AM. 2003. Conjugation to gold nanoparticles enhances polyethylenimine's transfer of plasmid DNA into mammalian cells. Proc Natl Acad Sci USA 100:9138–9143.
van MJ, Kaspers GJ, Cloos J. 2011. Cell sensitivity assays: the MTT assay. Methods Mol Biol 731:237–245.
Venticinque L, Meruelo D. 2012. Comprehensive proteomic analysis of nonintegrin laminin receptor interacting proteins. J Proteome Res 11:4863–4872.
Wall NR, Shi Y. 2003. Small RNA: can RNA interference be exploited for therapy? Lancet 362:1401–1403.
Whitehead KA, Langer R, Anderson DG. 2009. Knocking down barriers: advances in siRNA delivery. Nat Rev Drug Discov 8:129–138.
Zhang XD, Wu D, Shen X, Liu PX, Yang N, Zhao B, et al. 2011. Size-dependent in vivo toxicity of PEG-coated gold nanoparticles. Int J Nanomedicine 6:2071–2081.

Supplementary materials available online

Supplementary Table S1
Supplementary Figures S1–S4

Supplementary Information

Gold-Nanobeacons for gene therapy: evaluation of genotoxicity, cell toxicity and proteome profiling analysis

João Conde[1,2], Miguel Larguinho[1,3], Ana Cordeiro[1,4], Luís R. Raposo[5,6], Pedro M. Costa[7], Susana Santos[5,6], Mário S. Diniz[4], Alexandra R. Fernandes[5,6,8], Pedro V. Baptista[1,*]

[1]CIGMH, Departamento de Ciências da Vida, Faculdade de Ciências e Tecnologia, Universidade Nova de Lisboa, Caparica, Portugal.

[2]Instituto de Nanociencia de Aragón, Universidad de Zaragoza, Zaragoza, Spain.

[3]BioScope Group, Facultade de Ciencias de Ourense, Universidade de Vigo, Spain.

[4]REQUIMTE, Departamento de Química, Faculdade de Ciências e Tecnologia, Universidade Nova de Lisboa, Caparica, Portugal.

[5]Centro de Química Estrutural, Instituto Superior Técnico, Lisboa, Portugal.

[6]CB3, Faculdade de Engenharia e Ciências Naturais, Universidade Lusófona de Humanidades e Tecnologias, Lisboa, Portugal.

[7]IMAR-Instituto do Mar, Departamento de Ciências e Engenharia do Ambiente, Faculdade de Ciências e Tecnologia, Universidade Nova de Lisboa, Caparica, Portugal.

[8]Departamento de Ciências da Vida, Faculdade de Ciências e Tecnologia, Universidade Nova de Lisboa, Caparica, Portugal.

* Corresponding author

1. Physical characterization of Au-nanobeacons

Gold nanoparticles (AuNPs) were synthesized by the citrate reduction method described by Lee and Meisel (Lee, 1982).Briefly, 225 mL of 1 mM hydrogen tetrachloroaureate (III) hydrate (Sigma) (88.61 mg) was solved in 500 ml of distilled water and heated and stirred under reflux. When the solution boils, 25 mL of 38.8 mM sodium citrate dihydrate (285 mg) was added resulting in a red solution. The solution is kept under ebullition with vigorous stirring and protected from light for 30 minutes. Then, the solution is cooled down and kept protected from light. Citrate capped AuNPs were characterized by Transmission Electron Microscopy (TEM) and UV-Vis spectroscopy.

Functionalization of PEGylated AuNPs was carried out using commercial hetero-functional poly(ethylene glycol) (PEG) functionalized with a thiol group O-(2-Mercaptoethyl)-O'-methyl-hexa(ethylene glycol), $C_{15}H_{32}O_7S$, 356.48 Da (Sigma) as previously described (Rosa, 2012; Conde, 2013; Sanz, 2012).Briefly, 10 nM of the AuNPs were mixed with 0.003 mg/mL of O-(2-Mercaptoethyl)-O'-methyl-hexa(ethylene glycol) in an aqueous solution of SDS (0.028%). Then, NaOH was added to a final concentration of 25 mM and the mixture incubated for 16 hours at room temperature. Excess PEG was removed by centrifugation (21.460 ×g, 30 min, 4ºC), and quantified by the Ellman's Assay suitable for sulfhydryl group determination. Briefly, 0.05 mg/mL of 5,5'-dithio-bis-(2-nitrobenzoic acid) (DTNB) (Sigma), reacts with sulfhydryl under slightly alkaline conditions (0.5 M phosphate buffer, pH 7-8), to release 5-thio-2-nitrobenzoic acid (TNB) a highly chromogenic compound (412 nm), after 15 min at room temperature. The excess of O-(2-Mercaptoethyl)-O'-methyl-hexa(ethylene glycol) was determined following interpolation in a standard curve ($Abs_{412nm} = 26.034 \times [PEG, mg/mL] + 0.0627$).

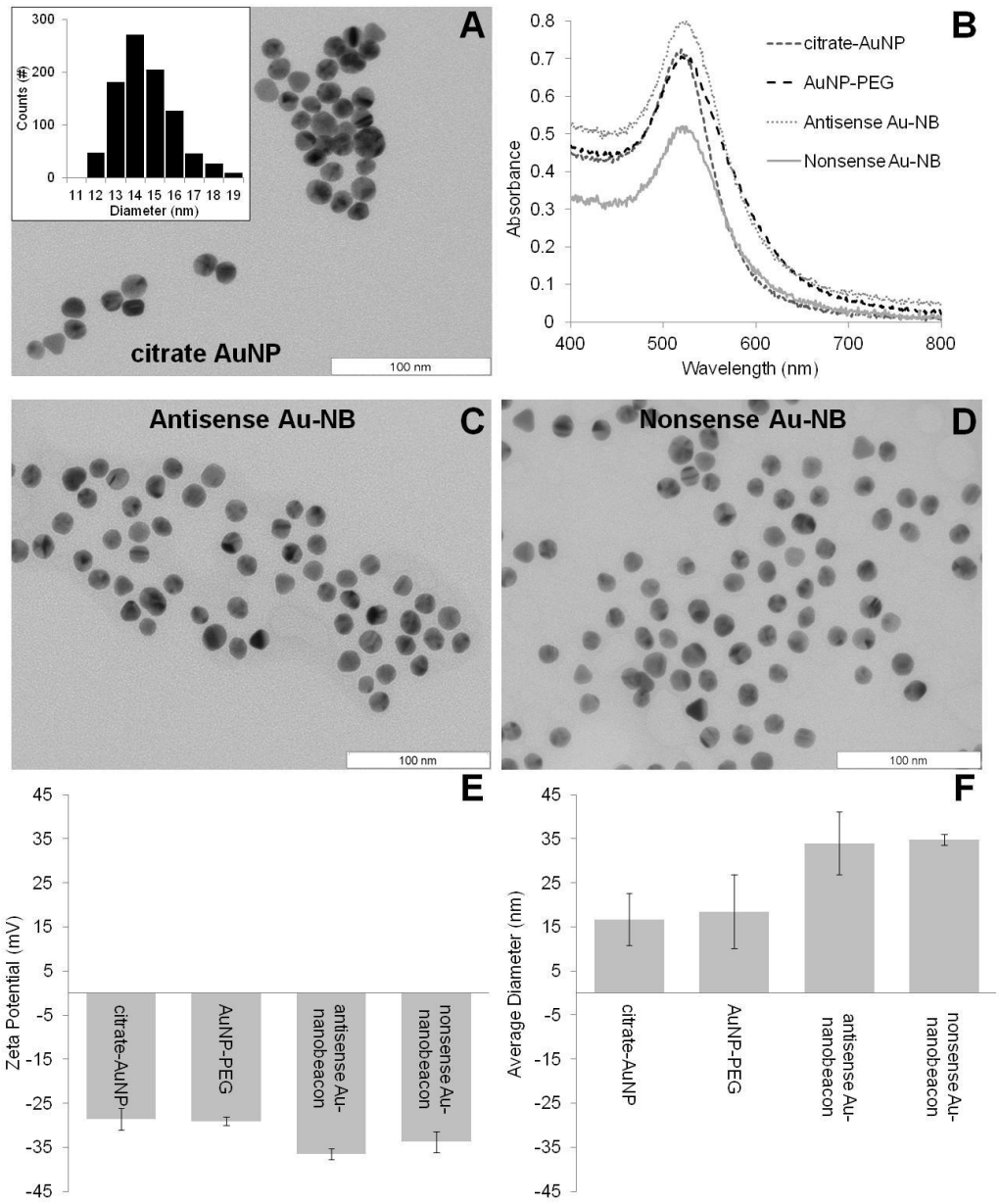

Figure S1. Physical characterisation of Au-nanobeacons. (A) Transmission Electron Microscopy (TEM) of citrate-AuNPs, Inset: size distribution histogram showing an average diameter of 14.6±1.7 nm. (**B**) UV/Vis Spectroscopy of citrate AuNPs and of Au-nanobeacons.TEM images for antisense (**C**) and nonsense (**D**) Au-nanobeacons. (**E**) Surface charge measurements by Zeta Potential. (**F**) Dynamic Light Scattering (DLS) showing average diameter of AuNPs conjugates.

2. EGFP vector transfection in HCT-116 cells

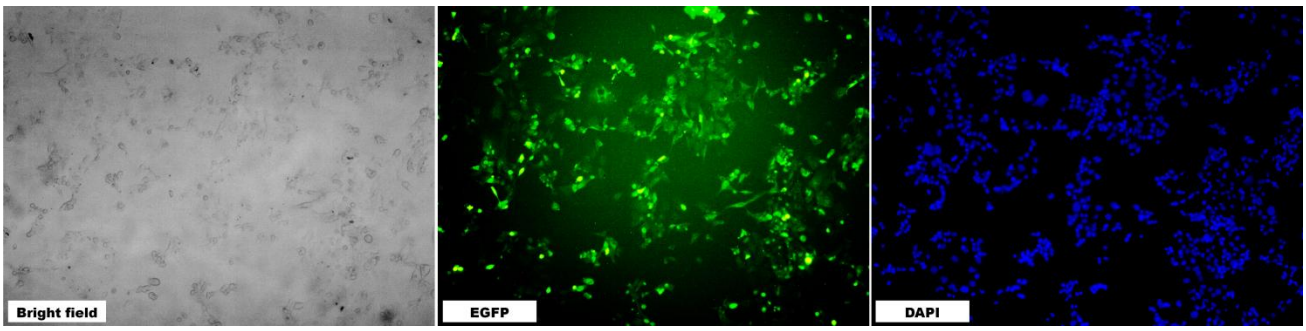

Figure S2.Representative images of HCT-116 cells 24 h after transfection with EGFP vector. From left to right: bright fieldmicroscopy images, green fluorescence channels corresponding to EGFP fluorescence, and nucleus stained with DAPI.

3. Comet class and nuclear abnormality frequency

A

			Au-nanobeacons			oligonucleotide	
	AuNP@PEG	PBS	antisense	nonsense	PBS + Lipo	antisense	nonsense
Class 0	0.17 ± 0.21	0.16 ± 0.19	0.25 ± 0.10	0.33 ± 0.08	0.13 ± 0.05	0.54 ± 0.16	0.49 ± 0.17
Class 1	0.22 ± 0.03	0.25 ± 0.09	0.30 ± 0.07	0.37 ± 0.13	0.32 ± 0.00	0.30 ± 0.23	0.29 ± 0.17
Class 2	0.30 ± 0.15	0.30 ± 0.13	0.25 ± 0.06	0.17 ± 0.09	0.25 ± 0.00	0.10 ± 0.02	0.13 ± 0.10
Class 3	0.21 ± 0.04	0.20 ± 0.07	0.13 ± 0.07	0.08 ± 0.04	0.22 ± 0.03	0.05 ± 0.05	0.07 ± 0.07
Class 4	0.10 ± 0.04	0.09 ± 0.06	0.08 ± 0.02	0.05 ± 0.03	0.09 ± 0.03	0.01 ± 0.02	0.01 ± 0.01

B

			Au-nanobeacons			oligonucleotide	
	AuNP@PEG	PBS	antisense	nonsense	PBS + Lipo	antisense	nonsense
N.A. Freq (%)	2.08 ± 0.64	2.60 ± 1.14	1.84 ± 0.69	1.93 ± 1.10	2.87 ± 0.63	3.23 ± 0.93	2.87 ± 1.22

Figure S3. Average frequencies for (**A**) scored comets per class, according to % of DNA in tail; (**B**) scored nuclear abnormalities, for each treatment.

4. Proteome evaluation – Two-dimensional gel electrophoresis

Protein samples (200 µg) were transferred onto strip holders along with 7 cm long IPG strips covering pH range from 3 to 10. Strips were positioned in the strip holders with gel side down, avoiding entrapment of bubbles underneath the strip. Strips were then covered with 3 mL DryStrip Cover Fluid (GE Healthcare) and the strip holders lidded. IEF was performed in five steps "step-n-hold" in the following order: 30 V for 720 minutes, 100 V for 30 minutes, 500 V for 30 minutes, 1000 V for 30 minutes and 5000 V for 60 minutes. After IEF, the strips were equilibrated 2×15 min with a mixture containing 75mM Tris-HCl (Sigma) (pH 8.8), 6 M urea, 2% SDS (Sigma), 30% glycerol (Merck) and traces of bromophenol blue. The buffer for the first equilibration step contained 1% DTT and the second 2.5% iodoacetamide (Sigma). The second dimension was performed in a mini-PROTEAN II electrophoresis Cell (Bio-Rad). IPG strips were placed on top of a 12% (w/v) acrylamide/bis-acrylamide (37.5:1) gel. The strips were sealed with an agarose solution of 0.5% (w/v) with traces of bromophenol blue and the electrophoresis was conducted at 50 V for 30 minutes until the proteins were incorporated in the polyacrylamide matrix, followed by 150 V for 90 minutes. Gels were soaked in a fixing solution (10% acetic acid; 30% ethanol) for at least 2 h, stained with hot Coomassie Brilliant Blue R350 (PhastGelTM Blue R, GE Healthcare) solution in 10% acetic acid for 30 min and washed overnight in 10% acetic acid. Gels were then dehydrated in a 2% glycerol, 35% ethanol solution and dried between two porous cellophane sheets for at least 48 h. All 2-DE gel images were digitalized (PIXMA M250, Canon) and analyzed with the Melanie 7.0Software (GeneBio). Each one of the conditions studied was evaluated in triplicate. The analysis was performed semi-automatically by the software, adhering to the following procedure: (1) spot detection; (2) spot matching from different gels; (3) background subtraction; and (4) assessment of the normalized intensity of each spot. Normalization was performed as the ratio of the spot intensity and the total intensity of the spots with a match in all gels in the experiment.

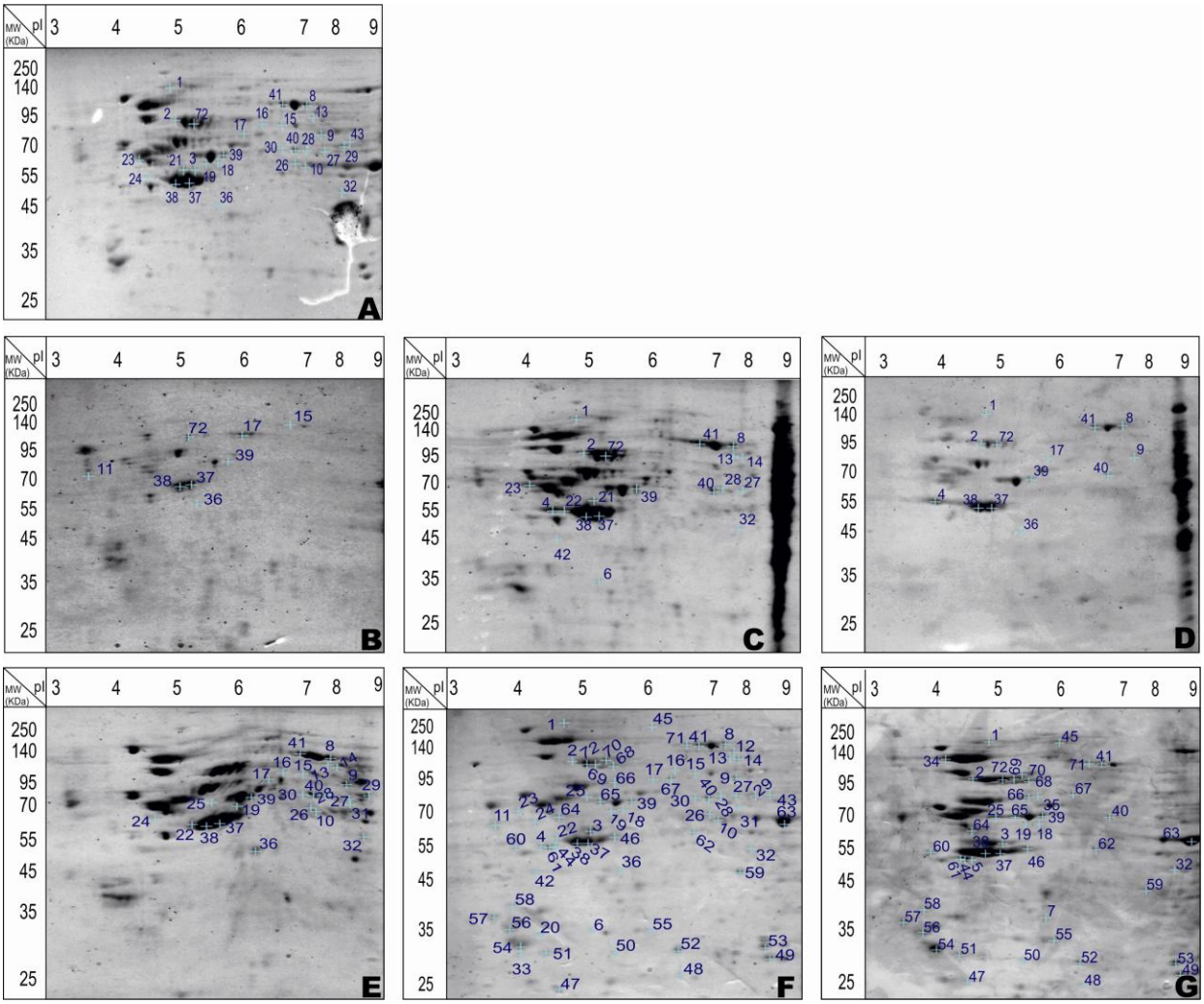

Figure S4. Two-dimensional gel electrophoresis of protein extracts for cells exposed to: (**A**) PBS, (**B**) PBS + Lipofectamine, (**C**) Antisense oligonucleotide, (**D**) Nonsense oligonucleotide, (**E**) AuNP@PEG, (**F**) Antisense Au-nanobeacon, (**G**) Nonsense Au-nanobeacon.

5. Proteome evaluation – MALDI-TOF Mass Spectrometry analysis

In-gel digestion and MALDI-TOF Mass Spectrometry analysis

Selected protein spots were manually excised from 2-DE gels and sent for Peptide Mass Fingerprinting analysis at Mass Spectrometry Laboratory in ITQB/IBET (Oeiras, Portugal). Briefly, excised gel spots were washed with MilliQ water and 50% acetonitrile (ACN) for Comassie dye removal and then dehydrated using 100% ACN. Reduction and alkylation steps followed by incubating the samples with agitation, first with 10 mM of DTT, 100 mM ammonium bicarbonate for 45 minutes at 56 °C followed by 55 mM of iodoacetamide, 100 mM ammonium bicarbonate for 30 minutes at room temperature in the dark. The spots were once more washed and dried with 100% ACN and vacuum centrifuged until completely dry. For in-gel digestion procedure the gel spots were rehydrated for 30 min on ice with digestion buffer (50 mM ammonium bicarbonate) and overnight digestion with 6.7 ng/µL of trypsin at 37 °C. Smaller protein digests were recovered from supernatant and larger protein digests were recovered by dehydration of the gels with 5% formic acid followed by 100% ACN and supernatant recovery. All samples were then completely dried under vacuum and stored at -20 °C. Sample preparation for mass spectrometry analysis was as follows: protein digests were resuspended in 5% formic acid, spotted onto the MALDI plate and covered with the same volume of matrix solution (α-cyano-4-hydroxycinnamic acid 10 mg/mL; 50% ACN, 5% form

Table 1.Protein identification via MALDI-TOF Mass Spectrometry analysis.

Spot ID	Protein Identification	Acession reference (HUMAN)	Protein Score (Mascot)	Isoelectric point	MW (KDa)	Description[a]
3	**Heat shock protein HSP 90-beta**	HS90B	259	4.97	83.212	Molecular chaperone that promotes the maturation, structural maintenance and proper regulation of specific target proteins involved for instance in cell cycle control and signal transduction. Undergoes a functional cycle that is linked to its ATPase activity. This cycle probably induces conformational changes in the client proteins, thereby causing their activation. Interacts dynamically with various co-chaperones that modulate its substrate recognition, ATPase cycle and chaperone function. Homodimer. Interacts with p53/TP53. Forms a complex with CDK6 and Hsp90/HSP90AB1. Interacts with UNC45A. Binding to UNC45A involves 2 UNC45A monomers per HSP90AB1 dimer. Interacts with CHORDC1 and DNAJC7. Interacts with FKBP4.
4	**Heat shock cognate 71 kDa protein**	HSP7C	807	5.37	70.8542	Acts as a repressor of transcriptional activation. Inhibits the transcriptional coactivator activity of CITED1 on Smad-mediated transcription.Chaperone. Component of the PRP19-CDC5L complex that forms an integral part of the spliceosome and is required for activating pre-mRNA splicing. May have a scaffolding role in the spliceosome assembly as it contacts all other components of the core complex. Identified in a mRNP granule complex, at least composed of ACTB, ACTN4, DHX9, ERG, HNRNPA1, HNRNPA2B1, HNRNPAB, HNRNPD, HNRNPL, HNRNPR, HNRNPU, HSPA1, HSPA8, IGF2BP1, ILF2, ILF3, NCBP1, NCL, PABPC1, PABPC4,

						PABPN1, RPLP0, RPS3, RPS3A, RPS4X, RPS8, RPS9, SYNCRIP, TROVE2, YBX1 and untranslated mRNAs. Interacts with PACRG. Interacts with HSPH1/HSP105. Interacts with IRAK1BP1 and BAG1. Interacts with DNAJC7. Interacts with CITED1 (via N-terminus); the interaction suppresses the association of CITED1 to p300/CBP and Smad-mediated transcription transactivation. Component of the PRP19-CDC5L splicing complex composed of a core complex comprising a homotetramer of PRPF19, CDC5L, PLRG1 and BCAS2, and at least three less stably associated proteins CTNNBL1, CWC15 and HSPA8. Interacts with SV40 VP1.
43	**Eukaryotic initiation factor 4A-I**	IF4A1	588	5.32	46.1246	ATP-dependent RNA helicase which is a subunit of the eIF4F complex involved in cap recognition and is required for mRNA binding to ribosome. In the current model of translation initiation, eIF4A unwinds RNA secondary structures in the 5'-UTR of mRNAs which is necessary to allow efficient binding of the small ribosomal subunit, and subsequent scanning for the initiator codon.
69	**Prohibitin**	PHB	629	5.57	29.7859	Prohibitin inhibits DNA synthesis. It has a role in regulating proliferation. As yet it is unclear if the protein or the mRNA exhibits this effect. May play a role in regulating mitochondrial respiration activity and in aging. Interacts with PHB2.
9	**Proteasome activator complex subunit 1**	PSME1	228	5.78	28.705	Implicated in immunoproteasome assembly and required for efficient antigen processing. The PA28 activator complex enhances the generation of class I binding peptides by altering the cleavage pattern of the proteasome.

19	**Ezrin**	EZRI	878	5.94	69.3697	Probably involved in connections of major cytoskeletal structures to the plasma membrane. In epithelial cells, required for the formation of microvilli and membrane ruffles on the apical pole. Along with PLEKHG6, required for normal macropinocytosis. Phosphorylated by tyrosine-protein kinases. Phosphorylation by ROCK2 suppresses the head-to-tail association of the N-terminal and C-terminal halves resulting in an opened conformation which is capable of actin and membrane-binding.
25	**T-complex protein 1 subunit zeta**	TCPZ	662	6.23	57.9876	Molecular chaperone; assists the folding of proteins upon ATP hydrolysis. Known to play a role, in vitro, in the folding of actin and tubulin.
33	**Proliferation-associated protein 2G4**	PA2G4	458	6.13	43.7592	May play a role in a ERBB3-regulated signal transduction pathway. Seems be involved in growth regulation. Acts a corepressor of the androgen receptor (AR) and is regulated by the ERBB3 ligand neuregulin-1/heregulin (HRG). Inhibits transcription of some E2F1-regulated promoters, probably by recruiting histone acetylase (HAT) activity. Binds RNA. Associates with 28S, 18S and 5.8S mature rRNAs, several rRNA precursors and probably U3 small nucleolar RNA. May be involved in regulation of intermediate and late steps of rRNA processing. May be involved in ribosome assembly. Mediates cap-independent translation of specific viral IRESs (internal ribosomal entry site). Interacts with the cytoplasmic domain of non-phosphorylated ERBB3; the interaction requires PKC activity. Interacts with AR. Treatment with HRG leads to dissociation from ERBB3 and increases association with AR. Interacts with NCL/nucleolin. Component of a

						ribonucleoprotein complex containing at least PA2G4, NCL, TOP1, PABPC2, RPLP0, acetylated histone H1 (HIST1H1A or H1F1), histone H1 2/4, RPL4, RPL8, RPL15, RPL18, RPL18A, RPL21, RPL11, RPL12, RPL28, RPL27, RPLP2 and RPL24. Interacts with HDAC2. Interacts with RB1; the interaction is enhanced upon PA2G4 dephosphorylation.
54	**Calumenin**	CALU	231	4.47	37.0835	Involved in regulation of vitamin K-dependent carboxylation of multiple N-terminal glutamate residues. Seems to inhibit gamma-carboxylase GGCX. Binds 7 calcium ions with a low affinity
22	**Moesin**	MOES	605	6.08	67.778	Probably involved in connections of major cytoskeletal structures to the plasma membrane. May inhibit herpes simplex virus 1 infection at an early stage. In resting T-cells, part of a PAG1-SLC9A3R1-MSN complex which is disrupted upon TCR activation. Binds SLC9A3R1. Interacts with PPP1R16B. Interacts with PDZD8. Interacts with SELPLG and SYK; mediates the activation of SYK by SELPLG.
24	**T-complex protein 1 subunit gamma**	TCPG	177	6.1	60.4953	Molecular chaperone; assists the folding of proteins upon ATP hydrolysis. As part of the BBS/CCT complex may play a role in the assembly of BBSome, a complex involved in ciliogenesis regulating transports vesicles to the cilia. Known to play a role, in vitro, in the folding of actin and tubulin.
23	**X-ray repair cross-complementing protein 6**	XRCC6	511	6.23	69.799	Single stranded DNA-dependent ATP-dependent helicase. Has a role in chromosome translocation. The DNA helicase II complex binds preferentially to fork-like ends of double-stranded DNA in a cell cycle-dependent manner. It works in the 3'-5' direction. Binding to DNA may be mediated by XRCC6. Involved in DNA non-homologous end joining (NHEJ) required for

						double-strand break repair and V(D)J recombination. The XRCC5/6 dimer acts as regulatory subunit of the DNA-dependent protein kinase complex DNA-PK by increasing the affinity of the catalytic subunit PRKDC to DNA by 100-fold. The XRCC5/6 dimer is probably involved in stabilizing broken DNA ends and bringing them together. The assembly of the DNA-PK complex to DNA ends is required for the NHEJ ligation step. Required for osteocalcin gene expression. Probably also acts as a 5'-deoxyribose-5-phosphate lyase (5'-dRP lyase), by catalysing the beta-elimination of the 5' deoxyribose-5-phosphate at an abasic site near double-strand breaks. 5'-dRP lyase activity allows to 'clean' the termini of abasic sites, a class of nucleotide damage commonly associated with strand breaks, before such broken ends can be joined. The XRCC5/6 dimer together with APEX1 acts as a negative regulator of transcription
17	**T-complex protein 1 subunit gamma**	TCPG	128	6.1	60.4953	Molecular chaperone; assists the folding of proteins upon ATP hydrolysis. As part of the BBS/CCT complex may play a role in the assembly of BBSome, a complex involved in ciliogenesis regulating transports vesicles to the cilia. Known to play a role, in vitro, in the folding of actin and tubulin.
16	**T-complex protein 1 subunit gamma**	TCPG	132	6.1		Molecular chaperone; assists the folding of proteins upon ATP hydrolysis. As part of the BBS/CCT complex may play a role in the assembly of BBSome, a complex involved in ciliogenesis regulating transports vesicles to the cilia. Known to play a role, in vitro, in the folding of actin and tubulin.
14	**T-complex**	TCPA	597	5.8	60.3056	Molecular chaperone; assists the folding of proteins upon ATP hydrolysis. As part of the

	protein 1 subunit alpha					BBS/CCT complex may play a role in the assembly of BBSome, a complex involved in ciliogenesis regulating transports vesicles to the cilia. Known to play a role, in vitro, in the folding of actin and tubulin.
37	**Cytochrome b-c1 complex subunit 1, mitochondrial**	QCR1	187	5.94	52.6124	This is a component of the ubiquinol-cytochrome c reductase complex (complex III or cytochrome b-c1 complex), which is part of the mitochondrial respiratory chain. This protein may mediate formation of the complex between cytochromes c and c1.
38	**RuvB-like 2**	RUVB2	571	5.49	51.1246	Possesses single-stranded DNA-stimulated ATPase and ATP-dependent DNA helicase (5' to 3') activity; hexamerisation is thought to be critical for ATP hydrolysis and adjacent subunits in the ring-like structure contribute to the ATPase activity. Component of the NuA4 histone acetyltransferase complex which is involved in transcriptional activation of select genes principally by acetylation of nucleosomal histones H4 and H2A. This modification may both alter nucleosome - DNA interactions and promote interaction of the modified histones with other proteins which positively regulate transcription. This complex may be required for the activation of transcriptional programs associated with oncogene and proto-oncogene mediated growth induction, tumour suppressor mediated growth arrest and replicative senescence, apoptosis, and DNA repair. The NuA4 complex ATPase and helicase activities seem to be, at least in part, contributed by the association of RUVBL1 and RUVBL2 with EP400. NuA4 may also play a direct role in DNA repair when recruited to sites of DNA damage. Proposed core component of

						the chromatin remodelling INO80 complex which is involved in transcriptional regulation, DNA replication and probably DNA repair.
61	**14-3-3 protein gamma**	1433G	310	4.8	28.2849	Adapter protein implicated in the regulation of a large spectrum of both general and specialised signalling pathways. Binds to a large number of partners, usually by recognition of a phosphoserine or phosphothreonine motif. Binding generally results in the modulation of the activity of the binding partner. Interacts with CDK16 and BSPRY. Interacts with WEE1 (C-terminal). Interacts with SAMSN1. Interacts with MLF1 (phosphorylated form); the interaction retains it in the cytoplasm. Interacts with Thr-phosphorylated ITGB2. Interacts with BCL2L11.Homodimer. Heterodimerizes with YWHAE. Homo- and hetero-dimerization is inhibited by phosphorylation on Ser-58. Interacts with FOXO4, NOXA1, SSH1 and ARHGEF2. Interacts with *Pseudomonas aeruginosa* exoS (unphosphorylated form). Interacts with BAX; the interaction occurs in the cytoplasm. Under stress conditions, MAPK8-mediated phosphorylation releases BAX to mitochondria. Interacts with phosphorylated RAF1; the interaction is inhibited when YWHAZ is phosphorylated on Thr-232. Interacts with TP53; the interaction enhances p53 transcriptional activity. The Ser-58 phosphorylated form inhibits this interaction and p53 transcriptional activity. Interacts with ABL1 (phosphorylated form); the interaction retains ABL1 in the cytoplasm. Interacts with PKA-phosphorylated AANAT; the interaction modulates AANAT enzymatic activity by increasing affinity for arylalkylamines and acetyl-CoA and protecting the enzyme from dephosphorylation and proteasomal degradation. It may also prevent

						thiol-dependent inactivation. Interacts with AKT1; the interaction phosphorylates YWHAZ and modulates dimerization. Interacts with GAB2 and TLK2.
50	**Actin, cytoplasmic 2**	ACTG	91	5.31	41.7658	Actins are highly conserved proteins that are involved in various types of cell motility and are ubiquitously expressed in all eukaryotic cells. Defects in ACTG1 are the cause of deafness autosomal dominant type 20 (DFNA20). DFNA20 is a form of sensorineural hearing loss. Sensorineural deafness results from damage to the neural receptors of the inner ear, the nerve pathways to the brain, or the area of the brain that receives sound information. DFNA20 is a form of sensorineural hearing loss. Sensorineural deafness results from damage to the neural receptors of the inner ear, the nerve pathways to the brain, or the area of the brain that receives sound information. Defects in ACTG1 are the cause of Baraitser-Winter syndrome type 2. A rare developmental disorder characterized by the combination of congenital ptosis, high-arched eyebrows, hypertelorism, ocular colobomata, and a brain malformation consisting of anterior-predominant lissencephaly. Other typical features include postnatal short stature and microcephaly, intellectual disability, seizures, and hearing loss.
51	**Secernin-1**	SCRN1	162	4.66	46.3525	Regulates exocytosis in mast cells. Increases both the extent of secretion and the sensitivity of mast cells to stimulation with calcium
52	**Ribonuclease inhibitor**	RINI	117	4.71	49.9411	Ribonuclease inhibitor which inhibits RNASE1, RNASE2 and ANG. May play a role in redox homeostasis.
41	**Peptidyl-**	FKBP4			51.7721	Immunophilin protein with PPIase and co-chaperone activities. Component of non-ligated steroid

	prolylcis-trans isomerase					receptors heterocomplexes through interaction with heat-shock protein 90 (HSP90). May play a role in the intracellular trafficking of heterooligomeric forms of steroid hormone receptors between cytoplasm and nuclear compartments. The isomerase activity controls neuronal growth cones via regulation of TRPC1 channel opening. Acts also as a regulator of microtubule dynamics by inhibiting MAPT/TAU ability to promote microtubule assembly.
10	**40S ribosomal protein SA**	RSSA	413	4.79	32.8334	Required for the assembly and/or stability of the 40S ribosomal subunit. Required for the processing of the 20S rRNA-precursor to mature 18S rRNA in a late step of the maturation of 40S ribosomal subunits. Also functions as a cell surface receptor for laminin. Plays a role in cell adhesion to the basement membrane and in the consequent activation of signalling transduction pathways. May play a role in cell fate determination and tissue morphogenesis. Acts as a PPP1R16B-dependent substrate of PPP1CA. Also acts as a receptor for several other ligands, including the pathogenic prion protein, viruses, and bacteria. This protein appears to have acquired a second function as a laminin receptor specifically in the vertebrate lineage. t is thought that in vertebrates 37/67 kDalaminin receptor acquired a dual function during evolution. It developed from the ribosomal protein SA, playing an essential role in the protein biosynthesis lacking any laminin binding activity, to a cell surface receptor with laminin binding activity.
32	**no id**	-	-	-	-	-
31	**T-complex protein 1**	TCPB	185	6.01	57.4521	Molecular chaperone; assists the folding of proteins upon ATP hydrolysis. As part of the BBS/CCT complex may play a role in the assembly of BBSome, a complex involved in

	subunit beta					ciliogenesis regulating transports vesicles to the cilia. Known to play a role, in vitro, in the folding of actin and tubulin
27	**no id**	-	-	-	-	-
15	**Cytosol aminopeptidase**	AMPL	350	8.03	56.1308	Presumably involved in the processing and regular turnover of intracellular proteins. Catalyzes the removal of unsubstituted N-terminal amino acids from various peptides.
35	**no id**	-	-	-	-	-
18	**T-complex protein 1 subunit beta**	TCPB	2080	6.01	57.4521	Molecular chaperone; assists the folding of proteins upon ATP hydrolysis. As part of the BBS/CCT complex may play a role in the assembly of BBSome, a complex involved in ciliogenesis regulating transports vesicles to the cilia. Known to play a role, in vitro, in the folding of actin and tubulin
20	**no id**	-	-	-	-	-
28	**Proteasome subunit alpha type-1**	PSA1	442	6.15	29.5369	The proteasome is a multicatalytic proteinase complex which is characterized by its ability to cleave peptides with Arg, Phe, Tyr, Leu, and Glu adjacent to the leaving group at neutral or slightly basic pH. The proteasome has an ATP-dependent proteolytic activity. Mediates the lipopolysaccharide-induced signal transduction in the macrophage proteasome. Might be involved in the anti-inflammatory response of macrophages during the interaction with C.albicans heat-inactivated cells.
11	**T-complex protein 1**	TCPQ	886	5.42	59.5825	Molecular chaperone; assists the folding of proteins upon ATP hydrolysis. As part of the BBS/CCT complex may play a role in the assembly of BBSome, a complex involved in

	subunit theta					ciliogenesis regulating transports vesicles to the cilia. Known to play a role, in vitro, in the folding of actin and tubulin.
6	**Glutamate dehydrogenase 1, mitochondrial**	DHE3	166	7.66	61.3592	May be involved in learning and memory reactions by increasing the turnover of the excitatory neurotransmitter glutamate. Defects in GLUD1 are the cause of familial hyperinsulinemichypoglycemia type 6 (HHF6) [MIM:606762]; also known as hyperinsulinism-hyperammonemia syndrome (HHS). Familial hyperinsulinemichypoglycemia [MIM:256450], also referred to as congenital hyperinsulinism, nesidioblastosis, or persistent hyperinsulinemichypoglycemia of infancy (PPHI), is the most common cause of persistent hypoglycemia in infancy and is due to defective negative feedback regulation of insulin secretion by low glucose levels. In HHF6 elevated oxidation rate of glutamate to alpha-ketoglutarate stimulates insulin secretion in the pancreatic beta cells, while they impair detoxification of ammonium in the liver.
30	**40S ribosomal protein SA**	RSSA	198	4.79	44.0791	Required for the assembly and/or stability of the 40S ribosomal subunit. Required for the processing of the 20S rRNA-precursor to mature 18S rRNA in a late step of the maturation of 40S ribosomal subunits. Also functions as a cell surface receptor for laminin. Plays a role in cell adhesion to the basement membrane and in the consequent activation of signalling transduction pathways. May play a role in cell fate determination and tissue morphogenesis. Acts as a PPP1R16B-dependent substrate of PPP1CA. Also acts as a receptor for several other ligands, including the pathogenic prion protein, viruses, and bacteria. This protein appears to have

						acquired a second function as a laminin receptor specifically in the vertebrate lineage. t is thought that in vertebrates 37/67 kDalaminin receptor acquired a dual function during evolution. It developed from the ribosomal protein SA, playing an essential role in the protein biosynthesis lacking any laminin binding activity, to a cell surface receptor with laminin binding activity.
45	**no id**	-	-	-	-	-
34	**Actin, cytoplasmic 2**	ACTG	819	5.31	41.7658	Actins are highly conserved proteins that are involved in various types of cell motility and are ubiquitously expressed in all eukaryotic cells. Defects in ACTG1 are the cause of deafness autosomal dominant type 20 (DFNA20). DFNA20 is a form of sensorineural hearing loss. Sensorineural deafness results from damage to the neural receptors of the inner ear, the nerve pathways to the brain, or the area of the brain that receives sound information. DFNA20 is a form of sensorineural hearing loss. Sensorineural deafness results from damage to the neural receptors of the inner ear, the nerve pathways to the brain, or the area of the brain that receives sound information. Defects in ACTG1 are the cause of Baraitser-Winter syndrome type 2. A rare developmental disorder characterized by the combination of congenital ptosis, high-arched eyebrows, hypertelorism, ocular colobomata, and a brain malformation consisting of anterior-predominant lissencephaly. Other typical features include postnatal short stature and microcephaly, intellectual disability, seizures, and hearing loss.
29	**T-complex protein 1**	TCPB	874	6.01	57.4521	Molecular chaperone; assists the folding of proteins upon ATP hydrolysis. As part of the BBS/CCT complex may play a role in the assembly of BBSome, a complex involved in

	subunit beta					ciliogenesis regulating transports vesicles to the cilia. Known to play a role, in vitro, in the folding of actin and tubulin
36	**Tubulin alpha-1B chain**	TBA1B	1170	4.94	50.1196	Tubulin is the major constituent of microtubules. It binds two moles of GTP, one at an exchangeable site on the beta chain and one at a non-exchangeable site on the alpha-chain. Undergoes a tyrosination/detyrosination cycle, the cyclic removal and re-addition of a C-terminal tyrosine residue by the enzymes tubulin tyrosine carboxypeptidase (TTCP) and tubulin tyrosine ligase (TTL), respectively.
40	**Endoplasmin**	ENPL	1330	4.76	92.4113	Molecular chaperone that functions in the processing and transport of secreted proteins. When associated with CNPY3, required for proper folding of Toll-like receptors. Functions in endoplasmic reticulum associated degradation (ERAD). Has ATPase activity.
12	**Alpha-enolase**	ENOA	386	7.01	47.1393	Multifunctional enzyme that, as well as its role in glycolysis, plays a part in various processes such as growth control, hypoxia tolerance and allergic responses. May also function in the intravascular and pericellularfibrinolytic system due to its ability to serve as a receptor and activator of plasminogen on the cell surface of several cell-types such as leukocytes and neurons. Stimulates immunoglobulin production. MBP1 binds to the myc promoter and acts as a transcriptional repressor. May be a tumour suppressor.
42	**Ezrin**	EZRI	1060	5.94	69.3697	Probably involved in connections of major cytoskeletal structures to the plasma membrane. In epithelial cells, required for the formation of microvilli and membrane ruffles on the apical pole. Along with PLEKHG6, required for normal macropinocytosis. Phosphorylated by tyrosine-

						protein kinases. Phosphorylation by ROCK2 suppresses the head-to-tail association of the N-terminal and C-terminal halves resulting in an opened conformation which is capable of actin and membrane-binding.
44	**L-lactate dehydrogenase B chain**	LDHB	443	5.71	36.6151	Responsible for the reaction (S)-lactate + NAD^+ = pyruvate + NADH.
53	**Adenine phosphoribosyltransferase**	APT	162	5.78	19.5954	Catalyses a salvage reaction resulting in the formation of AMPthat is energically less costly than de novo synthesis. Defects in APRT are the cause of adenine phosphoribosyltransferase deficiency (APRTD) [MIM:102600]; also known as 2,8-dihydroxyadenine urolithiasis. An enzymatic deficiency that can lead to urolithiasis and renal failure. Patients have 2,8-dihydroxyadenine (DHA) urinary stones.
55	**Translationally-controlled tumor protein**	TCTP	332	4.84	19.5826	Involved in calcium binding and microtubule stabilization. Found in several healthy and tumoral cells including erythrocytes, hepatocytes, macrophages, platelets, keratinocytes, erythroleukaemia cells, gliomas, melanomas, hepatoblastomas, and lymphomas. It cannot be detected in kidney and renal cell carcinoma (RCC). Expressed in placenta and prostate.
2	**Triosephosphateisomerase**	TPIS	152	5.65	30.7717	Catalytic activity D-glyceraldehyde 3-phosphate = glycerone phosphate.Defects in TPI1 are the cause of triosephosphateisomerase deficiency (TPI deficiency). TPI deficiency is an autosomal recessive disorder. It is the most severe clinical disorder of glycolysis. It is associated with neonatal jaundice, chronic haemolyticanaemia, progressive neuromuscular dysfunction,

						cardiomyopathy and increased susceptibility to infection.
59	**Rho GDP-dissociation inhibitor 1**	GDIR1	661	5.02	23.1927	Regulates the GDP/GTP exchange reaction of the Rho proteins by inhibiting the dissociation of GDP from them, and the subsequent binding of GTP to them. In glioma cells, inhibits cell migration and invasion by mediating the signals of SEMA5A and PLXNB3 that lead to inactivation of RAC1
68	**Heat shock protein beta-1**	HSPB1	579	5.98	22.7685	Involved in stress resistance and actin organization. Interacts with TGFB1I1. Associates with alpha- and beta-tubulin, microtubules and CRYAB. Interacts with HSPB8 and HSPBAP1
72	**Phosphoglycera temutase 1**	PGAM1	573	7.22	28.7858	Interconversion of 3- and 2-phosphoglycerate with 2,3-bisphosphoglycerate as the primer of the reaction. Can also catalyse the reaction of EC 5.4.2.4 (synthase) and EC 3.1.3.13(phosphatase), but with a reduced activity..
57	**14-3-3 protein zeta/delta**	1433Z	1030	4.73	27.7277	Adapter protein implicated in the regulation of a large spectrum of both general and specialised signalling pathways. Binds to a large number of partners, usually by recognition of a phosphoserine or phosphothreonine motif. Binding generally results in the modulation of the activity of the binding partner. Interacts with CDK16 and BSPRY. Interacts with WEE1 (C-terminal). Interacts with SAMSN1. Interacts with MLF1 (phosphorylated form); the interaction retains it in the cytoplasm. Interacts with Thr-phosphorylated ITGB2. Interacts with BCL2L11.Homodimer. Heterodimerises with YWHAE. Homo- and hetero-dimerization is inhibited by phosphorylation on Ser-58. Interacts with FOXO4, NOXA1, SSH1 and ARHGEF2. Interacts with *Pseudomonas aeruginosa* exoS (unphosphorylated form). Interacts with BAX; the

						interaction occurs in the cytoplasm. Under stress conditions, MAPK8-mediated phosphorylation releases BAX to mitochondria. Interacts with phosphorylated RAF1; the interaction is inhibited when YWHAZ is phosphorylated on Thr-232. Interacts with TP53; the interaction enhances p53 transcriptional activity. The Ser-58 phosphorylated form inhibits this interaction and p53 transcriptional activity. Interacts with ABL1 (phosphorylated form); the interaction retains ABL1 in the cytoplasm. Interacts with PKA-phosphorylated AANAT; the interaction modulates AANAT enzymatic activity by increasing affinity for arylalkylamines and acetyl-CoA and protecting the enzyme from dephosphorylation and proteasomal degradation. It may also prevent thiol-dependent inactivation. Interacts with AKT1; the interaction phosphorylates YWHAZ and modulates dimerization. Interacts with GAB2 and TLK2.
56	**14-3-3 protein zeta/delta**	1433Z	926	4.73	27.7277	Adapter protein implicated in the regulation of a large spectrum of both general and specialised signalling pathways. Binds to a large number of partners, usually by recognition of a phosphoserine or phosphothreonine motif. Binding generally results in the modulation of the activity of the binding partner. Interacts with CDK16 and BSPRY. Interacts with WEE1 (C-terminal). Interacts with SAMSN1. Interacts with MLF1 (phosphorylated form); the interaction retains it in the cytoplasm. Interacts with Thr-phosphorylated ITGB2. Interacts with BCL2L11.Homodimer. Heterodimerises with YWHAE. Homo- and hetero-dimerization is inhibited by phosphorylation on Ser-58. Interacts with FOXO4, NOXA1, SSH1 and ARHGEF2. Interacts with *Pseudomonas aeruginosa* exoS (unphosphorylated form). Interacts with BAX; the

						interaction occurs in the cytoplasm. Under stress conditions, MAPK8-mediated phosphorylation releases BAX to mitochondria. Interacts with phosphorylated RAF1; the interaction is inhibited when YWHAZ is phosphorylated on Thr-232. Interacts with TP53; the interaction enhances p53 transcriptional activity. The Ser-58 phosphorylated form inhibits this interaction and p53 transcriptional activity. Interacts with ABL1 (phosphorylated form); the interaction retains ABL1 in the cytoplasm. Interacts with PKA-phosphorylated AANAT; the interaction modulates AANAT enzymatic activity by increasing affinity for arylalkylamines and acetyl-CoA and protecting the enzyme from dephosphorylation and proteasomal degradation. It may also prevent thiol-dependent inactivation. Interacts with AKT1; the interaction phosphorylates YWHAZ and modulates dimerization. Interacts with GAB2 and TLK2.
1	**Proteasome activator complex subunit 1**	PSME1	295	5.78	28.705	Implicated in immunoproteasome assembly and required for efficient antigen processing. The PA28 activator complex enhances the generation of class I binding peptides by altering the cleavage pattern of the proteasome.
70	**Ran-specific GTPase-activating protein**	RANG	146	5.19	23.2956	Inhibits GTP exchange on Ran. Forms a Ran-GTP-RANBP1 trimeric complex. Increase GTP hydrolysis induced by the Ran GTPase activating protein RANGAP1. May act in an intracellular signalling pathway which may control the progression through the cell cycle by regulating the transport of protein and nucleic acids across the nuclear membrane.
63	**Proliferating**	PCNA	502	4.57	28.7503	Auxiliary protein of DNA polymerase delta and is involved in the control of eukaryotic DNA

	cell nuclear antigen					replication by increasing the polymerase's processibility during elongation of the leading strand. Induces a robust stimulatory effect on the 3'-5' exonuclease and 3'-phosphodiesterase, but not apurinic-apyrimidinic (AP) endonuclease, APEX2 activities. Has to be loaded onto DNA in order to be able to stimulate APEX2. Plays a key role in DNA damage response (DDR) by being conveniently positioned at the replication fork to coordinate DNA replication with DNA repair and DNA damage tolerance pathways. Acts as a loading platform to recruit DDR proteins that allow completion of DNA replication after DNA damage and promote postreplication repair: Monoubiquitinated PCNA leads to recruitment of translesion (TLS) polymerases, while 'Lys-63'-linked polyubiquitination of PCNA is involved in error-free pathway and employs recombination mechanisms to synthesize across the lesion.
58	**Annexin A3**	ANXA3	424	5.63	36.3527	Inhibitor of phospholipase A2, also possesses anti-coagulant properties. Also cleaves the cyclic bond of inositol 1,2-cyclic phosphate to form inositol 1-phosphate. A pair of annexin repeats may form one binding site for calcium and phospholipid.
60	**Small glutamine-rich tetratricopeptide repeat-containing protein alpha**	SGTA	66	4.81	44.0791	Co-chaperone that binds directly to HSC70 and HSP70 and regulates their ATPase activity.

13	**Elongation factor Tu, mitochondrial**	EFTU	317	7.26	49.5102	This protein promotes the GTP-dependent binding of aminoacyl-tRNA to the A-site of ribosomes during protein biosynthesis. Defects in TUFM are the cause of combined oxidative phosphorylation deficiency type 4 (COXPD4) [MIM:610678]. COXPD4 is characterized by neonatal lactic acidosis, rapidly progressive encephalopathy, severely decreased mitochondrial protein synthesis, and combined deficiency of mtDNA-related mitochondrial respiratory chain complexes.
62	**Actin, cytoplasmic 2**	ACTG	886	5.31	41.7658	Actins are highly conserved proteins that are involved in various types of cell motility and are ubiquitously expressed in all eukaryotic cells. Defects in ACTG1 are the cause of deafness autosomal dominant type 20 (DFNA20). DFNA20 is a form of sensorineural hearing loss. Sensorineural deafness results from damage to the neural receptors of the inner ear, the nerve pathways to the brain, or the area of the brain that receives sound information. DFNA20 is a form of sensorineural hearing loss. Sensorineural deafness results from damage to the neural receptors of the inner ear, the nerve pathways to the brain, or the area of the brain that receives sound information. efects in ACTG1 are the cause of Baraitser-Winter syndrome type 2. A rare developmental disorder characterized by the combination of congenital ptosis, high-arched eyebrows, hypertelorism, ocular colobomata, and a brain malformation consisting of anterior-predominant lissencephaly. Other typical features include postnatal short stature and microcephaly, intellectual disability, seizures, and hearing loss.
65	**Calreticulin**	CALR	477	4.29	48.1118	Calcium-binding chaperone that promotes folding, oligomeric assembly and quality control in the

						endoplasmic reticulum (ER) via the calreticulin/calnexin cycle. This lectin interacts transiently with almost all of the monoglucosylated glycoproteins that are synthesized in the ER. Interacts with the DNA-binding domain of NR3C1 and mediates its nuclear export. Involved in maternal gene expression regulation. May participate in oocyte maturation via the regulation of calcium homeostasis.
66	**Protein disulfide-isomerase A3**	PDIA3	557	5.98	56.7468	Catalyzes the rearrangement of -S-S- bonds in proteins. Subunit of the TAP complex, also known as the peptide loading complex (PLC). Can form disulphide-linked heterodimers with TAPBP. Interacts with ERP27 and CANX.
67	**Bifunctional purine biosynthesis protein PURH**	PUR9	247	6.27	64.5753	Bifunctional enzyme that catalyses 2 steps in purine biosynthesis
5	**Stress-induced-phosphoprotein 1**	STIP1	240	6.4	62.5994	Mediates the association of the molecular chaperones HSC70 and HSP90 (HSPCA and HSPCB).
7	**Stress-70 protein, mitochondrial**	GRP75	931	5.87	73.6348	Implicated in the control of cell proliferation and cellular aging. May also act as a chaperone. Interacts with FXN. Interacts with HSCB. Component of the MINOS/MitOS complex that includes IMMT, HSPA9 and CHCHD3 and associates with mitochondrial outer membrane proteins SAMM50, MTX1 and MTX2.

71	**Stress-70 protein, mitochondrial**	GRP75	876	5.87	73.6348	Implicated in the control of cell proliferation and cellular aging. May also act as a chaperone. Interacts with FXN. Interacts with HSCB. Component of the MINOS/MitOS complex that includes IMMT, HSPA9 and CHCHD3 and associates with mitochondrial outer membrane proteins SAMM50, MTX1 and MTX2.
73	**Ezrin**	EZRI	734	5.94	69.3697	Probably involved in connections of major cytoskeletal structures to the plasma membrane. In epithelial cells, required for the formation of microvilli and membrane ruffles on the apical pole. Along with PLEKHG6, required for normal macropinocytosis. Phosphorylated by tyrosine-protein kinases. Phosphorylation by ROCK2 suppresses the head-to-tail association of the N-terminal and C-terminal halves resulting in an opened conformation which is capable of actin and membrane-binding.
8	**Heat shock 70 kDa protein 1A/1B**	HSP71	1020	5.48	70.009	In cooperation with other chaperones, Hsp70s stabilize pre-existent proteins against aggregation and mediate the folding of newly translated polypeptides in the cytosol as well as within organelles. These chaperones participate in all these processes through their ability to recognize nonnative conformations of other proteins. They bind extended peptide segments with a net hydrophobic character exposed by polypeptides during translation and membrane translocation, or following stress-induced damage. In case of rotavirus A infection, serves as a post-attachment receptor for the virus to facilitate entry into the cell. Component of the CatSper complex. Identified in a mRNP granule complex, at least composed of ACTB, ACTN4, DHX9, ERG, HNRNPA1, HNRNPA2B1, HNRNPAB, HNRNPD, HNRNPL, HNRNPR, HNRNPU, HSPA1,

						HSPA8, IGF2BP1, ILF2, ILF3, NCBP1, NCL, PABPC1, PABPC4, PABPN1, RPLP0, RPS3, RPS3A, RPS4X, RPS8, RPS9, SYNCRIP, TROVE2, YBX1 and untranslated mRNAs. Interacts with TSC2. Interacts with IRAK1BP1. Interacts with TERT; the interaction occurs in the absence of the RNA component, TERC, and dissociates once the TERT complex has formed. Interacts with DNAJC7. Interacts with CHCHD3.
74	**Heat shock protein HSP 90-beta**	HS90B	1470	4.97	83.2121	Molecular chaperone that promotes the maturation, structural maintenance and proper regulation of specific target proteins involved for instance in cell cycle control and signal transduction. Undergoes a functional cycle that is linked to its ATPase activity. This cycle probably induces conformational changes in the client proteins, thereby causing their activation. Interacts dynamically with various co-chaperones that modulate its substrate recognition, ATPase cycle and chaperone function. Homodimer. Interacts with p53/TP53. Forms a complex with CDK6 and Hsp90/HSP90AB1. Interacts with UNC45A. Binding to UNC45A involves 2 UNC45A monomers per HSP90AB1 dimer. Interacts with CHORDC1 and DNAJC7. Interacts with FKBP4.

[a] **http://www.uniprot.org/**

❺

Final Conclusions

This Thesis gathered different points of view regarding the development of smart nanosystems to use in both diagnostics and therapy. Throughout this work, we diversified our objects of study from simple ssDNA-gold nanoparticles to complex and multifunctional gold nanoparticles functionalized with several types of biomolecules, which were tested in both *in vitro* and *in vivo* models.

All of this came together and allowed us to achieve the following:

i) Establishment of a detection and quantification method of the BCR-ABL gene fusion using thiol-modified ssDNA gold nanoparticles;

Here (**Article A**), we demonstrated the potential of an Au-nanoprobe based assay for the specific identification and quantification of aberrant expression of genes involved in cancer development. As far as we know, the potential for quantification of mRNA directly from total RNA extraction without retro-transcription or amplification was demonstrated here for the first time. The assay has a total work-up time of less than 45 minutes with comparable sensitivity settled to those demonstrated by traditional molecular biology methodologies. Our results show that the technique is quite robust for monitoring gene expression levels. This Au-nanoprobe strategy allows for detection of less than 100 $fmol.\mu l^{-1}$ of specific target, with the possibility of discriminating between a positive and negative sample from as little as 10 $ng.\mu l^{-1}$ of total RNA.

ii) Development of gold-silver alloy nanoparticles for multicolour Cancer diagnostics, by simultaneous identified several different mRNA targets using colour multiplexing;

Here (**Articles B** and **C**), we have demonstrated the functionalization of AuAg-alloy-NPs with ssDNA and the use of the resulting alloy nanoprobes for the specific detection of a target of interest. The attained AuAg-alloy-nanoprobes show a combination of the optical properties of Ag nanoparticles (high extinction coefficient) with the ease of functionalization via a thiol bond provided by the gold. Similarly to what is observed for Au-nanoprobes alone, these alloy nanoprobes are sensitive to variations in the quantity of target in solution and can, thus, be used for quantification assays. AuAg-alloy-nanoprobes with 25% gold and 75% silver were successfully synthesized and functionalized to produce nanoprobes that exhibit an SPR peak away from that of the Au-nanoprobes. This way, it is possible to better discriminate the

aggregation profiles of both types of nanoprobes once they are used in a one-pot assay. Based on the combination of AuAg-alloy- and Au-nanoprobes, it was possible to develop a differential gene expression assay using the *BCR-ABL* fusion product involved in chronic myeloid leukemia as a model. We further demonstrated that this dual-colour nanoparticle approach can be used as sensitive, selective, one-pot multicolour method for the simultaneous quantification of multiple RNA targets in a single reaction. The simultaneous differential quantification of two (or more) sequences is of utmost importance when performing genome based screening, where there is a mandatory need to assess whether a given transcript is present in a homo- or heterozygous form. This approach should be easily extendable to additional colours using the remarkable optical properties of nanoparticles of different sizes and compositions, i.e. different Au:Ag ratios, other metals may provide a multicolour homogenous system for application in array strategies and to rival fluorescence based assays.

iii) Clarify the role of ssDNA gold nanoparticles in *in vitro* Transcription and Translation Inhibition;

Here (**Article D**), we show that gold nanoparticles functionalized with promoter specific oligonucleotides strongly disrupts transcription even after extensive nuclease digestion, indicating the proficiency of these AuNP-DNA conjugates for application as gene silencing vectors. We also demonstrate that enhanced specific *in vitro* translation inhibition is achieved by means of the antisense oligonucleotides on AuNP surface. These AuNP-DNA conjugates seem to profit from the synergy between the specific sequence jamming and the steric hindrance provided by the AuNPs.

The described experimental setup can provide researchers with a simple yet robust means to assess the gene silencing potential of nanoparticle-DNA conjugates being developed for gene expression silencing purposes. These results show that a dual targeting approach for gene silencing could be explored - blocking transcription and translation, which can be achieved via combination of different oligonucleotide sequences on one or more nanoparticle vector.

Our experimental results show that we can create a two-way inhibition system using modified Au-nanoprobes to specifically block the *in vitro* transcription by binding the RNA polymerase promoter and the *in vitro* translation by suppressing the ribosome binding site.

Our results also demonstrate the greatly enhanced stability to nuclease attack of single stranded oligonucleotides functionalized at the surface of gold nanoparticles by the recovery

of DNA transcription. Surprisingly, the Au- nanoprobe show practically complete protection against nuclease-mediated degradation.

iv) Optimization and establishment of efficient methods to functionalized gold nanoparticles with several biomolecules like polymers, peptides/proteins and DNA/RNA;

v) Study the effect of polymer biofunctional spacers and peptides on dsRNA loading on gold nanoparticles;

In this work (**Article E**), an approach to bind specific biomolecules to the surface of AuNPs and study the effects in the combined functionalization was developed. The effect of thiolated PEG (PEG) spacers carrying different functional groups (carboxyl and azide) and the positively charged TAT peptide, functionalized by EDC reactions, on the dsRNA loading into the surface of AuNPs was studied. We demonstrated that there is a synergetic effect of the TAT peptide and the azide-containing PEG chain on the enhancement of the dsRNA loading into AuNPs. It was found that the loading of the oligonucleotide on the AuNP surface is controlled by the presence of ionic interactions between the negatively charged oligonucleotides and the positively charged molecules on the nanoparticles, such as the TAT peptide and the polarized azide group on one of the PEG chains. It was also demonstrated that weak interactions, e.g. hydrogen bounds, between PEG chains spacers and dsRNA enhance the loading of the dsRNA onto the AuNPs by steering its entry through the PEG layer.

vi) Demonstrate the implication in DNA Topology by histone-mimetic gold nanoparticles;

Here (**Article F**), we successfully report the use of gold nanoparticles functionalized with PEG-carboxylated and protamine to modify plasmid DNA topology. We demonstrated that AuNP@PEG@Protamine play an active role in controlling plasmid DNA structure, topology and levels of condensation and decondensation. Conversely to what occurs when using free protamine, AuNP@PEG@Prot may allow to control the levels of condensation and decondensation of DNA molecules in a stable and organized manner. By means of the theoretical equation, it is possible to exert control over the amount of each plasmid DNA conformation by constraining the initial conditions and the incubation time of AuNPs with plasmid DNA. Besides, although the functionalized AuNPs nanoparticles show an opposite

effect on DNA structure, plasmid DNA conformations could be selectively extracted to shift the equilibrium of the reaction towards the desired conformation.

We hypothesize that the effect of AuNP@PEG@Prot on plasmid DNA conformations probably mimics the interactions between AuNPs and DNA double helix in sperm chromatin. This hypothesis is supported by the fact that protamine proteins play an important role in condensation and stabilization of spermatic nuclear chromatin and that when combined with AuNPs of this particular size they may locate within the wide groove of DNA molecule, thus disturbing the structure of liquid crystals of DNA, changing its topology. Although plasmid DNA is different from genomic and sperm DNA, it can be used as a valuable model to study DNA topology. This study may constitute a good model study and to evaluate application of histone-mimetic gold nanoparticles – AuNP@PEG@Prot. If proven effective in cell models and on genomic DNA. Such a system may be considered for therapy and/or infertility procedures, for example in protamine-deficient sperm individuals. For this, further studies of *in vitro* experiments with intact nuclear membrane and nuclear core complexes, and with a relevant *in vivo* model of spermatogenesis will be needed to support this hypothesis.

vii) Design smart multifunctional gold nanoparticles for *in vitro* and *in vivo* gene silencing;

In this study (**Article G**), we show that two balanced formulations (ionic and covalent approaches), in terms of stability/electrostatic interactions, designed to produce smart multifunctional nanostructures succeeded to generate new innovative and versatile tools for efficient RNA interference in eukaryotic systems. Using three biological models of increasing complexity (cultured cells, *HeLa*; invertebrate, *Hydra*; and mammal, mice), both design and validation of multifunctional nanocarrier capable of selectively and specifically delivering siRNA *in vivo* were demonstrated. This functional screening approach allowed to finely tune concentrations, bonding and the combination of different chemical groups on the nanoparticle surface, addressing current ethical issues on unnecessary, cost-effective and time consuming vertebrate testing. These multifunctional nanocarriers are robust enough to preserve stability without showing acute toxicity or cell viability impairment, while simultaneously able to bypass biological barriers to perform RNAi activity without off-target effects. Our universal nanocarrier represents a valid gene delivery platform that can be exploited for clinical application in the near future.

viii) Development of a tumour targeting system using a nanoparticle-mediated therapeutic siRNA coupled to inflammatory response in lung cancer mouse models;

Here (**Article H**), we have developed a novel delivery systems that could achieve translocation of siRNA duplexes directly into the tumour cell cytoplasm and accomplish successful silencing of an oncogene expression. Our finding pave the way for new concepts, that gene therapy can offer to clinical cancer therapeutics. We successfully engineered fine-tuned RGD/siRNA-AuNPs capable to deliver siRNA into lung tumour cells and effectively to silence *c-Myc* proto-oncogene without side effects or toxicity. These novel AuNPs based carriers can both effectively enhance nanoparticle delivery efficiency and regulate gene expression in the context of RNA interference. Actually, RGD/siRNA-AuNPs can target preferentially and be taken up by tumour cells via integrin αvβ3-receptor-mediated endocytosis with no cytotoxicity, showing that can accumulate in tumour tissues overexpressing αvβ3 integrins and selectively delivered c-myc siRNA to suppress tumour growth and angiogenesis.

We propose that gene delivery based on selective expression of αvβ3 integrin in the tumour vasculature by using RGD/siRNA-AuNPs, might become applicable to lung cancer gene therapy. The work reported here, demonstrates the *in vivo* gene silencing and tumour regression by RGD/siRNA-AuNPs in two lung cancer mice models. This finding suggests that it is possible to use RGD/siRNA-AuNPs as a therapeutic agent for lung cancer and opens a new translational avenue to novel treatments of many diseases driven by deregulation of *c-Myc* gene expression.

ix) Propose an efficient nanotheranostic system – gold nanobeacons – for Real-Time Monitoring of RNA synthesis and for simultaneous gene specific silencing and intracellular tracking of the silencing events.

In this study (**Articles I, J, K**) we demonstrate the use of gold nanobeacons (Au-nanobeacons) capable of recognizing specific complementary sequences that can be easily synthesized by functionalization of gold nanoparticles with thiolated DNA hairpin oligonucleotides. Following Au-nanobeacons calibration, we used them to quantitatively monitor RNA synthesis in real-time and for kinetic quantification of RNA transcript synthesized by a RNA polymerase. We also demonstrate that by combining the use of a

reporter and an inhibitor Au-nanobeacon, we were able to create a dual colour system capable of quantify transcription and the level of inhibition in a single reaction vial. It is possible to quantify the level of inhibition of the RNA synthesis and relate it to the amount of template being effectively silenced, i.e. assessing actual silencing capability.

The proposed Au-nanobeacon biosensor allows for fast, accurate and sensitive RNA transcript expression profiling. A unique feature of this sensor, compared to conventional measurements of polymerase activities using intercalating dyes, is that the probes do not generate a signal from unrelated nucleic acids and polymerase activities can be distinguished from promoter-specific RNA polymerization. The simplicity and speed of the sensor are also great advantages.

Besides this, we also show that Au-nanobeacons are a new and versatile concept for genes specific silencing while simultaneously allowing for intra-cellular tracking of the silencing events. A significant attribute of these Au-nanobeacons is the ability to inhibit the endogenous and exogenous silencers with noticeably small amounts of effector molecule and without chemical co-transfectants. Our approach, combining a fluorescence nanobeacon with silencing capability is simple, inexpensive and straightforward as adjustment to any specific target, be it a specific mRNA or an endogenous or exogenous silencing nucleic acid, can be easily made. We demonstrate such potential by specifically silencing the expression of EGFP and overturning the knockdown effect of silencers after a first wave of silencing/delivery. Simultaneous studies of distinct cell populations should be feasible using multicolour labelling. Because the simple beacon-based scaffold of the Au-nanobeacons, our concept can be easily directed to any desired target without observable cytotoxicity, opening an important route towards tuned packaging and cargo delivery systems.

Finally, the possibility of silencing the silencers and of discriminating specific cells, where silencing is occurring, offers future prospects for studying and modulating cellular mechanisms involved in cancer. Combination of gold nanobeacons with other chemical functionalizations, e.g. targeting moieties, may enhance the therapeutic potential of our concept.

Moreover, an assessment of genome-related toxicity revealed no significant DNA damage increase, as well as no potential mutagenic or clastogenic consequences to the cell. Proteomics appears to be a relevant approach for mechanistic studies of cellular responses to Au-nanobeacons. The proteome profiling, as presented here, represents a useful tool for systematic analysis of toxicity of nanoconjugates, not only at the molecular level but also for the discovery of biomarkers and pathways towards the understanding of the mechanisms of

toxicity. It must be emphasised that such mechanistic studies must be ultimately verified on relevant *in vivo* models. Identification of response pathways to AuNP internalisation may assist in gathering relevant information on acute toxicity so as to optimise systems for translation to *in vivo* models, and eventually to clinical applications.

The studies presented here pave the way for novel approaches to better understand the mechanisms of interaction between multifunctional gold nanoparticles and targets (DNA/RNA), cells and tissues *in vitro* and *in vivo* biomedical applications.